THE UNIVERSITY OF READING
DEPARTMENT OF MATHEMATICS

Wave Scattering by Ice Sheets of Varying Thickness

Luke George Bennetts

Thesis submitted for the degree of
Doctor of Philosophy

March, 2007

Abstract

The problem of wave scattering by sea-ice of varying thickness and non-zero draught floating on water of finite depth is considered. To do so, the common idealisation of the ice as a thin-elastic plate, which is static in all but its flexural response, is adopted. Furthermore, the assumptions of linear and time harmonic motions are made.

The physical situation is initially formulated as a boundary-value problem but is subsequently reformulated as a variational principle. Here, the geometry is unconstrained and the ice covering may be either complete or partial. Additionally, the bed profile is permitted to undulate.

The solution method proceeds via application of the Rayleigh-Ritz method in conjunction with the variational principle. This restricts the vertical component of the velocity potential that represents the fluid motion to a finite-dimensional subspace and the stationary point of the variational principle over this finite space is sought. As the dimension of the subspace is increased, a sequence of approximations is generated, which can be made arbitrarily close to the full linear solution.

A judicious selection of the modes that span this subspace is given through a pointwise correspondence to the analogous problem in which the surrounding geometry is uniform. However, there are non-trivial issues related to this selection that require exploration.

Explicit solution methods are given for a number of specific geometries. Waves that are obliquely incident on two-dimensional geometries involving a finite interval of varying geometry, a finite ice floe, a semi-infinite ice sheet and an interval of periodic geometrical variations in an otherwise uniform ice sheet are all considered. A numerical formulation is also made for a three-dimensional axisymmetric floe. In all cases, comparisons are made to existing work before the scattering properties of geometries that fully exploit the generality of our solution method are investigated.

Acknowledgements

I owe a tremendous amount to the knowledge and ideas of my supervisors, Dr. Nick Biggs and Prof. David Porter. I would like to thank them for the time and effort that they have dedicated to helping me with my thesis. It has been a privilege to work with both of them.

I would also like to say how grateful I am for the constant support of my parents, Penny and David.

Finally, I wish to acknowledge the financial assistance given to me by the Department of Mathematics at the University of Reading.

Declaration

I confirm that this is my own work and the use of all material from other sources has been properly and fully acknowledged.

Contents

Chapter 1

Introduction

Beginning in earnest with Weitz & Keller in 1950, the mathematical study of the transfer of ocean wave energy into motion through a domain of ice-covered fluid has been an area of sustained research interest and much progress. Analysis of this problem can actually be traced back to a far earlier stage, with the work of Greenhill (1887) well-known.

However, the model adopted by Weitz & Keller, and other contemporaries such as Shapiro & Simpson (1953), was deficient in its view of the rôle of the ice covering as being that of an additional mass on the fluid surface. This 'mass-loading' model considered an area of ice-cover to be composed of a set of disconnected points and contained no information about its elastic response, which is now accepted as the leading component in the formation of motion in its presence (see Robin, 1963, and Squire, 1978).

At the present time, it is common practice to treat the ice as a 'thin-elastic plate', which forms a cohesive upper boundary of the fluid domain. Many authors cite the work of Evans & Davies (1968) as an early benchmark for the mathematical analysis of such a model. As with the majority of subsequent authors, Evans & Davies linearised the problem and considered it under time harmonic conditions.

Through the definition of a flexural rigidity, using a thin-elastic plate gives a more realistic view of the ice as having a horizontal structure. Such a description was conceived by the aforementioned Greenhill (1887), who was the first to consider the way that waves disperse in the presence of ice-cover.

Although a tremendous improvement on the mass-loading model, the use of an elastic plate still represents a substantial idealisation of the ice-cover. Notably, the plate has no vertical structure. That is, it is considered to be comprised of vertical strips that expand and contract without deformation. In contrast, a real sheet of ice will have a complicated vertical structure due to the differing states at its upper and lower surfaces that cause, for example, a temperature gradient to run through it (Fox & Squire, 1994). As an independent body with its own equations of motion, its hydrodynamic response will depend on this vertical structure. However, tests have indicated that its flexural response may be included by considering the properties in a vertically integrated fashion (Kerr & Palmer, 1972), which is consistent with its description as a thin plate.

The description 'thin' is a relative term that imposes some restrictions on the thickness of the plate in relation to the waves that pass through it. In particular, the plate must remain uniform under the deformation caused by its displacement. Essentially, this means that the strain imposed by the the passing wave cannot be too large. A complete theory of thin-elastic plates is outlined in Timoshenko & Woinowsky-Krieger (1959).

By using a thin plate to model the ice, it is possible to consider all of the motion within the plate in terms of the position of its lower surface, which is in contact with the fluid. Moreover, all of the stresses experienced by the ice may be calculated from knowledge of this interface. As we will discover in the following chapter, the problem presented by an elastic plate coupled to a fluid domain is formidable. In particular, the coupling at the interface between these two media requires a high-order boundary condition to be satisfied there.

There are also many properties of the ice which have no analogue in thin-elastic plate theory, such as dissipative effects, compressive stresses, rotational and shearing forces. These properties can and have been incorporated in more sophisticated idealisations of the ice, which allow for 'non-thin' ice for example. The dynamics of these plates, like the thin plate, may be entirely defined through the position of their lower surface. However, results calculated so far using these advanced models have provided no evidence to suggest that their inclusion is warranted in relation to the complexity they introduce (see Balmforth & Craster, 1999).

With the ice in the guise of an elastic plate, waves travel through the fluid-ice system in the form of flexural-gravity waves and are manifest as the transverse oscillations that appear at the horizontal interface between the two media. These waves are driven by the pressure disparity between the upper and lower surfaces of the ice sheet, which is generated by motion in the fluid-ice system. In our work we will consider this motion to be caused by ocean waves. A combination of gravity and the flexural rigidity of the plate is the counterbalance that attempts to restore the system towards its equilibrium state.

Like all other floating bodies, an ice sheet may respond to fluid motion with six degrees of freedom, namely heave, surge, sway, pitch, yaw and roll (Squire *et al.*, 1995). These are in addition to its ability to flex. For even the most simple geometry, to contemplate such a system would constitute a massive undertaking.

Fortunately, our wish is not to model the dynamics of large bodies of ice, such as the icebergs that calve from land masses, and for which the use of a thin plate would be inappropriate. Rather, we consider large expanses of ice whose spatial dimensions are such that their thickness is negligible in comparison to their width and breadth. Specifically, our interest is in these expanses as a source of scattering of wave energy. As we assume the horizontal dimensions of the ice that we focus on are vastly greater than its vertical dimensions, its displacement as an independent body is considered negligible in comparison with its ability to flex. Therefore, to investigate the way in which energy travels through an ice sheet, the scattering model we use assumes the ice to be static in all of its rigid-body motions and respond only with a transverse flexural displacement.

The type of ice sheets in which we are interested are formed, often on a seasonal basis, when the surface of the sea water freezes to produce a layer of ice covering. Such a phenomenon is prevalent in the polar and sub-polar seas. Any ice originating from freezing of sea water is termed 'sea-ice' and each contiguous frozen area is known as a 'floe'.

The structure of sea-ice is highly dependent on a number of factors. Primarily, the survival of sea-ice is dictated by the protection it receives from ocean waves, which if they are of sufficient strength may generate flexure that cracks, breaks, splits and even destroys weaker ice. The frequencies of the ocean waves that are incident on areas of sea-ice will vary from region to region. For example, Robin (1963) reports a normal wave spectrum of 4secs-24secs in the Weddell Sea in the Antarctic zone, although periods of as low as 2secs are recorded. In contrast, Hunkins (1962) reports that typically only waves of greater than 6sec periods penetrate the Arctic region. Fox (2001), on the other hand, who has contributed much to the work in the area of sea-ice, quotes the spectrum 2secs-20secs for typical sea-ice. We will use these figures only as a rough guide for our mathematical investigation.

In those situations in which the sea-ice receives protection from waves incident from the open ocean, say by the surrounding land mass near the coast or by other packs of ice, sea-ice may grow into sheets which extend for hundreds of kilometres (Squire, 2007). Smaller floes are then often created by the break-up of these larger expanses (Squire, 1984*b*). As it ages, sea-ice also becomes thicker, with ice that survives a single year typically 30cm-2m in thickness (WMO, 1970). Ice that survives for longer than a year, which is mainly a feature of the Arctic region, may develop to even greater thickness. Furthermore, non-thermodynamic processes, such as ridging, which will be discussed presently, can generate protrusions in the ice of thicknesses that far exceed those that could otherwise be created over time.

Despite the attenuation that occurs beneath sea-ice (Squire *et al.*, 1995), it is recognised that waves may propagate large distances into ice-covered waters in the form of flexural-gravity waves (Hunkins, 1962; Robin, 1963). It is also known that the wave energy that reaches the interior of an expanse of ice is of lower intensity and a higher pack period than that which exists at the edge (Squire *et al.*, 1995).

On encountering an ice-covered region from the open water, a wave is scattered by the ice edge, so that only a proportion of its energy transmits into the ice and part of it is reflected. During this scattering process a number of other motions, in addition to the transmitted wave and the reflected wave, are generated.

The stress that is induced within the ice by the scattering motion at an ice edge is regarded as the primary cause of fracture and subsequent break-up of the ice (Squire, 1984*a*). It is therefore of interest to construct a model which describes the hydroelastic process and will allow a theoretical insight into the fracturing phenomenon.

Once within an ice-covered region, the form of a travelling wave is highly dependent on the properties of the ice cover. As the properties of the ice change so do the waves. Additionally, irregularities or obstructions in the ice, the specifics of which will be discussed presently, provide extra sources of wave scattering, which further hinder the passage of a progressing wave.

In terms of the linear model, an ice edge, or any other source of scattering, produces a set of exponentially decaying 'evanescent' waves in its vicinity. Also, beneath the ice a pair of heavily damped progressing waves are generated. The dynamics of the ice edge itself are subject to two 'free-edge' conditions, which dictate that at this location the vertical shearing force and rotational bending moment it experiences both vanish.

Many different types and configurations of sea-ice have been observed and have their own scattering properties. The area of sea-ice in which we are interested in is termed the 'marginal ice zone' (MIZ). This description refers to "the parts of the ice cover which are close enough to the open ocean to be affected by its presence" (Wadhams, 1986). Two main divisions of the MIZ exist: those parts in which the ice is contiguous or in which the floes are close enough to act in unison, and areas in which a pack of smaller floes exist at a lower concentration so that the open water between them has an effect (Squire, 2007).

Near shorelines ice often forms a near-continuous covering and may extend over great distances. If these expanses are attached to the shore then they are described as 'shore-fast' sea-ice. Large expanses of ice may equally be found out to sea (Squire, 2007). Floes of a significant size may arise independently but are typically formed as a conglomeration of smaller floes and are hence very heterogeneous both in terms of their material properties and their geometrical structure (Chung & Fox, 2002). For example, the force of floes 'butting together' can form 'pressure ridges' where the ice bulges both at its upper surface but particularly at its lower surface. The former, a protrusion at the upper surface, is known as a 'sail', and the latter, a protrusion at the lower surface, which is in contact with the fluid, is known as a 'keel'. Pressure ridges have commonly been recorded at heights of around 10m (Vaughan & Squire, 2007).

Large floes also contain inhomogeneities in the form of cracks, which, as indicated earlier, form under the strain imposed by the flexing motion of the sheet. Under increasing pressure, these cracks extend to lengths up to many kilometres (WMO, 1970). Forced by currents and winds, cracks will separate to leave an area of clear water, which is loosely termed an ‘open lead’ (Squire, 2007). These leads may then quickly refreeze to produce an area of new ice within an expanse of thicker ice, a situation described as a ‘refrozen lead’. All of these features affect the passage of flexural-gravity waves through the fluid-ice system.

Rather than taking the form of a continuous sheet, ice-coverings are frequently composed of a number of individual ice floes. This often occurs at the edge of a larger floe, where the ice fractures into smaller parts, with the properties and dynamics of the ocean being the principle factor in determining the shape and alignment of the floes (Squire *et al.*, 1995). These packs of ice floes then serve as a barrier between the ocean waves and the inner ice. Scattering properties of such configurations depend not only on the response of the floes in isolation but also on the interaction of these responses.

The thin-elastic plate model has another important application, that of ‘pontoon-type very large floating structures’ (VLFSs). VLFSs are currently of high interest due to their use as a relatively cheap and environmentally friendly means of land reclamation. Examples of VLFSs already exist, particularly in Japan, where a proposal is in place for their use as an airport terminal and airstrip. The methods used by authors in the sea-ice and VLFSs areas are interchangeable in many aspects, although particular model geometries and parameters differ according to their application. In our work, for instance, we will concentrate on the rôle of geometrical variations in the vertical structure of the elastic plate, which are of a greater relevance to the case of sea-ice due to its inherent heterogeneity. However, the undulation of the sea-bed, which is only a secondary consideration in our work but is nevertheless a feature that is included in our model, is something that is of interest over the large horizontal scales of VLFSs (Wang & Meylan, 2002).

There exists a large catalogue of literature into the study of VLFSs, which is closely related to our research. In this field we note the work of Andrianov (2005), Andrianov & Hermans (2003, 2004), Belibassakis & Athanassoulis (2005), Hermans (2003*a*-*b*, 2004), Kaskiwagi (1998), Khabakhpasheva & Korobkin (2002), Sturova (2001), Takagi (2002), Takagi *et al.* (2000), Tkacheva (2001, 2004), and Wu *et al.* (1995) as being of particular relevance to the related study of sea-ice. A thorough appraisal of the work in the area of pontoon-type VLFSs may be found in the literature survey of Watanabe *et al.* (2003).

To date, the mathematical progress into the problem of ice covering has advanced to a stage at which numerical methods have been created for models that incorporate many of the sources of scattering, obstructions and heterogeneities discussed above, with differing degrees of generality. A number of the most relevant pieces of work in this area will now be discussed. Detailed reviews may be found in Squire *et al.* (1995) and the forthcoming article by Squire (2007).

Due mainly to the difficulty presented by the high-order condition imposed at the interface between the fluid and ice, many authors have chosen to investigate problems in which the geometry is piecewise uniform. These models consider regions or intervals of ice that are of constant thickness over a bed that is either flat or infinitely deep. Additionally, a zero draught, i.e. ice resting on the fluid surface, is often assumed to facilitate solution methods. Scattering is then caused by either the change from an ice-free state to an ice-covered state, or between states of ice-cover with differing properties, for example a change in thickness.

One example that has been repeatedly studied is the classic two-dimensional problem of ocean waves that are obliquely incident from a semi-infinite interval of ice-free fluid on a semi-infinite interval of ice-covered fluid, over a bed of finite depth. This may be considered a model of shore-fast sea-ice and was the problem that was studied by Evans & Davies (1968). These authors solved this problem via Fourier transforms and the Wiener-Hopf technique; unfortunately though, they deemed the complexity of the evaluation of certain integrals required in the solution procedure to be beyond their means. This meant that they were only able to conduct numerical calculations for shallow-water approximations.

Building on their earlier work (Fox & Squire, 1990, 1991), Fox & Squire (1994) were able to provide the first explicit calculations for the semi-infinite ice sheet problem considered by Evans & Davies, without the need to resort to simplified geometries. The solution method of these authors is different to that of Evans & Davies and is based on more numerical means. Fox & Squire used eigenfunction expansions of the solution in the ice-free and ice-covered domains and then matched these representations at the interface in an integral which minimised the jump in the pressure and velocity of the solution, subject to the free-edge conditions.

Further investigation of the semi-infinite ice sheet problem has been made by Balmforth & Craster (1999) and Linton & Chung (2003). Balmforth & Craster pursued the Wiener-Hopf method in the way suggested by Evans & Davies. These authors explicitly incorporate the ice edge conditions and show that the integrals considered difficult by Evans & Davies may be computed via quadrature. This method enables simple approximations to be derived in certain limits. On the other hand, Linton & Chung derive a method based on a mode-matching approach. Rather than turning to numerical methods though, they utilise integrals whose residues correspond to the unknown amplitudes, a method which is known as the ‘residue calculus technique’.

A smaller ice floe was treated as a two-dimensional model in which the ice-cover occupies a finite interval in an otherwise infinite interval of ice-free fluid by Wadhams (1973). Wadhams was, however, unable to provide a complete solution to this problem. This was later achieved by Meylan & Squire (1994), who considered cases of a finite and an infinite bed depth as well as the inclusion of a second floe. Their method of solution is to express the vertical derivative of the potential on the underside of the floe as an integral of the potential itself over this surface, which contains the ice edge conditions. This representation is then combined with the Green's function for the free-surface problem to produce a linear Fredholm integral equation of the second kind, which is solved numerically.

Instances of both cracks and leads that are approximately straight and long have been modelled in the style of piecewise uniform problems in two-dimensions. In such problems a crack is represented by a point at which two coupled ice regions meet. At this point the free-edge conditions apply to both sheets. An open lead is similarly represented by a non-zero finite interval of open water with ice-cover on either side. In contrast, for a refrozen lead the finite interval contains ice of a different property to the outer ice and the ice is connected throughout.

Investigations into the problem of leads have been less noteworthy than their crack problem counterparts. The case of an open lead, between two ice sheets of equal thickness and over a finite bed depth, was solved by Chung & Linton (2005) using the residue calculus technique that they applied to the semi-infinite ice sheet problem. Williams & Squire (2006) considered the same problem but one in which the central interval could contain ice, and the ice in the three intervals were of arbitrary thicknesses. This model is therefore clearly also applicable to a refrozen lead.

The two-dimensional crack problem has been solved by Evans & Porter (2003) for oblique incidence and a finite bed depth. This is accomplished by two means, the first being via a Green's function approach. Here, the solution is decomposed into its symmetric and antisymmetric parts and Green's identity, with an appropriate Green's function, is applied to each. Then, repeatedly applying integration by parts together with the edge conditions produces explicit expressions for the solution. The second method again decomposes the solution into odd and even functions but uses an eigenfunction expansion to represent these functions. As an aside, Evans & Porter prove that this expansion provides the complete solution.

Both Squire & Dixon (2000) and Williams & Squire (2002) solved the problem of a single crack over an infinite fluid depth, the former for normal incidence with the latter extending this to oblique incidence. The methods used by these authors are similar to the Green's function approach described above, although neither utilised the symmetry in the manner of Evans & Porter. The work of Squire & Dixon is extended to multiple cracks in Squire & Dixon (2001).

Multiple cracks are also dealt with by Porter & Evans (2006), although this work is far from a direct extension of their earlier method. Here, the authors solve for a single crack by deriving a pair of 'source' functions, which satisfy certain jump conditions across the crack. The full solution for any number of cracks may be expressed as a linear combination of these functions located at the cracks. Furthermore, Porter & Evans extend their analysis to a semi-infinite array of cracks using the properties of Bloch modes in an infinite array.

Porter & Evans (2007) have considered the more challenging, three-dimensional problem of an arbitrary number of cracks of a finite length in an ice sheet, where the restrictions of the cracks to straight parallel lines are enforced. Such finite cracks are subject to additional conditions at their ends. To solve this problem Porter & Evans solve hypersingular integral equations along the cracks. The sequence of papers concerning cracks is currently under development, with the forthcoming work of Porter (2007) tackling the problem of finite straight line cracks which are arranged arbitrarily, solved using source functions.

A number of techniques have also been formulated for other three-dimensional problems, specifically those that incorporate finite ice floes. Meylan & Squire (1996) considered the problem of a circular plate resting on the surface of an infinite fluid surface of infinite depth. In this work two solution methods were proposed, one of which was constructed in an entirely analogous fashion to the method of Meylan & Squire (1994) for finite two-dimensional floes, and resulted in a linear Fredholm integral equation of the second kind. A more computationally efficient option was also given. Here, the integral equation for the potential derived from the free-surface Green's function, in which both the potential and its vertical derivative appear in the integrand, is turned into a matrix system via expansions in the free modes of the plate taken *in vacuo*.

It was shown by Meylan (2002) that this method of expansion of the unknown functions in an integral equation in the *in vacuo* modes could be applied to plates of an arbitrary shape. However, for most non-circular floes these modes could only be found through numerical means. Meylan achieved this through the use of finite elements and produced results for triangular and quadrilateral floes.

Peter *et al.* (2004) also solved the circular ice floe problem but over a finite bed depth. Their solution procedure followed an eigenfunction matching method. The solution in both the ice-free and ice-covered regions were expanded as double infinite sums, in which the radial motion is defined in the form of Bessel functions, the azimuthal motion as a Fourier series and the vertical motion in the modes appropriate to the domain. An infinite set of equations is then generated by equating the two forms of the solution at their interface and integrating vertically and azimuthally, with the ice edge conditions also being applied. These equations are then truncated and solved directly.

To produce an accurate representation of the MIZ using a scattering model it is necessary to determine the combined effect of a multiplicity of three-dimensional floes. As in the two-dimensional setting, more realistic situations are formed by considering circumstances in which the scattering caused by individual floes may interact. Work in this area was conducted by Peter & Meylan (2004), who applied the method of Meylan (2002) for a single floe of an arbitrary shape to a finite number of multiple floes in any configuration.

For each individual floe the forcing upon it consists of not only the incident wave but of the waves scattered by all of the other floes. Peter & Meylan described this relationship explicitly via Graf's addition formula for Bessel functions, so that the scattered fields local to each floe could be coupled. Combining this with the scattering relation for individual floes results in a system of equations that must be solved simultaneously.

Another, related extension of the work of Meylan (2002), this time to an infinite straight line array of identical floes, was made by Peter *et al.* (2006). The interaction of the scattered fields of all of the floes is calculated via Graf's addition formula as in Peter & Meylan (2004) (albeit for a finite bed depth). At this point the periodicity of the problem is invoked, which reduces the problem to the consideration of only a single floe, and the resulting system of equations is solved directly.

The identical problem was also solved by Wang *et al.* (2007). In contrast, these authors used a Green's function to express the solution in terms of integrals of the potential and ice sheet displacement over the bases of all of the floes. Again, the periodicity of the problem meant that calculations for a single floe can be translated to all of the other floes, and the solution is then found from a suitable expansion of the unknown functions.

All of the models described above, although of great merit, are deficient in the aspect that they do not take account of the variable properties of the physical quantities they represent. Prominent in the application to ice sheets is the assumed uniformity of the elastic plate, both in its thickness and its material properties. Such variations cannot be expected to be realistically simulated by discrete jumps. Rather, the heterogeneous nature of the ice should be inherent in the model, so that the physical and material properties of the ice appear as continuous functions. However, the admittance of continuous variations incurs difficulties and there have consequently been relatively few attempts to solve such problems. For instance, it is not possible to obtain separation solutions in a domain for which the ice is non-uniform, which prevents standard eigenfunction matching methods being used.

Williams & Squire (2004) produced a solution procedure for a restricted class of variations in the properties of the ice. In a two-dimensional setting for which an infinite interval of otherwise uniform ice-cover is present, Williams & Squire allowed for a finite interval or finite intervals of continuous variations and concentrated on a changing thickness. The restriction imposed was that of a flat underside of the ice, which, along with the assumption of a finite flat bed, permits the use of the Green's function that was employed by Evans & Porter (2003), to reduce the problem to a Fredholm integral equation of the second kind. This method is elaborated on in the thesis of Williams (2006) and in particular a solution procedure is found for the more general situation of an ice shelf, where the finite interval of varying ice constitutes a transition in the thickness of the plate. For this problem Williams solved two coupled integral equations. The possibility of one of the semi-infinite intervals being ice-free is also considered.

Solutions for cases in which the shape of the quiescent bed undulates beneath a uniform floe of a finite extent have also been obtained. These models have far more relevance in relation to VLFSs than ice coverings as it is often assumed that, although of variable depth, the seabed beneath the MIZ is often deep enough to neglect these variations (Peter & Meylan, 2004). However, the mathematical models used are worthy of note. Both Wang & Meylan (2002) and Belibassakis & Athanassoulis (2005) considered bed variations beneath zero draught plates in a two-dimensional setting, although the Wang & Meylan model is slightly more general in that the interval of the variable bed may extend beyond the length of the plate. Wang & Meylan obtain a solution by reducing the problem to a finite domain enclosed by a boundary (including the varying part of the bed and the lower surface of the plate) on which the normal derivative of the potential is expressed as a function of the potential itself. The problem is then solved numerically using a boundary element method. Belibassakis & Athanassoulis, on the other hand, use a variational principle and express the solution as an infinite series in the vertical eigenfunctions, but add a further mode to improve convergence of the truncated series for a non-horizontal bed.

One feature that is common throughout the models that have been discussed so far, even those that incorporate continuous variations, is the unrealistic assumption of a 'zero' draught. This means that the surface of the ice that is in contact with fluid is flat and that the ice sheet rests on the fluid surface, which has a two-fold effect. Firstly, no variations in the lower surface of the ice may be included; for example the existence of a keel cannot be registered. Furthermore, the submergence at the edge of an ice sheet is neglected and the scattering caused by this is therefore absent.

Work on the inclusion of realistic draught conditions are sparse and we cite only two instances. Andrianov (2005) considers a small finite draught in a two-dimensional semi-infinite uniform plate. This is achieved by writing the unknowns of the problem in power series expansion in the draught, which are solved numerically for the leading two orders. In a forthcoming work, Williams & Squire (2007) investigate a non-zero draught in the form of a finite jump in the thickness of an infinite two-dimensional plate. Their method of solution is akin to that of Williams & Squire (2004), in that they use the Green's function based on the semi-infinite states to express the solution as an integral equation, where the integral in this case is over the contour that defines the part of the ice that protrudes from the uniform state.

The features of varying ice thickness, an undulating bed and a non-zero draught are all included in the model of Porter & Porter (2004). In this work the governing equations of full linear motion in a general three-dimensional setting are shown to be equivalent to a variational principle, whereby the stationary point of a given functional is sought.

Moreover, both cases of complete and partial ice-cover are permitted, with the latter requiring only modifications to the functional in the ice-free regions and a supplementary functional at the fluid-ice interfaces to couple the motion. Porter & Porter implement the 'modified mild-slope' approximation of Chamberlain & Porter (1995) for free-surface flows to situations of ice-cover by representing the vertical motion of their solution in terms of a single mode, which at each point in the domain corresponds to the wave bearing mode when the surrounding geometrical variations are neglected. Taken in conjunction with the variational principle, the 'mild-slope approximation' generates a set of approximate governing equations that are independent of the vertical coordinate. Numerical calculations in this work are made for selected two-dimensional geometries.

The ideas of Porter & Porter (2004) will be central to our work here. In particular, we will extend their single-mode (mild-slope) approximation, whose accuracy is dependent on the slow variation of the obstructions, to a multi-mode approximation, which does not impose any such restriction on the geometry. In conjunction with the same variational principle, the multi-mode approximation is an application of the Rayleigh-Ritz method that provides a means of constructing a sequence of increasingly accurate approximations, so that we may, in effect, obtain the full linear solution.

Certain aspects of the extension to multiple modes are not particularly straightforward. For instance, we will need to consider amendments to the interfacial functionals used to link solutions over jumps in the geometry. Moreover, we will need to look carefully at the properties of the modes that are used, as their rôle is essential to the accuracy of the approximation.

In addition to the consideration of multiple modes, we will elaborate on the numerical study of Porter & Porter by conducting a more detailed investigation of the two-dimensional configurations that they considered, which includes the extension to full linear solutions of certain problems selected from their work, as well as 'non-slow' variations. We also derive a solution method of a greater computational efficiency than that of Porter & Porter. Furthermore, our work will exceed that of Porter & Porter in the types of geometrical configurations that are formulated for numerical solution. This will include periodic variations in a two-dimensional setting and a three-dimensional axisymmetric construction.

It is pertinent at this point to give a brief review of the history of the solution method that we will use, in which a variational principle is taken in conjunction with a restiction of the vertical coordinate to a finite-dimensional space. For situations of free-surface flows, the modified mild-slope approximation was originally conceived by Chamberlain & Porter (1995) as an improvement to the 'mild-slope' approximation of Berkoff (1973). The motivation for this modification was that the mild-slope approximation of Berkoff neglected certain terms that proved to be significant in the case of rapid variations, such as might occur in ripple beds. In an extension that is analogous to ours here, Porter & Staziker (1995) expanded the modified mild-slope approximation to a multi-mode approximation by including a finite number of the modes that support evanescent waves in the corresponding flat bed problem.

Subsequently, many problems in the context of free-surface flows have been solved using the single-mode (modified mild-slope) or the multi-mode (extended modified mild-slope) approximations. For example, applications to two-dimensional ripple beds have been conducted by both Chamberlain & Porter (1995) and Porter & Porter (2003). Further examples examined include a plane wave incident on a three-dimensional domain of axisymmetric topography that has been considered by Chamberlain & Porter (1999), and the interaction of water waves with beds in the form of three-dimensional doubly-periodic undulations studied by Porter & Porter (2001). Inverse problems, in which a two-dimensional interval of varying topgraphy is reconstructed from knowledge of the reflection coefficient, have also been tackled (Chamberlain & Biggs, 2006). Finally, we note that the extended modified mild-slope (multi-mode) approximation has recently been reappraised by Chamberlain & Porter (2006) in the light of the additional accuracy gained through the inclusion of a ‘bed-mode’, which was first proposed by Belibassakis & Athanassoulis (1999).

Our outline for the work that will be carried out here is as follows. In the following chapter we will begin in §2.1 by giving the equations that govern motion in a situation in which a thin-elastic plate forms the upper surface of a fluid domain. We assume that the usual conditions of linear motion apply to the fluid and also that it is bounded below by a fixed impermeable bed. The motion of the thin plate is considered at the fluid surface using the linearised version of Bernouilli’s equation. These governing equations apply in the generality of a three-dimensional setting, for both full and partial ice coverings, and the geometrical surfaces are permitted to undulate so that the ice thickness and fluid depth may vary. A harmonic time dependence is removed and the oscillating interface between the fluid and ice linearised to leave a boundary-value problem in a fixed domain, which is to be solved for the motion within the fluid and the transverse displacement of the fluid-ice interface.

In the latter half of the second chapter, a variational principle is discussed. It is shown that the governing equations of the linear problem given earlier in the chapter arise as the natural conditions of the given functional when we seek its stationary point. Furthermore, this variational principle may be used to determine the natural conditions that must be satisfied by the full linear solution at any internal boundary, for example at the interface between ice-covered and ice-free domains.

At the beginning of §3 we apply the Rayleigh-Ritz method to the variational principle given in the preceding chapter to generate a means of calculating a hierarchy of approximations, abbreviated to the MMA, to the full linear solution. Our choice is to restrict the vertical motion to a finite-dimensional space, consisting of a set of vertical modes. We then determine the differential equations and accompanying boundary conditions that define the approximation. This new set of governing equations is independent of the vertical coordinate.

The remainder of the content of the chapter, section §3.2, is concerned with the choice of the vertical modes that define our approximation. Our wish is to follow the method of previous authors, for example Porter & Staziker (1995), who investigated analogous free-surface flows, by using a pointwise correspondence to the full linear solution of the problem in which no geometrical variations are present. However, it is found that the extra two 'complex' roots of the ice-covered dispersion relation cause bifurcations in the evanescent modes that may prevent their use in the multi-mode approximation. A further result is given, showing that there is a two-fold linear dependence in the set of vertical modes we wish to use and consequently that two of these vertical modes may be eliminated from our reckoning. This discovery has ramifications for the full linear solution in situations of uniform geometry and these are discussed. The linear dependence issue partially alleviates the problems caused by bifurcations but does not do so entirely and we give an example of an alternative expansion for cases in which their presence persists.

In §4 the multi-mode approximation is applied to the degenerate case in which variations only occur in one horizontal spatial coordinate and an incident wave propagates obliquely from the far-field. The governing equations therefore simplify to an ordinary differential system with accompanying point conditions. Over an interval of uniform geometry it is shown in §4.2 that it is possible to produce an analytic form for the approximation which mirrors the full linear solution over such an interval; however, unlike its free-surface equivalent, the form of the approximation when ice-cover is present is shown to not be a direct truncation of the full linear solution, due to the appearance of dimension-dependent complex waves.

Two particular two-dimensional geometrical configurations are formulated for numerical solution in §4.3. In the first we concentrate on the scattering caused by obstructions in the geometry alone. Here a finite interval of varying geometry is considered, with semi-infinite intervals of uniform geometry attached to it at either end. The solutions in the three subintervals are linked through the conditions that apply at the internal boundaries between states of connected ice-cover. These conditions are then combined with the expressions for the MMA in the uniform intervals to reduce the problem to the numerical calculation of the solution over the interval of varying geometry with appropriate boundary data. It is shown that we may manipulate the boundary data so that only two linearly independent solutions need to be calculated in order to obtain the solution, regardless of the dimension of the approximation.

A second problem, that of a finite ice floe, is also formulated. Here, the uniform intervals are ice-free rather than ice-covered. This is expected to be more demanding of the approximation due to the appearance of ice edges but can nevertheless be solved by following identical methods to the complete ice-cover problem.

Prior to using our approximation in situations in which the geometrical surfaces are permitted to vary, in §5 we investigate the effects of the difference we have found between our approximation and a truncated version of the full linear solution over intervals of uniform geometry. To do this, we take the problem of a semi-infinite ice sheet, which we solve using both our multi-mode approximation and an eigenfunction matching method. After a comparison to data produced by independent authors who used alternative methods of solution, we give a set of our own numerical calculations to compare the accuracy of our approximations and the eigenfunction matching method. It is found that our approximation provides superior accuracy to the eigenfunction matching method at low dimensions, especially when the jump between the two states is most pronounced, caused by either a large ice thickness or a high frequency. However, we also show that in certain extreme cases the higher-dimensional refinements of the multi-mode approximation are slow in comparison to the eigenfunction matching method.

In §§6-7 we undertake a numerical investigation of the scattering caused by the geometries that were formulated in §4.3. In both chapters we begin by providing comparisons to work produced by independent authors, who have used different methods of solution to our own. Furthermore, we consider extending some of the results given by the single-mode approximations of Porter & Porter (2004) to full linear solutions. In doing so, we discover in the continuous ice-cover problem that there is a close link between geometries that share certain features of their vertical structure. This observation leads to a full investigation in §6.4 of the relationship between obstructions related by a shared ice thickness or fluid depth or both. Certain régimes are deduced in which particular sources of scattering are significant, and a main conclusion is that variations to the ice thickness are dominant under many circumstances. The approximation used during the investigation of §6.4 is restricted to a single mode to aid analytical progress, and because a single mode has by then been proved to provide high accuracy, even in situations involving large obstructions.

For the situation of a finite floe the approximation must deal with discontinuities in the geometry caused by the ice edges. As expected, it is shown that this is detrimental to the accuracy of the multi-mode approximation, so that a greater dimension must be taken in order to achieve a desired accuracy in comparison with the continuous ice-cover problem. We find that this is particularly true in the vicinity of the ice edges, at which points the evanescent waves are strongly activated. Consequently, it is shown that approximations to quantities that are sensitive to the value of the solution at these points may contain qualitative inaccuracies at low dimensions but that these are quickly eradicated by the inclusion of supplementary evanescent modes. It is found that the scattering caused by the edges of the ice dominate over those induced by geometrical variations at high frequencies but that for lower frequencies the scattering caused by the two sources are comparable. Furthermore, we note the appearance of a fine structure in the results of the finite ice floe that were not present for the semi-infinite ice sheet.

As well as geometrical variations, the multi-mode approximation allows the inclusion of a realistic Archimedean draught and this is investigated for two-dimensional motions in §7.5. The effects of the existence of a draught are discovered to be significant in many circumstances. Primarily, we show that at mid to high frequencies the submerged portion of the floe causes it to reflect a greater proportion of the incident wave.

In §8 we progress to the problem of a finite interval containing periodic variations in an otherwise infinite ice sheet. Although we may use the formulation of §4.3.1, it is both computationally efficient and aids analysis if we reformulate the problem. This is done in §8.1 and §8.3 by using the transfer matrix approach devised by Porter & Porter (2003) for free-surface motions, which relates the amplitudes at either end of a single period, and we find that we are able to calculate the solution for any number of periods using the solution from a single such period. A wide-spacing approximation, analogous to that of Porter & Porter, which ignores the influence of the evanescent waves between periods, is also given and this allows us to relate the production of resonances to the eigenvalues of the transfer matrix. Although it is pointed out that the chance of Bragg values coinciding with realistic parameters is far less likely in the presence of ice-cover, we nevertheless examine this phenomenon in §8.4. We find that resonances do occur around Bragg values in this problem and that, in comparison to results of previous authors who investigated periodically varying beds for free-surface flows, these resonances are pronounced. Moreover, we make the discovery of rightward drift of Bragg peaks as well as the common leftward drift, as the magnitude of the periodic geometric variation is increased.

By returning to the general governing equations of the multi-mode approximation, in §9 we are able to formulate the three-dimensional problem of an axisymmetric ice floe forced by a plane wave. This is achieved using polar coordinates in the horizontal plane, and the axisymmetry of the geometry is then invoked to express all unknowns in terms of Fourier cosine series. The multi-mode approximation is therefore determined by a set of ordinary differential equations, which we truncate to a finite dimension to give a desired level of accuracy.

A restricted set of numerical results is presented in §§9.2-9.3 using the multi-mode approximation and it is found that the properties of the approximation are consistent with those shown in two-dimensional situations. In the following chapter (§10) we embark on a far more extensive investigation of the axisymmetric floe, although with the single-mode approximation. By taking only a single vertical mode we are able to produce explicit approximations in régimes in which the radius of the floe is either long or short with respect to the length of the propagating waves. These approximations are then used to aid our analysis of the numerical results that we produce. We are able to draw inferences about the behaviour of the floe as its properties vary, and pay particular attention to the prevalence of fine structure that leads to disproportionate responses for relatively short incident waves. This fine structure is shown to obscure the inferences that we may make about the effects of geometrical variations and an Archimedean draught. In §10.2.4 we are able to relate the occurrence of fine structure to full resonances in problems for which we allow a fictitious temporal decay.

To conclude, in §11 we give a summary of the findings that we have made, which is followed by a discussion of directions that we may wish to take in order to extend our work. All supplementary calculations are contained in Appendices A-C.

Chapter 2

Preliminaries

In this chapter we will define the problem of linear wave scattering by an ice sheet of varying thickness floating on fluid, which is bounded below by an undulating bed. The ice may fully or partially cover the fluid surface and our solution method for these two situations will be distinct. The setting considered here is three-dimensional, which will allow us to retain full generality in the approximation theory that is developed in §§2-3. The numerical methods that are formulated and utilised in §§4-9 are devised for specific geometrical configurations and make use of the degeneracies that they introduce; however, the general theory that is developed is available for further study.

The cartesian cordinates x, y, z are used to define the geometry, where x, y are horizontal coordinates and z is the vertical coordinate. This vertical coordinate is directed upwards and its origin is set to coincide with the equilibrium surface of the fluid in the absence of ice.

A typical two-dimensional cross-section ($y =$ constant) of geometry in equilibrium is shown in figure 2.1. The lower surface of the ice sheet is located at $z = -d(x, y)$, and its thickness is given by the function $D(x, y)$. Fluid is bounded above by the lower surface of the ice sheet and lies above a fixed impermeable bed located at $z = -h(x, y)$. The functions $D(x, y)$, $h(x, y)$ and $d(x, y)$ fully define the geometry; however, it will aid brevity to introduce the notation $H(x, y) = h(x, y) - d(x, y)$ to represent the fluid depth.

When motion is generated (by some means) in this system of fluid and ice, it is assumed that the fluid and ice remain in contact at all times. The ice then experiences flexural oscillations and the position, at time t, of the fluid-ice interface is given by

$$z = -d(x, y) + \zeta(x, y, t).$$

The *displacement function*, ζ, is an unknown.

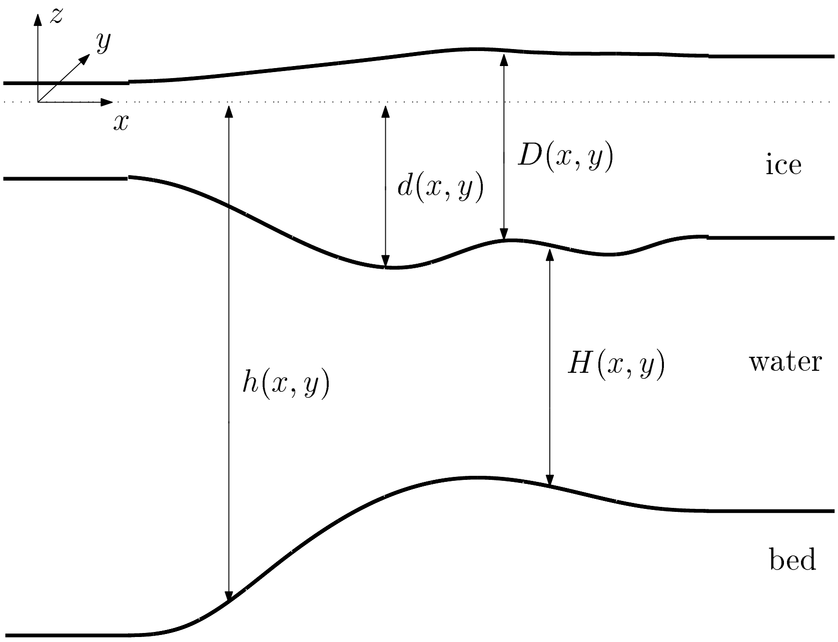

Figure 2.1: Two-dimensional cross-section of geometry.

2.1 The boundary-value problem

We are using linear theory. Therefore, on the basis that ζ is small in comparison to the vertical scales, the fluid is considered to occupy the fixed interval $-h < z < -d$. The usual assumptions regarding the properties of the fluid that are required for wave theory are also adopted. These are that the fluid is inviscid, incompressible, and homogeneous, and in irrotational motion. It follows that the fluid may be entirely defined through its *velocity potential* $\hat{\Phi} = \hat{\Phi}(x, y, z, t)$.

Within the fluid domain, the velocity potential satisfies Laplace's equation

$$\nabla^2 \hat{\Phi} + \partial_z^2 \hat{\Phi} = 0 \quad (-h < z < -d), \tag{2.1}$$

where $\nabla = (\partial_x, \partial_y)$ and the notation $\partial_x = \partial/\partial x$, and so on, is used throughout. The velocity potential must also satisfy the bed condition of no normal flow, namely

$$\nabla h \cdot \nabla \hat{\Phi} + \partial_z \hat{\Phi} = 0 \quad (z = -h). \tag{2.2}$$

The linearized version of Bernoulli's equation gives the pressure, $p(x, y, z, t)$, of the fluid in the form

$$p = p_0 - \rho_w \partial_t \hat{\Phi} - \rho_w g z \quad (-h < z < -d), \tag{2.3}$$

in which ρ_w is the density of the fluid and p_0 denotes the atmospheric pressure that we may take to be a constant (see, for example, Wehausen & Laitone, 1960). In order for linear theory to apply here, we have assumed that the potential, $\hat{\Phi}$, is small, so that the term $\rho_w(\nabla\hat{\Phi})^2/2$ may be omitted. The quantity g represents the acceleration due to gravity and will be set at $g = 9.81\text{ms}^{-2}$ throughout.

It has become standard practice to model the ice as a 'thin' elastic plate. A comprehensive study of elastic plates is contained in Timoshenko & Woinowsky-Krieger (1959). Such theory is based on the assumption that the ice is comprised of homogeneous vertical strips that expand and contract uniformly about a middle-plane, which experiences no deformation. Stresses that occur between adjacent vertical strips are considered negligible. A key feature of the elastic plate model is that the flexure of the ice is included through Hooke's law, rather than the ice appearing simply as a mass that rests on the fluid surface, as in the earlier 'mass-loading' models, such as that of Weitz & Keller (1950). Modifications to 'non-thin' elastic plates have been studied; for example, Balmforth & Craster (1999) incorporated rotational inertia, shear deformation, compressibility and dissipation in their model. This theory may be incorporated into our model; however, as it is yet to be shown that these modifications are of value we will not pursue this issue. All stresses within the ice may then be entirely described through calculation of its transverse displacement, ζ, at the interface between itself and the fluid.

By referring to Timoshenko & Woinowsky-Krieger (1959), on the basis that ζ is small, Porter & Porter (2004) deduced the linearised equation governing the motion of the ice to be

$$[p]_{z=-d} = p_0 + \rho_w g d + \rho_w g \mathscr{L}\zeta + \rho_i D \partial_t^2 \zeta, \tag{2.4}$$

where ρ_i is the density of the ice and

$$\mathscr{L}\zeta \equiv \nabla^2(\beta\nabla^2\zeta) - (1-\nu)\{\partial_x^2\beta\partial_y^2\zeta + \partial_y^2\beta\partial_x^2\zeta - 2\partial_x\partial_y\beta\partial_x\partial_y\zeta\},$$

in which ν denotes Poisson's ratio. The function

$$\beta(x,y) = \frac{ED^3(x,y)}{12\rho_w g(1-\nu^2)}, \tag{2.5}$$

where E is Young's modulus for ice, represents the flexural rigidity of the ice, which has been scaled by the factor $\rho_w g$. From expression (2.5), we note that β may be regarded as a function of the ice thickness, D. Equation (2.4) follows from an application of Newton's second law of motion that describes the motion of the ice, which is induced by pressure forces at its lower and upper surfaces.

At this point we note that we have assumed the density and resistive properties of the ice to be uniform horizontally as well as vertically. That is, the ice properties vary only with respect to its thickness, D. This is not a requirement of thin plate theory but is rather an expedient in the model for the following study of the rôle of the geometrical configuration.

In a state of equilibrium ($\hat{\Phi} = \zeta = 0$), consistency is ensured by the plate equation (2.4) coinciding with Bernoulli's equation (2.3) at $z = -d$. The motion of the fluid and the plate may be coupled by eliminating the pressure between the linearised equations (2.3) and (2.4), to give

$$\rho_w(\partial_t\hat{\Phi} + g\zeta) + \rho_w g\mathscr{L}\zeta + \rho_i D\partial_t^2\zeta = 0 \quad (z = -d). \tag{2.6}$$

Due to the presence of the two unknowns $\hat{\Phi}$ and ζ in (2.6), a second equation at the fluid-ice interface is required. This is provided by the linearised kinematic condition

$$\nabla d \cdot \nabla\hat{\Phi} + \partial_z\hat{\Phi} = \partial_t\zeta \quad (z = -d), \tag{2.7}$$

which equates the normal velocity of the fluid at its surface to the velocity of the displacement of the ice.

In situations of ice-free fluid ($D = d = 0$), equations (2.6)-(2.7) collapse to the standard free-surface condition

$$\partial_z\hat{\Phi} = \frac{1}{g}\partial_t^2\hat{\Phi} \quad (z = 0).$$

The displacement function $\zeta = [\partial_t\hat{\Phi}/g]_{z=0}$ then simply represents the free-surface elevation in terms of $\hat{\Phi}$.

By decomposing the time dependence of the problem into harmonic modes (see, for example, Linton & McIver, 2001), we may consider the problem in terms of individual frequencies, ω, over a range of significant values. By removing a harmonic time dependence with a given frequency ω, we express the steady-state behaviour of the velocity potential and displacement function as

$$\hat{\Phi}(x, y, z) = \Re\mathrm{e}\left(\frac{g}{\mathrm{i}\omega}\phi(x, y, z)\mathrm{e}^{-\mathrm{i}\omega t}\right), \quad \zeta(x, y, t) = \Re\mathrm{e}\left(\eta(x, y)\mathrm{e}^{-\mathrm{i}\omega t}\right), \tag{2.8}$$

where ϕ, the *reduced velocity potential*, and η, the *reduced displacement function*, are both complex functions. We also define the *wave period* $\tau = 2\pi/\omega$secs.

Equations (2.1)-(2.2) now become

$$\nabla^2\phi + \partial_z^2\phi = 0 \quad (-h < z < -d), \tag{2.9a}$$

and

$$\nabla h \cdot \nabla\phi + \partial_z\phi = 0 \qquad (z = -h). \tag{2.9b}$$

The time independent versions of the plate equation (2.6) and kinematic condition (2.7) are

$$(1 - \kappa\alpha)\eta + \mathscr{L}\eta - \phi = 0, \quad \nabla d \cdot \nabla\phi + \partial_z\phi = \kappa\eta \qquad (z = -d). \tag{2.9c}$$

Here, we have introduced the notation

$$\kappa = \frac{\omega^2}{g}, \quad \alpha(x,y) = \frac{\rho_i D(x,y)}{\rho_w g}, \tag{2.10}$$

where α denotes the mass of the ice, which has been scaled by the factor $\rho_w g$ and, like β, is a function of the ice thickness. For unloaded fluid, conditions (2.9a-c) degenerate to

$$\nabla^2\phi + \partial_z^2\phi = 0 \quad (-h < z < 0), \quad \nabla h \cdot \nabla\phi + \partial_z\phi = 0 \quad (z = -h), \tag{2.11a}$$

and the free-surface condition to

$$\partial_z\phi = \kappa\phi \qquad (z = 0). \tag{2.11b}$$

The reduced displacement becomes, trivially, the reduced free-surface elevation, $\eta = [\phi]_{z=0}$.

Unless otherwise stated, the physical parameters of the ice take the constant values values $E = 5 \times 10^9$Pa, $\rho_i = 922.5$kgm^{-3}, and $\nu = 0.3$, with the density of the water taken to be $\rho_w = 1025$kgm^{-3}. Although the properties of the ice will have a complicated dependency on the particular state of the ice that is being modelled, for instance the supposed dependency of the Young's modulus and Poisson's ratio on the brine content and tempreture of the ice (Hutter, 1975), these averaged values are those that are widely used at the present and are typical of MIZ conditions. Further information on the properties of the ice along with experimental data can be found in Hobbs (1974).

We have thus far considered only the conditions that apply at the vertical boundaries $z = -h$ and $z = -d$. There is also the question of the conditions that apply at the lateral boundaries, which may be the boundary of the overall domain under consideration. For the problems that we will deal with in §§5-9 these 'overall domain boundaries' will be infinite and therefore described as the *far-fields*. Then, there are the *internal boundaries* that separate differing states within the overall domain. Most commonly an internal boundary is an interface between ice-free and ice-covered states or it may define corners in the geometry. The mathematical description of the problem is not complete until conditions have been set at the lateral boundaries.

In §2.2.1 the internal boundary conditions will be determined under the present generality. These internal conditions dictate the continuity that must be maintained at such points and additionally impose constraints on the dynamics of the ice edge. Conversely, the far-field conditions are problem specific and will only be defined at the appropriate juncture. They take the form of *radiation conditions* and descibe the behaviour of the solution in this limit.

For each problem, the lateral conditions must be combined with equations (2.9) in order to obtain ϕ and η.

2.2 Variational principle

An alternative means of defining the linear, time-harmonic problem of wave scattering by an ice sheet of varying thickness over an undulating bed, in the form of a variational principle, was proposed by Porter & Porter (2004). In this setting, the governing equations (2.9a-c) and (2.11a-b) arise as the natural, stationary conditions of given functionals.

The functional formulation of the problem will provide the basis for our solution procedure, and as such warrants attention. The following mirrors the outline originally appearing in Porter & Porter (2004).

We introduce the simply connected and bounded domain Ω in the plane $z = 0$, with boundary $\delta\Omega$, and suppose that the region $\Omega \times [-h, -d]$ contains ice-covered fluid. Furthermore, we require the functions $\psi = \psi(x, y, z)$ and $\chi = \chi(x, y)$ to be sufficiently differentiable for what follows.

We will treat the motions of the fluid and ice through separate functionals. Consider first the fluid motion via the functional

$$L_1(\psi) = \frac{1}{2}\int\!\!\int_\Omega \int_{-h}^{-d} \{(\nabla\psi)^2 + (\partial_z\psi)^2\}\,\mathrm{d}z\,\mathrm{d}x\mathrm{d}y,$$

which has first variation

$$\delta L_1 = \int\!\!\int_\Omega \int_{-h}^{-d} \{(\nabla\psi)\cdot(\nabla\delta\psi) + (\partial_z\psi)(\partial_z\delta\psi)\}\,\mathrm{d}z\,\mathrm{d}x\,\mathrm{d}y.$$

Using Green's identity we may write

$$\begin{aligned}\delta L_1 \;=\; & -\int\!\!\int_\Omega \int_{-h}^{-d} \{\delta\psi\left(\nabla^2\psi + \partial_z^2\psi\right)\}\,\mathrm{d}z\,\mathrm{d}x\,\mathrm{d}y + \int_{\delta\Omega} \mathbf{n}\cdot\int_{-h}^{-d} \delta\psi\nabla\psi\,\mathrm{d}z\,\mathrm{d}s \\ & -\int\!\!\int_\Omega [\delta\psi\,(\nabla z\cdot\nabla\psi - \partial_z\psi)]_{z=-h}^{-d}\,\mathrm{d}x\,\mathrm{d}y.\end{aligned} \qquad (2.12)$$

This provides a form in which the variation $\delta\psi$ appears without differentiation. The vector $\mathbf{n}$ is the outward unit normal from the curve $\delta\Omega$ and s measures arclength on this boundary.

The second functional,

$$\begin{aligned}L_2(\psi,\chi) \;=\; & \frac{1}{2}\int\!\!\int_\Omega \left\{\beta\left((\nabla^2\chi)^2 - 2(1-\nu)\left((\partial_x^2\chi)(\partial_y^2\chi) - (\partial_x\partial_y\chi)(\partial_x\partial_y\chi)\right)\right)\right\}\mathrm{d}x\,\mathrm{d}y \\ & + \frac{1}{2}\int\!\!\int_\Omega \left\{(1-\kappa\alpha)\chi^2 - 2\chi[\psi]_{z=-d}\right\}\,\mathrm{d}x\,\mathrm{d}y,\end{aligned}$$

contains the motion of the ice sheet and a term that couples it to the fluid motion. This functional has the first variation

$$\begin{aligned}\delta L_2 \;=\;& \iint_{\Omega} \{\beta\left((\nabla^2\chi)(\nabla^2\delta\chi)\right.\\ &\left.-(1-\nu)\left((\partial_x^2\chi)+(\partial_y^2\delta\chi)(\partial_x^2\delta\chi)(\partial_y^2\chi)-2(\partial_x\partial_y\chi)(\partial_x\partial_y\delta\chi)\right)\right)\}\,\mathrm{d}x\,\mathrm{d}y\\ &+\iint_{\Omega}\{((1-\kappa\alpha)\chi-[\psi]_{z=-d})\,\delta\chi-\chi[\delta\psi]_{z=-d}\}\;\mathrm{d}x\,\mathrm{d}y.\end{aligned} \tag{2.13}$$

The removal of the derivative operators from the variations in L_2 is achieved through use of the identity

$$\begin{gathered}\beta\{(\partial_x^2\chi)(\partial_y^2\delta\chi)+(\partial_y^2\chi)(\partial_x^2\delta\chi)-2(\partial_x\partial_y\chi)(\partial_x\partial_y\delta\chi)\}=\\ \delta\chi\{(\partial_x^2\beta)(\partial_y^2\chi)+(\partial_y^2\beta)(\partial_x^2\chi)-2(\partial_x\partial_y\beta)(\partial_x\partial_y\chi)\}+\nabla\cdot\mathbf{g},\end{gathered}$$

where

$$\begin{aligned}\mathbf{g} \;=\;& \left\{\beta\left[(\partial_y^2\chi)(\partial_x\delta\chi)-(\partial_x\partial_y\chi)(\partial_y\delta\chi)\right]-\delta\chi\left[(\partial_x\beta)(\partial_y^2\chi)-(\partial_y\beta)(\partial_x\partial_y\chi)\right]\right\}\mathbf{i}\\ &+\;\left\{\beta\left[(\partial_x^2\chi)(\partial_y\delta\chi)-(\partial_x\partial_y\chi)(\partial_x\delta\chi)\right]-\delta\chi\left[(\partial_y\beta)(\partial_x^2\chi)-(\partial_x\beta)(\partial_x\partial_y\chi)\right]\right\}\mathbf{j},\end{aligned}$$

with $\mathbf{i}$ and $\mathbf{j}$ denoting the usual unit vectors. Green's identity may now be applied to the terms that contain the factor β in (2.13) to give

$$\begin{aligned}\delta L_2 \;=\;& \iint_{\Omega}\{((1-\kappa\alpha)\chi+\mathscr{L}\chi-[\psi]_{z=-d})\,\delta\chi-\chi[\delta\psi]_{z=-d}\}\;\mathrm{d}x\,\mathrm{d}y\\ &+\;\int_{\delta\Omega}\left\{\beta\nabla^2\chi(\partial_n\delta\chi)-\delta\chi(\partial_n\beta\nabla^2\chi)-(1-\nu)\mathbf{n}\cdot\mathbf{g}\right\}\mathrm{d}s.\end{aligned} \tag{2.14}$$

We therefore seek the stationary point of the functional $L_{\Omega}(\psi,\chi)\equiv L_1(\psi)+\kappa L_2(\psi,\chi)$. With reference to the form of the first variations (2.12) and (2.14) it is clear that $\delta L_{\Omega}=0$ for $(\psi,\chi)=(\phi,\eta)$ satisfying the governing equations of ice-covered fluid (2.9a-c). In addition to these natural conditions, there is a set of conditions to be satisfied at the boundary $\delta\Omega\times[-h,-d]$, which will be dealt with in the following section.

The derivation of the functional L_{Ω} is a form of Hamilton's principle, in that it is comprised of the difference between the kinetic and potential energies of the system. In our specification of the variational principle, we have implicitly made the assumption that our choice of approximation will be constructed on a real-valued basis. The extension of L_{Ω} to incorporate complex values is made in Bennetts *et al.* (2007).

Let us now suppose that we consider a domain $\Omega^{(0)}$, for which the fluid is unloaded. Equations (2.11a-b) arise as the natural conditions of the varational principle $\delta L_{\Omega^{(0)}}=0$, along with the identification of the reduced displacement function, η, with the reduced free-surface elevation, $[\phi]_{z=0}$. It is efficient to encapsulate this latter identity as an essential condition, by writing

$$L^{(0)}_{\Omega^{(0)}}(\psi) \equiv L_{\Omega^{(0)}}(\psi, [\psi]_{z=0}) = \frac{1}{2}\iint_{\Omega^{(0)}} \left\{ \int_{-h}^{0} \{(\nabla\psi)^2 + (\partial_z\psi)^2\}\mathrm{d}z - \kappa[\psi]^2_{z=0} \right\} \mathrm{d}x\,\mathrm{d}y.$$

The first variation of $L^{(0)}_{\Omega^{(0)}}$ is then easily deduced to be

$$\begin{aligned}\delta L^{(0)}_{\Omega^{(0)}} &= -\iint_{\Omega^{(0)}} \int_{-h}^{0} \{\delta\psi\left(\nabla^2\psi + \partial_z^2\psi\right)\}\,\mathrm{d}z\,\mathrm{d}x\,\mathrm{d}y + \int_{\delta\Omega^{(0)}} \mathbf{n}\cdot\int_{-h}^{-d} \delta\psi\nabla\psi\,\mathrm{d}z\,\mathrm{d}s \\ &\quad -\iint_{\Omega^{(0)}} [\delta\psi\left(\nabla z\cdot\nabla\psi - \partial_z\psi\right)]^0_{z=-h} + \kappa[\psi\delta\psi]_{z=0}\,\mathrm{d}x\,\mathrm{d}y,\end{aligned}$$

and the stationary point $\psi = \phi$ must therefore satisfy equations (2.11a-b) along with conditions at the lateral boundary $\delta\Omega^{(0)} \times [-h, 0]$.

2.2.1 Jump Conditions

It was noted at the end of §2.1 that the governing equations (2.9a-c) and (2.11a-b) lack conditions in the far-field and at the internal, lateral boundaries. Moreover, the satisfaction of (2.9a-c) and (2.11a-b) are not sufficient as stationary conditions; there remain boundary terms that must vanish.

In this section we will be primarily concerned with the conditions that must hold at internal boundaries, caused by either a corner in the geometry or by the interface between ice-covered and ice-free regions. To achieve this, we develop the boundary terms that appear in the variational principle into the form of *jump conditions*.

First though, let us consider $\delta\Omega \times [-h, -d]$ to form all or part of the far-field boundary. In each individual problem, sufficient conditions for ϕ and η will be specified at this boundary. These boundary conditions may be imposed on ψ and η in the variational problem, thus restricting the variations to

$$\delta\psi = 0 \quad \text{on } \delta\Omega \times [-h, -d], \quad \delta\chi = \partial_x\delta\chi = \partial_y\delta\chi = 0 \quad \text{on } \delta\Omega, \tag{2.15}$$

and the boundary contributions in δL_Ω vanish. Similarly, if $\delta\Omega^{(0)} \times [-h, 0]$ forms part or all of the far-field boundary then conditions on ϕ exist there and the boundary contribution to $\delta L^{(0)}_{\Omega^{(0)}}$ vanishes. If we were not able to impose the exact form of the solution as an essential condition in our variational principle then a modified (and far more complicated) functional would be required. This fact will have an important consequence for our solution procedure, which will be outlined in the following chapter, as it is necessary that the exact form of the far-field conditions is inherent in the approximation that we generate.

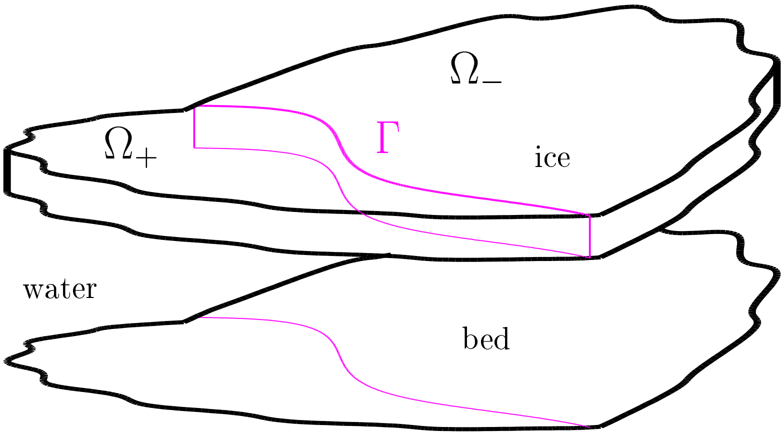

Figure 2.2: An internal boundary, Γ, that separates two regions of connected ice-cover, $\Omega_\pm$.

We now turn to the question of internal boundaries, beginning with their creation through corners in the geometry. In the derivation of the variational principle, it was implicitly assumed that the geometry possessed sufficient differentiability. Specifically, in Ω we require that the fluid boundaries, d and h, are continuous up to first derivatives and that the ice thickness, D, is continuous up to second derivatives. Let us suppose that such discontinuities occur along a smooth simple curve Γ, with end points Γ_0 and Γ_1, which partitions Ω into Ω_+ and Ω_-. A graphical reprentation of this situation is shown in figure 2.2. For algebraic convenience here, it is assumed that the fluid boundaries, h and d, are continuous. It is therefore not possible to apply the variational principle $\delta L_\Omega = 0$ but rather $\delta(L_{\Omega_+} + L_{\Omega_-}) = 0$. For all points $(x, y) \in \Omega/\Gamma$, the natural conditions (2.9a-b) once again apply; however, at the internal boundary, referring to (2.12) and (2.14), we have the boundary contribution

$$\int_\Gamma \mathbf{n} \cdot \int_{-h}^{-d} \langle\langle \delta\psi \rangle\rangle \, (\nabla\psi) \, \mathrm{d}z + \langle \kappa \left\{ (\beta\nabla^2\chi)(\nabla\delta\chi) - \delta\chi \, \nabla(\beta\nabla^2\chi) - (1-\nu)\mathbf{g} \right\} \rangle \mathrm{d}s, \quad (2.16)$$

where, for example, $\langle\langle \psi \rangle\rangle = \psi_+ - \psi_-$ denotes the jump in ψ across the surface $\Gamma \times [-h, -d]$ and $\langle \chi \rangle = \chi_+ - \chi_-$ denotes the jump in χ across the contour Γ. The subscripts $\pm$ indicate limits from the respective subdomains. Let the normal and tangential vectors, on Γ, $\mathbf{n}$ and $\mathbf{s}$ be defined by

$$\mathbf{n} = \mathbf{i} \cos\Theta + \mathbf{j} \sin\Theta, \quad \mathbf{s} = -\mathbf{i} \sin\Theta + \mathbf{j} \cos\Theta,$$

where $\Theta = \Theta(s)$ represents the angle of the curve Γ with respect to the Cartesian frame. It follows that

$$\partial_x = \cos\Theta\partial_n - \sin\Theta\partial_s, \quad \partial_y = \cos\Theta\partial_n + \sin\Theta\partial_s,$$

where $\partial_n = \mathbf{n}\cdot\nabla$ and $\partial_s = \mathbf{s}\cdot\nabla$, from which we find that

$$\mathbf{n}\cdot\mathbf{g} = (\partial_s^2\chi + \Theta'\partial_n\chi)(\beta\partial_n\delta\chi - (\partial_n\beta)\delta\chi) - (\partial_s\partial_n\chi - \Theta'\partial_s\chi)(\beta\partial_s\delta\chi - (\partial_s\beta)\delta\chi). \quad (2.17)$$

We also note the non-commutative identity

$$\partial_s\partial_n\chi - \Theta'\partial_s\chi \equiv \partial_n\partial_s\chi.$$

Using (2.17) and applying integration by parts to the terms involving $\partial_s(\delta\chi)$ in (2.17) leads to the representation of the expression in (2.16)

$$\begin{aligned} &\int_\Gamma\int_{-h}^{-d}\langle\langle\delta\psi\,(\partial_n\psi)\rangle\rangle\mathrm{d}z\,\mathrm{d}s \\ &+\kappa\int_\Gamma\Big\langle\delta\chi\Big\{-\partial_n(\beta\nabla^2\chi) + (1-\nu)\big((\partial_n\beta)(\partial_s^2\chi + \Theta'\partial_n\chi) \\ &\qquad -(2(\partial_s\beta)+\beta)(\partial_s\partial_n\chi - \Theta'\partial_s\chi)\big)\Big\}\Big\rangle\mathrm{d}s \\ &+\kappa\int_\Gamma\langle\partial_n(\delta\chi)\,\{\beta\nabla^2\chi - (1-\nu)\beta(\partial_s^2\chi + \Theta'\partial_n\chi)\}\rangle\,\mathrm{d}s \\ &-\kappa\,(1-\nu)\big[\,\langle\delta\chi\beta(\partial_s\partial_n\chi - \Theta'\partial_s\chi)\rangle\,\big]_{\Gamma_0}^{\Gamma_1}. \end{aligned} \quad (2.18)$$

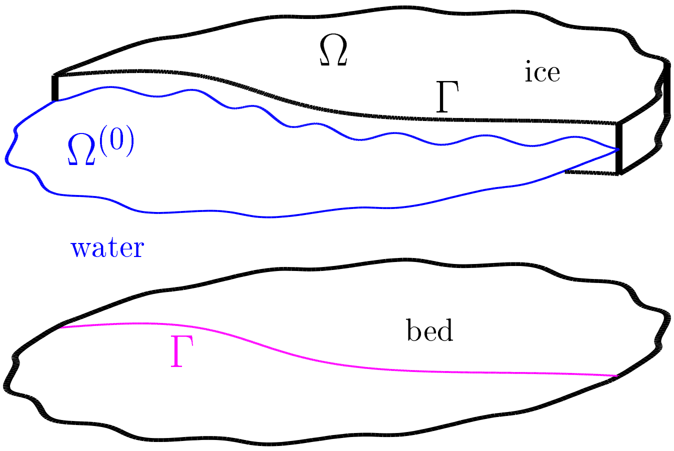

Figure 2.3: An internal boundary, Γ, that separates a region of ice-covered fluid, Ω, from a region of ice-free fluid, $\Omega^{(0)}$.

Let us now suppose that Γ occupies an interval of both $\delta\Omega$ and $\delta\Omega^{(0)}$, so that it forms the boundary between ice-covered and ice-free states. Such a situation is depicted in figure 2.3 and we may suppose that at the ice edge $D \neq 0$, so that the geometry is not continuous across Γ. Mimicking the steps that led to (2.18) we find the contribution to the first variation of $L_{\Omega^{(0)}} + L_{\Omega}$ on Γ to be

$$\begin{aligned}
&\int_{\Gamma}\int_{-h}^{-d} \delta\psi\,(\partial_n\psi)\,\mathrm{d}z\,\mathrm{d}s - \int_{\Gamma}\int_{-h}^{0} \delta\psi^{(0)}\,\big(\partial_n\psi^{(0)}\big)\,\mathrm{d}z\,\mathrm{d}s \\
&+\kappa\int_{\Gamma}\delta\chi\Big\{-\partial_n(\beta\nabla^2\chi) + (1-\nu)\big((\partial_n\beta)(\partial_s^2\chi + \Theta'\partial_n\chi) \\
&\qquad\qquad -(2(\partial_s\beta)+\beta)(\partial_s\partial_n\chi - \Theta'\partial_s\chi)\big)\Big\}\mathrm{d}s \\
&+\kappa\int_{\Gamma}\partial_n(\delta\chi)\,\big\{\beta\nabla^2\chi - (1-\nu)\beta(\partial_s^2\chi + \Theta'\partial_n\chi)\big\}\,\mathrm{d}s \\
&\qquad -\kappa\,(1-\nu)\,[\delta\chi\beta(\partial_s\partial_n\chi - \Theta'\partial_s\chi)]_{\Gamma_0}^{\Gamma_1},
\end{aligned}\tag{2.19}$$

where $\psi = \psi^{(0)} \in \Omega^{(0)}$ to distinguish the limits from the two opposing states.

Before we deduce the conditions that apply at each type of internal boundary, it will be beneficial to introduce the functional

$$I_{\Gamma}(\psi, u) = \int_{\Gamma}\int_{-h}^{-d_+} \langle\langle\psi\rangle\rangle u\ \mathrm{d}z\ \mathrm{d}s,$$

where u is an auxiliary function. This functional has first variation

$$\delta I_{\Gamma} = \int_{\Gamma}\int_{-h}^{-d_+} \{\langle\langle\delta\psi\rangle\rangle u + \langle\langle\psi\rangle\rangle\delta u\}\ \mathrm{d}z\ \mathrm{d}s. \tag{2.20}$$

Considering first the case of an internal boundary between two regions of connected ice, by enforcing the stationary condition $\delta(L_{\Omega_+} + L_{\Omega_-} - I_{\Gamma})$ along with the essential conditions

$$\langle\chi\rangle = \langle\partial_n\chi\rangle = 0, \tag{2.21a}$$

which ensures $\langle\delta\chi\rangle = \langle\partial_n\delta\chi\rangle = 0$, we obtain, by referring to (2.18), the natural conditions

$$\langle\langle\phi\rangle\rangle = \langle\langle\partial_n\phi\rangle\rangle = 0 \tag{2.21b}$$

and

$$\langle\mathfrak{M}\eta\rangle = \langle\mathfrak{S}\eta\rangle = 0, \tag{2.21c}$$

which must be satisfied by the stationary point on Γ. The essential conditions (2.21a) ensure continuity of the position and gradient of the ice and the natural conditions (2.21b) ensure continuity of fluid pressure and velocity. The quantities that appear in (2.21c) are defined by

$$\mathfrak{M}\eta \equiv \beta\nabla_h^2\eta - (1-\nu)\beta(\partial_s^2\eta + \Theta'(\partial_n\eta)), \tag{2.22a}$$

$$\begin{aligned}
\mathfrak{S}\eta \ \equiv\ & \partial_n(\beta\nabla_h^2\eta) - (1-\nu)\{(\partial_s^2\eta + \Theta'(\partial_n\eta))(\partial_n\beta) \\
& -2((\partial_s\partial_n\eta) - \Theta'(\partial_s\eta))(\partial_s\beta) - \beta\partial_s((\partial_s\partial_n\eta) - \Theta'(\partial_s\eta))\},
\end{aligned}\tag{2.22b}$$

and, respectively, represent the bending moment and shearing stress of the ice. If the ends, Γ_0 and Γ_1, of the internal boundary are finite and distinct, then the condition

$$\langle \beta(\partial_s \partial_n \chi - \Theta' \partial_s \chi) \rangle = 0, \tag{2.23}$$

applies at each of these points. This condition will not apply to any problems considered in this work.

If, instead, the internal boundary Γ separates ice-covered and ice-free regions then the stationary condition $\delta(L_\Omega + L^{(0)}_{\Omega^{(0)}} - I_\Gamma)$ provides, from (2.19) and (2.20), the natural conditions

$$\langle\langle \phi \rangle\rangle = \langle\langle \partial_n \phi \rangle\rangle = 0 \tag{2.24a}$$

$$\partial_n \phi^{(0)} = 0 \quad (x, y \in \Gamma, -d < z < 0), \tag{2.24b}$$

and

$$\mathfrak{M}\eta = \mathfrak{S}\eta = 0 \quad (x, y \in \Gamma), \tag{2.24c}$$

where we assume only that χ and $\partial_n \chi$ remain bounded along Γ and no essential conditions apply. If the contour is open and finite, for instance when it represents a crack or an edge of an open pool, there will also be corner conditions, which are akin to (2.23). However, in order to derive these conditions it is necessary to consider the limit from the opposing directions, and as this will not form part of our study we do not pursue this issue.

Condition (2.24b) states that there is no fluid flow from the ice-free domain through the submerged portion of the ice edge. For this form of internal boundary, the bending moment and shearing stress conditions now mean that both of these quantities vanish at the ice edge. These are the correct physical conditions applying at the edge on an ice sheet.

For both types of internal boundary, Γ, the auxiliary function u may be retrieved from

$$u = \partial_n \phi \quad (x, y \in \Gamma, -h < z < -d). \tag{2.25}$$

The use of the functional I_Γ was first proposed by Porter & Porter (2004) as a means of ensuring that the coupling between ice-covered and ice-free domains arises as a natural condition of the variational principle. We use it in a more wide ranging sense, so that it appears at the boundaries between regions of connected ice-cover. Through a straightforward modification it can be used for points at which discontinuities occur in the fluid boundaries between ice-covered states. Although, in all cases, the coupling of ϕ could be provided as an essential condition here, the use of I_Γ will have important ramifications for our solution method.

Finally, we note that an internal boundary need not necessarily define a set of points at which the geometry is not sufficiently smooth. The definition of an internal boundary in such situations is necessary; however, we may define an internal boundary along any contour and in doing so, partition the domain arbitrarily, linking the two sub-domains through jump conditions. Thus, we see that jump conditions apply at every point within the domain but are normally superceded by the governing equations (2.9a-c) or (2.11a-b). In our algebraic formulation of specific problems, it will prove to be benificial to partition the overall domain, regardless of whether the internal boundaries are necessitated by the particular geometrical properties.

2.3 Summary

On the basis of certain simplifying assumptions the problem of wave scattering by an ice sheet of varying thickness over an undulating bed has been formulated mathematically. Specifically, the motion of the system is described by a reduced velocity potential, ϕ, which exists within the fluid domain, and a reduced displacement function, η, which exists in ice-covered regions. These functions are unknowns that satisfy the governing equations (2.9a-c) when ice-cover is present and (2.11a-b) when the fluid is ice-free. At the interface between ice-covered and ice-free regions, solutions are connected through the lateral conditions (2.24a-c), and for any internal boundary within a connected ice-sheet the jump conditions (2.21a-c) apply. The boundary-value problem is completed by the imposition of the far-field behaviour of the solution, which is problem-specific.

All of the governing equations spoken of above arise as the natural conditions of a Hamiltonian formulation of the problem as a variational principle, so that the solution of the boundary-value problem coincides with the stationary point of a given functional. The correct joining conditions that apply at the internal boundaries were actually derived through this means, as the functionals contain all of the physical attributes that are required of the solution.

The formulation of the problem as a variational principle will provide the basis of our solution procedure, which will be outlined in the following chapter. Our motivation is that approximations to the stationary point of the functional are, clearly, approximations to the solution of the boundary-value problem. We may therefore utilise approximation methods that exist for variational principles.

Chapter 3

The multi-mode approximation

The set of governing equations (2.9a-c) is unsolvable by direct methods. Specifically, this is due to the presence of variations in the thickness of the ice and the fluid depth, and in particular that of the possibility of an undulating lower surface of the ice. This prevents, for instance, application of the Green's function method of solution that is utilised by Williams (2006), in the case of a horizontal bed and the assumption of a zero draught.

Our objective will be to create a sequence of increasingly accurate approximations, so that the full linear solution may be obtained to any degree of accuracy. Such approximations may be obtained in a number of ways; our chosen method is to restrict the vertical motion of the reduced velocity potential to a finite-dimensional space, seeking a solution of the form

$$\phi(x,y,z) \approx \psi_N(x,y,z) = \sum_{i=0}^{N} \varphi_i(x,y) w_i(x,y,z), \tag{3.1}$$

where the dimension $(N+1)$ and the *vertical modes* w_i $(i = 0, \ldots, N)$ are user-defined. The functions φ_i $(i = 0, \ldots, N)$ are unknowns that must be calculated by some means. For the remainder of our work, we will describe ψ_N as the *multi-mode approximation* (MMA). The specific choice of the vertical modes in the MMA is an important one and will be dealt with in §3.2.

In order to generate an approximation of the form (3.1), we make use of the variational principle derived in §2.2. If the argument ψ of the functional L_Ω (or $L^{(0)}_{\Omega^{(0)}}$) is restricted to be only functions of the form ψ_N, then by seeking the stationary point of the functionals over this restricted space we determine an approximation to the unrestricted stationary point and hence an approximation to the full linear solution of the boundary-value problem outlined in §2.1. The reduction of a variational principle to a chosen finite-dimensional subspace is known as the Rayleigh-Ritz method. We are therefore applying the Rayleigh-Ritz method to the coordinate z, using the *trial space* $\{w_0, \ldots, w_N\}$.

We expect that as the dimension, N, of the trial space is increased, through the inclusion of additional modes, the accuracy of our approximation will be improved. This property may be established in some settings, such as that of integral operator theory (see Porter & Stirling, 1990). In principle it is possible to convert the current problem into one involving integral equations, in which case we could obtain the assurance that by expanding our trial space we will gain a more accurate result. However, this conversion constitutes a substantial undertaking and we are content to rely on numerical support for the validity of this connection in the present work.

3.1 The governing equations of the MMA

The governing equations of the MMA, in a domain of ice-covered fluid, Ω, are generated by applying the stationary condition $\delta L_{\Omega} = 0$ in conjunction with the restriction of ψ to the form (3.1). Likewise, the governing equations of the MMA in a domain of ice-free fluid, $\Omega^{(0)}$, are generated through $\delta L^{(0)}_{\Omega^{(0)}} = 0$ in conjunction with the same restriction to ψ (although we will define different modes for this situation). We note at this juncture that approximations to the reduced displacement function, $\chi \approx \eta$, in domains of ice-covered fluid, are generated indirectly through this method. That is, the reduced displacement is only approximated through its relationship to the velocity potential.

We initially consider the case of a region of ice-covered fluid. Substituting the restricted version of ψ into L_{Ω} and noting that it has the variation

$$\delta\psi = \sum_{i=0}^{N} (\delta\varphi_i) w_i,$$

we find that, since the w_i are known, the stationary condition is

$$\begin{aligned} -\sum_{j=0}^{N} \iint_{\Omega} \delta\varphi_j \Big\{ \int_{-h}^{-d} w_j \sum_{i=0}^{N} (\nabla^2 + \partial_z^2)(\varphi_i w_i) \, \mathrm{d}z + \kappa\chi[w_j]_{z=-d} & \\ + \Big[w_j \sum_{i=0}^{N} \{\nabla z \cdot \nabla(\varphi_i w_i) - \varphi_i(\partial_z w_i)\}\Big]_{z=-h}^{-d} \Big\} \, \mathrm{d}x \, \mathrm{d}y & \\ + \kappa \iint_{\Omega} \delta\chi \big\{ (1 - \kappa\alpha)\chi + \mathscr{L}\chi - \sum_{i=0}^{N} \varphi_i [w_i]_{z=-d} \big\} \, \mathrm{d}x \, \mathrm{d}y &= 0, \end{aligned}$$

where, for the present, it has been assumed that the boundary $\delta\Omega \times [-h, -d]$ is in the far-field and can therefore be disregarded. It follows that the functional $L_{\Omega}(\psi, \chi)$ is stationary with respect to the variation $\delta\psi$ satisfying the boundary restriction (2.15) provided that the set of $(N+1)$ second-order partial differential equations

$$\int_{-h}^{-d} w_j \sum_{i=0}^{N} \nabla^2(\varphi_i w_i)\,\mathrm{d}z + \kappa\chi[w_j]_{z=-d} + \left[w_j \sum_{i=0}^{N} \{\nabla z \cdot \nabla(\varphi_i w_i) - \varphi_i(\partial_z w_i)\} \right]_{z=-h}^{-d} = 0 \tag{3.2}$$

is satisfied for $j = 0, \ldots, N$. Equations (3.2) may be simplified, by using the identity

$$\begin{aligned}\int_{-h}^{-d} w_j \nabla^2(w_i\varphi_i)\,\mathrm{d}z &= \int_{-h}^{-d} w_j(\nabla w_i)\cdot(\nabla\varphi_i) - (\nabla w_j)\cdot(w_i\nabla\varphi_i + \varphi_i\nabla w_i)\,\mathrm{d}z \\ &\quad - [w_j\nabla z\cdot\nabla(w_i\varphi_i)]_{z=-h}^{-d} + \nabla\cdot\left\{\int_{-h}^{-d} w_j w_i\,\mathrm{d}z\right\}\nabla\varphi_i + \left\{\nabla_h\cdot\int_{-h}^{-d} w_j(\nabla w_i)\,\mathrm{d}z\right\}\varphi_i,\end{aligned}$$

to

$$\sum_{i=0}^{N}\Big\{\nabla\cdot(a_{j,i}\nabla\varphi_i) + \tilde{\mathbf{d}}_{j,i}\cdot(\nabla\varphi_i) + b_{j,i}\varphi_i\Big\} + \kappa\chi[w_j]_{z=-d} = 0, \tag{3.3a}$$

where

$$a_{j,i} = \int_{-h}^{-d} w_j w_i\,\mathrm{d}z, \quad \tilde{\mathbf{d}}_{j,i} = \int_{-h}^{-d} \{w_j(\nabla w_i) - w_i(\nabla w_j)\}\,\mathrm{d}z,$$

and

$$b_{j,i} = \int_{-h}^{-d} w_j(\partial_z^2 w_i)\,\mathrm{d}z - [w_j(\partial_z w_i)]_{z=-h}^{-d} + \nabla\cdot\int_{-h}^{-d} w_j(\nabla w_i)\,\mathrm{d}z - \int_{-h}^{-d}(\nabla w_j)\cdot(\nabla w_i)\,\mathrm{d}z.$$

With respect to the variation $\delta\chi$, subject to the far-field restrictions (2.15), we have that the stationary point must further satisfy the fourth-order partial differential equation

$$(1-\kappa\alpha)\chi + \mathscr{L}\chi - \sum_{i=0}^{N}\varphi_i[w_i]_{z=-d} = 0. \tag{3.3b}$$

Equations (3.3a-b) thus govern the MMA over domains of ice-covered fluid and are to be solved for φ_i ($i = 0, \ldots, N$) and χ. These functions are dependent on the horizontal coordinates x and y only.

Our ability to assume that the arbitrary variations of ψ and χ, over the restricted space, should satisfy (2.15) is dependent on our choice of trial space. In particular, in the far-fields, we will always include the vertical mode that supports the propagating waves that contribute the only motion that exists in that limit. Our approximations will therefore maintain the exact form of the full linear solution in the far-fields.

Through the combination of an approximation of the form (3.1) with a variational principle we have succeeded in generating a new set of governing equations (3.3a-b) that are independent of the vertical coordinate, z. The elimination of a geometrical dimension contributes an enormous reduction in the complexity of the problem. Moreover, the dependence of the approximation on the vertical structure, and hence the choice of trial space, has been condensed into the coefficients through a process of vertical averaging. In particular, the difficulty of undulating vertical boundaries has been removed and the problem outlined in §2 had become manageable.

Similarly, in situations of ice-free fluid, the governing equations of the MMA may be deduced to be the set of $(N+1)$ second-order differential equations

$$\sum_{i=0}^{N} \Big\{ \nabla\cdot(a_{j,i}^{(0)}\nabla\varphi_i) + \widetilde{\mathbf{d}}_{j,i}^{(0)}\cdot(\nabla\varphi_i) + b_{j,i}^{(0)}\varphi_i \Big\} = 0 \quad (j=0,\ldots,N), \tag{3.4}$$

which are to be solved for the functions φ_i $(i=0,\ldots,N)$. The coefficients are defined as

$$a_{j,i}^{(0)} = \int_{-h}^{0} w_j w_i \,\mathrm{d}z, \quad \widetilde{\mathbf{d}}_{j,i}^{(0)} = \int_{-h}^{0} \{w_j(\nabla w_i) - w_i(\nabla w_j)\}\,\mathrm{d}z,$$

and

$$b_{j,i}^{(0)} = \int_{-h}^{0} w_j(\partial_z^2 w_i)\,\mathrm{d}z - [w_j(\partial_z w_i)]_{z=-h} + \nabla\cdot\int_{-h}^{0} w_j(\nabla w_i)\,\mathrm{d}z - \int_{-h}^{0}(\nabla w_j)\cdot(\nabla w_i)\,\mathrm{d}z.$$

For convenience, the system of equations (3.3a) will often be written as the more compact matrix equation

$$\nabla\cdot(A\nabla\mathbf{\Phi}_N) + \widetilde{D}\cdot(\nabla\mathbf{\Phi}_N) + B\mathbf{\Phi}_N + \kappa\chi C\mathbf{f} = 0, \tag{3.5}$$

where $\mathbf{\Phi}_N = (\varphi_0,\ldots,\varphi_N)^T$, $C = \mathrm{diag}\{[w_0]_{z=-d},\ldots,[w_N]_{z=-d}\}$, and $\mathbf{f} = (1,\ldots,1)^T$, while $A_{j,i} = a_{j-1,i-1}$, $B_{j,i} = b_{j-1,i-1}$ and $\widetilde{D}_{j,i} = \widetilde{\mathbf{d}}_{j-1,i-1}$ for $i,j = 1,\ldots,N+1$. Equivalently, the expression

$$\nabla\cdot(A^{(0)}\nabla\mathbf{\Phi}_N) + \widetilde{D}^{(0)}\cdot(\nabla\mathbf{\Phi}_N) + B^{(0)}\mathbf{\Phi}_N = 0, \tag{3.6}$$

will, on occasion, be used in place of (3.4), with the matrices defined analogously to those appearing in (3.5).

3.1.1 Jump conditions of the MMA

The conditions that must be satisfied by the MMA along any internal boundary, Γ, may be calculated through the same analysis used for the full linear solution in §2.2.1.

We begin by considering an internal boundary, Γ, that partitions a domain of ice-covered fluid Ω into Ω_+ and Ω_-. It is necessary to employ an approximation for the auxiliary function, u, introduced through the functional I_Γ in §2.2.1, which is consistent with the MMA, and so write

$$u \approx \sum_{i=0}^{N} u_i(x,y)v_i(x,y,z), \quad \delta u = \sum_{i=0}^{N} (\delta u_i) v_i,$$

where the modes v_i are supposed given but will be left unspecified for the present. With the restrictions to both ψ and u in place, the contribution of the variational principle $\delta(L_{\Omega_+} + L_{\Omega_-} - I_\Gamma) = 0$ on Γ gives

$$\begin{aligned} &\sum_{j=0}^{N}\sum_{i=0}^{N} \int_\Gamma \left\langle \int_{-h}^{-d} \{\delta\varphi_j w_j \left(\partial_n(\varphi_i w_i) - \tilde{u}_i v_i\right) - \delta u_j v_j w_i \varphi_i\} \, \mathrm{d}z \right\rangle \mathrm{d}s \\ &+ \kappa \int_\Gamma \langle \partial_n(\delta\chi)\mathfrak{M}\chi - \delta\chi\mathfrak{S}\chi \rangle \, \mathrm{d}s - \kappa\,(1-\nu)\left[\,\langle \delta\chi\beta(\partial_s\partial_n\chi - \Theta'\partial_s\chi)\rangle\,\right]_{\Gamma_0}^{\Gamma_1} \;=\; 0. \end{aligned}$$

For arbitrary variations $(\delta\psi)_\pm$ and $\delta\tilde{u}$, we deduce natural conditions, which are most conveniently given in the matrix form,

$$(V^T\mathbf{\Phi}_N)_+ = (V^T\mathbf{\Phi}_N)_-, \tag{3.7a}$$

and

$$(A\partial_n\mathbf{\Phi}_N)_\pm + (Q\mathbf{\Phi}_N)_\pm = V_\pm\mathbf{u}, \tag{3.7b}$$

where

$$Q_{m+1,n+1} = \int_{-h}^{-d} w_m \partial_n w_n \, \mathrm{d}z \quad (m,n = 0,\ldots,N), \tag{3.8}$$

$$V_{j+1,i+1} = v_{j,i} = \int_{-h}^{-d} w_j v_i \, \mathrm{d}z \quad (i,j = 0,\ldots,N), \tag{3.9}$$

and $\mathbf{u} = (u_0,\ldots,u_N)^T$. It is not necessary to explicitly calculate the auxiliary functions u_i $(i = 0,\ldots,N)$ and we therefore recast conditions (3.7b) as

$$V_+^{-1}\{(A\partial_n\mathbf{\Phi}_N)_+ + (Q\mathbf{\Phi}_N)_+\} = V_-^{-1}\{(A\partial_n\mathbf{\Phi}_N)_- + (Q\mathbf{\Phi}_N)_-\}, \tag{3.10}$$

where we have assumed that $V_\pm$ are invertible. It is possible that the relative choice of modes, w_i and v_i $(i = 0,\ldots,N)$, and particular geometrical parameters will cause the matrices $V_\pm$ to be singular; however, this is an unlikely scenario and has never proved to be an issue. Furthermore, we note that, if the geometry is continuous across Γ, the matrices $V_\pm$ satisfy $V_+ = V_-$. Retaining the essential conditions $\langle\chi\rangle = \langle\partial_n\chi\rangle = 0$, for arbitrary variations $\delta\chi$ and $\partial_n\delta\chi$, we find that the equations for continuity of bending moment and shearing stress, (2.21c), apply, as does the end-point condition (2.23). This is to be expected as the reduced displacement function is only indirectly approximated. The complete set of conditions to be satisfied by the MMA at a boundary dividing ice-covered states is given by (3.7a), (3.10), (2.21c) and the end-point condition (2.23).

Now suppose that the internal boundary Γ separates a region of ice-free fluid, $\Omega^{(0)}$, from a domain of ice-covered fluid, Ω. We will distinguish the MMA in the ice-free region through use of the superscript (0), that is,

$$\phi \equiv \phi^{(0)} \approx \psi_N^{(0)} = \sum_{i=0}^{N} \varphi_i^{(0)}(x,y) w_i^{(0)}(x,y,z) \quad (x,y \in \Omega^{(0)}).$$

The contribution of the variational principle $\delta(L_\Omega + L_{\Omega^{(0)}}^{(0)} - I_\Gamma) = 0$ along this interface implies

$$\begin{aligned} \sum_{j=0}^{N}\sum_{i=0}^{N} \int_\Gamma \Bigg\{ \int_{-h}^{-d} \{\delta\varphi_j w_j \left(\partial_n(\varphi_i w_i) - \widetilde{u}_i v_i\right) - \delta u_j v_j w_i \varphi_i\} \,\mathrm{d}z & \\ - \int_{-h}^{0} \{\delta\varphi_j^{(0)} w_j^{(0)} \left(\partial_n(\varphi_i^{(0)} w_i^{(0)}) - \widetilde{u}_i v_i\right) - \delta u_j v_j w_i^{(0)} \varphi_i^{(0)}\} \,\mathrm{d}z \Bigg\} \mathrm{d}s & \\ + \kappa \int_\Gamma \{\partial_n(\delta\chi)\mathfrak{M}\chi - \delta\chi\mathfrak{S}\chi\}\mathrm{d}s - \kappa\,(1-\nu)\,[\delta\chi\beta(\partial_s\partial_n\chi - \Theta'\partial_s\chi)]_{\Gamma_0}^{\Gamma_1} &= 0. \end{aligned}$$

The natural conditions

$$V^T \mathbf{\Phi}_N = (V^T \mathbf{\Phi}_N)^{(0)}, \tag{3.11a}$$

and

$$V^{-1} A \partial_n \mathbf{\Phi}_N + Q \mathbf{\Phi}_N = \{V^{-1} A \partial_n \mathbf{\Phi}_N + Q \mathbf{\Phi}_N\}^{(0)}, \tag{3.11b}$$

therefore apply across Γ. Note that, due to the assumption that $D \neq 0$ at the ice edge, $V \neq V^{(0)}$. For the approximate reduced displacement function, χ, the vanishing of bending moment and shearing stress conditions (2.24c) apply and there is the possibility of an end-point condition (see §2.2.1). The complete set of conditions to be satisfied by the MMA at an internal boundary that defines the interface between ice-covered and ice-free states is thus given by (3.11a-b), (2.24c) and the end-point condition.

We have succeeded in reducing the problem formulated in §2 to the calculation of a finite set of two-dimensional functions. This was achieved by restricting the vertical motion to a chosen (although, as yet undefined) finite-dimensional space. Application of the variational principle over this restricted space generates a new set of governing equations, from which the coordinate z has been removed through a process of vertical averaging. Our task, before we are able to implement this approximation, is now to make a judicious selection of the vertical modes that form the trial space. This is the subject of the next section.

3.2 Vertical Modes

The purpose of our work is in producing a sequence of increasingly accurate approximations to the full linear solution. We wish to balance this degree of accuracy with the computational effort undergone to achieve it. Primarily, the computational effort is dependent on the required dimension, N, of the approximation. Our remaining control over the MMA is through the choice of the vertical modes, w_i $(i = 0, \ldots, N)$. By judiciously selecting these vertical modes we will obtain approximations that reproduce the key qualitative and quantitative properties of the full linear solution with relatively few vertical modes.

If the geometrical configuration is uniform, such that the functions D, h and d are all constant, it is possible to solve the full linear problem (2.9a-c) by seeking separation solutions of the form $\phi(x, y, z) = X(x, y)Z(z)$. Through this approach, we obtain the representation of the full linear solution

$$\phi(x, y, z) = \sum_{i=0}^{\infty} \phi_i(x, y) \cosh k_i(z + h), \tag{3.12}$$

from which it is possible to obtain an expression for the reduced displacement, η. In (3.12), the vertical dependence of ϕ is defined through the hyperbolic functions $\cosh k_i(z + h)$ $(i = 0, \ldots)$, where the quantities k_i $(i = 0, \ldots)$ are the roots of the *(ice-covered) dispersion relation*

$$(1 - \kappa\alpha + \beta k^4)k \tanh kH = \kappa, \tag{3.13}$$

ordered in a way that will be discussed presently. Note that the quantities that appear in (3.13) are dependent on the harmonic frequency (through κ) and on the vertical distances D (through α and β) and H. A proof of the completeness of the expansion set that appears in (3.12) is given in Evans & Porter (2003).

The first mode $(i = 0)$ of expression (3.12) will represent the propagating waves of the solution. As we expect that the presence of a geometrical impediment will have the effect of modulating propagating waves and activating (to some degree) the remaining modes, we conjecture that a MMA of the form

$$\psi_N(x, y, z) = \sum_{i=0}^{N} \varphi_i(x, y) \cosh\{k_i(x, y)(z + h(x, y))\} \tag{3.14}$$

will provide a good approximation, for relatively small dimensions, to the exact solution ϕ, in regions where all fluid and ice boundaries are fully variable. We therefore define the *natural (vertical) modes* as

$$w_i(x, y, z) = \varpi_i(x, y) \cosh\{k_i(x, y)(z + h(x, y))\} \quad (i = 0, \ldots), \tag{3.15}$$

where ϖ_i $(i = 0, \ldots)$ is a *weight function* that is included for algebraic convenience and will be defined at the appropriate juncture. At each horizontal point (x, y), the roots k_i satisfy the dispersion relation (3.13) generated by the particular geometrical values D and H at (x, y). As such, they may equivalently be regarded as functions of (D, H). Subsequently, the natural vertical modes become functions of (D, h, d, z), so that they are dependent on the position of the fluid surfaces as well as the vertical distances. To emphasise the alternative dependences of the modes, we write

$$w_i(x, y, z) \equiv W_i(D, h, d, z) \quad (i = 0, \ldots, N).$$

In a region of ice-free fluid, we define the roots $k_i \equiv k_i^{(0)}$ to be the zeros of the free-surface dispersion relation

$$k^{(0)} \tanh k^{(0)} h = \kappa, \tag{3.16}$$

whose geometrical dependence is on the local fluid depth $h(x, y)$. The corresponding natural modes are

$$w_i^{(0)}(x, y, z) = \varpi_i^{(0)}(x, y) \cosh\{k_i^{(0)}(x, y)(z + h(x, y))\} \quad (i = 0, \ldots), \tag{3.17}$$

and may be taken to be functions of h and z, and we write $w_i^{(0)}(x, y, z) \equiv W_i^{(0)}(h, z)$ $(i = 0, \ldots, N)$.

It is appropriate to note at this juncture that, due to the dependence of the natural vertical modes on the geometry, any discontinuities in the structure will be manifest in the approximation. In particular, consider the interface between ice-covered and ice-free regions. At this point, the trial space will switch between $\{w_0, \ldots, w_N\}$ and $\{w_0^{(0)}, \ldots, w_N^{(0)}\}$. Consequently, it is not possible to ensure continuity of the MMA, throughout the fluid depth, at this interface. The same is true of any internal boundary over which the geometry is discontinuous. This provides the motivation for the use of the functional I_Γ, which is utilised to convert the condition $\langle\langle \psi \rangle\rangle = 0$ from essential to natural. That is, the condition $\langle\langle \psi_N \rangle\rangle = 0$ cannot be imposed, but is rather satisfied approximately as a natural condition.

Based on condition (2.25), we choose the vertical modes of the auxiliary function u to be $v_i = \cosh\{k_i(z + h)\}$ $(i = 0, \ldots, N)$. It is noted that, relative to our choice of vertical modes w_i and $w_i^{(0)}$, there may exist a more efficient choice of these modes. That is, there may be a choice that better balances the discontinuity across the internal boundary. Porter & Porter (2004) used an averaging method for their single-mode approximation; however, it was shown in Bennetts *et al.* (2007) that, for a particular problem, this does not improve accuracy. Furthermore, it is not possible to extend this method to a multi-mode approximation.

3.2.1 Coefficients of the MMA

Having made a suitable choice for the vertical modes that define the trial space for the MMA, we are able to explicitly calculate the coefficients that appear in the governing equations (3.3a) and (3.4) and the jump conditions (3.7a-b) and (3.11a-b). To ease calculations we utilise the dependence of the vertical modes, (3.15) and (3.17), on the geometrical functions. This is achieved by using the chain rule on the derivative operator to give

$$\nabla \equiv (\nabla D)\partial_D + (\nabla h)\partial_h + (\nabla d)\partial_d. \tag{3.18}$$

We note here that the equivalent transformation in Porter & Porter (2004) was made in terms of the vertical distances D and H only. The resulting approximations thus neglected variations to the fluid-ice interface d. In particular, this led to spurious results for non-constant d and the variations in this interface that appear in their work must be reinterpreted as equivalent variations in the bed and the upper surface of the ice.

It is possible to make the transformation, (3.18), from cartesian to geometrical coordinates, providing that the geometrical coordinate system fully describes the construction, including the positions of the horizontal interfaces. In ice-free regions transformation (3.18) reduces to

$$\nabla \equiv (\nabla h)\partial_h.$$

In terms of the inner-product notation

$$(f, g) = \int_{-h}^{-d} fg \; \mathrm{d}z, \qquad (f, g)^{(0)} = \int_{-h}^{0} fg \; \mathrm{d}z, \tag{3.19}$$

we express the coefficients involved in the governing equations of ice-free and ice-covered fluid as

$$a_{i,j} = (W_i, W_j), \quad a^{(0)}_{i,j} = (W_i, W_j)^{(0)}, \tag{3.20}$$

$$\widetilde{\mathbf{d}}_{j,i} = (P^{(D)}_{j,i} - P^{(D)}_{i,j})\nabla D + (P^{(h)}_{j,i} - P^{(h)}_{i,j})\nabla h + (P^{(d)}_{j,i} - P^{(d)}_{i,j})\nabla d,$$

$$\widetilde{\mathbf{d}}^{(0)}_{j,i} = (P^{(0)}_{j,i} - P^{(0)}_{i,j})\nabla h,$$

where we have written

$$P^{(X)}_{j,i} = (\partial_X W_i, W_j) \quad \text{for } X = D, h, d,$$

and

$$P^{(0)}_{j,i} = (\partial_h W^{(0)}_i, W^{(0)}_j)^{(0)}.$$

The remaining coefficients are defined as

$$\begin{aligned} b_{j,i} \; = \; & k_i^2 a_{j,i} - k_j \sinh(k_j H)\cosh(k_i H) + P_{j,i}^{(D)}\nabla^2 D + P_{j,i}^{(h)}\nabla^2 h + P_{j,i}^{(d)}\nabla^2 d \\ & + P_{j,i}^{(D,D)}(\nabla D)^2 + P_{j,i}^{(h,h)}(\nabla h)^2 + P_{j,i}^{(d,d)}(\nabla d)^2 \\ & + (P_{j,i}^{(D,h)} + P_{j,i}^{(h,D)})(\nabla D)\cdot(\nabla h) + (P_{j,i}^{(D,d)} + P_{j,i}^{(d,D)})(\nabla D)\cdot(\nabla d) \\ & + (P_{j,i}^{(d,h)} + P_{j,i}^{(h,d)})(\nabla d)\cdot(\nabla h), \end{aligned}$$

and

$$b_{j,i}^{(0)} \; = \; (k_i^{(0)})^2 a_{j,i}^{(0)} + P_{j,i}^{(0)}\nabla^2 h + P_{j,i}^{(0,0)}(\nabla h)^2,$$

with

$$P_{j,i}^{(X,Y)} = \partial_Y(\partial_X W_i, W_j) - (\partial_Y W_i, \partial_X W_j), \quad \text{for } X, Y = D, h, d,$$

and

$$P_{j,i}^{(0,0)} = \partial_h(\partial_h W_i^{(0)}, W_j^{(0)})^{(0)} - (\partial_h W_i^{(0)}, \partial_h W_j^{(0)})^{(0)},$$

and where we have used the properties $\partial_z^2 w_i = k_i^2 w_i$ and $[\partial_z w_i]_{z=-h} = 0$ of the vertical modes, and similarly for the ice-free modes. Using the same notation, the coefficients in the jump conditions are calculated via

$$v_{j+1,i+1} = (W_j, V_i), \quad v_{j+1,i+1}^{(0)} = (W_j^{(0)}, V_i), \tag{3.21}$$

and

$$Q_{j+1,i+1} = P_{j,i}^{(D)}\nabla D + P_{j,i}^{(h)}\nabla h + P_{j,i}^{(d)}\nabla d, \quad Q_{j+1,i+1}^{(0)} = P_{j,i}^{(0)}\nabla h,$$

where, in the same manner as we used for the vertical modes w_i and $w_i^{(0)}$, we have enforced the dependence of the modes v_i to be on the geometrical variables by writing $v_i(x, y, z) \equiv V_i(D, h, d, z)$ $(i = 0, \ldots, N)$.

Explicit calculations of the inner-products that appear in the above expressions are rather lengthy and for this reason are given separately in Appendix A. We note here that, with respect to the inner-products (3.19), the natural modes are non-orthogonal in ice-covered regions but are orthogonal in ice-free regions.

3.2.2 The roots of the dispersion relation

The roots of the dispersion relation (3.13) are of fundamental importance to the natural modes (3.15) and consequently to the MMA. In this section we investigate these roots and discover their properties to be non-trivial. We also discuss how they may be ordered.

To begin with though, we conduct a review of the roots of the free-surface dispersion relation (3.16), whose properties are comparatively simple. Each of the roots comes in a $\pm k^{(0)}$ pair and it is, therefore, only necessary to consider those that appear in the complex domain $k^{(0)} \in \mathbb{C}_1$ such that $\mathbb{C}_1 = \{R\mathrm{e}^{\mathrm{i}\theta} : R > 0, 0 \leq \theta < \pi\}$. In this domain, there exists a unique positive real root, which we denote $k_0^{(0)}$, whose corresponding vertical mode, $w_0^{(0)}$, supports *propagating waves* in regions of uniform fluid depth. The only waves that will exist in the far-fields are these propagating waves. By selecting the primary mode in our trial space to be that which supports these waves, we ensure that the exact form of the radiation conditions is mirrored exactly by the MMA, which is a requirement of our solution procedure.

There are also infinitely many purely imaginary roots, $k_n^{(0)}$ $(n = 1, \dots)$, ordered in ascending magnitude, and such that the inequality

$$\mathrm{i}\frac{(n-1)\pi}{h} < k_n^{(0)} < \mathrm{i}\frac{n\pi}{h} \quad (n = 1, \dots), \tag{3.22}$$

holds. In regions of uniform fluid depth, these purely imaginary roots support *evanescent waves* that attenuate exponentially according to the magnitude of the root. As they increase in magnitude, it is easily deduced that the purely imaginary roots approach the upper limit of (3.22), such that

$$k_n^{(0)}h = \mathrm{i}n\pi + \mathrm{O}(n^{-1}) \quad (n \to \infty). \tag{3.23}$$

We now turn to the roots of the ice-covered dispersion relation (3.13). Parallels run with the free-surface dispersion relation. Again, the roots come in $\pm k$ pairs and we restrict our attention to complex domain $k \in \mathbb{C}_1$. It will also be helpful to note that roots come in conjugate pairs, so that if one complex root k is present in $\mathbb{C}_1$ then a second, $-\overline{k} \in \mathbb{C}_1$, necessarily exists.

There is always one positive, real root of the dispersion relation (3.13), which we denote k_0. It can be shown that this root lies in the interval $(0, \mathcal{U})$, where $\mathcal{U} = \max\{\kappa \coth(\kappa), \kappa H^{-1}, (\kappa\alpha\beta^{-1})^{1/4}\}$, and it is therefore easily found numerically. In a region of uniform geometry, the corresponding vertical mode, w_0, supports propagating waves of length $\lambda = 2\pi/k_0$. Comments pertaining to the satisfaction of the radiation conditions in the far-field are again applicable.

The real root of the ice-covered dispersion relation, k_0, is typically smaller than that of the free-surface dispersion relation, $k_0^{(0)}$; however, for small angular frequencies $k_0 \approx k_0^{(0)}$. In figure 5.10(a) a graphical representation of the relationship between the respective roots is given for some example ice thicknesses and a typical range of frequencies. If the angular frequency is reasonably large we find that

$$k_0^{(0)} \approx \kappa, \quad k_0 \approx \left(\frac{\kappa\alpha}{\beta}\right)^{1/4}.$$

Thus, as the angular frequency (and hence κ) increases, so does the difference between these two roots.

Through application of the principle of the argument, it has been shown by Evans & Davies (1968) and Chung & Fox (2002) that the complex region $\mathbb{C}_2 = \{Re^{\mathrm{i}\theta} : 0 < R < n\pi/H, \pi/2 \leq \theta < 3\pi/2\}$ contains $(n+2)$ roots of the dispersion relation. In this aspect, the structure of the roots of the ice-covered dispersion relation differs from that of the free-surface dispersion relation, which has only n roots - its purely imaginary roots - in the analogous region.

Let us consider the possibility of purely imaginary roots. If we choose to write the roots as $k = \mathrm{i}\sigma$, such that $\sigma > 0$, then the dispersion relation may be given in the form

$$(1 - \kappa\alpha + \beta\sigma^4)\sigma = -\kappa \cot(\sigma H). \tag{3.24}$$

This expression makes it clear that at least one root, $\sigma_n = -\mathrm{i}k_n$, lies on each branch of $\cot(\sigma H)$, that is, in the interval (π_{n-1}, π_n), such that $\pi_n = n\pi/H$. In regions of uniform geometry, the corresponding vertical modes, w_n, support evanescent waves. These purely imaginary roots are (typically) simple and therefore account for n of the roots to be found in $\mathbb{C}_2$. As with the purely imaginary roots of the free-surface dispersion relation, the limit

$$k_n H = \mathrm{i}n\pi + \mathrm{O}(n^{-5}) \quad (n \to \infty), \tag{3.25}$$

is easily verified. Comparing (3.25) with (3.23) we see that the purely imaginary roots of the ice-covered dispersion relation attain their limit more rapidly and, taking $H = h$, are, in general, larger in magnitude than their free-surface counterparts.

We will describe the two remaining roots as *complex roots* and denote them $k_{-i} = \mu_i$ $(i = 1, 2)$. The full linear solution (3.12) and MMA (3.14) are therefore recast, in regions of ice-covered fluid, as

$$\phi = \sum_{i=-2}^{\infty} \phi_i \cosh\{k_i(z+h)\}, \quad \psi_{N+2} = \sum_{i=-2}^{N} \varphi_i w_i, \tag{3.26}$$

respectively. For most values of α, β, H and κ, the roots μ_i $(i = 1, 2)$ lie away from the imaginary axis, in which case $\mu_2 = -\overline{\mu}_1$. In intervals of uniform geometry, the corresponding modes support waves that attenuate as they propagate. Note that, as $\mu_i \in \mathbb{C}_2$, $\Im\mathrm{m}(|\mu_i|) > \Re\mathrm{e}(|\mu_i|)$. It is also possible that particular combinations of parameters produce values of μ_i that lie on the purely imaginary axis, occupying the same interval (π_{n-1}, π_n) of $\cot(\sigma H)$. The relationship between the values α, β, H and κ for which the complex roots bifurcate between these two states is significant to their rôle in the MMA and form the investigation of the subsequent section.

Bifurcations

A coalescence occurs at the point at which the complex roots, μ_i $(i = 1, 2)$, switch between being fully complex reflections of one another in the imaginary axis to being purely imaginary and being related only in that they exist on the same segment of the imaginary axis. A comprehensive study of the circumstances under which a bifurcation is created is conducted in Appendix B of Williams (2006). The following account, although closely linked, differs from that of Williams in its method and in that its intent is towards the use of the roots in the MMA.

The point at which the complex roots bifurcate between the two states described arises when a double root of the dispersion relation (3.24) occurs. Differentiating (3.24) with respect to σ, we deduce that a multiple root must satisfy

$$(1 - \kappa\alpha + 5\beta\sigma^4)\sigma = \kappa\sigma H \csc^2(\sigma H), \tag{3.27}$$

in addition to (3.24). Equations (3.24) and (3.27) may be rewritten

$$(A + B\sigma^4)\sigma = -\cot(\sigma H), \quad (A + 5B\sigma^4)\sigma = \sigma H \csc^2(\sigma H), \tag{3.28}$$

where

$$A = (1 - \kappa\alpha)/\kappa, \quad B = \beta/\kappa. \tag{3.29}$$

Isolating the factor $A\sigma$ in both expressions involved in (3.28) and equating leads to

$$-B\sigma^5 - \cot(\sigma H) = -5B\sigma^5 + \sigma H \csc^2(\sigma H)$$

which may be rearranged to give

$$4B\sigma^5 = \cot(\sigma H) + \sigma H \csc^2(\sigma H) \tag{3.30a}$$

and so

$$A\sigma = (A^5/4B)^{1/5}\{\cot(\sigma H) + \sigma H \csc^2(\sigma H)\}^{1/5}. \tag{3.30b}$$

Substituting expressions (3.30a-b) into the left hand equation of (3.28) and rearranging produces the equation

$$f_a(\hat{\sigma} : \hat{C}) \equiv 5\sin(\hat{\sigma}) + \hat{\sigma} + \hat{C}\{(1 - \cos(\hat{\sigma}))^4(\sin(\hat{\sigma}) + \hat{\sigma})\}^{1/5} = 0, \tag{3.31}$$

where $\hat{C}^5 \equiv 2^8 A^5/B$ and $\hat{\sigma} \equiv 2\sigma H$. The function f_a is an increasing, oscillatory function of the positive real variable $\hat{\sigma}$. The existence of zeros, $\hat{\sigma}$, is dependent on the value of the parameter $\hat{C}$, which, in turn, depends on the properties of the ice and also the incident wave through (3.29).

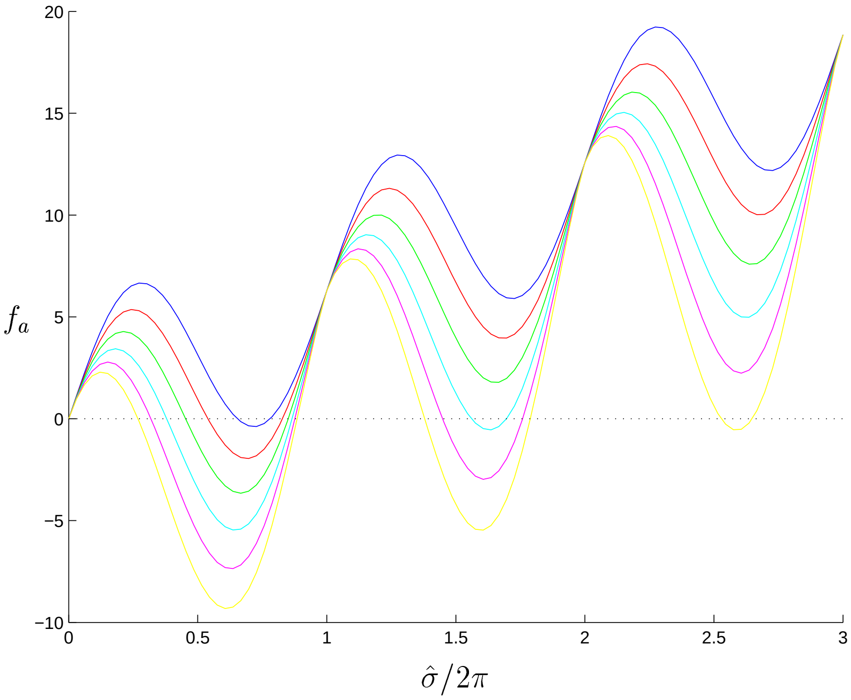

Figure 3.1: The function f_a given in equation (3.31), as a function of $\hat{\sigma}/2\pi$ for the parameter values $\hat{C} = 0$ (blue curve), $\hat{C} = -1$ (red), $\hat{C} = -2$ (green), $\hat{C} = -3$ (cyan), $\hat{C} = -4$ (magenta) and $\hat{C} = -5$ (yellow).

In figure 3.1, the function f_a is plotted in the interval $\hat{\sigma} \in (0, 6\pi)$, for the range of values of the parameter $\hat{C} \in [-5, 0] \cap \mathbb{Z}$. Decreasing the value of $\hat{C}$ has the effect of translating the curve f downwards, in doing so increasing the prevalence of zeros. For each interval (π_n, π_{n+1}) $(n = 0, 1, \dots)$ an oscillatory cycle occurs and there is the possibility of 2 isolated zeros, a single double zero or no zeros. If zeros exist in the interval (π_n, π_{n+1}) for $n = n_0$ then roots exist in all prior intervals, $n < n_0$. As $\hat{C}$ decreases and a particular interval passes from having no zeros to having 2, a double zero is created; for the interval (π_{n-1}, π_n) we label this point as $\hat{C} = \hat{C}_n$ $(n = 1, \dots)$. Hence, it is deduced that, on the nth purely imaginary branch of (3.24), for all $\hat{C} > \hat{C}_n$ there is no possibility of bifurcations as H varies; while, for $\hat{C} < \hat{C}_n$, there are two values of H that produce double roots. The finite interval between these values of H corresponds to the existence of purely imaginary μ_i $(i = 1, 2)$ (this may be deduced by noting that for any value of $\hat{C}$ we may select H such that we have a solitary root on the purely imaginary interval in question). As soon as we have calculated the relevant roots $\hat{\sigma}$, the value of σ (and consequently H) may be obtained from (3.30a-b). This assumes that B and/or A has been fixed (in addition to $\hat{C}$).

If the parameters α, β and κ are such that $\hat{C} = \hat{C}_n$, then there is an isolated value of H for which a triple root of the dispersion relation exists in the nth purely imaginary interval, although this is the only value of H for which multiple roots exist (in this interval). In order to investigate the values $\hat{C}_n$ $(n = 1, \dots)$ further, we differentiate the second equation of (3.28), with respect to σ, to obtain

$$10B\sigma^5 = -(\sigma H)^2 \cot(\sigma H) \csc^2(\sigma H). \tag{3.32}$$

A triple root is then defined by equations (3.28) and (3.32).

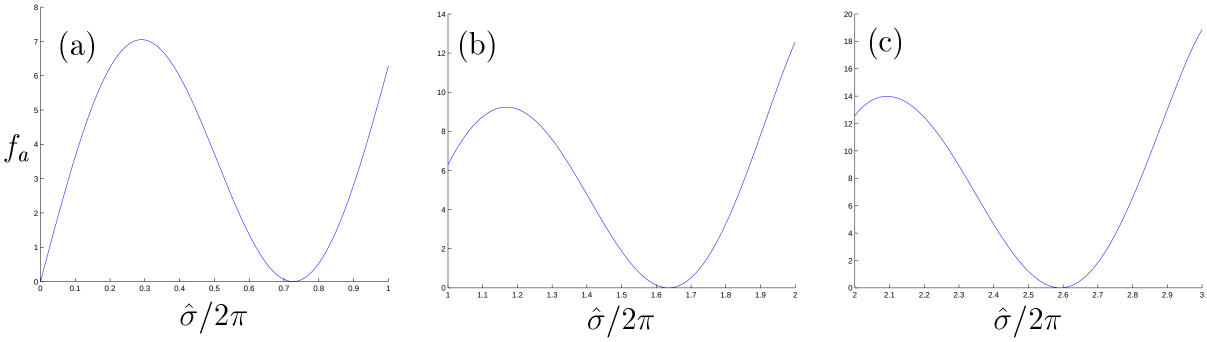

Figure 3.2: The function f_a as a function of $\hat{\sigma}/2\pi$ plotted for (a) $\hat{C} = \hat{C}_1$, (b) $\hat{C} = \hat{C}_2$ and (c) $\hat{C} = \hat{C}_3$ (see equation 3.34). The chosen interval of $\hat{\sigma}/2\pi$ in each subfigure corresponds to the specific parameter $\hat{C}_n$, in order that they demonstrate the existence of double roots for these values.

By eliminating $B\sigma^5$ between (3.30a) and (3.32) we deduce the triple root condition

$$5(\sin(\hat{\sigma}) + \hat{\sigma})(1 - \cos(\hat{\sigma})) + \hat{\sigma}^2 \sin(\hat{\sigma}) = 0. \tag{3.33}$$

This equation is independent of the parameters of the problem, specifically of the value $\hat{C}$. The zeros of (3.33) are denoted $\hat{\sigma}_n \in (\pi_{n-1}, \pi_n)$ $(n = 1, \dots)$ and may be easily found numerically. The corresponding values $\hat{C}_n$ may then be derived from, for example, equations (3.28), and we find the first three values to be

$$\hat{C}_1 \approx 2.65 \times 10^{-1}, \quad \hat{C}_2 \approx -2.77, \quad \hat{C}_3 \approx -4.80. \tag{3.34}$$

The value of $\hat{C}_1$ given above is consistent with the equivalent value that is given by Williams (2006). Further verification of these values is provided in figure 3.2, which plots the function f_a in the relevant interval of $\hat{\sigma}$ for the respective values of $\hat{C}_n$ appearing in (3.34).

Let us now turn to the physical interpretation of these values. It is clear from the definition of $\hat{C}$ that it decreases linearly with increasing κ and quadratically with increasing D. There is therefore a relationship between κ and D that must be satisfied in order to attain the values $\hat{C} = \hat{C}_n$. As n increases (and hence $\hat{C}_n$ decreases) this will require either a greater incident wavenumber or a greater ice thickness. It is clear that $\hat{C} = 0 < \hat{C}_1$ if

$\alpha = 1/\kappa$, which is satisfied by

$$\kappa D = \frac{10}{9} \left(= \frac{\rho_w}{\rho_i} \right).$$

In figure 3.3 the value of D that ensures $\hat{C} = 0$ is plotted for the interval of angular frequency $\omega \in (1, 5)$rads/secs. The corresponding bounding values of H, that separate the different states of the complex roots are also plotted; note that, the bounds are very close, which means that for each ω and D, there is only a narrow band of fluid depths for which the complex roots are purely imaginary. Using this information we may select, as an example, the combination $\omega = 3$rads/secs ($\kappa = 0.9174$), $D = 1.2111$m and $H \in (22.7870, 23.0060)$m as an interval of physically realistic parameters for which the μ_i ($i = 1, 2$) are purely imaginary, existing on the first imaginary segment, $(0, \pi_1)$.

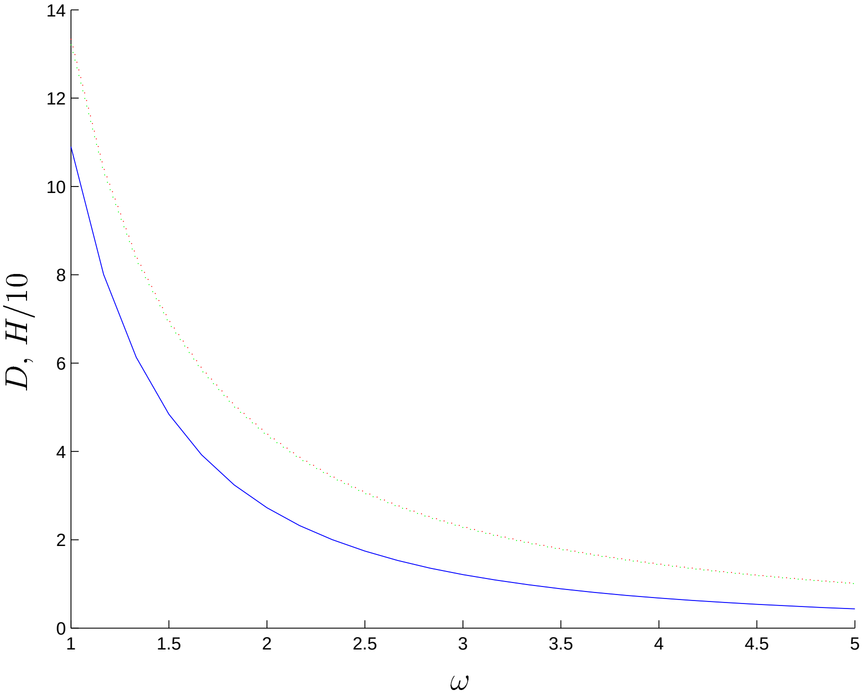

Figure 3.3: The values of D (solid blue curve) that ensure $\hat{C} = 0$ for differing frequency, and corresponding upper bound (dotted red) and lower bound (dotted green) of $H/10$ between which multiple roots exist on the first purely imaginary interval.

In the subsequent segments it is physically extremely unlikely that bifurcations will be encountered. In demonstration of this figure 3.4 displays the values of D and H against κ at the triple roots, $\hat{C} = \hat{C}_n$ ($n = 2, 3$), that bound the bifurcation points in the second and third imaginary intervals.

Finally in this section, we consider the relevance of these results to our model. In Appendix A, it will be shown that, in a neighbourhood of a bifurcation the derivative (with respect to any independent variable) of the constituent roots is unbounded. We are required to differentiate the natural modes (see §3.2.1), which implicitly necessitates

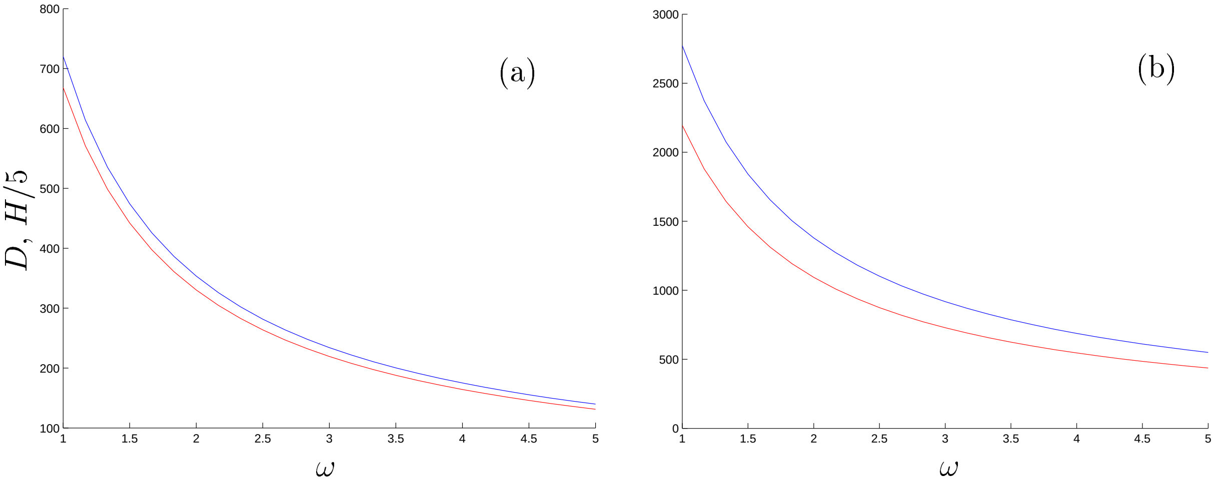

Figure 3.4: The unique values of D (blue curves) and H (red) that ensure (a) $\hat{C} = \hat{C}_2$ and (b) $\hat{C} = \hat{C}_3$, and hence the existence of a triple root in the corresponding interval of the imaginary axis, as functions of frequency.

the differentiation of the roots of the dispersion relation, and this is precluded if such a bifurcation arises.

In each particular problem there exists an fixed angular frequency (and hence fixed κ). The vertical structure of the geometry is allowed to vary, and let us suppose that $\max(D) = D_{mx}$ and $\max(H) = H_{mx}$. From the above argument it is legitimate to restrict our attention to only the first imaginary interval, $(0, \pi_1)$. For the set κ there exists a pair $(D, H) = (D_1, H_1)$ for which $\hat{C} = \hat{C}_1$. If $D_{mx} < D_1$ or $H_{mx} < H_1$ then there is no risk of bifurcations; however, if these inequalities do not hold then further investigation must be carried out. For $D \in (D_1, D_{mx})$ we may find the bounds in H of the bifurcation interval, say (D_l, H_u) and (D_u, H_l) represent the lower and upper bounds respectively. If this is plotted against $(D(x,y), H(x,y))$ then it is possible to deduce at which points (if any) bifurcations occur according to the number of times the path of the vertical structure cross the bounds of the bifurcation interval.

An example of a typical bifurcation is shown in figure 3.5. Part (a) shows the path of the constituent roots, namely μ_i $(i = 1, 2)$ and k_1, for a linearly increasing ice thickness, $D \in (1, 6)$m, and linearly decreasing fluid depth, $H \in (55, 60)$m, with $\kappa = 0.4245$. Part (b) plots the corresponding path of (D, H) along with the bifurcation bounds, (D_l, H_u) and (D_u, H_l), described above. Initially the complex roots, μ_i $(i = 1, 2)$, are genuinely complex. As the ice thickens and the fluid becomes more shallow they travel towards the imaginary axis. At the point at which the complex roots coalesce on the imaginary axis, the curve (D, H) meets the lower bound (D_l, H_u) and crosses so that it lies within the upper and lower bounds. During this period, as H and D vary, the complex roots, μ_i $(i = 1, 2)$, are travelling, respectively, down and up the imaginary axis. Whilst this has transpired, the purely imaginary root, k_1 has moved slowly up the imaginary axis towards the oncoming root μ_1. These roots inevitably collide, at which time the curve (D, H) crosses the upper bound upper bound (D_u, H_l). The curve (D, H) then crosses this boundary so that is no longer enclosed within the bifurcation bounds and concomitantly the roots μ_1 and k_1 bifurcate to form a new fully complex pair.

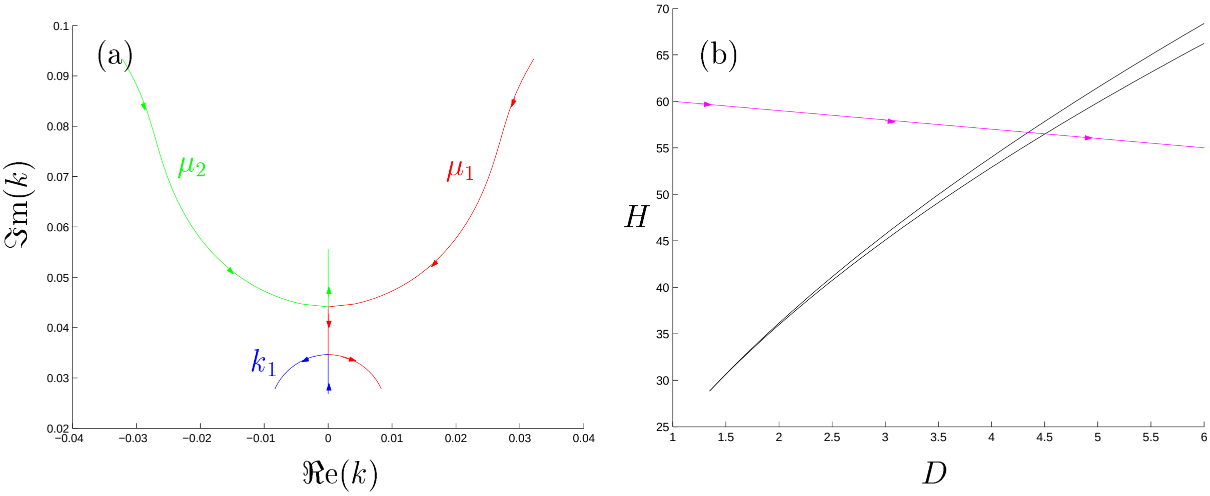

Figure 3.5: Graphical representation of a typical bifurcation. Part (a) plots the paths of the constituent roots, with k_1 (blue curve), μ_1 (red) and μ_2 (green). Part (b) plots the path of the vertical structure of the geometry, (D, H), (magenta curve) and bifurcation bounds, (D_l, H_u) and (D_u, H_l), (black).

Linear Dependence

There is a second result, concerning the natural modes, that will affect our ability to define the vertical structure of the MMA. In this section we will prove that the entire set of natural vertical modes, consisting of the single propagating mode, the two complex modes and the infinite number of evanescent modes has a two-fold linear dependence. To avoid numerical difficulties, we must then modify the finite subspace of these functions, that we intend to use as our trial space, by removing two of the salient members.

Consider the integral

$$\frac{1}{2\pi i}\oint \frac{f_b(\varsigma)}{\mathfrak{K}(\varsigma)}\cosh\varsigma(z+h)\mathrm{d}\varsigma, \tag{3.35}$$

integrated about a circle centred at the origin, of radius R, where

$$\mathfrak{K}(\varsigma) = (1-\kappa\alpha+\beta\varsigma^4)\varsigma\sinh(\varsigma H) - \kappa\cosh(\varsigma H),$$

is an even function, and f_b is a currently unspecified odd function that is holomorphic in the circle about which we are integrating.

Assuming that the parameter set used does not give rise to a multiple root (i.e. a point at which the complex roots $k_{-i} = \mu_i$ $(i = 1, 2)$ coalesce) application of the residue theorem to integral (3.35) gives

$$2\sum_{n=-2}^{N}\frac{f_b(k_n)}{\mathfrak{K}'(k_n)}\cosh k_n(z+h) = B_R, \tag{3.36}$$

where B_R is the contribution from the boundary, and we are supposing that only the roots $\pm k_n$ $(n=-2,\dots,N)$ are contained in the circle.

Suppose that f_b is selected such that the contribution from the boundary decays as $R\to\infty$, then

$$2\sum_{n=-2}^{\infty}\frac{f_b(k_n)}{\mathfrak{K}'(k_n)}\cosh k_n(z+h) = 0. \tag{3.37}$$

This result tells us that there exists a subset of the natural modes

$$\{\cosh k_n(z+h)\} \quad (n=-2,-1,0,1,\dots), \tag{3.38}$$

that spans the same space. The degree by which we may reduce the natural set (3.38) depends on how many linearly independent ways we may select the function f_b.

It may easily be deduced that the only admissable f_b are such that $f_b(\varsigma)=a_1\varsigma+a_3\varsigma^3$, for constants a_1 and a_3. Therefore $f_b(k_n)=k_n$ and $f_b(k_n)=k_n^3$ are the only two linearly independent possibilities. Integral (3.35) originally appeared in Evans & Porter (2003); however, its implication for the natural modes was not made explicit.

Although we work only with a finite number, $(N+1)$, of vertical modes, it can be expected that numerical problems will be experienced for small N, if the natural approximation is applied in the form (3.26). Specifically, the matrix A (defined after equation (3.5)) is found to be near-singular for MMAs of this form. Result (3.37) permits the removal of two modes from the trial space (3.38); the rôle of the removed modes will be compensated for, to an arbitrary degree of accuracy, through the addition of higher-order modes w_i $(i>N)$.

An obvious choice of modes to be removed from trial space (3.38) are those that correspond to the complex roots, namely w_{-i} $(i=1,2)$. This will leave a real-valued set, which is a computational advantage. It will also provide a consistent approximation in situations of partial ice-cover, so that each vertical mode used in the ice-free region has a clear analogue in the ice-covered region. To reflect this choice, we rewrite (3.37) as

$$\cosh\{\mu_j(z+h)\} = \sum_{i=0}^{\infty}\upsilon_{i,j}\cosh\{\mu_i(z+h)\} \quad (i=1,2), \tag{3.39}$$

in which the *redistribution weights* are

$$\upsilon_{i,j} = \frac{k_i \mathfrak{K}'(\mu_j)(k_i^2 - \mu_{j_-}^2)}{\mu_j \mathfrak{K}'(k_i)(\mu_j^2 - \mu_{j_-}^2)} \quad (i = 0, \ldots; \, j = 1, 2), \tag{3.40}$$

where $j_- = (3 - (-1)^j)/2$. By using the limiting value of the purely imaginary roots, $k_n \to \mathrm{i}n\pi/H$ as $n \to \infty$, we deduce that

$$\upsilon_{n,j} \approx (-1)^n \frac{H \mathfrak{K}'(\mu_j)}{n^2 \pi^2 \beta \mu_j (\mu_j^2 - \mu_{j_-}^2)} = \mathrm{O}\left(\frac{1}{n^2}\right) \quad (j = 1, 2), \tag{3.41}$$

for sufficiently large n.

In terms of the uniform geometry problem, we have shown that for any distribution of the roots of (3.13), in which the roots do not coincide, the vertical motion may be expressed by any subset of (3.38) with two members removed. The horizontal waves corresponding to the vertical modes that are no longer present are then redistributed amongst those remaining vertical modes. For example, by taking the choice to remove the vertical modes $\cosh\{\mu_i(z+h)\}$, the form of the full linear solution appearing in (3.26) becomes

$$\phi(x, y, z) = \sum_{i=0}^{\infty} \left\{ \phi_i(x, y) + \sum_{j=1,2} \upsilon_{i,j} \phi_{-j}(x, y) \right\} \cosh\{k_i(z + h)\}. \tag{3.42}$$

In situations in which any of the roots of the dispersion relation coincide, application of the residue theorem does not lead to equation (3.36). Instead, extra functions will arise in place of the repeated modes. As we are able to disregard two members of the trial space (3.38) knowledge of these additional functions is not required.

In terms of their relevance to the MMA, result (3.39) and the issue of bifurcations are not independent. By returning to the MMA of the form (3.14), any problems caused by bifurcations in the removed modes, $\cosh\{\mu_i(z + h)\}$ $(i = 1, 2)$, have been alleviated. However, if we consider the example given in figure 3.5, we see that the three roots k_1 and μ_i $(i = 1, 2)$ all bifurcate, hence invalidating the use of w_1 in (3.14). In terms of the type of bifurcations depicted in figure 3.5, we deduce that if the curve (D, H) only crosses one of the bifurcation boundaries then the MMA of the form (3.14) is valid by virtue of the linear dependence (3.39) but that if it passes through both upper and lower boundaries (as in figure 3.5) then it is not possible to utilise the natural modes in their current state.

3.2.3 Alternative vertical modes

We find ourselves in the position that, in our choice of vertical modes for situations of ice-covered fluid, (3.15), we are unable to guarantee sufficient differentiabilty to generate the governing equations. Specifically, the problem lies in the evanescent modes and in particular the primary evanescent mode, w_1.

This is an appropriate point at which to note that the issue of bifurcations is not one that reflects any failure in the full linear model, which was outlined in §2. It is rather an artifice of our solution method, in which the vertical motion is defined at each horizontal point as if the surrounding geometry were uniform.

In order that the MMA is available for all possible parameter ranges we must seek some resolution of the problem created by the occurence of bifurcations. If we wish to retain the natural modes, then it is sufficient that the composite quantities $\varphi_i w_i$ remain bounded up to second derivatives across the domain. However, there appears to be no practical way of implementing this condition. Alternatively, we may choose the weight functions, ϖ_i $(i = 1, \dots)$, to achieve sufficient differentiability. Unfortunately, as any numerical method will operate on a discretised space, such a method would inevitably lead to singular behaviour in the vicinity of a bifurcation. It would also be theoretically possible to partition the overall domain according to the existence of bifurcations, applying jump conditions between each subregion. This approach could not be realised practically as it would be difficult to manufacture the appropriate boundary values to be used in the jump conditions due to the unboundedness of the derivatives of k_i $(i = 1, \dots)$ in a neighbourhood of a bifurcation. Our choice of the natural modes was merely a judicious choice based on the reasoning that the key physical aspects of the vertical motion would be encompassed by a relatively small trial space. It is, however, in principle, possible to obtain convergence of the MMA to the full linear solution through use of any trial space, provided that a sufficiently large dimension is taken. Therefore, the problem of bifurcations may be simply overcome by employing an alternative trial space in situations for which the natural evanescent modes are not viable.

The specific alternative that we propose is the *hybrid* MMA $\psi_N = \tilde{\psi}_N$, so that

$$\tilde{\psi}_N(x, y, z) = \varphi_0(x, y)w_0(x, y, z) + \sum_{i=1}^{N} \varphi_i(x, y)\tilde{w}_i(x, y, z),$$

where the *hybrid (vertical) modes* are

$$\tilde{w}_i(x, y, z) = \varpi(x, y)\cosh\{\tilde{k}_i(x, y)(z + h(x, y))\} \quad (i = 1, \dots, N),$$

and

$$\tilde{k}_n = \mathrm{i}\pi_n = \mathrm{i}\frac{n\pi}{H} \quad (n = 1, \dots, N). \tag{3.43}$$

The hybrid MMA therefore shares the same single-mode approximation as the natural MMA, which is unaffected by bifurcations. The additional modes are modified versions of the natural evanescent modes, the quantities $\tilde{k}_i$ $(i = 1, \dots, N)$ being the limiting values of the purely imaginary roots k_i. We therefore have $k_n \to \tilde{k}_n$ as $n \to \infty$. It is clear from

(3.43), that unlike the k_i, which depend on both D and H, the quantities $\tilde{k}_i$ $(i = 1, \ldots, N)$ depend only on the fluid depth, H. As such, the hybrid modes have less correspondence to the structure of the problem and we therefore expect the convergence of the hybrid MMA to be (generally) slower than that of the natural MMA.

The form of the coefficients derived in §3.2.1 is equally applicable to the hybrid modes, with only $\tilde{k}_n$ replacing k_n $(n \neq 0)$. We however note the simplification

$$\nabla \tilde{W}_n = (\partial_h \tilde{W}_n)\nabla h + (\partial_d \tilde{W}_n)\nabla d \quad (n = 1, \ldots, N),$$

where $\tilde{w}_i(x, y, z) \equiv \tilde{W}_i(h, d, z)$ $(n = 1, \ldots, N)$. The same is true of the explicit expressions for the inner-products that are given in appendix 5.12. Only the derivatives of the quantities $\tilde{k}_n$ $(n = 1, \ldots, N)$ differ in structure from their natural counterparts and are given at the end of Appendix A.

Rather than considering the hybrid modes to be modified versions of the natural evanescent modes they may be viewed as the non-constant modes of a Fourier cosine series. The hybrid MMA therefore represents a truncated Fourier expansion of the vertical motion, with the constant term replaced by the mode that supports propagating waves. It is our assertion that the inclusion of this mode is fundamental to the MMA and significantly improves its accuracy.

It will be shown in §4 that it is necessary to move between alternative trial spaces across internal boundaries. In doing so, we will create discontinuities in the MMA, even when the geometry is continuous. This provides a further motivation for the use of the functional I_Γ.

3.3 Summary

We are now at a point at which we have at our disposal an approximation method, known as the MMA, that will provide solutions of any given accuracy. Moreover, we believe that in our specific formulation, we will receive a high degree of accuracy at minimal computational expense.

The task of solving the three-dimensional boundary-value problem that was outlined in §2 has been replaced by a more appealing set of governing equations, in which the coordinate z is absent. These equations were generated by the restriction of the vertical motion to a finite-dimensional space in the variational principle given in §2.2.

The accuracy of the MMA may be controlled through the choice of the trial space that defines the space in which the vertical motion of the solution exists. Specifically, the size of the trial space may be chosen large enough that we may, effectively, attain the full linear solution. Moreover, as we wish to minimise the computational expense, we proposed a set of vertical modes known as the natural modes. These modes, which comprise the trial space, were selected on the basis that they define the vertical motion of a ‘near-neighbour’ solution and we therefore expect that a relatively small number will accurately represent the vertical motion of the exact solution that is sought. Furthermore, the inclusion of the mode that supports the incident wave allows the exact form of the far-field to be retained in the MMA.

In situations of ice-cover, the properties of the natural modes were found to have non-trivial properties. Firstly, there is the difficulty of bifurcations; whereby, the complex roots of the ice-covered dispersion relation, which have no analogue in the free-surface case, switch between being genuinely complex and being purely imaginary and may collide with the purely imaginary roots as well as each other. This causes singularities in the derivatives of the resulting evanescent and complex modes and hence invalidates their use in the MMA. Secondly, there is the issue of a two-fold linear dependence in the complete set of natural modes. This necessitates the removal of two of the prominent modes from the trial space and the complex modes were seen to be the obvious choice.

For the trial space from which we have removed the complex modes, there is less chance of the modes becoming polluted by bifurcations; however, this was seen to still be a realistic possibility. To resolve this issue, we proposed an alternative set of evanescent modes, described as the hybrid evanescent modes. The hybrid modes do not suffer from bifurcations but also do not share the same level of association with the geometry as the natural modes and are hence expected to provide slightly less accurate approximations.

Chapter 4

Two-dimensional problems

The first application of the MMA that will be made is to two-dimensional problems in which the bed shape and ice shape are independent of y; take, for example, the situation shown in figure 2.1 of the §2, now assumed to represent every cross-section.

Two specific problems of this type are formulated for numerical solution and results are presented in §§6-7. Graphical representations of these geometries are given in figures 4.1-4.2. In both problems, the geometry is permitted to vary over a finite interval contained within semi-infinite intervals of uniform geometry that are either ice-covered and run on continuously from the varying geometry (see figure 4.1) or are ice-free (see figure 4.2). An obliquely incident plane wave propagates from the far-field $x \to -\infty$ with crests that meet the x-axis at a given angle, $\vartheta^{(-)}$. Problems of this type have been considered by previous authors and comparative results are therefore available for restricted cases.

This is an appropriate juncture at which to introduce the lateral conditions attached to the problem. In the *far-fields* $x \to \pm\infty$, the exact solution must behave like a superposition of propagating waves, such that the *radiation condition*

$$\phi(x,y,z) \sim \{A_0^{(\pm)}\mathrm{e}^{\pm\mathrm{i}\lambda_0^{(\pm)}x} + B_0^{(\pm)}\mathrm{e}^{\mp\mathrm{i}\lambda_0^{(\pm)}x}\}\mathrm{e}^{\mathrm{i}qy}\cosh k_0^{(\pm)}(z+h^{(\pm)}) \quad (x \to \pm\infty), \tag{4.1a}$$

holds if the far-fields are ice-covered and

$$\phi(x,y,z) \sim \{A_0^{(\pm)}\mathrm{e}^{\pm\mathrm{i}\lambda_0^{(0\pm)}x} + B_0^{(\pm)}\mathrm{e}^{\mp\mathrm{i}\lambda_0^{(0\pm)}x}\}\mathrm{e}^{\mathrm{i}qy}\cosh k_0^{(0\pm)}(z+h^{(\pm)}) \quad (x \to \pm\infty), \tag{4.1b}$$

holds if the far-fields are ice-free. Imposing these radiation conditions fully defines the two-dimensional problem.

The constants $A_0^{(-)}$ and $A_0^{(0-)}$ are the prescribed incident amplitudes and will be set as

$$A_0^{(-)} = \frac{\kappa}{k_0^{(-)}}\mathrm{csch}(k_0^{(-)}H^{(-)}), \quad A_0^{(0-)} = \frac{\kappa}{k_0^{(0-)}}\mathrm{csch}(k_0^{(0-)}h^{(-)}),$$

to ensure that the incident waves are of 1m amplitude. In numerical examples we will choose to consider no incident wave from the far-field $x \to \infty$ and thus set the constants $A_0^{(+)}$ and $A_0^{(0+)}$ as zeros; however, for generality and to ensure algebraic symmetry throughout the formulation, we leave these amplitudes unspecified. The constants $B^{(\pm)}$ and $B^{(0\pm)}$ are unknown outgoing amplitudes that must be determined as part of the solution process.

The quantities $k_0^{(\pm)}$ and $k_0^{(0\pm)}$ are the propagating wavenumbers in the respective far-fields and $q = k_0^{(-)} \sin \vartheta^{(-)}$ or $q = k_0^{(0-)} \sin \vartheta^{(-)}$. Using these values, we may calculate the wavenumbers in the x-direction from

$$(\lambda_0^{(\pm)})^2 = (k_0^{(\pm)})^2 - q^2, \quad (\lambda_0^{(0\pm)})^2 = (k_0^{(0\pm)})^2 - q^2.$$

By accepting the radiation conditions (4.1a-b), we have implicitly assumed that the angle of the reflected wave is identical to that of the incident wave, and that the angle, $\vartheta^{(+)}$, of the wave transmitted into the opposing far field ($x \to \infty$) satisfies the relation

$$k_0^{(+)} \sin(\vartheta^{(+)}) = k_0^{(-)} \sin(\vartheta^{(-)}),$$

so that it is dependent on the incident angle, $\vartheta^{(-)}$, as well as the ratio of the propagating wavenumbers in the respective far-fields. Both of these assumptions are consequences of Snell's law.

At this point we remark that when $k_0^{(+)} < k_0^{(-)}$ there exists a *critical angle*, $\vartheta^{(-)} = \vartheta_c$, beyond which no waves will propagate into the opposing far-field, $x \to \infty$. This critical angle is defined by

$$\vartheta_c = \sin^{-1}\left(\frac{k_0^{(+)}}{k_0^{(-)}}\right).$$

If the critical angle is attained or exceeded then all of the energy from the incident wave is reflected, $|R| = 1$. Moreover, the waves that we have assumed to be propagating in the far-field $x \to \infty$ are in fact exponentially growing or decaying. In this case, we must set the amplitude of the growing wave, $A_0^{(+)}$, to zero. However, this matter is of trivial concern and we will not need to touch upon it again. If, on the other hand, $k_0^{(+)} \geq k_0^{(-)}$ then waves will transmit to the far-field $x \to \infty$ for all incident wave angles, $\vartheta^{(-)} \in (0, \pi/2)$.

As a periodic variation has been assumed in the y-direction, it is pertinent to retain this in our approximation by setting

$$\varphi_i(x, y) = \tilde{\varphi}_i(x) \mathrm{e}^{\mathrm{i}qy} \quad (i = 0, \ldots, N), \quad \chi(x, y) = \tilde{\chi}(x) \mathrm{e}^{\mathrm{i}qy}.$$

The unknown functions are relabelled $\tilde{\varphi}(x) \equiv \varphi(x)$ and $\tilde{\chi}(x) \equiv \chi(x)$. They, along with the functions that define the surrounding ice and bed shape, are now functions of the variable x only and consequently the vertical modes are $w_i = w_i(x, z)$.

4.1 The governing equations of the MMA in 2-d

It is straightforward to reduce the partial differential system (3.5), for ice-covered fluid, to the ordinary differential system

$$\partial_x(A\partial_x\mathbf{\Phi_N}) + \widetilde{D}\partial_x\mathbf{\Phi_N} + (B - q^2A)\mathbf{\Phi_N} + \kappa\chi C\mathbf{f} = \mathbf{0}, \tag{4.3a}$$

and the associated fourth-order partial differential equation (3.3b) to the fourth-order ordinary differential equation

$$\{(\partial_x^2 - q^2)\beta(\partial_x^2 - q^2) + (1-\nu)(\partial_x^2\beta)q^2 + 1 - \kappa\alpha\}\chi - \sum_{i=0}^{N}[w_i]_{z=-d}\varphi_i = 0, \tag{4.3b}$$

where all of the matrices are defined in §3.1. The following, more compact, version of this system of differential equations

$$\partial_x(\mathcal{A}\partial_x\mathbf{\Psi}_N) + \widetilde{\mathcal{D}}\partial_x\mathbf{\Psi}_N + \mathcal{B}\mathbf{\Psi}_N = \mathbf{0}, \tag{4.4}$$

will prove to be convenient on occasion, where

$$\mathbf{\Psi}_N = \left(\mathbf{\Phi}_N^T, \chi^{(1)}, \chi^{(2)}\right)^T, \tag{4.5}$$

which is such that $\chi^{(1)} = \chi$, and $\chi^{(2)} = \beta(\partial_x^2 - q^2)\chi$, and

$$\mathcal{A}_{i,j} = A_{i,j}, \quad \mathcal{B}_{i,j} = B_{i,j}, \quad \widetilde{\mathcal{D}}_{i,j} = \widetilde{D}_{i,j} \quad (i,j = 1,\dots,N+1),$$

$$\mathcal{A}_{N+2,N+2} = \mathcal{A}_{N+3,N+3} = 1, \quad \mathcal{B}_{i,N+2} = \kappa\mathbf{I}_i^T C\mathbf{f} \quad (i = 1,\dots,N+1),$$

$$\mathcal{B}_{N+2,N+3} = -\beta^{-1}, \quad \mathcal{B}_{N+3,j} = -\mathbf{f}^T C\ \mathbf{I}_j \quad (j = 1,\dots,N+1),$$

$$\mathcal{B}_{N+2,N+2} = \mathcal{B}_{N+3,N+3} = -q^2, \quad \mathcal{B}_{N+3,N+2} = (1-\nu)(\partial_x^2\beta)q^2 + 1 - \kappa\alpha,$$

with all unspecified values equal to zero and where $[\ \mathbf{I}_1,\ \dots,\ \mathbf{I}_{N+1}\ ]$ is the identity matrix of size $(N+1)$. In an interval of ice-free fluid, the partial differential system (3.6) trivially collapses to the ordinary differential system

$$\partial_x(A^{(0)}\partial_x\mathbf{\Phi}_N) + \widetilde{D}^{(0)}(\partial_x\mathbf{\Phi}_N) + (B^{(0)} - q^2A^{(0)})\mathbf{\Phi}_N = 0. \tag{4.6}$$

Throughout the set of equations (4.3a-b), (4.4) and (4.6) we have tacitly redefined the differential operator ∂_x so that it now represents the full derivative $\partial_x \equiv \mathrm{d}/\mathrm{d}x$. The notation ∂_x has been retained simply for the sake of brevity and its new definition will hold throughout our investigation of two-dimensional motion in §§5-8.

The accompanying jump conditions must also be calculated. Given the restrictions of the problem, the contour Γ, over which the jump conditions are implemented, must be parallel to the y-axis and hence the normal to this contour is parallel to the x-axis.

If Γ separates two intervals of connected ice, the two-dimensional versions of the natural conditions (3.7a) and (3.10) are easily found to be

$$(V^T\mathbf{\Phi}_N)_+ = (V^T\mathbf{\Phi}_N)_-, \quad V_+^{-1}\{(A\partial_x\mathbf{\Phi}_N)_+ + (Q\mathbf{\Phi}_N)_+\} = V_-^{-1}\{(A\partial_x\mathbf{\Phi}_N)_- + (Q\mathbf{\Phi}_N)_-\},$$

respectively. Equivalently, if Γ defines the interface between ice-covered and ice-free regions, the natural conditions (3.11a-b) become

$$V^T\mathbf{\Phi}_N = (V^T\mathbf{\Phi}_N)^{(0)}, \quad V^{-1}A\partial_x\mathbf{\Phi}_N + Q\mathbf{\Phi}_N = \{V^{-1}A\partial_x\mathbf{\Phi}_N + Q\mathbf{\Phi}_N\}^{(0)}. \tag{4.7}$$

Again, all matrices that appear are defined in §3.1.

The expressions for the bending moment and shearing stress reduce to

$$\mathfrak{M}\chi = \chi^{(2)} + \beta(1-\nu)q^2\chi^{(1)},$$

and

$$\mathfrak{S}\chi = \partial_x\chi^{(2)} - (1-\nu)q^2(\beta\partial_x - (\partial_x\beta))\chi^{(1)}.$$

At a point between ice-covered intervals, the essential conditions $\langle\chi^{(1)}\rangle = \langle\partial_x\chi^{(1)}\rangle = 0$ apply. If the ice thickness is continuous across Γ, these essential conditions can be used to simplify the natural conditions that ensure continuity of bending moment and shearing stress to

$$\langle\hat{\chi}^{(2)}\rangle = 0, \tag{4.9a}$$

and

$$\langle\partial_x\hat{\chi}^{(2)} + (1-\nu)q^2(\partial_x\beta)\hat{\chi}^{(1)}\rangle = 0, \tag{4.9b}$$

respectively.

The full set of jump conditions at a point at which two intervals of connected ice meet may then be expressed as

$$(\mathcal{V}^T\mathcal{M}^{-1}\mathbf{\Psi}_N)_+ = (\mathcal{V}^T\mathcal{M}^{-1}\mathbf{\Psi}_N)_-, \tag{4.10a}$$

and

$$\mathcal{V}_+^{-1}\{(\mathcal{A}\mathcal{M}\partial_x\mathbf{\Psi}_N)_+ + (\mathcal{Q}\mathcal{N}\mathbf{\Psi}_N)_+\} = \mathcal{V}_-^{-1}\{(\mathcal{A}\mathcal{M}\partial_x\mathbf{\Psi}_N)_- + (\mathcal{Q}\mathcal{N}\mathbf{\Psi}_N)_-\}, \tag{4.10b}$$

where

$$\mathcal{Q}_{n,m} = Q_{n,m}, \quad \mathcal{Q}_{n,m} = Q_{n,m} \quad (n, m = 1, \ldots, N+1),$$

$$\mathcal{Q}_{N+2,N+2} = \mathcal{Q}_{N+3,N+3} = \mathcal{V}_{N+2,N+2} = \mathcal{V}_{N+3,N+3} = 1,$$

$$\mathcal{M}_{n,n} = 1 \quad (n = 1, \ldots, N+3), \quad \mathcal{N}_{n,n} = 1 \quad (n = 1, \ldots, N+1),$$

and

$$\mathcal{M}_{N+3,N+2} = -\beta(1-\nu)q^2, \quad \mathcal{N}_{N+3,N+2} = (1-\nu)q^2(\partial_x \beta).$$

As always, all unspecified entries are zeros. The matrices $\mathcal{M}$ and $\mathcal{N}$ therefore enforce the continuity of bending moment and shearing stress and may be simplified if the geometry allows; in particular, if the ice thickness is continuous then (4.9a-b) may be applied in place of $\langle \mathfrak{M}\chi \rangle = \langle \mathfrak{S}\chi \rangle = 0$ by replacing $\mathcal{M}$ with the identity matrix. Furthermore, the matrices $\mathcal{M}$ and $\mathcal{N}$ commute with all of the matrices that appear in the jump conditions.

If, however, the jump conditions are to be applied at a point separating ice-covered and free-surface fluid intervals then the conditions to be satisfied are given by (4.7) together with the conditions of zero bending moment and shearing stress, $\mathfrak{S}\chi^{(1)} = \mathfrak{M}\chi^{(1)} = 0$. These may be condensed into the expressions

$$(V^T \mathbf{\Phi}_N)_+ = (V^T \mathbf{\Phi}_N)_-, \tag{4.11a}$$

and

$$\mathcal{V}_+^{-1}\{(\mathcal{A}\widetilde{\mathcal{M}}\partial_x \mathbf{\Psi}_N)_+ + (\mathcal{Q}\widetilde{\mathcal{N}}\mathbf{\Psi}_N)_+\} = \mathcal{V}_-^{-1}\{(\mathcal{A}\widetilde{\mathcal{M}}\partial_x \mathbf{\Psi}_N)_- + (\mathcal{Q}\widetilde{\mathcal{N}}\mathbf{\Psi}_N)_-\}, \tag{4.11b}$$

where

$$\widetilde{\mathcal{M}}_{n,n} = \widetilde{\mathcal{N}}_{n,n} = 1 \quad (n = 1, \ldots, N+1),$$
$$\widetilde{\mathcal{M}}_{N+3,N+2} = -\beta(1-\nu)q^2, \quad \widetilde{\mathcal{M}}_{N+3,N+3} = 1,$$

and

$$\widetilde{\mathcal{N}}_{N+2,N+2} = \beta(1-\nu)q^2, \quad \widetilde{\mathcal{N}}_{N+2,N+3} = 1, \quad \widetilde{\mathcal{N}}_{N+3,N+2} = (\partial_x \beta)(1-\nu)q^2.$$

Note that, in both situations, end-point conditions, such as (2.23), do not apply.

4.2 Uniform geometry

In a situation in which the geometric variables D, h and d take constant values, it is possible to give an analytic expression for the natural MMA, as (4.4) reduces to a constant coefficient ordinary differential system that may be solved by standard methods. The expressions that we will derive for the MMA will provide boundary values for the numerical solution of the two-dimensional problems described at the beginning of this chapter. It is possible to obtain expressions for alternative trial spaces; however, these rely on complicated numerical procedures. For this section, it will make calculations more manageable to assume that the vertical modes take the weighting $\varpi_i = 1$ $(i = 0, \ldots, N)$, which is done without loss of generality.

Therefore, take $\mathbf{\Psi}_N(x) = \hat{\mathbf{c}}(\lambda)\mathrm{e}^{\mathrm{i}\lambda x}$, such that $\hat{\mathbf{c}}^T(\lambda) = \big(\mathbf{c}^T(\lambda), \gamma^{(1)}(\lambda), \gamma^{(2)}(\lambda)\big)$, where λ is a constant, $\hat{\mathbf{c}}$ is a vector depending on λ, and $\gamma^{(i)}$ $(i = 1, 2)$ are scalars depending on λ. The quantities λ and $\hat{\mathbf{c}}$ represent, respectively, eigenvalues and eigenvectors of the simplified system (4.4). Substituting these expressions into (4.3a-b) and making use of

$$\widetilde{d}_{j,i} = 0, \quad b_{j,i} = a_{j,i}k_i^2 - k_i \sinh(k_i H)\cosh(k_j H),$$

which apply on intervals of constant D, h and d, leaves the eigensystem defined by

$$\left\{A\left(K^2 - (\lambda^2 + q^2)I\right) - C\mathbf{f}\,\mathbf{f}^T KS\right\}\mathbf{c} + \kappa\gamma^{(1)}C\mathbf{f} = \mathbf{0}, \tag{4.12a}$$

and

$$\left(\beta(\lambda^2 + q^2)^2 + 1 - \kappa\alpha\right)\gamma^{(1)} - \mathbf{f}^T C\mathbf{c} = 0, \tag{4.12b}$$

where

$$C = \mathrm{diag}\{\cosh(k_0 H), \ldots, \cosh(k_N H)\}, \quad S = \mathrm{diag}\{\sinh(k_0 H), \ldots, \sinh(k_N H)\} \tag{4.13a}$$

and

$$K = \mathrm{diag}\{k_0, \ldots, k_N\}. \tag{4.13b}$$

Matrix A, which is defined by $A_{j+1,i+1} = a_{j,i} = (W_j, W_i)$ $(i, j = 0, \ldots, N)$, and the vector $\mathbf{f} = (1, \ldots, 1)^T$, were originally introduced in §3.1. The set of equations (4.12a-b) now represents an eigensystem that is to be solved for eigenvalues λ and corresponding eigenvector entries $\mathbf{c}(\lambda)$ and $\gamma^{(1)}(\lambda)$. Due to the dimension of this eigensystem, there will be $(2N + 6)$ of these eigenvalue-eigenvector pairs. Note that we have eliminated the constant $\gamma^{(2)}$ by using the identity $\gamma^{(2)} = -\lambda^2\beta\gamma^{(1)}$ from which it is therefore easily recovered.

Combining dispersion relation (3.13) and equation (4.12b) we deduce that

$$\begin{aligned} \kappa C\mathbf{f} &= (1 - \kappa\alpha)S\mathbf{f} + \beta K^4 KS\mathbf{f} \\ &= \beta(K^2 - (\lambda^2 + q^2))(K^2 + (\lambda^2 + q^2))KS\mathbf{f} + KS\mathbf{f}\mathbf{f}^T C\mathbf{c}. \end{aligned} \tag{4.14}$$

Furthermore, by using the formula

$$a_{j,i} = \frac{k_j \sinh(k_j H)\cosh(k_i H) - k_i \sinh(k_i H)\cosh(k_j H)}{k_j^2 - k_i^2} \quad (i \neq j), \tag{4.15}$$

which is given in Appendix A, the equality

$$A(K^2-\lambda^2)+(KS\mathbf{f}^T\mathbf{f}C-C\mathbf{f}^T\mathbf{f}KS)=(K^2-\lambda^2)A, \tag{4.16}$$

follows directly. Substituting equalities (4.14) and (4.16) into equation (4.12a) gives

$$\left(K^2-(\lambda^2+q^2)I\right)A\mathbf{c}+\beta\gamma^{(1)}\left(K^2-(\lambda^2+q^2)I\right)\left(K^2+(\lambda^2+q^2)I\right)KS\mathbf{f}=\mathbf{0}. \tag{4.17}$$

At this point, it may be noted that the $(2N+2)$ pairs

$$(\lambda^2,\mathbf{c})=(\lambda_i^2,\mathbf{I}_i)\equiv(k_i^2-q^2,\mathbf{I}_i) \quad (i=0,\ldots,N),$$

satisfy (4.17), and hence provide our first set of eigenvalue-eigenvector pairs. The values

$$\gamma^{(1)}(\lambda_i)=\kappa^{-1}k_i\sinh(k_iH) \quad (i=0,\ldots,N),$$

may then be recovered from (4.12b).

If $\lambda\neq\lambda_i$ $(i=0,\ldots,N)$ then the matrix $\Lambda\equiv K^2-(\lambda^2+m^2)I$ is non-singular, and hence equation (4.17) may be simplified to

$$A\mathbf{c}+\beta\gamma^{(1)}(K^2+(\lambda^2+q^2)I)KS\mathbf{f}=\mathbf{0}, \tag{4.18}$$

from which the vector $\mathbf{c}$ may be eliminated by multiplying through with $\mathbf{f}^T$ and using equation (4.12b), to give

$$(\beta(\lambda^2+q^2)^2+1-\kappa\alpha)+\beta\mathbf{f}^TCA^{-1}(K^2+(\lambda^2+q^2)I)KS\mathbf{f}=0. \tag{4.19}$$

Equation (4.19) is a quartic that defines the remaining four eigenvalues

$$\lambda^2=\lambda_{-i}^2\equiv\mu_{N,(i)}^2-q^2 \quad (i=1,2). \tag{4.20}$$

The corresponding eigenvectors, $\upsilon_{N,(i)}\equiv\mathbf{c}(\lambda_{-i})$, are then recovered from (4.18). Unlike the previous eigenvalue-eigenvector pairs, $(\lambda_i,\mathbf{I}_i)$ $(i=0,\ldots,N)$, the quantities $\mu_{N,(i)}$ and $\upsilon_{N,(i)}$ $(i=1,2)$ are dimension dependent. Note that the choice of $\gamma^{(1)}(\lambda_{-i})$ $(i=1,2)$ is free, and taking

$$\gamma^{(1)}(\lambda_{-i})=\frac{\lambda_{-i}\sinh(\lambda_{-i}H)}{\kappa} \quad (i=1,2), \tag{4.21}$$

will prove to be algebraically convenient.

On intervals of constant D, h and d the approximation may therefore be written as

$$\mathbf{\Psi}_N(x)=\mathcal{C}\{\mathrm{e}^{\mathrm{i}\Lambda x}\mathbf{A}+\mathrm{e}^{-\mathrm{i}\Lambda x}\mathbf{B}\}, \tag{4.22}$$

where

$$\Lambda = \mathrm{diag}\{\lambda_0, \dots, \lambda_N, \lambda_{-1}, \lambda_{-2}\}, \quad \mathrm{e}^{\pm \mathrm{i}\Lambda x} = \mathrm{diag}\{\mathrm{e}^{\pm \mathrm{i}\lambda_0 x}, \dots, \mathrm{e}^{\pm \mathrm{i}\lambda_N x}, \mathrm{e}^{\pm \mathrm{i}\lambda_{-1} x}, \mathrm{e}^{\pm \mathrm{i}\lambda_{-2} x}\}, \tag{4.23}$$

$$\mathcal{C} = \left[\begin{array}{ccccc} \hat{\mathbf{c}}(\lambda_0) & \dots & \hat{\mathbf{c}}(\lambda_N) & \hat{\mathbf{c}}(\lambda_{-1}) & \hat{\mathbf{c}}(\lambda_{-2}) \end{array} \right], \tag{4.24}$$

and

$$\mathbf{A} = (A_0, \dots, A_N, A_{-1}, A_{-2})^T, \quad \mathbf{B} = (B_0, \dots, B_N, B_{-1}, B_{-2})^T,$$

are constant vectors of length $(N+3)$. Equivalently, we may express the full MMA as

$$\psi_N(x,y,z) = \sum_{i=0}^{N} \left\{ \varphi_i(x) + \sum_{j=1,2} \upsilon_{N,(i,j)} \varphi_{-i}(x) \right\} \mathrm{e}^{\mathrm{i}qy} \cosh\{k_i(z+h)\}, \tag{4.25}$$

where

$$\varphi_i(x) = A_i \mathrm{e}^{\mathrm{i}\lambda_i x} + B_i \mathrm{e}^{-\mathrm{i}\lambda_i x} \quad (i = 0, \dots, N),$$

$$\varphi_{-j}(x) = A_{-j} \mathrm{e}^{\mathrm{i}\,(\mu_{N,(j)}^2 - q^2)^{1/2} x} + B_{-j} \mathrm{e}^{-\mathrm{i}\,(\mu_{N,(j)}^2 - q^2)^{1/2} x} \quad (j = 1, 2),$$

and the (dimension-dependent) constants are

$$\upsilon_{N,(i,j)} = \{\upsilon_{N,(j)}\}_i \quad (i = 0, \dots, N;\ j = 1, 2). \tag{4.26}$$

We may compare this with the two-dimensional version of the full linear solution (3.42)

$$\phi(x,y,z) = \sum_{i=0}^{\infty} \left\{ \phi_i(x) + \sum_{j=1,2} \upsilon_{i,j} \phi_{-j}(x) \right\} \mathrm{e}^{\mathrm{i}qy} \cosh\{k_i(z+h)\}, \tag{4.27}$$

where

$$\phi_i(x) = A_i \mathrm{e}^{\mathrm{i}\lambda_i x} + B_i \mathrm{e}^{-\mathrm{i}\lambda_i x} \quad (i = 0, \dots, N),$$

and

$$\phi_{-j}(x) = A_{-j} \mathrm{e}^{\mathrm{i}\,(\mu_j^2 - q^2)^{1/2} x} + B_{-j} \mathrm{e}^{-\mathrm{i}\,(\mu_j^2 - q^2)^{1/2} x} \quad (j = 1, 2).$$

Beyond the issue of truncation, expressions (4.25) and (4.27) differ only in the appearance of $\mu_{N,(j)}$ as opposed to μ_j, and $\upsilon_{N,(i,j)}$ as opposed to $\upsilon_{i,j}$ $(i = 0, \dots, N; j = 1, 2)$. As such, we may view the rôle of the dimension-dependent pairs $(\lambda_{-j}, \mathbf{c}(\lambda_{-j}))$ as compensating for the horizontal motion related to the complex roots that, in the full linear solution, are redistributed amongst the other vertical modes using (3.39). It is therefore natural to regard

$$\mu_{N,(j)} \approx \mu_j, \quad \upsilon_{N,(i,j)} \approx \upsilon_{i,j} \quad (i = 0, \dots, N;\ j = 1, 2). \tag{4.28}$$

It is possible to say a little more than (4.28) if we assume the approximations are replaced by equalities in the limit $N \to \infty$. It is then necessary to show that the eigensystem (4.18) is satisfied by these choices in this limit. To prove this we make use of the equality

$$\beta\gamma^{(1)}(\mu_j)(k_i^2+\mu_j^2)k_i\sinh(k_iH) = -\frac{k_i\sinh(k_iH)\cosh(\mu_jH)-\mu_j\sinh(\mu_jH)\cosh(k_iH)}{k_i^2-\mu_j^2},$$

for $i=0,\dots$ and $j=1,2$ (which may be derived from the dispersion relation (3.13)) and also the limit

$$\sum_{n=0}^{N} a_{i,n}v_{n,j} \to \frac{k_i\sinh(k_iH)\cosh(\mu_jH)-\mu_j\sinh(\mu_jH)\cosh(k_iH)}{k_i^2-\mu_j^2} \quad (N\to\infty),$$

for $i=0,\dots$ and $j=1,2$ (which is deduced via (3.39) and (4.15)). We may indeed therefore write

$$\mu_{N,(j)} \to \mu_j, \quad v_{N,(i,j)} \to v_{i,j} \quad (N\to\infty), \tag{4.29}$$

for $i=0,\dots,N$ and $j=1,2$.

Having substantiated assertion (4.28) through (4.29), we however note that the MMA of dimension N is unaware of our choice to redistribute the horizontal motion related to the complex roots; that is, we may equivalently have removed any of the vertical modes $w_{N+1},\dots$ in place of w_{-j} $(j=1,2)$ in (4.27) and have deduced different approximations (4.28). The effects of using the dimension-dependent values $\mu_{N,(j)}$ and $v_{N,(i,j)}$, as opposed to direct truncation of (4.27), are investigated in the following chapter.

In an interval of ice-free fluid, expression (4.22) degenerates to

$$\mathbf{\Phi}_N^{(0)}(x) = \mathrm{e}^{\mathrm{i}\Lambda x}\mathbf{A} + \mathrm{e}^{-\mathrm{i}\Lambda x}\mathbf{B}, \tag{4.30}$$

in which

$$\lambda_i^2 \equiv \left(\lambda_i^{(0)}\right)^2 = \left(k_i^{(0)}\right)^2 - q^2 \quad (i=0,\dots,N),$$

and

$$\mathbf{A} = \mathrm{diag}\left(A_0,\dots,A_N\right)^T, \quad \mathbf{B} = \mathrm{diag}\left(B_0,\dots,B_N\right)^T,$$

are now of length $(N+1)$. The analogues of expressions (4.25) and (4.27) are, respectively,

$$\psi_N(x,y,z) \equiv \psi_N^{(0)}(x,y,z)\sum_{i=0}^{N}\{A_i\mathrm{e}^{\mathrm{i}\lambda_i^{(0)}x} + B_i\mathrm{e}^{-\mathrm{i}\lambda_i^{(0)}x}\}\mathrm{e}^{\mathrm{i}qy}\cosh\{k_i^{(0)}(z+h)\}, \tag{4.31}$$

and

$$\phi(x,y,z)\sum_{i=0}^{\infty}\{A_i\mathrm{e}^{\mathrm{i}\lambda_i^{(0)}x} + B_i\mathrm{e}^{-\mathrm{i}\lambda_i^{(0)}x}\}\mathrm{e}^{\mathrm{i}qy}\cosh\{k_i^{(0)}(z+h)\}. \tag{4.32}$$

Therefore, in contrast with the case of ice-cover, for situations of ice-free fluid, the form of the MMA is a direct truncation of the full linear solution.

In this section we have ignored the possibility of the approximate roots $\mu_{N,(i)}$ $(i=1,2)$ coinciding, which could occur even though a multiple root of the dispersion relation is not present. The condition for a multiple root here is

$$\frac{1}{4}\left(\mathbf{f}^T CA^{-1}KS\mathbf{f}\right)^2 = \frac{1-\kappa\alpha}{\beta} + \mathbf{f}^T CA^{-1}K^3S\mathbf{f},$$

in which case

$$\mu^2_{N,(i)} = \frac{1}{2}\mathbf{f}^T CA^{-1}K^3S\mathbf{f}.$$

This situation is easily dealt with by standard methods; however, as this problem occurs only at isolated frequencies, we will not have to resort to an alternative expression but will rather take the pragmatic approach of perturbing the frequency to eliminate the multiple eigenvalue. It is also noted that, in the neighbourhood of a true bifurcation, it is not unlikely that the properties of the $\mu_{N,(i)}$ $(i=1,2)$ differ from those of the μ_i $(i=1,2)$. That is, for certain N, the $\mu_{N,(i)}$ $(i=1,2)$ may be purely imaginary, whilst the μ_i $(i=1,2)$ are complex and vice versa.

The fact that the inclusion of the vertical mode that bears the incident wave in the trial space would lead to the correct form of the far-field conditions being satisfied in the MMA was discussed in the previous chapter. Having derived the expressions (4.25) and (4.31) it is possible to explicitly witness this property in the case of two-dimensional motion and oblique incidence for which the radiation conditions (4.1a-b) must hold. Further and more specific reference will be made to this point in the following section.

For problems of two-dimensional geometry and obliquely incident waves, we have reduced the governing equations of the MMA, given in §3.1, to a finite system of ordinary differential equations, (4.4) and (4.6), with accompanying jump conditions. In intervals of uniform geometry, for which the geometrical functions take constant values, this system has been solved up to a set of unknown constants - the amplitudes - which are fixed by imposing the correct jump conditions dictated by the specific problem. These expressions will be used in the far-fields to allign the MMA with the exact radiation conditions that are attached to the problem. It now remains to formulate the specific solution procedures that will be used for our chosen geometrical constructions.

4.3 Numerical Formulation

In both of the two-dimensional problems to be considered, we define the finite interval over which the fluid and ice boundaries are permitted to vary as $x \in (0,l)$. Within this interval, the fluid therefore occupies the domain $(x,z) \in (0,l) \times (-h(x), -d(x))$ and the ice thickness is given by the function $D = D(x) \neq 0$. For the situation in which the ice-cover is complete, the two semi-infinite states of uniform geometry are defined as

$(x, z) \in (-\infty, 0) \times (-h^{(-)}, -d^{(-)})$ and $(x, z) \in (l, \infty) \times (-h^{(+)}, -d^{(+)})$, where $h^{(\pm)}$ and $d^{(\pm)}$ are constants, and the respective ice thicknesses are given by the constants $D^{(-)}$ and $D^{(+)}$. This is the geometrical configuration depicted in figure 4.1. The internal boundaries are defined by the points $x = 0, l$, regardless of whether the geometrical functions are insufficiently differentiable at these points or not (see §2.2.1). That is, even if the geometry were to be sufficiently smooth at either of the ends of the finite interval of varying geometry, it will suit our solution procedure to partition the x-axis at these points as if it were not.

The second problem involves partial ice-cover and, in particular, a solitary floe of finite length and is depicted in figure 4.2. The semi-infinite intervals of uniform geometry are ice-free, and the fluid occupies the domains $(x, z) \in (-\infty, 0) \times (-h^{(-)}, 0)$ and $(x, z) \in (l, \infty) \times (-h^{(+)}, 0)$. Again, the internal boundaries are defined by the points $x = 0, l$ and we recall that we have assumed that $D(x) \neq 0$ $(x = 0, l)$.

4.3.1 Complete ice-cover

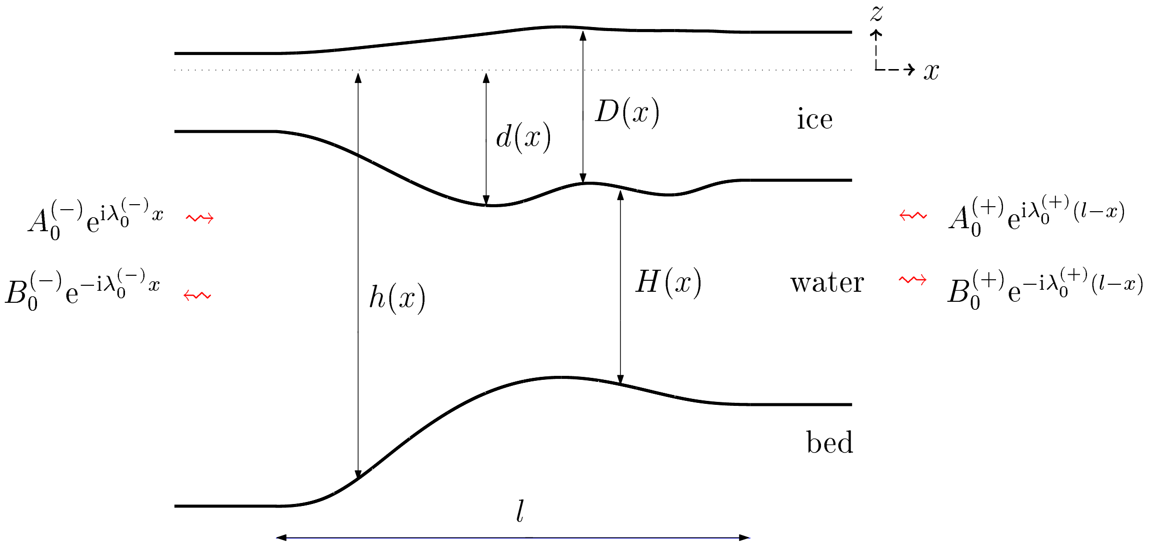

Figure 4.1: Schematic of the two-dimensional problem of complete ice-cover.

We assume the use of the natural modes in the two semi-infinite intervals $x \in (-\infty, 0)$ and $x \in (l, \infty)$. In this case, using the form (4.22), we may represent the unknown functions as

$$\begin{aligned} \boldsymbol{\Psi}_N^{(-)}(x) &= \mathcal{C}^{(-)}\{\mathrm{e}^{\mathrm{i}\Lambda^{(-)}x}\mathbf{A}^{(-)} + \mathrm{e}^{-\mathrm{i}\Lambda^{(-)}x}\mathbf{B}^{(-)}\} \qquad (x < 0), \\ \boldsymbol{\Psi}_N^{(+)}(x) &= \mathcal{C}^{(+)}\{\mathrm{e}^{\mathrm{i}\Lambda^{(+)}(l-x)}\mathbf{A}^{(+)} + \mathrm{e}^{-\mathrm{i}\Lambda^{(+)}(l-x)}\mathbf{B}^{(+)}\} \quad (x > l), \end{aligned} \tag{4.33}$$

where vectors $\mathbf{A}^{(\pm)} = (A_0^{(\pm)}, 0, \ldots, 0, 0, 0)^T$ contain the known incident amplitudes and

$\mathbf{B}^{(\pm)} = (B^{(\pm)}_{N,0}, \dots, B^{(\pm)}_{N,N}, B^{(\pm)}_{N,-1}, B^{(\pm)}_{N,-2})^T$ contain unknown outgoing amplitudes. The superscripts (±) are used to indicate that the particular quantity is evaluated using the corresponding geometrical constants. The approximation therefore mirrors the exact radiation conditions (4.1a), so that in the far-fields

$$\psi_N \sim \begin{cases} \{A_0^{(-)}\mathrm{e}^{\mathrm{i}\lambda_0^{(-)}x} + B^{(-)}_{N,0}\mathrm{e}^{-\mathrm{i}\lambda_0^{(-)}x}\}\mathrm{e}^{\mathrm{i}qy}\cosh\{k_0^{(-)}(z+h^{(-)})\} & (x\to-\infty),\\ \{A_0^{(+)}e^{i\lambda_0^{(+)}(l-x)} + B^{(+)}_{N,0}e^{-i\lambda_0^{(+)}(l-x)}\}\mathrm{e}^{\mathrm{i}qy}\cosh\{k_0^{(+)}(z+h^{(+)})\} & (x\to\infty),\end{cases}$$

and thus the only approximation is to the outgoing amplitudes $B^{(\pm)}_{N,0}$.

As discussed in §2.2.1, satisfaction by the MMA of the exact conditions in the far-fields is required so that we may assume that the appropriate variations vanish at these points. The point raised in §3.2.2 that it is essential to include the mode w_0 in the trial space in the far-fields is now particularly evident.

Over the interval of varying fluid and ice boundaries, $x \in (0, l)$, the system of governing equations (4.4) must be solved numerically for the vector of unknown functions $\boldsymbol{\Psi}_N$, up to a set of unknown constants. These constants are then determined through application of the jump conditions (4.10a-b). Using (4.33) we have

$$\big[\mathcal{V}^T\mathcal{M}^{-1}\boldsymbol{\Psi}_N\big]_{x=x_\pm} = \big(\mathcal{V}^T\mathcal{M}^{-1}\mathcal{C}\big)^{(\pm)}\{\mathbf{A}^{(\pm)}+\mathbf{B}^{(\pm)}\}, \tag{4.34a}$$

and

$$\big[\mathcal{V}^{-1}\{(\mathcal{A}\mathcal{M}\partial_x\boldsymbol{\Psi}_N) + (\mathcal{Q}\mathcal{N}\boldsymbol{\Psi}_N)\}\big]_{x=x_\pm} = \pm\mathrm{i}(\mathcal{V}^{-1}\mathcal{A}\mathcal{M}\Lambda)^{(\pm)}\{\mathbf{A}^{(\pm)}-\mathbf{B}^{(\pm)}\}, \tag{4.34b}$$

where $x^{(\pm)} = (l \pm l)/2$. In this finite interval the vertical modes may be chosen arbitrarily.

The number of constants up to which we determine the numerical solution, Ψ_N, is controlled by the number of unknown constants appearing in the jump conditions (4.34a-b). It is therefore computationally efficient to suppress as many unknowns as possible and, with this in mind, equations (4.34a-b) are reformulated as the vector

$$\mathfrak{B}_\pm\boldsymbol{\Psi}_N(x^{(\pm)}) = \mp\mathrm{i}\lambda_0(A_0^{(\pm)} - B^{(\pm)}_{N,0})(\mathcal{V}^{-1}\mathcal{A}\mathcal{M}\mathcal{C})^{(\pm)}\mathcal{I}_1, \tag{4.35a}$$

where $\mathcal{I}_1 = (1, 0 \dots, 0)^T$ is of length $(N+3)$, and the scalar

$$\mathfrak{b}_\pm\boldsymbol{\Psi}_N(x^{(\pm)}) = A_0^{(\pm)} + B^{(\pm)}_{N,0}, \tag{4.35b}$$

where

$$\mathfrak{B}_\pm\mathbf{v}(x) \equiv \mathcal{V}^{-1}(x_\mp)\big(\mathcal{A}(x_\mp)\mathcal{M}(x_\mp)\partial_x + \widehat{\mathcal{Q}}_\pm(x)\big)\mathbf{v}(x_\mp),$$

and

$$\mathfrak{b}_{\pm}\mathbf{v}(x) \equiv \mathcal{I}_1^T \mathcal{C}^{-1}(x_{\pm})\mathcal{M}(x_{\pm})\mathcal{V}^{-T}(x_{\pm})\mathcal{V}^{T}(x_{\mp})\mathcal{M}^{-1}(x_{\mp})\mathbf{v}(x_{\mp}),$$

where

$$\widehat{\mathcal{Q}}_{\pm}(x) \quad = \quad \mathcal{Q}(x_{\mp})\mathcal{N}(x_{\mp}) \mp \mathrm{i}\widetilde{\mathcal{Q}}_{\pm}(x), \tag{4.36a}$$

and

$$\begin{aligned}\widetilde{\mathcal{Q}}_{\pm}(x) \quad = \quad & \mathcal{V}(x_{\mp})\mathcal{V}^{-1}(x_{\pm})\mathcal{A}(x_{\pm})\mathcal{M}(x_{\pm})\mathcal{C}(x_{\pm})\mathit{\Lambda}(x_{\pm})\mathcal{F}\times \\ & \mathcal{C}^{-1}(x_{\pm})\mathcal{M}(x_{\pm})\mathcal{V}^{-T}(x_{\pm})\mathcal{V}^{T}(x_{\mp})\mathcal{M}^{-1}(x_{\mp}),\end{aligned} \tag{4.36b}$$

with $\mathcal{F} = \mathrm{diag}\{0, 1, \dots, 1\}$. Note that the only unknown amplitudes appearing in these new conditions are those of the outgoing amplitudes that appear in the far-field, namely $B^{\pm}_{N,0}$. However, the amplitudes of the evanescent waves, $B_{N,n}$ ($n = 1, \dots, N$), are unavailable through jump conditions (4.35a-b). Our objective in these two-dimensional problems will be to obtain information relating to the properties of the ice over the varying interval, specifically its displacement, and the far-field response. Therefore, the loss of knowledge of the evanescent waves, in the intervals of uniform geometry, will not deter us. It is mentioned in passing that, having obtained the MMA, the missing amplitudes may be retrieved from conditions (4.34a-b).

The approximation may now be expressed over the interval $x \in (0, l)$ as a linear combination of numerically determinable functions, with

$$\mathbf{\Psi}_N(x) = \mathrm{i}(A_0^{(-)} - B_{N,0}^{(-)})\mathcal{L}_{-}(x) + \mathrm{i}(A_0^{(+)} - B_{N,0}^{(+)})\mathcal{L}_{+}(x), \tag{4.37}$$

where $\mathcal{L}_{\pm}$ satisfy the system of equations (4.4), along with boundary conditions

$$\mathfrak{B}_{-}\mathcal{L}_{-}(0) = (\lambda_0\mathcal{V}^{-1}\mathcal{AMC})^{(-)}\mathcal{I}_1, \quad \mathfrak{B}_{+}\mathcal{L}_{+}(l) = -(\lambda_0\mathcal{V}^{-1}\mathcal{AMC})^{(+)}\mathcal{I}_1, \tag{4.38a}$$

and

$$\mathfrak{B}_{+}\mathcal{L}_{-}(l) = \mathfrak{B}_{-}\mathcal{L}_{+}(0) = \mathbf{0}, \tag{4.38b}$$

where, again, $\mathcal{I}_1 = (1, 0, \dots, 0)^T$.

The form of the solution (4.37) along with conditions (4.38a-b) ensure satisfaction of the jump conditions (4.35a). The remaining unknowns in (4.37), the outgoing amplitudes $B^{(\pm)}_{N,0}$, are found through application of the conditions (4.35b) that are yet to be used. Specifically, this produces

$$\begin{pmatrix} B_{N,0}^{(-)} \\ B_{N,0}^{(+)} \end{pmatrix} = S \begin{pmatrix} A_0^{(-)} \\ A_0^{(+)} \end{pmatrix}, \tag{4.39a}$$

which defines the outgoing amplitudes in terms of the incident amplitudes through the *scattering matrix*

$$S = -(I_2 + \mathrm{i}S_0)^{-1}(I_2 - \mathrm{i}S_0), \tag{4.39b}$$

with I_2 representing the two-dimensional identity matrix, and

$$S_0 = \begin{pmatrix} \mathfrak{b}_-\mathcal{L}_-(0) & \mathfrak{b}_-\mathcal{L}_+(0) \\ \mathfrak{b}_+\mathcal{L}_-(l) & \mathfrak{b}_+\mathcal{L}_+(l) \end{pmatrix}. \tag{4.39c}$$

4.3.2 Partial ice-cover

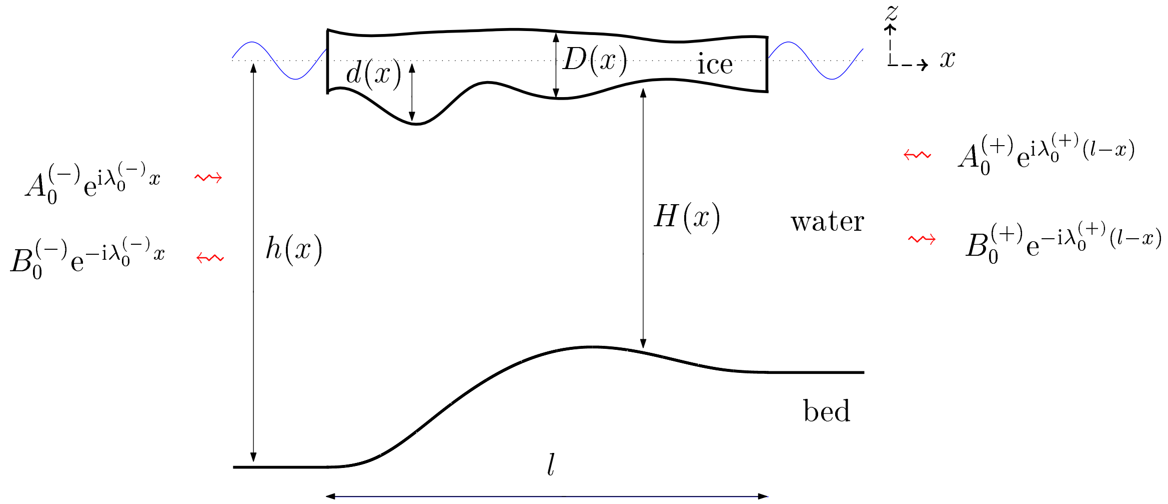

Figure 4.2: Schematic of the two-dimensional problem of partial ice-cover.

In the second problem, the two semi-infinite intervals are ice-free, and consequently, using (4.30), we may denote the solution

$$\begin{aligned} \mathbf{\Phi}_N^{(0-)}(x) &= \mathrm{e}^{\mathrm{i}\Lambda^{(-)}x}\mathbf{A}^{(-)} + \mathrm{e}^{-\mathrm{i}\Lambda^{(-)}x}\mathbf{B}^{(-)} \qquad (x<0), \\ \mathbf{\Phi}_N^{(0+)}(x) &= \mathrm{e}^{\mathrm{i}\Lambda^{(+)}(l-x)}\mathbf{A}^{(+)} + \mathrm{e}^{-\mathrm{i}\Lambda^{(+)}(l-x)}\mathbf{B}^{(+)} \quad (x>l), \end{aligned} \tag{4.40}$$

where now the vectors $\mathbf{A}^{(\pm)} = \left(A_0^{(\pm)}, 0, \ldots, 0\right)^T$ contain the incident amplitudes and $\mathbf{B}^{(\pm)} = \left(B_{N,0}^{(\pm)}, \ldots, B_{N,N}^{(\pm)}\right)^T$ the unknown outgoing amplitudes. The comments relating to the satisfaction of the the exact form of the radiation conditions, here (4.1b), are again applicable.

By using (4.40) in the jump conditions (4.11a-b) we provide the boundary conditions

$$[V^T\mathbf{\Phi}_N]_{x=x_\pm} = (V^{(\pm)})^T\{\mathbf{A}^{(\pm)} + \mathbf{B}^{(\pm)}\}, \tag{4.41a}$$

and

$$\Big[\mathcal{V}_+^{-1}\{(\mathcal{A}\widetilde{\mathcal{M}}\partial_x\mathbf{\Psi}_N)_+ + (\mathcal{Q}\widetilde{\mathcal{N}}\mathbf{\Psi}_N)_+\}\Big]_{x=x_\pm} = \pm\mathrm{i}\widetilde{\mathcal{F}}(V_-^{-1}A\Lambda)^{(\pm)}\{\mathbf{A}^{(\pm)} - \mathbf{B}^{(\pm)}\}, \tag{4.41b}$$

for the numerical solution $\boldsymbol{\Psi}_N(x)$ $(0 < x < l)$, in which $\widetilde{\mathcal{F}}$ is a $(N+3) \times (N+1)$ matrix consisting of the identity matrix of dimension $(N+1)$ appended with two rows of zeros. To calculate $\boldsymbol{\Psi}_N$, in this finite interval, any vertical modes may be chosen.

Following §4.3.1, we recast the conditions (4.41a-b) to reduce the number of unknowns that appear. The reformulated versions are

$$\mathfrak{B}_\pm \boldsymbol{\Psi}_N(x^{(\pm)}) = \mp \mathrm{i}\lambda_0^{(\pm)}(A_0^{(\pm)} - B_0^{(\pm)})\widetilde{\mathcal{F}}(V_-^{-1}A)^{(\pm)}\mathbf{I}_1, \tag{4.42a}$$

and

$$\mathfrak{b}_\pm \boldsymbol{\Psi}_N(x^{(\pm)}) = A_0^{(\pm)} + B_0^{(\pm)}, \tag{4.42b}$$

where we have redefined $\mathfrak{B}_\pm$ and $\mathfrak{b}_\pm$ as

$$\mathfrak{B}_\pm \mathbf{v}(x) \equiv \mathcal{V}^{-1}(x_\mp)(\mathcal{A}(x_\mp)\widetilde{\mathcal{M}}(x_\mp)\partial_x + \widehat{\mathcal{Q}}_\pm(x))\mathbf{v}(x_\mp)$$

and

$$\mathfrak{b}_\pm \mathbf{v}(x) \equiv \mathbf{I}_1^T V^{-T}(x_\pm)V^T(x_\mp)\widetilde{\mathcal{F}}^T \mathbf{v}(x_\mp),$$

with

$$\widehat{\mathcal{Q}}_\pm(x) = \mathcal{Q}(x_\mp)\widetilde{\mathcal{N}}(x_\mp) \mp \mathrm{i}\widetilde{\mathcal{F}}V(x_\mp)V^{-1}(x_\pm)A(x_\pm)\Lambda(x_\pm)FV^{-T}(x_\pm)V^T(x_\mp),$$

where $F = \mathrm{diag}\{0, 1, \ldots, 1\}$ is a square matrix of dimension $(N+1)$. Again, the reformulated conditions (4.42a-b) contain only the amplitudes that exist in the far-fields.

We then numerically calculate the functions $\mathcal{L}_\pm(x)$ $(0 < x < l)$ satisfying the system of equations (4.4) and the boundary conditions

$$\mathfrak{B}_-\mathcal{L}_-(0) = \widetilde{\mathcal{F}}(\lambda_0^{(0)}V^{-1}A)^{(-)}\mathbf{I}_1, \quad \mathfrak{B}_+\mathcal{L}_+(l) = -\widetilde{\mathcal{F}}(\lambda_0^{(0)}V^{-1}A)^{(+)}\mathbf{I}_1, \tag{4.43a}$$

and

$$\mathfrak{B}_+\mathcal{L}_-(l) = \mathfrak{B}_-\mathcal{L}_+(0) = \mathbf{0}. \tag{4.43b}$$

The approximation may be expressed as the linear combination

$$\boldsymbol{\Psi}_N(x) = \mathrm{i}(A_0^{(-)} - B_0^{(-)})\mathcal{L}_-(x) + \mathrm{i}(A_0^{(+)} + B_0^{(+)})\mathcal{L}_+(x),$$

and the outgoing amplitudes are obtained from the scattering relation (4.39a-c).

4.4 The scattering matrix

Many of the results presented in §§5-8 will be based on the scattering matrix, S, defined in (4.39a). This is because it gives a concise representation of the reflection and transmission of energy through an obstacle. We will also write

$$S = \begin{pmatrix} R_- & T_+ \\ T_- & R_+ \end{pmatrix}, \tag{4.44}$$

where the entries $R_\pm$ denote the *reflection coefficients* and $T_\pm$ the *transmission coefficients.* The squares of the moduli of these quantities we will refer to as the *reflected energies* and *transmitted energies* respectively, which are clearly proportional to the square of the incident amplitudes.

As the vertical modes have been chosen to be real-valued, all of the coefficients involved in the governing equations of the MMA are real-valued. It follows that $\overline{\boldsymbol{\Psi}}_N$ is a solution to the same problem as $\boldsymbol{\Psi}_N$, with the only concession being that the amplitudes $(\overline{B}^{(\pm)}_{N,0}, \overline{A}^{(\pm)}_0)$ replace $(A^{(\pm)}_0, B^{(\pm)}_{N,0})$. In particular, the scattering process (4.39a-c) remains consistent, so that

$$\begin{pmatrix} \overline{A}^{(-)}_0 \\ \overline{A}^{(+)}_0 \end{pmatrix} = S \begin{pmatrix} \overline{B}^{(-)}_{N,0} \\ \overline{B}^{(+)}_{N,0} \end{pmatrix}. \tag{4.45}$$

Comparison of (4.39a) with (4.45) reveals the identity $S\overline{S} = I$. From this equality the Kreisel relationships

$$|R_- R_+| + |T_- T_+| = 1, \tag{4.46a}$$

$$|R_-| = |R_+| \equiv |R|, \tag{4.46b}$$

$$\arg(T_-) - \arg(T_+) = 2n\pi \quad (n \in \mathbb{Z}), \tag{4.46c}$$

and

$$\arg(R_- R_+) - \arg(T_- T_+) = (2n+1)\pi \quad (n \in \mathbb{Z}), \tag{4.46d}$$

which are well-known for free-surface flows (see Porter & Chamberlain, 1997), may be obtained. It is therefore necessary to only consider the one value, $|R|^2$, for the reflected energy.

In Appendix B the energy balance

$$\Big[\boldsymbol{\Psi}^T_{(1)}\mathcal{O}\mathcal{A}(\partial_x \boldsymbol{\Psi}_{(0)}) - (\partial_x \boldsymbol{\Psi}^T_{(1)})\mathcal{O}\mathcal{A}\boldsymbol{\Psi}_{(0)} + \boldsymbol{\Psi}^T_{(1)}\widetilde{\mathcal{D}}\boldsymbol{\Psi}_{(0)}\Big]_{x_0}^{x_1} = 0, \tag{4.47}$$

is derived, with x_i $(i = 0, 1)$ arbitrary points, within ice-covered intervals, and $\boldsymbol{\Psi}_{(i)}$ $(i =$

$0, 1)$ any two solutions of the differential system of equations (4.4). The matrix

$$\mathcal{O} = \begin{pmatrix} I & \mathbf{0} & \mathbf{0} \\ \mathbf{0}^T & 0 & -\kappa \\ \mathbf{0}^T & -\kappa & 0 \end{pmatrix}, \tag{4.48}$$

is of size $(N+3) \times (N+3)$.

Taking $(\mathbf{\Psi}_{(0)}, \mathbf{\Psi}_{(1)}) = (\mathcal{L}_-, \mathcal{L}_+)$ in (4.47), where $\mathcal{L}_\pm$ satisfy the complete ice-cover boundary conditions (4.38a-b), it is possible to show that

$$\left[\mathcal{I}^T \mathcal{A}\mathcal{C}^T \mathcal{O}\mathcal{A}\mathcal{C}\mathcal{I}\right]_{x=0_-} \mathfrak{b}_- \mathcal{L}_+(0) = \left[\mathcal{I}^T \mathcal{A}\mathcal{C}^T \mathcal{O}\mathcal{A}\mathcal{C}\mathcal{I}\right]_{x=l_+} \mathfrak{b}_+ \mathcal{L}_-(l). \tag{4.49}$$

This makes use of the identity

$$\widetilde{D} = Q - Q^T,$$

and the diagonality of the matrix $\mathcal{C}^T \mathcal{O}\mathcal{A}\mathcal{C}$, which is proved in Appendix B. We deduce that, if the matrices satisfy

$$\left[\mathcal{A}\mathcal{C}^T \mathcal{O}\mathcal{A}\mathcal{C}\right]_{x=0_-}^{l_+} = 0, \tag{4.50}$$

then

$$\mathfrak{b}_- \mathcal{L}_+(0) = \mathfrak{b}_+ \mathcal{L}_-(l). \tag{4.51}$$

Equality (4.50) is clearly satisfied if the far-field geometries are identical.

From the definition (4.39c), it can readily be shown that

$$\det(S_0) T_- = 2\mathfrak{b}_-^{i-i}(\mathcal{L}_1)(0),$$

and

$$\det(S_0) T_+ = 2\mathfrak{b}_+^{i-i}(\mathcal{L}_0)(l),$$

and hence that if equality (4.51) is satisfied, then we have equality of the transmission coefficients, $T_- = T_+$.

Similarly, for the case of partial ice-cover, when the functions $\mathcal{L}_\pm$ satisfy the boundary conditions (4.43a-b), the relation

$$\left[\mathbf{I}^T \Lambda A \mathbf{I}\right]_{x=0_-} \mathfrak{b}_- \mathcal{L}_+(0) = \left[\mathbf{I}^T \Lambda A \mathbf{I}\right]_{x=l_+} \mathfrak{b}_+ \mathcal{L}_-(l),$$

can be deduced in place of (4.49). The equality of the transmission coefficients then follows if the far-field fluid depths are identical.

If the transmission coefficients are equal, say $T_\pm = T$, then using (4.46a),

$$|T|^2 = 1 - |R|^2.$$

It is therefore only necessary to consider the value $|R|$ to describe the scattering of energy by any two-dimensional obstacle.

Chapter 5

Piecewise uniform geometry

Before we consider the two-dimensional models formulated in §§4.3.1-4.3.2, in which there exists an interval for which we permit the geometrical surfaces to undulate, it is pertinent to explore the properties of the MMA in comparison to an alternative solution method. This will serve to establish the MMA as an efficient approximation method and highlight some of its strengths and weaknesses.

To make this comparison, we consider a restricted class of problem, involving only piecewise uniform geometry, in which the sole sources of scattering are at the interfaces between different uniform regions. For such problems there is a range of alternative solution methods available, some of which are mentioned in §1. In particular, we will make use of the analytic expression for the MMA in intervals of uniform geometry, which was derived in §4.2, and explore the issues that were raised about this approximation.

The derivation of the MMA was a consequence of the consideration of geometry that varies over a domain as a continuous function of the horizontal spatial variables. An approximation method was produced by a combination of the following:

- The separation of the vertical and horizontal motion of the fluid;
- Restriction of the vertical motion to a judiciously chosen finite-dimensional space;
- Application of the Rayleigh-Ritz method in a variational principle.

This results in the elimination of the vertical coordinate from our calculations via a process of vertical averaging through integration.

Our specific aim in this chapter is to examine the rôle of the vertical averaging in the MMA. To do so, we will compare the MMA against an *eigenfunction matching method* (EMM) that does not invoke any such vertical averaging. For the investigations of this chapter, it is sufficient to consider only the most simple version of piecewise uniform geometry, which is a two-dimensional model involving only a single source of scattering. The EMM is introduced through one such example below.

5.1 The semi-infinite ice sheet problem

As stated above, we will restrict our comparison of the MMA and EMM to a piecewise uniform problem that incorporates only a single source of scattering. The example that will be used here is the classical problem of ocean waves normally incident from a semi-infinite interval on an ice sheet of a semi-infinite extent. This problem has been used to describe shore-fast sea-ice (see §1) and has been studied by Evans & Davies (1968), Fox & Squire (1994), Balmforth & Craster (1999) and Linton & Chung (2003) amongst others, although a zero draught has always been assumed.

Therefore, we consider the geometrical configuration defined by

$$D(x) = \begin{cases} 0 & (x < 0), \\ D_0 & (x > 0), \end{cases} \qquad H(x) = \begin{cases} h_0 & (x < 0), \\ H_0 & (x > 0), \end{cases}$$

and $h = h_0$ throughout. The draught of the ice is given by $d_0 = h_0 - H_0$. All values with subscripts are positive constants. A graphical representation of the semi-infinite ice sheet geometry is given in figure 5.1.

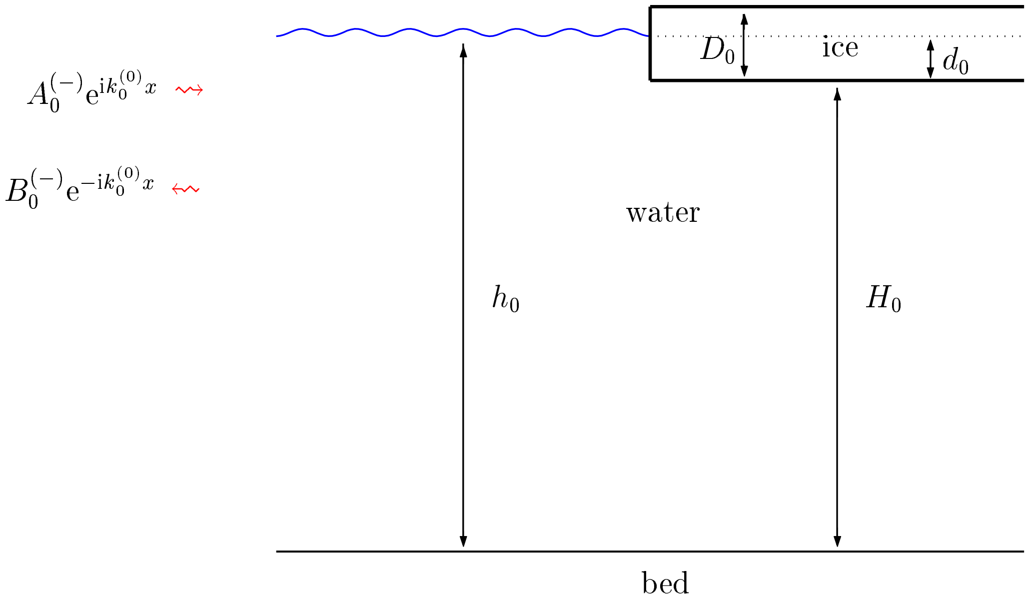

Figure 5.1: Schematic of the semi-infinite ice sheet problem.

We wish to approximate the reduced velocity potential $\phi(x, z)$ satisfying (2.9a-c) for $x > 0$ and (2.11a-b) for $x < 0$. Additionally, there are the continuity conditions

$$\langle\langle \phi \rangle\rangle = \langle\langle \partial_x \phi \rangle\rangle = 0 \quad (x = 0, -h_0 < z < -d_0), \tag{5.1a}$$

and the draught condition

$$\partial_x\phi(0_-,z) = 0 \quad (-d_0 < z < 0). \tag{5.1b}$$

The no bending moment and shearing stress conditions are given by

$$\partial_x^2\eta(0) = \partial_x^3\eta(0) = 0, \tag{5.2a}$$

or, alternatively,

$$\partial_x^2\partial_z\phi(0_+,-d_0) = \partial_x^3\partial_z\phi(0_+,-d_0) = 0. \tag{5.2b}$$

In the far-fields, the radiation conditions

$$\phi(x,z) \sim \begin{cases} (A_0^{(-)}\mathrm{e}^{\mathrm{i}k_0^{(0)}x} + B_0^{(-)}\mathrm{e}^{-\mathrm{i}k_0^{(0)}x})\cosh k_0^{(0)}(z+h_0) & (x \to -\infty), \\ (A_0^{(+)}\mathrm{e}^{-\mathrm{i}k_0 x} + B_0^{(+)}\mathrm{e}^{\mathrm{i}k_0 x})\cosh k_0(z+h_0) & (x \to \infty), \end{cases} \tag{5.3}$$

must hold, where k_0 is the propagating wavenumber beneath the ice and $k_0^{(0)}$ is the propagating free-surface wavenumber. As usual, the constants $A_0^{(\pm)}$ and $B_0^{(\pm)}$ represent, respectively, the incident and reflected amplitudes. The incident wave amplitude from the ice-covered far-field, $A_0^{(+)}$, will usually be set to zero; however, we retain it in our numerical formulation for completeness.

5.1.1 The multi-mode approximation (MMA)

Assuming unit weighting, $\varpi_n = 1$ $(n = 0,\dots,N)$, the reduced velocity potential ϕ, under the constraints of (5.3), is approximated in the MMA as

$$\phi(x,z) \approx \begin{cases} \psi_N^{(0)}(x,z) = \mathbf{f}^T C^{(0)}(z)\mathbf{\Phi}_N^{(0)}(x) & (x<0), \\ \psi_N(x,z) = \mathbf{f}^T C(z)\mathbf{\Phi}_N(x) & (x>0), \end{cases}$$

where $\mathbf{f} = (1,\dots,1)^T$ is a vector of length $(N+1)$ and

$$C(z) = \mathrm{diag}\{\cosh\{k_0(z+h_0)\},\dots,\cosh\{k_N(z+h_0)\}\}$$

and

$$C^{(0)}(z) = \mathrm{diag}\{\cosh\{k_0^{(0)}(z+h_0)\},\dots,\cosh\{k_N^{(0)}(z+h_0)\}\}$$

have been (for this chapter only) redefined to include z dependence. From equation (4.30)

$$\mathbf{\Phi}_N^{(0)}(x) = \mathrm{e}^{\mathrm{i}K^{(0)}x}\mathbf{A}^{(-)} + \mathrm{e}^{-\mathrm{i}K^{(0)}x}\mathbf{B}^{(-)},$$

and, similarly, from equation (4.25),

$$\mathbf{\Phi}_N(x) = \mathrm{e}^{-\mathrm{i}Kx}\mathbf{A}^{(+)} + \mathrm{e}^{\mathrm{i}Kx}\mathbf{B}^{(+)} + \sum_{j=1,2} B_{-j}\mathrm{e}^{\mathrm{i}\mu_{N,(j)}x}\upsilon_{N,(j)}, \tag{5.4}$$

where $\mathbf{A}^{(\pm)}$ are vectors whose only non-zero entries are the incident amplitudes and $\mathbf{B}^{(\pm)}$ are vectors of the unknown reflected amplitudes.

The vertical displacement of the underside of the ice, η, is indirectly approximated in the MMA by χ. By using (5.4) in (4.12a), it is straightforward to give χ in the explicit form

$$\chi(x) = \kappa^{-1}\mathbf{f}^T K S(-d_0)\{\mathrm{e}^{-\mathrm{i}Kx}\mathbf{A}^{(+)} + \mathrm{e}^{\mathrm{i}Kx}\mathbf{B}^{(+)}\} + \sum_{j=1,2}\gamma^{(1)}(\mu_{N,(j)})B_{-j}\mathrm{e}^{\mathrm{i}\mu_{N,(j)}x}, \tag{5.5}$$

where $S(z) = \mathrm{diag}\{\sinh\{k_0(z+h)\},\ldots,\sinh\{k_N(z+h)\}\}$, like $C(z)$, has been redefined for this chapter only. Using this definition, conditions (5.2a), which here translate to $\partial_x^2\chi(0) = \partial_x^3\chi(0) = 0$, may be interpreted as a means of defining the amplitudes B_{-j} $(j = 1, 2)$ in terms of $\mathbf{A}^{(+)}$ and $\mathbf{B}^{(+)}$, with

$$\begin{gathered}\gamma^{(1)}(\mu_{N,(j)})B_{-j}\mu_{N,(j)}^2(\mu_{N,(j)} - \mu_{N,(j_-)}) = \\ \kappa^{-1}\mathbf{f}^T K S(-d) K^2\{(K + \mu_{N,(j_-)}I)\mathbf{A}^{(+)} + (K - \mu_{N,(j_-)}I)\mathbf{B}^{(+)}\},\end{gathered} \tag{5.6}$$

where $j_- = (3 - (-1)^j)/2$.

The approximations $\psi_N^{(0)}$ and ψ_N are joined at $x = 0$ through the conditions

$$(V^{(0)})^T\mathbf{\Phi}^{(0)}(0) = V^T\mathbf{\Phi}(0), \tag{5.7a}$$

and

$$A^{(0)}\partial_x\mathbf{\Phi}^{(0)} = V^{(0)}\mathbf{u}, \quad A\partial_x\mathbf{\Phi} = V\mathbf{u}. \tag{5.7b}$$

This fully defines the MMA approximation. The auxiliary vector $\mathbf{u}$, which is usually omitted from these continuity conditions, is retained to aid comparison with the EMM.

5.1.2 The eigenfunction matching method (EMM)

In order to examine the EMM, it is convenient to utilise notation that includes infinite arrays. The difference between infinite and finite arrays will be understood through a subscript attached to all matrices where confusion could arise.

Seeking separation solutions (see §3.2) and applying radiation conditions (5.3), the reduced velocity potential may be expressed as the infinite sum over the vertical modes

$$\begin{aligned}\phi(x,z) &= \sum_{n=0}^{\infty}\{A_n^{(-)}\mathrm{e}^{\mathrm{i}k_n^{(0)}x} + B_n^{(-)}\mathrm{e}^{-\mathrm{i}k_n^{(0)}x}\}\cosh\{k_n^{(0)}(z+h_0)\} \\ &= \mathbf{f}^T C_{\infty}^{(0)}(z)\{\mathrm{e}^{\mathrm{i}K_{\infty}^{(0)}x}\mathbf{A}^{(-)} + \mathrm{e}^{-\mathrm{i}K_{\infty}^{(0)}x}\mathbf{B}^{(-)}\} \\ &\equiv \mathbf{f}^T C_{\infty}^{(0)}(z)\mathbf{\Phi}^{(0)}(x),\end{aligned} \tag{5.8a}$$

in $x < 0$, and

$$\begin{aligned}\phi(x,z) &= \sum_{n=0}^{\infty}\{A_n^{(+)}\mathrm{e}^{-\mathrm{i}k_n x} + B_n^{(+)}\mathrm{e}^{\mathrm{i}k_n x} + \sum_{j=1,2}\upsilon_{n,j}B_{-j}\mathrm{e}^{\mathrm{i}\mu_j x}\}\cosh\{k_n(z+h_0)\} \\ &= \mathbf{f}^T C_{\infty}(z)\{\mathrm{e}^{-\mathrm{i}K_{\infty}x}\mathbf{A}^{(+)} + \mathrm{e}^{\mathrm{i}K_{\infty}x}\mathbf{B}^{(+)} + \sum_{j=1}^{2}B_{-j}\mathrm{e}^{\mathrm{i}\mu_j x}\upsilon_j\} \\ &= \mathbf{f}^T C_{\infty}(z)\mathbf{\Phi}(x),\end{aligned} \tag{5.8b}$$

for $x > 0$, where $\mathbf{A}^{(\pm)} = \left(A_0^{(\pm)}, 0, \dots\right)^T$, $\mathbf{B}^{(\pm)} = \left(B_0^{(\pm)}, \dots\right)^T$, $\mathbf{f} = (1, \dots)^T$ and $\upsilon_j = (\upsilon_{0,j}, \dots)^T$ are all vectors of infinite length. The quantities μ_j $(j = 1, 2)$ are the complex roots of the dispersion relation (3.13), which were discussed in §3.2.2, and the values $\upsilon_{n,j}$ $(n = 0, \dots)$ are the corresponding redistribution weights defined in equation (3.40). It is appropriate to again note that the recasting of the full linear solution ϕ through the redistribution of the horizontal motion associated to the vertical modes $\cosh\{\mu_j(z+h)\}$ $(j = 1, 2)$ is non-unique. The particular selection to remove the complex vertical modes is here made to maintain consistency with the MMA and this choice will have a bearing on the resulting truncated form of the EMM.

Following the MMA approach, the constants B_{-j} $(j = 1, 2)$ are determined in terms of $\mathbf{A}^{(+)}$ and $\mathbf{B}^{(+)}$ by application of the no bending moment and shearing stress conditions, here equations (5.2b), to (5.8b)

$$\begin{gathered}\mu_j \sinh(\mu_j H_0)B_{-j}\mu_j^2(\mu_j - \mu_{j_-}) = \\ -\kappa^{-1}\mathbf{f}^T K_{\infty}S_{\infty}(-d_0)(K_{\infty})^2\{(K_{\infty} + \mu_{j_-}I_{\infty})\mathbf{A}^{(+)} + (K_{\infty} - \mu_{j_-}I)\mathbf{B}^{(+)}\},\end{gathered} \tag{5.9}$$

where, again $j_- = (3 - (-1)^j)/2$ $(j = 1, 2)$, and the identity

$$\mathbf{f}^T K_{\infty}^{(+)}S_{\infty}^{(+)}(z)\upsilon_j = \kappa\mu_j\sinh\{\mu_j(z+h)\},$$

has been used.

Let the condition of continuity of fluid velocity at $x = 0$ be expressed as

$$\partial_x\phi(0_-, z) = \partial_x\phi(0_+, z) = u(z) \quad (-h_0 < z < -d_0), \tag{5.10}$$

where u again denotes an auxiliary function, and note that, due to the condition (5.1b) we may define $u(z) = 0$ $(-d_0 < z < 0)$, so that

$$\int_{-h_0}^{0} g(z)u(z)\mathrm{d}z = \int_{-h_0}^{-d_0} g(z)u(z)\mathrm{d}z \quad (j = 1, 2),$$

for arbitrary function g. Taking the inner-products, with respect to z, of the two limits involved in (5.10), with $C_{\infty}^{(0)}\mathbf{f}$ and $C_{\infty}\mathbf{f}$ respectively, and noting that

$$A_{\infty}^{(0)} = \int_{-h_0}^{0} C_{\infty}^{(-)}(z)\mathbf{f}^T\mathbf{f}C_{\infty}^{(-)}(z)\,\mathrm{d}z, \quad A_{\infty} = \int_{-h_0}^{-d_0} C_{\infty}^{(+)}(z)\mathbf{f}^T\mathbf{f}C_{\infty}^{(+)}(z)\,\mathrm{d}z,$$

yields the conditions

$$A^{(0)}\partial_x\mathbf{\Phi}(\mathbf{0}_-) = \int_{-h_0}^{-d_0} C^{(0)}(z)\mathbf{f}\,u(z)\,\mathrm{d}z, \quad A\partial_x\mathbf{\Phi}(\mathbf{0}_+) = \int_{-h_0}^{-d_0} C(z)\mathbf{f}\,u(z)\,\mathrm{d}z.$$

The function $u(z)$ may be expanded as

$$u(z) = \sum_{i=0}^{\infty} v_i(z)u_i = \mathbf{f}^T\mathrm{diag}\{v_n(z)\}\mathbf{u}, \quad \mathbf{u} = (u_0, \dots)^T,$$

where $\{v_0, \dots\}$ is the trial space employed for the analogous auxiliary function in the MMA (see §3.2). This approach is equivalent to Galerkin's method. Conditions (5.10) may then be recast as

$$A^{(0)}\partial_x\mathbf{\Phi}^{(0)}(0_-) = V_{\infty}^{(0)}\mathbf{u}. \tag{5.11a}$$

Furthermore, if we take inner-products of the remaining continuity condition, $\langle\langle\phi\rangle\rangle = 0$, with $v_0(z), \dots$, the resulting condition is

$$(V^{(0)})^T\mathbf{\Phi}(0_-) = V^T\mathbf{\Phi}(0_+). \tag{5.11b}$$

The unknown outgoing amplitudes $\mathbf{B}^{(\pm)}$ are theoretically obtained through conditions (5.11a-b), which determines the EMM solution.

In practice the EMM solution must be found by setting a truncation level for the vertical fluid structure, N say, and also for the auxiliary, interfacial function $u(z)$, M say. All infinite matrices are therefore reduced to the relevant finite dimension. Note that the structure of the EMM approximation of dimension $N = M$ differs from that of the MMA in only one respect, that the wavenumbers μ_j and associated vectors υ_j $(j = 1, 2)$ appearing in the EMM are, respectively, the exact complex roots of dispersion relation (3.13) and redistribution weights (3.39), whereas the corresponding entries in the MMA, $\mu_{N,(j)}$ and $\upsilon_{N,(j)}$ $(j = 1, 2)$, are dimension-dependent values generated by the variational principle and are such that $\mu_{N,(j)} \to \mu_j$ and $\upsilon_{N,(j)} \to \upsilon_j$ as $N \to \infty$ for $j = 1, 2$ (see §4.2).

Consequently, at finite dimensions, the calculated values of the outgoing amplitudes, $\mathbf{B}^{(\pm)}$, differ between the two methods but will converge to the same values as the dimension is increased.

In both methods, the vertical and horizontal motions of the fluid have been separated. The process of vertical averaging results in horizontal modes in the MMA that can be viewed as attempting to compensate for all of the absent modes. In contrast, in the EMM the level of truncation does not affect the horizontal modes retained. However, due to the separation of the spatial coordinates, the structure of both methods is unrelated to the scattering which takes place over a horizontal boundary. These last comments are not restricted to the case of a semi-infinite ice sheet but are true of all geometrical configurations. As our primary concern is in exposing characteristics of the MMA, throughout the remainder of this chapter we will restrict the truncated EMM to dimensions such that $N = M$ and refer to this as the EMM approximation of dimension N.

5.1.3 Comparison to the work of Linton & Chung (2003)

Linton & Chung (2003) also solved the semi-infinite ice sheet problem being considered in this chapter, albeit with the restriction to zero draught and with the introduction of oblique incidence. Their method of solution follows our EMM closely, in that the solutions in the differing states, expressed as infinite series involving unknown amplitudes (see (5.8a-b)), are matched at the vertical interface $x = 0$. However, the resulting system of equations are solved by Linton & Chung via an application of the residue calculus technique, whereby a function whose poles correspond to the required unknowns, is derived and utilised. The work of Linton & Chung provides a means of testing the validity of the approximation methods presented in this chapter.

The extension of both approximations to oblique incidence is straightforward - the presentation of normal incidence was made only so that the similarity between the EMM and MMA could be clearly distinguished. The introduction of oblique incidence, other than modifying the wavenumbers used in a horizontal direction, requires only the use of the modified bending moment and shearing stress conditions

$$\partial_x^2 \chi(0_+) - \nu \chi(0_+) = \partial_x^3 \chi(0_+) - (2 - \nu)\partial_x \chi(0) = 0,$$

or

$$\partial_x^2 \partial_z \phi(0_+, -d) - \nu \partial_z \phi(0_+, -d) = \partial_x^3 \partial_z \phi(0_+, -d) - (2 - \nu)\partial_x \partial_z \phi(0_+, -d) = 0,$$

which somewhat complicates expressions (5.6) and (5.9) but does nothing to affect the structure of the solutions.

Throughout the results produced in our work, we will refer to the *normalised difference* of two functions, say f and g over the interval (a,b), which we define as

$$\epsilon(f,g)=\int_a^b \frac{|f(\varsigma)-g(\varsigma)|}{|f(\varsigma)|}\mathrm{d}\varsigma, \tag{5.13}$$

where the parameter ς is either spatially or frequency dependent as required. If we take the sequence of functions $\{f_0,\dots\}$ to be particular quantities of interest, approximated with the subscripted dimension, then the normalised differences $\epsilon(f_n,f_m)$ will be used as a measure of the convergence of the approximations. For instance, in the following example f_n is the MMA or EMM approximation of dimension n to $|R|$ over the interval of κ $(a,b)=(0.2,2)$. It is noted that the normailised difference of the sequence of approximations merely gives a reflection of the convergence rate. In many cases we will revert to the notation $\epsilon_{n,m}\equiv\epsilon(f_n,f_m)$ and moreover $\epsilon_n\equiv\epsilon_{n-1,n}$. We will regularly, although not always, consider results to be converged when $\epsilon_n=\mathrm{O}(10^{-3})$. We may, for example, have the case that across an interval of frequencies, say, results for a certain subinterval of frequencies take longer to converge than the remaining frequencies and, therefore, deficiencies at certain points are smoothed away in ϵ_n by rapid convergence at other points. The normalised difference will also be used to compare the difference between two different approximations, for example the MMA and the EMM, and contrast the results given by two related problems, for example the displacement experienced by a floe of a zero draught to the corresponding floe with the correct physical draught.

Figures 5.2-5.3 display both the convergence of the EMM and MMA and comparisons to the results obtained by Linton & Chung for the problem in which the constant (dimensionless) parameters $\alpha=0$, $\beta=1$ and $H=\pi/5$ are chosen, with an incident wave such that $q=k_0^{(0)}\sin(\pi/9)$. Although, from an algebraic point of view, the present theory admits the value $\alpha=0$, this has no physical interpretation in our model. Figure 5.2 concentrates on the modulus of the reflection coefficient, $|R|$, whereas figure 5.3 gives the argument of the reflected part of the wave propagating from the ice-covered far-field, here denoted by Θ_2. Parts (a) plot the convergence of both the EMM and MMA and parts (b) plot EMM and MMA approximations, taken to be converged, alongside the results given found by Linton & Chung.

The EMM and MMA single-mode approximations, to both $|R|$ and Θ_2, are clearly distinct from one another but, nevertheless, both capture the key qualitative and quantitative properties of the converged solutions. We further observe that the two approximation methods tend towards one another as their respective dimensions are increased. In these problems the EMM approximations of low dimension are more accurate than the MMA of the same dimension. This is particularly evident in the approximations to Θ_2, for which $\epsilon_{0,3}\approx 6\times10^{-2}$ for the EMM compared to $\epsilon_{0,3}\approx 1.1\times10^{-1}$ for the MMA. Parts (b) confirm

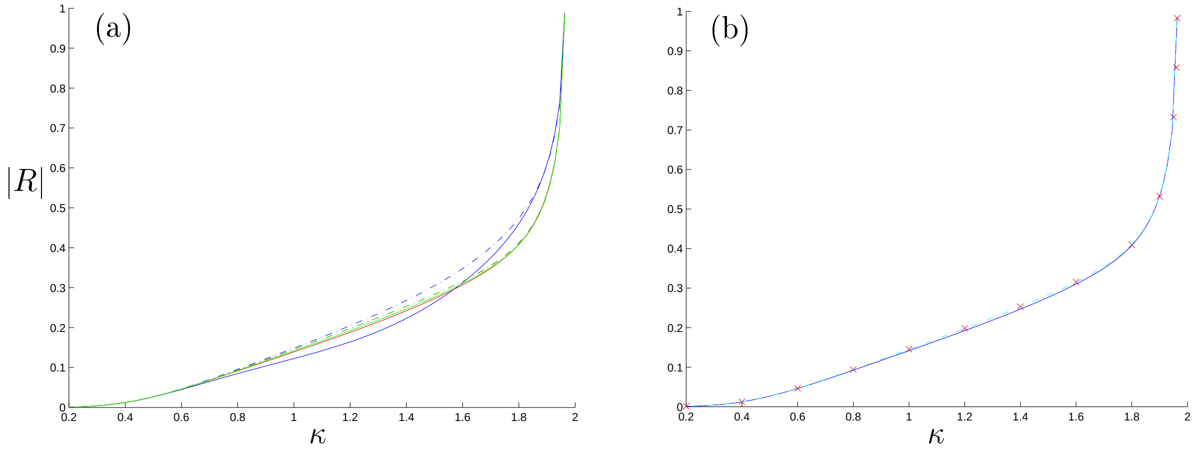

Figure 5.2: Comparison with the results of table 1 of Linton & Chung (2003) for the semi-infinite ice sheet problem, with parameters $\alpha = 0$, $\beta = 1$, $h_0 = H = \pi/5$, and an incident wave of angle $\pi/9$rads. MMAs (solid curves) and EMM approximations (dot-dash) to the modulus of the reflected amplitude as a function of the frequency parameter κ. Part (a) plots the convergence of the MMA and the EMM. The dimensions of the approximations are $N = 0$ (blue curves), $N = 2$ (red) and $N = 4$ (green). Parts (b) plots the converged MMA ($N = 6$) and converged EMM approximation ($N = 4$) along with the values calculated by Linton & Chung (×).

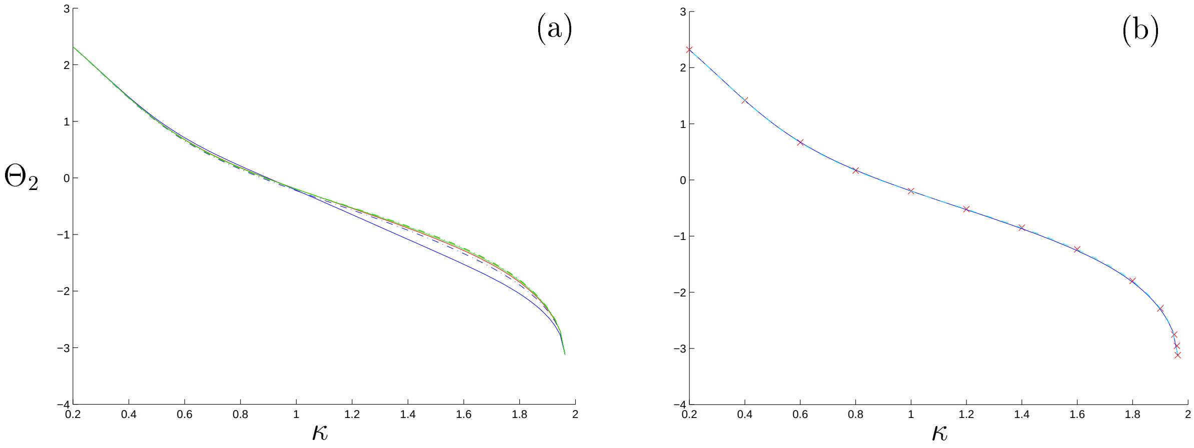

Figure 5.3: As in figure 5.2 but for the argument of the reflected amplitude , Θ_2

that our approximations are converging to the correct full linear solution. However, we note that for the approximations presented in parts (b), marginal yet clear gaps remain between the two methods. These discrepancies are attributed to slow refinement of the MMA and are observed in a slower convergence rate (ϵ_n). This is substantiated by the results of Linton & Chung for which we observe greater agreement with our EMM, which is particularly visible in figure 5.2. The noted behaviours are further investigated in the following section.

5.2 Results

Having validated the solutions produced by the MMA and EMM with independent data, we will now conduct an investigation into the respective convergence properties of these two methods of solution. In particular, we are interested in exposing the properties of the MMA that we intend to implement in cases for which there is scattering caused by continuously varying fluid and ice boundaries, in addition to that instigated by the ice edges.

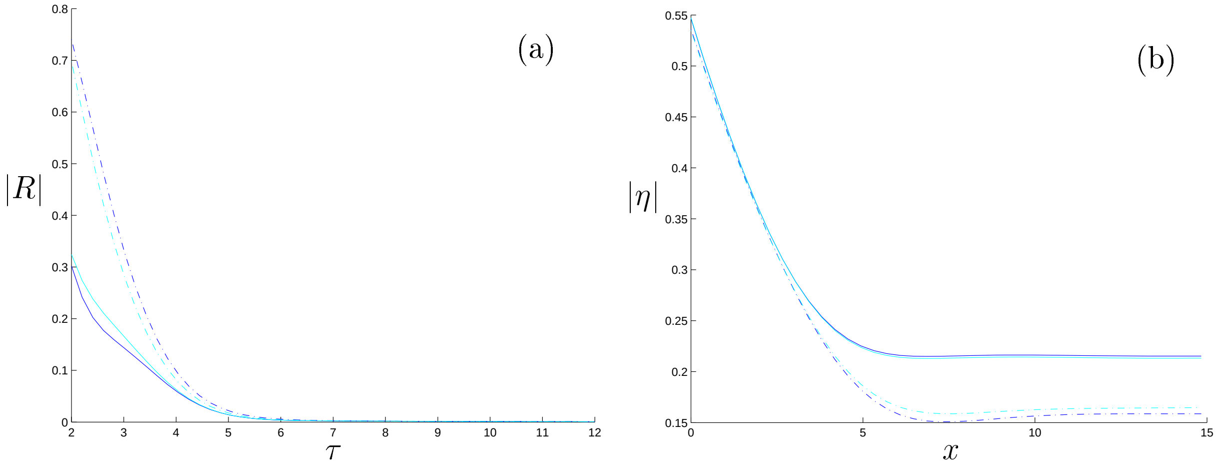

Figure 5.4: Comparison of low-dimensional MMAs (solid curves) and EMM approximations (dot-dash) to (a) the modulus of the reflected amplitude as a function of wave period and (b) the modulus of the reduced displacement when $\tau = 2$secs, for the semi-infinite ice sheet problem. The ice has thickness $D = 0.1$m and a zero draught $h_0 = H_0$, with $h_0 = 20$m. The dimensions of the approximations are $N = 0$ (blue curves) and $N = 3$ (cyan).

In this section we revert to normal incidence. The remaining parameters are the ice thickness, the fluid depth, the draught of the ice and the wave frequency. For the purposes of comparing the MMA against the EMM, the rôle of the draught is immaterial as the differences in the two methods are independent of this issue. For this reason, we may apply the simplifying assumption that the ice floats on the fluid surface. A full investigation of the physical implications of a non-zero draught as well as its effect on the convergence of the MMA is conducted in §7.5.1. The fluid depth is normalised to $H = 20$m and we therefore vary only the ice thickness, D, and wave period, τ.

Figures 5.4-5.9 plot the convergence of the MMA and EMM. In each part (a) approximations to the modulus of the reflected amplitude, $|R|$, are given as a function of wave period in the interval $\tau \in (2, 12)$secs. Parts (b) plot approximations of the modulus of the reduced displacement function, $|\eta|$, which is shown over a single wavelength beneath the ice, $x \in (0, 2\pi/k_0)$, with the incident wave of period $\tau = 2$secs and originating from the

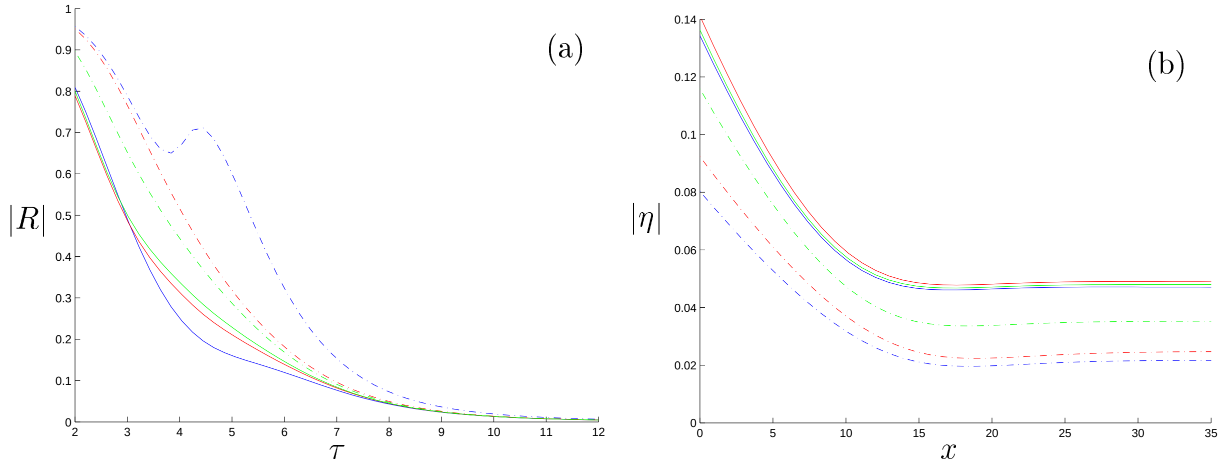

Figure 5.5: As in figure 5.4 but with an ice thickness $D_0 = 0.5$m. The dimensions of the approximations are $N = 0$ (blue curves), $N = 1$ (red) and $N = 2$ (green).

ice-free far-field, $x \to -\infty$, with an amplitude of 1m. Between the figures, three different ice thicknesses are used, $D_0 = 0.1$m, 0.5m and 1m. Also, we distinguish between the convergence that occurs at low dimensions and convergence at higher dimensions that refines the full linear solution, when a sufficient number of modes are present; this is reflected in the presentation of the figures.

At the interface between the ice-covered and ice-free states, $\{x = 0,\ -h_0 < z < -d_0\}$, both methods are required to adequately resolve the continuity conditions (5.1a), which are lost through truncation of the vertical modes. In order to regain continuity the evanescent waves become activated around the interface and it is the level of disparity between the two states that will dictate the number of evanescent modes required to achieve the desired degree of convergence. The MMA must also satisfactorily recreate the complex waves beneath the ice; however, we conjecture that the dimension-dependent complex waves in the MMA will improve the method's ability to resolve the continuity at the interface in comparison to the EMM.

The convergence of both methods at low dimensions is shown in figures 5.4-5.6. Here we observe that, as the ice thickness, D_0, increases, the accuracy of the low-dimensional approximations of both methods decreases; for example, $\epsilon_0 \approx 1.9 \times 10^{-2}$ when $D_0 = 0.1$m compared to $\epsilon_0 \approx 1.0 \times 10^{-1}$ when $D_0 = 0.5$m for the MMA approximations to $|R|$. Intuitively, we understand this phenomenon to be a property of the increasing disparity between the ice-covered and ice-free states as the ice thickens. By way of demonstration of this, figure 5.10(a) displays the respective propagating wavenumbers, k_0 and $k_0^{(0)}$, over the chosen interval of wave periods, for ice thicknesses between 0.1m and 1m. We note that the difference between the ice-covered and ice-free wavenumbers increases as the ice thickens. Moreover, it is evident that the differences become pronounced at the smaller

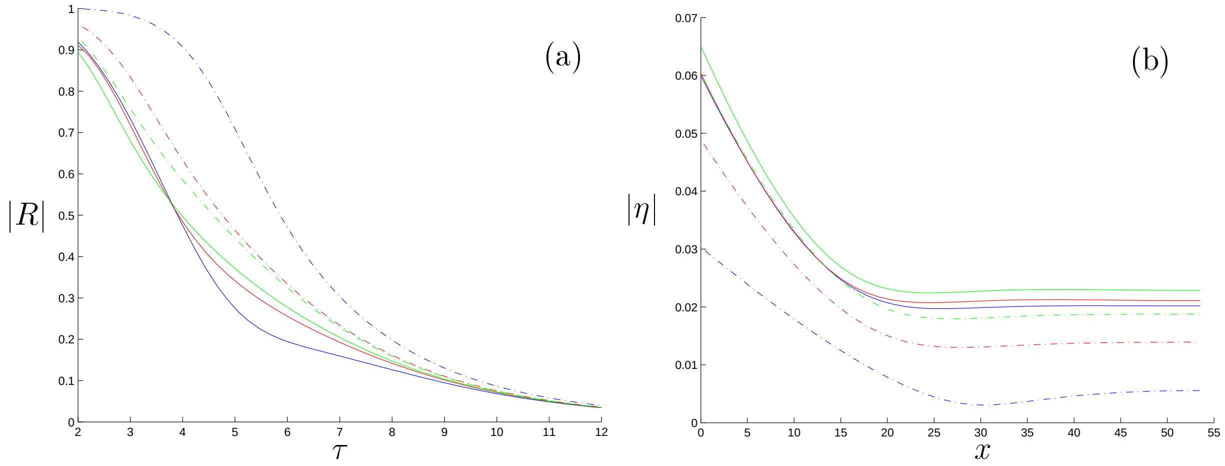

Figure 5.6: As in figure 5.4 but with the ice thickness $D_0 = 1$m. The dimensions of the approximations are $N = 0$ (blue curves), $N = 1$ (red) and $N = 2$ (green).

wave periods, which is reflected in the need for evanescent modes to be used in order to obtain accuracy for $|R|$ in this limit. It may, therefore, be assumed that the wave period of $\tau = 2$secs chosen for parts (b) provides the stiffest test of convergence in the current interval. Comments pertaining to the noted properties of the propagating wavenumbers were made in §3.2.2.

For the low-dimensional approximations shown in 5.4-5.6, the supremacy of the MMA over the EMM becomes evident as the ice thickens and, in relation to the approximations to $|R|$, as the wave period decreases. That is, the low-dimensional approximations of the MMA are superior to those of the EMM at those points for which there is a significant amount of scattering. For example, with $D_0 = 1$m, $\epsilon_n = \mathrm{O}(10^{-2})$ $(n = 0, \dots, 3)$ for MMA approximations to both $|R|$ and $|\eta|$, compared to $\epsilon_n = \mathrm{O}(10^{-1})$ for corresponding EMM approximations. This implication is contrary to the inference from the example considered in §5.1.3; however, we note that $\beta = 1\text{Pa m}^5\ \text{s}^2/\text{kg}$ corresponds to the extremely thin ice thickness $D_0 \approx 2.8$mm.

The shape of the displacement function is dominated by the propagating wave as the evanescent waves are confined to the vicinity of the ice edge. The rôle of the evanescent modes is primarily in quantitative adjustments to the approximations. In contrast, we note, in particular, a significant qualitative inaccuracy in the single-mode EMM approximation to $|R|$ for $D = 0.5$m. This reflects the sensitivity of this value to the accuracy of the approximation at $x = 0$ that we have noted to be a source of difficulty at low dimensions.

The implication of these results is that the dimension dependence of the MMA, which is derived through the process of vertical averaging, compensates somewhat for the evanescent waves missing from the approximation. In contrast, the truncated EMM approxima-

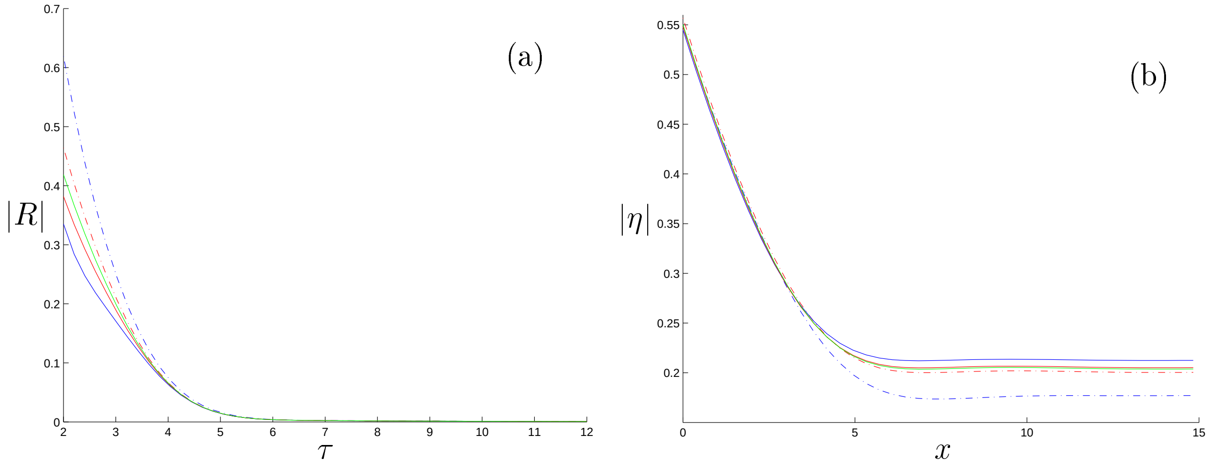

Figure 5.7: High-dimensional refinements of the approximations shown in figure 5.4. The dimensions of the approximations in part (a) are $N = 4$ (blue curves), $N = 12$ (red) and $N = 29$ (green), and in part (b) are $N = 4$ (blue), $N = 24$ (red) and $N = 36$ (green).

tion is insensitive to these missing terms. This result was anticipated in §4.2. However, with the possible exception of the MMA approximation to $|\eta|$ with $D = 0.1$m for which $\epsilon_3 \approx 4.1\times10^{-3}$, the approximations shown in figures 5.4-5.6 have not sufficiently converged to the full linear solution.

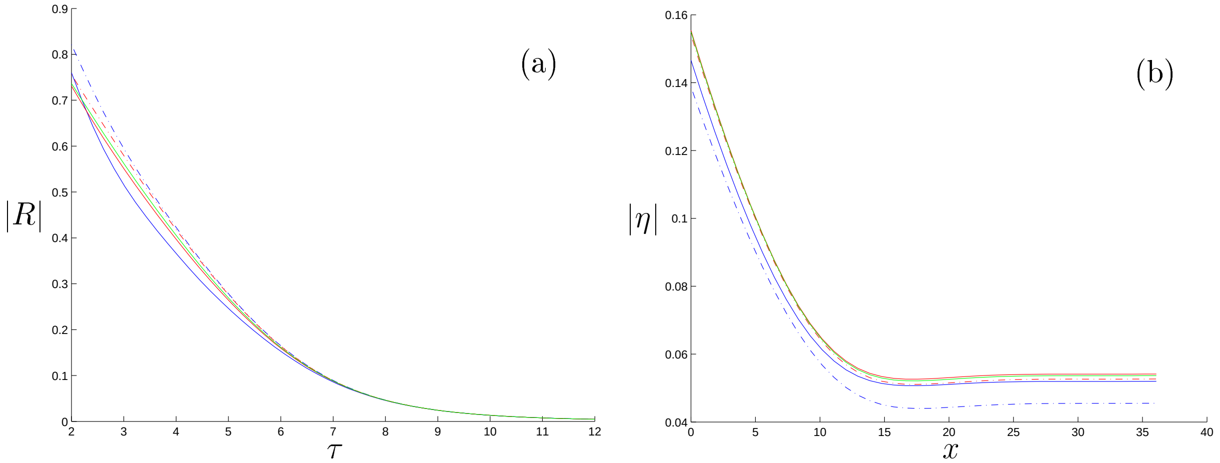

Figure 5.8: High-dimensional refinements of the approximations shown in figure 5.8. The dimensions of the approximations in part (a) are $N = 4$ (blue curves), $N = 12$ (red) and $N = 21$ (green), and in part (b) are $N = 4$ (blue), $N = 19$ (red) and $N = 33$ (green).

Figures 5.7-5.9 plot the refinements of near-converged approximations to the problems considered in figures 5.4-5.6. The performance of the two methods here is contrasting, with the EMM providing highly accurate approximations where the MMA struggles to fully resolve the solution. For example, with $D = 0.1$m, $\epsilon_{29} \approx 1.8 \times 10^{-3}$ for the MMA approximation to $|R|$ compared to $\epsilon_{29} \approx 1.0 \times 10^{-4}$ for the EMM. Our findings here are consistent with the example considered in §5.1.3.

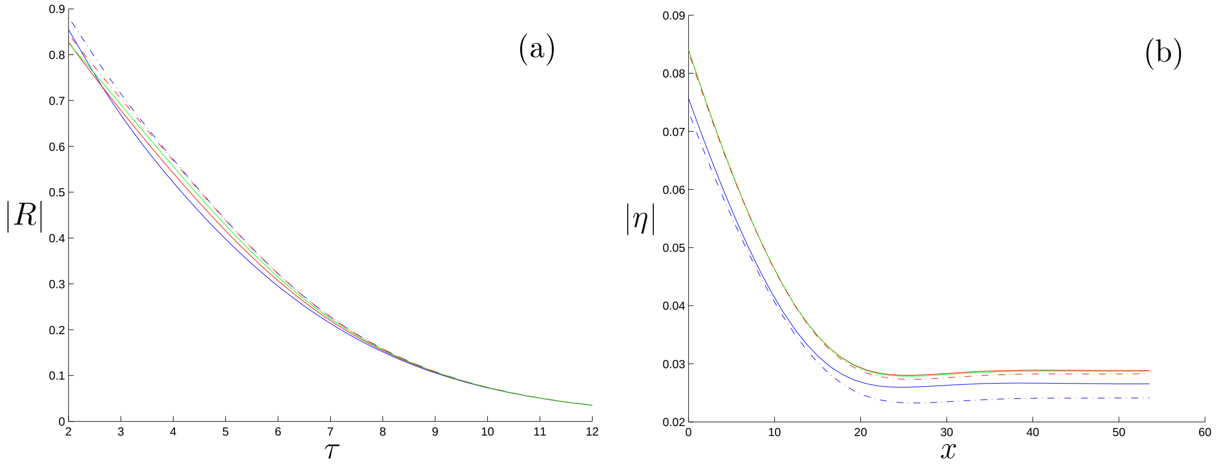

Figure 5.9: High-dimensional refinements of the approximations shown in figure 5.6. The dimensions of the approximations in part (a) are $N = 4$ (blue curves), $N = 8$ (red) and $N = 19$ (green), and in part (b) are $N = 4$ (blue), $N = 19$ (red) and $N = 29$ (green).

This observation indicates that the complex waves, those of wavenumbers μ_j ($j = 1, 2$), are strongly activated in this problem. It is these waves that differentiate the two methods of approximation. Unlike the EMM, for which the exact values of μ_j are in-built, in the MMA, the absence of these waves is compensated for by the inclusion of waves of dimension-dependent wavenumbers $\mu_{N,(j)}$. However, as previously discussed in the concluding paragraph of §5.1, the horizontal modes of MMA approximations are formed independently of the source of scattering and subsequently no precedence is given to the missing wavenumbers μ_j over the other wavenumbers omitted from the approximation, although they are clearly of greater importance in this problem. Therefore, the same process that distinguishes the MMA approximation at low dimensions is also responsible for slow small-scale refinements at higher dimensions. Despite this latter deficiency, we note that, as seen through figures 5.7-5.9, the MMA is capable of obtaining the full linear solution to a desired degree of accuracy, if a large enough dimension is taken.

It is evident that the refinement problems shown by the MMA are of greater significance for thinner ice; for example, the difference between the two methods' approximations to $|R|$ at $N = 29$ is approximately 5.6×10^{-2} for $D_0 = 0.1$m and 1.3×10^{-2} for $D_0 = 1$m. A possible explanation for this is the variation of the magnitude of the complex roots μ_j ($j = 1, 2$), which, as depicted in figure 5.10(b), increase as D_0 decreases. It therefore seems reasonable to expect the motion relating to these roots to be more significant for thinner ice. A second possibility is that the dimension-dependent wavenumbers in the MMA, $\mu_{N,(j)}$, converge more slowly to the complex wavenumbers, μ_j, for thinner ice. However, this issue is not explored further in this work.

By way of comparison to the semi-infinite ice sheet problem studied above, we consider

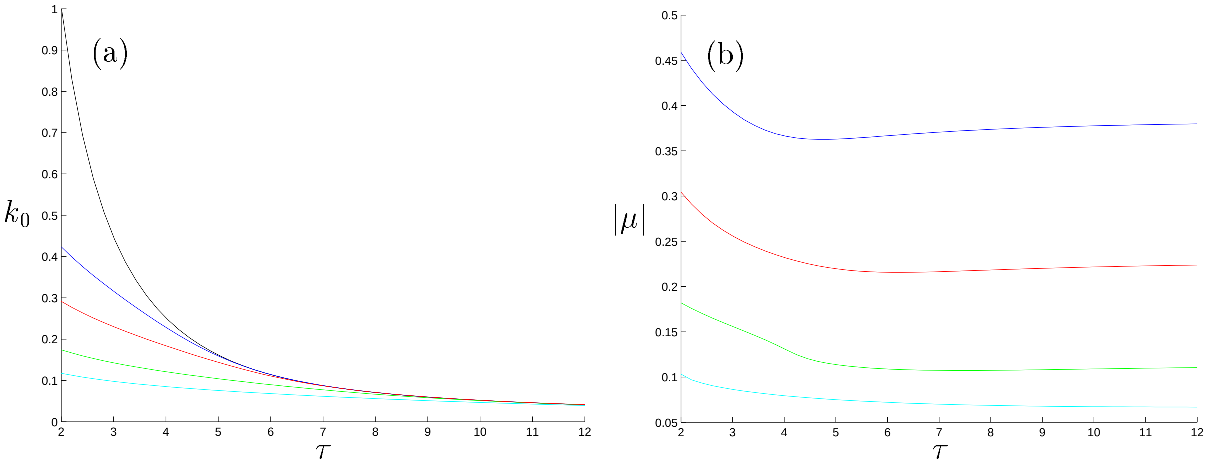

Figure 5.10: Part (a) plots propagating wavenumbers, and part (b) plots the modulus of the complex wavenumber, as functions of wave period. The ice thicknesses are $D_0 = 0.1$m (blue curves), $D_0 = 0.2$m (red), $D_0 = 0.5$m (green), and $D_0 = 1$m (cyan). In part (a) the free-surface wavenumber is also shown (black curve). In all cases the bed depth is 20m.

a related problem in which there is still a single source of scattering produced by a geometrical discontinuity but one for which the ice-cover is now complete. Let us therefore define the geometrical functions as

$$D = \begin{cases} D_0 \neq 0 & (x < 0), \\ D_1 \neq 0 & (x > 1), \end{cases} \qquad H = \begin{cases} H_0 & (x < 0), \\ H_1 & (x > 1), \end{cases}$$

and $h = h_0 (= 20\text{m})$, for constants D_i, H_i $(i = 0, 1)$ and h_0, which may be formulated for both the MMA and EMM in a similar fashion to the semi-infinite ice sheet problem. The difference between the two approximation methods is again confined to the terms corresponding to the complex roots.

Figure 5.11 plots the convergence of MMA and EMM approximations to $|R|$ for two choices of ice discontinuity and may be compared to the semi-infinite ice sheet problems of figures 5.4-5.9 parts (a). In both problems shown in figure 5.11 the discontinuity occurs in the underside of the ice, so that $H_1 = H_0 + D_0 - D_1$, with $D_0 = 0.1$m fixed. In figure 5.11(a), $D_1 = 0.2$m, giving a discontinuity of 0.1m in the ice thickness, which is comparable to the geometrical discontinuity caused by the semi-infinite ice sheet of 0.1m thickness. The convergence here is rapid, with $\epsilon_3 = \mathrm{O}(10^{-3})$ for both methods, and we may consider the three-mode MMA and four-mode EMM approximation to be sufficiently converged. Moreover, the single-mode approximations provide high accuracy, with $\epsilon_{0,3} \approx 1.3 \times 10^{-2}$ for the MMA and $\epsilon_{0,3} \approx 5.1 \times 10^{-2}$ for the EMM. This again indicates that at low dimensions the MMAs are more accurate than their EMM counterparts. As with the semi-infinite ice sheet problems, at higher dimensions the EMM demonstrates

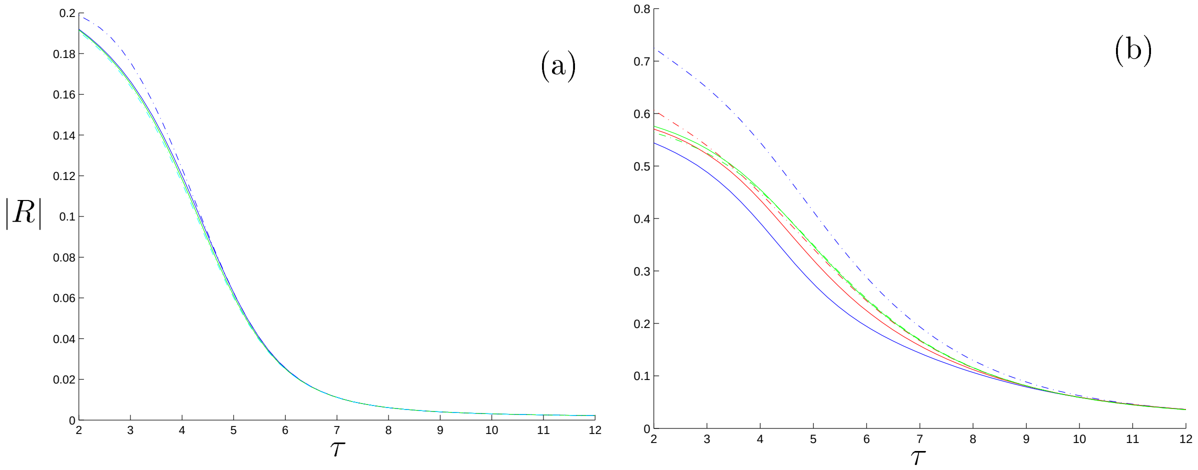

Figure 5.11: Comparison of MMAs (solid curves) and EMM approximations (dot-dash) to the modulus of the reflected amplitude as functions of wave period for the complete ice-cover problem. The ice thicknesses in part (a) are $D_0 = 0.1$m and $D_1 = 0.2$m and in part (b) are $D_0 = 0.1$m and $D_1 = 1$m. The bed depths are $H_0 = 20$m and $H_1 = H_0 + D_0 - D_1$. The dimensions of the approximations in part (a) are $N = 0$ (blue curves), $N = 2$ (red) and $N = 3$ (cyan), and in part (b) are $N = 0$ (blue), $N = 1$ (red) and $N = 14$ (green).

superior convergence to the MMA, for example, $\epsilon_{14} \approx 1.6 \times 10^{-4}$ for the MMA and $\epsilon_{14} \approx 2.6 \times 10^{-5}$ for the EMM, which is again attributed to the rôle of the wavenumbers μ_j $(j = 1, 2)$. However, as we have already accepted lower dimension approximations as adequately converged, the negligible size of the refinements at high dimensions in this problem indicate that, unlike the semi-infinite ice sheet problems studied, these waves are not activated significantly. This may be anticipated by considering the small jump between the relevant propagating wavenumbers of this problem (see figure 5.10(a)) relative to the jumps that occurred between the propagating wavenumber when moving from ice-free to ice-covered states.

By taking the ice thickness $D_1 = 1$m in figure 5.11(b), we create a more significant discontinuity and amplify the rôle of the complex waves. The difference between the propagating wavenumbers in the two opposing states is now of comparable size to those considered in the semi-infinite ice sheet problem. High-dimensional refinements in this case are no longer negligible, with, for example, the difference between the MMA and EMM approximation of dimension $N = 19$ approximately 7.5×10^{-3}, whilst $\epsilon_{19} \approx 2.7 \times 10^{-3}$ for the MMA and $\epsilon_{19} \approx 5.5 \times 10^{-4}$ for the EMM. Consequently, we accept a converged EMM of lower dimension than MMA, although the low-dimensional MMAs maintain better accuracy. It should be noted that the inaccuracies shown in this final complete ice-cover problem are smaller than those of all of the semi-infinite ice sheet problems seen, and that a large discontinuity in a continuous ice sheet is not a model that we are interested in studying. Rather, we will model changes in the properties of an ice sheet as continuous functions, as in the two-dimensional problem of complete ice-cover formulated in §4.3.1. In contrast, the geometrical jump produced by an ice edge is a feature that is prevalent in our investigations.

5.3 Conclusions

In this chapter, two alternative methods of solution are proposed for geometrical configurations in which the defining functions are piecewise constant. The first method is the application of the MMA, using the natural vertical modes, to this degenerate class of geometries, and we have sought to emphasise the process of vertical averaging inherent in the method. The alternative method, known as the EMM, is valid only for piecewise uniform geometry. Approximations are produced by directly truncating an expression for the full linear solution as an infinite sum of separation solutions, where the unknown amplitudes are determined through application of Galerkin's method at the scattering interfaces.

Both the MMA and the EMM were explicitly formulated for the classical problem of a semi-infinite ice sheet and normal incidence, in two-dimensions. It was noted that the sole disparity between the two methods derives from the additional complex waves that are attached to each vertical mode in the ice-covered interval. In the MMA these waves are dimension-dependent quantities, generated through the process of vertical integration. In contrast, in the EMM, irrespective of the dimension of truncation, these waves are given by the exact complex waves that appear in the full linear solution.

For the results presented in this chapter, a single source of scattering was considered in order to isolate the primary characteristics of the two methods. It was seen to be advantageous to separate the convergence at low dimensions, where the methods must attempt to resolve the continuity conditions, and the higher dimension refinements. We highlighted both relative properties of the two methods and the influence of the geometry, specifically the thickness of the ice, on the accuracy of approximations. In terms of the latter, it was concluded that a greater jump between the uniform states causes inaccuracies in the low-dimensional approximations of both methods. As expected, the jump from ice-free to ice-covered states is a relatively strong source of scattering, even at a small ice thickness, as opposed to cases of complete ice-cover. At low dimensions, the MMA regularly provided higher accuracy than the EMM, a phenomenon attributed to the MMA's property of being 'dimension-aware'.

For those problems in which the complex waves are strongly activated, the high dimension refinements of the MMA are slow compared to those of the EMM. This is a consequence of the separation of spatial coordinates, making the dimension-dependent terms unaware of the relative dominance of the complex waves. In the EMM the exact structure of these waves is in-built.

We conclude that, for cases of partial ice-cover, in which scattering of the complex waves is generally significant, the implementation of a method based on a variational principle generates accurate approximations at relatively low dimensions. However, the ability to attain highly refined solutions may require the use of a high dimension, which could prove to be numerically costly over continuously varying geometry for which differential equations of order $(2N + 4)$ must be obtained numerically.

Chapter 6

Numerical Results: complete ice-cover in two-dimensions

In this chapter we are concerned with presenting numerical results for problems of complete ice-cover, of the two-dimensional form outlined in §4.3.1.

6.1 Alternative modes

During the investigation of §3.2.2 it was found that, under certain circumstances, the natural evanescent modes, in particular the first evanescent mode, may be invalidated by the presence of bifurcations in the roots of the dispersion relation (3.13). This led us to propose an alternative trial space in §3.2.3, consisting of what we call hybrid modes. It is expected that the ramification of the switch of natural to evanescent modes in the MMA will be a slight loss of accuracy and hence the requirement of a larger number of modes to achieve the desired convergence. Our basis for this assertion, as discussed in §3.2.3, is that the hybrid modes lack an awareness of the ice thickness. Furthermore, by combining the hybrid approximation in the interval of varying geometry with natural approximations in the intervals of uniform geometry, we introduce a jump in the trial space which is not the product of a geometrical feature. This creates a fictitious source of scattering that must be resolved.

In this section we will provide numerical results, in terms of the two-dimensional complete ice-cover problem, to substantiate the conjecture regarding the respective convergence rates, as well as showing that convergence is achieved with either choice of modes. We will also consider the *Fourier cosine trial space*

$$\{1, \cos\left(\frac{\pi}{H}(z+h)\right), \cos\left(\frac{2\pi}{H}(z+h)\right), \dots\},$$

over the interval of varying geometry ($0 < x < l$), and compare it with the trial spaces we intend to implement.

The results presented here will use the geometrical configuration defined by

$$D(x) = \begin{cases} 1 & (x < 0,\, x > 10), \\ 1 + \sin^2\left(\frac{\pi x}{5}\right) & (0 < x < 10), \end{cases} \quad d(x) = \begin{cases} 0 & (x < 0,\, x > 10), \\ \frac{1}{2}\sin^2\left(\frac{\pi x}{5}\right) & (0 < x < 10), \end{cases} \tag{6.1a}$$

and

$$h(x) = \begin{cases} h_0 & (x < 0), \\ h_0 + \frac{h_1 - h_0}{10}x & (0 < x < 10), \\ h_1 & (x > 10), \end{cases} \tag{6.1b}$$

where h_i $(i = 0, 1)$ are constants such that $h_0 > h_1$. This represents a symmetric pressure ridge in the ice thickness, in which the protrusions in the upper and lower surfaces are equal, over a linearly shoaling bed. In this configuration all of the geometrical functions vary and by making appropriate choices of the bed depths, h_i $(i = 0, 1)$, we may manipulate the vertical modes to produce the behaviour that we wish to expose.

Figure 6.1 displays results comparing the natural and hybrid MMAs for two choice of bed depth. In parts (a.i-iii) $h_0 = 20$m and $h_1 = 10$m, whereas in parts (b.i-iii) $h_0 = 40$m and $h_1 = 30$m. The wave period is set at $\tau = 2.5$secs.

As the purely imaginary roots of the dispersion relation attain their limiting value rapidly (see equation (3.25)), differences in the natural and hybrid approximations are mainly a product of discrepancies in their respective lower-order evanescent modes. In particular, the presence of bifurcations plays a leading rôle in this issue. The choice of bed depths made for parts (a.i-iii) and (b.i-iii) ensures that the path of the root $\sigma_1 = -\mathrm{i}k_1$, where k_1 is the initial purely imaginary root of the dispersion relation (3.13), lies to either either side of a pair of bifurcations. This is shown graphically in parts (a-b.i) of figure 6.1 and the resulting roots σ_1 are plotted against their corresponding limiting values, π_1, which are used in the hybrid approximation, in parts (a-b.ii).

We note that the root resulting from the shallower bed of part (a) is far closer to its limiting value than the analogous root resulting from the deeper bed of part (b). With reference to the form of the dispersion relation (3.24), we understand this to be a property of how the quintic on the left-hand-side intersects the first branch of the right-hand-side. For example, consider the fluid depth to be fixed and suppose that the ice thickness lies within the bifurcation bounds $D_l < D < D_u$. Let the three imaginary roots that exist on the first branch be denoted in ascending order as σ_{1i} $(i = a, b, c)$ (see figure 6.3). Then, if $D > D_u$ we have $\sigma_1 \geq \max(\sigma_{1c})$ and if $D < D_l$ we have $\sigma_1 \leq \min(\sigma_{1a})$. Therefore, for points (D, H) that lie below the bifurcation bounds, take the example of figure 6.1(a.i), the purely imaginary root will lie in the vicinity of its limiting value but if (D, H) lies

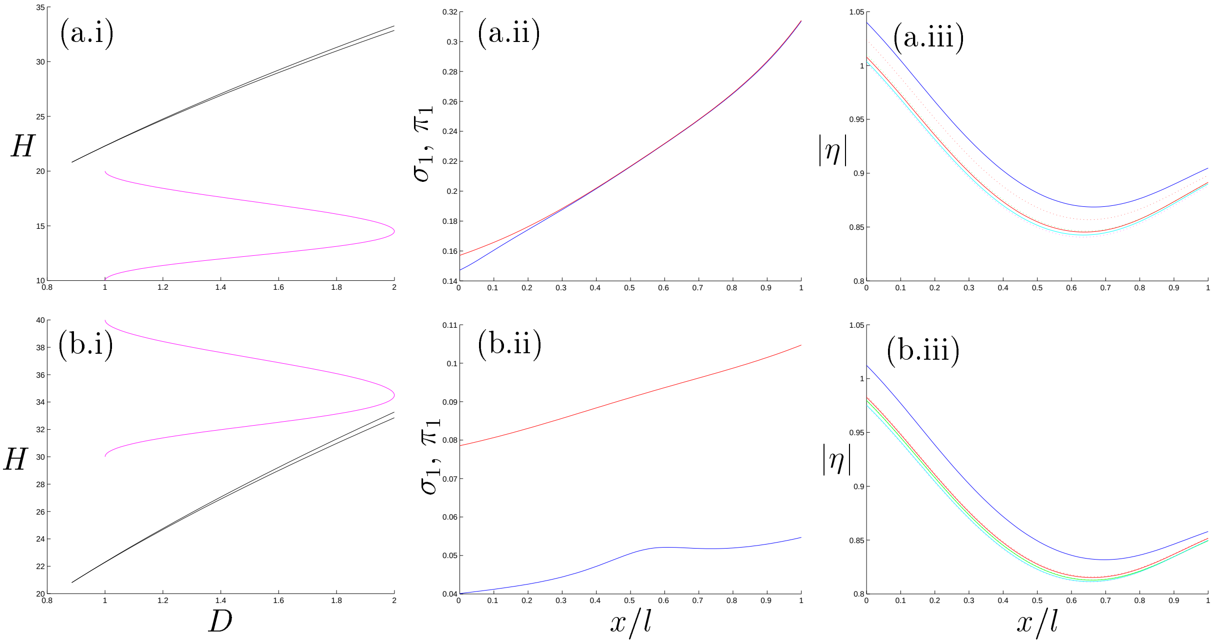

Figure 6.1: Comparison of natural and hybrid MMAs for the geometry defined in equations (6.1a-b) and wave period $\tau = 2.5$secs. In parts (a.i-iii) $h_0 = 20$m and $h_1 = 10$m, and in parts (b.i-iii) $h_0 = 40$m and $h_1 = 30$m. Parts (i) plot the path of the vertical structure of the geometry, (D, H), (magenta curves) and bifurcation bounds, (D_l, H_u) and (D_u, H_l), (black). Parts (ii) plot the modulus of the first purely imaginary root of the dispersion relation, σ_1, (blue curves) and their limiting value, π_1, (red). Parts (iii) plot MMAs to the modulus of the reduced displacement function, $|\eta|$, using the natural modes (solid curves) and the hybrid modes (dotted). The dimensions of the approximations in part (a.iii) are $N = 0$ (blue curves), $N = 1$ (red), $N = 2$ (green), $N = 3$ (cyan) and $N = 5$ (magenta), and in part (b.iii) are $N = 0$ (blue curves), $N = 1$ (red), $N = 2$ (green), $N = 5$ (cyan) and $N = 7$ (magenta).

above the bifurcation bounds, take the example of figure 6.1(b.i), there will be a significant difference between the root and the limiting value.

The corresponding convergence of the natural and hybrid MMAs to the modulus of the reduced displacement, $|\eta|$, are plotted in figure 6.1 parts (a-b.iii). As predicted, the convergence of the hybrid MMA is seen to be slightly inferior, with approximations having the appearance of 'following behind' their natural counterparts. This is particularly evident in the double-mode approximations, where the disparity between the two trial spaces is most acute. Recall that we have defined the quantity ϵ to be the normalised difference between two functions, and use it as a measure of the rate of convergence of the MMA. In this context we have

$$\epsilon_n = \epsilon(\chi_{n-1}, \chi_n) = \int_0^l \frac{|\chi_{n-1} - \chi_n|}{|\chi_{n-1}|}\,\mathrm{d}x,$$

where χ_n is the MMA approximation of dimension n to the displacement function. In the most extreme case, the deeper bed of part (b), we have $\epsilon_1 \approx 2.8 \times 10^{-2}$ for the natural approximation as opposed to $\epsilon_1 \approx 1.4 \times 10^{-4}$ for the hybrid approximation, which here implies a slower convergence rate in the hybrid approximation. For these results, convergence is taken to at least $\epsilon_N = \mathrm{O}(10^{-4})$ and in each case we obtain converged natural approximations at a lower dimension than than their hybrid counterparts.

Given what has been noted about the relationship between the values of σ_1 and π_1 for the two problems, it is unsurprising to find that the convergence rates are most distinct for the problem that incorporates the deeper bed. In this case, the maximum normalised difference between the two approximations is 1.4×10^{-2}, which is, obviously, at $N = 1$. However, it only takes one additional mode for this difference to reduce to $\mathrm{O}(10^{-3})$. For the shallower bed the natural and hybrid approximations never have a normalised difference that exceeds $\mathrm{O}(10^{-3})$.

We conclude that the hybrid approximation is a competitive alternative to replace the natural approximation, for points at which bifurcations invalidate the natural evanescent modes. Specifically, we have seen that the hybrid approximation will converge rapidly to the full linear solution, although, as expected, the natural approximation has proven to be the superior of the two methods and we retain its use whenever possible. Our investigation has incorporated only two example problems; however, numerous tests not presented have shown identical behaviour. It is possible to construct much stiffer tests of the hybrid modes but these are somewhat spurious as they generally involve unrealistic parameters in circumstances for which the natural modes may be used. For more typical geometry, the natural and hybrid approximations are closer than the examples presented. Here we have chosen a relatively short incident wave to highlight the differences in the approximations.

In figure 6.2 the convergence of Fourier MMAs to $|\eta|$ are plotted for the problems used in figure 6.1. To enable comparison, the natural single-mode approximations and converged results are also shown. It is evident that, although the Fourier approximations are reasonable both quantitatively and qualitatively, they are significantly inferior to those produced by the natural and hybrid modes. The approximations given by a single Fourier mode - the constant mode - are particularly weak. We note that the difference between the natural and Fourier single-mode approximations is most prominent for the shallower bed, part (a), for which the normalised difference is $\epsilon(\chi, \chi_F) \approx 1.3 \times 10^{-1}$, where χ is the natural approximation and χ_F is the Fourier approximation. This case coincides with the greatest difference between the vertical mode $w_0 = \cosh\{k_0(z + h)\}$ and the constant term, although in the deeper bed case these primary modes are only narrowly closer. Ten modes are required to reach sufficient convergence of the Fourier approximation in part (b), and it can be seen that it gives the same aproximation to the full linear solution as that achieved via the natural modes. In part (a), the Fourier approximation has not

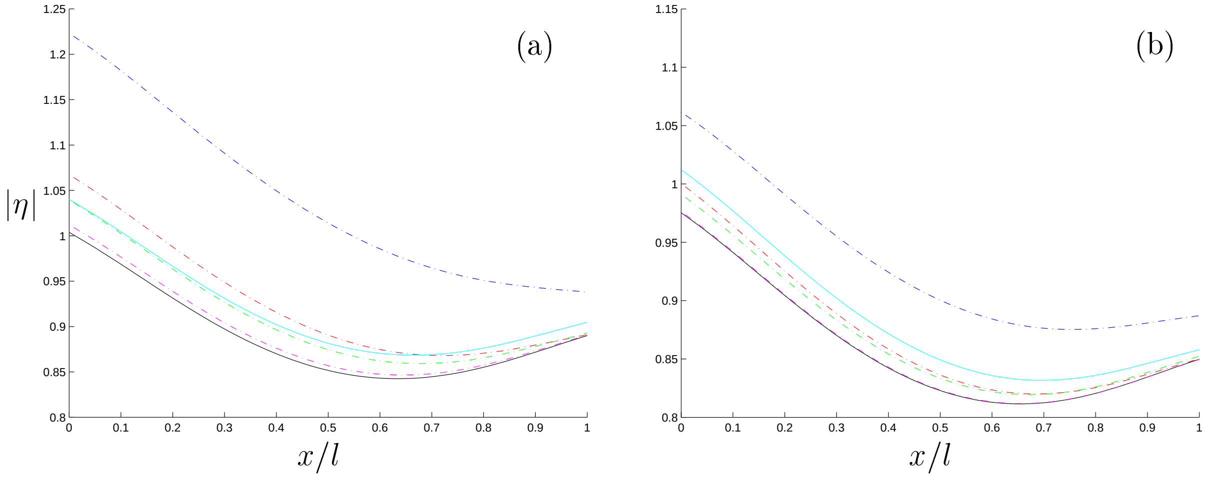

Figure 6.2: The convergence of the Fourier MMA (dot-dash curves) to the modulus of the reduced diplacement, for the geometry defined in equation (6.1a-b) and the wave period $\tau = 2.5$secs. In part (a) $h_0 = 20$m and $h_1 = 10$m, and in part (b) $h_0 = 40$m and $h_1 = 30$m. The single-mode natural approximations are displayed by cyan curves and converged natural approximations are the black curves. The dimensions of the Fourier approximations are $N = 0$ (blue curves), $N = 1$ (red), $N = 2$ (green) and $N = 9$ (magenta).

converged with ten modes. At this point, it has a normalised distance of approximately 5.6×10^{-3} from the converged natural approximation. However, it is clear that it is tending to the correct solution and will provide the full linear solution with additional modes.

Having conducted this examination of the Fourier approximation, we discard it forthwith. Its purpose has primarily been in highlighting the efficiency of the natural approximation.

6.1.1 Choice of evanescent modes

There exists a subtle issue regarding the choice of vertical evanescent modes included in our approximation, connected to the subject of bifurcations and linear dependence and capable of becoming manifest in the results that we obtain. Although it is worthy of note it is of a purely academic nature. The problem, that will presently be outlined, is a general property of the natural MMA and it is pertinent to discuss it at this juncture in terms of the two-dimensional complete ice-cover problem.

In the problems considered, we will often record quantities as a particular parameter is varied continuously. So, let us suppose that the geometry has been fixed and that the angular frequency, ω, is varied. It was shown in §3.2.2 that, as this parameter varies, the complex roots of the dispersion relation (3.13) may bifurcate and that there is a two-fold linear dependence in the set of natural modes $\{w_j\}$ $(j = -2, \dots)$. For the reasons discussed in §3.2.2, when they exist, we wish to omit the modes relating to the pair of symmetric, complex roots and, at all times, retain only one mode per purely imaginary branch of the dispersion relation. However, in order to retain these conditions we must sacrifice the assurance of continuity of our vertical basis, $\{w_j\}$ $(j = 0, \dots N)$, as a function of frequency. For example, we may envisage the type of situation depicted in figure 3.5(a), in which the complex roots, μ_i $(i = 1, 2)$, bifurcate from being a symmetric pair onto the first purely imaginary interval, $(0, \pi_1)$, already supporting the root k_1, followed by one of the complex roots, μ_1 say, coalescing with k_1 to create a new complex pair. However, in the current context, we regard this transition as a function of the wave frequency rather than of the geometry.

At the point at which three roots exist in the first interval, there is a choice as to which of them, μ_i $(i = 1, 2)$ or k_1, is chosen for use in the MMA. To either side of this interval, as we pass through a bifurcation, the choice reverts to either k_1 or μ_2. As the paths of k_1 and μ_2 never cross there is necessarily a frequency, between the two instances of bifurcation, that the user may control, at which the path of the chosen root from this segment is discontinuous. Under the same circumstances, when continuously varying the geometry, with incoming frequency fixed, we revert to the hybrid approximation.

If we consider approximations generated by the MMA, of fixed dimension $N \geq 1$, to a particular quantity, the reflected amplitude, $|R|$, say, as a function of frequency, through a situation such as the one described above, then the function $|R(\omega)|$ will contain a discontinuity. As the dimension N is increased, and the full linear solution is attained, this discontinuity will be resolved.

The size of the discontinuity in $|R(\omega)|$ is dependent on a number of factors, in particular, the level of activation of the subject mode, here w_1, in the problem and thus this phenomenon may often pass unnoticed. Furthermore, suppose that the issue only occurs in the interval of varying geometry, for instance, let us suppose that it is not possible to select the root $k_1(x)$ $(0 < x < l)$ as a continuous function, as the frequency is varied. In this case a discontinuity in $|R(\omega)|$ may be overcome by consistently reverting to the hybrid approximation throughout the chosen interval, regardless of whether bifurcations occur in each individual problem. For a bifurcation caused by a non-geometrical parameter in a domain of uniform geometry, the problem will persist due to our wish to employ the natural approximation in all uniform domains surrounding those containing the geometrical variations.

In figures 6.3-6.4, an example of the above issue is given. Here, we use a trigonometric keel of 10m amplitude and 80m length protruding from an otherwise uniform sheet of 1m thickness, over a flat bed depth of 20m with an incident wave of length 53.45m. In the uniform intervals, $x < 0$ and $x > l$, there exists three roots on the first imaginary interval,

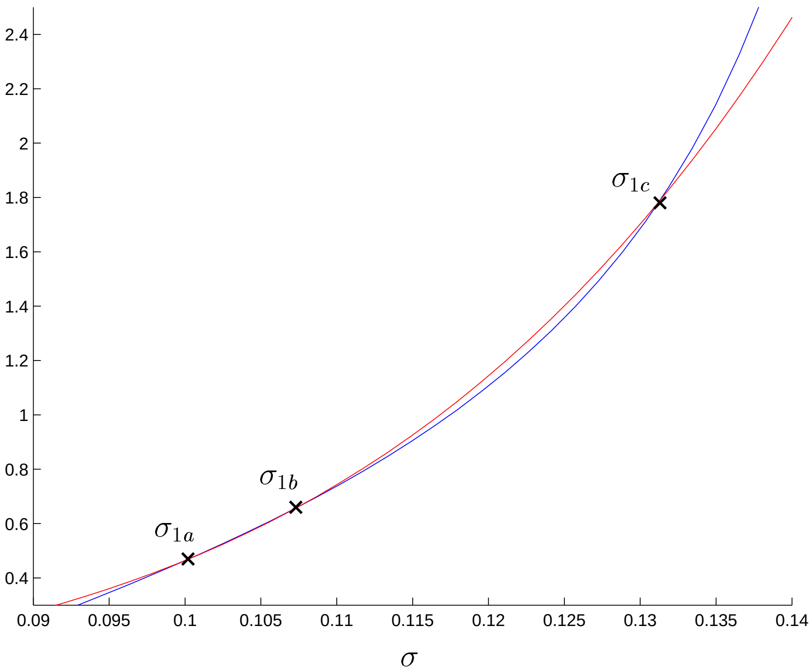

Figure 6.3: Graphical representation of the existence of three roots, $k_i = \sigma_i$ $(i = a, b, c)$, in the first imaginary interval, $(0, \pi_1)$. The functions shown are $-\kappa \cot(\sigma H)$ (blue curve) and $(1 - \alpha\kappa + \beta\sigma^4)\sigma$ (red).

as shown in figure 6.3. These roots will be denoted σ_{1j} $(j = a, b, c)$ in ascending order of magnitude. For all of these roots, and the parameters used here, the roots remain purely imaginary across the geometrical variation. There is, therefore, a choice to be made as to which of the three roots are used in the MMA in the uniform intervals. Across the varying interval, bifurcations restrict our choice to the root that runs on continuously from the largest of these roots, σ_{1c}.

Figure 6.4 compares approximations to $|\eta|$ generated by approximations using σ_{1a} and σ_{1c}. Double-mode approximations $(N = 1)$ are used in part (a) and the normalised difference between the two is approximately 1.8×10^{-2}. With the addition of supplementary modes, $N = 11$ and $N = 14$ respectively, this difference falls to 3.1×10^{-3} in part (b). It should be noted that the problem that is used here is an extreme case, chosen to clearly highlight the current issue.

Despite the lack of continuity of the function $k_1(x)$ at $x = 0$ and $x = l$, the convergence of the approximation using σ_{1a} is superior to that of σ_{1c}, with, for example, $\epsilon_N = \mathrm{O}(10^{-4})$ when $N = 11$ compared to $N = 14$. If we refer to the values of $\mu_{N,(i)}$ $(i = 1, 2)$ generated by the opposing roots then we find that, at $N = 10$, those generated by k_{1a} agree with k_{1b} to two decimal places and with k_{1c} to one decimal place, whereas at $N = 14$, k_{1c} still produces $\mu_{N,(i)}$ $(i = 1, 2)$ that form a symmetric, complex pair. The question of choice of the optimal root in these circumstances is perceived to be of unwarranted difficulty and will not concern us further.

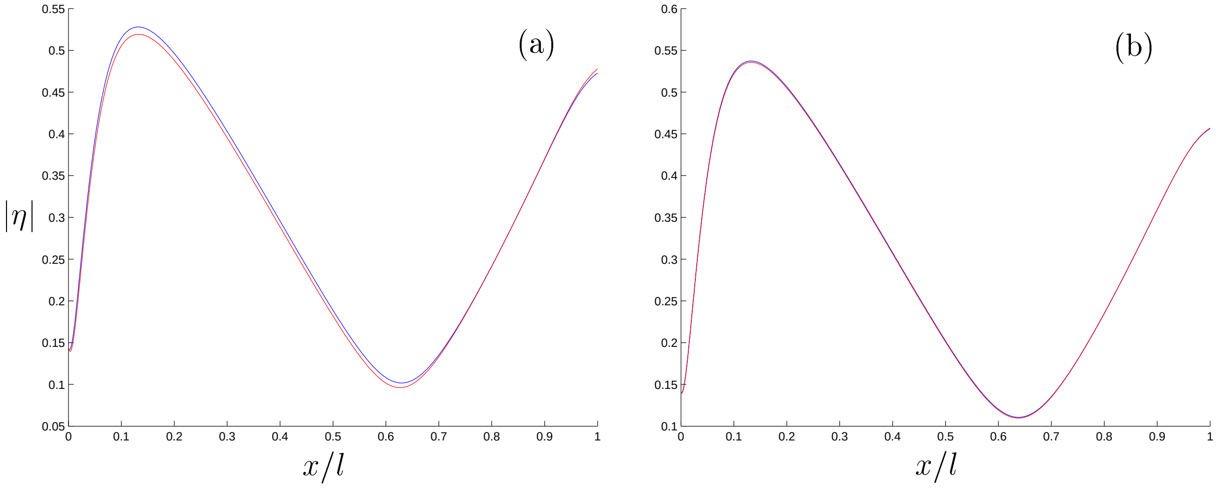

Figure 6.4: Natural approximations to the modulus of the reduced displacement function over the interval of varying geometry, using the roots $k_1 = \mathrm{i}\sigma_{1a}$ (blue curve) and $k_1 = \mathrm{i}\sigma_{1c}$ (red) in the semi-infinite intervals of uniform geometry, $x < 0$ and $x > l$. The approximations in part (a) have dimension $N = 1$, and in part (b) have dimensions $N = 11$ (blue) and $N = 14$ (red).

6.2 Comparison to the work of Williams & Squire (2004)

Our attention now turns to the analysis of the rôle of geometrical variations in the process of wave scattering. Having established that we may produce consistent results with either the natural or hybrid evanescent modes, the MMA will, from this point on, be chosen with the natural modes where available and the hybrid modes when bifurcations invalidate the natural modes. Reference will only be made to the specific choice of modes if it is felt to be relevant.

Initially, we will consider solving a problem for which numerical results already exist in the literature. This is done primarily to aid validation of our method of solution.

A restricted case of varying ice thickness, in two dimensions, was solved by Williams & Squire (2004), who considered variations of finite length in the upper surface of the ice (sail heterogeneities) in infinite intervals of complete ice-cover. Their method of solution utilised a Green's function that allowed the vertical displacement of the underside of the ice to be obtained from an integral equation, which leads to a knowledge of the reduced velocity potential everywhere.

The particular geometrical configuration that we will compare results against at this stage was described as *type 2* by Williams & Squire and is defined by

$$D(x) = \begin{cases} 1 & (x < 0,\, x > 15), \\ 2 & (0 < x < 15), \end{cases}$$

with $d = 0$ and $h = 70$m.

We note that this is the only geometrical configuration to be considered, in the context of complete ice-cover, for which the geometry will contain discontinuities. We have previously studied isolated discontinuities in an infinite interval of ice-covered fluid in §5.2. As type 2 geometry is piecewise uniform, following the method adopted in §5.2, it is possible to obtain approximations by means of the approach outlined (for partial ice-cover) in §5.1.1, where we must now deal with the two scatterers at the interfaces $x = 0$ and $x = 15$m.

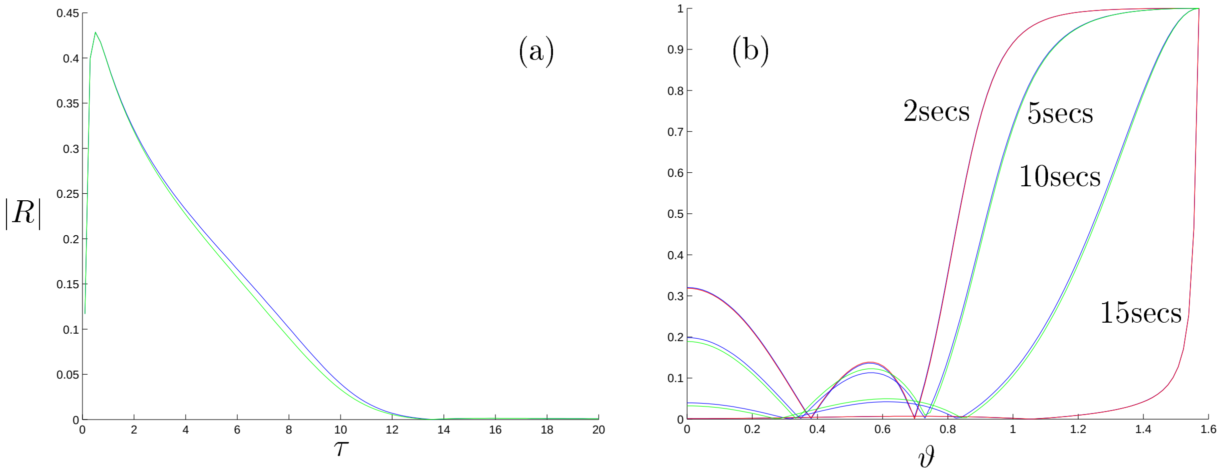

Figure 6.5: Comparison with figures 4(h) & 4(i) of Williams & Squire (2004), in which type 2 geometry (see equation (6.2)) is used with the geometrical values $d = 0$ and $h = 70$m. Part (a) plots the convergence of approximations to the modulus of the reflected amplitude as a function of wave period for normal incidence ($\vartheta = 0$). Part (b) plots the convergence of approximations to the moduli of reflected amplitudes as functions of incident angle for the wave periods $\tau = 2$secs, 5secs, 10secs and 15secs. The dimensions of the approximations are $N = 0$ (blue curves), $N = 1$ (red) and $N = 2$ (green).

Figures 6.5(a-b) are for comparison with figures 4(h) and 4(i) of Williams and Squire (2004), where the graphs of the transmitted amplitudes have been omitted for clarity. Both plot the convergence of natural approximations to the magnitude of the reflected amplitude, $|R|$, against incident wave period, τ, in part (a) or incident angle, ϑ, in part (b). For figure 6.5(a), although the single-mode approximation provides good accuracy, it is necessary to take three modes to achieve $\epsilon_N = \mathrm{O}(10^{-3})$, which is primarily due to the need for convergence in the middle range of wave periods taken.

Indeed, the need for the greatest number of vertical modes in a middle interval of wave periods proves to be a general trait. The middle interval is relative to the size on the obstruction and this indicates that the evanescent modes are activated with most strength when the incident wave is not particularly long or short with respect to the obstruction.

Consistently, we find for 6.5(b) that $\epsilon_1 = \mathrm{O}(10^{-3})$ for $\tau = 2$, 15secs, and $\epsilon_1 = \mathrm{O}(10^{-2})$

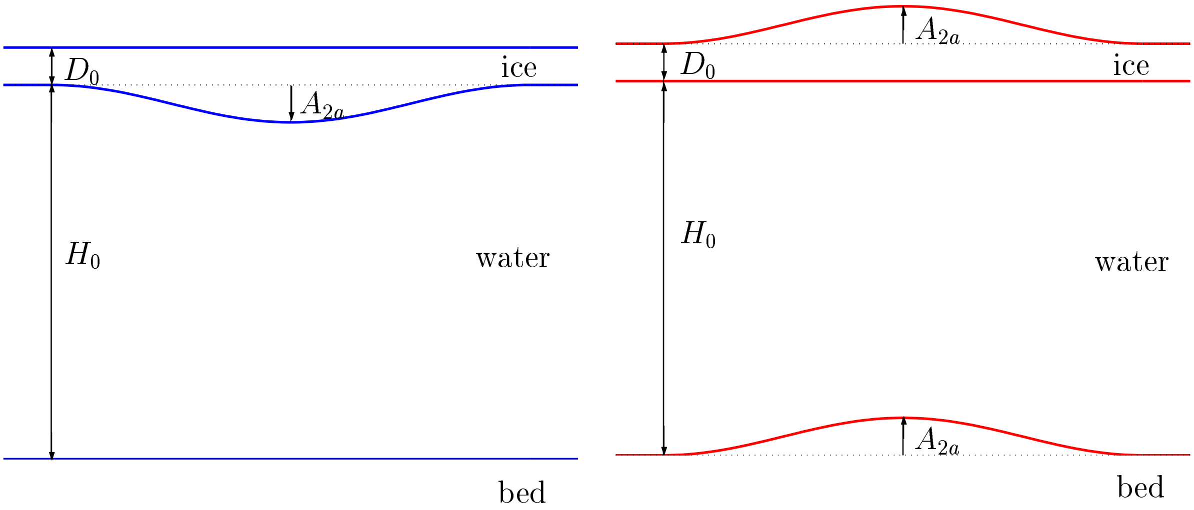

Figure 6.6: Schematics of the keel and the sail with a bed protrusion geometries defined in equation (6.2a).

for $\tau = 5$secs, 10secs. This extends the relatively slow convergence seen for normal incidence in the interval $4 \lesssim \tau \lesssim 11$. In all four curves, we observe that $|R| \to 1$ as $\vartheta \to \pi$. This limit is more readily attained at smaller wave periods.

All of the converged solutions are consistent with the relevant data of Williams & Squire (2004). A fuller analysis of the results may be found therein.

6.3 Comparison with the work of Porter & Porter (2004)

In this section we revisit two problems of continuous ice-cover, which were originally considered via the single-mode approximation of Porter & Porter (2004). We are able to present full linear solutions for these problems through use of the MMA. The two problems taken from their work, are those of figures 2(a) and 5(a), which involve the variations

$$p_{2a}(x) = \begin{cases} 0 & (x < 0,\, x > l), \\ \frac{1}{2}A_{2a}(1 - \cos\left(\frac{2\pi x}{l}\right)) & (0 < x < l), \end{cases} \tag{6.2a}$$

and

$$p_{5a}(x) = \begin{cases} 0 & (x < 0), \\ A_{5a}\frac{x}{l} & (0 < x < l), \\ A_{5a} & (x > l), \end{cases} \tag{6.2b}$$

respectively, where A_i $(i = 2a, 5a)$ are constant amplitudes. In Porter & Porter the geometrical configurations intended for figures 2(a) and 5(a) involved variations to the underside of the ice; however, as discussed in §3.2.1, these must be reinterpreted in terms of equivalent variations to the upper surface of the ice and the fluid bed. For protrusions, such as the trigonometric variation of figure 2(a) of Porter & Porter, these geometries are described as a *keel* problem and a *sail with a bed protrusion* problem. These two geometries are depicted in figure 6.6 for the trigonometric variations given in (6.2a).

Due to this correction of Porter & Porter, in figure 6.7, results are presented for both the intended problems, $D(x) = D_0 + p_i(x)$, $d(x) = p_i(x)$, $h = h_0$ $(i = 2a, 5a)$, in figures 6.7(a-b.i), and the unintended problem, $D(x) = D_0 + p_i(x)$, $d(x) = 0$, $h = h_0 - p_i(x)$ $(i = 2a, 5a)$, in figures 6.7(a-b.ii). The constant values $D_0 = 1$m and $h_0 = 20$m are maintained for both problems. Bifurcations occur in subintervals of the independent variables, λ and k_0, for all of the geometries used to produce results in figure 6.7. For consistency, the hybrid MMA is therefore used throughout the entire intervals of wavelength and wavenumber.

The choices of geometrical configurations made in Porter & Porter (2004) were influenced by the restriction of the single-mode approximation, so that only ‘slow variations’ were considered. This is reflected in the results presented in figure 6.7, for which the single-mode approximations are seen to require very little refinement in order to obtain the full linear solutions; in fact, for many of the problems the single-mode approximation is adequate. For both the original and corrected versions of Porter & Porter’s figure 2a, which are shown in figures 6.7(a.i-ii), the only obstruction length for which $\epsilon_1 = \mathrm{O}(10^{-2})$ is that of $l = 20$m, with all other lengths producing $\epsilon_1 = \mathrm{O}(10^{-3})$. Equivalently, for Porter & Porter’s figure 5a, which is shown in figures 6.7(b.i-ii), $\epsilon_0 = \mathrm{O}(10^{-2})$ only for the amplitude $A_{5a} = 2$m, with all other amplitudes producing $\epsilon_0 = \mathrm{O}(10^{-3})$. The $l = 20$m case of figures 6.7(a.i-ii) and the $A_{5a} = 2$m case of figures 6.7(b.i-ii) are the steepest variations in their respective figures. It is only necessary to include typically one, or at most two, additional modes to achieve convergence to $\mathrm{O}(10^{-3})$ in these problems. As, in all other problems $\epsilon_1 = \mathrm{O}(10^{-3})$, we accept the single-mode approximations as the converged solutions. A significant feature of these curves is the striking similarity between results from the original problem and their corrected counterparts. This indicates a strong link between these geometrical configurations that will be analysed in §6.4.

The problems considered in figure 6.7 do not provide a suitable test of the convergence of the MMA as they were biased by the need for slowly-varying geometry. In figure 6.8, figures 2(a) and 5(a) of Porter & Porter are reconsidered with the (clearly ‘non-slowly varying’) amplitudes $A_{2a} = 10$m and $A_{5a} = 6.5$m. Only the corrected geometries, $d = p_i$ $(i = 2a, 5a)$, are used as the results for the original problems, $d = 0$, remain nearly identical.

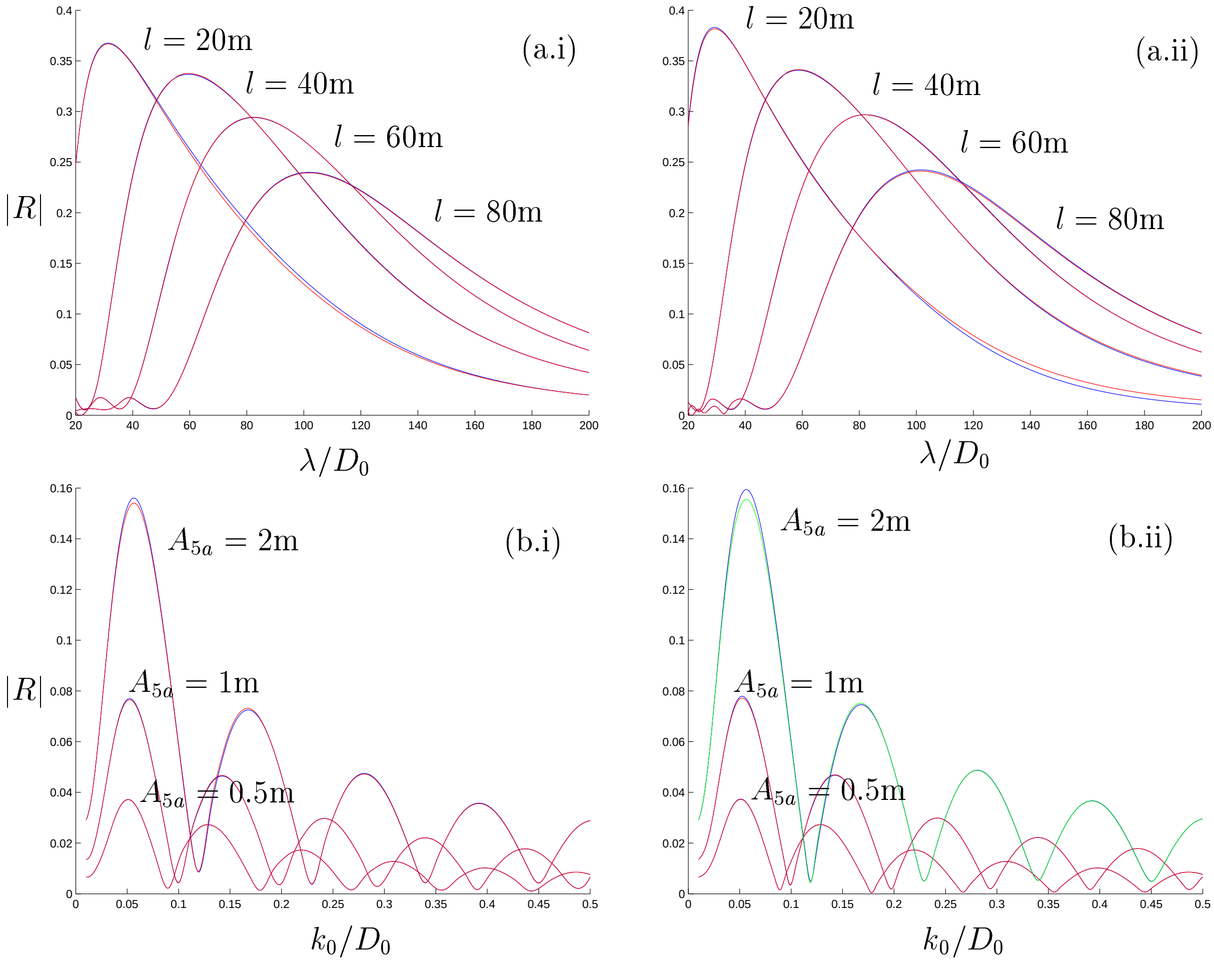

Figure 6.7: The extension to full linear solutions of the approximations given in figures 2(a) & 5(a) of Porter & Porter (2004). The geometrical variations in parts (a.i-ii) are of type p_{2a} (see equation (6.2a)) with amplitude $A_{2a} = 1$m, and lengths $l = 20$m, 40m, 60m and 80m. In parts (b.i-ii) the geometrical variations are of type p_{5a} (see equation (6.2b)) with length $l = 40$m, and amplitudes $A_{5a} = 0.5$m, 1m and 2m. Parts (a-b.i) are the keel variations intended by Porter & Porter, and parts (a-b.ii) are the sails with bed protrusions that were actually produced in Porter & Porter (2004). The dimensions of the approximations are $N = 0$ (blue curves), $N = 1$ (red) and $N = 2$ (green). The values $D_0 = 1$m and $h_0 = 20$m are used throughout.

By comparing the results of figure 6.8 to their counterparts in figure 6.7, it is clear that the accuracy of the single-mode approximation decreases with increasing amplitudes. This is reflected in the values $\epsilon_1 \approx 10^{-1}$ for $l = 20$m in figure 6.8(a) and $\epsilon_1 \approx 5 \times 10^{-2}$ for the other two problems of figure 6.8. Consequently, a larger number of modes are required to achieve convergence, with up to five modes required to give $\epsilon_N = \mathrm{O}(10^{-3})$. Despite this, it is evident here that, even for these rapidly varying obstructions, a single-mode provides a good approximation, in all cases shown, managing to accurately represent the shape and magnitude of the full linear solution.

In particular, we may make a comparison between the accuracy of the single-mode

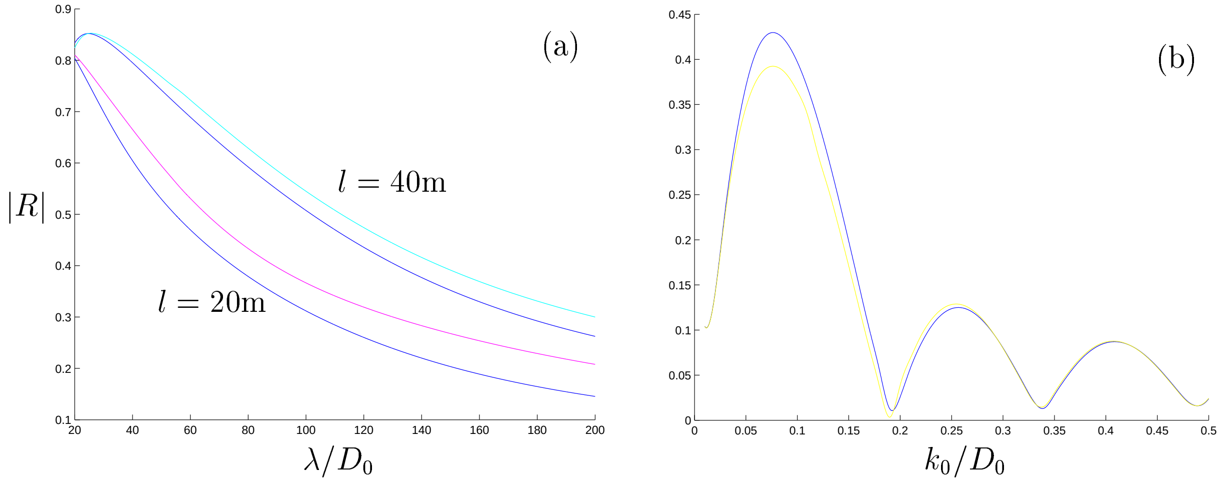

Figure 6.8: The convergence of MMAs to the modulus of the reflected amplitude as a function of (a) non-dimensional incident wavelength, and (b) non-dimensional incident wavenumber, for geometries that extend those used by Porter & Porter (2004) to 'non-slow' variations. The geometry in part (a) is a keel of type p_{2a} with amplitude $A_{2a} = 10$m and lengths $l = 20$m and 40m. In part (b) the obstruction is on the lower surface of the ice and is of type p_{5a} for amplitide $A_{2a} = 6.5$m, and length $l = 40$m. The dimensions of the approximations are $N = 0$ (blue curves), $N = 3$ (cyan), $N = 4$ (magenta) and $N = 5$ (yellow). The values $D_0 = 1$m and $h_0 = 20$m are used throughout.

approximation to the reflected amplitude for these 'non-slow' variations in the geometrical surfaces with the low-dimensional MMAs for the semi-infinite ice sheet problem of §5.2. In that problem, the geometrical surfaces were flat and the scattering was produced by the single geometrical discontinuity at the ice edge. The low-dimensional approximations to the reflected amplitudes, although reasonable, were adversely affected by the strong activation of the evanescent modes at the ice edge and were consequently more susceptible to qualitative inaccuracies. At high frequencies there was also a need to take a relatively large number of modes to fully refine the solution.

6.4 The single-mode approximation

Through the results that have thus far been produced for cases of continuous ice-cover it has been noted that:

1. The single-mode approximation provides high levels of accuracy;
2. There are similarities in the results produced by geometries that share the same ice thickness and fluid depth.

In this section we provide a mathematical interpretation of the causes of the similarities that have been observed and the limits in which they hold, which is done using the single-mode approximation. The relatively simple structure of the single-mode approximation allows for a great deal of analytical progress to be made and the inferences that are made are deemed to be applicable to the full linear solution due to the high levels of accuracy that have been displayed thus far.

For the single-mode approximation and normal incidence the system of equations that govern the two-dimensional motion of the MMA, equations (4.3a-b), degenerate to

$$\partial_x(a\partial_x\varphi) + b\varphi + w\kappa\chi = 0, \tag{6.3a}$$

and

$$\{\partial_x^2\beta\partial_x^2 + 1 - \kappa\alpha\}\chi - w\varphi = 0, \tag{6.3b}$$

where $\varphi \equiv \varphi_0$, $w \equiv [w_0]_{z=-d}$, $a \equiv a_{0,0}$ and $b \equiv b_{0,0}$. Analysis is most easily carried out if we eliminate the approximate displacement, χ, from (6.3a-b), to leave the sixth-order differential equation

$$\sum_{i=0}^{6} c_i\partial_x^i\varphi = 0, \tag{6.4}$$

where

$$c_6 = \beta\frac{1}{w}, \tag{6.5a}$$

$$c_5 = 4\beta\left(\partial_x\frac{1}{w}\right) + 2\left(\partial_x\beta\right)\frac{1}{w}, \tag{6.5b}$$

$$c_4 = 6\beta\left(\partial_x^2\frac{1}{w}\right) + 6\left(\partial_x\beta\right)\left(\partial_x\frac{1}{w}\right) + \left(\partial_x^2\beta\right)\frac{1}{w} + \beta\frac{b}{w}, \tag{6.5c}$$

$$\begin{aligned} c_3 = {} & 4\beta\left(\partial_x^3\frac{1}{w}\right) + 6\left(\partial_x\beta\right)\left(\partial_x^2\frac{1}{w}\right) + 2\left(\partial_x^2\beta\right)\left(\partial_x\frac{1}{w}\right) \\ & + 4\beta\partial_x\left(\frac{b}{w}\right) + 2\left(\partial_x\beta\right)\frac{b}{w}, \end{aligned} \tag{6.5d}$$

$$\begin{aligned} c_2 = {} & \beta\left(\partial_x^4\frac{1}{w}\right) + 2\left(\partial_x\beta\right)\left(\partial_x^3\frac{1}{w}\right) + \left(\partial_x^2\beta\right)\left(\partial_x^2\frac{1}{w}\right) \\ & + 6\beta\partial_x^2\left(\frac{b}{w}\right) + 6\left(\partial_x\beta\right)\left(\partial_x\frac{b}{w}\right) + \left(\partial_x^2\beta\right)\frac{b}{w} + (1-\alpha\kappa)\frac{1}{w}, \end{aligned} \tag{6.5e}$$

$$c_1 = 4\beta\partial_x^3\left(\frac{b}{w}\right) + 6\left(\partial_x\beta\right)\left(\partial_x^2\frac{b}{w}\right) + 2\left(\partial_x^2\beta\right)\left(\partial_x\frac{b}{w}\right), \tag{6.5f}$$

$$c_0 = \beta\partial_x^4\left(\frac{b}{w}\right) + 2\left(\partial_x\beta\right)\left(\partial_x^3\frac{b}{w}\right) + \left(\partial_x^2\beta\right)\left(\partial_x^2\frac{b}{w}\right) + (1-\alpha\kappa)\frac{b}{w} + \kappa w. \tag{6.5g}$$

Here

$$w = \left(\frac{4k\cosh^2 kH}{\sinh K + K}\right)^{\frac{1}{2}},$$

where $k = k_0$ and $K = 2kH$, uses the *normal weighting*

$$\varpi_0 = (\cosh\{k(z+h)\}, \cosh\{k(z+h)\})^{-1/2},$$

so that $a = 1$. The function b may be written in terms of the derivatives of the wavenumber, k, and the those of the fluid boundaries h and d

$$\begin{aligned} b &= b_c(k,H) + (\partial_x k)^2 b_{k_x^2}(k,H) \\ &+(\partial_x k)(\partial_x h) b_{k_x h_x}(k,H) + (\partial_x k)(\partial_x d) b_{k_x d_x}(k,H) \\ &+(\partial_x h)^2 b_{h_x^2}(k,H) + (\partial_x h)(\partial_x d) b_{h_x d_x}(k,H) + (\partial_x d)^2 b_{d_x^2}(k,H) \\ &+(\partial_x^2 h) b_{h_{xx}}(k,H) + (\partial_x^2 d) b_{d_{xx}}(k,H), \end{aligned} \tag{6.6a}$$

where the coefficients appearing in this expression are dependent on the wavenumber and the fluid depth. Alternatively, we may use the fluid depth H in place of d and write

$$\begin{aligned} b &= b_c(k,H) + (\partial_x k)^2 b_{k_x^2}(k,H) \\ &+(\partial_x k)(\partial_x H) b_{k_x H_x}(k,H) + (\partial_x k)(\partial_x h) \tilde{b}_{k_x h_x}(k,H) \\ &+(\partial_x H)^2 b_{H_x^2}(k,H) + (\partial_x H)(\partial_x h) \tilde{b}_{H_x h_x}(k,H) + (\partial_x h)^2 \tilde{b}_{h_x^2}(k,H) \\ &+(\partial_x^2 H) b_{H_{xx}}(k,H) + (\partial_x^2 h) \tilde{b}_{h_{xx}}(k,H). \end{aligned} \tag{6.6b}$$

The various coefficients appearing in expressions (6.6a-b) are given by

$$\begin{aligned} Fb_c(k,H) &= \frac{k}{4}\{K^2 - \sinh^2 K\}, \\ Fb_{k_x^2}(k,H) &= \frac{1}{48k^3}\{-3\sinh^2 K - 6K\sinh K \\ &\quad +3K^2(1+2\cosh K) - 2K^3\sinh K + K^4\}, \\ Fb_{k_x h_x}(k,H) &= \frac{1}{8k}\{-4\sinh K + 4K\cosh K - K^2\sinh K + K^3\}, \\ Fb_{k_x d_x}(k,H) &= -\frac{1}{4k}\{-\sinh K(1+\cosh K) + K(1+\cosh K) - K^2\sinh K\}, \\ Fb_{h_x^2}(k,H) &= \frac{k}{4}\{2(1+\cosh K) + K^2\}, \\ Fb_{h_x d_x}(k,H) &= -\frac{k}{2}\{2(1+\cosh K) - K\sinh K\}, \\ Fb_{d_x^2}(k,H) &= \frac{k}{4}\{2(1+\cosh K) - 2K\sinh K - \sinh^2 K\}, \\ Fb_{h_{xx}}(k,H) &= -\frac{1}{2}(K + \sinh K), \end{aligned}$$

$$Fb_{d_{xx}}(k,H) = \frac{1}{4}(1+\cosh K)(K + \sinh K),$$

and

$$\begin{aligned}
b_{k_x H_x}(k,H) &= -b_{k_x d_x}(k,H), \\
\tilde{b}_{k_x h_x}(k,H) &= b_{k_x h_x}(k,H) + b_{k_x d_x}(k,H), \\
b_{H_x^2}(k,H) &= -b_{d_x^2}(k,H), \\
\tilde{b}_{H_x h_x}(k,H) &= -b_{h_x d_x}(k,H) - 2b_{d_x^2}(k,H), \\
\tilde{b}_{h_x^2}(k,H) &= b_{h_x^2}(k,H) + b_{h_x d_x}(k,H) + b_{d_x^2}(k,H), \\
b_{H_{xx}}(k,H) &= -b_{d_{xx}}(k,H), \\
\tilde{b}_{h_{xx}}(k,H) &= b_{h_{xx}}(k,H) + b_{d_{xx}}(k,H).
\end{aligned}$$

with

$$F = \frac{1}{4k}\{\sinh K + K\}^2.$$

Comparisons between differing geometries are made using the trigonometric variation $p_{2a}(x)$ (see equation (6.2a) and figure 6.6) with the amplitude of this obstruction set as $A_{2a} = 1$m and with the constant values $D_0 = 1$m and $H_0 = 10$m throughout. We begin by considering geometries that share the upper case geometrical variables D and H. Initially, this is interpreted as a keel against a sail with a bed protrusion, for which D and H vary subject to $D + H$ remaining constant. These two geometrical configurations are depicted in figure 6.6.

As α and β may be considered to be functions of the ice thickness, and k and w are functions of the ice thickness and the fluid depth, it is clear that the only differences between these problems are manifest in the coefficient b, due to the terms endowed with a tilde, which are only present in the latter geometrical configuration.

Figures 6.9-6.11 compare single-mode approximations to $|\eta|$ along with the relevant functions $b(x)$, across the interval of varying geometry, for the two problems described. The length of the obstructions is $l = 10$m in figures 6.9-6.10 and $l = \pi$m in figure 6.11, with incident waves of length $\lambda = 200$m in figure 6.9, $\lambda = 20$m in figure 6.10 and $\lambda = \pi$m in figure 6.11.

We observe that the functions b shown in figure 6.9(b) are extremely similar and, inevitably, this leads to corresponding approximations of $|\eta|$, shown in figure 6.9(a), that are also extremely similar. The closely matched functions b for the incident wavelength $\lambda = 200$m are to be expected here. If we consider the second definition of b (6.6b), which

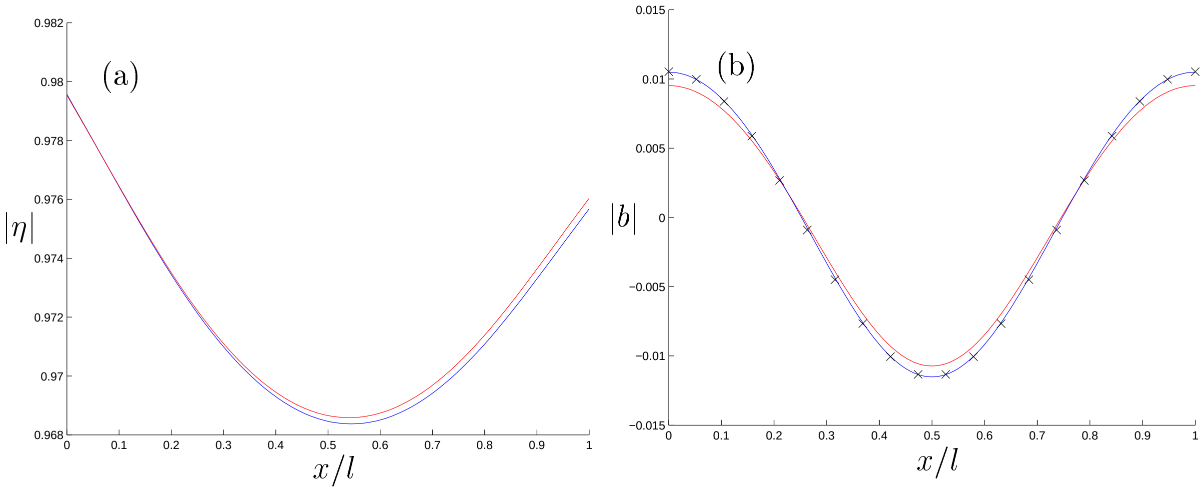

Figure 6.9: Part (a) plots single-mode approximations to the modulus of the reduced displacement caused by an incident wavelength of $\lambda = 200$m, for obstructions of form p_{2a} (see equation (6.2a)) with amplitude $A_{2a} = 1$m, length $l = 10$m, thickness $D_0 = 1$m, and fluid depth $H_0 = 10$m. The obstructions are in the form of a keel (blue curve) and a sail with a bed protrusion (red). Part (b) plots the corresponding moduli of the function b (see equation (6.6b)), with the dominant term $\partial_x^2 H b_{H_{xx}}$ superimposed (×).

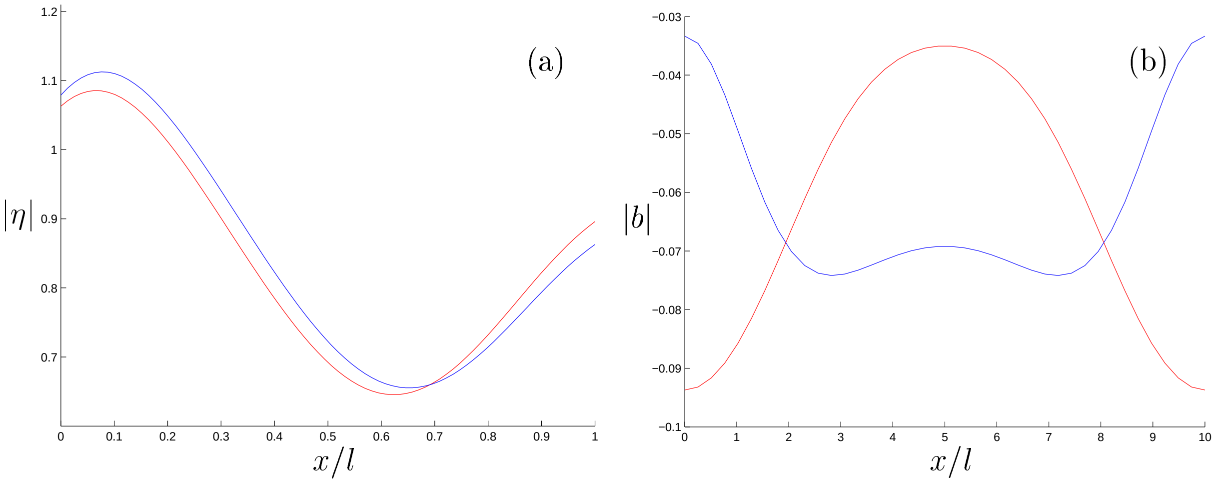

Figure 6.10: As in figure 6.9 but with incident wavelength $\lambda = 20$m

is made in terms of the geometrical variables D, H and h, then it is possible to show that

$$\begin{array}{lll} b_c \sim -\dfrac{1}{12}(kK)^2, & b_{k_x^2} \sim -\dfrac{1}{180}\left(\dfrac{K^2}{k}\right)^2, & b_{k_x H_x} \sim -\dfrac{1}{3}K, \\ \tilde{b}_{k_x h_x} \sim \dfrac{1}{2}K, & b_{H_x^2} \sim \left(\dfrac{k}{K}\right)^2, & \tilde{b}_{H_x h_x} \sim k^2, \\ \tilde{b}_{h_x^2} \sim -\dfrac{1}{12}(kK)^2, & b_{H_{xx}} \sim \dfrac{k}{K}, & \tilde{b}_{h_{xx}} \sim \dfrac{1}{4}kK, \end{array} \tag{6.9}$$

as $k \to 0$. Therefore, for fixed geometry, as the incident wavelength becomes large, all terms involved in (6.6b) tend to zero except for $b_{H_x^2}$ and $b_{H_{xx}}$ that tend to the constant values $1/4H^2$ and $1/2H$ respectively (recall that $K = 2kH$). These two terms are shared by the respective geometries. Due to the choice of geometry, specifically our choice of $H_0 = 10$m, the term involving $b_{H_{xx}}$ is dominant, which may be seen in figure 6.9(b). To emphasise this, the function $\partial_x^2 H b_{H_{xx}}$ is superimposed over the functions b in figure 6.9(b).

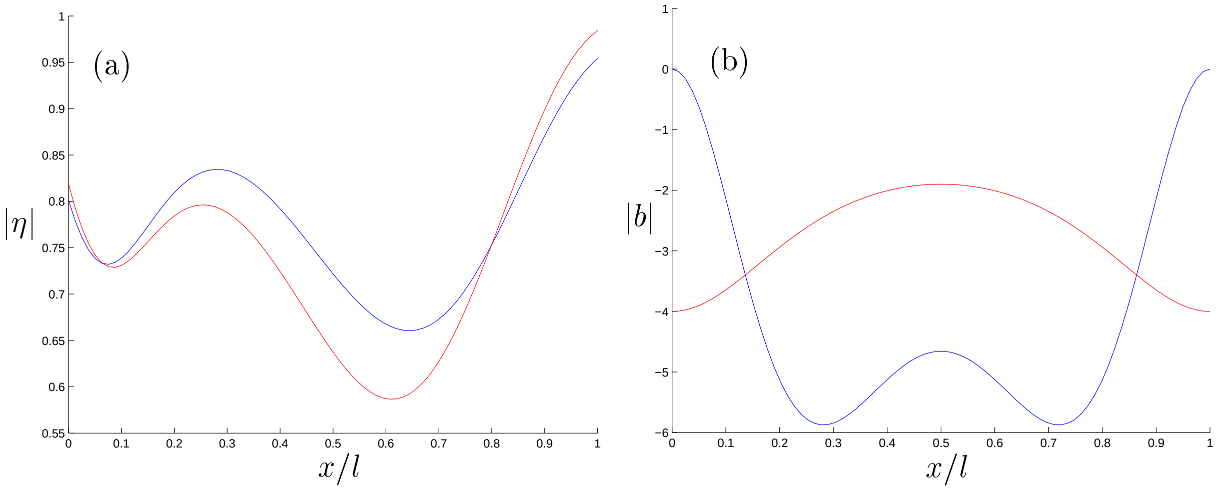

Figure 6.11: As in figure 6.9 but with obstructions of length $l = \pi$m and incident wavelength $\lambda = \pi$m.

Conversely, the corresponding functions b for an incident wave of $\lambda = 20$m, which are plotted in figure 6.10(b), are quite distinct from one another as the coefficients that separate the respective geometries (those that take the tilde notation) are now of a comparable magnitude to the other terms. However, although the functions b have clearly become different, the corresponding approximations to $|\eta|$, shown in figure 6.10(a), are still quantitatively and qualitatively very close.

In figure 6.12(a) the coefficients of the governing equation (6.4) that differ between the keel and sail with a bed protrusion geometries, namely c_i $(i = 0, \dots, 4)$ defined in (6.5c-g), are plotted for the problem considered in figure 6.10. With reference to the transform (3.18), we note that the derivative operator is inversely proportional to the length of the obstruction. As the differential operator becomes more dominant in the lower-order coefficients, in this case, where $l = 10$m, the coefficients decrease in magnitude from c_4 to c_0. The coefficients c_5 and c_6, that are shared by the two geometries and are not shown in figure 6.12(a), are of magnitude $\mathrm{O}(10^5)$ and therefore outweigh the coefficients c_4 to c_0. We also note that, in this case, the relative size of the only variation between the two problems, the function b, is negligible in the coefficient c_4.

The more extreme example $l = \lambda = \pi$m is considered in figure 6.11. As in the case $l = 10$m and $\lambda = 20$m, the functions b shown in figure 6.11(b) are dissimilar. The resulting

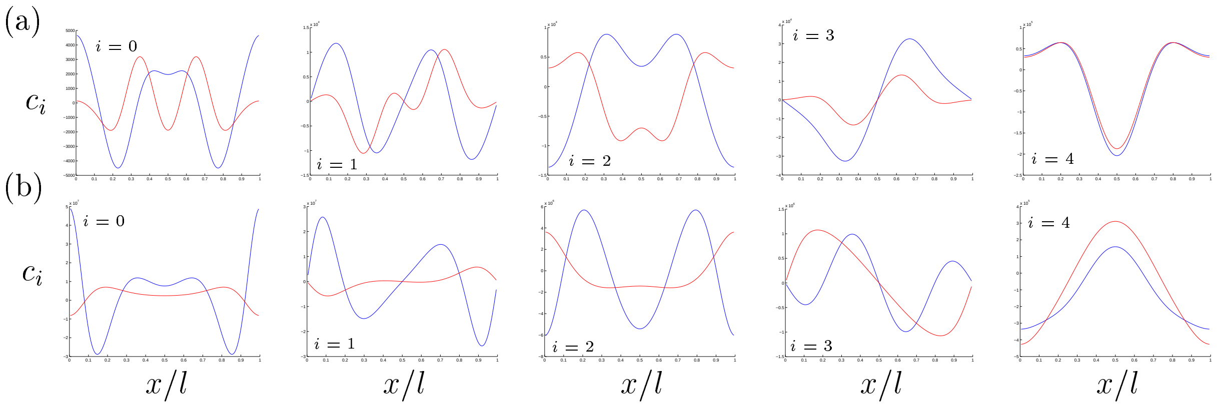

Figure 6.12: The coefficients c_i ($i = 0, \ldots, 4$) of the governing differential equation of the single-mode approximation. These are the coefficients that differ for problems that share the same vertical structure, D and H. The geometry used in part (a) is as in figure 6.10 ($l = 10$m and $\lambda = 20$m). In part (b) the geometry is as in figure 6.11 ($l = \pi$m and $\lambda = \pi$m). In both, the obstructions appear as a keel (blue curves) and a sail with a bed protrusion (red).

approximations to $|\eta|$, which are shown in figure 6.11(a), differ to a greater extent than those that appear in figure 6.10(a); however, their agreement, both quantitatively and qualitatively, remains.

As with the case $l = 10$m and $\lambda = 20$m, the coefficents c_i ($i = 0, \ldots, 4$), corresponding to figure 6.11, are displayed in figure 6.12(b). The magnitude of the shared coefficients c_5 and c_6 (not shown) is $\mathrm{O}(10^4)$, which is smaller than those of the displayed coefficients that are not shared by the two geometries. This is due to the reduction in length of the obstruction. Furthermore, by shortening the incident wave, the relative magnitude of the function b in the coefficients increases. The difference between the respective coefficients is therefore greater here than in the previous example of figure 6.12(a). Despite this, as already commented, the approximate displacements shown in figure 6.10(a) are similar. This indicates that the sources of scattering contained in the coefficients c_5 and c_6, which are produced through variations in the ice thickness and the fluid depth, are dominant.

Figure 6.13(a) displays single-mode approximations to $|R|$, over an interval of incident wavelengths, for the keel and sail with a bed protrusion geometries described, where $l = 10$m. As expected from our previous analysis, we see the results for these two problems tending towards one another as λ increases and only a slight difference for $\lambda \approx 20$m.

A further curve denoting the reflected amplitude arising from an isolated sail geometry is also shown in figure 6.13(a). This geometrical configuration shares its ice thickness D but not its fluid depth H with the previous geometries; thus, the sail problem does not share the functions w or b with the previous problems. The differences in these functions are produced by differences in the values of k and K caused by the absence of variations in H, as well as the extra terms that appear in b when d or h vary.

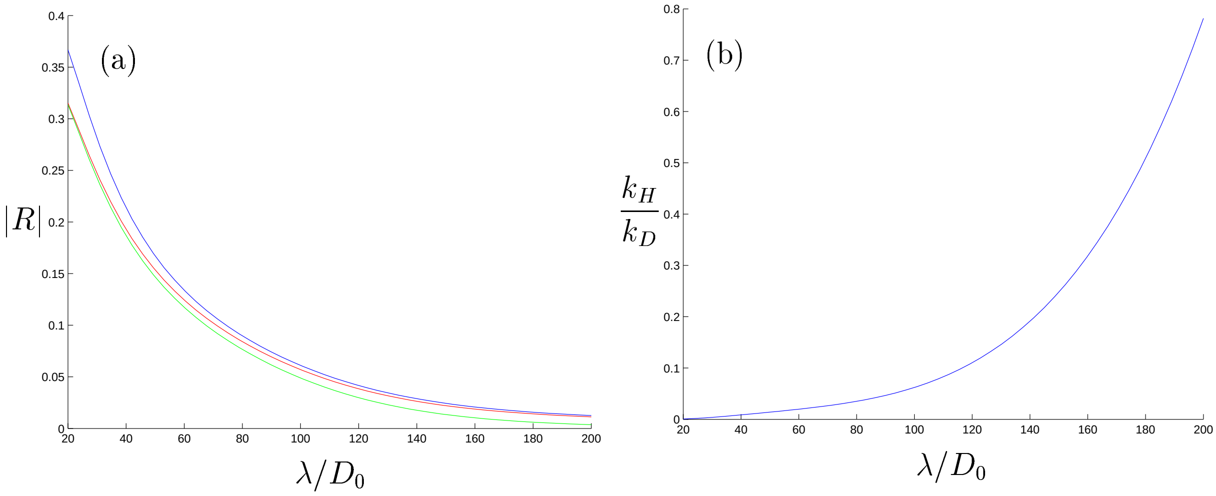

Figure 6.13: Part (a) plots single-mode approximations to the modulus of the reflected amplitude as functions of non-dimensional incident wavelength, for obstructions of form p_{2a} with amplitude $A_{2a} = 1$m, thickness $D_0 = 1$m, length $l = 10$m and bed depth $h_0 = 10$m. The obstruction takes the form of a keel (blue curve), a sail with a bed protrusion (red) and a sail (green). Part (b) plots the corresponding ratio k_H/k_D, where k is the incident wavenumber.

It is evident in figure 6.13(a) that the far-field behaviour of the sail problem closely resembles that of the two other problems. In particular, we observe the results of the sail and the sail with a bed protrusion geometries tending towards one another as $\lambda \to 20$m. As $\lambda \to 200$m the reflection caused by the solitary sail is negligible in comparison to that from the other two geometrical obstructions.

We are primarily concerned with how the rôle of the wavenumber, k, dictates the scattering properties of each of the chosen geometrical configurations. Therefore, consider the partial derivatives

$$k_D = \frac{k(\alpha\kappa - 3\beta k^4)\sinh K}{DE}, \quad k_H = -\frac{2(1 - \alpha\kappa + \beta k^4)k^2}{E}, \tag{6.10}$$

where

$$E = (1 - \alpha\kappa + 5\beta k^4)\sinh K + (1 - \alpha\kappa + \beta k^4)K.$$

These derivatives have the properties that

$$k_D \sim \begin{cases} \dfrac{\alpha k^3}{2D} & (k \to 0), \\ -\dfrac{k}{2D} & (k \to \infty), \end{cases} \qquad k_H \sim \begin{cases} -\dfrac{k}{2H} & (k \to 0), \\ -\dfrac{k}{2\alpha}\text{csch}K & (k \to \infty). \end{cases}$$

We deduce that, for a large incident wavenumber, the variation of k, in relation to the ice thickness, is proportional to the wavenumber itself but, in relation to the fluid depth, becomes negligible. For a small incident wavenumber, the derivatives of k tend to zero and do so more rapidly with respect to D than H. Consequently, for short incident waves, the shape of the wavenumber, k, for the sail problem will be almost identical to that of the keel and sail with a bed protrusion geometries, whereas for long incident waves, due to the uniform fluid depth in the solitary sail geometry, this relationship will cease. This latter remark is consistent with the conclusion drawn from the limits (6.9). We can, therefore, partially attribute the similarity of results of the solitary sail to the keel and sail with a bed protrusion geometries, used in figure 6.13(a), to a close relationship in their respective wavenumbers, which is a product of the shared ice thickness profile, over much of the chosen interval. The relationship between the derivatives (6.10) is displayed graphically, for the problem in hand, in figure 6.13(b).

Having investigated the influence of the vertical distances, D and H, on the single-mode approximation, further understanding of geometrical relations may be gained by considering the rôle of variations to the fluid boundaries, d and h. This is achieved by considering two problems, one in which only d varies and another in which only h varies. In both problems the ice thickness is constant and the variations to the fluid depth, H are the same.

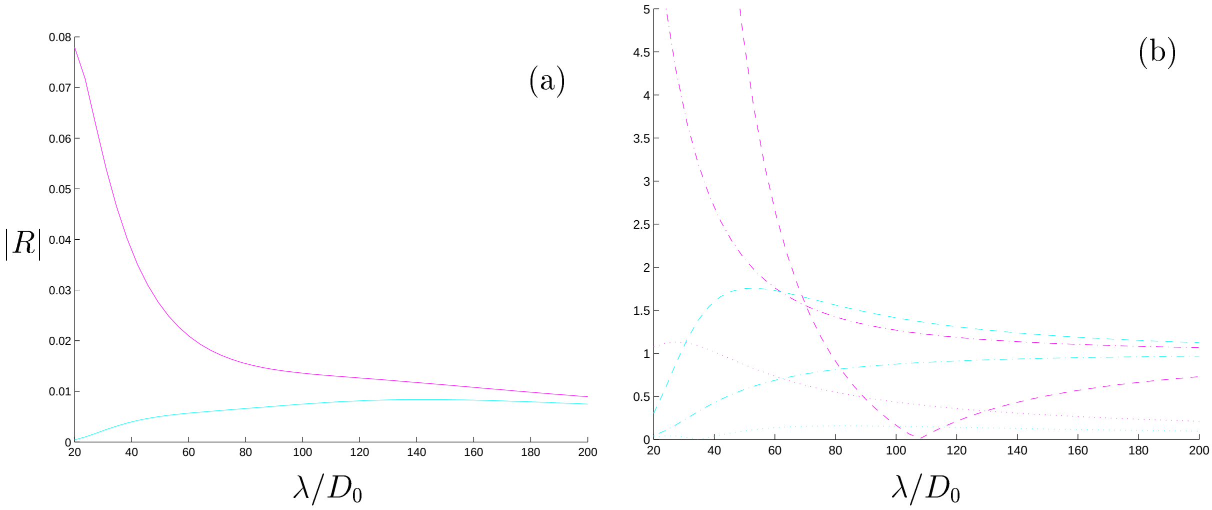

Figure 6.14: Part (a) plots single-mode approximations to the modulus of the reflected amplitude, for obstructions of form p_{2a}, with amplitude $A_{2a} = 1$m, length $l = 10$m, thickness $D_0 = 1$m and bed depth $h_0 = 10$m. The obstruction takes the form of an undulating fluid-ice interface (magenta curve) and an undulating bed (cyan). In both, the ice thickness remains constant. Part (b) plots the corresponding terms that differentiate the function b, namely $4H^2 b_{X_x^2}$ (dashed curves), $b_{k_x X_x}$ (dotted) and $2Hb_{X_{xx}}$ (dot-dash) $(X = d, h)$.

Figure 6.14(a) displays single-mode approximations to $|R|$ resulting from variations in H derived in the two ways described. Figure 6.15 plots approximations to $|\eta|$ along with the relevant functions b, taken at either end of the interval of incident wavelength, $\lambda = 20$m and 200m.

As the two problems share the upper case geometrical variables, D and H, differences in the solutions are again caused by the function b; specifically, considering the first definition of b (6.6a), the differences appear through the terms with the coefficients $b_{k_x h_x}$, $b_{h_x^2}$ and $b_{h_{xx}}$, and $b_{k_x d_x}$, $b_{d_x^2}$ and $b_{d_{xx}}$. The analysis of b for small k, given in equation (6.9), once more applies and is substantiated by the similarities that are visible between the two problems in figure 6.15(b.i-ii) and the behaviour of the reflected amplitudes as $\lambda \to 200$m, shown in figure 6.14(a). Note that, as D is constant, the problem is more sensitive to the variations in b and hence the solutions are proportionately further apart around $\lambda = 200$m than for the keel and sail with a bed protrusion problems at corresponding incident wavelengths.

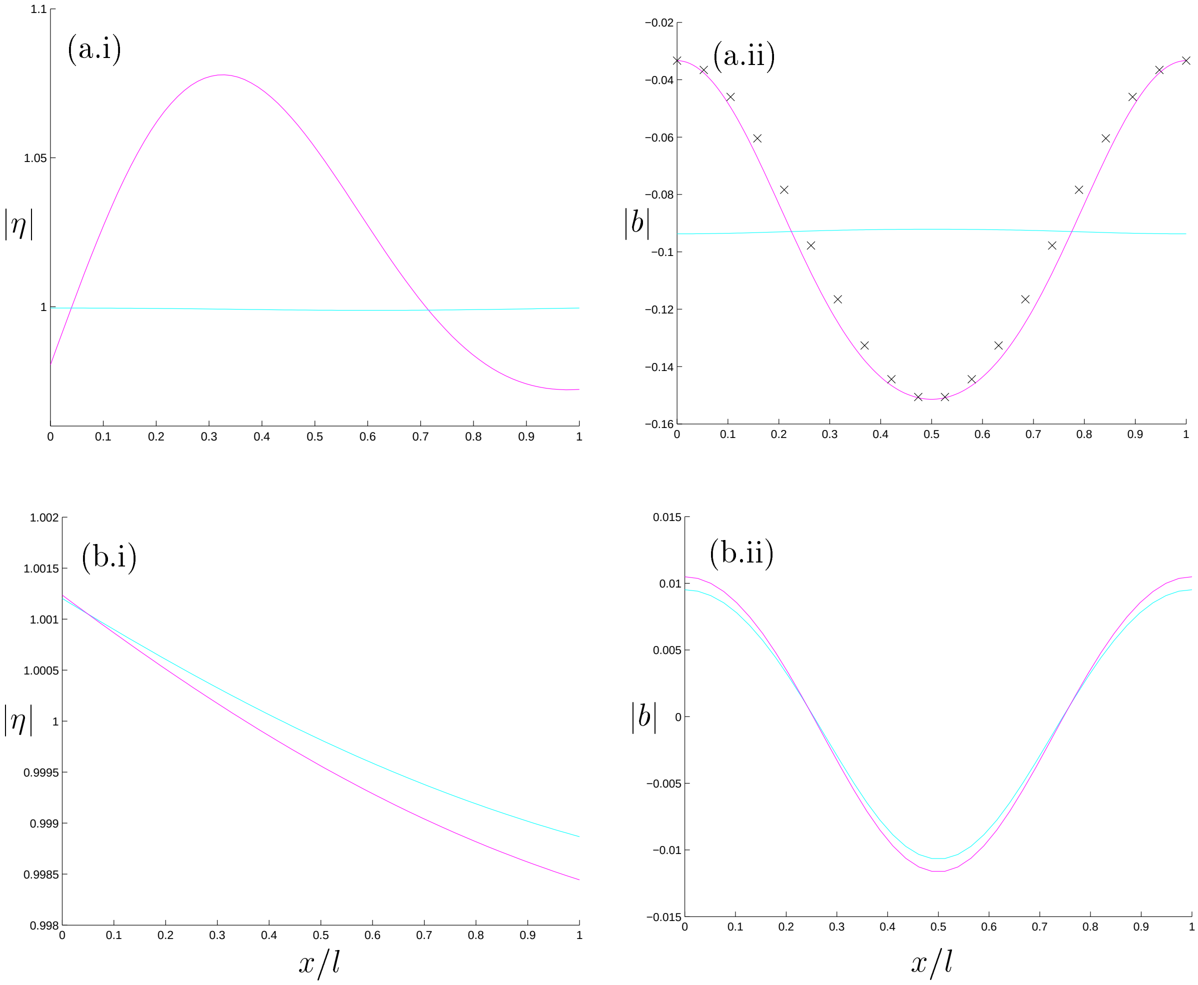

Figure 6.15: Parts (a-b.i) plot single-mode approximations to the modulus of the reduced displacement for the geometries used in figure 6.14. In part (a) the incident wave is of length $\lambda = 20$m, and in part (b) it is $\lambda = 200$m. Parts (a-b.ii) plot the corresponding moduli of function b, and in part (a.ii) the dominant term $|b_0 + \partial_x^2 d b_{d_{xx}}|$ is superimposed ($\times$).

It is clear in figure 6.14(a) that, for the majority of the interval of incident wavelengths, variations in d cause greater reflection than equivalent variations in h. This is confirmed by the response of the lower surface of ice at $\lambda = 20$m, which is shown in figure 6.15(a.i). To examine this phenomenon we consider b in the limit $k \to \infty$, for which it can be shown that

$$\begin{array}{lll} b_c \sim -k^2, & b_{k_x^2} \sim -\dfrac{1}{4k^2}, & b_{k_x h_x} \sim -\dfrac{1}{2}K^2 \mathrm{csch} K, \\ b_{k_x d_x} \sim 1, & b_{h_x^2} \sim 2k^2 \mathrm{csch} K, & b_{d_x^2} \sim -k^2, \\ b_{h_{xx}} \sim -2k \mathrm{csch} K, & b_{d_{xx}} \sim k. & \end{array} \tag{6.11}$$

Therefore, as k increases the terms corresponding to variations in d increase or tend to a non-zero constant. In contrast, the analogous terms corresponding to variations in h tend to zero, so that variations to the underside of the ice dominate over bed variations. These tendencies are shown graphically, over the interval of incoming wavelengths $\lambda \in (20, 200)$m, for the current problem in figure 6.14(b). They are also observed in the shapes of the respective functions b at $\lambda = 20$m in figure 6.15(a.ii). The dominant terms in b in the short wave limit, for $l = 10$m, are deduced from (6.11) to be $b_c + \partial_x^2 d b_{d_{xx}}$ and this function is overlaid on figure 6.15(a.ii).

It is now possible to further clarify the relationships shown in figure 6.13(a). As the influence of the variations in h die out in b as k increases, which coincides with the weak response in k to variations in H, the sail with a bed protrusion problem tends towards the sail problem. In this limit, the influence of the fluid-ice boundary, d, in b remains significant and so a gap remains between the keel and sail problems even when the response of k to variations in H is weak.

6.5 Conclusions

The problems considered in this chapter have been those of a two-dimensional nature in the context of complete ice-cover. The formulation of such problems was outlined in section §4.3.1.

In §6.1, this form of geometry was used to demonstrate the respective convergence rates of the natural and hybrid approximations. By judiciously selecting two example problems, the slight superiority of the natural approximation over the hybrid approximation was demonstrated. Nevertheless, the hybrid modes provided rapid convergence and the full linear solutions gained by using the two alternative trial spaces were consistent. It was therefore concluded that the hybrid modes would be used in all cases in which the natural evanescent modes became invalidated by bifurcations. A third trial space, comprised of the Fourier cosine modes, was used to further highlight the excellent performance of the natural approximation.

A technical issue, regarding the choice of modes was then investigated. This centred around the possibility that we would be unable to select a continuous trial space as a non-geometrical parameter (e.g. frequency ω) was varied. Consequently, it was shown that a spurious jump would become manifest in our results. However, these jumps are normally negligible and vanish as more modes are included and the MMA converges.

In §§6.2-6.3, we compared results produced by the MMA to results available in previous literature. The comparison to Williams & Squire (2004), whose method is entirely independent of our own, served to verify the effectiveness and accuracy of the MMA. It was observed that the convergence of the MMA is weakest in an intermediate interval of frequency for which the parameters cause the incident wave to most strongly excite the evanescent waves. The single-mode approximations of Porter & Porter (2004) were advanced to full linear solutions using the MMA. It was prominent that only a small number of modes was required to find the full linear solution, with, in many cases, a single mode producing approximations to the reflected amplitude and displacement for which the addition of each evanescent mode causes at most only $O(10^{-3})$ improvements. Even when the geometry was extended to 'non-slow' variations, the low-dimensional approximations retained their accuracy, although a larger number of modes was required to attain the full linear solution. This compares to the resolution of the scattering caused by an ice edge, which was seen in the case of a semi-infinite ice sheet. There, qualitative inaccuracies were far more evident in low-dimensional approximations.

Correction of the erroneous transformation employed in Porter & Porter (2004) led us to observe a close link between geometries that share their ice thickness and fluid depth. This relationship was thoroughly investigated in §6.4. Due to the high levels of accuracy that it demonstrated, the analysis that was carried out in this section was made using the relatively simple structure of the single-mode approximation. Through a series of results and examination of the relevant quantities involved, it was shown that the ice thickness is the dominant factor in determining the shape of the solution, whilst the fluid depth only becomes a factor in the long wave régime. This indicated that configurations that share the same ice thickness, such as equivalent keels, sails and sails with bed protrusions, can be expected to give similar results under most circumstances. Additionally, it was shown that undulations in the fluid-ice interface, d, affect long incident waves in the same way as bed undulations, h, but that for shorter incident waves the effects of the bed variations die out, whereas those due to the ice variations grow.

Chapter 7

Numerical Results: partial ice-cover in two-dimensions

Having considered the effects of variations to the geometrical surfaces in isolation during the previous chapter, we now progress to problems involving partial ice-covering. This adds the feature of ice edges, which are an additional source of scattering to the incident wave. In this chapter we will mainly look at those problems that incorporate a single ice floe of a finite extent, which is the problem that was formulated in §4.3.2. This means that we will now be dealing with the scattering caused by and interactions of two ice edges and undulating surfaces. In situations of partial ice-cover there is also the question of the inclusion of the correct physical draught and this is addressed at the end of the results.

7.1 Comparison with the work of Belibassakis & Athanassoulis (2005)

As with the previous two chapters, our numerical investigations are prefaced by a comparison to results produced by independent authors.

Belibassakis & Athanassoulis (2005) also used a variational approach to solve two-dimensional finite ice floe problems of the form outlined in §4.3.2; however, they imposed the ice sheet restrictions of uniform thickness and a zero draught, so that only the bed topography may vary continuously over the finite interval beneath the ice floe. Noting that the natural modes satisfy $[\partial_z w_i]_{z=-h} = 0$ and building on their earlier work for free surface motions (Belibassakis & Athanassoulis, 1999), an extra expansion mode was included, $\hat{w}$ say, satisfying $[\partial_z \hat{w}]_{z=-h} \neq 0$, thereby accelerating the convergence of the approximation.

A similar approach could be utilised in our MMA. That is, we note that both the natural and hybrid modes satisfy

$$\partial_z w_i = 0 \quad (z = -h),$$

for $i = 0, \ldots, N$. It is therefore impossible for the no-flow condition (2.9b) to be satisfied exactly by the MMA when the bed undulates and convergence around this point is expected to be slow. If we chose to pursue this issue, it is likely that we would closely follow the method of Chamberlain & Porter (2006). In the work of these authors the trial space used on a free-surface flow is extended consistently with the addition of a vertical mode that both allows the bed condition to be satisfied and decays in the far-fields, so that the exact radiation conditions are not compromised.

However, the addition of a supplementary 'bed-mode' would only be an issue if we wished to investigate the motion in a vicinity of this surface. Our concern is with the fluid-ice interface, and the excellent convergence we find in the results presented in this section confirm that the bed-mode would only have a marginal effect. Furthermore, we will most often use situations in which the bed is flat. Therefore, the bed-mode is left only as an area of possible further study.

In the particular problem, chosen from Belibassakis & Athanassoulis (2005) for comparison, the parameter values are $\alpha = 0$, $\beta = 10^5$Pa m^{5}s^2/kg and $l = 500$m, with

$$h(x) = \frac{h_0 + h_1}{2} - \frac{h_0 - h_1}{2} \tanh 3\pi(x/l - 1/2) \quad (0 < x < l), \tag{7.1}$$

which represents a monotonic decrease in the depth when $h_0 > h_1$. Using the parameter values given in §2, $\beta = 10^5$Pa m^{5}s^2/kg corresponds to an ice thickness $D_0 \approx 1.3$m. The value $\alpha = 0$ is inconsistent with any parameter values for the model problem we have developed and the comments pertaining to the semi-infinite ice sheet problem studied by Linton & Chung (see §5.1.3) are again relevant.

Figures 7.1(a-b) are the counterparts of figures 10-11 of Belibassakis & Athanassoulis (2005). Both figures plot MMAs to the magnitude of the sheet elevation $|\eta|/2$ across the ice floe; the single incident wave has angular frequency $\omega = 0.4$ rads/secs. Only the most significant two sets of data are plotted on each graph to keep them uncluttered. The four parameter sets each demonstrate extremely rapid convergence with $\epsilon_1 \approx 1 \times 10^{-3}$ and $\epsilon_1 \approx 3 \times 10^{-4}$ and the single-mode approximations are considered sufficiently accurate. In all cases the converged curves of figure 7.1 appear identical to their counterparts presented in Belibassakis & Athanassoulis (2005).

The rapid convergence displayed in figure 7.1 can be explained by the large length of the ice floe. Referring back to the investigation into the convergence of approximations to the ice sheet displacement for the semi-infinite ice sheet conducted in section §5.2, we learnt that the rôle of the additional evanescent modes is confined to the vicinity of the

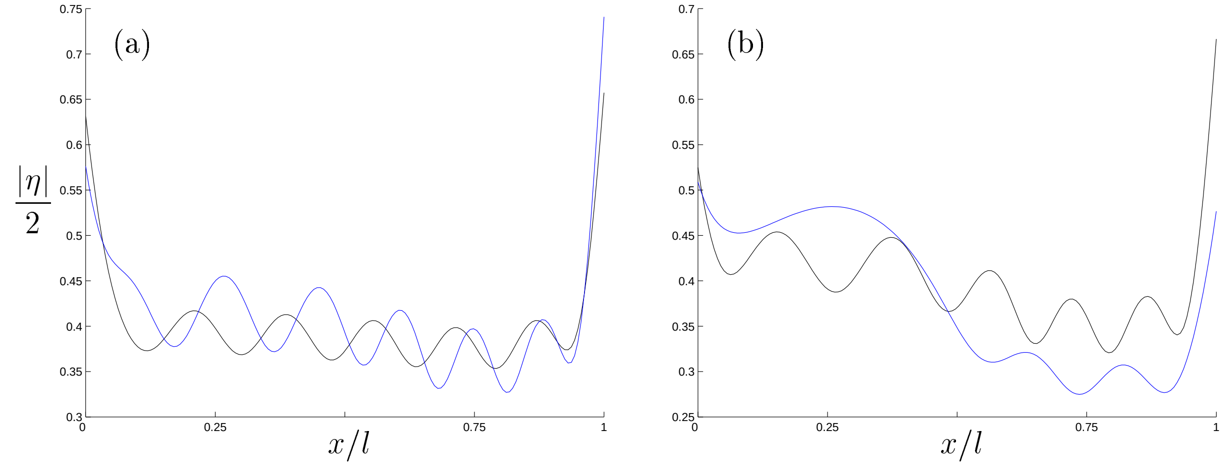

Figure 7.1: Single-mode approximations for comparison with figures 10-11 of Belibassakis & Athanassoulis (2005), in which the plate is of uniform thickness, a zero draught and length $l = 500$m, and the bed varies beneath it, as defined in equation (7.1). Part (a) plots scaled moduli of the reduced displacements of floes for normal incidence ($\vartheta = 0$) and bed depths $h_0 = 12$m and $h_1 = 8$m (black line), and $h_0 = 15$m and $h_1 = 5$m (blue). In part (b) the bed depths are $h_0 = 15$m and $h_1 = 5$m and the incident angles $\vartheta = \pi/6$ (black line) and $\vartheta = \pi/3$ (blue) are used.

ice edges. For a long floe such as this, the lengths of these regions are small compared to the floe length and thus it is the propagating wave that dominates. The question of the length of the floe is further investigated in §7.3.

7.2 Comparison with the work of Porter & Porter (2004)

We continue by again returning to Porter & Porter (2004) in order to study the effects of the inclusion of evanescent modes in the approximation. In addition to the issue of the missing terms relating to variations in d (see §3.2.1), the results presented in §6 of Porter & Porter (2004) differ from the results taken from our single-mode approximation ($N = 0$) due to the expansion of the auxiliary function, u, that exists in the interfacial jump conditions (see §3.1.1).

Figure 7.2 displays the convergence of the natural approximation to the non-dimensional sheet elevation, $|\eta/A_0^{(0-)}|$, of a uniform floe of a zero draught, length $l = 10$m and thickness $D_0 = 38$mm over a uniform bed of depth $h_0 = 1.1$m for two incident wavelengths, $\tau = 0.7$secs and 1.429secs. In this problem only, Young's modulus is $E = 103$MPa and the density of the ice is $\rho_i = 220.5\text{kgm}^3$. The corresponding single-mode approximations of Porter & Porter (originally appearing in figures 8(a) and 9(a) of that paper) are also shown. Note that the ice thickness used here is far less than any of those that we have considered previously but that the length of the incident waves is also shorter.

As the underside of the ice is flat, the only difference between our single-mode approximations and the single-mode approximations of Porter & Porter is derived through the reformulation of the matching conditions. For the incident wave of angular frequency $\tau = 0.7$secs, shown in figure 7.2(a), there is negligible difference between the accuracies of the single-mode approximations; however, for the incident wave of angular frequency $\tau = 1.429$secs, shown in figure 7.2(b), the reformulated matching conditions lead to a clear improvement in accuracy.

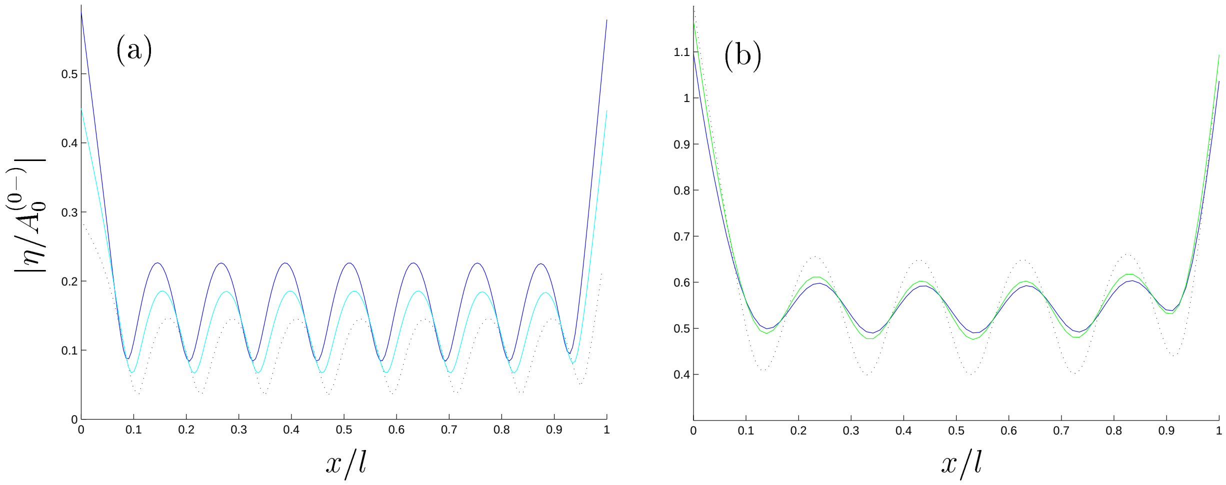

Figure 7.2: Extensions to full linear solutions of the approximation given in figures 8(a) & 9(a) of Porter & Porter (2004). The floe is of uniform thickness $D_0 = 38$mm, length $l = 10$m and with a zero draught ($d = 0$) over a bed depth of $h_0 = 1.1$m. The figures plot the convergence of the MMA to a scaled version of the modulus of the reduced displacement of the floe, with wave period (a) $\tau = 0.7$secs and (b) $\tau = 1.429$secs. The dimensions of the approximation are (a) $N = 0$ (blue curves) and $N = 3$ (cyan), and (b) $N = 0$ (blue) and $N = 2$ (green). The single-mode approximations of Porter & Porter are also superimposed (black dotted curves).

Here, we find that the convergence of the natural approximation for the longer incident wave is far more rapid than that of the shorter incident wave, with $\epsilon_2 \approx 7.2 \times 10^{-3}$ for the longer wave compared to $\epsilon_3 \approx 3.7 \times 10^{-2}$ for the shorter wave. The stronger activation of the evanescent modes seen in figure 7.2(a) may be attributed to a greater jump in the propagating wavenumber as it passes into the interval occupied by the ice sheet; we have $k_0/k_0^{(0)} = 0.1550$ for $\tau = 0.7$secs and $k_0/k_0^{(0)} = 0.4588$ for $\tau = 1.429$secs. Similar comments were made for the semi-infinite ice sheet problem in §5.2. Convergence for the $\tau = 0.7$rads/secs problem was terminated at four modes with $\epsilon_3 \approx 3.7 \times 10^{-2}$.

It is again evident that the accuracy gained by adding the evanescent modes is significant at the ends of the ice floe, particularly the left hand end at which the incoming wave is incident. The qualitative nature of the propagating wave passing through the ice is

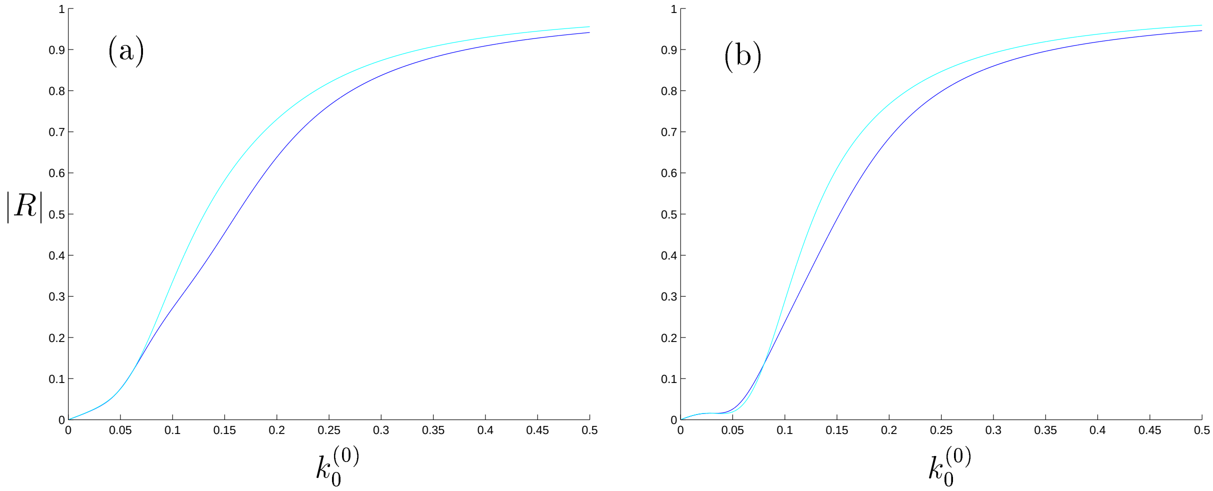

Figure 7.3: Convergence of the MMA to the modulus of the reflected amplitude as a function of incident wavenumber, which extends to full linear solutions the single-mode approximations given in figure 11 of Porter & Porter (2004). The floe is of length $l =$ 40m and thicknesses $D_0 = 0.1$m, with the bed depth $h_0 = 20$m. The variations of the geometrical surfaces are those defined in equation (7.2) with amplitude $A_{11} = 1.35$m. The variations take the form of (a) the keel intended by Porter & Porter and (b) the sail with bed protrusion actually given in Porter & Porter (2004). The dimensions of the approximations are $N = 0$ (blue curves) and $N = 3$ (cyan).

accurate in the single-mode approximation; however, slight quantitative refinements are achieved through the addition of extra modes.

The results given in figure 11 of Porter & Porter (2004) were intended for a set of keels of the parabolic form

$$p_{11}(x) = \begin{cases} 0 & (x < 0, x > l), \\ 4A_{11}(1 - x/l)x/l & (0 < x < l), \end{cases} \tag{7.2}$$

where A_{11} is a constant amplitude. However, we now understand that these results must be reinterpreted as equivalent sails with bed variations.

In figures 7.3-7.5 we investigate and contrast the results of both the intended keel geometries with the actual sail with bed protrusion geometries. The results are of the modulus of the reflected amplitude, $|R|$, over the interval of incident wavelengths $k_0^{(0)} \in (0, 0.5)$rads/m, where the geometrical values $D_0 = 0.1$m, $h_0 = 20$m and $A_{11} = 13.5D_0$m are used, along with the three floe lengths $l = 40$m, 80m and 160m. Over the chosen interval of incident wavelengths the wave period decreases to approximately 4secs at $k_0^{(0)} = 0.25$rads/m and 2.84secs at $k_0^{(0)} = 0.5$rads/m. Due to bifurcations, in all problems the hybrid evanescent modes are used.

Convergence has been taken to be complete when $\epsilon_N \approx 10^{-3}$, which requires four vertical modes for the two shorter floe lengths and five modes for the longest floe length. In all problems the convergence rates are extremely similar; the marginally slower convergence caused by the longest floe is understood to be due to an increase in interference effects between propagating modes. In §7.3 we will observe convergence difficulties produced by interference between evanescent waves when the floe length is short.

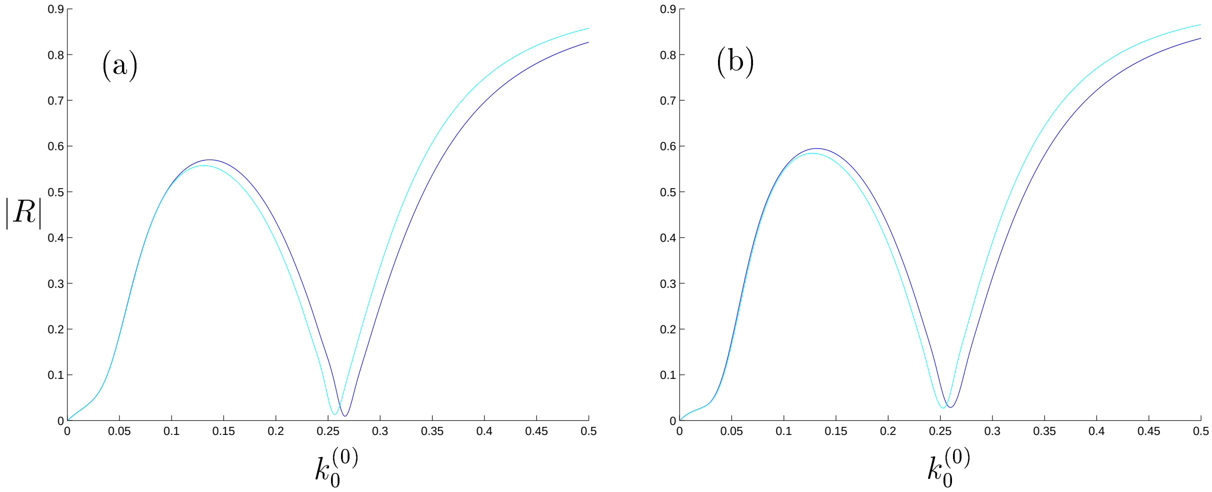

Figure 7.4: As in figure 7.3 but with floe length $l = 80$m. The dimensions of the approximations are $N = 0$ (blue curves) and $N = 3$ (cyan).

In all problems the single-mode approximation provides good accuracy, containing the essential characteristics of the converged solution. This is a consequence of the relatively small geometrical jump at the edges of the floe, a feature that was observed for the semi-infinite ice sheet problem in §5.2. Following the findings of that chapter, we anticipate that the fine-scale refinement of the solution will be slow. By way of confirmation of this assertion we note that it takes twelve modes for the error, ϵ_N, to gain an extra order of magnitude in accuracy for the keel of length 40m, that is $\epsilon_{11} \approx 10^{-4}$.

During our study of the semi-infinite ice sheet problem we noted the deterioration of accuracy of low-dimensional approximations as the frequency increased, which was attributed to the difference of the propagating wavenumbers between the ice-free and ice-covered states. In §6 we observed that the convergence of the MMA when there are geometrical variations is weakest in a middle range of frequencies. The current problem combines both scattering by ice edges and undulating surfaces and we hence expect a combination of the above convergence traits. We can certainly distinguish weak convergence in a mid-interval for the shorter floes, in figure 7.3, and at the higher wavenumbers of the longer floes, in figures 7.4-7.5.

It is evident that the scattering properties of the corresponding geometries are almost identical to one another. This phenomenon is consistent with our investigations of the complete ice-cover problems of the previous chapter and again indicates that the variations in the ice thickness are dominant. However, the problems presented in figures 7.3-7.5

are limited, especially in relation to the ice thickness used. The issue of dominance of variations to the ice thickness, in the context of partial ice-cover, is investigated further in §7.4.

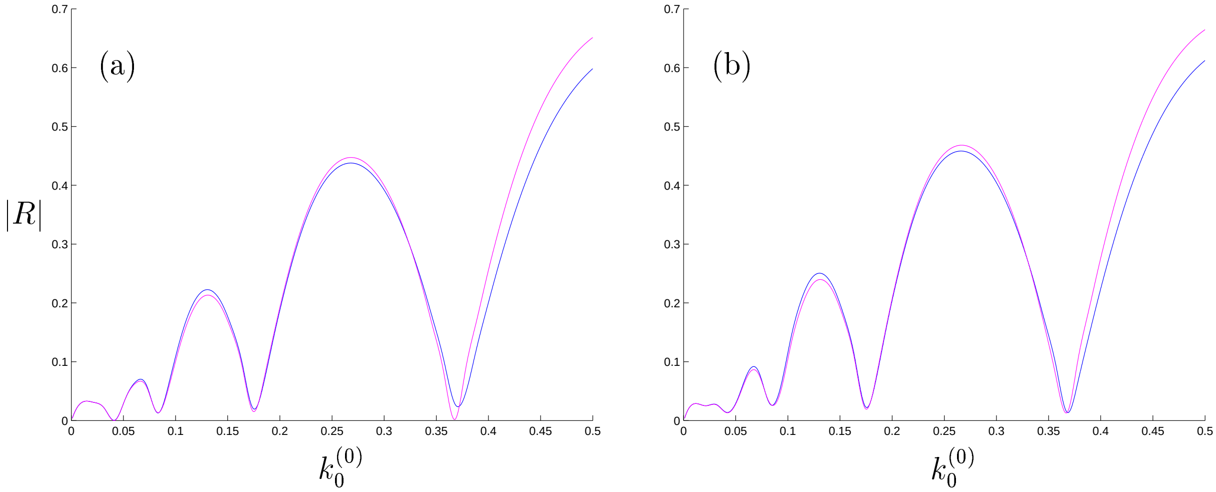

Figure 7.5: As in figure 7.3 but with floe length $l = 160$m. The dimensions of the approximations are $N = 0$ (blue curves) and $N = 4$ (magenta).

7.3 Piecewise uniform geometry

For our first set of independent numerical results in this chapter, we restrict ourselves to floes of uniform thickness and a zero draught over flat beds. This situation is closely related to the semi-infinite ice sheet problem studied in §5 and may be analysed by similar means to those outlined in that chapter. A finite uniform floe contains two sources of scattering - one at each ice edge - and is thus more complicated than that of the semi-infinite ice sheet in which there is only a single ice edge. It is therefore necessary to consider the interaction of the scatterers in addition to their isolated properties, which were investigated as part of our analysis of the semi-infinite ice sheet problem.

In figures 7.6-7.8 we consider $|R|$ for the three floe lengths $l = 10$m, 30m and 100m, and the three ice thicknesses $D_0 = 0.1$m, 0.5m and 1m over a bed depth of $h_0 = 20$m. The interval of incident wave periods, $\tau \in (2, 12)$secs, translates to $k_0 \in (0.0413, 0.424)$rads/m for $D = 0.1$m, $k_0 \in (0.0411, 0.174)$rads/m for $D = 0.5$m, $k_0 \in (0.0393, 0.117)$rads/m for $D = 1$m.

As in §5.2, the assumption of a zero draught is made to isolate other properties. Specifically, here we are interested in the effects of varying l and D_0.

The characteristics observed in §5.2 are again present: low-dimensional approximations display large inaccuracies for the thicker ice but are resolved rapidly; small-scale refinements of the full solution are slow; and convergence problems are confined to short

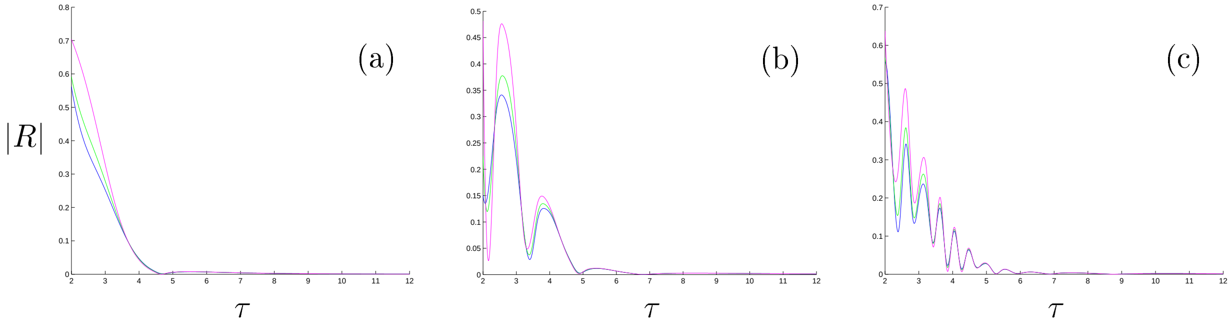

Figure 7.6: The convergence of the MMA to the modulus of the reflected amplitude as a function of wave period. The ice floe is of uniform thickness $D = 0.1$m and a zero draught, over a flat bed $h = 20$m, with length (a) $l = 10$m, (b) $l = 30$m and (c) $l = 100$m. The dimensions of the approximations are $N = 0$ (blue curves), $N = 2$ (green) and $N = 14$ (magenta).

incident waves. A feature of these finite floes, not seen in the semi-infinite ice sheet, is the existence of fine structure in the far-field response. This is attributed to interactions between the two sources of scattering - the ice edges - and is dependent on the length of the floe relative to that of the incident wave, so that it is a feature that is more prevalent for longer floes.

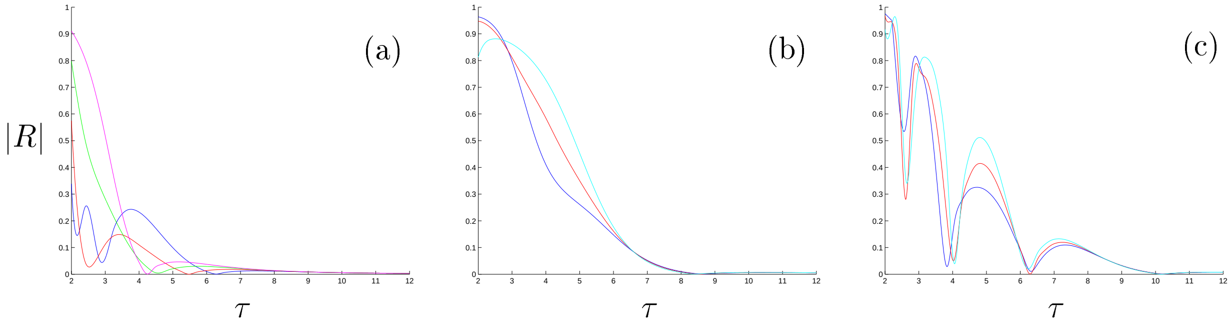

Figure 7.7: As in figure 7.6 but for ice thickness $D = 0.5$m. The dimensions of the approximations are $N = 0$ (blue curves), $N = 1$ (red), $N = 4$ (green), $N = 12$ (cyan) and $N = 14$ (magenta).

A shorter floe length is seen to exacerbate any convergence difficulties experienced by the MMA. This is attributed to interactions of the evanescent waves generated by the scattering at each ice edge. As these evanescent waves are only significant locally to the scattering source, interactions between scatterers are only possible if the floe length is relatively small. Above a certain distance the only non-trivial motion under the ice, away from the edges, is that of the propagating waves. It is therefore unsurprising to find that, for example, with an ice thickness of 1m, $\epsilon_1 \approx 5.8 \times 10^{-1}$ when $l = 10$m compared to $\epsilon_1 \approx 2.0 \times 10^{-1}$ when $l = 100$m. The importance of the floe length in this issue is actually somewhat understated in these relative values due to the shorter floe going 'unnoticed' by the incident wave at a far smaller wave period than the longer floe. Specifically, for the ice floe of a 1m thickness, the reflected amplitude is approximately zero from around 9secs onwards when the floe is of a 10m length. Whereas, for the floe of an 100m length, the reflected amplitude remains significant throughout the given interval of wave periods. In addition to the conclusion of §5 that increased thickness of the ice edge adversely affects the accuracy of low-dimensional approximations, we may therefore add that, for a finite floe, at short floe lengths, the distance between the edges is inversely proportional to the accuracy of low-dimensional MMAs but that beyond a certain point this relationship no longer applies.

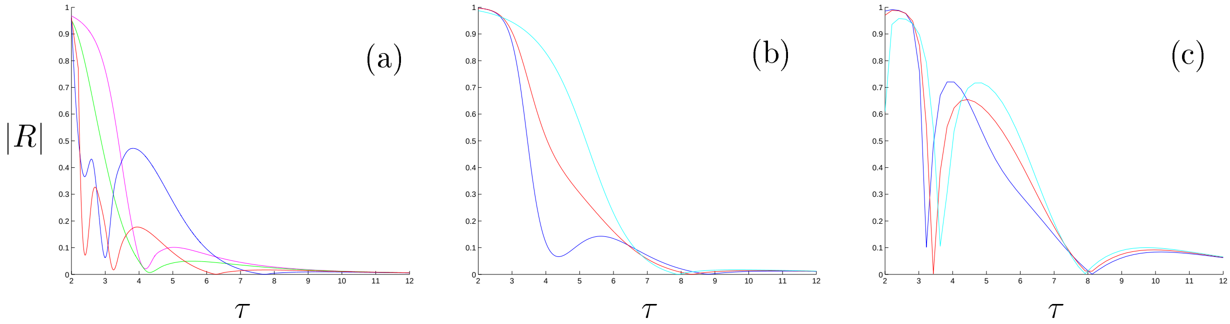

Figure 7.8: As in figure 7.6 but with ice thickness $D = 1$m. The dimensions of the approximations are $N = 0$ (blue curves), $N = 1$ (red), $N = 4$ (green), $N = 11$ (cyan) and $N = 14$ (magenta).

7.4 Sinusoidal variations

In this section we study the complete problem formulated in §4.3.2, for which the geometrical surfaces are permitted to undulate in the finite interval occupied by the ice floe. The addition of variations to the ice thickness and bed shape creates an extra source of scattering and we are concerned with how this influences the problem.

As with our investigations of continuous ice-cover in §6.4, we will be content to work with sinusoidal variations of the form

$$A_{2a} \sin^2\left(\frac{\pi x}{l}\right), \tag{7.3}$$

where A_{2a} is the amplitude of the protrusion. As a simplifying measure for this section, the floe is assumed to have no submergence at its edges. That is, we set $d = 0$ at $x = 0, l$.

In figures 7.9-7.12 we consider the addition of sinusoidal variations (7.3) to an ice floe of thickness $D_0 = 1$m and lengths $l = 10$m and 50m over a bed of depth $h_0 = 20$m. Specifically, we are again interested in comparing the results given by a keel against an equivalent sail with a bed protrusion, all of amplitude $A_{2a} = 1$m. The 1m ice edge

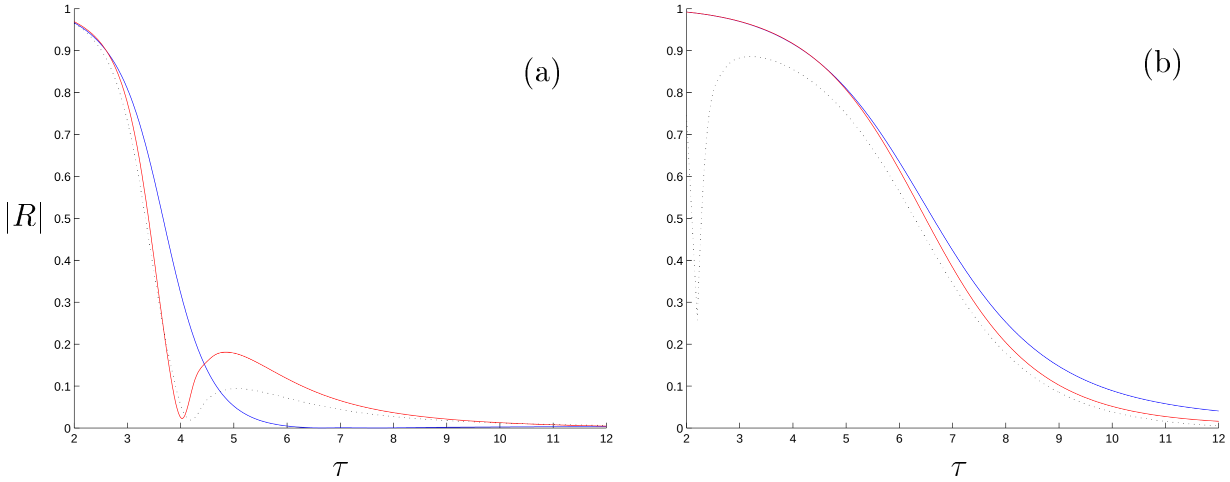

Figure 7.9: Moduli of reflected amplitudes as functions of wave period for geometries that include variations. The floes are of length (a) $l = 10$m and (b) $l = 50$m. The variations are defined by equation (6.2a) with amplitude $A_{2a} = 1$m, and take the form of a keel (blue curves), and a sail with a bed protrusion (red). In all cases, the ice thickness $D_0 = 1$m, the edge submergence of the floe is zero, and the bed depth is 20m. The result from the corresponding uniform floe is also shown (black dotted). The dimension of the approximations is (a) $N = 11$ and (b) $N = 6$.

thickness provides a stronger source of scattering than that of the 10cm ice edge used in figures 7.3-7.5 and is hence a better test of the approximation to the partial ice-cover problem.

Figure 7.9 plots approximations to the reflected amplitude as a function of incident wave period, over the interval $\tau \in (2, 12)$secs, for the two geometrical constructions described and also includes the corresponding piecewise uniform problem ($A_{2a} = 0$). Approximations to $|\eta|$, at the three incident wave periods $\tau = 2$secs, 5.06secs and 12secs, are given in figures 7.10-7.12. All approximations are converged so that $\epsilon_N < 10^{-2}$.

For the floe of length $l = 10$m, a far greater effect is caused by the addition of the keel than the sail with a bed protrusion. Thus, the energy reflected by the keel behaves quantitatively differently to that reflected by the uniform floe, whereas the effect of introducing the sail with a bed protrusion is mainly quantitative.

In figure 7.10(a) it can be seen that the approximations for the three geometries to the reduced displacement at $\tau = 2$secs virtually overlap one another. From figure 7.9(a), we also note that the reflected amplitudes coalesce as $\tau \to 2$secs. We therefore infer that at shorter wavelengths the effect of the ice edge scattering is dominant. It is again noted that, in the short wave limit, the energy carried by the incident wave is almost entirely reflected and hence the magnitude of the displacement experienced by the floe diminishes.

Considering the opposing limit, $\tau \to 12$secs, as expected, in all three instances the reflected amplitudes decay to $|R| \approx 0$. The corresponding ice displacements seen in figure

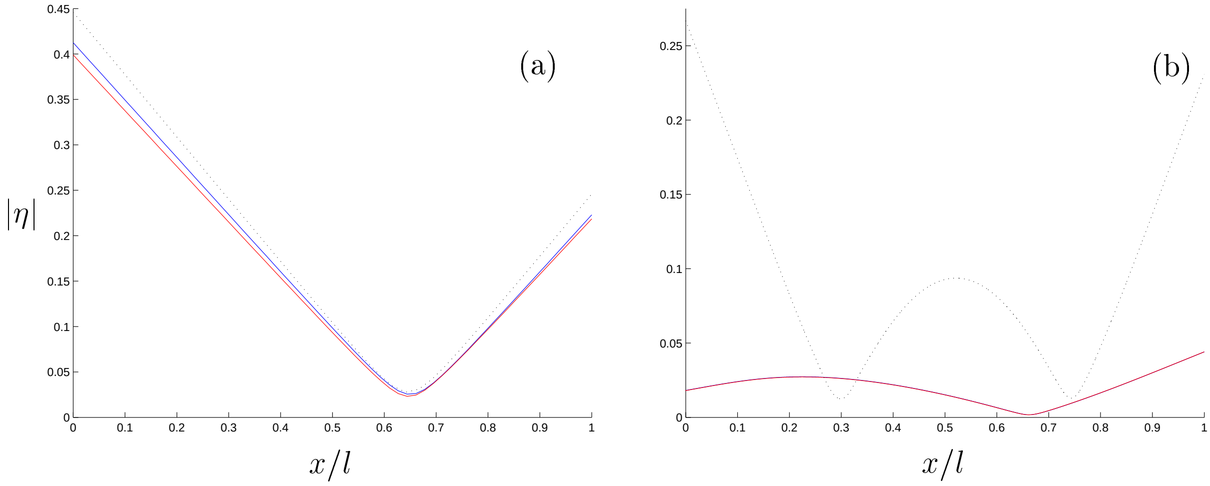

Figure 7.10: Moduli of the reduced displacements of the floes used in figure 7.9, for a wave period $\tau = 2$secs. The floes are of length (a) $l = 10$m and (b) $l = 50$m. The approximations are of dimension $N = 11$.

7.12(a) display trivial flexure, so that the floe merely rests on the incident wave. It is clear that the incident wavelength is such that the scattering by both the ice edges and the geometrical variations is negligible.

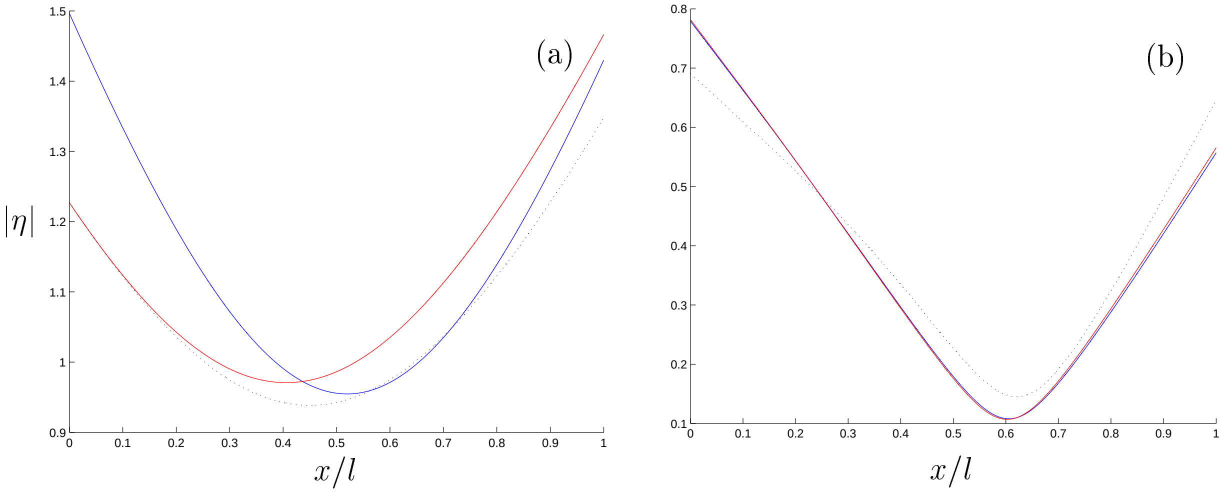

Figure 7.11: As in figure 7.10 but with wave period $\tau \approx 5.06$secs. The approximations are of dimension (a) $N = 11$ and (b) $N = 5$.

Between these two limits there is an interval in which both sources of scattering are distinguishable. In figure 7.9(a), this interval is approximately $\tau \in (4, 8)$secs, although this can be extended to $\tau \in (3, 10)$secs, if we consider the addition of the keel only. This issue is further evident in the approximations of the reduced displacement shown in figure 7.11(a). The observation that a geometrical obstruction has its greatest influence for a middle range of incident wavelengths is consistent with the findings of §6 for complete ice-cover.

In parts (b) of figures 7.9-7.12, we see that the keel and sail with bed protrusion variations agree far more closely for the floe of length $l = 50$m than the $l = 10$m case just studied. As with complete ice-cover, this is due to the diminishing importance of the position of the interfaces relative to that of the vertical scales, which are shared by these geometrical configurations, as l is increased.

As $\tau \to 12$secs, we again note the results for the three geometrical configurations tending towards each other, with $|R| \to 0$ shown in figure 7.9(b) and little displacement shown in 7.12(b). However, it is clear that these effects are weaker for the longer floe. This is clearly a property of the relative length of the 50m floe to the incident wave as opposed to the 10m floe.

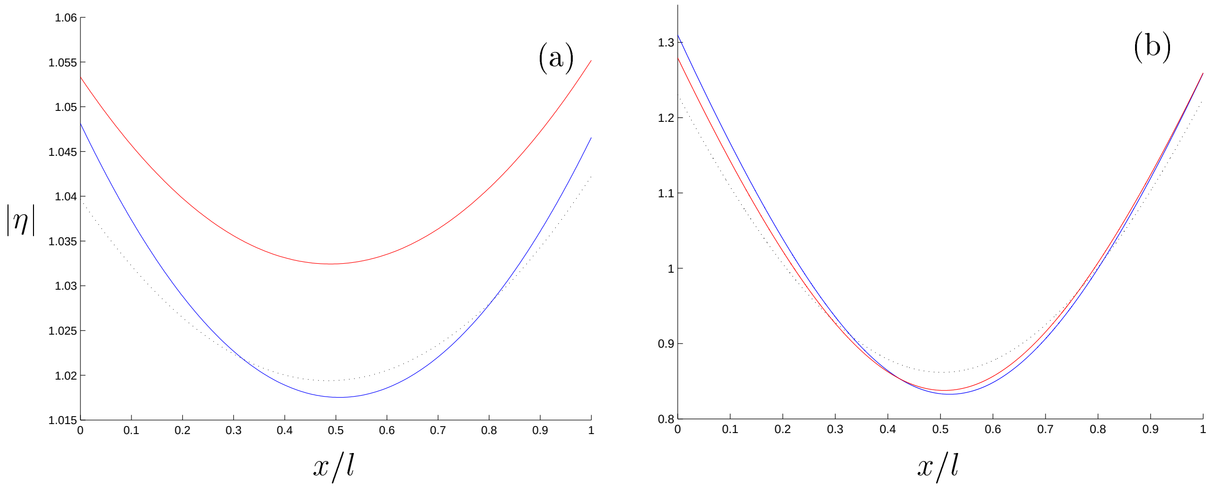

Figure 7.12: As in figure 7.10 but with wave period $\tau = 12$secs. The approximations are of dimension (a) $N = 11$ and (b) $N = 5$.

Unlike the floes of 10m length, as the wave period decreases to 2secs, the behaviour of the geometrically varying problems is markedly different to that of the piecewise uniform problem both in terms of the reflected amplitude, shown in figure 7.9(b), and ice displacement, shown in figure 7.10(b). Around the wave period of 2secs we see the beginnings of fine structure, which was observed earlier in §7.3, in the reflected amplitude produced by the uniform floe. The presence of a keel or a sail with a bed protrusion completely eliminates the minimum experienced by the uniform floe in this case. As the uniform floe reflects relatively little of the incident wave around this sharp dip in the reflected amplitude, we expect more energy to be transferred into the ice floe. This is confirmed by the displacement functions given in figure 7.10(b), where we see that the uniform floe has a displacement which is of a magnitude that is significantly greater than that of the varying floes.

In §10, the question of locally disproportionate responses in the ice displacement is explored in the context of a fully three-dimensional ice floe. It will be seen that such behaviour is more prevalent for larger floes and this is reflected in these two-dimensional results.

We may question why the connection between geometrical configurations that share the same vertical structure (D and H) is weaker in cases of partial ice-cover than for continuous ice-cover. That is, why do we observe, over an interval of wave periods corresponding to $\lambda^{(0)} = 2\pi/k_0^{(0)} \in (53.5, 160)$m, the present response of keels versus sails with bed protrusions in figure 7.9(a), when, for almost identical geometrical variations in the context of continuous ice-cover (see figures 6.9-6.11 and 6.13(a)) there is little to distinguish between the two configurations?

The investigation of §6.4, into the relationship between geometries related by their vertical structure, in the context of continuous ice-cover, was restricted to the single-mode approximation on the basis that it provides high levels of accuracy. All of the analysis that was carried out in that section also holds for cases of partial ice-cover, and we may therefore expect that single-mode approximations will display generally good agreement between keels and equivalent sails with bed protrusions for these finite floe problems. In demonstration of this, figure 7.13 displays the single-mode approximations corresponding to figures 7.9(a) and 7.11(a). The piecewise uniform configurations are disregarded as they do not form part of the current issue.

Comparing the single-mode approximations of figure 7.13 to their converged counterparts, we find that they are, evidently, not of sufficient accuracy. The single-mode approximation of the reduced displacement is deficient quantitatively and also qualitatively, in that it does not reproduce the larger modulus at the far end from the incident wave; however, it does correctly reproduce the concavity of the full linear solution. The accuracy of the single-mode approximations to the reflected amplitude is far worse. This is especially true in the middle range of incident wave periods, for which spurious extrema appear. Poor accuracy of the single-mode approximation to the reflected amplitude has been noted for the semi-infinite ice sheet problem in §5.2, and is attributed to the sensitivity of the far-field to the boundary values of the numerical solution.

It is in the process of convergence, which is achieved through the addition of evanescent modes, that the association between the two configurations is lost. The reason for this is an accumulation of interface-dependent terms, in which the problems differ, as N increases, combined with the stronger impact of the additional modes that are generated by the ice edge scattering. However, referring to figures 7.3-7.5 and 7.9(b), we note that in situations in which the floe is long and hence the gradient of the geometrical functions is small, the vertical structure of the geometry is again dominant.

A detailed analysis of factors that determine such geometrical associations, akin to that carried out for cases of continuous ice-cover in §6.4, will not be pursued here. In situations of partial ice-cover matters are obscured both by the coupling of geometrical

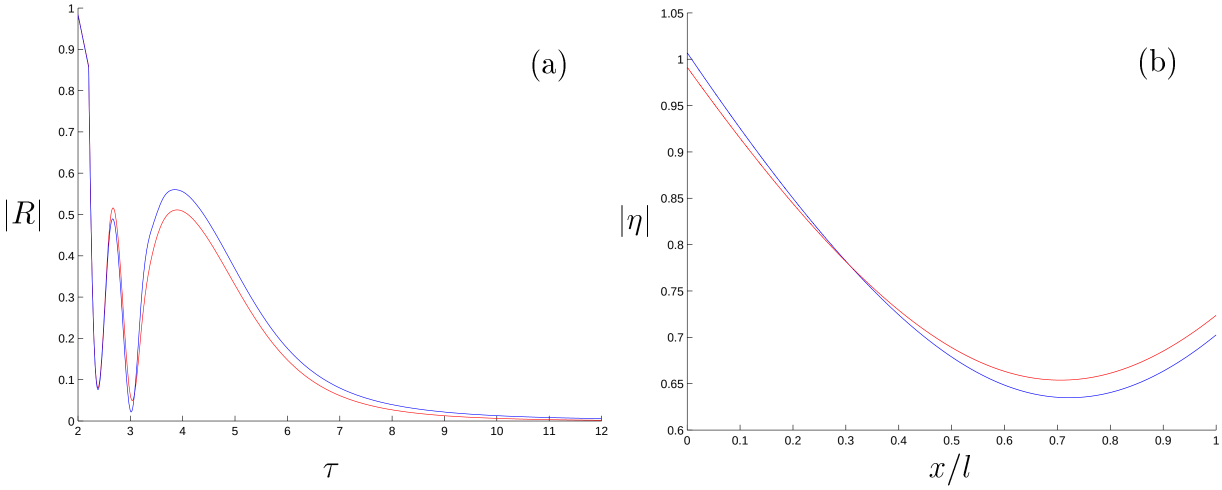

Figure 7.13: The single-mode approximations corresponding to (a) figure 7.9(a) and (b) 7.11(a).

variations to the scattering at the ice edges and by the complicated behaviour of the evanescent modes.

7.5 Archimedean draught

Thus far in our consideration of problems that involve partial ice-cover, pertaining to §5.2 as well as this chapter, the uniform floes have been restricted to a zero draught and the floes of varying thickness to zero submergence at their edges. This leads to a physically unrealistic model of the floes, as all floes will experience some submergence. Importantly, the inclusion of a non-zero draught at the edge of a floe introduces a supplementary source of scattering through the condition

$$\partial_x \phi^{(0)} = 0 \quad (-d < z < 0), \tag{7.4}$$

which applies at each ice edge. This condition ensures that there is no flow through these submerged portions (see equation (2.24b)).

A non-zero edge submergence is readily permitted in our model. The physically correct draught of an ice floe is calculated using Archimedes's principle, which here takes the form

$$\int_0^l \{\rho_i D(x) - \rho_w d(x)\} \,\mathrm{d}x = 0, \tag{7.5}$$

and, given the floe's shape, determines its buoyancy.

In this section we conduct an investigation into the effects of introducing an Archimedean draught in various circumstances.

7.5.1 Semi-infinite ice sheet

Before we consider introducing an Archimedean draught to the finite floes that have been the study of this chapter, we return to the simpler problem of the semi-infinite ice sheet of §5. By initially dealing with a single source of scattering, we are able to isolate the influence of the no flow condition (7.4) without the interference of additional influences, specifically those due to geometrical variations and floe length.

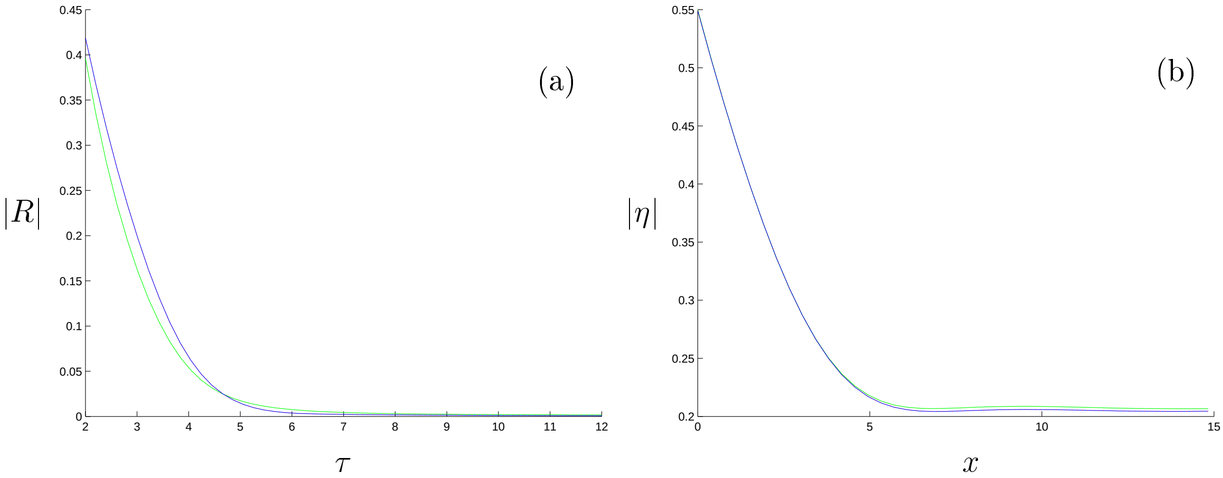

Figure 7.14: Comparison of results of a zero draught (blue curves) and the corresponding Archimedean draught (green) semi-infinite ice sheet. The ice is of thickness $D_0 = 0.1$m and the bed has the depth $h_0 = 20$m. Part (a) plots the moduli of the reflected amplitudes as functions of wave period, and part (b) plots the moduli of the reduced displacement functions, for wave period $\tau = 2$secs. The dimension of the approximations is $N = 29$. Also plotted are the results given by the altered bed depth $H_0 = h_0 - d_A$ with a zero draught (red dotted curves).

For ice of uniform thickness D_0, the Archimedean draught, $d_0 = d_A(D_0)$, is calculated from condition (7.5) to be

$$d_A(D_0) = \frac{\rho_i D_0}{\rho_w}.$$

Moving from a zero draught to an Archimedean draught both alters the wavenumber beneath the ice and the limits between which vertical integrals are calculated beneath the ice, which affect the values $a_{j,i}$ and $v_{j,i}$ $(i, j = 0, \ldots, N)$ given in equations (3.20) and (3.21) respectively.

We also consider a third geometrical configuration, in which the bed depth is replaced by $h_0 - d_A$ and a zero draught is again imposed. This will allow us to judge the influence of the change in bed depth caused by the introduction of a non-zero draught in separation from condition (7.4). Having a bed depth of $h_0 - d_A$ and a zero draught differs from having a bed depth of h_0 and a draught of d_A due to the free-surface wavenumbers, $k_i^{(0)}$ $(i = 0, \ldots, N)$, and the limits of vertical integration used to calculate the $a_{j,i}^{(0)}$ $(i, j = 0, \ldots, N)$, which is defined in equation (3.20).

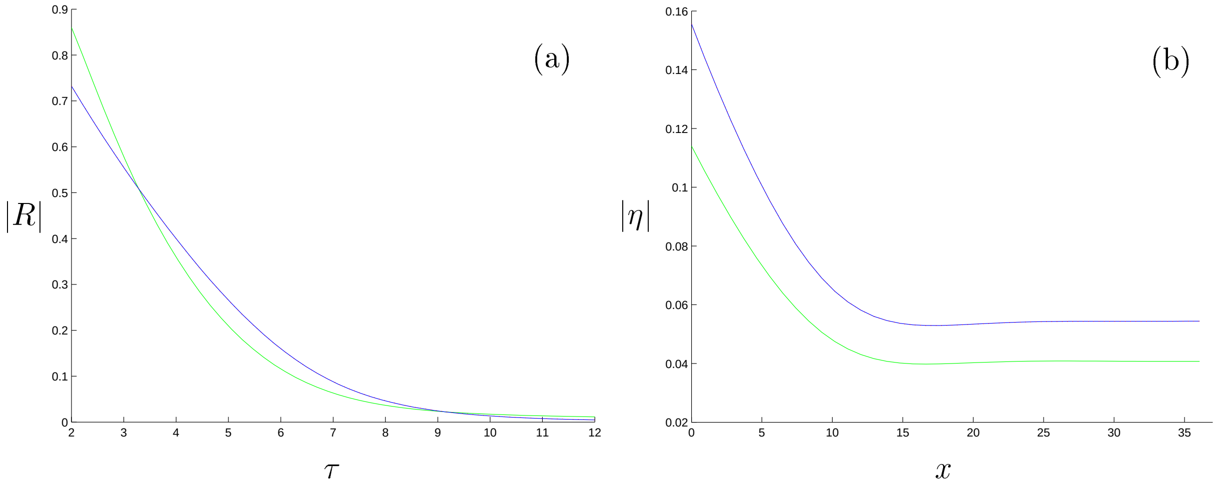

Figure 7.15: As in figure 7.14 but with $D_0 = 0.5$m. The dimension of the approximations is (a) $N = 14$ and (b) $N = 20$.

Figures 7.14-7.16 plot sufficiently converged MMAs to the reflected amplitude, $|R|$, over the interval $\tau \in (2, 12)$secs, and the modulus of the reduced displacement, $|\eta|$, at $\tau = 2$secs, for the three geometrical variations described. The incident wave again originates in the ice-free far-field, and we consider the three ice thicknesses $D_0 = 0.1$m, 0.5m and 1m.

As may be anticipated, the differences between the problems increase as the ice becomes thicker. This is particularly evident in the displacement of the ice, for which the zero draught and Archimedean draught geometries are approximately 6.8×10^{-3} apart when $D_0 = 0.1$m and 6.1×10^{-1} when $D_0 = 1$m. There appears to be a tendency for the magnitude of the displacement to be greater for ice sheets of a zero draught and this will be analysed presently. Intuitively, it is interpreted as additional reflection of the incident wave by condition (7.4).

Between figures 7.14-7.16, the ice sheet becomes thicker and qualitative differences in $|R|$ become visible between the zero draught and Archimedean draught problems. These are apparent for much of the incident wavelength interval when $D_0 = 0.5$m and 1m but do die out as the wavelengths increase.

The altered bed depth and original zero draught problems give virtually identical results, with their greatest deviation being $\mathrm{O}(10^{-3})$ when $D_0 = 1$m, which makes the red dotted curves for the altered bed depth problem difficult to identify. This implies that it is the introduction of condition (7.4) that is responsible for the transformation in results caused by the addition of an Archimedean draught, rather than the change in fluid depth.

Although throughout figures 7.14-7.16 the approximations are plotted as converged at the same dimensions for the zero draught and Archimedean draught problems, we note

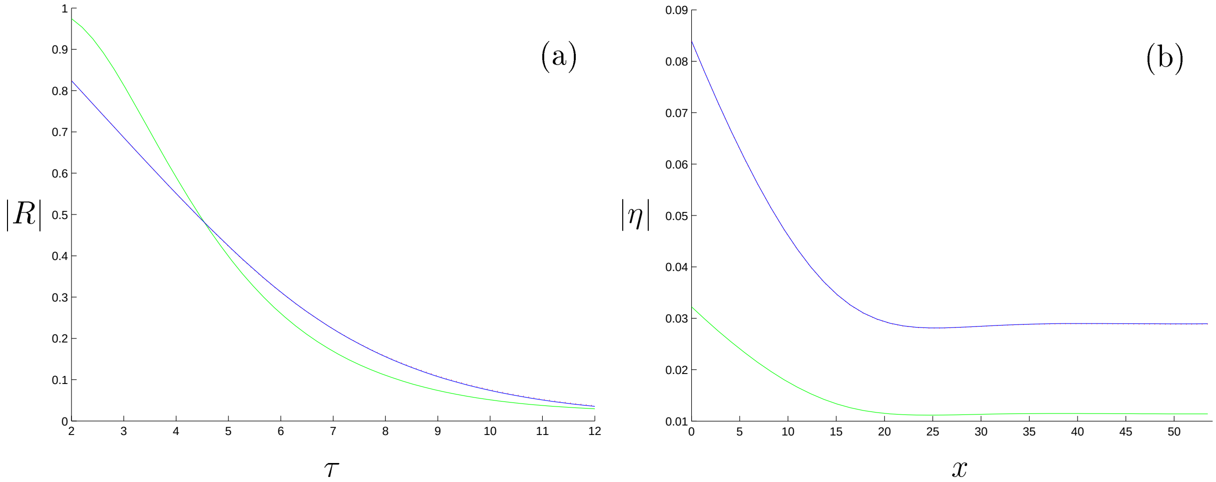

Figure 7.16: As in figure 7.14 but with $D_0 = 1$m. The dimension of the approximations is (a) $N = 13$ and (b) $N = 14$.

that the convergence rate of the latter is marginally slower than that of the former. In the most extreme case here, we have $\epsilon_N = \mathrm{O}(10^{-1})$ for the zero draught problem and $\epsilon_N = \mathrm{O}(10^{-2})$ for the Archimedean draught problem ($N = 0, \ldots, 4$) for the approximations to $|\eta|$ when $D_0 = 0.1$m, which in this instance demonstrates that the approximations for the zero draught problem move more rapidly towards the full solution than those for the Archimedean draught problem. This trait persists for the finite ice floe problems considered in §§7.5.2-7.5.3 and is attributed to the extra scattering that must be resolved when edge submergence is present. However, for convenience we often continue to plot approximations of the same converged dimension.

Single-mode approximation: short waves

It has been noted that, for 2sec incident waves, there is a tendency for the ice sheet to be displaced to a lesser extent when an Archimedean draught is included. This tendency is relative to the thickness of the ice, so that a greater reduction in the displacement is produced for thicker ice. Let us examine this phenomenon further.

In order to conduct an analysis of the displacement function, we will restrict ourselves to the single-mode approximation. Although the single-mode approximation contains inaccuracies in the magnitude of the displacement, particularly at the ice edge, it has, nevertheless, been proven to contain the key feature of the displacement. Without loss of generality, we suppose that $\varpi_0 = 1$ and that there is a single normally incident wave propagating from the ice-free far-field.

Referring to equations (5.5)-(5.6), the approximate displacement is given by

$$\chi(x) = \left\{ \mathrm{e}^{\mathrm{i}k_0 x} + \sum_{j=1,2} \hat{\gamma}_j \, \mathrm{e}^{\mathrm{i}\mu_{0,(j)}x} \right\} \hat{B}_0,$$

where

$$\hat{B}_0 = \kappa^{-1} k_0 \sinh(k_0 H) B_0, \quad \hat{\gamma}_j = \frac{k_0^2(k_0 - \mu_{0,(j_-)})}{\mu_{0,(j)}^2(\mu_{0,(j)} - \mu_{0,(j_-)})}. \tag{7.6}$$

Recall that $j_- = (3 - (-1)^j)/2$ $(j = 1, 2)$. For the remainder of this section we shall endow quantities with a subscript A if they relate to the Archimedean draught problem, for example $H_A \equiv H_0$, $k_A \equiv k_0$ and $\hat{B}_A \equiv \hat{B}_0$. Quantities that retain the zero subscript will refer to the zero draught problem.

Let us suppose that the limits $k_0 H_0 \ll \sinh(k_0 H_0)$ and $k_A H_A \ll \sinh(k_A H_A)$ hold, which is the case for most of the geometrical parameters in which we are interested. We therefore have $\tanh(k_A H_A) \approx \tanh(k_0 H_0) \approx 1$ and consequently

$$(1 - \kappa\alpha + \beta k_0)k_0 \approx \kappa, \; (1 - \kappa\alpha + \beta k_A)k_A \approx \kappa,$$

from which $k_A \approx k_0$ follows and then also $\mu_{A,(j)} \approx \mu_{0,(j)}$ $(j = 1, 2)$. This implies that $\widetilde{\chi}_0 \approx \widetilde{\chi}_A$, where

$$\widetilde{\chi}_0 = \frac{\chi}{\hat{B}_0}, \quad \widetilde{\chi}_A = \frac{\chi_A}{\hat{B}_A},$$

and we deduce that the respective magnitudes of the displacements are controlled by the values $\hat{B}_0$ and $\hat{B}_A$.

Similarly, take the functions

$$\varphi_0 = \left\{ \mathrm{e}^{\mathrm{i}k_0 x} + \sum_{j=1,2} \hat{\upsilon}_j \mathrm{e}^{\mathrm{i}\mu_{0,(j)}x} \right\} B_0, \quad \varphi_A = \left\{ \mathrm{e}^{\mathrm{i}k_A x} + \sum_{j=1,2} \hat{\upsilon}_j \mathrm{e}^{\mathrm{i}\mu_{A,(j)}x} \right\} B_A,$$

where

$$\hat{\upsilon}_j = \frac{k_0^3(k_0 - \mu_{0,(j_-)}) \sinh(k_0 H)}{\mu_{0,(j)}^3(\mu_{0,(j)} - \mu_{0,(j_-)}) \sinh(\mu_{0,(j)})},$$

or

$$\hat{\upsilon}_j = \frac{k_A^3(k_A - \mu_{A,j_-}) \sinh(k_A H)}{\mu_{A,(j)}^3(\mu_{A,(j)} - \mu_{A,(j_-)}) \sinh(\mu_{A,(j)})},$$

according to its context. We find that $\widetilde{\varphi}_0 \approx \widetilde{\varphi}_A$, where

$$\widetilde{\varphi}_0 = \frac{\varphi_0}{B_0}, \quad \widetilde{\varphi}_A = \frac{\varphi_A}{B_A},$$

and it can be shown that

$$\partial_x\varphi_0(0)=\mathrm{O}(k_0)\varphi_0(0)\quad \partial_x\varphi_A(0)=\mathrm{O}(k_A)\varphi_A(0).$$

For both problems, the unknown amplitudes B_0 and B_A are found from application of the jump conditions (5.7a-b), in the form

$$\left\{\frac{a}{a^{(0)}}\frac{v^{(0)}}{v}\partial_x\widetilde{\varphi}_0(0)+\mathrm{i}k_0^{(0)}\frac{v}{v^{(0)}}\widetilde{\varphi}_0(0)\right\}\hat{B}_0=2\mathrm{i}k_0^{(0)}\frac{k_0\sinh(k_0H_0)}{k_0^{(0)}\sinh(k_0^{(0)}H_0)}, \tag{7.7a}$$

and

$$\left\{\frac{a_A}{a^{(0)}}\frac{v_A^{(0)}}{v_A}\partial_x\widetilde{\varphi}_A(0)+\mathrm{i}k_0^{(0)}\frac{v_A}{v_A^{(0)}}\widetilde{\varphi}_A(0)\right\}\hat{B}_A=2\mathrm{i}k_0^{(0)}\frac{k_A\sinh(k_AH_A)}{k_0^{(0)}\sinh(k_0^{(0)}h)}, \tag{7.7b}$$

in which $a=a_{0,0}$, $v=v_{0,0}$, $a^{(0)}=a_{0,0}^{(0)}$, $v^{(0)}=v_{0,0}^{(0)}$ and the A-subscripted versions are calculated from the Archimedean draught problem. By explicitly evaluating these coefficients, and using $\sinh(k_0H_0)\gg k_0H_0$ and $\sinh(k_AH_A)\gg k_AH_A$ we find that

$$\frac{a}{a^{(0)}}\frac{v^{(0)}}{v}\approx\frac{2k_0^{(0)}}{k_0+k_0^{(0)}}\left\{\frac{\sinh(k_0H_0)}{\sinh(k_0^{(0)}H_0)}\right\},\quad \frac{a_A}{a^{(0)}}\frac{v_A^{(0)}}{v_A}\approx\frac{2k_0^{(0)}}{k_0+k_0^{(0)}}\left\{\frac{\sinh(k_0^{(0)}H_A)\sinh(k_AH_A)}{\sinh^2(k_0^{(0)}h_0)}\right\}, \tag{7.8a}$$

and

$$\frac{v}{v^{(0)}}\approx\frac{k_0+k_0^{(0)}}{2k_0}\left\{\frac{\sinh(k_0H_0)}{\sinh(k_0^{(0)}H_0)}\right\},\quad \frac{v_A}{v_A^{(0)}}\approx\frac{k_A+k_0^{(0)}}{2k_A}\left\{\frac{\sinh(k_AH_A)}{\sinh(k_0^{(0)}H_A)}\right\}. \tag{7.8b}$$

The terms that differ strongly between the zero draught and Archimedean draught problems are bracketed $\{\cdot\}$. Taking these bracketed terms, we have for most situations that

$$\frac{\sinh(k_0H_0)}{\sinh(k_0^{(0)}H_0)}<\frac{\sinh(k_AH_A)}{\sinh(k_0^{(0)}H_A)}, \tag{7.9a}$$

and

$$\frac{\sinh(k_0^{(0)}H_A)\sinh(k_AH_A)}{\sinh^2(k_0^{(0)}h)}<\frac{\sinh(k_0H_0)}{\sinh(k_0^{(0)}h)}. \tag{7.9b}$$

Unfortunately, straightforward application of inequalities (7.9a-b) to (7.8a-b) gives no indication of the tendency for change in magnitude of the amplitudes in question, as we switch between a zero draught and an Archimedean draught. However, for relatively short incident waves $k_0^{(0)}\gg k_0\approx k_A$ (see §3.2.2) and consequently

$$k_0^{(0)}\frac{k_0+k_0^{(0)}}{2k_0}\gg k_0\frac{2k_0^{(0)}}{k_0+k_0^{(0)}},\quad k_0^{(0)}\frac{k_A+k_0^{(0)}}{2k_A}\gg k_A\frac{2k_0^{(0)}}{k_A+k_0^{(0)}} \tag{7.10}$$

from which we deduce that

$$\frac{a}{a^{(0)}}\frac{v^{(0)}}{v}\partial_x\widetilde{\varphi}_0(0)+\mathrm{i}k_0^{(0)}\frac{v}{v^{(0)}}\widetilde{\varphi}_0(0)\approx\mathrm{i}k_0^{(0)}\frac{v}{v^{(0)}}\widetilde{\varphi}_0(0)\quad(k_0^{(0)}\gg k_0),\tag{7.11a}$$

and

$$\frac{a_A}{a^{(0)}}\frac{v_A^{(0)}}{v_A}\partial_x\widetilde{\varphi}_A(0)+\mathrm{i}k_0^{(0)}\frac{v_A}{v_A^{(0)}}\widetilde{\varphi}_A(0)\approx\mathrm{i}k_0^{(0)}\frac{v_A}{v_A^{(0)}}\widetilde{\varphi}_A(0)\quad(k_0^{(0)}\gg k_A).\tag{7.11b}$$

The validity of the inequalities given in equation (7.10) and the approximations (7.11a-b) is shown graphically in figure 7.17. This is done for the same three ice thicknesses, $D_0 = 0.1$m 0.5m and 1m, which have been used previously.

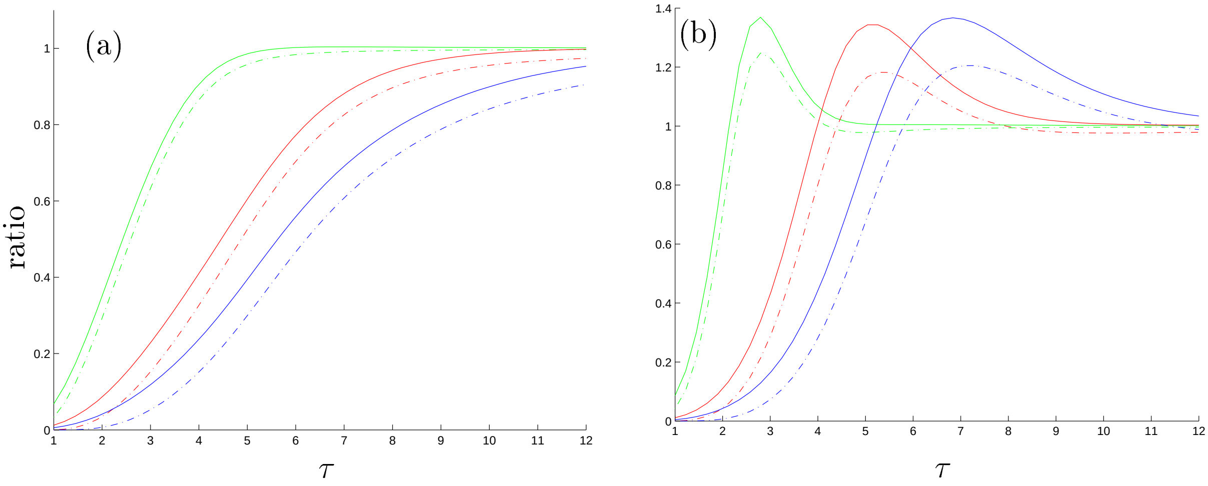

Figure 7.17: Graphical representations of the inequalities given in equation (7.10) and the approximations given in equations (7.11a-b), which hold in the small wave period régime. Part (a) plots the ratio of the coefficients of the non-derivative to the derivative parts of the jump conditions (7.7a-b). Part (b) plots the ratio of the non-derivative to the derivative terms on the left-hand side of the jump conditions (7.7a-b). The ice is of thickness $D_0 = 0.1$m (green curves), $D_0 = 0.5$m (red) and $D_0 = 1$m (blue). Ratios are given for the zero draught problem (solid curves) and the Archimedean draught problem (dot-dash).

Applying approximations (7.11a-b), in conjunction with (7.8b), to equations (7.7a-b) gives, respectively,

$$\hat{B}_0\approx 4\left(\frac{k_0}{k_0^{(0)}}\right)^2\left(\frac{\varphi_0(0)}{B_0}\right)^{-1}=\mathrm{O}\left(\frac{k_0}{k_0^{(0)}}\right)^2,\tag{7.12a}$$

for $k_0^{(0)} \gg k_0$, and

$$\begin{aligned} \hat{B}_A &\approx 4\frac{\sinh(k_0^{(0)}H_A)}{\sinh(k_0^{(0)}h_0)}\left(\frac{k_A}{k_0^{(0)}}\right)^2\left(\frac{\varphi_A(0)}{B_A}\right)^{-1} \\ &= \mathrm{O}\left(\left(\frac{k_A}{k_0^{(0)}}\right)^2\frac{\sinh(k_0^{(0)}H_A)}{\sinh(k_0^{(0)}h_0)}\right) \end{aligned} \tag{7.12b}$$

for $k_0^{(0)} \gg k_A$. The accuracy of the approximations given in (7.12a-b) are shown graphically in figure 7.18(a) for the three ice thicknesses $D_0 = 0.1$m, 0.5m and 1m.

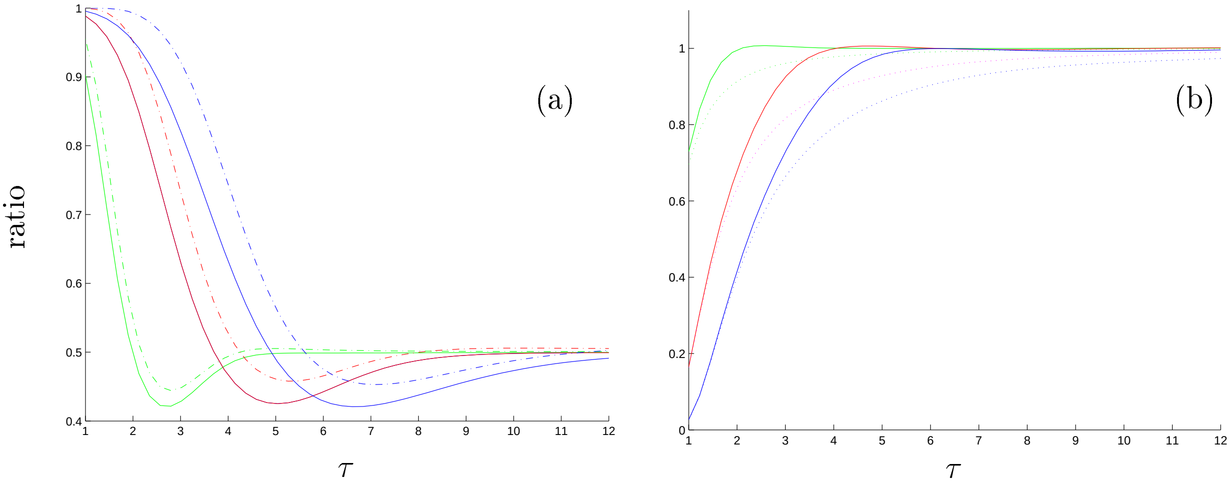

Figure 7.18: Graphical representation of the validity of approximations (7.12a-b) and the relationship (7.13) between the zero draught and Archimedean draught problems. Part (a) plots the ratio of the approximate amplitudes given in equations (7.12a-b) to the exact amplitudes, for the zero draught problem (solid lines) and the Archimedean draught problem (dot-dash). Part (b) plots the ratio of the amplitude of the Archimedean draught problem to that of the zero draught problem, for the exact amplitudes (solid curves) and the approximate amplitudes (dotted). The ice is of thickness $D_0 = 0.1$m (green curves), $D_0 = 0.5$m (red) and $D_0 = 1$m (blue).

From (7.12a-b) we deduce that, as the incident wave becomes shorter, the magnitude of the amplitude of the displacement function decreases - a feature that has been noted for problems of partial ice-cover. Furthermore, when an Archimedean draught is included, the decay of the amplitude is more rapid due to the extra term $\sinh(k_0^{(0)}H_A)\mathrm{csch}(k_0^{(0)}h)$. This is demonstrated in 7.18(b), which plots the ratio of the amplitudes, $\hat{B}_A/\hat{B}_0$, and we observe that

$$\hat{B}_A/\hat{B}_0 \to 0, \tag{7.13}$$

as $\tau \to 0$.

In figures 7.18(a-b) it is clear that the approximations that have been found and the conclusions that have been drawn, for short incident waves, are more appropriate for for

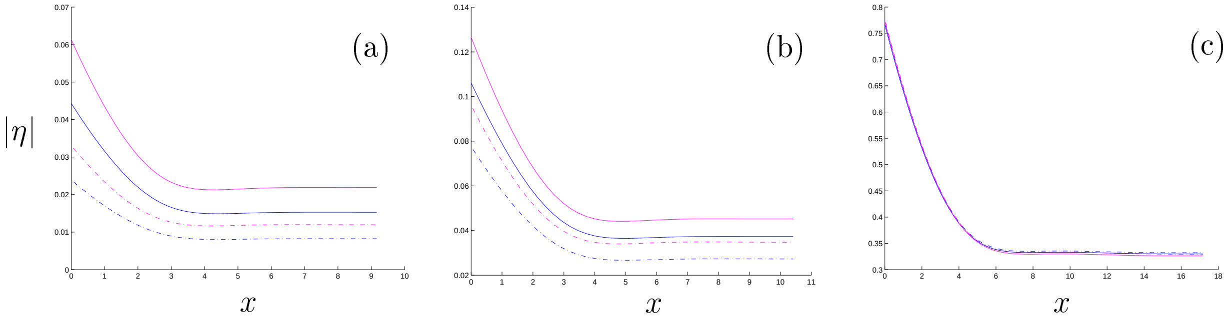

Figure 7.19: Comparison of the moduli of the reduced displacement functions of a zero draught (solid curves) and the corresponding Archimedean draught (dot-dash) semi-infinite ice sheet. Both the single-mode approximations (blue curves) and converged approximations (magenta) are given. The ice is of thickness $D_0 = 0.1$m and the bed of depth $h_0 = 20$m, with the wave period (a) $\tau = 0.75$secs, (b) $\tau = 1$sec and (c) $\tau = 2.5$secs. The dimensions of the converged approximations are (a) $N = 38$, (b) $N = 29$ and (c) $N = 4$ for the zero draught problem, and (a) $N = 44$, (b) $N = 29$ and (c) $N = 4$ for the Archimedean draught problem.

thicker ice. This is easily explained if we consider the limits, $k_0^{(0)} \gg k_0$ and $k_0^{(0)} \gg k_A$, on which our approximations are based. These inequalities are satisfied in the short wave limit; however, they take a shorter incident wave to be attained for thinner ice. Such relationships between the free-surface and ice-covered propagating wavenumbers have already been discussed in §3.2.2 and quantified in figure 5.10. Therefore, for thinner ice, the incident waves are required to be shorter in order for the reduction in displacement, which is caused by the introduction of an Archimedean draught, to take effect.

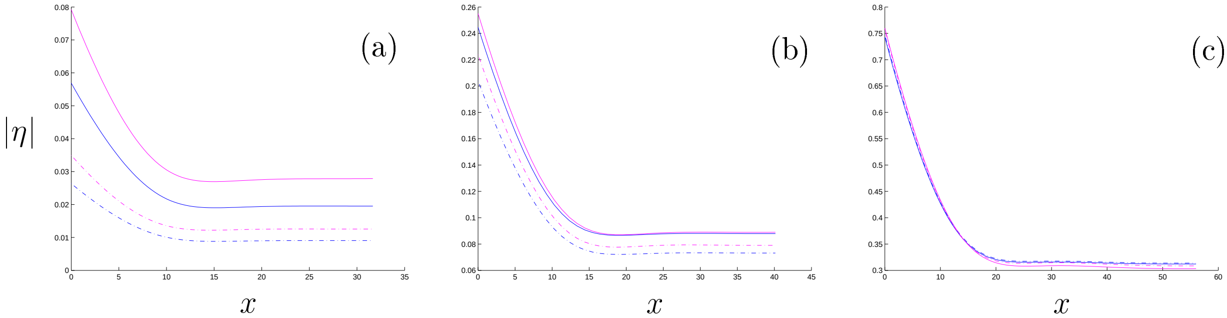

Figure 7.20: As in figure 7.19 but with ice thickness $D_0 = 0.5$m and wave period (a) $\tau = 1.5$secs, (b) $\tau = 2.5$secs and (c) $\tau = 4.5$secs. The dimensions of the converged approximations are (a) $N = 18$, (b) $N = 14$ and (c) $N = 3$ for the zero draught problem, and (a) $N = 25$, (b) $N = 24$ and (c) $N = 2$ for the Archimedean draught problem.

Figures 7.19-7.21 plot single-mode approximations to the reduced displacement for the zero draught and the Archimedean draught problems, along with the corresponding converged approximations. Three different wave periods are used in each figure, chosen at points for which the ratio of the amplitudes is $\hat{B}_A/\hat{B}_0 \approx 0.5$, 0.75 and 1. We note that, as the ice thickness increases, the wave period for which the above ratios are attained increases, which is consistent with our predictions. It is also clear that the relative properties displayed by the single-mode approximations are mirrored by the converged solutions.

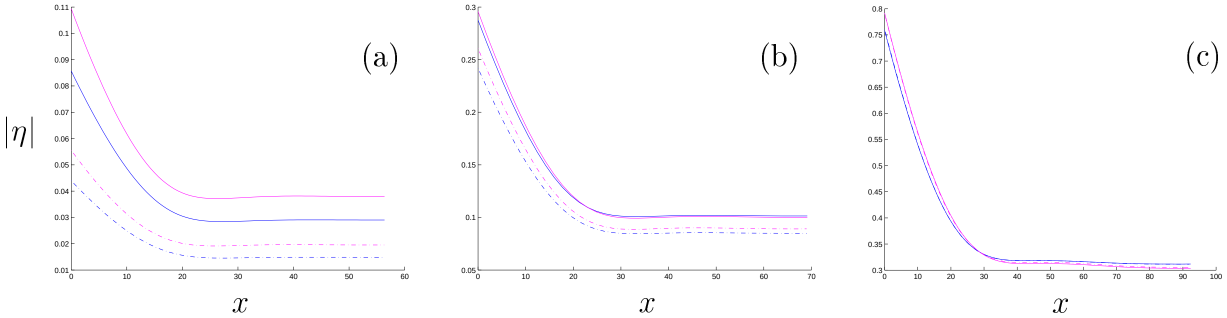

Figure 7.21: As in figure 7.19 but with ice thickness $D_0 = 1$m and wave period (a) $\tau = 2.25$secs, (b) $\tau = 3.5$secs and (c) $\tau = 6$secs. The dimensions of the converged approximations are (a) $N = 7$, (b) $N = 10$ and (c) $N = 3$ for the zero draught problem, and (a) $N = 14$, (b) $N = 16$ and (c) $N = 2$ for the Archimedean draught problem.

Single-mode approximation: long waves

It is reasonable to speculate from observation of figure 7.18 and parts (c) of figures 7.19-7.21 that, in the long wave limit, the zero draught and the Archimedean draught problems are tending towards the same solution. We may analyse this issue by similar means to those employed for short waves.

Recall that $\kappa = 4\pi^2/(g\tau^2)$. As τ increases and therefore κ decreases, we have the following approximations of the wavenumbers

$$k_0^{(0)} \approx \sqrt{\frac{\kappa}{h}}, \quad k_0 \approx \sqrt{\frac{\kappa}{H}} \quad (\tau \gg 1),$$

which therefore decay at the same rate as τ grows. In making the approximation of the wavenumber beneath the ice, k_0, we have specifically assumed that τ is large enough that $\beta k_0^4 \ll 1$. Furthermore, it can be shown that

$$\beta \mu_{0,(j)}^4 \approx -1 \quad (j = 1, 2),$$

and therefore the dimension-dependent wavenumbers, unlike the propagating wavenumbers, remain bounded as τ increases. Consequently, the coefficients, $\hat{\gamma}_j$ $(j = 1, 2)$, of the complex waves, which are defined in (7.6), decay as the wave period grows. It follows that the motion under the ice is dominated by the propagating wave. We also note that the values of the coefficients of equations (7.7a-b) approach the fluid depths over which the integrals that produce their values are calculated, so that, for example,

$$a_0 \approx H_0, \quad v_A \approx H_A, \quad a_A^{(0)} \approx h_0.$$

Using the above approximations, we are able to deduce from equations (7.7a-b) that

$$\hat{B}_0 \approx 1, \quad \hat{B}_A \approx \frac{2\sqrt{h_0}}{\sqrt{h_0} + \sqrt{H_A}}.$$

The value of $\hat{B}_A$ is, unsurprisingly, the long wave limit of the transmitted amplitude across a depth discontinuity in a free surface flow (see Lamb, 1932). Although they are extremely similar, the amplitudes of the displacements of the two problems do not, therefore, reach the same long wave limit. The amplitude of the Archimedean draught problem is marginally greater than that of its zero draught counterpart, and, as would be expected, this disparity increases for thicker ice. We attribute the slight difference in the solutions here to the change in the fluid depth. This long wave property is undetectable in figure 7.18(b) but can be verified through numerical calculations.

7.5.2 A finite uniform floe

We now return to a floe of finite length and consider the effect of introducing an Archimedean draught in this context. In this section, a uniform ice thickness is retained. The inclusion of the correct submergence, $d = d_A$, to such a floe is shown graphically in figure 7.22.

We are particularly interested in the rôle of the floe length. The findings of the previous section, concerning variations of the ice thickness, are also applicable for a finite floe. For this reason, only the thicker ice values, $D_0 = 0.5$m and 1m, are used, in order to highlight the submergence effects.

Figure 7.23 compares converged approximations to the reflected amplitude for a zero draught ($d = 0$) against an Archimedean draught ($d = d_A(D_0)$). The floes are of thickness $D_0 = 0.5$m. As with the investigation of the semi-infinite ice sheet, the addition of submergence at the ice edges is seen to be considerable here. The effects are greatest when the two sources of scattering are closest, with a relative difference of approximately 4.0×10^{-1} for $l = 10$m compared to 2.0×10^{-1} for $l = 100$m. Again, the strength of this effect is somewhat obscured in these values due to the shorter floe going 'unnoticed' by for an incident wave of a smaller wave period than the longer floe. Specifically, for $l = 10$m, we note that the minimum around $\tau = 4$secs in the zero draught problem is eliminated by the inclusion of submergence.

Converged approximations to the reduced displacement of the floe when $D_0 = 1$m, for the two types of draught, are given in figure 7.24. The incident waves are taken at either end of the intervals used for figure 7.23 and the floe lengths $l = 10$m and 50m are used. For

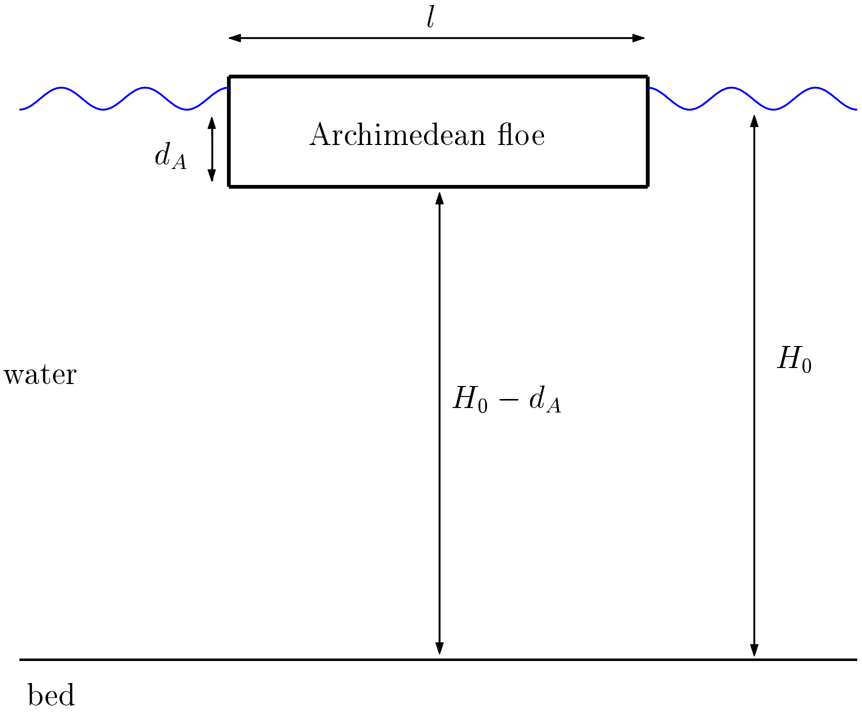

Figure 7.22: Schematic of a uniform floe with the inclusion of an Archimedean draught.

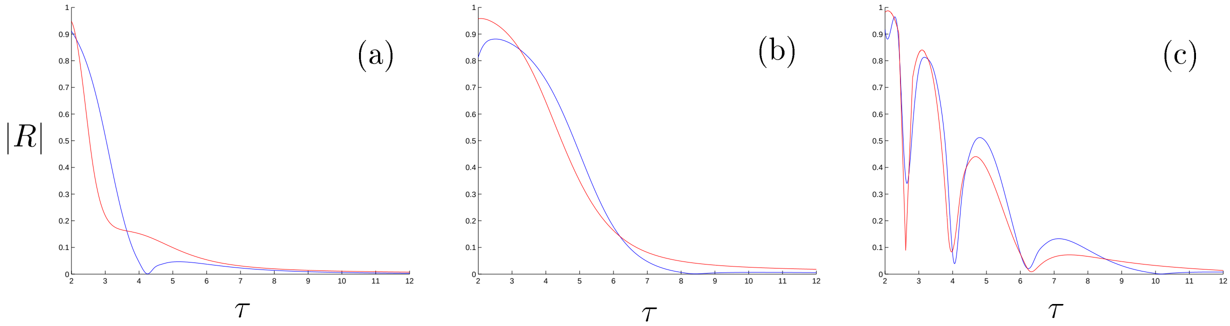

Figure 7.23: Comparison of moduli of the reflected amplitudes given by a zero draught (blue curves) and the corresponding Archimedean draught (red) uniform floe of a finite length. The ice is of thickness $D_0 = 0.5$m, with a flat bed of depth $h = 20$m. The floe length is (a) $l = 10$m, (b) $l = 30$m and (c) $l = 100$m. The dimension of the approximations is (a) $N = 14$ and (b-c) $N = 12$.

both of the 2sec incident waves the relative difference between the corresponding curves is 6×10^{-1}; for the 12sec incident waves this value reduces to 2×10^{-2} (both correct to one significant figure). Therefore, unlike the quantity $|R|$, there is no evidence to suggest that the size of the change in the oscillations of the ice, caused by the inclusion of a non-zero draught, is affected by the length of the floe. Rather, as in §7.5.1, the inclusion of an Archimedean draught causes the floe to experience less displacement at smaller wave periods but becomes trivial when the incident wave is relatively long. The former is again interpreted as the extra reflection caused by the submergence at the ice edges, and the latter is due to the insignificance of the floe to long waves.

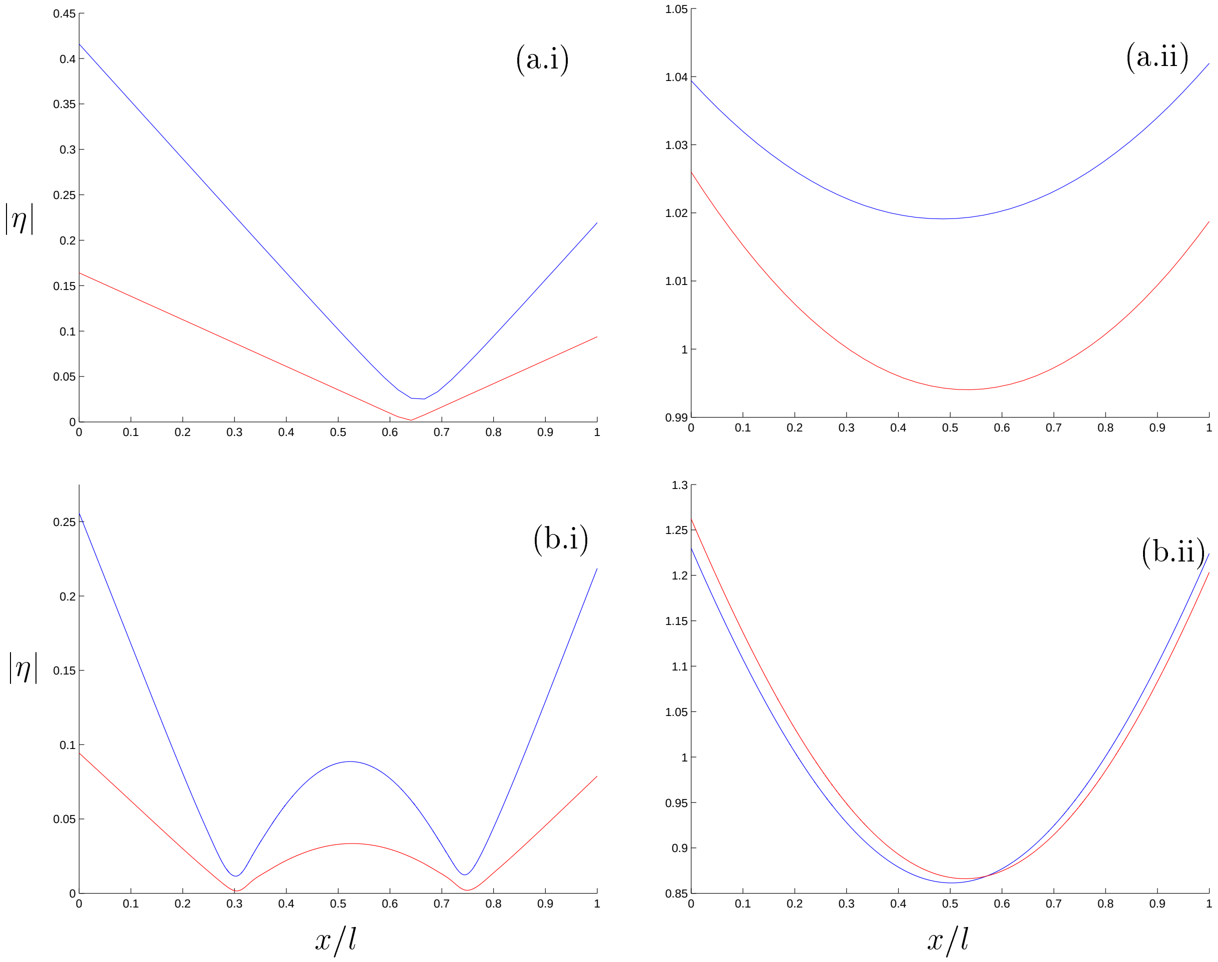

Figure 7.24: Comparison of the moduli of reduced displacement functions of a zero draught (blue curves) and the corresponding Archimedean draught (red) uniform floe of a finite length. The ice is of thickness $D = 1$m, with a flat bed of depth $h = 20$m. The floe length is (a.i-ii) $l = 10$m, and (b.i-ii) $l = 50$m. The wave period in parts (a-b.i) is $\tau = 2$secs and in parts (a-b.ii) is $\tau = 12$secs. The dimension of the approximations is (a.i) $N = 19$, (a.ii) $N = 9$, (b.i) $N = 17$ and (b.ii) $N = 4$.

7.5.3 Inclusion of trigonometric variations

In this section we study the addition of the correct physical draught to floes that include trigonometric protrusions of the form (7.3). Such trigonometric variations were considered earlier, for floes of a zero edge submergence, in §7.4 with the protrusion occurring as either a keel or a sail. Our attention in that section was in comparing the results that are produced by the respective positions of the protrusion. To accurately compare different geometrical configurations, the respective floes must obey the Archimedean draught condition (7.5). In particular, the way in which the weight of the floe is distributed will affect its buoyancy, so that, for instance, a sail will weigh the ice down more than a keel.

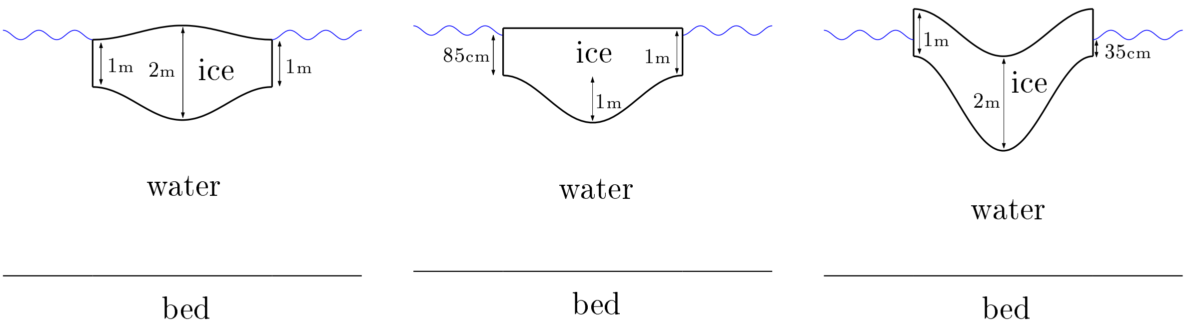

Figure 7.25: Schematics showing the submergence experienced by floes of the same thickness, D, but with different shapes in their upper and lower surfaces.

Let us suppose that the ice floe we are considering, which is of thickness

$$D_0 + A_d \sin\left(\frac{\pi x}{l}\right), \tag{7.14}$$

where A_d is the amplitide of the protrusion, has a lower surface defined by

$$d_0 + pA_d \sin\left(\frac{\pi x}{l}\right). \tag{7.15}$$

The value p denotes the proportion of the protrusion that is a keel, so that $p = 1$ is the ice floe with a keel studied in §7.4, and $p = 0$ is the corresponding ice floe with a sail (the values $d_0 = 0$ and $D_0 = A = 1$m were used earlier). We may calculate the Archimedean draught for this ice floe from (7.5) to be

$$d_0 = \frac{9}{10}D_0 + \frac{1}{2}\left(\frac{9}{10} - p\right)A_d,$$

where we have used $\rho_i = 9\rho_w/10$. Our model requires that the ice edges do not become fully submerged beneath the fluid surface, and this imposes the restriction that $d_0 \leq 1$, and therefore the proportion p must satisfy $p \geq 0.7$. Due to this restriction, we may not study the ice floe with a sail protrusion and a flat lower surface that appeared in §7.4 as it leads to the value $d_0 = 1.35$m. Instead, as well as a floe with a keel and a flat upper surface, we will investigate floes that vary in both their upper and lower surfaces, with the possibility of an indentation on the upper surface. As in §7.4 we will use the values $A = 1$m and $D_0 = 1$m. The three floes that will be used are shown in figure 7.25.

In figure 7.26 we compare the reflected amplitudes produced by floes of a zero edge submergence with the corresponding floes of an Archimedean draught over an interval of incident wave periods. Results for the two configurations shown in figure 7.25 that produce the largest draught are displayed. These are $p = 0.7$ which gives $d_0 = 1$m so that the entire ice edge is submerged, and $p = 1$, the floe with a keel that was studied when a zero edge submergence was maintained in §7.4, which gives an 85cm edge submergence.

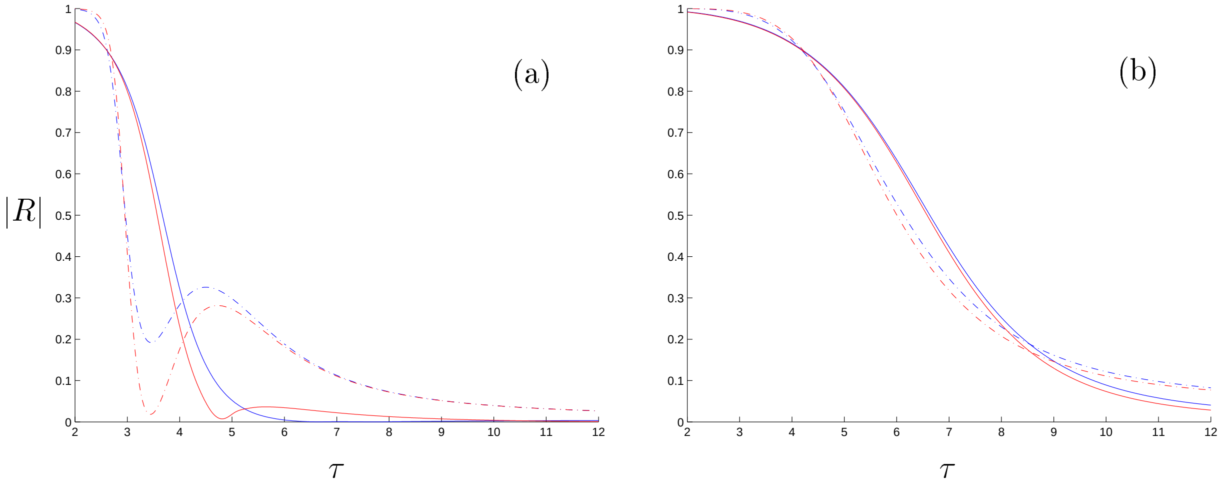

Figure 7.26: Comparison of the moduli of the reflected amplitudes given by a floe with zero edge submergence (solid curves) and the corresponding floe with an Archimedean submergence (dot-dash). The floes have varying thickness, as defined in equation (7.14), with $D_0 = 1$m and $A = 1$m over a flat bed of depth 20m. The lower surface of the floes is defined by equation (7.15) with keel proportion $p = 1$ (blue curves) and $p = 0.7$ (red). The floes are of length (a) $l = 10$m and (b) $l = 50$m. The dimension of the approximations is (a) $N = 11$ and (b) $N = 6$.

The two floe lengths $l = 10$m and 50m are used.

For floes of a 10m length the inclusion of an Archimedean draught has a significant effect on the reflected amplitude. Prominent in figure 7.26(a) is that the reflected amplitude decays far more slowly as the incident period becomes larger when the floes have an edge submergence, and we see that, unlike the floes that lack a realistic draught, at $\tau = 12$secs a non-trivial amount of reflection is caused by the Archimedean floes. For shorter incident waves the addition of submergence creates qualitative differences in $|R|$, with a pronounced maximum and minimum seen in the response of both floes. The change in the reflection is marginally larger for the floe with the greater submergence, $p = 0.7$, with the normalised difference 7.2×10^{-1} for this floe compared to 6.8×10^{-1} for the $p = 1$ floe.

In comparison, the effect that the introduction of an Archimedean draught has on the reflected amplitude is small for the two floes when their length is 50m, which is shown in figure 7.26(b). Although clear changes in the reflection coefficient are produced here when the Archimedean draught is included, both curves only move $\mathrm{O}(10^{-2})$ and no new qualitative properties are created. As before, the difference in the results for the two different floes are increased when the correct edge submergence is included, particularly around the middle range of wave periods, but this is only marginal and the reflection coefficients remain extremely similar.

The effect on the displacement of the floe caused by the change from a zero edge

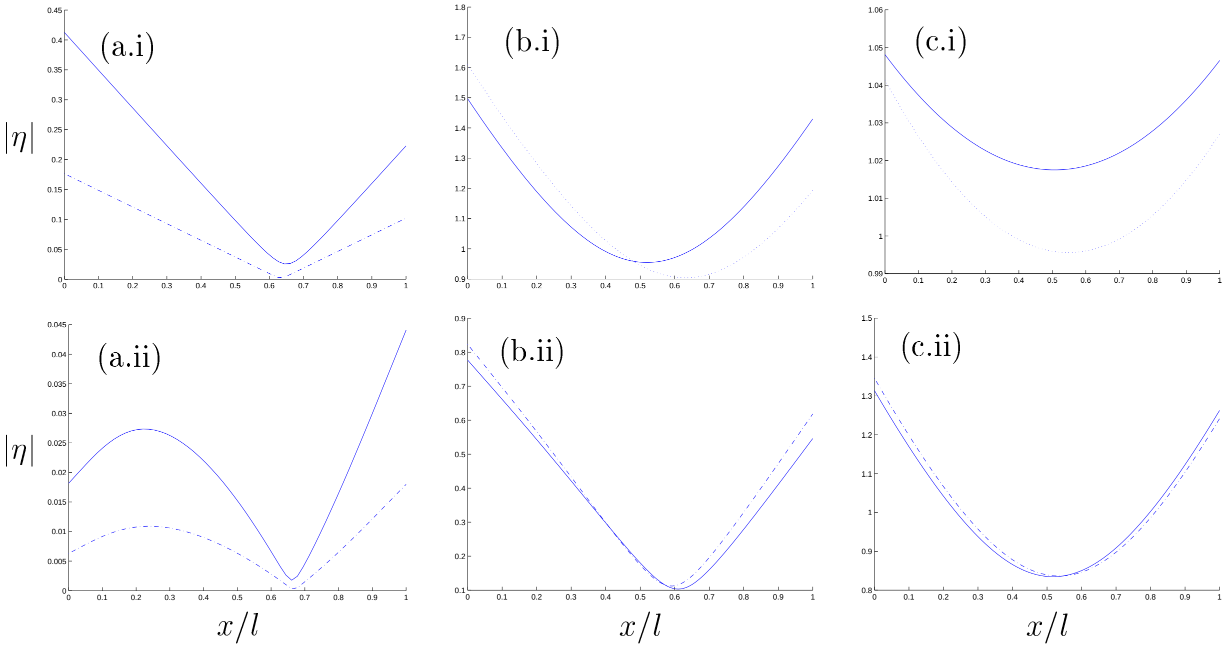

Figure 7.27: Comparison of the moduli of the reduced displacement functions of a floe of zero edge submergence (solid curves) and the corresponding floe of an Archimedean submergence (dot-dash). The floes have varying thickness, as defined by equation (7.15) in the form of a keel, with thickness $D_0 = 1$m, amplitude $A = 1$m and length (a-c.i) $l = 10$m, and (a-c.ii) $l = 50$m. The incident wave period is (a.i-ii) $\tau = 2$secs, (b.i-ii) $\tau \approx 5.06$secs and (c.i-ii) $\tau = 12$secs.

submergence to an Archimedean draught is investigated in figures 7.27-7.28. Figure 7.27 displays a floe with a keel ($p = 1$) for the two floe lengths used previously, $l = 10$m and 50m, and the three periods $\tau = 2$secs, 5.06secs and 12secs. Our findings here parallel those made for the uniform floe in the previous section. Specifically, as the incident period becomes smaller the additional scattering produced by the submerged portion of the ice edge causes the Archimedean floe to be displaced to a lesser extent than the same floe of a zero edge submergence. For the larger period, $\tau = 12$secs, the corresponding displacements are almost identical both qualitatively and quantitatively. At the smaller wave periods, we again see that the Archimedean floes experience less flexure than their non-Archimedean counterparts, a property that becomes more pronounced as the period decreases. At the middle period, $\tau \approx 5.06$secs, which we have previously found to be in the régime for which the scattering caused by the undulating surfaces is most distinguishable, there are no additional features observed when the non-zero draught is introduced. This is not surprising as the influence of the draught around such periods has been attributed to the extra source of scattering it produces at the edges of the floe. We also note that, as with the uniform floe, the effect of the edge submergence is again insensitive to the length of the floe.

It is evident that the difference between a floe when it has a zero edge submergence and when it has an Archimedean draught is very similar for both the uniform floes of 1m thickness seen in the previous section and the floes of figure 7.27. This similarity is undoubtedly due to the close values of their edge Archimedean edge submergences, with this value being 90cm for the uniform floes and 85cm when a keel is included. We can corroborate this observation with the values of the normalised differences. For example, for the incident wave period of 2secs, both the 10m and 50m length floes move by a distance of approximately 6×10^{-1} when the Archimedean draught is included, which is identical to the uniform problem.

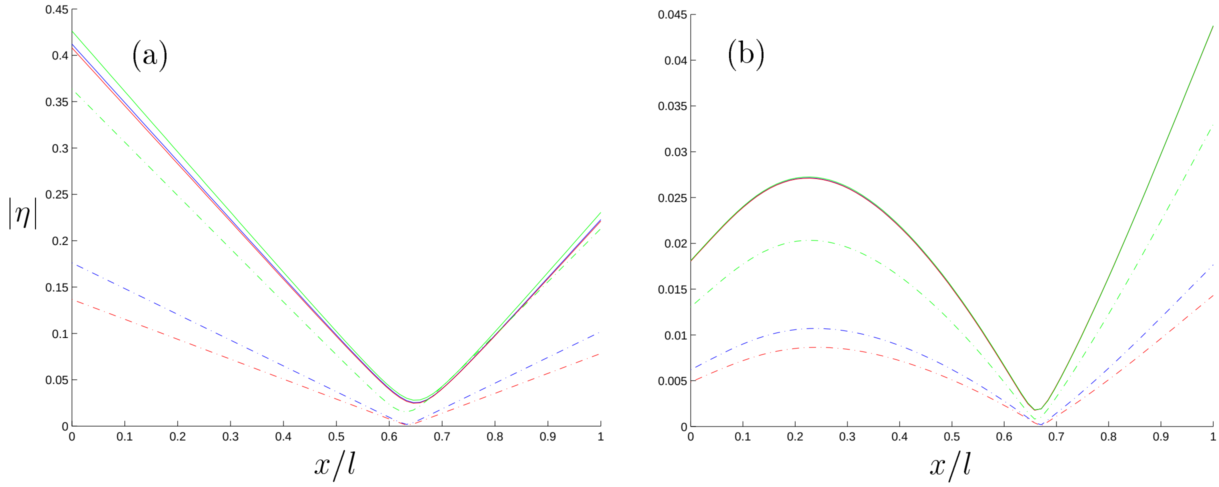

Figure 7.28: Comparison of the moduli of the reduced displacement functions of a floe of zero edge submergence (solid curves) and the corresponding floe of an Archimedean submergence (dot-dash). The floes have varying thickness, as defined in (7.15), with thickness $D_0 = 1$m, amplitude $A = 1$m, and length (a) $l = 10$m and (b) $l = 50$m. A wave period of $\tau = 2$secs is used. The lower surface of the floes is defined by equation (7.15) and the proportion of the variation that is a keel is $p = 1$ (blue curves), $p = 0.7$ (red) and $p = 2$ (green).

The change in the displacement of the floe is further investigated in figure 7.28. Here, we look at how the influence of the introduction of an Archimedean draught depends on the position of the variation in the ice thickness. To do this we take the wave period that maximises the effect of the submergence, namely 2secs. In the results presented we use the three keel proportions $p = 0.7$, 1 and 2, and, again, the floe lengths $l = 10$m and 50m.

As the keel proportion, p, increases more of the weight of the floe is transferred downwards. Consequently, the edge submergence diminishes and it is clear that the effect of the draught decreases markedly. For example, the normalised difference between the zero draught and Archimedean draught floes are 1.7×10^{-1} when $l = 10$m, and 3.4×10^{-1} when $l = 50$m, for the proportion $p = 2$, whereas for $p = 0.7$ these values are 2.0 and 2.1 respectively.

As expected, we may therefore conclude that the addition of the correct physical draught has a negligible impact on the scattering caused by a geometrical variation. In contrast, the size and position of the variation may have a strong influence on the degree to which the ice edge becomes submerged and hence the impact of the satisfaction of the Archimedean condition. The fact that the position of the variation also has an influence on the scattering caused by the floe indirectly through the edge submergence it induces further compounds the weaker relationship that we have found for floes related by a shared ice thickness in this chapter.

7.6 Conclusions

Results presented in this chapter have been concerned with cases of partial-ice cover in a two-dimensional setting. In particular, we have been occupied by the problem of a single floe of finite length, which was formulated in §4.3.2. Such problems are of a more complex nature than those of continuous ice-cover due to the additional sources of scattering provided by the ice edges.

In §7.3 we studied only the scattering caused by the ice edges, with the ice floe assumed to be uniform and the bed flat. This extended the investigation of the semi-infinite ice sheet of §5.2 to two sources of scattering - one at each edge of the finite floe. The findings made for the semi-infinite ice sheet were seen to hold for the finite floe. In terms of the convergence of the MMA, we again observed that low-dimensional approximations could contain qualitative as well as quantitative inaccuracies. This is particularly true of quantities that are sensitive to the accuracy at the sources of scattering (for example $|R|$) at which the evanescent waves are strongly activated. Convergence issues are prominent for large wavenumbers and thick ice, as these are the régimes for which the jump in the propagating waves between the ice-free and ice-covered intervals is greatest.

The addition of a second scattering source results in the possibility of interaction between the evanescent waves, which was deemed to be the cause of the need for extra vertical modes in the MMA to gain convergence. However, this is only true if the two sources of scattering are in close proximity, as the evanescent waves decay rapidly.

At high frequencies, the ice edges reflect most of the incident wave and the magnitude of the ice displacement is small. The reflection property is relative to the thickness of the ice, so that, for a fixed frequency, thicker floes tend to reflect the incident wave more strongly. This is again consistent with our study of the semi-infinite ice sheet problem.

Furthermore, incident waves which are long compared to the length of the floe pass by relatively undisturbed. Between the long and short wave limits, we found the existence of fine structure in the far-field response of the incident wave to the ice floe. This was not observed in the case of a semi-infinite ice sheet and is attributed to the effects of cross-scatterer interactions within the floe. The fine structure takes the form of sharp minima in the reflected amplitude, which was complemented by disproportionately large responses in the floe displacement.

The addition of keels and sails to the ice floe, as well as bed undulations, was investigated in §7.4. Typically, these continuous geometrical variations did not activate the evanescent waves as strongly as the ice edges and the convergence rate of the MMA went unaffected. For high frequencies, we found that the reflection of the incident wave caused by the ice edges dominated. However, at intermediate frequencies, for which a significant wave penetrates the ice, scattering properties due to the undulating geometrical surfaces were evident. This was especially true in the case of keels, for which qualitative differences were produced.

As in situations of continuous ice-cover studied in §6.4, we were again concerned with the relationship between geometries that share the same vertical structure, in particular keels and sails with bed protrusions. For finite ice floes, it was found that, although a similarity remains between these geometries, it is far weaker than in the case of continuous ice-cover.

A significant issue for cases of partial ice-cover is the question of how the addition of a physically correct submergence affects results. In §7.5 we considered some of the problems of the semi-infinite ice sheet problem of §5.2 and finite ice floe problems of §§7.3-7.4 with the inclusion of an Archimedean draught and compared them to their zero draught counterparts.

In particular, we found that at relatively high frequencies, the submerged portion of the ice edge reduces the amount of displacement experienced by the ice. This was attributed to reflection of the incident wave by these additional sources of scattering. Unsurprisingly, the effects of a non-zero draught depended on the thickness of the ice and length of the incident wave. Thus, results were perturbed most for thick ice and short incident waves. It was also seen that the extra source of scattering produced by edge submergence caused slower convergence of the MMA.

For floes that have a varying thickness, the satisfaction of Archimedes's principle will depend on the way in which the variations are manifest. In particular, adding more weight to the top of the floe rather than the bottom will result in a greater submergence and hence cause greater scattering of the incident wave. The difference in the edge submergence for floes of a shared thickness profile serves to further exacerbate the weakness in their relationship that has been seen in this chapter.

Chapter 8

Periodic structures in two-dimensions

It is possible to investigate many variants of the two-dimensional problems formulated in §4. One such is the subject of this chapter.

In the following section a method is devised in which the scattering caused by a two-dimensional periodic stucture, consisting of an arbitrary number of periods, may be determined using only a fixed set of solutions of differential equations taken over a single period. This represents a substantial numerical saving. Moreover, for free-surface flows periodic arrays are known to be the cause of resonances; for instance, see the work of Chamberlain & Porter (1995) and Porter & Porter (2003), which we will refer to frequently. It is on this issue of resonance that the results of this chapter are concentrated.

The scope for the study of periodic arrays is such that we confine ourselves to cases of continuous ice-cover and normal incidence. However, the extensions to partial ice-cover and/or oblique incidence may be easily made.

8.1 Reformulation of the complete ice-cover problem in two-dimensions

Before we consider cases of periodic geometry, let us begin in the general setting of the complete ice-cover problem defined in §4.3.1 but such that the interval $(0, l)$ is divided into the M subintervals (l_{i-1}, l_i) for $i = 1, \ldots, M$, where $l_0 = 0$ and $l_M = l$. This subdivision is chosen either on the basis of geometrical discontinuities or simply for convenience. The periodic problem is then a specific sub-class of this configuration.

The MMA is subdivided correspondingly, by writing

$$\mathbf{\Psi}_N(x) \equiv \mathbf{\Psi}_{N,(i)}(x) \quad (l_{i-1} \le x \le l_i),$$

for $i = 1, \ldots, M$. At the boundaries that have been created between the subintervals, the solutions, $\mathbf{\Psi}_{N,(i)}$ $(i = 1, \ldots, M)$, are linked through the jump conditions (4.10a-b). This is so regardless of whether or not the geometry is sufficiently differentiable at these points and, in fact, we will assume at a later stage that the geometry is smooth, so that the boundaries are artifices of the method.

We may therefore consider the waves scattered by a particular period to be the incident waves for the adjacent period and this means that the full solution can be composed by solving the scattering problem defined by each individual period. So, let the function $\mathbf{\Psi}_{N,(i)}$ be defined as the solution of the differential system (4.4) that governs the MMA in two-dimensions (with normal incidence, $q = 0$) in the interval (l_{i-1}, l_i), with

$$\mathbf{\Psi}_{N,(i)}(x) = \left[\mathcal{C}\{\mathrm{e}^{\mathrm{i}\mathcal{K}(l_{i-1}-x)}\mathbf{l}_{i-1} + \mathrm{e}^{-\mathrm{i}\mathcal{K}(l_{i-1}-x)}\mathbf{r}_{i-1}\}\right]_{x=l_{i-1}} \quad (l_{i-1} - \hat{l} < x < l_{i-1}), \tag{8.1a}$$

and

$$\mathbf{\Psi}_{N,(i)}(x) = \left[\mathcal{C}\{\mathrm{e}^{\mathrm{i}\mathcal{K}(l_i-x)}\mathbf{l}_i + \mathrm{e}^{-\mathrm{i}\mathcal{K}(l_i-x)}\mathbf{r}_i\}\right]_{x=l_i} \quad (l_i < x < l_i + \hat{l}), \tag{8.1b}$$

where $\hat{l}$ is an arbitrary positive value, $\mathcal{K} = \mathrm{diag}\{k_0, \ldots, k_N, \mu_{N,(1)}, \mu_{N,(2)}\}$ is the matrix $\mathit{\Lambda}$ of equation (4.23) evaluated for normal incidence ($\vartheta = 0$) and the matrix $\mathcal{C}$ is defined in equation (4.24). The constant vectors $\mathbf{l}_j$ and $\mathbf{r}_j$ $(j = i-1, i)$ represent, respectively, the amplitudes of the leftward and rightward waves. We suppose that these vectors are full, as the waves incident on any subinterval will consist of the evanescent waves scattered by the neighbouring periods in addition to propagating waves. The only exception is at the extreme ends of the periodic interval, where $\mathbf{r}_0 = \mathbf{A}^{(-)}$ and $\mathbf{l}_M = \mathbf{A}^{(+)}$, each containing a single amplitude from the wave that propagates from the relevant far-field. Using the jump conditions (4.10a-b) to link the expressions (8.1a-b) to the solution over the period of varying geometry, we deduce the boundary conditions

$$\left[\mathcal{V}^T\mathcal{M}^{-1}\mathbf{\Psi}_{N,(i)}\right]_{x=l_{(i-1)+}} = \left[\mathcal{V}^T\mathcal{M}^{-1}\mathcal{C}(\mathbf{r}_{i-1} + \mathbf{l}_{i-1})\right]_{x=l_{(i-1)-}}, \tag{8.2a}$$

$$\left[\mathcal{V}^T\mathcal{M}^{-1}\mathbf{\Psi}_{N,(i)}\right]_{x=l_{i-}} = \left[\mathcal{V}^T\mathcal{M}^{-1}\mathcal{C}(\mathbf{r}_i + \mathbf{l}_i)\right]_{x=l_{i+}}, \tag{8.2b}$$

$$\left[\mathcal{V}^{-1}\{\mathcal{A}\mathcal{M}\partial_x\mathbf{\Psi}_{N,(i)} + \mathcal{Q}\mathcal{N}\mathbf{\Psi}_{N,(i)}\}\right]_{x=l_{(i-1)+}} = \mathrm{i}\left[\mathcal{V}^{-1}\mathcal{A}\mathcal{M}\mathcal{C}\mathcal{K}(\mathbf{r}_{i-1} - \mathbf{l}_{i-1})\right]_{x=l_{(i-1)-}}, \tag{8.2c}$$

and

$$\left[\mathcal{V}^{-1}\{\mathcal{A}\mathcal{M}\partial_x\mathbf{\Psi}_{N,(i)} + \mathcal{Q}\mathcal{N}\mathbf{\Psi}_{N,(i)}\}\right]_{x=l_{i-}} = -\mathrm{i}\left[\mathcal{V}^{-1}\mathcal{A}\mathcal{M}\mathcal{C}\mathcal{K}(\mathbf{r}_i - \mathbf{l}_i)\right]_{x=l_{i+}}. \tag{8.2d}$$

The matrices $\mathcal{M}$, $\mathcal{N}$ and $\mathcal{V}$ are defined in §4.1.

Each of the solutions $\mathbf{\Psi}_{N,(i)}$ $(i = 1, \ldots, M)$ may therefore be expressed in terms of a linear combination of calculated functions, and we write

$$\boldsymbol{\Psi}_{N,(i)}(x) = \mathrm{i}\mathcal{L}_{-,(i)}(x)(\mathbf{r}_{(i-1)} - \mathbf{l}_{(i-1)}) + \mathrm{i}\mathcal{L}_{+,(i)}(x)(\mathbf{l}_{(i)} - \mathbf{r}_{(i)}) \quad (i = 1, \ldots, M). \tag{8.3}$$

The functions $\mathcal{L}_{\pm,(i)}$ are $(N+3)$ square matrices whose columns satisfy the system of differential system (4.4), so that

$$\partial_x(\mathcal{A}\partial_x\mathcal{L}_{\pm,(i)}) + \widetilde{\mathcal{D}}\partial_x\mathcal{L}_{\pm,(i)} + \mathcal{B}\mathcal{L}_{\pm,(i)} = 0 \quad (i = 1, \ldots, M), \tag{8.4}$$

and boundary conditions derived from (8.2c-d)

$$\left[\mathcal{V}^{-1}\{\mathcal{A}\mathcal{M}\partial_x\mathcal{L}_{\pm,(i)} + \mathcal{Q}\mathcal{N}\mathcal{L}_{\pm,(i)}\}\right]_{x=l_{(i-1)+}} = \left[\mathcal{V}^{-1}\mathcal{A}\mathcal{M}\mathcal{C}\mathcal{K}I_{\mp}\right]_{x=l_{(i-1)-}}, \tag{8.5a}$$

and

$$\left[\mathcal{V}^{-1}\{\mathcal{A}\mathcal{M}\partial_x\mathcal{L}_{\pm,(i)} + \mathcal{Q}\mathcal{N}\mathcal{L}_{\pm,(i)}\}\right]_{x=l_{i-}} = -\left[\mathcal{V}^{-1}\mathcal{A}\mathcal{M}\mathcal{C}\mathcal{K}I_{\mp}\right]_{x=l_{i+}}, \tag{8.5b}$$

where I_+ is the identity matrix of size $(N+3)$ and I_- is the zero matrix of the same size, for the solutions of equation (8.4). Note that, unlike the formulation of the standard two-dimensional complete ice-cover problem in §4.3.1, we have not modified the jump conditions (8.2a-d) to suppress the amplitudes of the evanescent waves. Instead, we retain all of the amplitudes in (8.3), not only those corresponding to propagating waves, which is necessary as, at the intermediate boundaries, all of the evanescent waves have an active rôle.

The constant amplitudes $\mathbf{r}_{(i)}$ and $\mathbf{l}_{(i)}$ $(i = 0, \ldots, M)$ are as yet undetermined; nonetheless, we are able to relate the neighbouring amplitudes through the *extended scattering matrices*

$$\begin{pmatrix} \mathbf{l}_{(i-1)} \\ \mathbf{r}_{(i)} \end{pmatrix} = \mathcal{S}_{N,(i)} \begin{pmatrix} \mathbf{r}_{(i-1)} \\ \mathbf{l}_{(i)} \end{pmatrix} \quad (i = 1, \ldots, M), \tag{8.6}$$

which, unlike the scattering matrix discussed in §4.4 that refers to only those of the propagating waves, includes the amplitudes of all of the waves that are relevant to the subinterval. The scattering matrix (8.6) describes the scattering on the single subinterval (l_{i-1}, l_i) and relates the incoming amplitudes to the outgoing. Alternatively, it is possible to define the *transfer matrices* $P_{N,(i)}$ and the *extended transfer matrices* $\mathcal{P}_{N,(i)}$, which relate amplitudes at either side of a subinterval, with

$$\begin{pmatrix} r_{0,(i)} \\ l_{0,(i)} \end{pmatrix} = P_{N,(i)} \begin{pmatrix} r_{0,(i-1)} \\ l_{0,(i-1)} \end{pmatrix}, \quad \begin{pmatrix} \mathbf{r}_{(i)} \\ \mathbf{l}_{(i)} \end{pmatrix} = \mathcal{P}_{N,(i)} \begin{pmatrix} \mathbf{r}_{(i-1)} \\ \mathbf{l}_{(i-1)} \end{pmatrix} \quad (i = 1, \ldots, M), \tag{8.7}$$

where $l_{0,(j)}$ and $r_{0,(j)}$ $(j = i-1, i)$ are the amplitudes of the propagating waves. We will use these transfer matrices to compose our solution over the full interval of periods, an approach that was first proposed by Porter & Porter (2003).

If we isolate the scattering problem in each subinterval, then the remaining conditions to be satisfied by $\boldsymbol{\Psi}_{N,(i)}$, equations (8.2a-b), may be expressed as

$$\mathfrak{Q}_0(l_{(i-1)+})\boldsymbol{\Psi}_{N,(i)}(l_{i-1}) = \mathfrak{Q}_1(l_{(i-1)-})(\mathbf{r}_{(i-1)} + \mathbf{l}_{(i-1)}), \tag{8.8a}$$

and

$$\mathfrak{Q}_0(l_{i-})\boldsymbol{\Psi}_{N,(i)}(l_i) = \mathfrak{Q}_1(l_{i+})(\mathbf{r}_{(i)} + \mathbf{l}_{(i)}), \tag{8.8b}$$

for $i = 1, \ldots, M$, where

$$\mathfrak{Q}_0(x_\pm) = \mathcal{K}(x_\mp)\mathcal{C}^T(x_\mp)\mathcal{A}(x_\mp)\mathcal{M}^T(x_\mp)\mathcal{V}^{-T}(x_\mp)\mathcal{V}^T(x_\pm)\mathcal{M}^{-T}(x_\pm)\mathcal{O},$$

$$\mathfrak{Q}_1(x_\pm) = \mathcal{K}(x_\pm)\mathcal{C}^T(x_\pm)\mathcal{A}(x_\pm)\mathcal{O}\mathcal{C}(x_\pm),$$

and, as previously defined in (4.48), the block matrix $\mathcal{O}$ is

$$\mathcal{O} = \begin{pmatrix} I & \mathbf{0} & \mathbf{0} \\ \mathbf{0}^T & 0 & -\kappa \\ \mathbf{0}^T & -\kappa & 0 \end{pmatrix}.$$

By applying the conditions (8.8a-b) to the form of the solutions given in (8.3), it is straightforward to derive the following expression for the scattering matrix in each subinterval, with

$$\mathcal{S}_{N,(i)} \equiv \begin{pmatrix} R_{(i)-} & T_{(i)+} \\ T_{(i)-} & R_{(i)+} \end{pmatrix} = -(\widetilde{\mathcal{S}}_{0,(i)} + \mathrm{i}\widetilde{\mathcal{S}}_{1,(i)})^{-1}(\widetilde{\mathcal{S}}_{0,(i)} - \mathrm{i}\widetilde{\mathcal{S}}_{1,(i)}), \tag{8.9}$$

where

$$\widetilde{\mathcal{S}}_{0,(i)} = \begin{pmatrix} \mathfrak{Q}_1(l_{(i-1)-}) & 0 \\ 0 & \mathfrak{Q}_1(l_{i+}) \end{pmatrix},$$

and

$$\widetilde{\mathcal{S}}_{1,(i)} = \begin{pmatrix} \mathfrak{Q}_0(l_{(i-1)+})\mathcal{L}_{-,(i)}(l_{i-1}) & \mathfrak{Q}_0(l_{(i-1)+})\mathcal{L}_{+,(i)}(l_{i-1}) \\ \mathfrak{Q}_0(l_{i-})\mathcal{L}_{-,(i)}(l_i) & \mathfrak{Q}_0(l_{i-})\mathcal{L}_{+,(i)}(l_i) \end{pmatrix}.$$

The transfer matrices across each subinterval are similarly calculated from

$$\mathcal{P}_{N,(i)} \equiv \begin{pmatrix} T_{(i)-} - R_{(i)+}T^{-1}_{(i)+}R_{(i)-} & R_{(i)+}T^{-1}_{(i)+} \\ -T^{-1}_{(i)+}R_{(i)-} & T^{-1}_{(i)+} \end{pmatrix} = -\widetilde{\mathcal{P}}^{-1}_{0,(i)}\widetilde{\mathcal{P}}_{1,(i)}, \tag{8.10}$$

where

$$\widetilde{\mathcal{P}}_{0,(i)} = \begin{pmatrix} \mathrm{i}\mathfrak{Q}_0(l_{(i-1)+})\mathcal{L}_{-,(i)}(l_{i-1}) & -\mathrm{i}\mathfrak{Q}_0(l_{(i-1)+})\mathcal{L}_{-,(i)}(l_{i-1}) \\ \mathfrak{Q}_1(l_{i+}) + \mathrm{i}\mathfrak{Q}_0(l_{i+})\mathcal{L}_{-,(i)}(l_i) & \mathfrak{Q}_1(l_{i+}) - \mathrm{i}\mathfrak{Q}_0(l_{i-})\mathcal{L}_{-,(i)}(l_i) \end{pmatrix},$$

and

$$\widetilde{\mathcal{P}}_{1,(i)} = \begin{pmatrix} \mathfrak{Q}_1(l_{(i-1)-}) - \mathrm{i}\mathfrak{Q}_0(l_{(i-1)+})\mathcal{L}_{+,(i)}(l_{i-1}) & \mathfrak{Q}_1(l_{(i-1)-}) + \mathrm{i}\mathfrak{Q}_0(l_{(i-1)+})\mathcal{L}_{+,(i)}(l_{i-1}) \\ -\mathrm{i}\mathfrak{Q}_0(l_{i-})\mathcal{L}_{+,(i)}(l_i) & \mathrm{i}\mathfrak{Q}_0(l_{i-})\mathcal{L}_{+,(i)}(l_i) \end{pmatrix}.$$

It is clear from equations (8.9) and (8.10) that the entries of the scattering matrix may be deduced from those of the transfer matrix and vice versa.

If the extended transfer matrix for the entire interval, $(0, l)$, is denoted $\mathcal{P}_N$, then it is immediate from (8.7) that

$$\mathcal{P}_N = \mathcal{P}_{N,(M)}\mathcal{P}_{N,(M-1)} \dots \mathcal{P}_{N,(1)}. \tag{8.11}$$

Using the above noted relationship between the transfer and scattering matrices, the scattering matrix for the entire interval, $\mathcal{S}_N$, is then easily obtained from $\mathcal{P}_N$.

The problem of two-dimensional scattering in the context of complete ice-cover, originally considered in §4.3.1, has now been reformulated in view of the forthcoming periodic problem. Our motivation in §4.3.1 was to minimise the computations required to produce a numerical solution, and the jump conditions used were thus manipulated to suppress the maximum possible number of unknown amplitudes. However, due to our current desire to investigate the periodic problem, we consider the overall interval of varying geometry to be arbitrarily subdivided and find the scattering properties of the entire interval from the individual properties of the subintervals, which necessitates an explicit knowledge of the amplitudes that were previously disregarded in the modified jump conditions.

8.2 Comparison to the work of Williams and Squire (2004)

In addition to the advantages it yields for instances of periodic geometry, the method of transfer matrices, outlined in §8.1, may be utilised in circumstances where the interval of varying geometry contains points at which the geometry is not smooth enough to generate the equations (4.4) and the jump conditions (4.10a-b) are instead applicable. One such example is provided by Williams & Squire (2004), who solve for the geometry

$$D(x) = \begin{cases} 1 & (x < 0), \\ 1 + 2x/15 & (0 < x < 15/2), \\ 51/15 - 2x/15 & (15/2 < x < 15), \\ 1 & (x > 15), \end{cases} \tag{8.12}$$

with $H = 70$m and $d = 0$, which they describe as *type 1*. Their solution method is, as with type 2 geometry (see §6.2), a Green's function approach.

Type 1 geometry is non-differentiable at the points $x = 0, 15/2, 15$ and we will therefore subdivide the interval of varying geometry $x \in (0, 15)$ into the two subintervals $x \in (0, 15/2)$ and $x \in (15/2, 15)$ with the corresponding transfer matrices $\mathcal{P}_{N,(1)}$ and $\mathcal{P}_{N,(2)}$, respectively. Due to the symmetry of the geometry,

$$\mathcal{P}_{N,(2)} = \begin{pmatrix} 0 & \mathcal{I}_{N+3} \\ \mathcal{I}_{N+3} & 0 \end{pmatrix} \mathcal{P}_{N,(1)}^{-1} \begin{pmatrix} 0 & \mathcal{I}_{N+3} \\ \mathcal{I}_{N+3} & 0 \end{pmatrix},$$

and therefore the transfer matrix for the interval $x \in (0, 15)$, $\mathcal{P}_N = \mathcal{P}_{N,(2)}\mathcal{P}_{N,(1)}$, is produced from one set of linearly independent solutions.

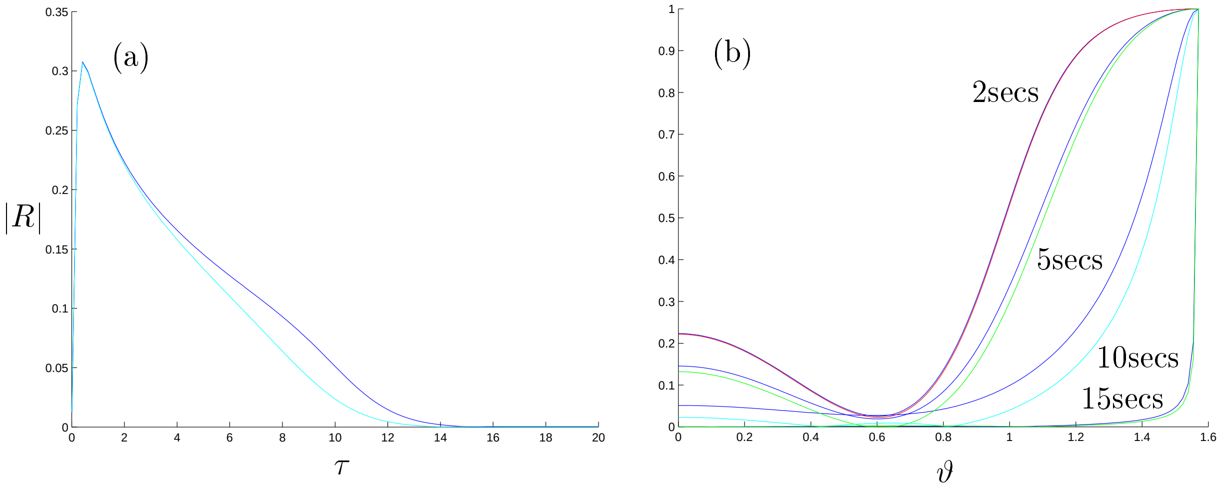

Figure 8.1: Comparison with figures 4(e) & 4(f) of Williams & Squire (2004), in which type 1 geometry (see equation (8.12)) is used with the geometrical values $d = 0$ and $h = 70$m. Part (a) plots the convergence of approximations to the modulus of the reflected amplitude as a function of wave period for normal incidence ($\vartheta = 0$). Part (b) plots the convergence of approximations to the moduli of reflected amplitudes as functions of incident angle for the wave periods $\tau = 2$secs, 5secs, 10secs and 15secs. The dimensions of the approximations are $N = 0$ (blue curves), $N = 1$ (red), $N = 2$ (green) and $N = 3$ (cyan).

Figure 8.1 displays the convergence of approximations to the reflected amplitude as a function of wave period, τ, and incident angle, ϑ, for type 1 geometry. These are directly comparable to figures 4(e-f) of Williams & Squire (2004) and it is evident that the converged MMAs match these figures. The convergence properties of the MMA remain smooth here and are very close to those seen for type 2 geometry in §6.2. Convergence rates are found to be adversely affected by the addition of an extra interface; for example, the value ϵ_1 in relation to the function $|R(\tau)|$, for type 1 geometry is an order of magnitude greater than its corresponding value for type 2 geometry. However, the accuracy of the single-mode approximation is maintained for large and small wave periods, and it is only in the middle interval that convergence worsens. This implies that, in this middle interval, the scattering caused by an additional interface significantly increases the activation of the evanescent modes.

8.3 Formulation of the periodic problem

We now return to the formulation of the periodic problem. Each subinterval (l_{i-1}, l_i) $(i = 1, \ldots, M)$ will henceforth be of the same length and contain identical geometrical variations, so that we have $l_i - l_{i-1} \equiv \hat{l}_0$ $(i = 1 \ldots M)$ and

$$D(x_0 + i\hat{l}_0) = D(x_0), \;\; h(x_0 + i\hat{l}_0) = h(x_0), \;\; d(x_0 + i\hat{l}_0) = d(x_0) \quad \text{for } x_0 \in (0, \hat{l}_0), \tag{8.13}$$

for $i = 0 \ldots M - 1$. The definition of periodic geometry (8.13) implicitly imposes the restriction of continuity of the geometrical functions D, h and d. As such, the matrices $\mathcal{M}$ that appear in the interfacial conditions (8.5a-b) and (8.8a-b) may be replaced by identity matrices. This is also true of the matrices $\mathcal{V}$ if we use the natural modes.

8.3.1 The transfer matrix

Before we outline our method of solution for the periodic problem, it is pertinent to consider certain properties of the transfer matrices $\mathcal{P}_{N,(i)}$. These may be deduced as follows.

Firstly, by noting the relevant changes that must be made to the amplitudes, the function $\overline{\boldsymbol{\Psi}}_{N,(i)}$ satisfies the same scattering conditions as $\boldsymbol{\Psi}_{N,(i)}$, which may be represented as

$$\widehat{\mathcal{I}} \begin{pmatrix} \overline{\mathbf{r}}_{(i)} \\ \overline{\mathbf{l}}_{(i)} \end{pmatrix} = \mathcal{P}_{N,(i)} \widehat{\mathcal{I}} \begin{pmatrix} \overline{\mathbf{r}}_{(i-1)} \\ \overline{\mathbf{l}}_{(i-1)} \end{pmatrix} \quad (i = 1, \ldots, M), \tag{8.14}$$

where $\widehat{\mathcal{I}}$ is a matrix that interchanges the first and the $(N+4)$th entries of a vector only if the dimension dependent wavenumbers, $\mu_{N,(i)}$ $(i = 1, 2)$, are distinct and purely imaginary, and also the $(N+2)$nd and the $(2N+6)$th, and the $(N+3)$rd and the $(2N+5)$th entries if the $\mu_{N,(i)}$ form a symmetric, complex pair. In either case $\widehat{\mathcal{I}}$ is self-inverse and simple manipulation of (8.7) and (8.14) leads to

$$\mathcal{P}_{N,(i)} = \widehat{\mathcal{I}}\overline{\mathcal{P}}_{N,(i)}\widehat{\mathcal{I}}.$$

This relation implies that the eigenvalues of the transfer matrices are either real or arise in conjugate pairs. This property was proved by Porter & Porter (2003) for free-surface flows over periodically undulating beds.

Secondly, the identities

$$\mathfrak{Q}_0(l_{(i-1)+})\mathcal{L}_{+,(i)}(l_{i-1}) = (\mathfrak{Q}_0(l_{(i-1)+})\mathcal{L}_{+,(i)}(l_{i-1}))^T, \tag{8.15a}$$

$$\mathfrak{Q}_0(l_{i-})\mathcal{L}_{-,(i)}(l_i) = (\mathfrak{Q}_0(l_{i-})\mathcal{L}_{-,(i)}(l_i))^T, \tag{8.15b}$$

and

$$\mathfrak{Q}_0(l_{i-})\mathcal{L}_{+,(i)}(l_i) = (\mathfrak{Q}_0(l_{(i-1)+})\mathcal{L}_{-,(i)}(l_{i-1}))^T, \tag{8.15c}$$

result from the application of the two-dimensional multi-mode energy balance

$$\Big[\mathbf{\Psi}_{(1)}^T\mathcal{O}\mathcal{A}(\partial_x\mathbf{\Psi}_{(0)}) - (\partial_x\mathbf{\Psi}_{(1)}^T)\mathcal{O}\mathcal{A}\mathbf{\Psi}_{(0)} + \mathbf{\Psi}_{(1)}^T\widetilde{\mathcal{D}}\mathbf{\Psi}_{(0)}\Big]_{x_0}^{x_1} = 0,$$

(see Appendix B) where $(\mathbf{\Psi}_{(0)}, \mathbf{\Psi}_{(1)})$ is taken to be the pairs

$$(\mathcal{L}_{-,(i)}\mathcal{I}_m, \mathcal{L}_{-,(i)}\mathcal{I}_n), \quad (\mathcal{L}_{+,(i)}\mathcal{I}_m, \mathcal{L}_{+,(i)}\mathcal{I}_n), \quad (\mathcal{L}_{+,(i)}\mathcal{I}_m, \mathcal{L}_{-,(i)}\mathcal{I}_n)$$

for $(m, n = 1, \ldots, N+3)$ respectively. This derivation is very similar to that which produced (4.49) and again uses the diagonality of the matrix $\mathcal{C}^T\mathcal{O}\mathcal{A}\mathcal{C}$. Identities (8.15a-c) may then be directly used to establish the equality

$$\widetilde{\mathcal{P}}_{1,(i)}\widehat{\mathcal{S}}_{0,(i)}^{-1}\widetilde{\mathcal{P}}_{1,(i)}^T = \widetilde{\mathcal{P}}_{0,(i)}\widehat{\mathcal{S}}_{0,(i)}^{-1}\widetilde{\mathcal{P}}_{0,(i)}^T,$$

where

$$\widehat{\mathcal{S}}_{0,(i)} = \widetilde{\mathcal{S}}_{0,(i)}\begin{pmatrix} 0 & \mathcal{I}_{N+3} \\ -\mathcal{I}_{N+3} & 0 \end{pmatrix}$$

when the geometrical functions D, h and d are identical at the two boundaries. Therefore, under this condition, we find that

$$\mathcal{P}_{N,(i)}^T = \widehat{\mathcal{S}}_0\mathcal{P}_{N,(i)}^{-1}\widehat{\mathcal{S}}_0^{-1} \tag{8.16}$$

holds, from which we conclude that the eigenvalues of the transfer matrices must come in reciprocal pairs. Again, this property is proved in Porter & Porter (2003) for the free-surface case.

Finally, consider the transfer matrix that gives the left-hand amplitudes in terms of the right-hand rather than the usual construction (8.7) that performs the transfer in the opposite direction. Referring to equation (8.10) it is easily seen that

$$\begin{pmatrix} \mathbf{l}_{(i-1)} \\ \mathbf{r}_{(i-1)} \end{pmatrix} = \begin{pmatrix} T_{(i)+} - R_{(i)-}T_{(i)-}^{-1}R_{(i)+} & R_{(i)-}T_{(i)-}^{-1} \\ -T_{(i)-}^{-1}R_{(i)+} & T_{(i)-}^{-1} \end{pmatrix} \begin{pmatrix} \mathbf{l}_{(i)} \\ \mathbf{r}_{(i)} \end{pmatrix} \quad (i = 1, \ldots, M). \tag{8.17}$$

Alternatively, we may define the right-to-left transfer matrix in terms of the inverse of the left-to-right transfer matrix to be

$$\begin{pmatrix} 0 & \mathcal{I}_{N+3} \\ \mathcal{I}_{N+3} & 0 \end{pmatrix} \mathcal{P}_{N,(0)}^{-1} \begin{pmatrix} 0 & \mathcal{I}_{N+3} \\ \mathcal{I}_{N+3} & 0 \end{pmatrix}. \tag{8.18}$$

Equating our two expressions for the right-to-left transfer matrix, (8.17)-(8.18), and assuming symmetry of the geometrical boundary values, so that (8.16) holds, we have that

$$\begin{pmatrix} T_{(i)+} - R_{(i)-}T_{(i)-}^{-1}R_{(i)+} & R_{(i)-}T_{(i)-}^{-1} \\ -T_{(i)-}^{-1}R_{(i)+} & T_{(i)-}^{-1} \end{pmatrix} =$$

$$\begin{pmatrix} \mathcal{I}_{N+3} & 0 \\ 0 & -\mathcal{I}_{N+3} \end{pmatrix} \widetilde{\mathcal{S}}_{0,(i)}^{-1} \mathcal{P}_{N,(0)}^{T} \widetilde{\mathcal{S}}_{0,(i)} \begin{pmatrix} \mathcal{I}_{N+3} & 0 \\ 0 & -\mathcal{I}_{N+3} \end{pmatrix}.$$

Matching the block entries in this equation gives a set of four equalities. Most notably we have that

$$T_{(i)+}^{T}\mathfrak{Q}_0(l_i) = \mathfrak{Q}_0(l_i)T_{(i)-} \quad (i = 0, \ldots, M),$$

and hence $\mathrm{diag}(T_{(i)+}) = \mathrm{diag}(T_{(i)-})$. This result supercedes that of the equality of the transmission coefficients of the propagating waves, which was given in §4.4.

We will now utilise the above properties of the transfer matrices in our formulation of the periodic problem.

As the geometry in each subinterval has been assumed to be identical, each period necessarily defines the same scattering problem, whence

$$\mathcal{S}_{N,(i)} = \mathcal{S}_{N,(j)} \equiv \mathcal{S}_{N,(0)} \quad (i, j = 1, \ldots, M),$$

and

$$\mathcal{P}_{N,(i)} = \mathcal{P}_{N,(j)} \equiv \mathcal{P}_{N,(0)} \quad (i, j = 1, \ldots, M).$$

It is convenient at this juncture to revise the context of the problem, so that the individual period under consideration is taken to be fixed and that the length, l, of the entire interval varies according to the number, M, of these periods that are present.

By virtue of the reciprocal and conjugate properties of its eigenvalues, the transfer matrix, $\mathcal{P}_{N,(0)}$, may be decomposed as

$$\mathcal{P}_{N,(0)} = \mathcal{H} \begin{pmatrix} \Delta & 0 \\ 0 & \Delta^{-1} \end{pmatrix} \mathcal{H}^{-1},$$

where Δ is a diagonal matrix whose entries are the eigenvalues of $\mathcal{P}_{N,(0)}$ of magnitude less than unity or lying on the upper half of the unit circle and the matrix $\mathcal{H}$ contains the eigenvectors of the transfer matrix, ordered accordingly. Referring to (8.11), the transfer matrix for the entire interval, $\mathcal{P}_N$, is therefore given by

$$\mathcal{P}_N = \mathcal{P}_{N,(0)}^M = \mathcal{H} \begin{pmatrix} \Delta^M & 0 \\ 0 & \Delta^{-M} \end{pmatrix} \mathcal{H}^{-1}. \tag{8.20}$$

All other quantities are now readily available; however, as we are likely to have terms in Δ^M that are growing and terms in Δ^{-M} that are decaying, for large M this creates the possibility of extreme values in the diagonal matrix on the right-hand side of equation (8.20). In order to avoid numerical complications that may arise from these extreme values, we mimic Porter & Porter (2003) by writing

$$\mathcal{S}_N = -\begin{pmatrix} \mathcal{H}_{22} & -\Delta^M \mathcal{H}_{21} \\ \Delta^M \mathcal{H}_{12} & -\mathcal{H}_{11} \end{pmatrix}^{-1} \begin{pmatrix} \mathcal{H}_{21} & -\Delta^M \mathcal{H}_{22} \\ \Delta^M \mathcal{H}_{11} & -\mathcal{H}_{12} \end{pmatrix}, \tag{8.21}$$

where the $\mathcal{H}_{ij}$ are such that

$$\mathcal{H}^{-1} = \begin{pmatrix} \mathcal{H}_{11} & \mathcal{H}_{12} \\ \mathcal{H}_{21} & \mathcal{H}_{22} \end{pmatrix}.$$

Similarly, the amplitudes are retrieved by simultaneously solving the relations

$$\left.\begin{array}{rcl} \mathcal{H}_{11}\mathbf{r}_i + \mathcal{H}_{12}\mathbf{l}_i & = & \Delta\mathcal{H}_{11}\mathbf{r}_{i-1} + \Delta\mathcal{H}_{12}\mathbf{l}_{i-1} \\ \Delta\mathcal{H}_{21}\mathbf{r}_i + \Delta\mathcal{H}_{22}\mathbf{l}_i & = & \mathcal{H}_{21}\mathbf{r}_{i-1} + \mathcal{H}_{22}\mathbf{l}_{i-1} \end{array}\right\} (i = 1, \ldots, M). \tag{8.22}$$

In equations (8.20)-(8.22) we have developed a means of calculating the response to an incident wave over an interval of an arbitrary number of periods of identical geometry from a single such period. This constitutes a significant numerical saving, as it is now not necessary to discretise each period in order to calculate the solutions of the differential system (4.4). As will be seen in the following section, this method also allows for some analytical understanding of the process of resonance to be gained.

8.3.2 A wide-spacing approximation

Expression (8.21) is particularly recondite when it comes to the issue of resonance. If the so-called 'wide spacing approximation' is implemented, which supposes that the only interaction between adjacent periods is through propagating waves, then certain properties may be determined. This method has been used in the case of free-surface flows with periodic bedforms by authors including Porter & Porter (2003) and Chamberlain & Porter (1995) and our analysis mirrors much of their work.

In order to implement the wide-spacing approximation, we require the transfer matrix

$$P_{N,(0)} = T^{-1} \begin{pmatrix} -\det(S_{N,(0)}) & R_+ \\ -R_- & 1 \end{pmatrix}, \tag{8.23a}$$

where

$$S_{N,(0)} = \begin{pmatrix} R_- & T \\ T & R_+ \end{pmatrix} \tag{8.23b}$$

is the 2 × 2 scattering matrix discussed in §4.4 and calculated throughout §6. These matrices relate the amplitudes of the propagating waves on either side of an obstruction and may be constructed for any dimension N using two linearly independent solutions (see §4.3.1). The scattering matrix (8.23b) is a truncated version of the extended scattering matrix defined in equation (8.6), and, as such, the outgoing amplitudes it provides are only approximate. This is because, in the periodic problem, the waves that are incident on each period are not only propagating waves but also evanescent waves. Consequently, the transfer matrix (8.23a) is not exact.

The equality of the transmission coefficients, $T = T_+ = T_-$, for periodic constructions, was most recently proved in §8.3.1. Moreover, the Kreisel relations (see Porter & Chamberlain, 1997) given in equations (4.46a-d) hold. Note that, unlike their free-surface equivalents, the scattering matrix $S_{N,(0)}$ and transfer matrix $P_{N,(0)}$ are not equal to the extended scattering and transfer matrices in the single-mode approximation, $\mathcal{S}_{0,(0)}$ and $\mathcal{P}_{0,(0)}$, due to the suppression of the amplitudes of the dimension-dependent evanescent waves.

Following Porter & Porter (2003) and Chamberlain & Porter (1995), it can be shown that the eigenvalues of $P_{N,(0)}$ may be expressed as $\mathrm{e}^{\pm \mathrm{i} p_0}$, where p_0 is chosen to satisfy

$$T(\mathrm{e}^{\mathrm{i}p_0} + \mathrm{e}^{-\mathrm{i}p_0}) = 1 - \det(S_{N,(0)}) = \frac{T(\mathrm{e}^{\mathrm{i}\arg(T)} + \mathrm{e}^{-\mathrm{i}\arg(T)})}{|T|}.$$

Therefore, p_0 may be restricted to the interval $[0, \pi]$ if

$$-|T| \le \mathrm{e}^{\mathrm{i}\arg(T)} + \mathrm{e}^{-\mathrm{i}\arg(T)} \le |T|, \tag{8.24a}$$

in which case the eigenvalues form a complex conjugate pair lying on the unit circle; and to the form $p_0 \in \mathrm{i}\mathbb{R}$ if

$$\mathrm{e}^{\mathrm{i}\arg(T)} + \mathrm{e}^{-\mathrm{i}\arg(T)} > |T|, \tag{8.24b}$$

or $p_0 \in \pi + \mathrm{i}\mathbb{R}$ if

$$\mathrm{e}^{\mathrm{i}\arg(T)} + \mathrm{e}^{-\mathrm{i}\arg(T)} < -|T|, \tag{8.24c}$$

in which case the eigenvalues are a real-valued, reciprocal pair. The corresponding eigenvectors are also readily available, and we may decompose $P_{N,(0)}$ into

$$P_{N,(0)} = H \begin{pmatrix} \mathrm{e}^{\mathrm{i}p_0} & 0 \\ 0 & \mathrm{e}^{-\mathrm{i}p_0} \end{pmatrix} H^{-1},$$

where

$$H^{-1} = \begin{pmatrix} 1 - T\mathrm{e}^{\mathrm{i}p_0} & -R_+ \\ 1 - T\mathrm{e}^{-\mathrm{i}p_0} & -R_+ \end{pmatrix}.$$

We now apply the wide-spacing approximation, in which we assume that the effect of the evanescent waves on the scattering of the propagating waves, between neighbouring periods, is negligible. If this is true, then the scattering process may then be represented by

$$\begin{pmatrix} l_{0,(i-1)} \\ r_{0,(i)} \end{pmatrix} = S_{N,(0)} \begin{pmatrix} r_{0,(i-1)} \\ l_{0,(i)} \end{pmatrix}, \quad \begin{pmatrix} r_{0,(i)} \\ l_{0,(i)} \end{pmatrix} = P_{N,(0)} \begin{pmatrix} l_{0,(i-1)} \\ r_{0,(i-1)} \end{pmatrix}$$

for $i = 1, \dots, M$, and this results in the approximation of the transfer matrix for the entire interval, $P_N \approx \widehat{P}_N$, where

$$\widehat{P}_N = P_{N,(0)}^M = H \begin{pmatrix} \mathrm{e}^{\mathrm{i}Mp_0} & 0 \\ 0 & \mathrm{e}^{-\mathrm{i}Mp_0} \end{pmatrix} H^{-1}.$$

The complementary approximation of the scattering matrix for the entire interval, $S_N \approx \widehat{S}_N$, is given by

$$\widehat{S}_N = -\begin{pmatrix} -R_+ & \mathrm{e}^{\mathrm{i}Mp_0}(1 - T\mathrm{e}^{-\mathrm{i}p_0}) \\ \mathrm{e}^{\mathrm{i}Mp_0}(1 - T\mathrm{e}^{\mathrm{i}p_0}) & -R_+ \end{pmatrix}^{-1} \begin{pmatrix} (1 - T\mathrm{e}^{-\mathrm{i}p_0}) & -\mathrm{e}^{\mathrm{i}Mp_0}R_+ \\ -\mathrm{e}^{\mathrm{i}Mp_0}R_+ & (1 - T\mathrm{e}^{\mathrm{i}p_0}) \end{pmatrix}. \tag{8.25}$$

To aid brevity, we will write

$$\widehat{S}_N \equiv \begin{pmatrix} \widehat{R}_- & \widehat{T} \\ \widehat{T} & \widehat{R}_+ \end{pmatrix}. \tag{8.26}$$

Straightforward manipulations of (8.25) and (8.26) lead to the expression

$$|\widehat{T}|^2 = \frac{|T|^2 \sin^2(p_0)}{|T|^2 \sin^2(p_0) + |R|^2 \sin^2(Mp_0)}.$$

It can easily be deduced and verified that the entries of the approximate scattering matrix $\widehat{S}_N$ satisfy the Kreisel relations (4.46a-d). In particular, from $|\widehat{R}|^2 = 1 - |\widehat{T}|^2$ we have that

$$|\widehat{R}|^2 = \frac{|R|^2 \sin^2(Mp_0)}{|T|^2 \sin^2(p_0) + |R|^2 \sin^2(Mp_0)}.$$

Two distinct possibilities are now clear: the first is that inequality (8.24a) holds and p_0 is real, in which case $\sin^2(Mp_0)$ oscillates with varying M but remains bounded. Following Porter & Porter (2003), we may then deduce the complementary envelopes

$$|\widehat{T}|^2 \geq \frac{|T|^2 \sin^2(p_0)}{|T|^2 \sin^2(p_0) + |R|^2} \quad (M = 1, 2, \dots), \tag{8.28a}$$

and

$$|\widehat{R}|^2 \leq \frac{|R|^2}{|T|^2 \sin^2(p_0) + |R|^2} \quad (M = 1, 2, \dots). \tag{8.28b}$$

Alternatively, if either of inequalities (8.24b-c) hold, then p_0 has an imaginary part and $\sin^2(Mp_0)$ will be unbounded as M increases, so that $|\widehat{T}| \to 0$ $(M \to \infty)$ and $|\widehat{R}| \to 1$ $(M \to \infty)$.

Under the wide-spacing assumption of non-interaction of the evanescent waves with the propagating waves between neighbouring periods, we have generated an approximation to the scattering properties of the entire interval that requires the calculation of only two linearly independent solutions over an individual period. This not only represents a substantial numerical saving but also allows the prediction of resonance based on the scattering properties of a single period. Specifically, having calculated the eigenvalues of the transfer matrix of one such period, we may determine whether or not the wide-spacing approximation of the far-field response will display resonant behaviour as the number of periods increases. The validity of this method will be substantiated in the numerical results of the following section.

8.4 Results

In this results section we will study the issue of resonance in the setting of continuous ice-cover with periodic variations, described in §8.3. Resonances about the so-called Bragg values $k_0\hat{l}_0/\pi = 1, 2, \ldots$ are often observed in other problems; see, for example, Chamberlain & Porter (1995) and Porter & Porter (2003).

Due to the tendency of ice to elongate propagating waves (see §3.2.2), for suitable period lengths, the parameter régimes that we have thus far used will not typically coincide with points of Bragg resonance. This is particularly true of ice sheets of considerable thickness as they more severely extend propagating waves. As our initial concern is with the existence and behaviour of these Bragg resonances, for the remainder of this section we will be content to work with often unrealistically short incident waves, whilst retaining the single period length $\hat{l}_0 = 2\pi$m throughout. This period length is suitable for our purposes as it allows us to investigate a reasonable number of periods without the entire period $(0, l)$ becoming particularly long or short. We do however note that, due to this issue, the occurrence of Bragg resonance in practical models is extremely sensitive to the thickness of the ice in question and hence is unlikely to occur in many situations.

With reference to the investigation of §6.4, it is here justifiable to restrict our attention to variations in the ice thickness, D, using the single-mode approximation. Calculations not given indicate that, in the problems presented in this section, the single-mode approximation retains the high accuracy previously shown for instances of continuous ice-cover, and that geometries that share their ice thicknesses give near identical results.

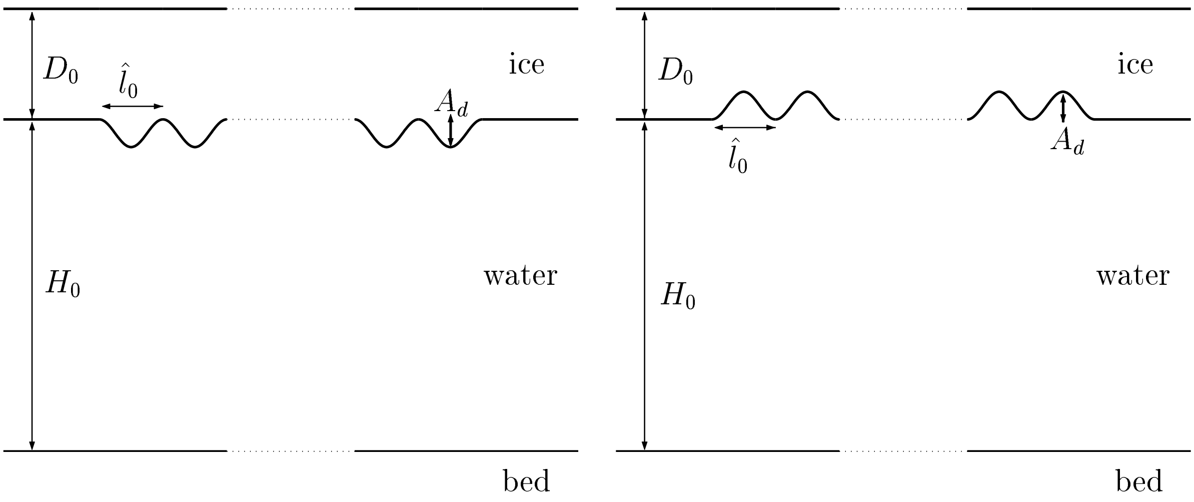

Figure 8.2: Schematics of the periodic geometrical configurations defined in equation (8.29), which here appear as protrusions and indentations in the lower surface of the ice.

In figures 8.3-8.4 reflected amplitudes are plotted as functions of the non-dimensional frequency parameter $k_0\hat{l}_0/\pi$, which, in this case, varies with the incident wavenumber, k_0.

The periodic variations are in the ice thickness and are of the form

$$D(x_0) = D_0 + A_d \sin^2\left(\frac{\pi x_0}{\hat{l}_0}\right) \quad (0 < x_0 < \hat{l}_0), \tag{8.29}$$

where A_d is the amplitude of the obstruction. We use the thickness $D_0 = 1$m and a flat bed, which is of depth $h = 20$m. The four amplitudes $A_d = \pm 0.1$m and ± 0.5m are used and results are shown for one, two, five and ten periods. Two examples of these geometrical configurations are shown in figure 8.2. It is worth noting that the obstruction defined in equation (8.29) may be rewritten

$$D_0 + \frac{A_d}{2} + A_d \cos\left(\frac{2\pi x_0}{\hat{l}_0}\right),$$

and it is clear that it represents a sinusoidal variation, which is based around the fixed level $D_0 + A_d/2$ and is of period $\hat{l}_0$.

Curves indicating the corresponding wide-spacing approximations are overlaid on figures 8.3-8.4 and the envelope of the reflected amplitude, which is given in (8.28b), is also included. For the results presented, the ice thickness was varied by the inclusion of a protrusion or an indentation on the lower surface of the ice; however, as previously mentioned, any other means of producing the same variations in the ice (for example, a protrusion or an indentation on the upper surface of the ice) will give rise to near identical results.

The scaling of the horizontal axes is such that integer values coincide with Bragg resonance points. Here, the interval of incident wavenumbers is chosen such that we pass through the first three Bragg values, which, for an far-field ice thickness of 1m, corresponds to wave periods ranging from $\tau \approx 3.3 \times 10^{-1}$secs to $\tau \approx 3.7 \times 10^{-3}$secs. As noted earlier, this interval represents far shorter waves than have previously been considered.

For the less severe amplitudes, $A_d = \pm 0.1$m, which are shown in figure 8.3, resonant effects are prominent about the primary Bragg value, $k_0\hat{l}_0/\pi = 1$, and also exist around the secondary Bragg value, $k_0\hat{l}_0/\pi = 2$, although to a far lesser degree. This behaviour is consistent with that noted for analogous free surface motion over ripple beds (see Porter & Porter, 2003). At these primary and secondary Bragg values, full resonance, i.e. $|R| = 1$, is not achieved, and effects are rather observed as being extreme relative to the local behaviour. This is especially true if we consider the wide-spacing envelope, which indicates the maximum effect caused by the inclusion of additional periods. More generally, the wide-spacing approximations display excellent agreement with their corresponding single-mode approximations in figure 8.3.

In figure 8.4 the accuracy of the wide-spacing approximations is only slightly diminished by the stronger activation of the evanescent waves when the amplitudes are increased

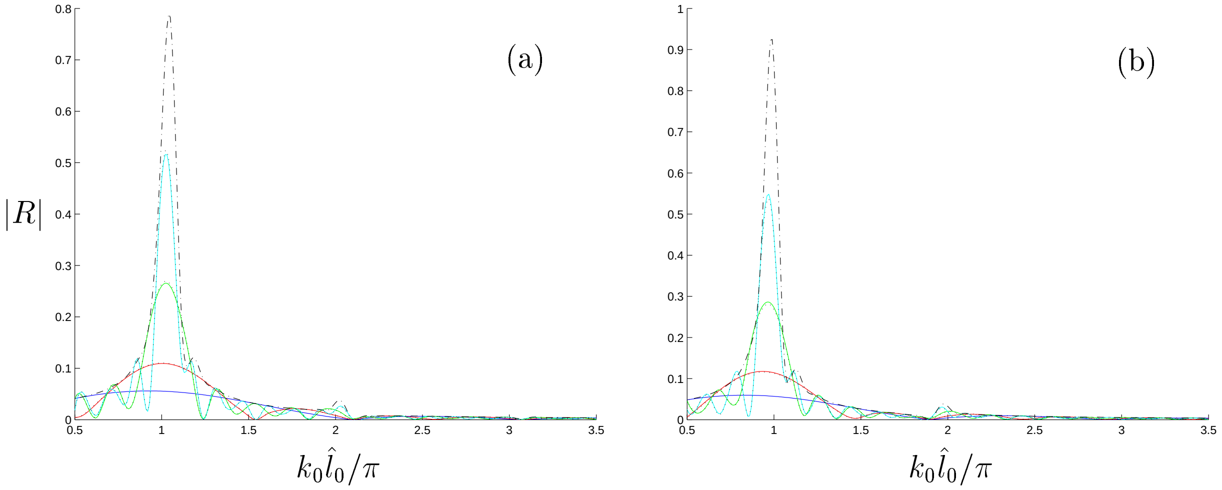

Figure 8.3: The modulus of the reflected amplitude as a function of a non-dimensional wavenumber, using the periodic ice thickness defined in (8.29) with $D_0 = 1$m, and period length $\hat{l}_0 = 2\pi$m, over a flat bed depth $h = 20$m. The number of periods is $M = 1$ (blue curves), $M = 2$ (red), $M = 5$ (green) and $M = 10$ (cyan). In part (a) the variations take the form of protrusions on the lower surface of the ice, $A_d = 0.1$m, and in part (b) they are indentations on the lower surface of the ice, $A_d = -0.1$m. Also plotted is the corresponding wide-spacing approximations (dotted curves) and wide-spacing envelope (black dot-dash).

to $A_d = \pm 0.5$m. Resonant effects are far more pronounced in these problems, with, for ten periods around the primary Bragg value, full resonance reached for the indentation of figure 8.4(b). At the corresponding Bragg value for the protrusion, shown in figure 8.4(a), full resonance is not achieved by ten periods; however, the wide-spacing envelope indicates that it will be realised if an increased number of periods is taken.

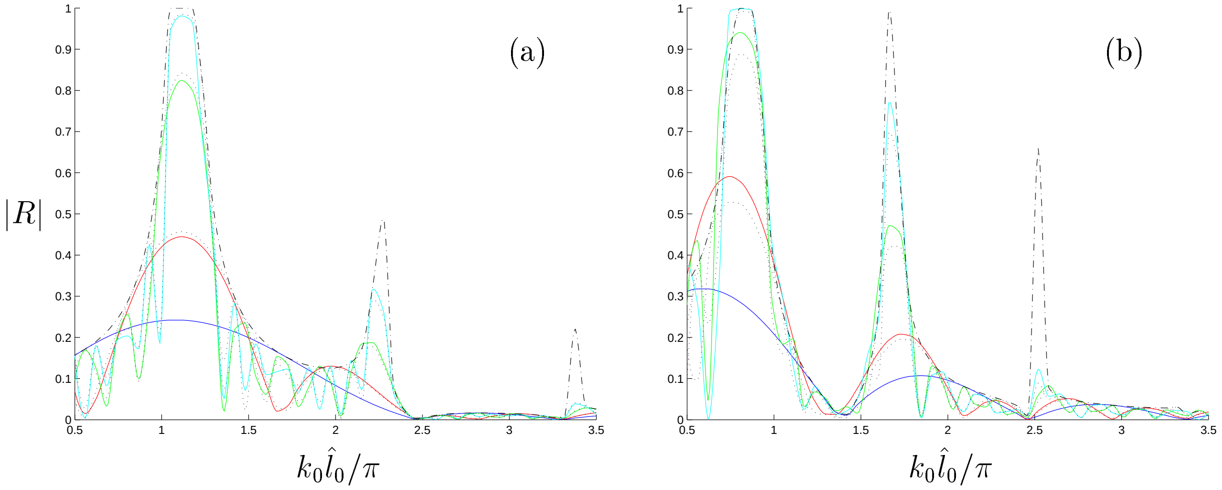

Figure 8.4: As in figure 8.3 but with amplitudes (a) $A_d = 0.5$m and (b) $A_d = -0.5$m.

It is observed that the intervals around the primary Bragg value, for which full resonance is captured in figures 8.4(a-b), are wide and are of approximately the same length.

The resonances at secondary Bragg values are also far more significant with the increased amplitudes, and, moreover, there are pronounced resonances developed at tertiary Bragg values. The strength of the resonant effects shown in this figure is notably larger than that discovered for free-surface flows, for instance that found by Porter & Porter (2003). Again, referring to §6.4, this phenomenon may be attributed to the considerable response given by waves of decreasing length to variations in the ice compared to the decaying response given when only bed variations are present.

We further note that resonances seen in figures 8.3-8.4 are not centred about the Bragg values but rather have a tendency to drift in a particular direction, a tendency that is exacerbated by the increased amplitude of the variations and as the Bragg value increases. For ripple beds this drift is well established but occurs in a leftward direction. In figures 8.3-8.4 we observe both rightward and leftward drifts, with the former appearing to be a property of a protrusion and the latter likewise of an indentation.

To investigate the occurrence of resonances it is illuminating to consider the behaviour of the wide-spacing approximation. In §8.3.2 it was shown that resonance is caused by one of the eigenvalues, $\mathrm{e}^{\pm\mathrm{i}p_0}$, of the transfer matrix for a single period, $P_{N,(0)}$, departing from the unit circle. Figure 8.5 plots these eigenvalues, for the problems considered in figure 8.4, where the amplitudes are of magnitude 0.5m, in the vicinity of a resonance. Figure 8.5(a) is the primary resonance for the protrusion problem and figure 8.5(b) the secondary resonance for the indentation problem.

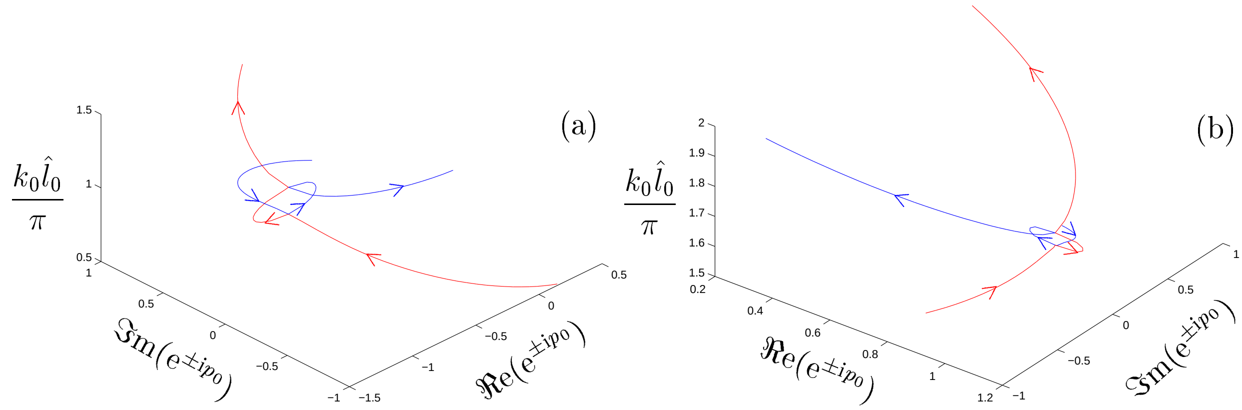

Figure 8.5: The eigenvalues, $\mathrm{e}^{\pm\mathrm{i}p_0}$, of the transfer matrix, $P_{1,(0)}$, as functions of the non-dimensional wavenumber, in vicinity of a Bragg resonance. In part (a) the geometry is as in figure 8.4(a), and in part (b) it is as in 8.4(b).

In both subfigures of figure 8.5 we see that the respective eigenvalues meet at the real axis as they approach from opposing directions along the unit circle, whence their paths temporarily cut onto the real axis, before returning to the unit circle. During this process their paths form a single loop, the length and amplitude of which are major factors in determining the size and strength of resonance caused. This behaviour is consistent with that seen for periodic problems in other settings, for example in free-surface flows (see Porter & Porter, 2003).

Taking the examples given in figure 8.5, we see that the resonance loop in figure 8.5(a) is far wider and of greater amplitude than that of figure 8.5(b), which corresponds to a more rapid build-up and a wider capture interval for the primary resonance of figure 8.4(a) than the secondary resonance of figure 8.4(b).

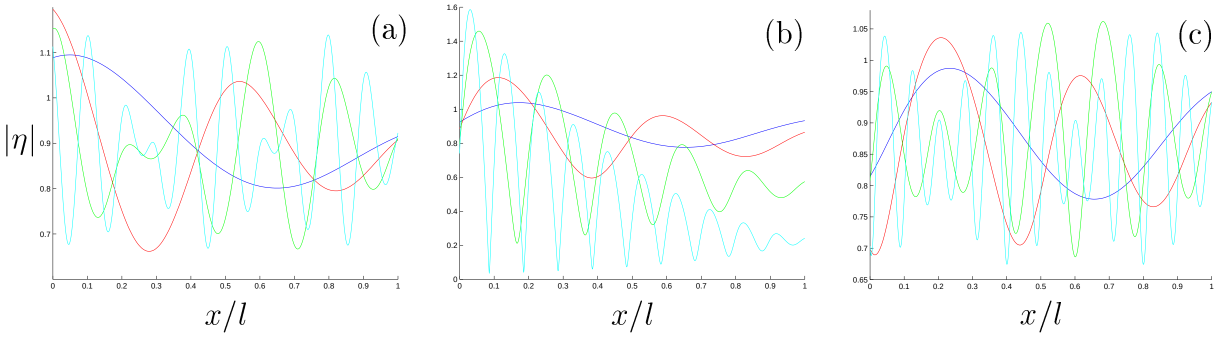

Figure 8.6: The modulus of the displacement function with the wave period passing through a primary resonance. The thickness of the ice is defined by equation (8.29) with $D_0 = 1$m, and period length $\hat{l}_0 = 2\pi$m, over a flat bed depth $h = 20$m. The number of periods is $M = 1$ (blue curves), $M = 2$ (red), $M = 5$ (green) and $M = 10$ (cyan). Each period of the lower surface of the ice contains a protrusion of amplitude $A_d = 0.5$m The non-dimensional wavenumbers used are (a) $k_0\hat{l}_0/\pi \approx 0.81$, (b) $k_0\hat{l}_0/\pi \approx 1.17$ and (c) $k_0\hat{l}_0/\pi \approx 1.42$.

The effects of resonance are also visible in the transverse oscillations of the ice sheet. In each of figures 8.6-8.8 a series of three subfigures display how the modulus of the reduced displacement function, $|\eta|$, behaves as the incident wavenumber passes through an interval of resonance. To enable comparison with the corresponding reflected amplitudes, the geometrical configurations are those considered in figures 8.3-8.4 and results are again given for one, two, five and ten periods.

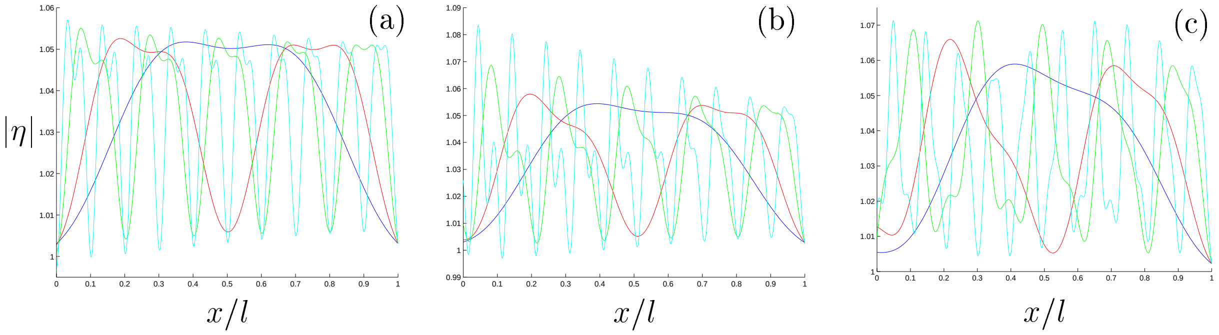

Figure 8.7: As in figure 8.6 but for indentations, $A_d = -0.1$m. The wavenumber passes through secondary resonance, with (a) $k_0\hat{l}_0/\pi \approx 1.91$, (b) $k_0\hat{l}_0/\pi \approx 1.97$ and (c) $k_0\hat{l}_0/\pi \approx 2.10$.

To either side of a resonant interval the maximum displacement of the ice is bounded as the number of periods is increased. In some cases the bounds are those attained by the single period (see figures 8.8(a),(c)). Conversely, at resonant frequencies, the amplitude of the waves travelling along the underside of the ice sheet increases with the number of periods. As may be expected, the magnitude of amplification is related to the degree of resonance displayed by the reflected energy; so that, the resonance around the primary Bragg values seen in figure 8.6(b) for amplitude $A_d = 0.5$m, are more extreme than the $A_d = -0.1$m secondary resonance of figure 8.7(b) or the $A_d = 0.5$m tertiary resonance of figure 8.8(b).

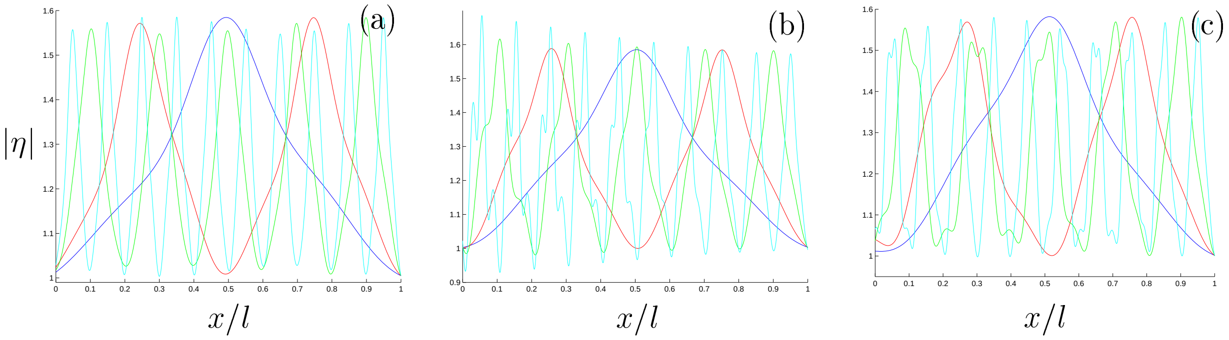

Figure 8.8: As in figure 8.6 but for indentations, $A_d = -0.5$m. The wavenumber passes through tertiary resonance, with (a) $k_0\hat{l}_0/\pi \approx 2.40$, (b) $k_0\hat{l}_0/\pi \approx 2.52$ and (c) $k_0\hat{l}_0/\pi \approx 2.64$.

At this point, it is of interest to consider a property of the ice other than its transverse displacement, namely the bending moment imposed on the ice by the incident wave. This is the quantity defined in (2.22a) and is one for which continuity is dictated at the interface between ice-covered domains. The bending moment is a vertically integrated measure of the stress experienced by the ice (see Timoshenko & Woinowsky-Kreiger, 1959). It is therefore associated with the issue of fracture and is consequently of physical interest. For two-dimensional motion and normal incidence, the bending moment, parallel to the x-axis, is defined by

$$\mathfrak{M}\eta = \beta\partial_x^2\eta.$$

Our solution method, therefore, directly supplies us with an approximation to this quantity via the function $\chi^{(2)} \equiv \beta\partial_x^2\chi$ (see section §4.1).

In figure 8.9 approximations to the maximum value of $\mathfrak{M}\eta$, attained across the interval $x \in (0, l)$, are considered as continuous functions of $k_0\hat{l}_0/\pi$, for the parameters and geometrical configurations used in figures 8.3(a) and 8.4(b). Again, it is only the incident wavenumber, k_0, that varies and it is clear that maximum bending moment and incident wavenumber have a typically positive correlation. This is easily understood if we consider the bending moment of the incident wave, which is

$$\chi_I^{(2)} = \beta k_0^2 \mathrm{e}^{\mathrm{i}k_0 x},$$

(see §4.2) and hence has an amplitude that increases quadratically with k_0. Intuitively, we infer that shorter incident waves impose a greater bending force on the ice.

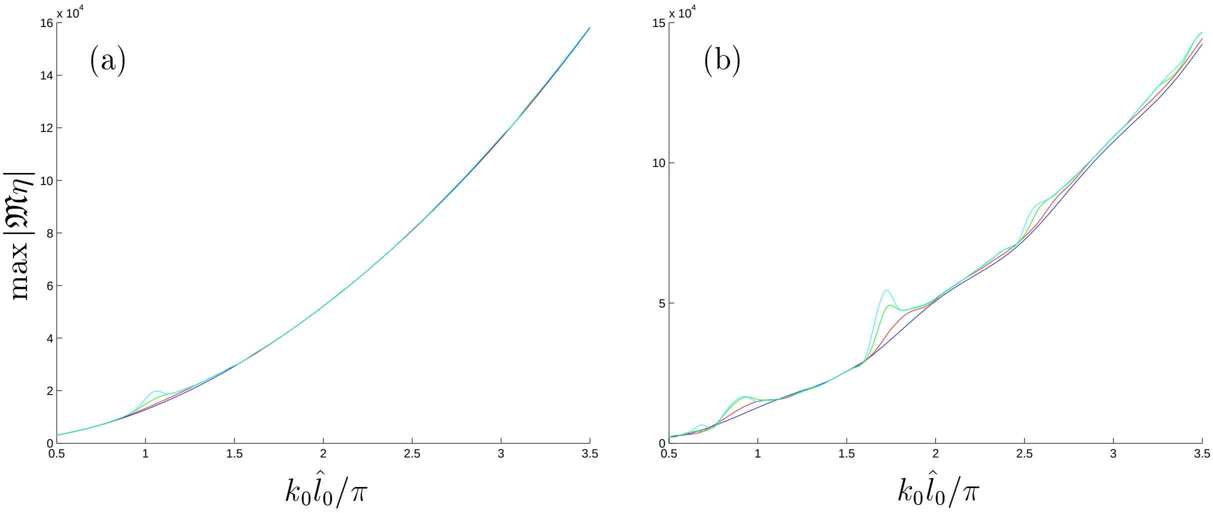

Figure 8.9: The maximum bending moment experienced by ice over the periodic array as a function of non-dimensional wavenumber. The geometry used is that of (a) figure 8.3(a) and (b) figure 8.4(b). The number of periods is $M = 1$ (blue curves), $M = 2$ (red), $M = 5$ (green) and $M = 10$ (cyan).

The monotonic relationship between the maximum bending moment and the incident wavenumber is broken only by resonant effects. If we consider the size of the maximum value of $\mathfrak{M}\eta$ after ten periods, attained at each incident wavelength, in the context of the wide interval of incident wavelengths used here, these resonant effects are insignificant compared to the quadratic shape of the curve. However, in the subintervals of resonance bandwidth, their effect is notable. The most prominent case is the secondary resonance seen in figure 8.9(b), where the maximum bending moment increases by a factor of approximately 1.51 from one to ten periods. Thus, in an interval of wavenumber centred on a Bragg value, the occurrence of Bragg resonance is the primary factor in determining the possibility of fracture.

The drift of the resonant intervals away from the Bragg values has already been noted in this section. A tendency for leftward drift to be associated with thinning ice and rightward drift to be associated with thickening ice was also remarked upon. The occurrence of rightward drift, we believe, is a phenomenon hitherto unseen in mathematical models of fluid flow. In figure 8.10 we continue to investigate the properties and causes of these drifts.

It was observed through figures 8.3-8.4 that the extent of the drift is largely governed by

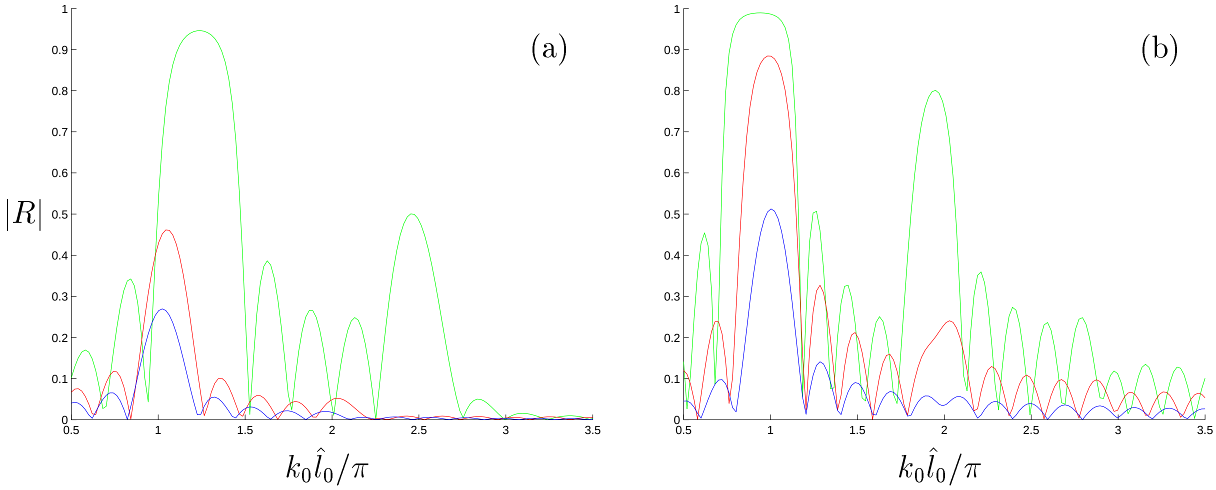

Figure 8.10: Moduli of reflected amplitudes as functions of non-dimensional wavenumber after five periods ($M = 5$). In part (a) the lower surface of the ice contains protrusions and the ice thickness is defined by (8.29), with amplitude $A_d = 0.1$ and $D_0 = 1$m (blue curve), $D_0 = 0.5$m (red) and $D_0 = 0.1$m (green). In part (b) the lower surface of the ice undulates with the ice thickness defined by (8.30), for $D_0 = 1$m and amplitudes $A_p = 0.1$m (blue curve), $A_p = 0.25$m (red) and $A_p = 0.5$m (green). In both situations $h = 20$m and the period length is $\hat{l}_0 = 2\pi$m.

the relative magnitude of obstruction present. Furthermore, the drift is more pronounced around higher order Bragg values. Both of these properties are clearly visible in figure 8.10(a) with drifts around the primary Bragg value growing as the size of the keel grows in relation to the overall ice thickness, and, for the $D = 0.1$m problem, the drift increasing with Bragg value, so that the secondary resonance is actually clear of $k_0\hat{l}_0 = 2\pi$.

If the scattering problem is considered in terms of formal perturbation theory then these issues may be attributed to the rôle of the second-order terms. A full investigation of the generation of drifts using perturbation methods is an area left open for further work.

We have thus far only considered geometrical configurations in which the ice is either thicker in the varying interval than the far-fields or likewise thinner. In figure 8.10(b) sinusoidal periods of the form

$$D(x_0) = D_0 + A_p \sin\left(\frac{2\pi x_0}{\hat{l}_0}\right), \tag{8.30}$$

are taken so that the variation about the surrounding states is equal. The tendency displayed is for leftward drift, from which we deduce that there are factors, independent of the direction of geometrical variation, that determine the drift, and that these work with the effects caused by thinning ice and against those of thickening ice. This explains why the responses shown to thinning ice are greater than those of thickening ice.

8.5 Conclusions

The periodic problem that has been formulated and numerically solved in this chapter is a modification of the two-dimensional complete ice-cover problem that appeared in §4.3.1 and §6. In §8.1 the numerical solution of the complete ice-cover problem provided in §4.3.1 was reformulated through the addition of intermediate boundaries. This necessitated the retention of the evanescent amplitudes, which were disregarded previously, as they play an active rôle between neighbouring subintervals. As well as providing a platform for the periodic problem, this formulation gives a means of solving for geometries in which there are more than two internal boundaries. One such problem was available in existing literature and we compared MMAs successfully with this data in §8.2.

For the periodic problem, the overall interval is built up of an arbitrary number of identical periods. Our method allows the solution to such a scattering problem to be found using information calculated from a single period only. This constitutes a substantial numerical saving and allows insight into the occurrence of resonances. A wide-spacing approximation that is more efficient and accessible but ignores the interaction of evanescent waves with the propagating waves, between the periods, was also constructed.

The data that were produced for the results section of this chapter centred on the production of resonances around Bragg values. It was noted that, due to the tendency of the ice to elongate propagating waves, these Bragg values are less inclined to coincide with physically realistic values than, for instance, those in the analogous free-surface situation.

Strong resonant effects were found to be created in the far-field, for modest geometrical constructions, around the primary, secondary and tertiary Bragg values, with large responses quickly generated as the number of periods was increased and often wide intervals of resonance capture. Although full resonance was only observed at the primary Bragg value for the steepest obstruction, a significant local response was seen for all Bragg values considered and even for reasonably mild obstructions. The far-field resonances were seen to be reflected in the properties of the ice. Specifically, around Bragg values the ice experiences a locally disproportionate displacement and bending force. Consequently, it is more susceptible to fracture at these points.

For approximations to the reflected amplitude, the wide-spacing method provided a good approximation in all of the examples used. As expected, its accuracy decreased with an increased amplitude of the obstruction. Significantly, the resonances predicted by the wide-spacing approximations were found to be consistent with the true resonances displayed by the full approximation. As in periodic problems in other settings, for example free-surface flows, the onset of resonance in the wide-spacing approximation can be attributed to a coalescence of the eigenvalues of the transfer matrix on a single period and is therefore easily classified.

It is well known for free-surface flows that the peaks of resonance never exactly coincide with Bragg values and this was seen to be consistent when ice-cover is present. Rather, a drift appears and is found to increase with the relative amplitude of the impediment and order of Bragg value about which the resonance emerged. We found drifts in both directions from the Bragg values and a link was drawn between leftward drift and thinning ice, and rightward drift and thickening ice. In the absence of any bias towards thickening or thinning of the ice the drift was leftward. The occurrence of rightward drift is a property that does not appear to have previously been documented in fluid flow problems.

Chapter 9

An axisymmetric ice floe

Thus far, we have formulated numerical procedures only for problems of a two-dimensional nature. The presentation of the structure of the MMA in §3 was made in three dimensions, which allows us to consider more realistic models of ice floes. One such example is the subject of this chapter.

In the following section we will outline a technique for solving the problem of a circular ice floe in an otherwise ice-free domain that stretches to infinity in all horizontal directions. Scattering is induced by a plane incident wave that propagates from the far-field. The ice is, of course, permitted to contain geometrical variations; however, we restrict these geometrical variations to be of an axisymmetric form. In particular, this allows its azimuthal dependence to be represented in the form of a Fourier cosine series, so that computations may be made at a reduced cost. A graphical representation of this configuration is given in figures 9.1-9.2.

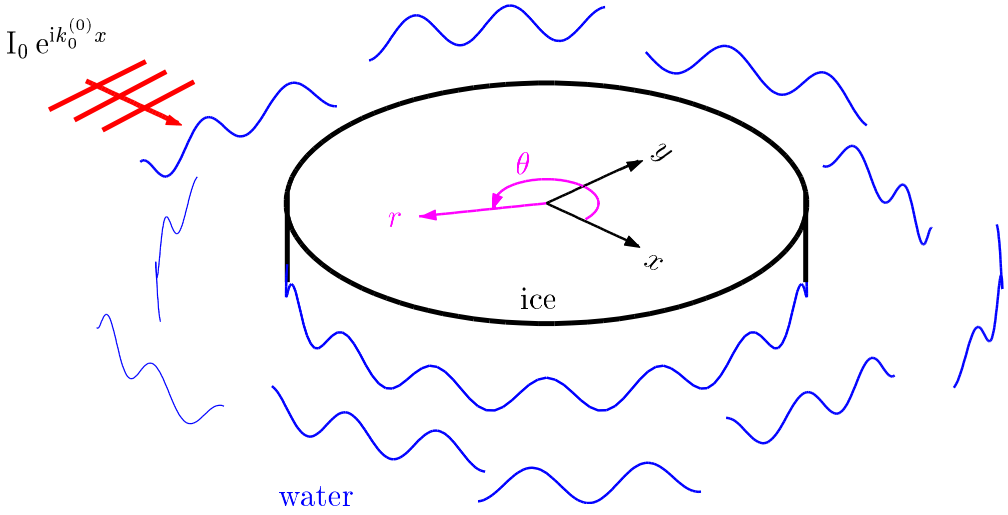

Figure 9.1: Three-dimensional representation of the geometry.

9.1 Formulation

In this section we will outline the procedure that will be used to calculate MMAs to the axisymmetric ice floe problem described above. Recall that the general form of the differential system that governs the MMA in an ice-covered domain is given by

$$\sum_{i=0}^{N}\Big\{\nabla\cdot(a_{j,i}\nabla\varphi_i)+\widetilde{\mathbf{d}}_{j,i}\cdot(\nabla\varphi_i)+b_{j,i}\varphi_i\Big\}+\kappa\chi[w_j]_{z=-d}=0\quad(j=0,\ldots,N),\tag{9.1a}$$

where the coefficients $a_{j,i}$, $\widetilde{\mathbf{d}}_{j,i}$ and $b_{j,i}$ are defined in §3.2.1, and

$$(1-\kappa\alpha)\chi+\mathscr{L}\chi-\sum_{i=0}^{N}\varphi_i[w_i]_{z=-d}=0.\tag{9.1b}$$

The equivalent equations in an ice-free domain are

$$\sum_{i=0}^{N}\Big\{\nabla\cdot(a_{j,i}^{(0)}\nabla\varphi_i^{(0)})+\widetilde{\mathbf{d}}_{j,i}^{(0)}\cdot(\nabla\varphi_i^{(0)})+b_{j,i}^{(0)}\varphi_i^{(0)}\Big\}=0\quad(j=0,\ldots,N),\tag{9.2}$$

where the coefficients are also given in §3.2.1.

Without loss of generality, we suppose that the origin of the horizontal coordinate system is set to coincide with the centre of the ice floe, so that equations (9.1a-b) hold in the disc $x^2+y^2<R^2$, where R denotes the radius of the floe. Equations (9.2) then hold in the region $x^2+y^2>R^2$. At the edge of the floe, $x^2+y^2=R^2$, the solutions from the ice-covered and ice-free regions are linked by the jump conditions

$$V^T\mathbf{\Phi}_N=(V^T\mathbf{\Phi}_N)^{(0)},\tag{9.3a}$$

and

$$V^{-1}A\partial_n\mathbf{\Phi}_N+J\mathbf{\Phi}_N=\{V^{-1}A\partial_n\mathbf{\Phi}_N+J\mathbf{\Phi}_N\}^{(0)},\tag{9.3b}$$

where

$$\mathbf{\Phi}_N=(\varphi_0,\ldots,\varphi_N)^T,\quad \mathbf{\Phi}_N^{(0)}=\left(\varphi_0^{(0)},\ldots,\varphi_N^{(0)}\right)^T.$$

There are also the conditions that dictate that the bending moment and shearing stress both vanish at the ice edge, which are defined by

$$\mathfrak{M}\chi=\mathfrak{S}\chi=0,$$

where the operators $\mathfrak{M}$ and $\mathfrak{S}$ are defined in equations (2.22a-b).

We are free to set the incident wave so that it propagates along the x-axis from the far-field $x \to -\infty$ and it is therefore given by

$$\phi_I(x, y, z) = \mathrm{I}_0 \mathrm{e}^{\mathrm{i}k_0^{(0)}x} \cosh\{k_0^{(0)}(z + h_0)\}, \tag{9.4}$$

where, as usual, h_0 is the bed depth in the far-field and $k_0^{(0)}$ is the corresponding propagating wavenumber. As previously, the incident amplitude will be set as

$$\mathrm{I}_0 = \frac{\kappa}{\sinh(k_0^{(0)}h_0)k_0^{(0)}}, \tag{9.5}$$

to ensure that the incident wave has a displacement of 1m amplitude at the free-surface, regardless of its frequency. The problem is therefore symmetric about the y-axis and this will be utilised in our method of solution.

Considering the circular shape of the floe, it is pertinent to switch from the horizontal cartesian coordinates, (x, y), to the polar coordinates, (r, θ), using the transformation

$$x = r\cos(\theta), \quad y = r\sin(\theta), \tag{9.6}$$

in which $r > 0$ and $0 \leq \theta < 2\pi$.

The floe therefore occupies the domain $r < R$, for all θ. Under the constraints of axisymmetry, the geometrical variations that occur, within this circular region, must be independent of the azimuthal coordinate θ, so that

$$D = D(r), \quad h = h(r), \quad d = d(r) \quad (r \leq R),$$

for all θ. Note that, for generality, we also permit the bed to vary beneath the ice floe; however, bed undulations are not our primary concern and thus are not investigated in the results section. Outside of the ice-covered region the bed depth is assumed to be uniform, with $h = h_0$ a constant in $r > R$.

Having made the transformation to polar coordinates, we redefine the MMA in terms of these variables. In the ice-covered region, $r < R$, we have the MMA to the reduced velocity potential $\phi \approx \psi_N$, where, assuming the use of the natural modes,

$$\psi_N = \psi_N(r, \theta, z) = \sum_{n=0}^{N} \varphi_n(r, \theta) w_n(r, z), \quad w_n = \varpi_n(r) \cosh\{k_n(r)(z + h(r))\} \tag{9.7a}$$

and the associated, indirect approximation of the reduced displacement function $\eta \approx \chi = \chi(r, \theta)$. In the ice-free region, $r > R$, the MMA is $\phi^{(0)} \approx \psi_N^{(0)}$, where

$$\psi_N^{(0)} = \psi_N^{(0)}(r, \theta, z) = \sum_{n=0}^{N} \varphi_n^{(0)}(r, \theta) w_n^{(0)}(r, z), \quad w_n^{(0)} = \varpi_n^{(0)} \cosh\{k_n^{(0)}(z + h_0)\}. \tag{9.7b}$$

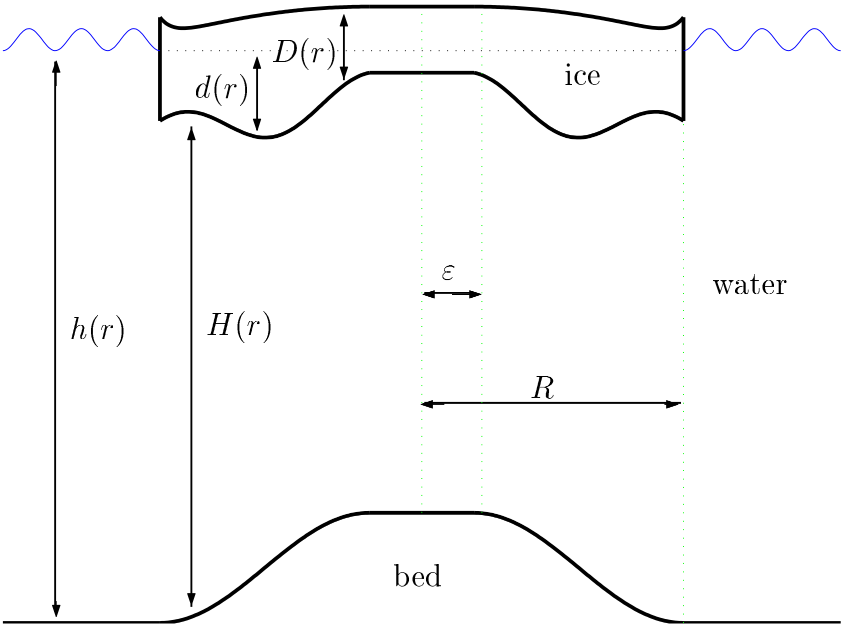

Figure 9.2: Two-dimensional cross-section of the axisymmetric floe.

The roots $k_n^{(0)}$ $(n=0,\ldots,N)$ are constants, due to the uniform bed in this region.

9.1.1 Governing equations

In §4.1 we used the specific degeneracies of the two-dimensional geometry with oblique incidence to reduce the governing equations of the MMA, equations (9.1a-b) and (9.2), to (4.3a-b) and (4.6) with accompanying jump conditions. In the same manner, we must use the properties of the current, axisymmetric problem to generate a set of equations to be satisfied by the MMA that is numerically solvable.

Making the transformation to polar coordinates, the gradient operator becomes

$$\nabla \equiv \left(\cos(\theta)\partial_r - \frac{1}{r}\sin(\theta)\partial_\theta, \sin(\theta)\partial_r + \frac{1}{r}\cos(\theta)\partial_\theta\right), \tag{9.8}$$

and the Laplacian operator is given by

$$\nabla^2 \equiv \partial_r^2 + \frac{1}{r}\partial_r + \frac{1}{r^2}\partial_\theta^2.$$

The polar differential operators are defined as $\partial_r \equiv \partial/\partial r$ and $\partial_\theta \equiv \partial/\partial\theta$.

Using the axisymmetry of the geometry, we find that, in terms of the polar coordinates, the system of partial differential equations (9.1a), for this problem, degenerates to

$$\frac{1}{r}\partial_r(rA\partial_r\mathbf{\Phi}) + \widetilde{D}\partial_r\mathbf{\Phi} + \left(B + \frac{1}{r^2}A\partial_\theta^2\right)\mathbf{\Phi} + \kappa C\mathbf{f}\chi = \mathbf{0}, \tag{9.9a}$$

which is to be solved for the vector of unknown functions $\mathbf{\Phi}(r,\theta)$. As always, the entries of the matrices are defined as $A_{j,i}=a_{j-1,i-1}$, $\widetilde{D}_{j,i}=\widetilde{d}_{j-1,i-1}$ and $B_{j,i}=b_{j-1,i-1}$ $(i,j=1,\dots,N+1)$, where, in this case

$$a_{j,i}=(W_j,W_i),\quad \widetilde{d}_{j,i}=(P^{(D)}_{j,i}-P^{(D)}_{i,j})\partial_r D+(P^{(h)}_{j,i}-P^{(h)}_{i,j})\partial_r h+(P^{(d)}_{j,i}-P^{(d)}_{i,j})\partial_r d,$$

and

$$\begin{aligned} b_{j,i} \;=\;& k_i^2 a_{j,i}-k_j\sinh(k_jH)\cosh(k_iH)+P^{(D)}_{j,i}\partial_r^2 D+P^{(h)}_{j,i}\partial_r^2 h+P^{(d)}_{j,i}\partial_r^2 d\\ &+P^{(D,D)}_{j,i}(\partial_r D)^2+P^{(h,h)}_{j,i}(\partial_r h)^2+P^{(d,d)}_{j,i}(\partial_r d)^2\\ &+(P^{(D,h)}_{j,i}+P^{(h,D)}_{j,i})(\partial_r D)(\partial_r h)+(P^{(D,d)}_{j,i}+P^{(d,D)}_{j,i})(\partial_r D)(\partial_r d)\\ &+(P^{(d,h)}_{j,i}+P^{(h,d)}_{j,i})(\partial_r d)(\partial_r h), \end{aligned}$$

with the quantities $P^{(X)}_{j,i}$ and $P^{(X,Y)}_{j,i}$ $(X,Y=D,h,d)$ being defined in §3.2.1. We also remind ourselves that the matrix $C=\mathrm{diag}\{[w_0]_{z=-d},\dots,[w_N]_{z=-d}\}$ and the vector $\mathbf{f}=(1,\dots,1)^T$. Similarly, the coupled fourth-order equation (9.1b) becomes

$$(1-\kappa\alpha)\chi+\mathscr{L}\chi-\mathbf{f}^TC\mathbf{\Phi}=0, \tag{9.9b}$$

where the operator $\mathscr{L}$ is now defined by

$$\mathscr{L}\chi\equiv\nabla^2\left(\beta\nabla^2\chi\right)-(1-\nu)\left\{\frac{1}{r}\partial_r\left((\partial_r\beta)(\partial_r\chi)\right)+\frac{1}{r^2}(\partial_r^2\beta)(\partial_\theta^2\chi)\right\}.$$

In the ice-free region, equivalent simplifications change (9.2) into

$$\frac{1}{r}\partial_r(rA^{(0)}\partial_r\mathbf{\Phi}^{(0)})+\widetilde{D}^{(0)}\partial_r\mathbf{\Phi}^{(0)}+\left(B^{(0)}+\frac{1}{r^2}A^{(0)}\partial_\theta^2\right)\mathbf{\Phi}^{(0)}=\mathbf{0}, \tag{9.10}$$

which is to be solved for $\mathbf{\Phi}^{(0)}(r,\theta)$. The matrices are defined as $A^{(0)}_{j,i}=a^{(0)}_{j-1,i-1}$, $\widetilde{D}^{(0)}_{j,i}=\widetilde{d}^{(0)}_{j-1,i-1}$ and $B^{(0)}_{j,i}=b^{(0)}_{j-1,i-1}$ $(i,j=1,\dots,N+1)$, for the coeffficients

$$a^{(0)}_{i,j}=(W_i,W_j)^{(0)},\quad \widetilde{d}^{(0)}_{j,i}=(P^{(0)}_{j,i}-P^{(0)}_{i,j})\partial_r h,$$

and

$$b^{(0)}_{j,i}=(k_i^{(0)})^2a^{(0)}_{j,i}+P^{(0)}_{j,i}\nabla^2 h+P^{(0,0)}_{j,i}(\nabla h)^2.$$

Again, the quantities $P^{(0)}_{j,i}$ and $P^{(0,0)}_{j,i}$ are defined in §3.2.1. Note that, we have not, as yet, utilised the degeneracies that result from the flat bed in the ice-free region in (9.10).

We will denote the circular contour that defines the edge of the floe as $\Gamma=\{r=R,\ 0\le\theta<2\pi\}$. In §2.2.1 the normal and tangential vectors to this contour were represented by

$$\mathbf{n} = (\cos\Theta, \sin\Theta), \quad \mathbf{s} = (-\sin\Theta, \cos\Theta),$$

respectively, where Θ is the angle of Γ with respect to the cartesian frame. Here $\Theta = \Theta(\theta) = \theta$. Using (9.8), the corresponding derivative operators may be expressed in polar coordinates as

$$\partial_n = \mathbf{n} \cdot \nabla = \partial_n, \quad \partial_s = \mathbf{s} \cdot \nabla = \frac{1}{r}\partial_\theta, \tag{9.12}$$

and it follows that $\partial_s \Theta = r^{-1}$.

From definitions (9.12), we find that the jump conditions (9.3a-b) applied at Γ take the form

$$V^T \mathbf{\Phi}_N = (V^T \mathbf{\Phi}_N)^{(0)} \quad (r, \theta) \in \Gamma, \tag{9.13a}$$

and

$$V^{-1}\{A\partial_r \mathbf{\Phi}_N + Q\mathbf{\Phi}_N\} = (V^{(0)})^{-1} A^{(0)} \partial_r \mathbf{\Phi}_N^{(0)} \quad (r, \theta) \in \Gamma. \tag{9.13b}$$

Furthermore, the bending moment and shearing stress along a circular contour, such as Γ, are deduced to be

$$\mathfrak{M}\chi \equiv \beta\nabla^2\chi - (1-\nu)\beta\left(\frac{1}{r}\partial_r + \frac{1}{r^2}\partial_\theta^2\right)\chi,$$

and

$$\mathfrak{S}\chi \equiv \partial_r\left(\beta\nabla^2\chi\right) - (1-\nu)\left\{(\partial_r\beta)\left(\frac{1}{r}\partial_r + \frac{1}{r^2}\partial_\theta^2\right)\chi - \frac{1}{r}\beta\partial_r\left(\frac{1}{r}(\partial_\theta^2\chi)\right)\right\}.$$

These quantities must vanish at the ice edge, which means that

$$\mathfrak{M}\chi = \mathfrak{S}\chi = 0 \quad (r, \theta) \in \Gamma. \tag{9.15}$$

The problem also requires the specification of its far-field behaviour. For a three-dimensional problem, such as this, the scattered solution must decay according to the *Sommerfeld radiation condition* (see, for example, Wehausen & Laitone, 1960), which states that

$$\sqrt{r}\left(\partial_r - \mathrm{i}k_0^{(0)}\right)(\phi - \phi_I) \to 0 \quad (r \to \infty) \tag{9.16}$$

uniformly in θ, where $\phi - \phi_I$ represents the scattered solution. Therefore, the only motion that exists in the far-field is that of the incident wave. The governing equations of the MMA are now fully defined by the differential systems (9.9a-b) and (9.10), the jump conditions (9.13a-b), the ice edge conditions (9.15) and the Sommerfeld radiation condition (9.16).

9.1.2 Decomposition of the azimuthal motion

As we include the vertical mode, $w_0^{(0)}$, that bears propagating waves, in our trial space, the incident wave (9.4) is represented exactly in the MMA by

$$\begin{aligned} \psi_I &= \mathrm{I}_0 \mathrm{e}^{\mathrm{i}k_0^{(0)}x} \cosh\{k_0^{(0)}(z+h_0)\} \\ &= \mathrm{I}_0 \mathrm{e}^{\mathrm{i}k_0^{(0)}r\cos(\theta)} \cosh\{k_0^{(0)}(z+h_0)\} \\ &= \mathrm{I}_0 \left\{ \mathrm{J}_0(k_0^{(0)}r) + 2\sum_{m=1}^{\infty} \mathrm{i}^m \mathrm{J}_m(k_0^{(0)}r)\cos(m\theta) \right\} \cosh\{k_0^{(0)}(z+h_0)\}. \end{aligned} \tag{9.17}$$

The final expression given for the incident wave, for which the azimuthal motion appears in the form of a Fourier cosine series, is produced via the identity

$$\mathrm{e}^{\frac{1}{2}\xi(\varsigma-\frac{1}{\varsigma})} = \sum_{m=-\infty}^{\infty} \varsigma^m \mathrm{J}_m(\xi),$$

(see, for example, Tranter, 1968). The functions J_m ($m = 0, \dots$) are Bessel functions of the first kind, of order m.

It will prove to be beneficial to decompose all of the azimuthal motion into its Fourier cosine modes, which reflects the form given in the final expression, (9.17), of the incident wave. Therefore, we write the unknown functions as

$$\varphi_n(r,\theta) = \mathrm{I}_0 \left\{ \varphi_{n,0}(r) + 2\sum_{m=1}^{\infty} \mathrm{i}^m \varphi_{n,m}(r)\cos(m\theta) \right\},$$

$$\chi(r,\theta) = \mathrm{I}_0 \left\{ \chi_0(r) + 2\sum_{m=1}^{\infty} \mathrm{i}^m \chi_m(r)\cos(m\theta) \right\},$$

and

$$\varphi_n^{(0)}(r,\theta) = \mathrm{I}_0 \left\{ \varphi_{n,0}^{(0)}(r) + 2\sum_{m=1}^{\infty} \mathrm{i}^m \varphi_{n,m}^{(0)}(r)\cos(m\theta) \right\}$$

for $n = 0, \dots, N$, and the corresponding vectors are

$$\mathbf{\Phi}_N(r,\theta) = \mathrm{I}_0 \left\{ \mathbf{\Phi}_{N,0}(r) + 2\sum_{m=1}^{\infty} \mathrm{i}^m \mathbf{\Phi}_{N,m}(r)\cos(m\theta) \right\},$$

and

$$\mathbf{\Phi}_N^{(0)}(r,\theta) = \mathrm{I}_0 \left\{ \mathbf{\Phi}_{N,0}^{(0)}(r) + 2\sum_{m=1}^{\infty} \mathrm{i}^m \mathbf{\Phi}_{N,m}^{(0)}(r)\cos(m\theta) \right\}. \tag{9.19}$$

Our job is now to calculate the unknowns $\varphi_{n,m}$, $\varphi_{n,m}^{(0)}$ ($n = 0, \dots, N$) and χ_m for $m = 0, \dots,$ which are functions of the radial coordinate only. Each of these functions is then forced by the corresponding azimuthal mode of the incident wave, (9.17). Note that the representation in terms of a Fourier cosine series reflects the symmetry of the problem about the y-axis.

If we substitute the above expressions for $\mathbf{\Phi}_N$ and χ into the governing differential equations (9.9a) and (9.9b), then the azimuthal modes decouple and we are left to solve the ordinary differential system

$$\frac{1}{r}\partial_r(rA\partial_r\mathbf{\Phi}_{N,m}) + \widetilde{D}\partial_r\mathbf{\Phi}_{N,m} + \left(B - \frac{m^2}{r^2}A\right)\mathbf{\Phi}_{N,m} + \kappa C\mathbf{f}\chi_m = \mathbf{0}, \tag{9.20a}$$

and the coupled fourth-order ordinary differential equation

$$(1-\kappa\alpha)\chi_m + \mathscr{L}_m\chi_m - \mathbf{o}^T C\mathbf{\Phi}_{N,m} = 0, \tag{9.20b}$$

for $m = 0, \ldots,$ where

$$\mathscr{L}_m\chi_m \equiv \nabla_m^2\left(\beta\nabla_m^2\chi_m\right) - (1-\nu)\left\{\frac{1}{r}\partial_r\left((\partial_r\beta)(\partial_r\chi_m)\right) - \frac{m^2}{r^2}(\partial_r^2\beta)\chi_m\right\},$$

and

$$\nabla_m^2\chi_m \equiv \frac{1}{r}\partial_r(r\partial_r\chi_m) - \frac{m^2}{r^2}\chi_m.$$

Mimicking the two-dimensional case of §4.1, we condense equations (9.20a-b) into the single expression

$$\frac{1}{r}\partial_r(r\mathcal{A}\partial_r\mathbf{\Psi}_{N,m}) + \widetilde{\mathcal{D}}\partial_r\mathbf{\Psi}_{N,m} + \mathcal{B}^{(m)}\mathbf{\Psi}_{N,m} = \mathbf{0} \quad (m = 0, \ldots), \tag{9.21}$$

which is to be solved for the vector of unknowns

$$\mathbf{\Psi}_{N,m} = \left(\mathbf{\Phi}_{N,m}^T, \chi_m^{(1)}, \chi_m^{(2)}\right)^T,$$

where $\chi_m^{(1)} = \chi_m$ and $\chi_m^{(2)} = \beta\nabla_m^2\chi_m$. The entries of the three matrices that appear in (9.21) are defined by

$$\mathcal{A}_{j,i} = A_{j,i}, \quad \mathcal{B}_{j,i}^{(m)} = B_{j,i} - \frac{m^2}{r^2}A_{j,i}, \quad \widetilde{\mathcal{D}}_{j,i} = \widetilde{D}_{j,i} \quad (i,j = 1, \ldots, N+1),$$

$$\mathcal{A}_{N+2,N+2} = \mathcal{A}_{N+3,N+3} = 1, \quad \mathcal{B}_{i,N+2}^{(m)} = \kappa\mathbf{I}_i^T C\mathbf{f} \quad (i = 1, \ldots, N+1),$$

$$\mathcal{A}_{N+3,N+2} = -(1-\nu)\frac{1}{r}(\partial_r\beta), \quad \mathcal{B}_{N+2,N+3}^{(m)} = -\beta^{-1}, \quad \mathcal{B}_{N+3,j}^{(m)} = -\mathbf{f}^T C\,\mathbf{I}_j$$

for $j = 1, \ldots, N+1$, and

$$\mathcal{B}_{N+2,N+2}^{(m)} = \mathcal{B}_{N+3,N+3}^{(m)} = -\frac{m^2}{r^2}, \quad \mathcal{B}_{N+3,N+2}^{(m)} = (1-\nu)(\partial_r^2\beta)\frac{m^2}{r^2} + 1 - \kappa\alpha,$$

with all unspecified values equal to zero and where, again, $[\ \mathbf{I}_1, \ \ldots, \ \mathbf{I}_{N+1}\ ]$ is the identity matrix of size $(N+1)$. Similarly, inserting expression (9.19) into the partial differential system (9.10) results in

$$\frac{1}{r}\partial_r(rA^{(0)}\partial_r\mathbf{\Phi}^{(0)}_{N,m}) + \widetilde{D}^{(0)}\partial_r\mathbf{\Phi}^{(0)}_{N,m} + \left(B^{(0)} - \frac{m^2}{r^2}A^{(0)}\right)\mathbf{\Phi}^{(0)}_{N,m} = \mathbf{0} \quad (m = 0, \ldots), \tag{9.22}$$

after decoupling the azimuthal modes. As in the case of two-dimensional motion, we have redefined the notation of the active differential operator, namely ∂_r, so that it now represents the full derivative, that is $\partial_r \equiv \mathrm{d}/\mathrm{d}r$.

We have succeeded in reducing the partial differential equations that govern the MMA, for an axisymmetric ice floe, to a set of ordinary differential equations in the radial coordinate. This reduction was possible since we were able to take advantage of the properties of the geometry, specifically the axisymmetry, to define a set of azimuthal modes that decouple and hence remove the coordinate θ from our calculations. In practice, we will set a tolerance on the accuracy of the MMA with respect to the convergence in the azimuthal modes. We therefore restrict the azimuthal modes to a finite number, $(M+1)$ say, so that the MMA of vertical dimension N is approximated as

$$\varphi_n(r,\theta) \approx \mathrm{I}_0\left\{\varphi_{n,0}(r) + 2\sum_{m=1}^{M}\mathrm{i}^m\varphi_{n,m}(r)\cos(m\theta)\right\}, \tag{9.23a}$$

$$\chi(r,\theta) \approx \mathrm{I}_0\left\{\chi_0(r) + 2\sum_{m=1}^{M}\mathrm{i}^m\chi_m(r)\cos(m\theta)\right\}, \tag{9.23b}$$

and

$$\varphi^{(0)}_n(r,\theta) \approx \mathrm{I}_0\left\{\varphi^{(0)}_{n,0}(r) + 2\sum_{m=1}^{M}\mathrm{i}^m\varphi^{(0)}_{n,m}(r)\cos(m\theta)\right\} \tag{9.23c}$$

for $n = 0, \ldots, N$, and it is our conjecture that only a relatively small number of these azimuthal modes will provide good accuracy. This is the topic of results section §10.2.1.

Having made the approximations (9.23a-c) to the MMA, by restricting the azimuthal motion to a finite set of Fourier cosine modes, we are left to solve a set of $(M+1)$ ordinary differential equations in the radial coordinate. In a region of ice-covered fluid each ODE is of dimension $(2N+6)$, whereas in ice-free regions the dimension is $(2N+2)$. It is now necessary to calculate the conditions that link the approximations at the edge of the circular floe.

By applying the jump conditions (9.13a-b) to our approximations (9.23a-c), it is a simple matter to decouple the azimuthal modes and deduce that the conditions

$$V^T\mathbf{\Phi}_{N,m} = (V^T\mathbf{\Phi}_{N,m})^{(0)} \quad (r,\theta) \in \Gamma, \tag{9.24a}$$

and

$$V^{-1}\{A\partial_r\mathbf{\Phi}_{N,m}+Q\mathbf{\Phi}_{N,m}\}=(V^{(0)})^{-1}A^{(0)}\partial_r\mathbf{\Phi}^{(0)}_{N,m}\quad (r,\theta)\in\Gamma. \tag{9.24b}$$

must be satisfied by each of the unknown vectors, $\mathbf{\Phi}_{N,m}$ ($m=0,\dots,M$). In (9.24b) we have used the property of a flat bed to set $Q^{(0)}=0$. Similarly, the vanishing of the bending moment and shearing stress conditions (9.15) decouple to give

$$\mathfrak{M}_m\chi_m=\mathfrak{S}_m\chi_m=0\quad (r,\theta)\in\Gamma, \tag{9.25}$$

for $m=0,\dots,M$. In (9.25), the operators $\mathfrak{M}_m$ and $\mathfrak{S}_m$ satisfy $\mathfrak{M}_m\chi_m\equiv\widetilde{\mathfrak{M}}_m(\chi^{(1)}_m,\chi^{(2)}_m)$ and $\mathfrak{S}_m\chi_m\equiv\widetilde{\mathfrak{S}}_m(\chi^{(1)}_m,\chi^{(2)}_m)$, where

$$\widetilde{\mathfrak{M}}_m(\chi^{(1)}_m,\chi^{(2)}_m)\equiv\chi^{(2)}_m-(1-\nu)\beta\left(\frac{1}{r}\partial_r-\frac{m^2}{r^2}\right)\chi^{(1)}_m, \tag{9.26a}$$

and

$$\widetilde{\mathfrak{S}}_m(\chi^{(1)}_m,\chi^{(2)}_m)\equiv\partial_r\chi^{(2)}_m-(1-\nu)\left\{(\partial_r\beta)\left(\frac{1}{r}\partial_r-\frac{m^2}{r^2}\right)\chi^{(1)}_m+\frac{m^2}{r}\beta\partial_r\left(\frac{1}{r}\chi^{(1)}_m\right)\right\}. \tag{9.26b}$$

In addition to the conditions to be applied at the ice edge (9.24a-b) and (9.25), outside of the ice-covered region, each of the unknown functions, $\varphi^{(0)}_{n,m}$, must satisfy the Sommerfeld radiation condition (9.16). This fully defines the set of governing equations from which we may calculate the MMA for the problem of an axisymmetric ice floe. However, before we are able to perform explicit calculations, we must note that the transformation from cartesian to polar coordinates is singular at the origin and this will lead to numerical difficulties. For this reason, it is convenient to assume that there exists a positive value $\varepsilon<R$ for which, within the disc $r<\varepsilon$, the ice is of uniform thickness and has a uniform draught, and the bed does not undulate (see figure 9.2). As will be seen presently, this allows us to analytically remove the singular part of the solution at this point without resorting to complicated numerical techniques. Although we now only allow variations of the geometry in the annulus $\varepsilon<r<R$, we have not compromised the generality of our model as we may select ε to be arbitrarily small.

By making the above assumption to facilitate calculations around the origin, we have created the additional internal interface $\Gamma_\varepsilon=\{r=\varepsilon,\,0\le\theta<2\pi\}$. This contour separates two regions of connected ice-cover and it is therefore necessary to obtain the jump conditions that apply here from (3.7a) and (3.10). Following the same procedure that produced the ice edge conditions, we can easily deduce that these jump conditions are given by

$$(V^T\mathbf{\Phi}_{N,m})_+=(V^T\mathbf{\Phi}_{N,m})_-\quad (r,\theta)\in\Gamma_\varepsilon, \tag{9.27a}$$

and

$$V_+^{-1}\{(A\partial_r\boldsymbol{\Phi}_{N,m})_+ + (Q\boldsymbol{\Phi}_{N,m})_+\} = (V^{-1}A\partial_r\boldsymbol{\Phi}_{N,m})_- \quad (r,\theta)\in\Gamma_\varepsilon, \tag{9.27b}$$

for $m = 0,\ldots,M$, where the positive subscript is used to denote the solution in the annulus of varying geometry and the negative subscript likewise for the solution in the disc of uniform geometry. As in (9.24b), the matrix $Q_- = 0$ results from the uniform geometry in this region. The continuity of the position and velocity of the ice's displacement must be ensured at this point, so that

$$\langle\chi_m\rangle = \langle\partial_r\chi_m\rangle = 0 \qquad (r,\theta)\in\Gamma_\varepsilon, \tag{9.28}$$

for $m = 0,\ldots,M$, where the brackets $\langle\cdot\rangle$ are again used to denote the jump in the included quantity. We assume the ice thickness to be continuous and this means that conditions (9.28) may be used to reduce the continuity of bending moment and shearing stress to

$$\langle\chi_m^{(2)}\rangle = 0, \tag{9.29a}$$

and

$$\langle\partial_r\chi_m^{(2)} - (1-\nu)(\partial_r\beta)\left(\frac{1}{r}\partial_r - \frac{m^2}{r^2}\right)\chi_m^{(1)}\rangle = 0. \tag{9.29b}$$

The entire set of conditions (9.27a-b), (9.28) and (9.29a-b), that apply at $r=\varepsilon$, may be collected into the more compact notation

$$(\mathcal{V}^T\boldsymbol{\Psi}_{N,m})_+ = (\mathcal{V}^T\boldsymbol{\Psi}_{N,m})_- \quad (x,y)\in\Gamma_\varepsilon, \tag{9.30a}$$

and

$$\mathcal{V}_+^{-1}\{(\mathcal{A}\partial_r\boldsymbol{\Psi}_{N,m})_+ + (\mathcal{Q}\mathcal{N}^{(m)}\boldsymbol{\Psi}_{N,m})_+\} = \mathcal{V}_-^{-1}(\mathcal{A}\partial_r\boldsymbol{\Psi}_{N,m})_- \quad (x,y)\in\Gamma_\varepsilon, \tag{9.30b}$$

where the matrix $\mathcal{N}^{(m)}$ is given by

$$\mathcal{N}_{n,n}^{(m)} = 1 \quad (n = 1,\ldots,N+3), \quad \mathcal{N}_{N+3,N+2}^{(m)} = (1-\nu)(\partial_r\beta)\frac{m^2}{r^2},$$

and, as always, all unspecified entries are zero. The matrix $\mathcal{Q}$ is defined in §4.1.

9.1.3 Uniform geometry

In our current problem, we have two regions in which we have assumed that the geometrical functions, D, h and d, take constant values. Within the disc $r<\varepsilon$ the situation is that of ice-cover, whereas in the infinite region $r>R$ no ice is present, $D=d=0$. As we did for the two-dimensional problems formulated in §4.2, we will use the simplifications that uniform geometry introduces to produce analytic forms of the solutions in these regions, which will subsequently provide boundary data for the annulus of varying geometry.

Let us first assume the presence of ice-cover, so that the governing equations (9.20a-b) apply. As in §4.2, the simplifications $\widetilde{d}_{j,i} = 0$, and $b_{j,i} = a_{j,i}k_i^2 - k_i \sinh(k_i H)\cosh(k_j H)$ result from the uniform geometry and the governing equations reduce to

$$A\left(\frac{1}{r}\partial_r r \partial_r - \frac{m^2}{r^2}\right)\mathbf{\Phi}_{N,m} + \left(AK^2 - C\mathbf{f}\mathbf{f}^T KS\right)\mathbf{\Phi}_{N,m} + \kappa C\mathbf{f}\chi_n^{(1)} = \mathbf{0} \quad (m = 0, \ldots, M),$$

and

$$(1-\kappa\alpha)\chi_m^{(1)} + \nabla_m^2 \chi_m^{(2)} - \mathbf{o}^T C\mathbf{\Phi}_{N,m} = 0 \quad (m = 0, \ldots, M),$$

where the matrices C, S and K are defined by

$$C = \mathrm{diag}\{\cosh(k_0 H), \ldots, \cosh(k_N H)\}, \quad S = \mathrm{diag}\{\sinh(k_0 H), \ldots, \sinh(k_N H)\}$$

and

$$K = \mathrm{diag}\{k_0, \ldots, k_N\},$$

just as they were in §4.2.

We note that the above system of ODEs has the solution

$$\mathbf{\Phi}_{N,m} = \mathbf{c}(\lambda)\mathrm{Bes}_m(\lambda r), \quad \chi_m^{(1)} = \gamma^{(1)}\mathrm{Bes}_m(\lambda r), \quad \chi_m^{(2)} = \gamma^{(2)}\mathrm{Bes}_m(\lambda r) \quad (m = 0, \ldots, M),$$

where $\mathbf{c}(\lambda)$ and $\gamma^{(i)}(\lambda)$ $(i = 1, 2)$ are constants, and Bes_m is any Bessel function of order m, which satisfies

$$r^2\partial_r^2\mathrm{Bes}_m + r\mathrm{Bes}_m + (\lambda^2 r^2 - m^2)\mathrm{Bes}_m = 0 \quad (m = 0, \ldots, M). \qquad (9.32)$$

Specification of precisely which Bessel functions are appropriate is left until a later stage. The value λ represents an eigenvalue with the corresponding eigenvector $\hat{\mathbf{c}} = (\mathbf{c}^T, \gamma^{(1)}, \gamma^{(2)})^T$, which are calculated from the eigensystem

$$(A(K^2 - \lambda^2 I) - C\mathbf{f}\,\mathbf{f}^T KS)\mathbf{c} + \kappa\gamma^{(1)}C\mathbf{f} = \mathbf{0},$$

and

$$\beta(\lambda^4 + 1 - \kappa\alpha)\gamma^{(1)} - \mathbf{f}^T C\mathbf{c} = 0,$$

with $\gamma^{(2)} = -\beta\lambda^2\gamma^{(1)}$. This eigensystem is, unsurprisingly, identical to that of the two-dimensional case (4.12a-b), with normal incidence $(q = 0)$, which has already been solved to find the eigenvalue-eigenvector pairs

$$(\lambda, \hat{\mathbf{c}}) = \left(k_i, [\mathbf{I}_i^T, \kappa^{-1}k_i\sinh(k_i H), -\kappa^{-1}\beta k_i^3\sinh(k_i H)]^T\right) \quad (i = 0, \ldots, N),$$

and

$$(\lambda, \hat{\mathbf{c}}) = \big(\mu_{N,(i)}, [\upsilon^T_{N,(i)}, \kappa^{-1}\mu_{N,(i)} \sinh(\mu_{N,(i)}H), -\kappa^{-1}\beta\mu^3_{N,(i)} \sinh(\mu_{N,(i)}H)]^T\big) \quad (i = 1, 2),$$

where $\mu_{N,(i)}$ and $\upsilon_{N,(i)}$ are dimension-dependent quantities that are defined in §4.2.

Therefore, in a region of ice-covered fluid, we may represent the unknown vectors that define the MMA as

$$\mathbf{\Psi}_{N,m}(r) = \mathcal{C}\{\mathcal{J}_m(r)\mathbf{A} + \mathcal{H}_m(r)\mathbf{B}\} \quad (m = 0, \dots, M), \tag{9.34}$$

where $\mathcal{C}$ is a matrix, previously defined in equation (4.24), whose columns contain the eigenvectors of the system and $\mathbf{A}$ and $\mathbf{B}$ are constant vectors of length $(N + 3)$, which are fixed with appropriate lateral conditions. The matrices $\mathcal{J}_m$ and $\mathcal{H}_m$ are defined by

$$\mathcal{J}_m(r) = \mathrm{diag}\{\mathrm{J}_m(k_0r), \dots, \mathrm{J}_m(k_Nr), \mathrm{J}_m(\mu_{N,(1)}r), \mathrm{J}_m(\mu_{N,(2)}r)\},$$

and

$$\mathcal{H}_m(r) = \mathrm{diag}\{\mathrm{H}_m(k_0r), \dots, \mathrm{H}_m(k_Nr), \mathrm{H}_m(\mu_{N,(1)}r), \mathrm{H}_m(\mu_{N,(2)}r)\},$$

where J_m and H_m are, respectively, Bessel functions of the first kind and Hankel functions of the first kind, of order m.

Similarly, in a domain of ice-free fluid, we may simplify the governing equations (9.22) and seek solutions of the form $\mathbf{\Phi}^{(0)}_{N,m}(r) = \mathrm{Bes}_m(\lambda r)$. Solving the resulting eigensystem leads to the expressions

$$\mathbf{\Phi}^{(0)}_{N,m}(r) = J^{(0)}_m(r)\mathbf{A} + H^{(0)}_m(r)\mathbf{B} \quad (m = 0, \dots, M), \tag{9.36}$$

in which

$$J^{(0)}_m(r) = \mathrm{diag}\{\mathrm{J}_m(k^{(0)}_0r), \dots, \mathrm{J}_m(k^{(0)}_Nr)\}, \quad H^{(0)}_m(r) = \mathrm{diag}\{\mathrm{H}_m(k^{(0)}_0r), \dots, \mathrm{H}_m(k^{(0)}_Nr)\},$$

and the constant vectors $\mathbf{A}$ and $\mathbf{B}$ are now of length $(N + 1)$.

We therefore have, at our disposal, representations for the MMA in the disc of uniform geometry centred at the origin and the infinite region of ice-free fluid, for which we have assumed a flat bed. The structure of the solutions here, (9.34) and (9.36), mirror their two-dimensional counterparts, (4.22) and (4.30) respectively, almost exactly, with the only difference being in the substitution of Bessel functions for the exponential functions. This is to be expected, as both must represent incoming and outgoing propagating waves and exponentially decaying waves, with respect to the same wavenumbers. Note that, in both (9.34) and (9.36) the specific choice of Bessel functions was arbitrary in the sense that we could have chosen any two linearly independent functions that satisfy the differential equation (9.32). However, the reason behind the particular choice of J_m and H_m will become clear in the next section.

9.1.4 Numerical calculation

The problem of an axisymmetric ice floe, forced by a single incident plane wave, is now ready for numerical solution. Our solution procedure will follow that of the two-dimensional problems given in §4.3, with the representation for the MMA in domains of uniform geometry, derived in the previous section, providing boundary data for the solution in the annulus of varying geometry, which must be calculated numerically.

By using the result (9.34), we may deduce that, in the inner disc of uniform geometry, the MMA may take the form

$$\boldsymbol{\Psi}_{N,m}(r) = \mathcal{C}^{(\varepsilon)}\mathcal{J}_m^{(\varepsilon)}(r)\mathbf{A}_m \quad (r < \varepsilon), \tag{9.37a}$$

for $m = 0, \dots, M$, where the superscript (ε) is used to indicate evaluation of the particular quantity inside this region. For each m, the vectors $\mathbf{A}_m = (A_{m,0}, \dots, A_{m,N}, A_{m,-1}, A_{m,-2})^T$ contain a set of $(N+3)$ unknown amplitudes.

In (9.37a) the Hankel functions of the first kind have been disregarded due to unboundedness at the origin. This explicitly displays the advantage that we have gained by assuming a region of constant geometry about this point. That is, the singularity that has been created by the transformation to polar coordinates is encapsulated in the Hankel functions, which we have been able to remove analytically.

Outside of the ice, the expression for the MMA,

$$\boldsymbol{\Phi}_{N,m}^{(0)}(r) = J_m^{(0)}(r)\mathbf{I}_1 + H_m^{(0)}(r)\mathbf{B}_m \quad (r > R), \tag{9.37b}$$

for $m = 0, \dots, M$, may be obtained from result (9.36). The motion represented by the Bessel functions of the first kind is that of the incident wave. Whereas, the Hankel functions of the first kind represent the scattered waves, with the vectors $\mathbf{B}_m = (B_{m,0}, \dots, B_{m,N})^T$ containing their unknown amplitudes. In the far-field we note that the Hankel functions have the asymptotic behaviour

$$\mathrm{H}_m(k_n^{(0)}r) \sim \mathrm{i}^{-m}\left(\frac{2}{\pi k_n^{(0)}r}\right)^{1/2} \mathrm{e}^{\mathrm{i}(k_n^{(0)}r - \pi/4)} \quad (r \to \infty), \tag{9.38}$$

(see, for example, Tranter, 1968) and therefore comply with the Sommerfeld radiation condition. Using equation (9.38), we can be more precise about the behaviour of the Hankel functions as they tend towards the far-field and say that they represent outward-travelling circular waves that decay at the rate $r^{-1/2}$.

Expression (9.37a) is then combined with the continuity conditions at the boundary within the floe, (9.30a-b), and we find that

$$\left[\mathcal{V}^T \mathbf{\Psi}_{N,m}\right]_{r=\varepsilon_+} = \left((\mathcal{V}^T \mathcal{C}\right) \mathcal{J}_m(\varepsilon)^{(\varepsilon)} \mathbf{A}_m, \tag{9.39a}$$

and

$$\left[\mathcal{V}_+^{-1}\{(\mathcal{A}\partial_r \mathbf{\Psi}_{N,m}) + (\mathcal{Q}\mathcal{N}^{(m)} \mathbf{\Psi}_{N,m})\}\right]_{r=\varepsilon_+} = \left(\mathcal{V}^{-1}\mathcal{A}\mathcal{C}(\partial_r \mathcal{J}_m(\varepsilon))\right)^{(\varepsilon)} \mathbf{A}_m, \tag{9.39b}$$

must be satisfied at this interface by the numerical solutions, $\mathbf{\Psi}_{N,m}$ $(m = 0, \ldots, M)$, over the interval of varying geometry. Likewise, expression (9.37b) is used in the joining conditions at the ice edge, (9.24a-b) and (9.25), and we have

$$\left[V^T \mathbf{\Phi}_{N,m}\right]_{r=R_-} = \left(V^{(0)}\right)^T \left\{J_m^{(0)}(R)\mathbf{I}_1 + H_m^{(0)}(R)\mathbf{B}_m\right\}, \tag{9.40a}$$

$$\left[V^{-1}\{A\partial_r \mathbf{\Phi}_{N,m} + Q\mathbf{\Phi}_{N,m}\}\right]_{r=R_-} = \left(V^{-1}A\right)^{(0)} \left\{(\partial_r J_m^{(0)}(R))\mathbf{I}_1 + (\partial_r H_m^{(0)}(R))\mathbf{B}_m\right\}, \tag{9.40b}$$

and

$$\mathfrak{M}_m \chi_m = \mathfrak{S}_m \chi_m = 0 \quad (r = R_-), \tag{9.40c}$$

as the conditions to be satisfied by $\mathbf{\Psi}_{N,m}$ $(m = 0, \ldots, M)$ at this boundary.

As with the two-dimensional problems that were formulated in §4.3, we wish to provide the solutions of the differential systems (9.21), over the varying interval, with boundary conditions that contain as few of the unknown amplitudes as possible. Therefore, we manipulate (9.39a-b) and (9.40a-c), to produce

$$\mathfrak{B}_\varepsilon^{(m)} \mathbf{\Psi}_{N,m}(\varepsilon) = \mathbf{0}, \quad \mathfrak{B}_R^{(m)} \mathbf{\Psi}_{N,m}(R) = -\frac{2\mathrm{i}}{\pi R}\mathcal{I}_1 \quad (m = 0, \ldots, M), \tag{9.41}$$

which are in terms of only known values. The operators $\mathfrak{B}_\varepsilon^{(m)}$ and $\mathfrak{B}_R^{(m)}$ are defined by

$$\begin{aligned} \mathfrak{B}_\varepsilon^{(m)} \mathbf{\Psi}(r) \ \equiv \ & (\mathcal{J}_m(\varepsilon)(\mathcal{A}\mathcal{C})^{-1}\mathcal{V})^{(\varepsilon)} \left[\mathcal{V}^{-1}\mathcal{A}\right]_{r=\varepsilon_+} \partial_r \mathbf{\Psi}(r) \\ & + \Big\{ (\mathcal{J}_m(\varepsilon)(\mathcal{A}\mathcal{C})^{-1}\mathcal{V})^{(\varepsilon)} \left[\mathcal{V}^{-1}\mathcal{Q}\mathcal{N}^{(m)}\right]_{r=\varepsilon_+} \\ & \quad - \left((\partial_r \mathcal{J}_m(\varepsilon))\mathcal{C}\mathcal{V}^{-T}\right)^{(\varepsilon)} \left[\mathcal{V}^T\right]_{r=\varepsilon_+} \Big\} \mathbf{\Psi}(r), \end{aligned}$$

$$\begin{aligned} \{\mathfrak{B}_R^{(m)} \mathbf{\Psi}(r)\}_i \ \equiv \ & \mathbf{I}_i^T (H_m(R)A^{-1}V)^{(0)} \left[V^{-1}A\right]_{r=R_-} \widetilde{\mathcal{F}}(\partial_r \mathbf{\Psi}(r)) \\ & + \mathbf{I}_i^T \Big\{ (H_m(R)A^{-1}V)^{(0)} \left[V^{-1}Q\right]_{r=R_-} \\ & \quad - (\partial_r H_m^{(0)}(R))(V^{(0)})^{-T} \left[V^T\right]_{r=R_-} \Big\} \widetilde{\mathcal{F}}\mathbf{\Psi}(r) \end{aligned} \tag{9.42}$$

for $i = 1, \ldots, N+1$, and

$$\{\mathfrak{B}_R^{(m)}\mathbf{\Psi}(r)\}_{N+2} \equiv \widetilde{\mathfrak{M}}\left(\mathbf{\Psi}_{N+2}(r), \mathbf{\Psi}_{N+3}(r)\right), \quad \{\mathfrak{B}_R^{(m)}\mathbf{\Psi}(r)\}_{N+3} \equiv \widetilde{\mathfrak{S}}\left(\mathbf{\Psi}_{N+2}(r), \mathbf{\Psi}_{N+3}(r)\right).$$

In definition (9.42) the notation $\widetilde{\mathcal{F}}$ has again been used to denote the $(N+1) \times (N+3)$ matrix comprised of the $(N+1)$ identity matrix appended with two columns of zeros. The Wronskian identity

$$\mathrm{J}_m(z)\mathrm{H}'_m(z) - \mathrm{J}'_m(z)\mathrm{H}_m(z) = \frac{2\mathrm{i}}{\pi z},$$

has been used to simplify the right-hand side of the condition at the ice edge ($r = R$) given in (9.41).

To obtain the MMA, we must therefore numerically solve the differential system (9.21) over the interval $\varepsilon < r < R$, with boundary conditions (9.41), for the vectors $\mathbf{\Psi}_{N,m}$ ($m = 0, \ldots, M$). The value of M is chosen so that a desired level of accuracy is achieved in the convergence of the azimuthal coordinate. Note that, due to the reformulation of the boundary conditions, we need only calculate a single numerical solution for each of the azimuthal modes. If we had retained (9.30a-b) at $r = \varepsilon$, and (9.24a-b) and (9.25) at $r = R$, as our boundary conditions, then it would have been necessary to calculate $(2N+4)$ linearly independent solutions for each azimuthal mode. Having calculated $\mathbf{\Psi}_{N,m}$, the unknown amplitudes, $\mathbf{A}_m$ and $\mathbf{B}_m$ may be easily obtained from (9.39a) and (9.40a) respectively. This method will fail to deliver an amplitude if its corresponding Bessel function vanishes at the particular internal boundary; in this case we must revert to the appropriate derivative condition, (9.39b) or (9.40b), although this will require the numerical calculation of the derivative $\partial_r \mathbf{\Psi}_{N,m}$ at the relevant boundary.

9.2 Comparison to the work of Peter *et al.* (2004)

Consistent with all of the previous geometrical constructions considered, our first set of numerical results use a problem for which independent data exists in the literature for comparison. Peter *et al.* (2004) also solved the circular ice floe problem that we consider in this chapter, albeit imposing the restrictions of a uniform ice thickness, a zero draught and a flat bed.

The solution method of Peter *et al.* is based on a decomposition of the reduced velocity potential into a double infinite sum of azimuthal and vertical modes, and the displacement function into azimuthal modes, akin to our expressions (9.7a-b) and (9.23a-c). Representations of the potential are matched through the continuity conditions

$$\langle\langle \phi \rangle\rangle = \langle\langle \partial_r \phi \rangle\rangle = 0 \quad (r, \theta) \in \Gamma,$$

which hold throughout the fluid depth, and the ice edge conditions $\mathfrak{M}\eta = \mathfrak{S}\eta = 0$ for $(r, \theta) \in \Gamma$, are applied to the reduced displacement. The numbers of azimuthal modes and of vertical modes are then truncated to finite dimensions and the resulting systems of equations solved. This procedure is closely related to the EMM that was derived in §5.1.2 for the semi-infinite ice sheet problem, and, as in the EMM, the complex wavenumbers that appear in their expansions are exact.

It is possible to calculate the MMA for this problem without the need for the numerical solution of a differential equation to be calculated. To do this, we abandon the interface $r = \varepsilon$ within the floe, and employ the analytic structure of the MMA, given in equation (9.37a), at all points of the ice-covered domain, $r < R$. The ice edge conditions are then dealt with in a similar manner to the method outlined in §5.1.1 for the semi-infinite ice sheet problem. We will use this approach explicitly in §10.1 for the single-mode approximation and hence obtain analytical information about the solution.

Here, we compare results obtained from the MMA to a selection of the results that appear in Peter *et al.* (2004). We begin by considering the convergence of the MMA, both vertically and azimuthally, to the solution of a chosen problem. Figure 9.3 displays the convergence of the MMA for the modulus of the displacement function on the contour $\theta = 0$ for the problem in which the properties of the ice are described by $\alpha = 0$ and $\beta = 10^5$Pa m^{5}s^2 kg^{-1}, the radius of the floe is $R = 100$m, the incident wave is of length $\lambda^{(0)} = 50$m and the constant bed depth is $h = 25$m. For five vertical modes, $M = 12$ produces azimuthal convergence of approximately 2.2×10^{-3}; this convergence is shown in figure 9.3(a).

The use of five vertical modes is sufficient for convergence as displayed in figure 9.3(b), where $M = 12$ is fixed. Note from this figure that a single vertical mode gives a good approximation, retaining the key qualitative and quantitative features of the converged solution. The incident wavelength of 50m along with the bed depth of 25m corresponds to an incident wave period of approximately 5.67secs and, as in the comparison to the work of Athanassoulis & Belibassakis (2005) in §7.1, we deduce the value $\beta = 10^5$Pa m^{5}s^2 kg^{-1} to be given by ice of thickness of approximately 1.3m. We may therefore conclude that the performance of the single-mode approximation here appears to be consistent with that seen around equivalent parameter values for the two-dimensional cases of §5 and §7. The convergence of the vertical modes will be investigated independently in §9.3.

Figures 9.4-9.5 display MMAs that are directly comparable to results that appear in Peter *et al.* (2004). The approximations are to the real and imaginary parts of the displacement function, η, and have converged both azimuthally and vertically. The results shown in figure 9.4 use the parameters that appear in figure 9.3 and should be compared, respectively, to figures 3(a-b) of Peter *et al.*.

Figure 9.5 differs from the previous problem in that a shallow bed depth of 1m is used.

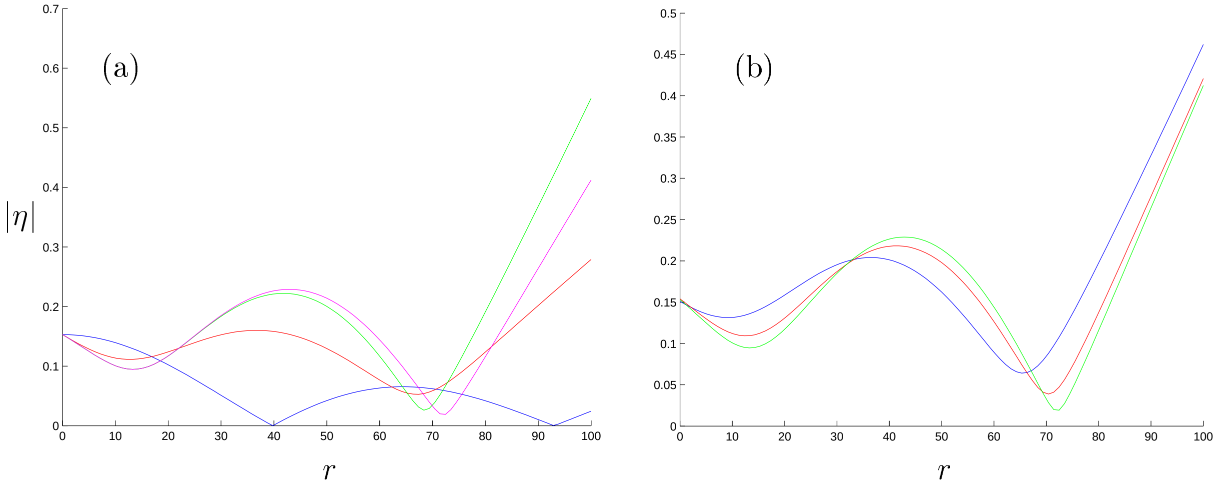

Figure 9.3: Convergence of the MMA to the modulus of the reduced displacement function along the contour $\theta = 0$, with respect to (a) the azimuthal modes and (b) the vertical modes. The problem is that solved by Peter *et al.* (2004) in which the floe is of uniform thickness, a zero draught and radius $R = 100$m, over a flat bed of depth 25m, with an incident wavelength of 50m. In part (a) the approximation uses six vertical modes ($N = 5$), and $M = 0$ (blue curve), $M = 2$ (red), $M = 4$ (green) and $M = 12$ (magenta) azimuthal modes. In part (b) the approximation uses thirteen azimuthal modes ($M = 12$), and $N = 0$ (blue curve), $N = 2$ (red) and $N = 5$ (green) vertical modes.

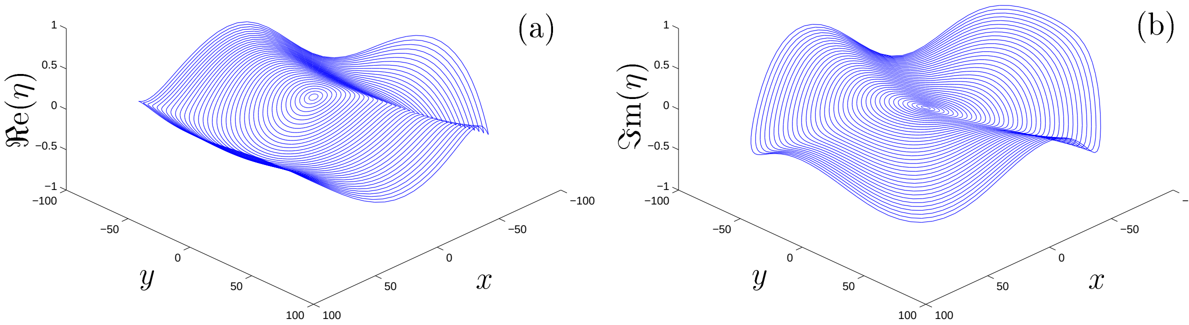

Figure 9.4: Comparison with figure 4(a) of Peter *et al.* (2004), in which the floe is of uniform thickness, a zero draught and radius $R = 100$m, over a flat bed of depth 25m, with an incident wave of length 50m. Part (a) displays the real part of the reduced displacement function and part (b) the corresponding imaginary part. The dimensions of the approximation are $N = 5$ and $M = 12$.

The incident wavelength of 50m now corresponds to a wave period of approximately 16secs. Figure 9.5(a-b) are, respectively, for comparison figures 4(a-b) of to Peter *et al.*. The azimuthal convergence of the shallow bed depth problem is very similar to the greater fluid depth problem and an identical M is chosen in each problem for convergence; however, as may be expected in a case of shallow water, the effect of the introduction of evanescent modes to the $h = 1$m problem is unnoticeable and the approximation is taken as converged when only a single vertical mode is included. This compares to $N = 4$ when $h = 25$m. Results given figures 9.4-9.5 match their counterparts in Peter *et al.* (2004).

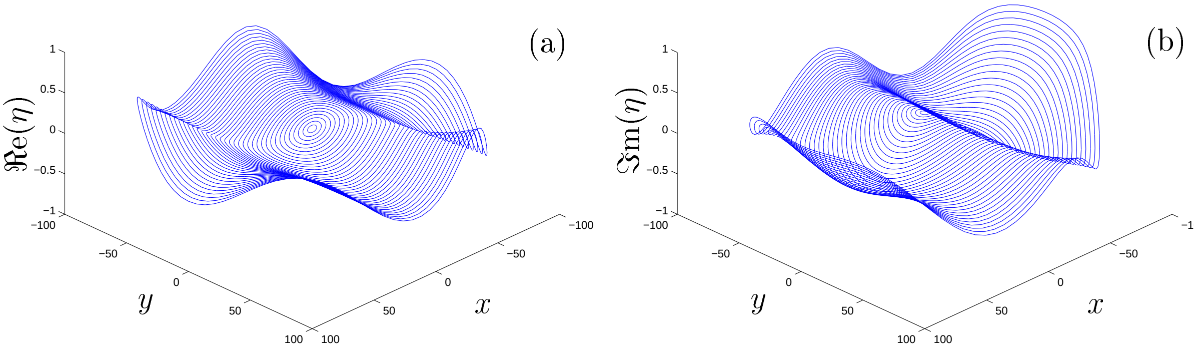

Figure 9.5: Comparison with figure 4(b) of Peter *et al.* (2004). As in figure 9.4 but with bed depth of 1m and a single vertical mode ($N = 0$).

9.3 Convergence of the MMA with respect to the vertical modes

We have already seen in the previous section that, for a particular problem, the convergence with respect to the vertical modes is rapid and that a single vertical mode provides a good approximation. In this section, we conduct a brief investigation of the convergence of the MMA with respect to the vertical modes for our axisymmetric problem. Results given in this section will use only ice of uniform thickness and a zero draught, as numerical experiments (not presented) have shown that, consistent with our investigation of two-dimensional motion, it is the scattering caused by the ice edge, not undulations, that dominate this convergence issue.

Let us consider the form of the scattered solution in the far-field. Earlier, in equation (9.38), we defined the asymptotic behaviour of the Hankel functions to be outgoing circular waves that decay at the rate $r^{-1/2}$. Substituting this expression into the scattered solution, we find that

$$\psi_N \sim \left(\frac{2}{\pi k_0^{(0)} r}\right)^{1/2} \mathrm{e}^{i(k_0^{(0)} r - \pi/4)} \mathcal{S}_B(\theta) \cosh\{k_0^{(0)}(z+h)\} \quad (r \to \infty),$$

where

$$\mathcal{S}_B(\theta) = B_0 + 2\sum_{m=1}^{\infty} B_m \cos(m\theta).$$

Therefore, in the far-field the scattered solution can be separated into its radial, azimuthal and vertical motions. Hence, the function $\mathcal{S}_B$, which contains the amplitudes B_m that are calculated as part of the solution process, describes the azimuthal variation of the most slowly decaying part of the scattered wave.

The scattered far-field is a quantity of importance. However, in the current context we regard the response of the floe itself as our principal interest. To enable us to concentrate on the properties of the floe, the main body of results that will be given in the following chapter will on the whole neglect the form of the scattering outside of the ice-covered region. For completeness, isolated approximations to the far-field will be presented in §10.2.2, as in that section we will give an overview of the scattering caused by circular floes of different thicknesses and radii and at different incident wavelengths. Of course, it would be possible to use the solution procedure outlined in this chapter to investigate the solution away from the ice. For this reason, we feel that it is warranted to display the accuracy of low dimensional approximations to the far-field in this section.

Figures 9.6-9.7 plot the convergence of the MMA to both $|\eta|_{\theta=0}$ and the function $\mathcal{S}_B$ for the three incident wave periods $\tau = 2$secs, 5secs and 10secs and the two ice thicknesses $D = 0.1$m and 1m. The radius of the floe $R = 50$m is maintained throughout as its value is only important relative to the varied parameters, specifically the incident wavelength.

In figures 9.6-9.7(a-c.ii) the modulus of the function $\mathcal{S}_B$ is given as a ribbon plot, in which the azimuthal dependence is traced around the circle. The magnitude of the function is represented by the distance of the curve from the origin. However, to prevent the generally dominant scattering in the direction of the incident wave from obscuring the convergence of the MMA, the magnitude of the functions in these figures is distorted, so that the dotted circles shown in fact represent ellipses. Consequently, there is no reason to indicate the magnitude of the functions in these figures. In similar figures that will be given later, in which we are concerned with the magnitude and true shape of the far-field scattering, curves of $\mathcal{S}_B$ will not be distorted and its magnitude will be labelled.

As we found in the previous section, the convergence properties displayed in figures 9.6-9.7 are consistent with those observed for the two dimensional problems of partial ice-cover considered in §5 and §7. For instance, we note that more vertical modes are required for convergence at smaller wave periods. Also, in relation to the thickness of the ice, we again observe the trait that low-dimensional approximations are clearly less accurate for the thicker ice; however, these inaccuracies are eradicated rapidly as the dimension of the approximation is increased.

Here, a close relationship is seen to exist between the convergence properties of the MMA (with respect to the vertical modes) for two-dimensional problems of partial ice-cover and the current three-dimensional problem. This is not unexpected, as we understand the need for the addition of the evanescent modes to resolve the full linear solution to

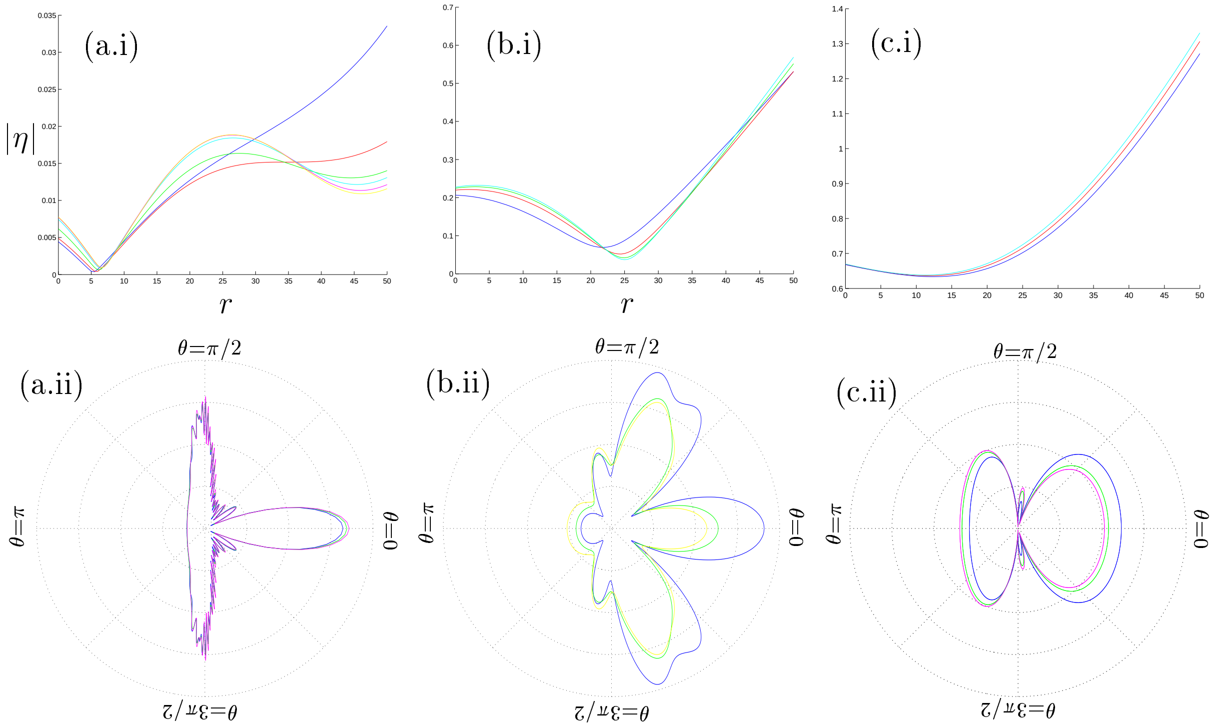

Figure 9.6: Convergence of the MMA with respect to the vertical modes. Parts (a-c.i) are approximations of the modulus of the reduced displacement function on the contour $\theta = 0$. Parts (a-c.ii) are approximations of the function $\mathcal{S}_B(\theta)$. The floe is of uniform thickness 1m, a zero draught and radius 50m, over a flat bed depth of 20m. The incident wave period is (a.i-ii) 2secs, (b.i-ii) 5secs and (c.i-ii) 10secs. The dimensions of the vertical coordinate are $N = 0$ (blue curves) and: (a.i) $N = 1$ (red), $N = 3$ (green), $N = 7$ (cyan), $N = 12$ (magenta) and $N = 19$ (yellow), with $M = 15$; (b.i) $N = 1$ (red), $N = 3$ (green) and $N = 9$ (cyan), with $M = 8$; (c.i) $N = 1$ (red) and $N = 4$ (cyan), with $M = 4$; (a.ii) $N = 3$ (cyan) and $N = 12$ (magenta), with $M = 60$; (b.ii) $N = 3$ (green) and $N = 12$ (yellow), with $M = 15$; (c.ii) $N = 2$ (green) and $N = 9$ (magenta), with $M = 5$.

be related to their activation by the sources of scattering that are present in the geometry. In particular, for scattering at an ice edge, the strength of the activation of the evanescent modes will be dominated by the frequency of the incident wave and the thickness of the ice edge, regardless of whether we are in a two-dimensional or a three-dimensional setting.

Furthermore, it is noted that the azimuthal convergence of the MMA is consistent as the number of vertical modes is varied. Therefore, we may be confident that no important azimuthal motion is neglected by approximations that have not fully converged with respect to the vertical modes.

Throughout the results that have been calculated, which extend beyond those that appear in this section, a single vertical mode consistently provides a high level of accuracy. In the results displayed in this section, the only point at which the single-mode approximation does not sufficiently represent the qualitative properties of the full linear solution is in the approximation to $|\eta|_{\theta=0}$ in a vicinity of the ice edge for $D = 1$m and

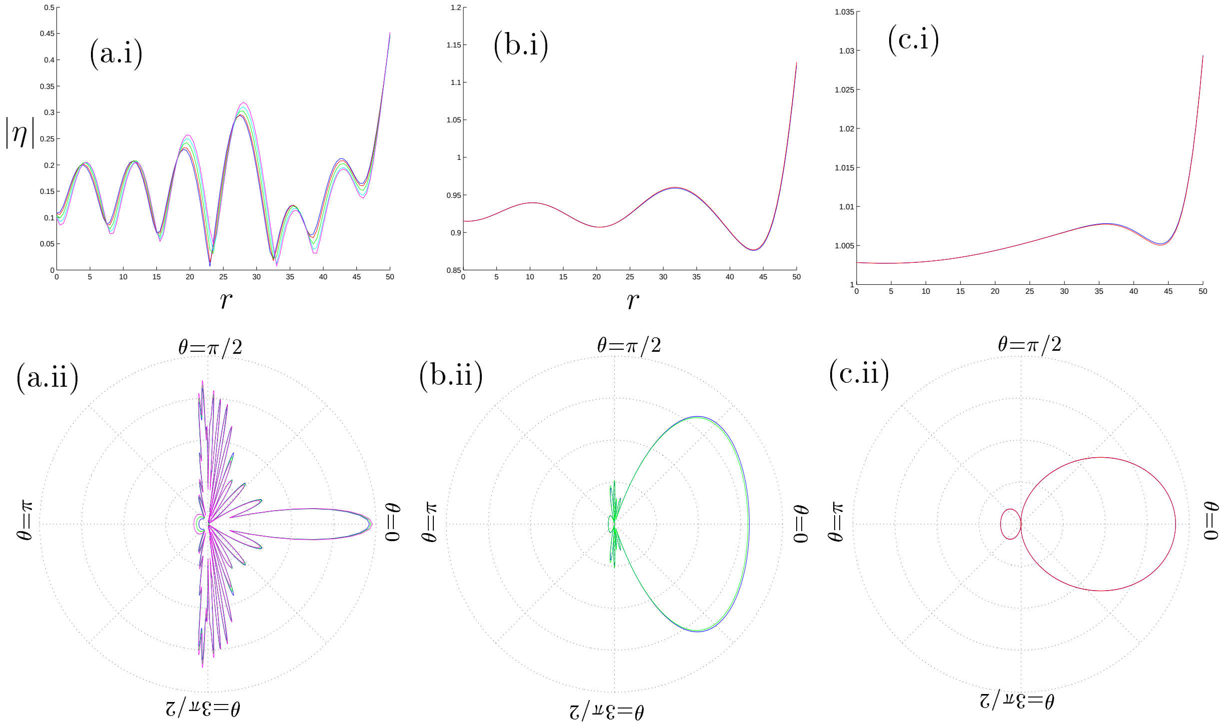

Figure 9.7: As in figure 9.6 but with ice thickness $D = 0.1$m, and vertical dimensions $N = 0$ (blue curves): (a.i) $N = 2$ (red), $N = 5$ (green), $N = 10$ (cyan) and $N = 20$ (magenta), with $M = 40$; (b.i) $N = 1$ (red), with $M = 15$; (c.i) $N = 1$ (red), with $M = 9$; (a.ii) $N = 5$ (green) and $N = 19$ (magenta), with $M = 60$; (b.ii) $N = 3$ (green) and $N = 7$ (cyan), with $M = 15$; (c.ii) $N = 1$ (red), with $M = 5$.

$\tau = 2$secs. Nevertheless, the corresponding approximation of the scattered far-field does not suffer qualitatively.

It is therefore deemed acceptable to use a single vertical mode to gauge the scattering properties of axisymmetric ice floes. For the numerical and analytical investigation of the axisymmetric floe problem that will be made in the following chapter we consider only the single-(vertical)-mode approximation. In doing so, we will find that its relatively simple structure allows for greater transparency when analysing the results and hence a more comprehensive understanding of the scattering process. Of course, the accuracy of the results given by the single-mode approximation can always be checked by taking the full MMA; however, this is not an avenue that we will pursue in this account of the work carried out.

9.4 Conclusions

During this chapter we have used the governing equations of the MMA set out in §3 to formulate a solution procedure for a problem involving three-dimensional geometry. Specifically, we have considered the problem of an ice floe under axisymmetric constraints being forced by a plane incident wave.

It was natural to transform from the horizontal cartesian coordinates to polar coordinates in order to perform calculations. The imposed axisymmetry could then be utilised by expanding the azimuthal dependence of the unknown functions in the form of Fourier cosine series. This allows the azimuthal modes to be decoupled, which results in a system of ordinary differential equations, dependent on the radial coordinate only, with corresponding lateral conditions at the ice edge.

In regions of uniform geometry, both ice-covered and ice-free, it is possible to calculate solutions of these ordinary differential equations and thus provide an analytical form for the MMA. The structure of these solutions is closely related to the analogous expressions we obtained for two-dimensional problems. However, in the three-dimensional setting the horizontal motion is defined in terms of Bessel functions.

A further assumption was made that a disc of an arbitrarily small radius exists around the centre of the floe in which the geometry is uniform, so that the geometry is permitted to vary only in the surrounding annulus. This assumption only minimally compromises the generality of the model, the loss of which is far outweighed by the advantage it affords. By assuming this disc of uniform geometry we are able to deal with the singularity introduced by the transformation to polar coordinates analytically, which means that we do not need to resort to complicated numerical means.

In order to calculate a solution we truncate the azimuthal motion to a finite number of Fourier modes. We expect the key azimuthal motion to be carried by a relatively small number of the Fourier modes and hence it to be possible to calculate the MMA at a low computational cost. Therefore, to calculate the MMA we are required to numerically calculate the solution of the governing differential equations over the annulus of varying geometry. The analytical forms of the solution in the uniform regions are used in the jump conditions to provide the necessary boundary data.

As in the two-dimensional problems considered in §4, it was shown that by manipulating the jump conditions it is possible to reduce the number of calculations that are needed in order to obtain the approximation. To do this, we removed the amplitudes of the scattered waves that appear in certain conditions, so that only one numerical solution over the annulus of varying geometry is required per azimuthal mode.

In §§9.2-9.3 a limited number of numerical results for the problem of a circular uniform floe was given. Initially, we compared our converged approximations with results obtained by independent authors and found them to be consistent. This was followed by a brief study of the convergence properties of the MMA with respect to the vertical modes. As expected, it was found that these properties were identical to those seen in two-dimensional problems. Notably we have the result that low-dimensional approximations, in particular the single-mode approximation, give accurate representations of the displacement of the floe. Difficulties were only experienced in a vicinity of thicker ice edges at high frequencies.

Chapter 10

An axisymmetric ice floe: the single-mode approximation

During the previous chapter the MMA was formulated for numerical solution to the problem of an axisymmetric floe forced by a plane wave. The resulting approximation method required convergence in the azimuthal coordinate in addition to the vertical coordinate. We have already made a thorough investigation of the convergence of the MMA in respect of the vertical coordinate on numerous two-dimensional geometries in §§5-7, and, in the numerical results presented in the previous chapter, have seen these properties to be retained for three-dimensional constructions.

It is therefore of a far greater interest to study the convergence of the approximation with respect to the azimuthal coordinate. Thus, for consistency when considering the azimuthal convergence and in order to focus the attention of the more extensive investigation of this chapter on the properties of the floe we here restrict our approximation to a single vertical mode. In cases of large obstructions, such as a thick ice edge or a high frequency, our single-mode approximations will undoubtedly contain inaccuracies, particularly around the perimeter of the floe. Whilst we accept this, we note that in most cases the single-mode approximation has proved to be highly accurate and, even for difficult problems will give a good representation of the displacement of the floe.

As we will now only be dealing with a single vertical mode, the unknown functions that form the MMA are redefined by

$$\varphi_{0,m} \equiv \varphi_m, \quad \varphi_{0,m}^{(0)} \equiv \varphi_m^{(0)} \quad (m = 0, \dots, M).$$

Similarly, we will also relabel the propagating and complex wavenumbers by

$$k_0 \equiv k, \quad k_0^{(0)} \equiv k^{(0)}, \quad \mu_{0,(i)} \equiv \mu_{(i)} \quad (i = 1, 2),$$

and the coefficients of the governing equations as

$$a_{0,0} \equiv a, \quad v_{0,0} \equiv v, \quad a^{(0)}_{0,0} \equiv a^{(0)}, \quad v^{(0)}_{0,0} \equiv v^{(0)}.$$

Our analysis of the scattering properties of an axisymmetric floe, using the single-mode approximation, will consist mainly of numerical calculations. However, as in previous problems, the relatively simple structure of the single-mode approximation enables some purely analytical understanding of the solution to be gained. This work is the subject of the following section and directly precedes the numerical investigation.

10.1 Piecewise uniform geometry

If we assume an ice floe of uniform thickness and a zero draught over a flat bed, then we may easily adapt the analysis of the semi-infinite ice sheet problem in §5.1.1, to the current circular ice floe problem. The difference in the structure of these two geometrical constructions means that the formulation of the current problem in this context is worthy of presentation. A zero draught is taken here to isolate other properties; however, in the following analysis a submergence may be easily implemented, as it was for the semi-infinite ice sheet problem in §7.5.1.

The form of the single-mode approximation, for a floe of uniform thickness and uniform draught over a flat bed, may be deduced from (9.34) to be

$$\varphi_m(r) = \mathrm{J}_m(kr)A_{m,0} + \sum_{i=1,2} v_{(i)}\mathrm{J}_m(\mu_{(i)}r)A_{m,-i} \quad (m = 0, \ldots, M), \tag{10.1a}$$

and

$$\chi_m(r) = \mathrm{J}_m(kr)\hat{A}_m + \sum_{i=1,2} \mathrm{J}_m(\mu_{(i)}r)\gamma(\mu_{(i)})A_{m,-i} \quad (m = 0, \ldots, M), \tag{10.1b}$$

where $\gamma(\mu) = \mu\sinh(\mu H)/\kappa$,

$$v_{0,(0,i)} \equiv v_{(i)} = -\frac{\beta\gamma(\mu_{(i)})k\sinh(kH)(k^2 + \mu^2_{(i)})}{a} \quad (i = 1, 2), \tag{10.2}$$

and

$$\hat{A}_m = \frac{k\sinh(kH)}{\kappa}A_{m,0} \quad (m = 0, \ldots, M).$$

In fact, we are actually interested in the amplitudes $\widetilde{A}_m = \mathrm{I}_0\hat{A}_m$ $(m = 0, \ldots, M)$, as these are the correct physical amplitudes beneath the floe, having their dimension in units metres. Outside of the ice-covered domain, the single-mode approximation may be easily deduced from (9.36) to be

$$\varphi_m^{(0)}(r) = \mathrm{J}_m(k^{(0)}r) + \mathrm{H}_m(k^{(0)}r)B_m \quad (m = 0, \ldots, M), \tag{10.3}$$

where we have redefined the scattered amplitudes $B_{m,0} \equiv B_m$.

Due to the constant ice thickness and the property (9.32) of the Bessel functions, the conditions of zero bending moment and shearing stress at the ice edge applied to (10.1b), here take the form

$$\begin{aligned} \left\{\left((kR)^2 - (1-\nu)m^2\right)\mathrm{J}_m(kR) + R(1-\nu)\left(\partial_r \mathrm{J}_m(kR)\right)\right\}\hat{A}_m + \\ \sum_{i=1,2}\left\{\left((k\mu_{(i)})^2 - (1-\nu)m^2\right)\mathrm{J}_m(\mu_{(i)}R) + R(1-\nu)\left(\partial_r \mathrm{J}_m(\mu_{(i)}R)\right)\right\}\gamma(\mu_{(i)})A_{m,-i} &= 0, \end{aligned} \tag{10.4a}$$

and

$$\begin{aligned} \left\{\left((kR)^2 + (1-\nu)m^2\right)\left(\partial_r \mathrm{J}_m(kR)\right) + (1-\nu)m^2\mathrm{J}_m(kR)\right\}\hat{A}_m + \\ \sum_{i=1,2}\left\{\left((\mu_{(i)}R)^2 + (1-\nu)m^2\right)\left(\partial_r \mathrm{J}_m(\mu_{(i)}R)\right) + (1-\nu)m^2\mathrm{J}_m(\mu_{(i)}R)\right\}\gamma(\mu_{(i)})A_{m,-i} &= 0. \end{aligned} \tag{10.4b}$$

Following the case of a semi-infinite ice sheet, we use conditions (10.4a-b) to express the amplitudes associated with the complex wavenumbers, $A_{m,-i}$ $(i = 1, 2)$, in terms of the amplitude associated with the propagating wavenumber, $\hat{A}_m$, by writing

$$\triangle_m(\mu_{(1)}R, \mu_{(2)}R)\begin{pmatrix} \gamma(\mu_{(1)})A_{m,-1} \\ \gamma(\mu_{(2)})A_{m,-2} \end{pmatrix} = -\begin{pmatrix} \triangle_m(kR, \mu_{(2)}R) \\ -\triangle_m(kR, \mu_{(1)}R) \end{pmatrix}\hat{A}_m, \tag{10.5}$$

where we define

$$\triangle_m(w, z) = \mathscr{X}_m(w)\mathscr{Y}_m(z) - \mathscr{X}_m(z)\mathscr{Y}_m(w), \tag{10.6a}$$

with

$$\mathscr{X}_m(w) = \left(w^2 - (1-\nu)m^2\right)\mathrm{J}_m(w) + w(1-\nu)(\partial_w \mathrm{J}_m(w)), \tag{10.6b}$$

and

$$\mathscr{Y}_m(w) = \left(w^2 + (1-\nu)m^2\right)w(\partial_w \mathrm{J}_m(w)) - (1-\nu)m^2\mathrm{J}_m(w). \tag{10.6c}$$

Thus, using equality (10.5) to remove the amplitudes $A_{m,-i}$ $(i = 1, 2)$ from expression (10.1a) we have $\varphi_m(r) \equiv \widetilde{\varphi}_m(r)A_m$, where

$$\widetilde{\varphi}_m(r) = \mathrm{J}_m(kr) - \sum_{i=1,2}\hat{v}_{(i)}\frac{\triangle_m(kR, \mu_{(i_-)}R)}{\triangle_m(\mu_{(i)}R, \mu_{(i_-)}R)}\mathrm{J}_m(\mu_{(i)}r) \quad (m = 0, \ldots, M), \tag{10.7}$$

with

$$\hat{v}_{(i)} = \frac{k \sinh(kH) v_{(i)}}{\gamma(\mu_{(i)})\kappa} \quad (i = 1, 2), \tag{10.8}$$

and we recall that $j_- = (3 - (-1)^j)/2$ $(j = 1, 2)$. The unknown amplitudes, A_m, are then obtained through the continuity conditions (9.24a-b), which we here write as

$$\left\{ \mathrm{H}_m(k^{(0)}R) \frac{a}{a^{(0)}} \frac{v^{(0)}}{v} \left(\partial_r \widetilde{\varphi}_m(R)\right) - \left(\partial_r \mathrm{H}_m(k^{(0)}R)\right) \frac{v^{(0)}}{v} \widetilde{\varphi}_m(R) \right\} A_m = -\frac{2\mathrm{i}}{\pi R} \tag{10.9a}$$

for $m = 0, \ldots, M$. In order to explicitly calculate the amplitudes A_m from equation (10.9a) we must assume that the bracketed quantity on the left hand side is non-vanishing. A situation in which this quantity were to vanish would correspond to a resonance in that particular mode. Further investigation of this issue will be made later in this chapter.

If required, the scattered amplitudes B_m $(m = 0, \ldots, M)$ are then recovered via

$$\frac{2\mathrm{i}}{\pi R} B_m = \left\{ \mathrm{J}_m(k^{(0)}R) \frac{a}{a^{(0)}} \frac{v^{(0)}}{v} \left(\partial_r \widetilde{\varphi}_m(R)\right) - \left(\partial_r \mathrm{J}_m(k^{(0)}R)\right) \frac{v^{(0)}}{v} \widetilde{\varphi}_m(R) \right\} A_m. \tag{10.9b}$$

Hence, we may completely define the single-mode approximation by explicitly calculating the required amplitudes, A_m and B_m, from equations (10.9a-b), for use in expressions (10.1a-b) and (10.3).

The complex wavenumbers $\mu_{(i)}$ are defined by the $N = 0$ case of (4.19), and this may be solved straightforwardly to give

$$\begin{aligned} \mu_{(i)}^2 \quad = \quad & -\frac{k^2 \sinh(kH)\cosh(kH)}{\sinh(kH)\cosh(kH) + kH} - (-1)^i \mathrm{i} \left(\frac{(1 + \beta k^4)\cosh(kH)}{\beta(\cosh(kH) + \alpha k \sinh(kH))} \right. \\ & \left. + \frac{k^4 \sinh(kH)\cosh(kH)(\sinh(kH)\cosh(kH) + 2kH)}{(\sinh(kH)\cosh(kH) + kH)^2} \right)^{1/2}, \end{aligned} \tag{10.10}$$

for $i = 1, 2$, where we have used the dispersion relation (3.13) and the equality

$$a = \frac{\sinh(kH)\cosh(kH) + kH}{2k},$$

in which the weighting $\varpi_0 = 1$ has been taken. Equation (10.10) explicitly defines the complex wavenumbers in terms of the propagating wavenumber, k, the vertical distances D and H and the frequency (through κ). The solution (10.7) is therefore likewise defined in terms of these quantities, as well as the radius of the floe.

Supposing that the complex wavenumbers, $\mu_{(i)}$ $(i = 1, 2)$, form a symmetric pair (in the imaginary axis), i.e. $\mu_{(1)} = -\overline{\mu_{(2)}}$, we have that

$$\mathrm{J}_m(\mu_{(1)}r) = (-1)^m \overline{\mathrm{J}_m(\mu_{(2)}r)}, \quad \partial_r \mathrm{J}_m(\mu_{(1)}r) = (-1)^m \overline{\partial_r \mathrm{J}_m(\mu_{(2)}r)} \quad (m = 0, \ldots, M),$$

from which it can be verified that

$$\mathscr{X}_m(\mu_{(1)}r) = (-1)^m\overline{\mathscr{X}_m(\mu_{(2)}r)}, \quad \mathscr{Y}_m(\mu_{(1)}r) = (-1)^m\overline{\mathscr{Y}_m(\mu_{(2)}r)}.$$

The above equalities lead to the simplification

$$\sum_{i=1,2}\hat{v}_{(i)}\frac{\triangle_m(kR,\mu_{(i_-)}R)}{\triangle_m(\mu_{(i)}R,\mu_{(i_-)}R)}\mathrm{J}_m(\mu_{(i)}r) = \frac{\Im\mathrm{m}\left(\hat{v}_{(1)}\overline{\triangle_m(kR,\mu_{(1)}R)}\mathrm{J}_m(\mu_{(1)}r)\right)}{\Im\mathrm{m}\left(\mathscr{X}(\mu_{(1)}R)\overline{\mathscr{Y}(\mu_{(1)}R)}\right)},$$

for use in expression (10.7).

Let us now investigate certain régimes that are of interest. By analysing the behaviour of our single-mode approximation in these régimes we will be able to draw inferences from the numerical results that are produced in §10.2. This approximation will then allow us to make predictions about the response of the ice floe to the incident wave. Details of the calculations which follow may be found in Appendix C.

Short waves

It will be supposed throughout the following analysis that the frequency, the ice thickness and the fluid depth produce a propagating wavenumber, k, such that

$$kH \ll \sinh(kH).$$

This simply states that the wavelength within the ice-covered region is not particularly long in relation to the fluid depth. This régime has previously been used in §7.5.1, to investigate the addition of an Archimedean draught to the semi-infinite ice sheet problem.

When $kH \ll \sinh(kH)$ holds we have already seen in equation (7.8a-b) that the approximations

$$\frac{a}{a^{(0)}}\frac{v^{(0)}}{v} \approx \frac{2k_0^{(0)}}{k+k^{(0)}}\frac{\sinh(kH)}{\sinh(k^{(0)}H)}, \quad \frac{v}{v^{(0)}} \approx \frac{k+k^{(0)}}{2k}\frac{\sinh(kH)}{\sinh(k^{(0)}H)}, \tag{10.11}$$

are valid when the ice rests on the fluid surface. The approximations

$$\mu_{(j)}^2 \approx -k^2 - (-1)^j\mathrm{i}\left(\frac{1+\beta k^4}{\beta(1+\alpha k)}\right)^{1/2} \quad (j=1,2), \tag{10.12a}$$

and

$$\hat{v}_{(j)} \approx -\frac{2\beta(1+\alpha k)k^2(k^2+\mu_{(j)}^2)}{1+\beta k^4} \quad (j=1,2), \tag{10.12b}$$

also result from applying $kH \ll \sinh(kH)$ in (10.10) and (10.8) respectively. If we further assume that $\alpha k \ll 1 \ll \beta k^4$, which is typical of the values that occur for the parameters used in our numerical calculations, then approximations (10.12a-b) simplify to

$$\mu_{(j)}^2 \approx -(1+(-1)^j\mathrm{i})k^2 \quad (j=1,2), \tag{10.13a}$$

and

$$\hat{v}_{(j)} \approx (-1)^j 2\mathrm{i} \quad (j=1,2). \tag{10.13b}$$

From (10.13a) we can indeed conclude that the complex wavenumber form a symmetric pair, with

$$\mu_{(1)} \approx 2^{1/4}k\mathrm{e}^{\mathrm{i}3\pi/8}, \qquad \mu_{(2)} \approx 2^{1/4}k\mathrm{e}^{\mathrm{i}5\pi/8}. \tag{10.14}$$

These approximations will now be combined with other régimes that concern the radius of the floe in relation to the wavelengths.

Large floes

Initially, we assume that the radius of the floe is large in relation to the wavelength in the presence of ice-cover and the free-surface wavelength, so that the inequalities $kR \gg 1$ and $k^{(0)}R \gg 1$ hold. Note that as the free-surface wavenumber, $k^{(0)}$, is greater than the ice-covered wavenumber, k, in all but exceptional circumstances, the requirement $kR \gg 1$ will suffice here.

In this case, we may use standard Bessel function expansions (see Tranter, 1968, for example) to determine the relevant approximations

$$\mathrm{J}_m(kR) \sim \left(\frac{2}{\pi kR}\right)^{1/2} \cos\left(kR - \frac{2m+1}{4\pi}\right), \tag{10.15a}$$

$$[\partial_r \mathrm{J}_m(kr)]_{r=R} \sim -k\left(\frac{2}{\pi kR}\right)^{1/2} \sin\left(kR - \frac{2m+1}{4\pi}\right), \tag{10.15b}$$

$$\mathrm{J}_m(\mu_{(i)}R) \sim \left(\frac{1}{2\pi\mu_{(i)}R}\right)^{1/2} \mathrm{e}^{\Im\mathrm{m}(\mu_{(i)})R}\mathrm{e}^{-\mathrm{i}\Re\mathrm{e}(\mu_{(i)})R+\mathrm{i}\frac{2m+1}{4\pi}}, \tag{10.15c}$$

$$[\partial_r \mathrm{J}_m(\mu_{(i)}r)]_{r=R} \sim -\mathrm{i}\mu_{(i)}\left(\frac{1}{2\pi\mu_{(i)}R}\right)^{1/2} \mathrm{e}^{\Im\mathrm{m}(\mu_{(i)})R}\mathrm{e}^{-\mathrm{i}\Re\mathrm{e}(\mu_{(i)})R+\mathrm{i}\frac{2m+1}{4\pi}}, \tag{10.15d}$$

$$\mathrm{H}_m(k^{(0)}R) \sim \left(\frac{2}{\pi k^{(0)}R}\right)^{1/2} \mathrm{e}^{\mathrm{i}k^{(0)}R-\mathrm{i}\frac{2m+1}{4\pi}}, \tag{10.15e}$$

and

$$[\partial_r \mathrm{H}_m(k^{(0)}r)]_{r=R} \sim \mathrm{i}k^{(0)}\left(\frac{2}{\pi k^{(0)}R}\right) \mathrm{e}^{\mathrm{i}k^{(0)}R-\mathrm{i}\frac{2m+1}{4\pi}}, \tag{10.15f}$$

for $m=0,\dots,M$, to be used in conditions (10.9a-b).

It follows from (10.15a-d) that

$$\mathscr{X}_m(w) \sim w^2 \mathrm{J}_m(w), \quad \mathscr{Y}_m(w) \sim w^3(\partial_w \mathrm{J}_m(w)) \quad (m = 0, \dots, M), \tag{10.16}$$

for $w = kR$, $\mu_{(i)}R$ $(i = 1, 2)$, which will be of use in finding the approximate values of $\widetilde{\varphi}_m(R)$ and $\partial_r\widetilde{\varphi}_m(R)$. Specifically, we combine the approximations given in equations (10.13b), (10.14), (10.15a-d) and (10.16) in (10.7), to deduce that, in the chosen régimes,

$$\widetilde{\varphi}_m(R) \sim \left(\frac{2}{\pi kR}\right)^{1/2} X_m, \quad \partial_r\widetilde{\varphi}_m(R) \sim -k\left(\frac{2}{\pi kR}\right)^{1/2} Y_m \quad (m = 0, \dots, M) \tag{10.17}$$

where

$$X_m = (1 - 2^{1/2})\cos\left(kR - \frac{2m+1}{4\pi}\right) - 2^{-1/4}\csc\left(\frac{\pi}{8}\right)\sin\left(kR - \frac{2m+1}{4\pi}\right), \tag{10.18}$$

and

$$Y_m = 2^{1/4}\csc\left(\frac{\pi}{8}\right)\cos\left(kR - \frac{2m+1}{4\pi}\right) + \left(1 + 2^{1/2}\cot\left(\frac{\pi}{8}\right)\right)\sin\left(kR - \frac{2m+1}{4\pi}\right).$$

It is now possible to settle on an approximation to the amplitudes, $\widetilde{A}_m$, within the ice-covered domain. Using (10.17) in (10.9a), along with the approximate coefficients (10.11) and approximate Hankel functions (10.15e-f), results in

$$\left\{\frac{2k^2}{k^{(0)}(k + k^{(0)})}Y_m + \mathrm{i}\frac{k + k^{(0)}}{2k}X_m\right\}\widetilde{A}_m \approx \mathrm{i}\left(\frac{k}{k^{(0)}}\right)^{3/2} \mathrm{e}^{-\mathrm{i}k^{(0)}R + \mathrm{i}\frac{2m+1}{4\pi}} \quad (m = 0, \dots, M), \tag{10.19a}$$

which holds for $kH \ll \sinh(kH)$, $\alpha k \ll 1 \ll \beta k^4$ and $kR \gg 1$. As the frequency increases or the ice becomes thicker the régime $k^{(0)} \gg k$ is attained (see figure 5.10(a)) and the above approximation may be simplified to

$$\widetilde{A}_m \approx \frac{2}{X_m}\left(\frac{k}{k^{(0)}}\right)^{5/2} \mathrm{e}^{-\mathrm{i}k^{(0)}R + \mathrm{i}\frac{2m+1}{4\pi}} \quad (m = 0, \dots, M). \tag{10.19b}$$

The validity of the approximations (10.19a-b) is represented graphically in figure 10.1. In this figure, the exact amplitude $\widetilde{A}_m$ is plotted as a function of kR for the first two azimuthal modes $(m = 0, 1)$, alongside the approximations derived above. The quantity kR is varied through the frequency rather than the radius of the floe, so that the geometry remains fixed throughout. Varying the frequency leads to a non-constant relationship between values of the wavenumbers k and $k^{(0)}$, which affects the assumption $k \ll k^{(0)}$ that produced the simpler of the approximations, given in (10.19b). Therefore, two particular values of the quotient $k/k^{(0)}$ are plotted on each of the subfigures, so that we may judge

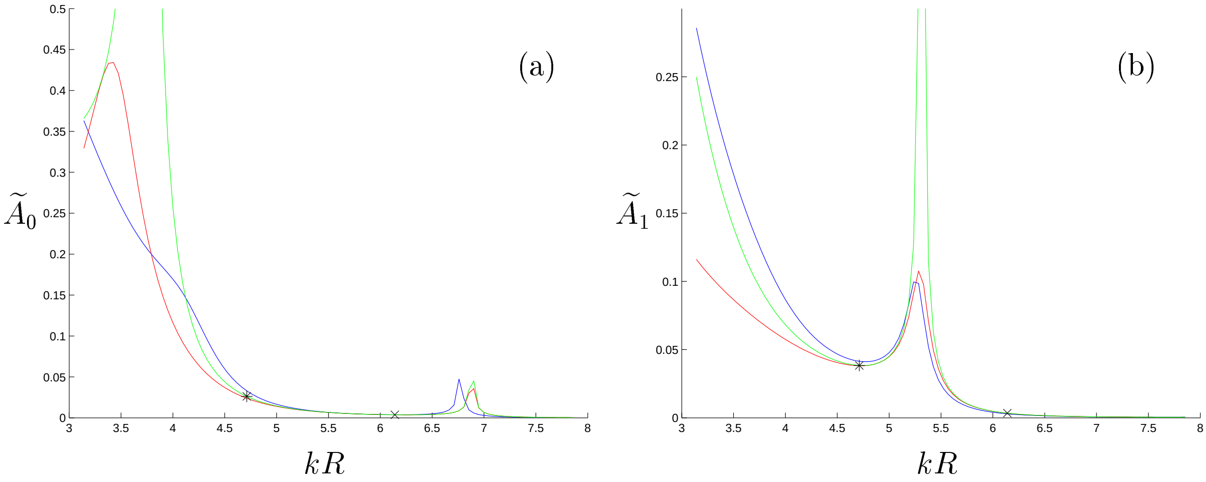

Figure 10.1: Comparison of the exact amplitudes, $\widetilde{A}_m$ $(m = 0, 1)$, (blue curves) in the uniform problem with their approximations, which are derived for the régimes $kH \ll \sinh(kH)$ and $kR \gg 1$ in equation (10.19a) (red) and additionally $k \ll k^{(0)}$ in equation (10.19b) (green). Amplitudes are plotted as functions of non-dimensional wavenumber kR. Two values of the ratio of the ice-covered and free-surface propagating wavenumbers are also plotted, with $k/k^{(0)} \approx 0.25$ $(*)$ and $k/k^{(0)} \approx 0.1$ $(\times)$.

the validity of the simpler approximation.

As predicted, we note from figure 10.1 that there is good agreement of the approximations of $\widetilde{A}_m$ to its exact value as the régime $kR \gg 1$ is attained. Moreover, consistent with the derivation of approximation (10.19b), the two approximations tend towards one another as the relative values of the wavenumbers $k/k^{(0)}$ decreases.

For the larger values of kR, the approximations are deficient in one aspect. This is in their accuracy around the fine structure of the amplitudes. Such fine structure has been noted previously at high frequencies for finite floes in the context of partial ice-cover, and was attributed to interactions within the floe. We note that the fine structure is a product of the oscillatory nature of the coefficient of the amplitude $\widetilde{A}_m$ in (10.9a). Specifically, it is a minimum in this coefficient that results in the observed maximum in the amplitudes. Such behaviour is particularly sensitive and it should not be surprising that it is difficult to approximate. Moreover, as the effect of the trigonometric functions in the relative magnitudes of the values X_m and Y_m were not considered when deriving approximation (10.19b), its sensitivity around these points is most acute.

The difficulty in the approximation of the fine structure is particularly evident in figure 10.1(b) at the point $kR \approx 5.3$. Here, the approximation that assumes $k^{(0)} \gg k$ predicts a resonance rather than a finite maximum, as is attained by the exact amplitude and the other approximation. The spurious resonance arises due to the quantity X_1 vanishing, which, with reference to its definition (10.18), occurs when

$$\tan\left(kR - \frac{3}{4\pi}\right) = \frac{2^{1/4}\sin\left(\frac{\pi}{8}\right)}{1 - 2^{1/2}}.$$

We deduce that approximation (10.19b) will predict an infinite number of (spurious) resonances in each azimuthal mode.

By retaining the term relating to the quantity Y_m in approximation (10.19a) the spurious resonance is avoided and the fine structure is represented well. We may therefore deduce that resonance does not occur in the exact solution for large kR due to the oscillatory parts of the terms involving $\widetilde{\varphi}_m$ and $\partial_r\widetilde{\varphi}_m$, in equation (10.9a), not vanishing concurrently. Furthermore, this indicates that the maxima result from zeros in the oscillatory part of the dominant term (involving $\widetilde{\varphi}_m$), at which point the magnitude of the bracketed quantity on the left-hand side of (10.9a) becomes dependent on the magnitude of the non-dominant term (involving $\partial_r\widetilde{\varphi}_m$).

Note that, our approximation of the oscillatory part of the dominant term, i.e. the oscillatory part of X_m, is identical to the oscillatory part of the corresponding Bessel function of the first kind $\mathrm{J}_m(kR)$ in the régime $kR \gg 1$ (see equation (10.15a)). We can therefore relate the maxima in the amplitude A_m to the points at which the values kR coincide with the zeros of the Bessel function J_m. The behaviour of the Bessel function of the first kind is such that for a finite floe length R and $k < k_{mx}$, where k_{mx} is finite, the limit (10.15a) will only be attained for orders $m < m_{mx}$ for some finite number m_{mx} (see Tranter, 1968, for example). These Bessel functions may then contain zeros at some values of k through the oscillatory part of (10.15a); however, all higher orders will be non-vanishing. This leads us to conclude that, for a fixed floe and frequency range, only a finite number of modes will experience a fine structure for large kR. Consequently, we can be confident that a disproportionally large response is very unlikely in high order modes and we will not eliminate any significant motion through truncation of the azimuthal coordinate.

Small floes

We now turn to the opposing limit, in which the radius of the floe is small in comparison to the ice-covered and free-surface wavelengths. This is described by the régimes $kR \ll 1$ and $k^{(0)}R \ll 1$. Repeating our argument that, under most circumstances, $k < k^{(0)}$, we need only consider that $k^{(0)}R \ll 1$. We note that the case in which $k^{(0)}R \ll 1$ is of less interest than the case $kR \gg 1$, as we expect the floe to go relatively unnoticed when the incident wave is long in relation to the diameter of the floe. However, it is still worthy of investigation and we will also use the asymptotic limits required here to help describe the motion near the centre of the floe in the next section.

For small arguments wR, where $w = k$ or $\mu_{(i)}$ $(i = 1, 2)$, the Bessel function of the first kind is such that

$$\mathrm{J}_m(wR) \sim \frac{1}{m!}\left(\frac{wR}{2}\right)^m, \tag{10.20a}$$

and

$$\partial_r[\mathrm{J}_m(wr)]_{r=R} \sim \begin{cases} -\dfrac{w^2 R}{2} & (m = 0), \\ \dfrac{w(wR)^{m-1}}{2^m(m-1)!} & (m \neq 0). \end{cases} \tag{10.20b}$$

Similarly, the Hankel function of the first kind is seen to behave as

$$\mathrm{H}_m(k^{(0)}R) \sim \begin{cases} \dfrac{2\mathrm{i}}{\pi}\ln(k^{(0)}R) & (m = 0), \\ -\dfrac{\mathrm{i}(m-1)!}{\pi}\left(\dfrac{2}{k^{(0)}R}\right)^m & (m \neq 0), \end{cases} \tag{10.20c}$$

and

$$[\partial_r \mathrm{H}_m(k^{(0)}r)]_{r=R} \sim \begin{cases} \dfrac{2\mathrm{i}}{\pi R} & (m = 0), \\ \dfrac{\mathrm{i}m!}{\pi R^{m+1}}\left(\dfrac{2}{k^{(0)}}\right)^m & (m \neq 0), \end{cases} \tag{10.20d}$$

for small arguments $k^{(0)}R$.

It is convenient to consider the behaviour of quantities in the current régime in terms of orders of magnitude. By using the form of the Bessel functions J_m given in (10.20a-b), with $w = k$ and $\mu_{(i)}$ $(i = 1, 2)$, and taking the limits (10.13a-b), derived for the case $kH \ll \sinh(kH)$, in (10.7), we find that

$$\widetilde{\varphi}_m(R) = \mathrm{O}\left((kR)^m\right), \quad k^{-1}\partial_r\widetilde{\varphi}_m(R) = \mathrm{O}\left((kR)^{m-1}\right) \quad (m = 1, \ldots, M). \tag{10.21}$$

Applying (10.21) to (10.7) along with the corresponding approximations of the Hankel functions via (10.20c-d) and the approximations of the coefficients, which are given in (10.11), we obtain the following relation

$$G_m(k, k_0)\widetilde{A}_m = \mathrm{O}\left(\frac{k^{(0)}}{k}\right)^{m-1} \quad (m = 0, \ldots, M), \tag{10.22}$$

where the function G_m is given in Appendix C. This is not particularly helpful unless we consider the frequency to be large enough or the ice thickness to be great enough that $k \ll k^{(0)}$, in which case

$$\widetilde{A}_m = \mathrm{O}\left(\frac{k^{(0)}}{k}\right)^{m-2} \quad (m = 0, \ldots, M). \tag{10.23}$$

The equations (10.22) and (10.23) allow us to describe the behaviour of the amplitudes

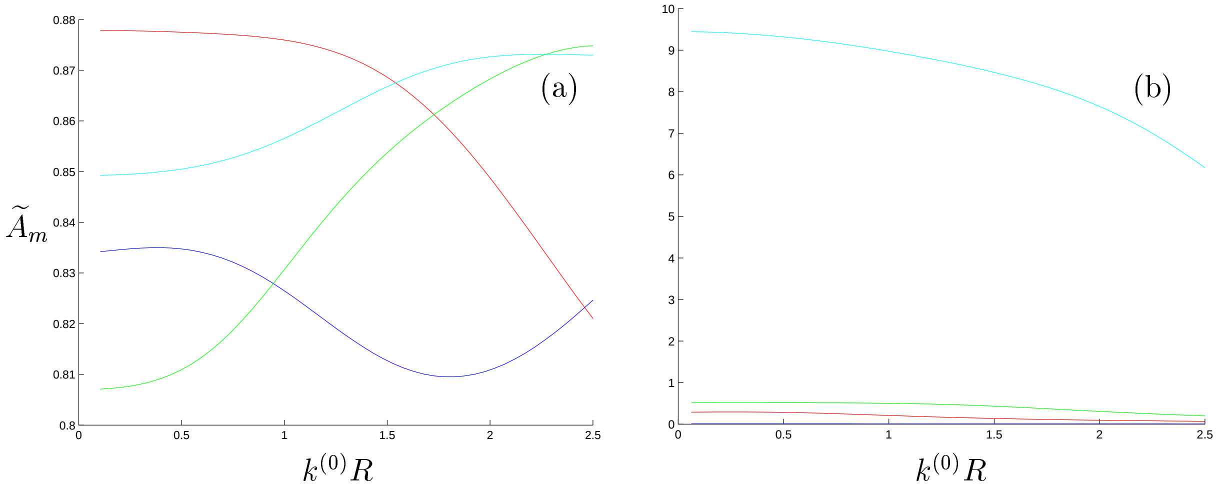

Figure 10.2: Comparison of the amplitudes $\widetilde{A}_m$ $(m = 0, \ldots, 3)$ for small $k^{(0)}R$. In part (a) the ratio of the ice-covered and free-surface wavenumbers $k/k^{(0)} \approx 0.95$, which refers to equation (10.22). In part (b) $k/k^{(0)} \approx 0.055$, which refers to equation (10.23). The orders of the amplitudes are $m = 0$ (blue curves), $m = 1$ (red), $m = 2$ (green) and $m = 3$ (cyan).

beneath the ice, when $k^{(0)}R \ll 1$, to some extent. In figure 10.2 exact values of the amplitudes $\widetilde{A}_m$ $(m = 0, \ldots, 3)$ are plotted as functions of $k^{(0)}R$ for two different ratios of the wavenumbers. Here, the quantity $k^{(0)}R$ varies with the radius and all other parameters are held constant. When the wavenumbers in the ice-covered and ice-free regions are similar, as in figure 10.2(a), the relation (10.23) does not hold and we deduce only from (10.22) that the amplitudes will be of approximately the same magnitude. However, when the free-surface wavenumber is far greater than the ice-covered wavenumber, as in figure 10.2(b), relation (10.23) applies, so that the ratio of these two wavenumbers dominates and the magnitude of the amplitudes will increase with m. Both of these predictions are consistent with the relevant results presented in figure 10.2.

10.2 Results

In this section we conduct a numerical investigation of the problem of an axisymmetric ice floe forced by a single plane incident wave, using the single-mode approximation. As has been mentioned previously, we are particularly concerned with the properties of the ice floe itself, under such forcing. We will consider how changes to the properties of the floe, specifically its thickness, radius and draught as well as the introduction of undulations, affects the displacement it experiences. These issues will be studied for a range of incident wavelengths. The influence of the bed is not our primary concern and a constant depth of 20m will be retained throughout. We note that if one wished to do so, our formulation permits a full investigation of the response away from the floe.

10.2.1 Azimuthal convergence of the MMA

Before we begin to draw physical conclusions from the results of our single-mode approximation, it is necessary to consider the issue of the convergence of the approximation with respect to the number of azimuthal modes. In particular, we wish to establish our conjecture that only a relatively small number of these modes will allow us to accurately describe the motion within the ice-covered region. This investigation is restricted to ice of uniform thickness and a zero draught, as the inferences that we draw may be readily extended to varying geometry.

Here, we wish to attain the single-mode approximation to the reduced displacement, η, through the choice of a suitably large number of azimuthal modes, M. The rate of convergence will, clearly, be closely linked to the relative magnitudes of the amplitudes $\widetilde{A}_m$ $(m = 0, \ldots, M)$, and, as such, we make use of the discussion and findings of §10.1. At each point within the domain occupied by the ice floe $(r < R)$, it is actually the relative magnitudes of the compound quantities $\widetilde{A}_m \mathrm{J}_m(r)\cos(m\theta)$ that govern the convergence rate. Although we do not study the issue in detail here, it is noted that the free-surface region depends on different compound quantities and will therefore have a separate convergence rate. We will confine our examination to the contour $\theta = 0$, so that each azimuthal mode is weighted equally. It is accepted that the convergence of $[\eta]_{\theta=0}$ does not necessarily imply convergence at all points within the ice; however, it proves to be sufficient for our purposes.

We will consider the convergence issues as we vary the ice thickness, D, and the floe radius, R, as well as the incident wavelength, $\lambda^{(0)}$. Each of figures 10.3-10.5 plots the convergence of the single-mode approximation against the modulus of the reduced displacement, for the three incident wavelengths $\lambda^{(0)} = 10$m, 30m and 100m and the two thicknesses $D = 0.1$m and 1m, where a radius $R = 10$m, 50m or 100m is maintained respectively.

Let us again note that $\mathrm{J}_m(z) = \mathrm{O}(z^m)$ as $z \to 0$. There is therefore a value of $r < R$ in all of the floes for which the mth mode dominates over the $(m+1)$th mode to any given tolerance, which is relative to the amplitudes $\widetilde{A}_m$ and the wavenumber k. Note that the behaviour we are referring to is separate from the limit $k^{(0)}R \ll 1$, which was studied in the previous section. The dominance of the lower-order modes is clear in the convergence shown in figures 10.3-10.5. The physical implication of this finding is that the flexure of the ice towards the centre of a circular floe is less than at its edge.

As the value of $r < R$ increases, and hence so does kr, more of the Bessel functions become significant. Therefore, a greater number of azimuthal modes is required to achieve convergence around the edge of the floe (and hence throughout the floe). Considering the wavenumber k fixed, the scope for the growth of kr is evidently dependent on the radius of the floe, R, so that the number of azimuthal modes required increases with the radius

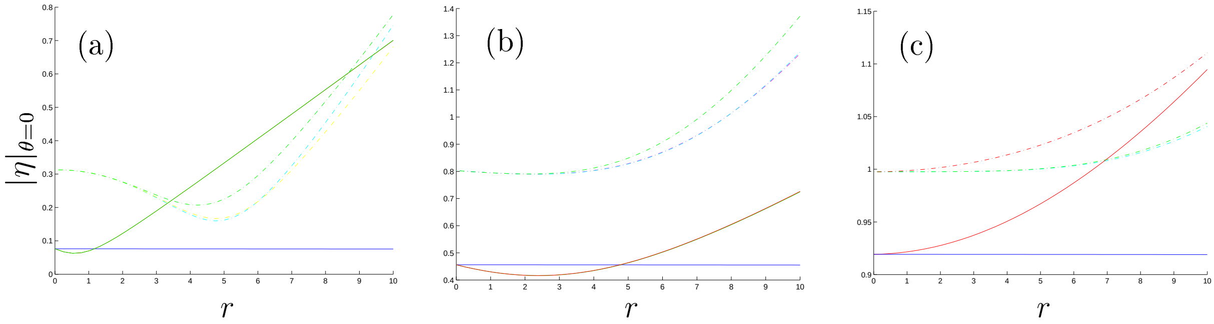

Figure 10.3: Azimuthal convergence of the single-mode aproximation to $|\eta|_{\theta=0}$. The floe has uniform thickness $D = 1$m (solid curves) and $D = 0.1$m (dot-dash), with a zero draught and radius 10m. The incident wave has length (a) $\lambda^{(0)} = 10$m, (b) $\lambda^{(0)} = 30$m and (c) $\lambda^{(0)} = 100$m. The azimuthal dimensions of the approximations are $M = 0$ (blue curves) $M = 1$ (red) $M = 2$ (green), $M = 3$ (cyan), $M = 4$ (magenta) and $M = 5$ (yellow).

of the floe. We infer from this observation that the motion within a larger floe is generally more complicated than that within a smaller floe, which is to be expected on intuitive grounds.

We have seen previously, for example in figure 5.10(a), that the wavenumber, k, decreases in value as the ice thickens or the incident wave lengthens. The value of kr is therefore smaller when the ice is thicker or the incident wave is longer (at each fixed r) and hence the lower-order modes dominate for a greater proportion of floe in such circumstances. This is reflected in the results that show that a smaller number of azimuthal modes is required for convergence both as $\lambda^{(0)}$ increases and as the ice thickness increases.

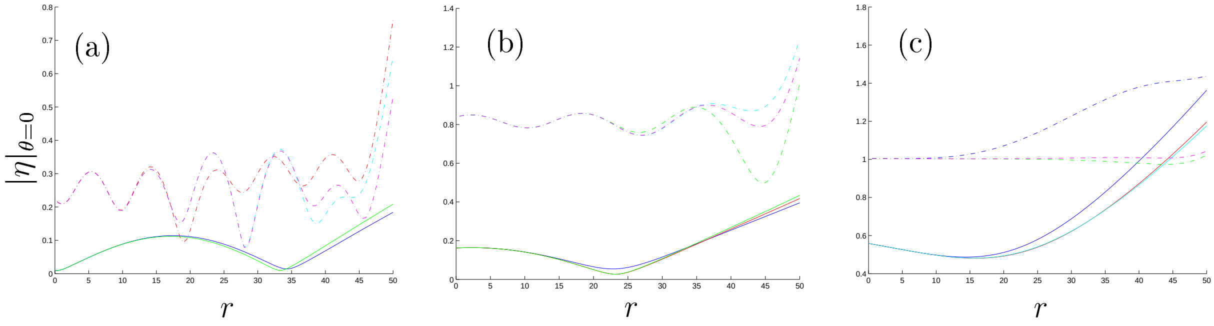

Figure 10.4: As in figure 10.3 but with floe of radius 50m. The azimuthal dimensions of the approximations are: in part (a) $M = 2$ (blue curves) $M = 7$ (red) $M = 8$ (green), $M = 14$ (cyan) and $M = 25$ (magenta); in part (b) (b) $M = 2$ (blue curves) $M = 4$ (red) $M = 8$ (green), $M = 10$ (cyan) and $M = 14$ (magenta); and in part (c) $M = 2$ (blue curves) $M = 3$ (red) $M = 4$ (green), $M = 8$ (cyan) and $M = 9$ (magenta).

In §10.1 we deduced an approximation for the amplitudes $\widetilde{A}_m$ that holds under the conditions $kR \gg 1$ and $\sinh(kH) \gg kH$. To do so, we used an asymptotic limit of the

Bessel functions of the first kind, which is given in equations (10.15a-b); however, for any combination of k and R, this limit will only have been attained by a finite number of these Bessel functions, with all such functions of a higher order being negligible. Clearly then, we have the result that a larger value of kR leads to a greater number of modes significant in resolving this issue. We note that, for $kR \gg 1$, the limit reached by the Bessel functions, J_m, of contributing magnitude differ only in their oscillatory phase, with a magnitude dependent on the value of kR. Similarly, the approximations (10.19a-b) suggest that the limits attained by the significant amplitudes, $\widetilde{A}_m$, have a magnitude that is largely dependent on the relationship between the wavenumbers k and $k^{(0)}$ and not the order m. However, this ignores the complications of the fine structure these amplitudes are prone to in this limit, which are introduced through the values X_m and Y_m. We will look into the issue of fine structure more closely at a later point of this chapter. Consequently, at the edge of the ice we find that the non-trivial modes are of comparable weight and hence all of these contributing modes must be included to achieve convergence at this point. Again we conclude that a larger floe or a larger wavenumber beneath the ice, the latter caused by a shorter incident wave and or thinner ice, will necessitate inclusion of a greater number of azimuthal modes for convergence.

Although for large values of kR there may be a relatively high number of modes that contribute to the motion at the edge of the floe, we have already seen that the higher-order Bessel functions decay rapidly towards the centre of the floe. We therefore find that waves within the floe become damped away from the edge to a degree that depends on the number of significant modes at the edge. This feature is noticeable in a number of the sets of results, particularly the $D = 0.1$m case of figure 10.4(a).

The régime $kR \gg 1$ can be attained in two ways. The first is through the radius, R, increasing, for which the limiting magnitude of the amplitudes remains fixed. The second is through the incident wavelength, $\lambda^{(0)}$, decreasing, for which we have $k \to \infty$ and $k^{(0)} \to \infty$ and $k/k^{(0)} \to 0$ as $\lambda^{(0)} \to 0$. In this case we refer to the second approximation (10.19b) and deduce that a shortening of the incident wavelength will typically result in a decrease in the magnitude of the amplitudes. As the magnitude of the displacement, towards the centre of the floe, is dependent on the size of the amplitudes of the primary modes, we infer that, away from the ice edge, as the incident wavelength shortens, the magnitude of the displacement function decreases. This may be interpreted as a resistance to the incident wave. We note that this is relative to the thickness of the ice, so that, since k decreases as D increases, the phenomenon is more prevalent for thicker ice floes.

The second régime ivestigated in §10.1 was $k^{(0)}R \ll 1$, which may be attained by a relatively small radius R or a relatively long incident wavelength. Assuming $k \ll k^{(0)}$, we see that the limit (10.23) holds, so that the amplitudes grow in magnitude as the order increases. By combining equation (10.23) with the corresponding limit of the Bessel

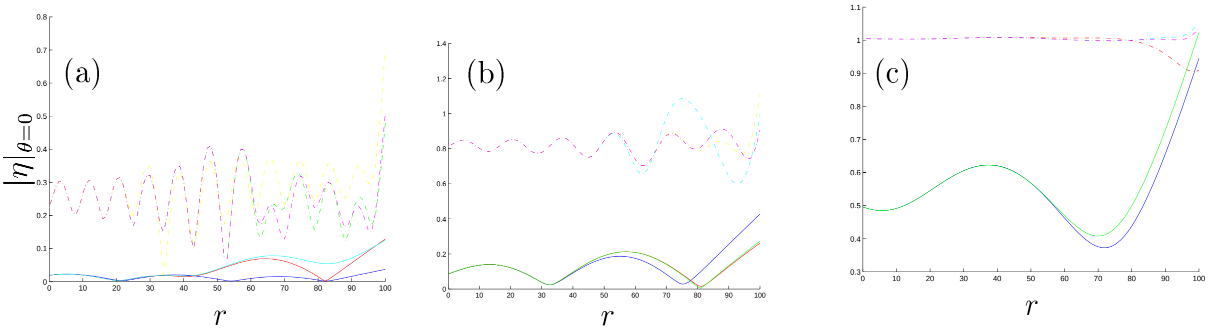

Figure 10.5: As in figure 10.3 but with floe of radius 100m. The azimuthal dimensions of the approximations are: in part (a) $M = 2$ (blue curves) $M = 6$ (red) $M = 10$ (green), $M = 12$ (cyan), $M = 23$ (yellow) and $M = 38$ (magenta); in part (b) (b) $M = 5$ (blue curves) $M = 7$ (red) $M = 11$ (green), $M = 14$ (cyan), $M = 19$ (yellow) and $M = 27$ (magenta); and in part (c) $M = 5$ (blue curves) $M = 7$ (red) $M = 8$ (green), $M = 9$ (cyan) and $M = 13$ (magenta).

functions of the first kind (10.20a), we deduce that

$$\mathrm{J}_m(kR)\widetilde{A}_m = \mathrm{O}\left(\left(\frac{kR}{k^{(0)}R}\right)^2 (k^{(0)}R)^m\right), \tag{10.24}$$

which implies that the lower-order azimuthal modes dominate throughout the floe. If we cannot assume that the wavenumber beneath the ice is significantly less than the free-surface wavenumber, then equation (10.22) rather than (10.23) holds. In figure 10.2(a) we saw that in this case the amplitudes are of approximately the same magnitude and this means that the dominance of the lower-order modes within the floe is more pronounced.

Expression (10.24) closely resembles the behaviour of the incident wave in this limit, reduced by a factor which is proportional to the difference in the two wavenumbers. As predicted, we therefore infer that, for small $k^{(0)}R$, the motion beneath the ice is that of the incident wave, whose amplitude is damped by the presence of a surface load. As the floe is small in its extent in relation to the wavelength, we envisage this situation as that of the floe merely resting on the passing wave with its flexure being negligible.

10.2.2 Uniform floes

From this point on we will consider only approximations that have converged sufficiently, with respect to the azimuthal coordinate, to the single-vertical-mode approximation. Our investigation of the scattering properties of axisymmetric floes starts with the restriction to floes of a uniform thickness and a zero draught (over a flat bed) and will incorporate some of the observations made in our discussion of the azimuthal convergence in the previous section. We note that a similar investigation was made by Meylan & Squire (1995) over an infinite fluid depth for $R = 50\text{m}-400\text{m}$, $D = 0.5\text{m}-5\text{m}$ and $\lambda^{(0)} = 100\text{m}$.

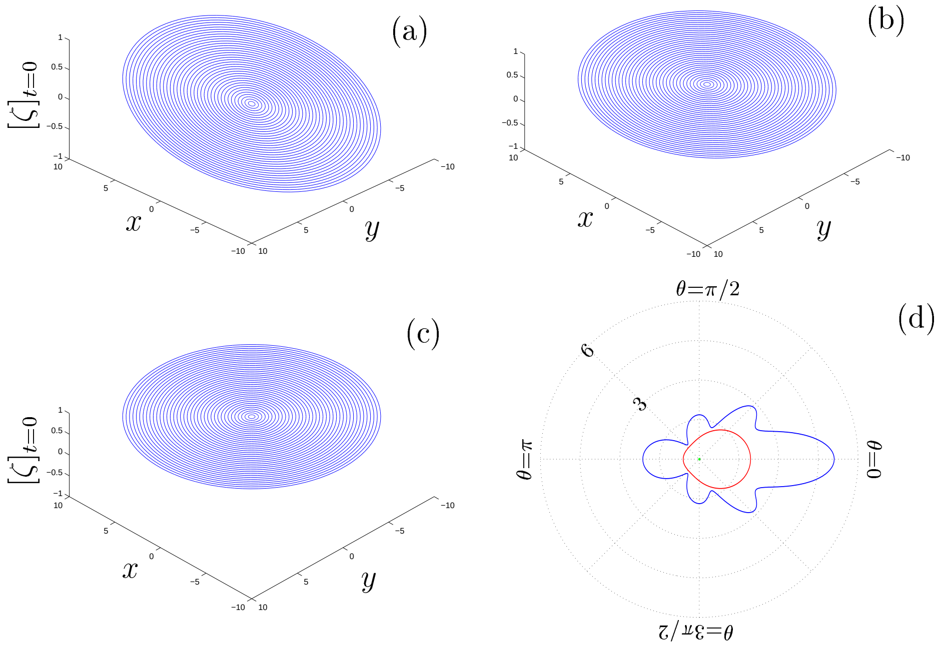

Figure 10.6: Parts (a-c) display single-mode approximations of the floe displacement at $t = 0$, for a floe of uniform thickness $D = 1$m, a zero draught and radius 10m. The incident wavelength is (a) $\lambda^{(0)} = 10$m, (b) $\lambda^{(0)} = 30$m and (c) $\lambda^{(0)} = 100$m. Part (d) gives the corresponding ribbon plots of the 'far-field scattering', $|2\mathcal{S}_B/\pi k^{(0)}|$, as functions of the azimuthal coordinate. The dotted circles define the level surfaces of the function and two of the values are indicated on the contour $\theta = 3\pi/4$. Here, the wavelengths are $\lambda^{(0)} = 10$m (blue curve), $\lambda^{(0)} = 30$m (red) and $\lambda^{(0)} = 100$m (green). In parts (a-c) the dimension of the azimuthal coordinate is $M = 2$; and in part (d) $M = 10$ (blue), $M = 5$ (red) and $M = 4$ (green).

For figures 10.6-10.11 we reintroduce the harmonic time dependence to the displacement function, which was removed in equation (2.8) by writing

$$\zeta(x, y, t) = \Re\mathrm{e}\left(\eta(x, y)\mathrm{e}^{-\mathrm{i}\omega t}\right).$$

These figures then display azimuthally converged single-mode approximations to the displacement function, at the initial moment in its harmonic cycle, $[\zeta]_{t=0} = \Re\mathrm{e}(\eta)$, for the sets of parameters that were used in the previous section. Corresponding ribbon plots of the coefficient,

$$\left(\frac{2}{\pi k^{(0)}}\right)^{1/2} \mathcal{S}_B(\theta) = \left(\frac{2}{\pi k^{(0)}}\right)^{1/2} \left\{ \left(B_0 + 2\sum_{m=1}^{\infty} B_m \cos(m\theta) \right) \right\},$$

of the outgoing circular wave

$$r^{-1/2}\mathrm{e}^{\mathrm{i}(k^{(0)}R-\pi/4)},$$

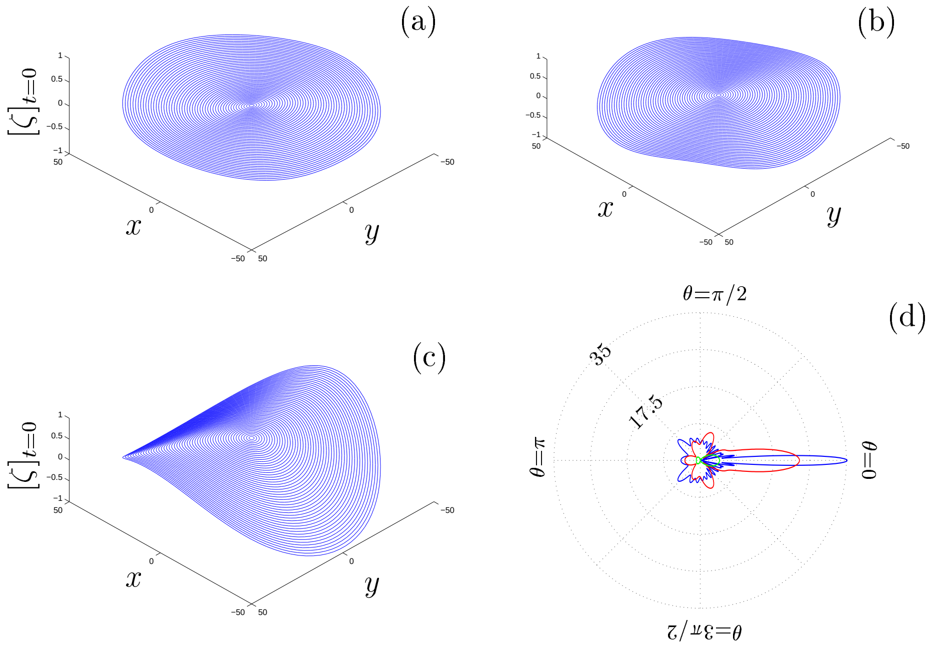

Figure 10.7: As in figure 10.6 but with floe of radius 50m. In parts (a-c) the dimension of the azimuthal coordinate is $M = 8$; and in part (d) $M = 36$ (blue), $M = 13$ (red) and $M = 7$ (green).

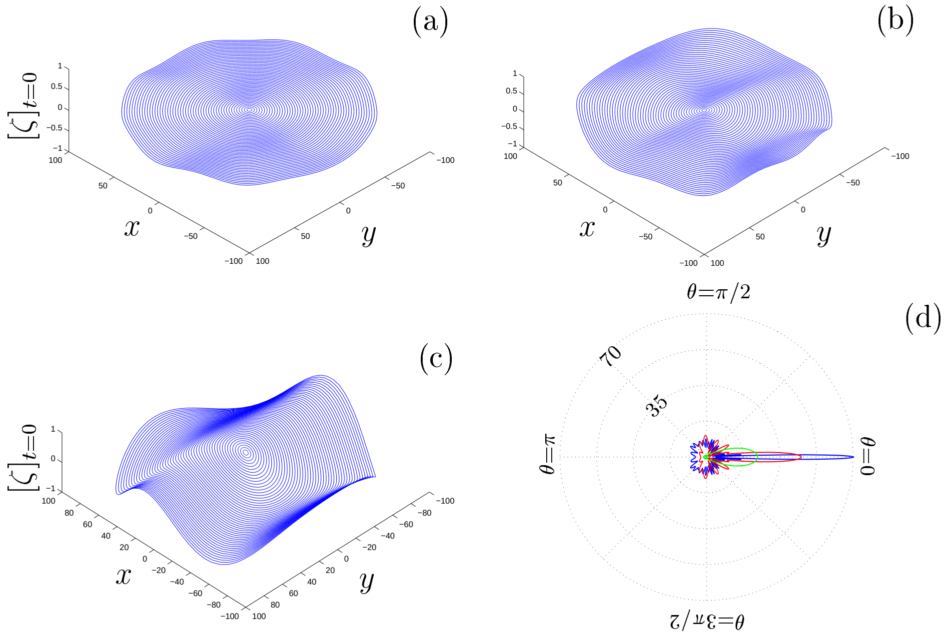

Figure 10.8: As in figure 10.6 but with floe of radius 100m. In part (a) the dimension of the azimuthal coordinate is $M = 12$; in parts (b-c) $M = 11$; and in part (d) $M = 68$ (blue), $M = 36$ (red) and $M = 10$ (green).

which is the slowest decaying part of the scattered wave in the far-field, are also given in parts (d). Unlike figures 9.6-9.7, here we are interested in the physical implications of

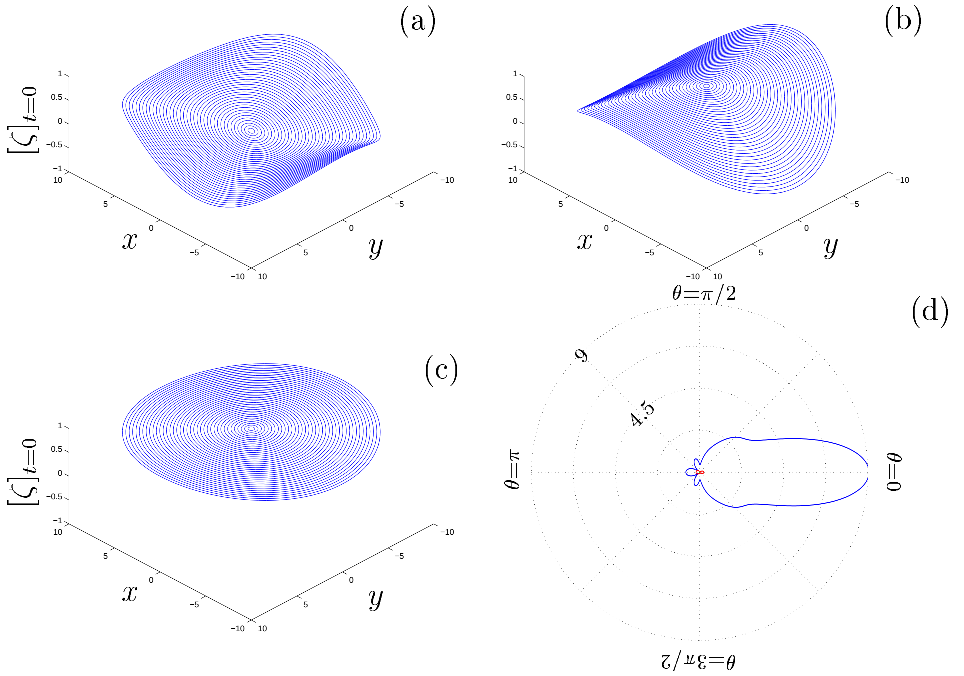

Figure 10.9: As in figure 10.6 but with floe of thickness 0.1m. In parts (a-c) the dimensional of the azimuthal coordinate is $M = 5$; and in part (d) $M = 10$ (blue), $M = 6$ (red) and $M = 4$ (green).

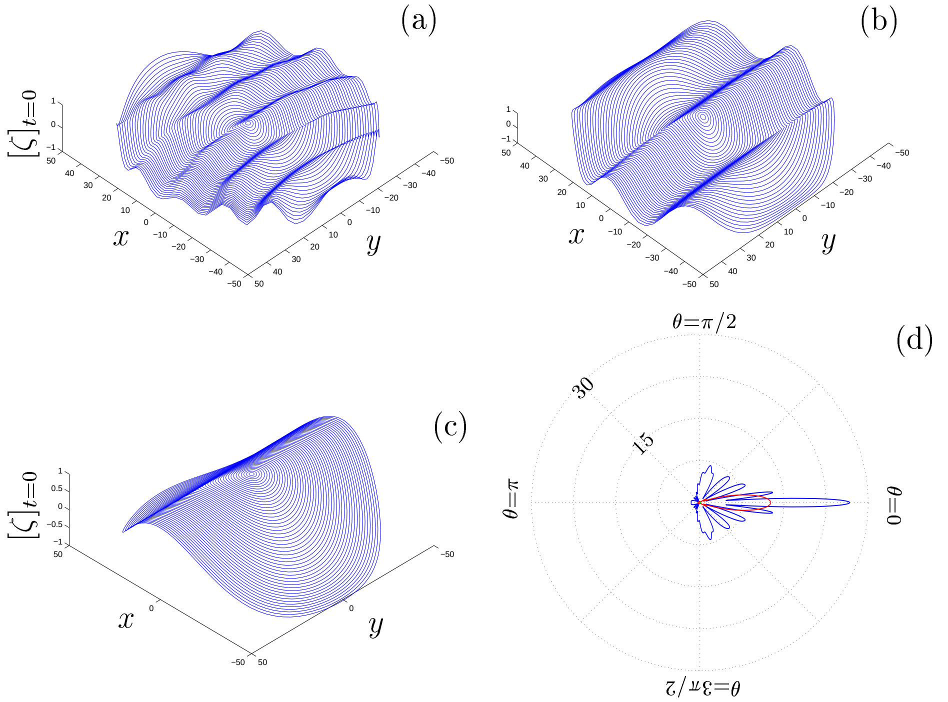

Figure 10.10: As in figure 10.9 but with floe of radius 50m. In part (a) the dimension of the azimuthal coordinate is $M = 25$; in part (b) $M = 14$; in part (c) $M = 11$; and in part (d) $M = 39$ (blue), $M = 14$ (red) and $M = 6$ (green).

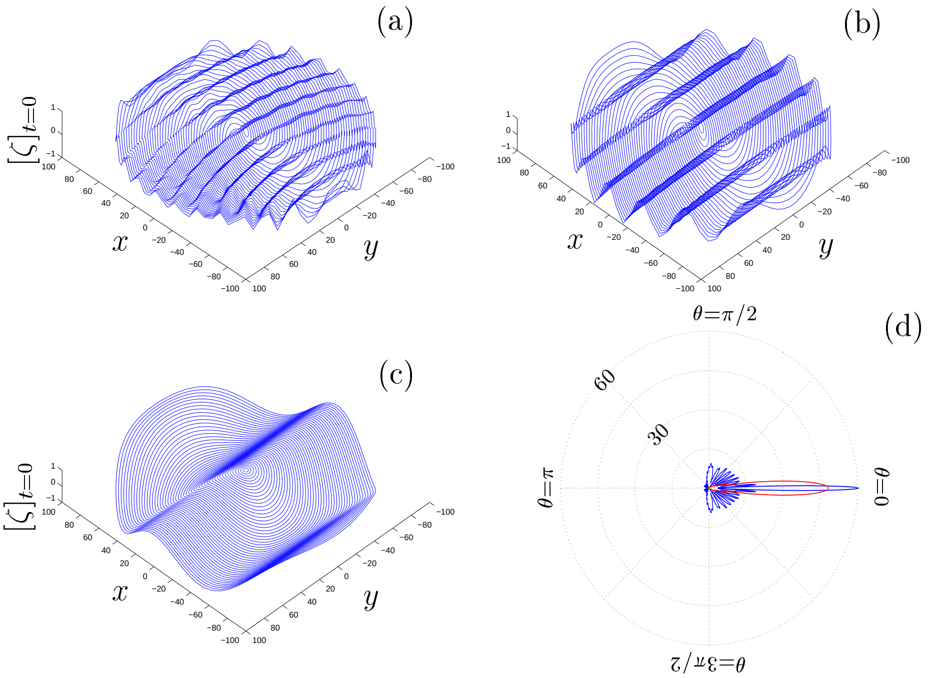

Figure 10.11: As in figure 10.9 but with floe of radius 100m. In part (a) the dimension of the azimuthal coordinate is $M = 38$; in part (b) $M = 27$; in part (c) $M = 18$; and in part (d) $M = 71$ (blue), $M = 27$ (red) and $M = 9$ (green).

these functions and hence plot the above scattered coefficients in ribbon plots where the aspect ratio is fixed.

For $D = 0.1$m the ice is generally compliant with the incident wave and we observe near-plane waves travelling through the ice floes. The ice displays the tendency to elongate the incident wave and we see the phenomenon of damping of the amplitude away from the ice edge. Observe also, in figure 10.11(a) for example, that the circular shape of the ice also slightly curves the plane wave. For $D = 1$m the ice is less prone to become displaced, which may be interpreted as the ice resisting the incident wave. In those situations for which wave motion exists within the ice floe of 1m thickness, for instance in figure 10.8(a), the plane incident wave is distorted by the greater influence exerted by the thicker ice and the displacement of the floe is consequently complicated.

The far-field scattering of the incident wave by the floes of both thicknesses is generally strongest in the direction of the incident wave, $\theta = 0$. We note that the thicker ice, which is more resistive to the incident wave, tends to reflect more of the incident wave into the region $x < 0$ ($\pi/2 < \theta < 3\pi/2$), whereas the thinner ice, for which the incident wave propagates through the floe, scatters almost entirely into the region $x > 0$ ($\pi/2 > \theta, \theta > 3\pi/2$).

As the length of the incident wave increases, we have seen that the wave beneath the ice tends to behave like the incident wave and this effect can be seen in the figures. For example, compare the effect of a 30m incident wavelength in 10.11(b) to the 10m incident

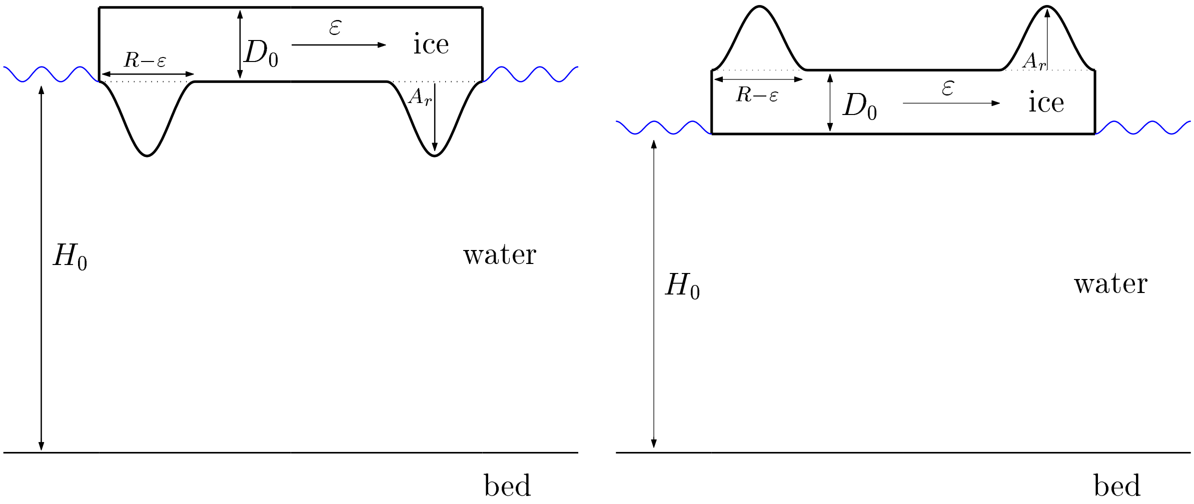

Figure 10.12: Two-dimensional cross-sections of floes with trigonometric edge rims, defined by equation (10.25), which here take the form of both a submergence and a surface protrusion.

wavelength of 10.11(a) and note that it leads to a far less pronounced curvature within the floe. A second example is the near plane wave that travels through the 1m thick floe of 100m radius when the incident wavelength is 100m, which is shown in figure 10.8(c). Correspondingly, it is unsurprising to find that a relatively small amount of scattering is caused for long incident waves compared to short incident waves, for which it has been noted that the ice is more resistant to the incident wave.

10.2.3 The addition of axisymmetric variations

We will now consider how the addition of axisymmetric variations to the thickness affects the deformation the ice experiences. We therefore reintroduce the positive value $\varepsilon < R$, and assume again that the geometry is uniform in the disc $r < \varepsilon$. The full model formulated in §9.1 is only restricted in that, for the present, we retain zero submergence at the edge of the floe.

As in §9.3, the results presented in this section will be only for a floe radius of 50m. However, all of the conclusions that are drawn may be easily interpreted for floes of different sizes.

The first variation is the addition of a trigonometric rim to the edge of the floe, of the form

$$D(r) = \begin{cases} D_0 & (0 < r < \varepsilon), \\ D_0 + A_r \sin^2\left(\dfrac{\pi(r-\varepsilon)}{R-\varepsilon}\right) & (\varepsilon < r < R), \end{cases} \tag{10.25}$$

where D_0 is a positive constant and A_r is the amplitude of the rim. Figure 10.13 plots a series of approximations to the modulus of the reduced displacement function along the x-axis. Ice floes including a trigonometric rim of the form (10.25), are shown for thicknesses $D_0 = 0.1$m and 1m and rim amplitudes $A_r = 0$ (uniform thickness), D_0 and $5D_0$. Furthermore, the rim takes the form of both a submergence, so that

$$d(r) = A_r \sin^2 \left(\frac{\pi(r - r_\varepsilon)}{R - r_\varepsilon} \right) \quad (r_\epsilon < r < R),$$

and also a protrusion on the upper surface of the ice with $d = 0$ instead. These two configurations are shown in figure 10.12. The three incident wavelengths $\lambda^{(0)} = R/10$, $R/4$ and R are used and the width of the protrusion is 20m throughout ($\varepsilon = 30$m).

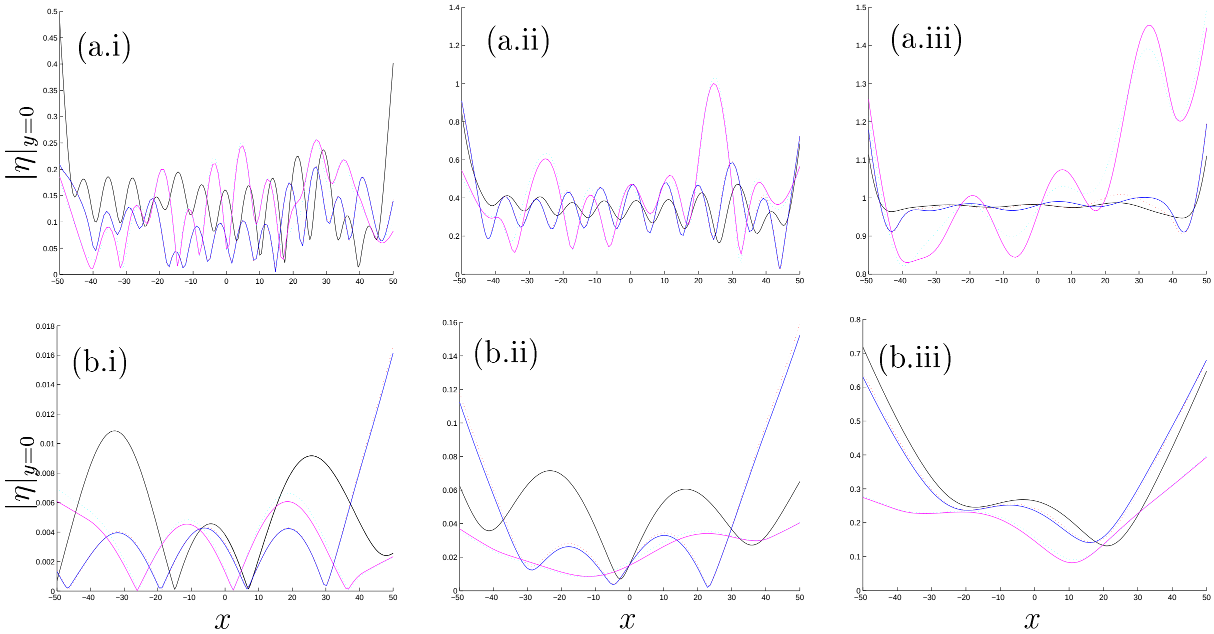

Figure 10.13: Comparison of the moduli of reduced displacement functions along the x-axis of floes of radius 50m and including a trigonometric edge rim, as defined in equation (10.25). The rims are of length 20m, and are in the form of a submergence (solid curves) and a surface protrusion (dotted). The amplitudes are $A_r = 0$ (black curves), $A_r = D_0$ (blue and red) and $A_r = 5D_0$ (cyan and magenta). The incident wavelength is (a-b.i) $\lambda^{(0)} = 5$m, (a-b.ii) $\lambda^{(0)} = 12.5$m and (a-b.iii) $\lambda^{(0)} = 50$m. In parts (a.i-iii) $D_0 = 0.1$m, and in parts (b.i-iii) $D_0 = 1$m.

In our study of two-dimensional scattering by ice of varying thickness, conducted in §§6-7, it was shown that there is a close relationship between geometries that share the same ice thickness, D. Analysis of this phenomenon was carried out in §6.4 for the single-mode approximation and in §7.4 it was shown that the similarity may weaken for those problems that converge more slowly, which is particularly evident in situations of partial ice-cover.

The analysis of §6.4 may be trivially modified to be applicable to the single-mode approximation for the current, three-dimensional problem and it is therefore unsurprising

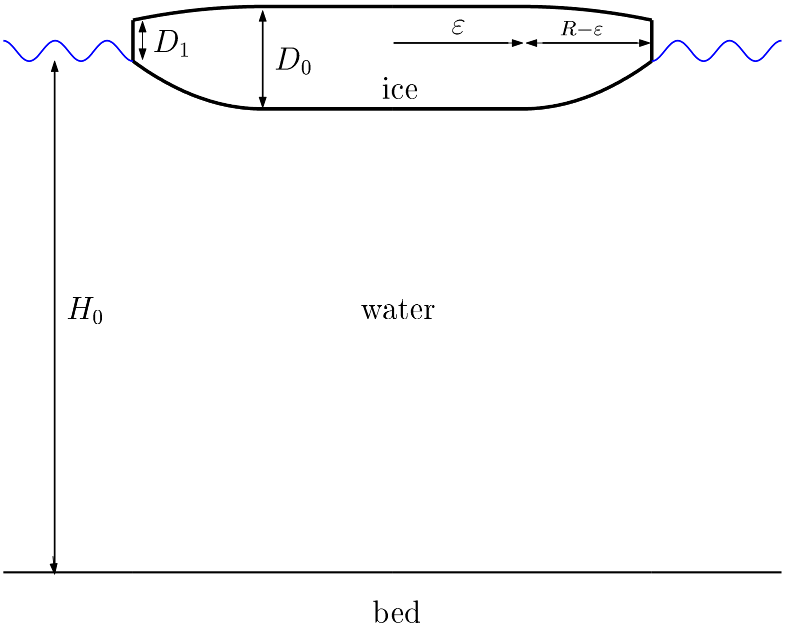

Figure 10.14: Two-dimensional cross-section of a floe with a quadratic increase in thickness, which is defined in equation (10.26), and here appears in the form of a pressure ridge.

to find that the correspondence between the submerged rim and the upper surface rim follows the behaviour witnessed for two-dimensional flows. That is, those geometrical variations that share a common ice thickness, D, produce similar results. Any differences between the two are exaggerated by a (relatively) large amplitude, A_r, and a thinner ice thickness, D_0. Moreover, as variations to the fluid depth become more significant for longer incident waves, from the plots that use the largest value of $\lambda^{(0)}$, we observe a greater deviation between the results for the corresponding positions of the rim. It follows that the displacement caused by the submerged rim and the upper surface rim are most distinct for the instance of the largest amplitude, $A_r = 5D_0$, the thinnest ice thickness, $D_0 = 0.1\text{m}$ and the longest incident wave, $\lambda^{(0)} = R$, which appears in figure 10.13(c).

We also consider a second geometrical variation, which is of the form

$$D(r) = \begin{cases} D_0 & (0 < r < r_\epsilon), \\ D_0 + (D_1 - D_0)\left(\dfrac{r - r_\epsilon}{R - r_\epsilon}\right)^2 & (r_\epsilon < r < R), \end{cases} \tag{10.26}$$

and describes a quadratic increase, away from the edge of the floe, in the ice thickness. The values D_i $(i = 0, 1)$ are positive constants, such that $D_0 > D_1$, with D_0 denoting the ice thickness in the disc of uniform geometry and D_1 the ice thickness at the edge of the floe. An example of a cross-section of a floe that varies in this fashion is shown in figure 10.14.

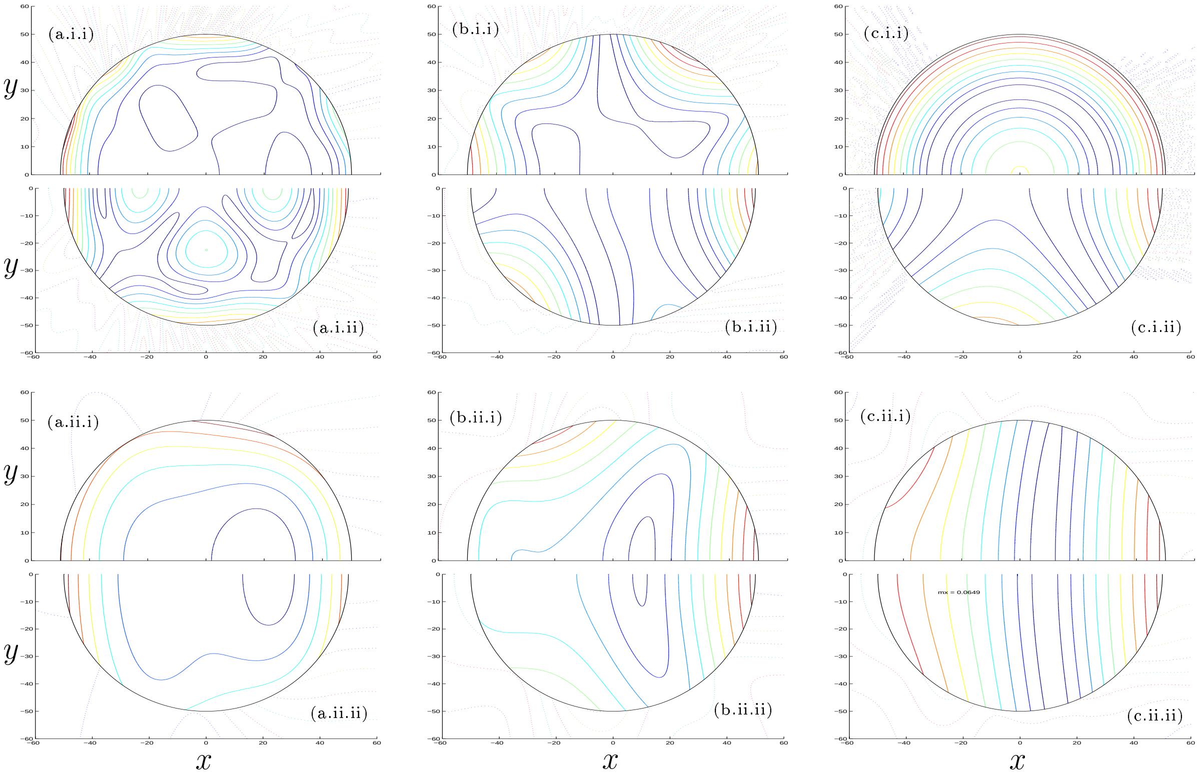

Figure 10.15: Contour plots of the moduli of the reduced displacements of floes along with scattered free-surface profiles surrounding the floes, comparing the results of quadratically varying floes (parts (a-c.i-ii.i)) with corresponding uniform floes (parts (a-c.i-ii.ii)). The thicknesses of the quadratically varying floes are defined by equation (10.26) with $\varepsilon = 10$m and with $D_0 = 10D_1$, and are in the form of pressure ridges. In parts (a.i-ii.i) the thickness is $D_1 = 0.1$m, in parts (b.i-ii.i) $D_1 = 0.25$m and in parts (c.i-ii.i) $D_1 = 0.5$m. The uniform floes have thicknesses chosen to be equal to the avereges of their corresponding varying floes. Each floe has the radius $R = 50$m. The incident wavelength is (a.i.i-ii) $\lambda^{(0)} = 7.15$m, (b.i.i-ii) $\lambda^{(0)} = 6.6$m, (c.i.i-ii) $\lambda^{(0)} = 1.25$m, (a.ii.i-ii) $\lambda^{(0)} = 80$m, (b.ii.i-ii) $\lambda^{(0)} = 40$m and (c.ii.i-ii) $\lambda^{(0)} = 25$m. In each subdomain, depending on which function is being displayed, there are ten contours eqispaced between 0 and either $0.95 \times M_i$ or $0.95 \times M_w$, where $M_i \equiv \max|\eta|$ and $M_w \equiv \max|\partial_z[\phi - \phi_I]_{z=0}\eta|$. We have (a.i.i) $M_i \approx 2.27 \times 10^{-1}$ and $M_w| \approx 1.34$; (a.i.ii) $M_i \approx 1.72 \times 10^{-1}$ and $M_w \approx 1.22$; (b.i.i) $M_i \approx 9.62 \times 10^{-2}$ and $M_w \approx 1.26$; (b.i.ii) $M_i \approx 1.59 \times 10^{-2}$ and $M_w \approx 1.12$; (c.i.i) $M_i \approx 1.55 \times 10^{-2}$ and $M_w \approx 1.27$; (c.i.ii) $M_i \approx 5.18 \times 10^{-5}$ and $M_w \approx 1.23$; (a.ii.i) $M_i \approx 1.10$ and $M_w \approx 7.24 \times 10^{-1}$; (a.ii.ii) $M_i \approx 1.18$ and $M_w \approx 7.72 \times 10^{-1}$; (b.ii.i) $M_i \approx 3.22 \times 10^{-1}$ and $M_w \approx 1.32$; (b.ii.ii) $M_i \approx 3.45 \times 10^{-1}$ and $M_w \approx 1.24$; (c.ii.i) $M_i \approx 8.33 \times 10^{-2}$ and $M_w \approx 1.16$; (c.ii.ii) $M_i \approx 6.49 \times 10^{-2}$ and $M_w \approx 1.14$.

Figure 10.15 gives contour plots of approximations to the reduced displacement function over the floe, along with the surrounding free-surface elevation of the scattered wave, $[\partial_z(\phi - \phi_I)]_{z=0}$. Each contour plot is subdivided such that the upper half domain ($0 < \theta < \pi$) and the lower half domain ($\pi < \theta < 2\pi$) display different but related problems. The upper half domain features a floe whose thickness varies as in equation (10.26) in the form of a pressure ridge, with $D_0 = 10D_1$, which is the particular form of variation displayed in figure 10.14. Following Vaughan & Squire (2006), the ridge is set so that the increment in the upper surface of the ice to the lower surface is in the ratio $2:7$. (For this problem, results not presented show again that ice floes sharing the same thickness, D, have almost idential behaviour to one another). The lower half domain contains results from uniform floes of a thickness chosen to match the mean thickness of the corresponding floe of varying thickness.

In figure 10.15 three edge thicknesses are investigated, namely $D_1 = 0.1$m, 0.25m and 0.5m. For each, a pair of subfigures display the differing response of the floes to a relatively short and a relatively long incident wave. It is clear that, for each pair, the shorter of the two incident waves distinguishes the response of the varying floe from that of the uniform floe, whereas for the longer incident waves, the two floes behave in a similar manner both qualitatively and quantitatively.

Our choice of incident wavelengths was made judiciously in order to highlight these characteristics. The longer of the incident waves was chosen to be as short as possible whilst the floes retained their similarity. We note that the value of the longer incident wave decreases as the ice edge, D_1, becomes thicker. Likewise, it is noted that length of the shorter of the incident waves that we use decreases as the ice edge becomes thicker. The values of the shorter incident waves were selected to demonstrate extreme cases of differing behaviour; however, for an interval of relatively short incident waves, these extremes are by no means unique. The use of the description 'relatively' is dependent on both the radius of the floe and on the wavelength beneath the ice (through the thickness of the ice).

10.2.4 Fine structure

In figures 10.15(a-c.i) the differences in the displacement experienced by the quadratically varying floes and the uniform floes can be attributed to the excitation of a particular azimuthal mode. In part (a.i) the excitation is of the third mode ($m = 2$) of the uniform floe; in part (b.i) the fourth mode ($m = 3$) of the quadratically varying floe and in part (c.i) the primary mode ($m = 0$) of the quadratically varying floe. Note that, due to the dominance of the lower-order Bessel functions towards the centre of the floe, which was discussed in our investigation of the azimuthal convergence earlier in this section, the higher the order of the excited mode the further away from the centre of the floe its dominance becomes apparent. This effect is evident in the disproportionate magnitude of the fourth mode seen in the upper half plane of figure 10.15(b.ii), which manifests itself only in a vicinity of the ice edge, whereas in the upper half plane of part (c.ii) the primary mode prevails throughout the floe.

The excitation of a particular azimuthal mode is the product of a local peak in the value of the corresponding amplitude, $\widetilde{A}_m$. Such peaks have been observed previously in figures 10.1 for $kR \gg 1$, which describes incident waves that are short in relation to the radius of the floe, relative to the ice thickness. The occurrence of such local maxima has been described by the use of the term ‘fine structure’. Fine structure has also been noted for finite ice floes in a two-dimensional context in §7.3.

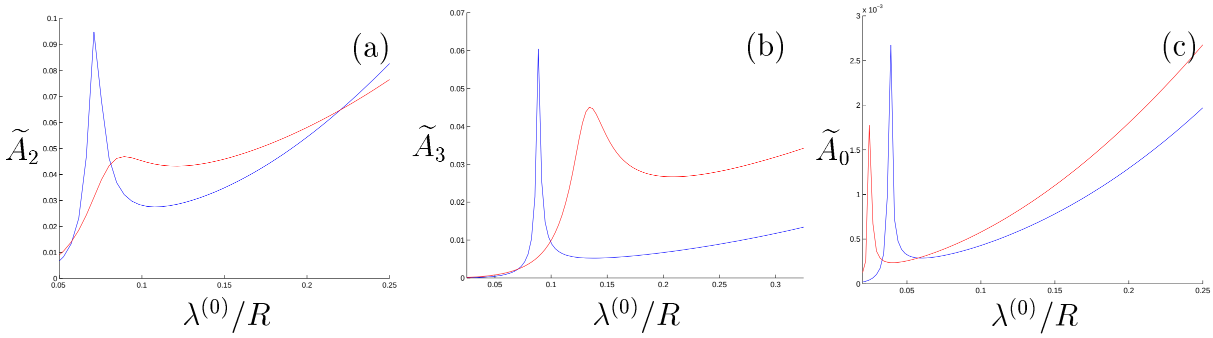

Figure 10.16: Comparison of the amplitudes $\widetilde{A}_m$ of a uniform floe (blue curves) and the corresponding quadratically varying floe (red), as functions of non-dimensional incident wavelength. The floes are as in figure 10.15, with (a) $D_1 = 0.1$m, (b) $D_1 = 0.25$m and (c) $D_1 = 0.5$m. The amplitudes are chosen to be those that appear dominant in the displacement of one of each of the pairs of floes for the problems displayed in figures 10.15(a-c.i.i-ii).

In figures 10.16(a-c) the amplitudes pertinent to figures 10.15(a-c.i) respectively, are plotted as functions of incident wavelength. These figures confirm that the extreme behaviour appearing in figures 10.15(a-c.i) coincides with peaks in the amplitudes. It is noted that each peak that relates to a short wave value of figure 10.15 is accompanied by a peak in the related ice configuration at a nearby incident wavelength. Comparison of the corresponding amplitudes indicates that the peaks caused by the quadratically varying ice are less severe than those of the uniform ice and will consequently lead to less extreme displacement of the floe. We also note that the peaks are locally significant to a greater degree for shorter incident waves.

With reference to equation (10.9a), the peaks observed in the amplitude $\widetilde{A}_m$, for floes of an uniform thickness, are caused by minima in the function

$$F_m(\kappa) \equiv \mathrm{H}_m(k^{(0)}R)\frac{a}{a^{(0)}}\frac{v^{(0)}}{v}\left(\partial_r\widetilde{\varphi}_m(R)\right) - \left(\partial_r\mathrm{H}_m(k^{(0)}R)\right)\frac{v^{(0)}}{v}\widetilde{\varphi}_m(R) \quad (m = 0, \ldots, M). \tag{10.27}$$

In this context we consider the geometry to be fixed, so that the function F_m is only dependent on the frequency parameter κ.

Equation (10.27) is easily extended to floes of varying geometry. To do so, we consider the vectors of unknown functions as the linear combinations

$$\boldsymbol{\Psi}_{0,m} = \boldsymbol{\Psi}_{m,0}(r)A_{m,0} + \sum_{i=1,2}\boldsymbol{\Psi}_{m,-i}(r)A_{m,-i} \quad (m = 0, \ldots, M),$$

where the vectors $\boldsymbol{\Psi}_{m,j} = \left(\varphi_{m,j}, \chi^{(1)}_{m,j}, \chi^{(2)}_{m,j}\right)^T$ $(j = 0, -1, -2)$ are solutions of the initial-value problem defined by the differential equation (9.21), and also satisfy the conditions

$$\left[\mathcal{V}^T\boldsymbol{\Psi}_{m,0}\right]_{r=\varepsilon_+} = \left(\mathcal{V}^T\mathcal{C}\mathcal{J}_m(\varepsilon)\right)^{(\varepsilon)}\mathbf{I}_1, \quad \left[\mathcal{V}^T\boldsymbol{\Psi}_{m,-i}\right]_{r=\varepsilon_+} = \left(\mathcal{V}^T\mathcal{C}\mathcal{J}_m(\varepsilon)\right)^{(\varepsilon)}\mathbf{I}_{i+1} \quad (i = 1, 2)$$

$$\left[\mathcal{V}_+^{-1}\{(\mathcal{A}\partial_r\boldsymbol{\Psi}_{m,0}) + (\mathcal{Q}\mathcal{N}^{(m)}\boldsymbol{\Psi}_{m,0})\}\right]_{r=\varepsilon_+} = \left(\mathcal{V}^{-1}\mathcal{A}\mathcal{C}(\partial_r\mathcal{J}_m)(\varepsilon)\right)^{(\varepsilon)}\mathbf{I}_1,$$

and

$$\left[\mathcal{V}_+^{-1}\{(\mathcal{A}\partial_r\boldsymbol{\Psi}_{m,-i}) + (\mathcal{Q}\mathcal{N}^{(m)}\boldsymbol{\Psi}_{m,-i})\}\right]_{r=\varepsilon_+} = \left(\mathcal{V}^{-1}\mathcal{A}\mathcal{C}(\partial_r\mathcal{J}_m)(\varepsilon)\right)^{(\varepsilon)}\mathbf{I}_{i+1} \quad (i = 1, 2),$$

for $m = 0, \ldots, M$. The functions $\widetilde{\varphi}_m$, satisfying $\varphi_m = \widetilde{\varphi}_m A_m$ are then defined by

$$\widetilde{\varphi}_m(r) = \varphi_{m,0}(r) + \sum_{i=1,2} \hat{v}_{(i)}\frac{\triangle_m^{0,i_-}}{\triangle_m^{i,i_-}}\varphi_{m,-i}(r),$$

where

$$\triangle_m^{i,j} \equiv \widetilde{\mathfrak{M}}_m(\chi^{(1)}_{m,i}, \chi^{(2)}_{m,i})\widetilde{\mathfrak{S}}_m(\chi^{(1)}_{m,j}, \chi^{(2)}_{m,j}) - \widetilde{\mathfrak{M}}_m(\chi^{(1)}_{m,j}, \chi^{(2)}_{m,j})\widetilde{\mathfrak{S}}_m(\chi^{(1)}_{m,i}, \chi^{(2)}_{m,i}),$$

using the definitions of the bending moment and shearing stress operators given in (9.26a-b).

The amplitides A_m may then be calculated via

$$F_m(\kappa)A_m = -\frac{2\mathrm{i}}{\pi R},$$

where the function F_m has been redefined through the addition of an extra term, and is now given by

$$\begin{aligned} F_m(\kappa) \equiv{}& \mathrm{H}_m(k^{(0)}R)\frac{a}{a^{(0)}}\frac{v^{(0)}}{v}(\partial_r\widetilde{\varphi}_m(R)) + \Big\{\mathrm{H}_m(k^{(0)}R)\frac{\widetilde{q}}{a^{(0)}}\frac{v^{(0)}}{v} - \\ & \left(\partial_r\mathrm{H}_m(k^{(0)}R)\right)\frac{v^{(0)}}{v_+}\Big\}\widetilde{\varphi}_m(R), \end{aligned}$$

for $m = 0, \ldots, M$. The quantity $\widetilde{q} = Q_{0,0}$, where the matrix Q is defined in equation (3.8), is associated with the jump condition that replaces the continuity of fluid velocity at the water-ice interface.

A zero of the function F_m at κ would correspond to a resonance in the function φ_m at that particular frequency; however, this phenomenon has not been observed throughout extensive numerical simulations. The peaks that we have observed, resulting from minima in F_m, have been only of local significance, which is a consequence of the short wave régime, in which they occur, coinciding with the limit in which the ice experiences diminishing displacement. This would be somewhat counteracted if we were to consider the bending moment of the floe rather than its displacement, due to the factor of k^2 that it introduces (see §8.4).

Following Chamberlain & Porter (1998), the minima of F_m, for positive real-valued κ, are related to zeros at complex values of κ, whose imaginary part is small and negative. Such values of κ correspond an imaginary component in the frequency and thus relate to waves that decay slowly in time.

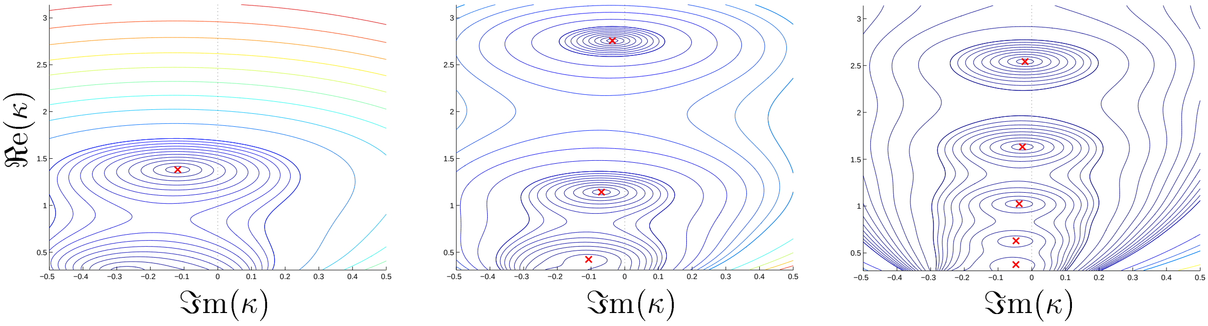

Figure 10.17: The function $\widehat{F}$, which is defined in equation (10.30), as a function of the complex frequency parameter κ, using an uniform floe of thickness $D = 0.25$m and a zero draught. From left to right the floe has radius $R = 25$m, $R = 50$m and $R = 100$m, respectively. The zeros of $\widehat{F}$ are marked with an $\times$.

By further following Chamberlain & Porter (1998), the zeros of F_m may be obtained through use of the iterative scheme

$$\kappa_{n+1} = \kappa_n - \frac{F_m(\kappa_n)}{\widetilde{F}'_m(\kappa_n)}, \quad \widetilde{F}'_m(\kappa) \equiv \frac{F_m(\kappa+\delta) - F_m(\kappa)}{\delta}, \quad (n = 0, \ldots), \tag{10.29}$$

where κ_0 is an appropriate initial guess. Equation (10.29) defines an approximate version of Newton's method and δ must be chosen suitably (here $\delta = 10^{-12}\mathrm{i}$ was used). This method is applicable to all of the problems considered in this chapter; however, as it necessitates intricate numerical calculations for cases of varying geometry, it is expedient to consider only uniform ice floes and flat beds. We may now relate, for example, the peak in $\widetilde{A}_2$ at $\lambda^{(0)} \approx 7.15$m, which is shown in figure 10.16(a), to a zero of F_2 at $\kappa = 0.8818 - 0.0425\mathrm{i}$, for which $\lambda^{(0)} = 7.1089 + 0.3426\mathrm{i}$.

Figures 10.17-10.19 plot the modulus of the function

$$\widehat{F}_m(\kappa) \equiv \left(k^{(0)}R\right)^{1/2} \mathrm{e}^{-\mathrm{i}k^{(0)}R} F_m(\kappa) \quad (m = 0, \ldots, M), \tag{10.30}$$

for the primary azimuthal mode ($m = 0$), using the normalised weighting, $\varpi_0 = 1/a^{1/2}$, over the complex domain $\Re\mathrm{e}(\kappa) \in (\pi/10, \pi)$, $\Im\mathrm{m}(\kappa) \in (-0.5, 0.5)$. The function $\widehat{F}_m$ is chosen for display as it reduces the exponential growth/decay that occurs in the function

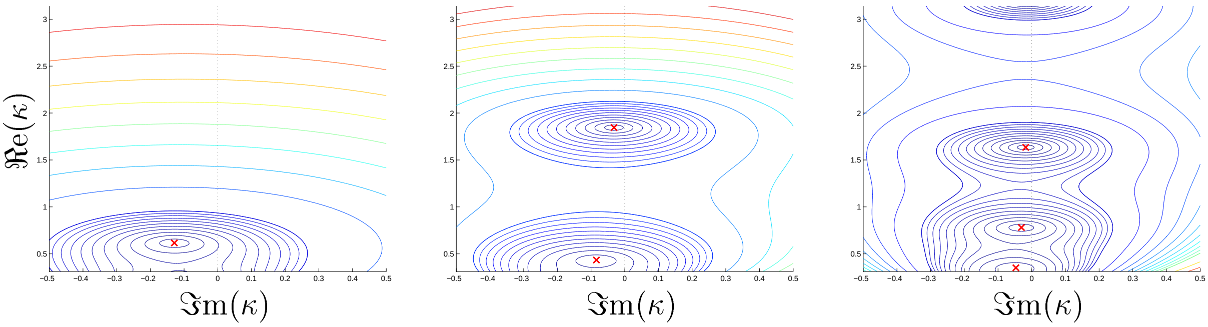

Figure 10.18: As in figure 10.17 but for an ice thickness of $D = 0.5$m.

F_m as the imaginary part of κ increases. The positions of the zeros occurring in this domain are also indicated. It is only necessary to present results for the primary azimuthal mode as calculations indicate that higher-order modes behave in an analogous fashion.

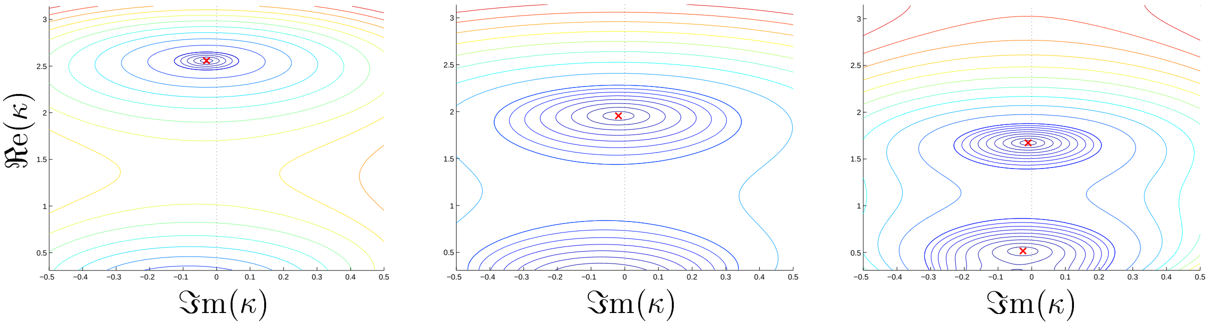

Figure 10.19: As in figure 10.17 but for an ice thickness of $D = 1$m.

Along the real κ-axis the incident wavenumber varies from $\lambda^{(0)} = 2$m at $\kappa = \pi/10$ to $\lambda^{(0)} = 20$m at $\kappa = \pi/10$. The three ice thicknesses $D = 0.25$m, 0.5m and 1m and three radii $R = 25$m, 50m and 100m are displayed. It is clear that the number of zeros increases as the size of the radius increases or the ice becomes thinner, both of which are consistent with the hypothesis that the peaks are caused by interactions within the ice when the wavelength beneath the ice is shorter than the diameter of the floe. We further note that the location of the zeros drifts away from the real axis as the real value of the root decreases. This is consistent with the earlier observation that the peaks in the amplitudes are more severe at lower wavelengths.

10.2.5 An Archimedean draught

For our final set of numerical results, we will consider the effect of introducing an Archimedean draught to the ice floe. The models of the ice floe that have been used in this chapter up until this point have all assumed no submergence at the edge of the floe, in order that we may investigate other issues. However, we now wish to study a model that is as realistic as possible. For an axisymmetric floe, the physically correct draught, d, is calculated from the Archimedean condition

$$\int_0^R \{\rho_i D(r) - \rho_w d(r)\}\mathrm{d}r = 0.$$

If the floe is uniform, then the Archimedean draught, $d = d_A$, is given by

$$d_A(D_0) = \frac{\rho_i D_0}{\rho_w}, \tag{10.31}$$

where $D = D_0$ is the constant thickness of the ice.

A similar investigation was carried out for two-dimensional structures in §7.5 and it was seen that the inclusion of an Archimedean draught had the ability to significantly affect the scattering produced by the ice. Many of the conclusions that were drawn for those two-dimensional problems studied are true of general structures and have been verified (in results not presented) for the problem of an axisymmetric floe that we study in this chapter. We may therefore narrow our investigation.

The work of §7.5 indicated that it is the extra source of scattering introduced by a submerged portion of the ice edge that is the dominant factor in distinguishing the Archimedean problem from that of ice with zero edge submergence. Unsurprisingly, the effects of the inclusion of an Archimedean draught increased as the edge submergence became greater. This is also true of the current three-dimensional problem, and hence results need only be displayed for an edge thickness of 1m.

Furthermore, for two-dimensional problems, the influence of an Archimedean draught was shown to be related to the length of the incident wave. For short incident waves, an Archimedean floe is typically displaced with a lesser magnitude than the equivalent floe with no edge submergence. This was attributed to the submerged portion of the ice edge preventing the incident waves from penetrating beneath the floe to a certain extent. For long incident waves, the influence of the submerged portion of the ice edge is negligible and the small difference produced by the inclusion of an Archimedean draught was ascribed to the change in fluid depth beneath the ice.

In this section we will be primarily concerned with the régime in which the submerged portion of the ice edge is significant, namely incident waves that are short relative to the dimensions of the floe. More specifically, we will look at the relationship between the introduction of an Archimedean draught and the fine structure that has been observed for short incident waves within axisymmetric floes. Fine stucture has also been noted in two-dimensional floes of a finite extent but was not studied in relation to a physically correct draught. This is because fine structure has proven to be far more prevalent in the results presented in this chapter and an investigation is therefore more justified at this juncture.

We will also restrict our investigation to uniform floes. This is because it allows us to directly study the effect of the scattering caused by the submerged portion of the ice edge. For the finite length two-dimensional floes with an Archimedean draught used in §7.5.3, it was found that the addition of variations to the ice surfaces had the effect of changing the solution by varying the amount of edge submergence but achieved little else. This also proves to be the case in the current context (although, again, we display no results to this end).

In figures 10.20-10.22, we consider introducing a non-zero submergence to a uniform floe of a 50m radius. The ice thickness is 1m and hence the Archimedean draught is $d = d_A = 90$cm, via equation (10.31).

The amplitudes of the first two azimuthal modes, $\widetilde{A}_i$ $(i = 0, 1)$, are shown in figure 10.20 as functions of a normalised incident wavelength. This is done for both the floe of an Archimedean draught and that of a zero draught so that we can judge the effect of the introduction of submergence.

Figures 10.20(a-b.i) display the amplitudes over a wide range of incident wavelengths. For the longer incident waves, the amplitudes do not display any fine structure and although a gap between the corresponding amplitudes of the two problems is evident they are very closely matched and resulting approximations (not shown) are extremely similar qualitatively and quantitatively. This behaviour is consistent with that of the two-dimensional configurations that we have studied.

As the incident wavelength decreases, we observe the onset of fine structure in each of the amplitudes. For the primary amplitude, $\widetilde{A}_0$, this occurs around $\lambda^{(0)}/R = 0.55$, and it is clear that the local maximum obtained by the Archimedean amplitude is greater than the value of the zero draught amplitude. In fact, the zero draught amplitude does not actually produce a local maximum at this point but merely an inflection point. Both problems do, however, produce a local maximum for the amplitude $\widetilde{A}_1$ around $\lambda^{(0)}/R = 0.2$. Again, the value attained by the Archimedean amplitude is greater than that of the zero draught amplitude. This is despite the Archimedean amplitudes, in both cases, tending to be smaller than the zero draught amplitude away from their local peaks.

Comparison of the respective amplitudes in figures 10.20(a-b.i) becomes difficult at small incident wavelengths, due to the relatively small values of the amplitudes in this limit. For this reason, figures 10.20(a-b.ii) plot the same amplitudes over small intervals of short incident waves, centred around an occurrence of fine structure. This allows us to clearly observe that the Archimedean amplitudes are typically smaller in magnitude than their zero draught counterparts, a tendency that was commented upon for two-dimensional configurations in §7.5 and was again alluded to above. This short wave relationship is broken only by the fine structure, so that the Archimedean amplitude often exceeds that of the zero draught amplitude at these points, for instance in the case seen in figure 10.20(b.ii). However, as displayed in figure 10.20(a.ii), it is not necessarily the Archimedean amplitude that attains the greatest magnitude at a peak. Although we must therefore conclude that we are unable to predict if a submergence will cause a greater magnitude in the peaks, we note that peaks appear to occur around the same points as when no submergence is included. This phenomenon has been observed in other similar problems not presented here. That is, the introduction of an Archimedean draught appears to modify the maxima of the zero draught floe rather than creating new maxima. We may relate this to our argument of §10.1 that the peaks in the amplitudes of uniform floes are determined by the occurrence of zeros in the Bessel functions with the argument kR. As an Archimedean floe is of the same dimensions as its zero draught counterpart and the slight change in fluid depth caused by the submergence will do little to the value of the wavenumber, k, then the reasoning that led to this link may be repeated. It is therefore unsurprising to find that the peaks in the amplitudes of these two problems occur at almost identical frequencies. Conversely, earlier we saw that the inroduction of a varying ice thickness caused drifts in the position of the amplitude peaks (see figure 10.16).

The displacement experienced over the floe for three specific incident wavelengths is shown in figure 10.21. As in figure 10.15 the displacement is displayed in the form of contour plots, with the upper half ($y > 0$) and lower half planes ($y < 0$) representing the solutions for differing floes. Here, the upper half plane is the floe with an Archimedean draught and the lower half is the floe that has a zero draught. The free-surface profile around the floe is again included.

Our choice of incident wavelengths is made to highlight different situations that occur in the short wave limit. In figure 10.21(b) the sixteen amplitudes, $\widetilde{A}_m$ ($m = 0, \dots, 15$), used to represent the motion within the floe, are free of fine structure, which may be seen graphically for the first six amplitudes in figure 10.22. Consequently, we find that scattering caused by the two floes are qualitatively almost identical. The smaller magnitude of the Archimedean amplitudes for short wavelengths, away from fine structure, results in the displacement experienced by the Archimedean floe being significantly less than the zero draught floe, in this case. This is again attributed to the greater reflection of the incident wave caused by the submerged portion of the ice edge, which is supported by the greater displacement of the free-surface around the Archimedean floe.

The case of the incident wavelength $\lambda^{(0)} = 7$m is shown in figure 10.21(c). It is clear that the fifth azimuthal mode dominates within both floes and this is confirmed if we refer to figure 10.22 around $\lambda^{(0)}/R = 0.14$. Although the displacement within both floes again match qualitatively, it is the magnitude of the Archimedean floe that is the greater in this case. This is easily attributed to the greater maximum attained by the dominant amplitude, $\widetilde{A}_4$, in the case of the Archimedean draught.

As the amplitude attached to each azimuthal mode experiences fine structure, it is

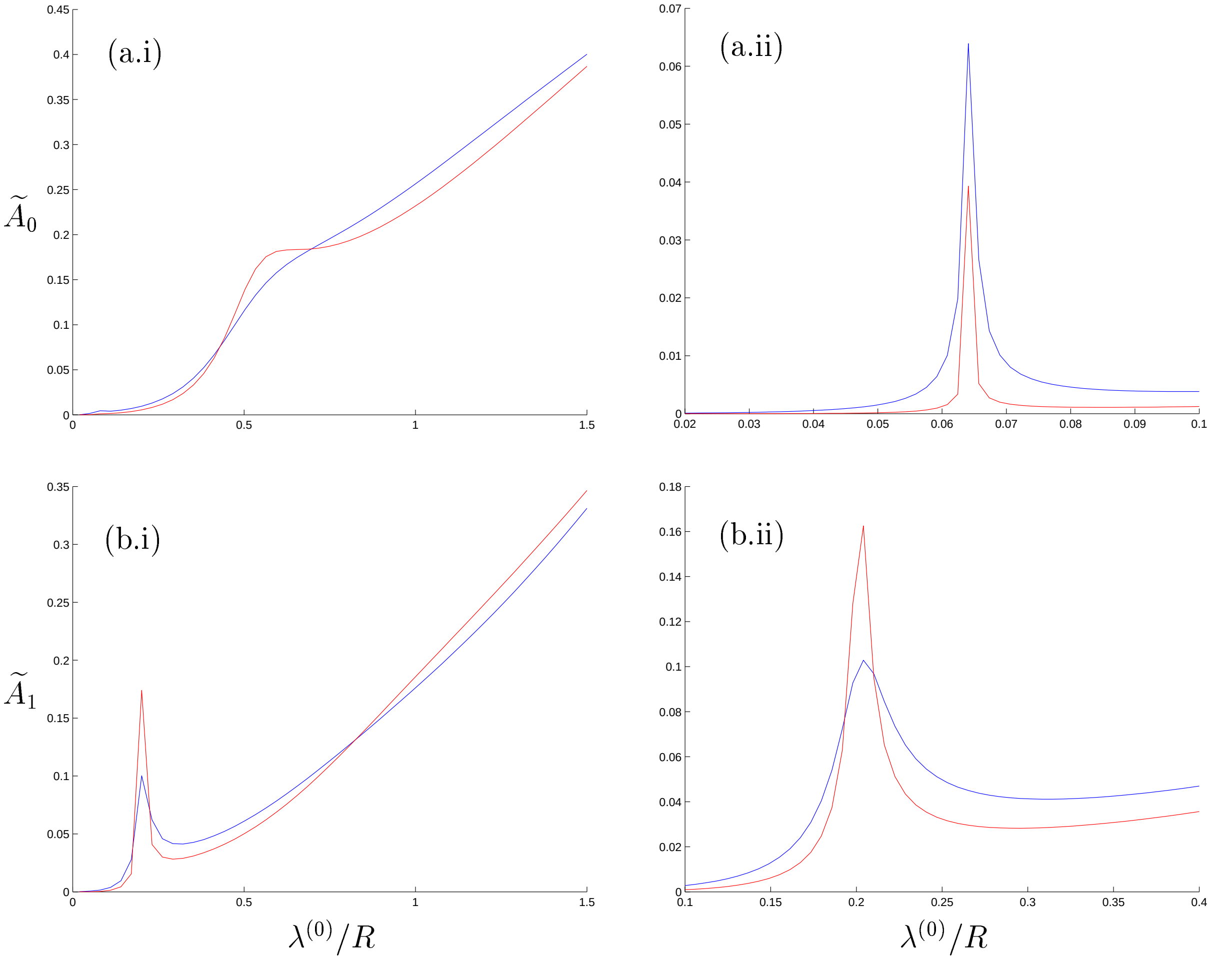

Figure 10.20: Comparison of the amplitudes $\widetilde{A}_m$ $(m = 0, 1)$ of a zero draught (blue curves) and the corresponding Archimedean draught (red) floe, as functions of non-dimensional incident wavelength. The floes have thickness $D_0 = 1$m and radius $R = 50$m.

possible for more than one of the amplitudes used in the approximation to be passing through a local maximum concomitantly. Such a situation is given here by the incident wavelength $\lambda^{(0)} = 3.25$m and is displayed in figure 10.21(a). We note from figure 10.22 around $\lambda^{(0)}/R = 0.065$ that, at this wavelength, both the primary amplitude, $\widetilde{A}_0$, and the sixth amplitude, $\widetilde{A}_5$, are peaking or are in the process of peaking.

As the amplitudes of the Archimedean draught and zero draught problems peak at significantly different values, the relative size of the primary and sixth amplitudes are very different for the two different floes. This makes the question of dominance of a particular azimuthal mode more complicated in this case. Hence, for this wavelength, we have the greatest qualitative difference caused by the introduction of an Archimedean draught seen in figure 10.21. Nevertheless, the two problems remain extremely close in the structure of their response, with the primary azimuthal mode dominant around the centre of the floe and the sixth mode likewise at the edge of the floe.

It would be possible to find more complicated interactions of the fine structures of

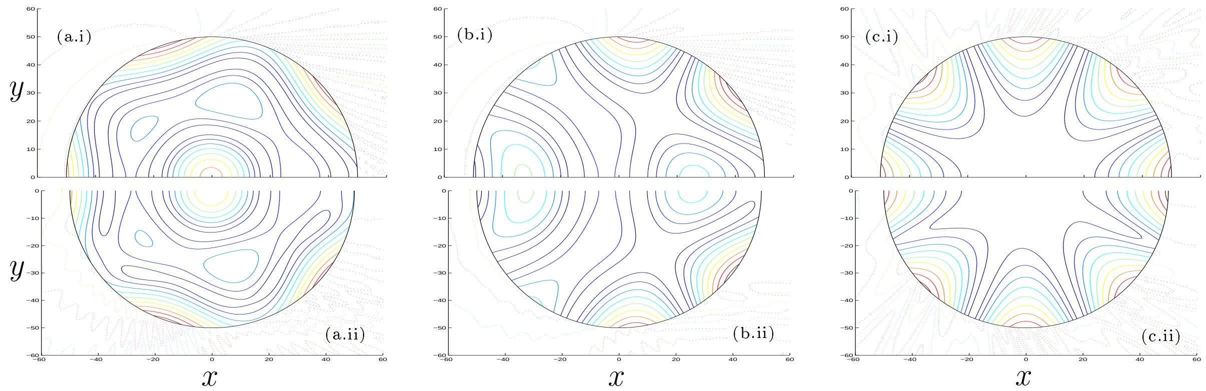

Figure 10.21: Comparison of the scattering caused by floes of an Archimedean draught (upper half planes, parts (a-c.i)) and the corresponding zero draught floes (lower half planes, parts (a-c.ii)). Contours plots are as in figure 10.15. The floes are uniform, of thickness $D_0 = 1$m and radius $R = 50$m. The incident wavelength is (a.i-ii) $\lambda^{(0)} = 3.25$m, (b.i-ii) $\lambda^{(0)} = 5$m and (c.i-ii) $\lambda^{(0)} = 7$m. Using $M_i \equiv \max|\eta|$ and $M_w \equiv M_w$, we have (a.i) $M_i \approx 5.72 \times 10^{-2}$ and $M_w \approx 1.33$; (a.ii) $M_i \approx 1.23 \times 10^{-2}$ and $M_w \approx 1.16$; (b.i) $M_i \approx 6.4 \times 10^{-3}$ and $M_w \approx 1.27$; (b.ii) $M_i \approx 1.99 \times 10^{-2}$ and $M_w \approx 1.10$; (c.i) $M_i \approx 1.95 \times 10^{-1}$ and $M_w \approx 1.33$; (c.ii) $M_i \approx 1.33 \times 10^{-1}$ and $M_w \approx 1.25$.

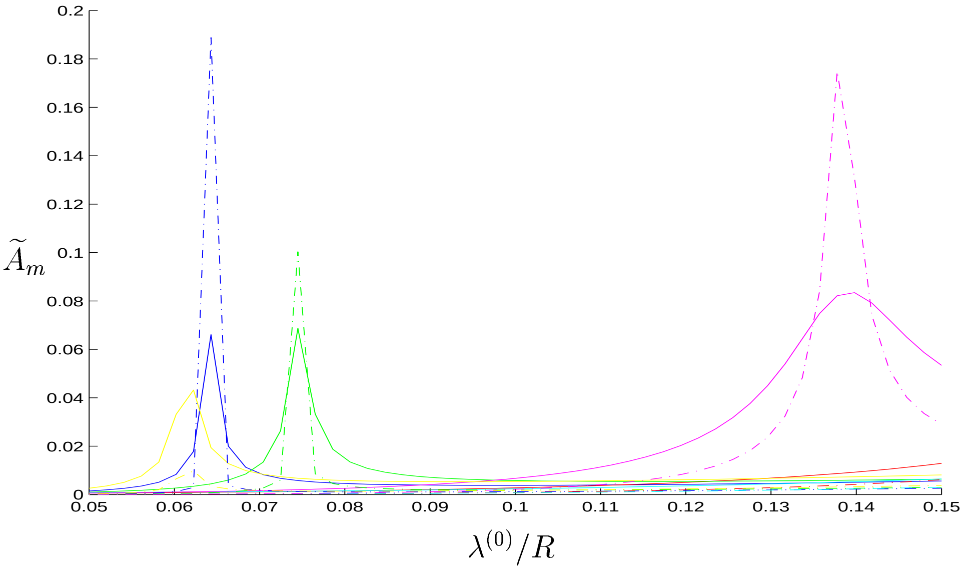

Figure 10.22: Comparing the amplitudes $\widetilde{A}_m$ ($m = 0, \ldots, 5$) of a zero draught (solid curves) and the corresponding Archimedean draught (dot-dash) floe, as functions of non-dimensional incident wavelength. The amplitudes have orders $M = 0$ (blue curve), $M = 1$ (red), $M = 2$ (green), $M = 3$ (cyan),$M = 4$ (magenta) and $M = 5$ (yellow).

the salient amplitudes in other problems, which would differentiate the zero draught and Archimedean draught problems to a greater degree. However, we conclude that in most situations the effect of the introduction of an Archimedean draught is mainly quantitative.

10.3 Conclusions

The study conducted in this chapter was into the scattering of a plane wave by an axisymmetric floe. This followed directly from the numerical formulation given in the preceding chapter. For the purposes of our investigation in this chapter the approximation was restricted to a single vertical mode, as it was felt that a more comprehensive study both numerically and particularly analytically could be achieved by these means.

An analysis of the approximation under certain conditions of interest was given in §10.1 and prefaced the numerical results. Specifically, we considered floes of a uniform thickness and a zero draught, which allowed the amplitudes of the complex waves to be calculated in terms of the amplitude of the propagating waves via the free-edge conditions. Our method here followed a similar procedure to that outlined in §5 for the semi-infinite ice sheet problem. By then concentrating on relatively short waves, we were able to devise an approximation in which the complex wavenumbers are replaced by functions of the propagating wavenumber. This approximation was then combined with régimes in which the radius of the floe is either large or small in relation to the wavelengths contained in the problem, and approximate values of the unknown amplitudes that appear in the domain occupied by the floe were obtained by using the relevant limits of the Bessel functions. Using the approximate solutions this method generates we were then, for instance, able to deduce the degree to which the floe reflects the incident wave as the frequency increases.

In §10.2 we conducted a numerical investigation of the scattering properties of an axisymmetric ice floe using the single-mode approximation. Our attention was centred on the response of the ice floe itself to an incident wave. However, at certain points we also considered the scattering at the free-surface about the floe and the far-field response.

It was of interest to study how the properties of the floe and the incident wave affected the convergence of the azimuthal modes. We deduced that the lower-order modes dominate around the centre of the floe but that towards the edge of the floe that the higher-order modes may be of equal importance. This is particularly true for larger, thinner floes and is relative to the incident wavelength. The motion within such floes is of a more complicated nature and a greater number of modes is required to resolve this, especially at the ice edge.

Certain physical implications were deduced. Firstly, thinner ice is far more responsive to the incident wave, with the disturbance generated in the ice being close to that of a plane wave passing through the floe. Conversely, thicker ice tends to resist the forcing wave and when waves are present within such floes, they are typically curved by the circular shape of the ice. Another trait observed was of the amplitudes of the flexural-gravity waves becoming damped away from the ice edge towards the centre of the floe as the higher-order modes decay. This is therefore more evident in the larger, thinner floes at shorter incident wavelengths, for which a greater number of modes contribute to the scattering motion in a vicinity of the ice edge.

We studied extensions of uniform floes by including variations to its thickness and undulating surfaces, and also through the introduction of a physically correct Archimedean draught. The differences caused were most noticeable around the fine structure that appears for axisymmetric floes, when we consider relatively short incident waves. This fine structure manifests itself as maxima in the amplitudes of the azimuthal modes and results in a locally disproportionate displacement of the floe. From our analysis of §10.1 we could clearly attribute these maxima to the zeros of the Bessel functions of the first kind, in the case of uniform floes. Modifications to the floe, specifically undulating surfaces and an edge submergence, were seen to modulate and displace the maxima, which produces both qualitative and quantitative differences in the scattering caused by similar floes around these points.

The effect of the maxima on the motion of the floe was only found to be of a local significance due to the diminishing displacement experienced by the ice as the incident wave shortens. By extending the frequency domain to include complex values, so that the waves decay in time, we were able to relate the maxima at real frequencies to full resonance at nearby complex frequencies.

Despite the issue of fine structure, typically similar scattering is caused by floes of the same diameter and average thickness. The same is true of the introduction of an Archimedean draught to a floe, although as in two-dimensional problems, away from peaks in the amplitudes, we expect the submerged portion of the ice edge to reflect relatively short incident waves and hence displace the floe to a lesser extent.

Chapter 11

Final discussion

11.1 Overall summary

In areas of the ocean in which the surface layer of fluid freezes to form a sheet of sea-ice, motion that is generated primarily by ocean waves may propagate large distances through the ice-covered region in the form of flexural-gravity waves. These flexural-gravity waves manifest themselves as oscillations in the position of the fluid-ice interface and exist by virtue of the ability of the ice sheet to flex. The amount of wave energy that transfers from ocean waves into oscillations beneath the ice sheet is dependent on the reflection that occurs at the ice edge. The subsequent form of the flexural-gravity waves is highly dependent on the properties of the ice and their passage through the ice is conditioned by the way in which these properties change.

Our interest is in the part of the ice-cover that is affected by ocean waves, termed the 'marginal ice zone' (MIZ). Ocean waves are thought to play the primary rôle in the fracturing of larger floes and determining the distribution of smaller floes (Squire *et al.*, 1995). Many different configurations of MIZ may be found, with the constituent ice floes spanning a broad range of sizes and thicknesses that depend on the means of their formation. For example, we may consider one of the vast ice sheets that are often created by a conglomeration of smaller floes. Consequently, the properties of the ice may be highly variable with pressure ridges, cracks and refrozen leads being rife. Waves that enter the ice will be modified and scattered by these features. Alternatively, there is the case of groups of smaller ice floes. Here, the propagation of ocean waves is determined by interactions between the floes as well as the response of individual floes.

The motivation of our work has been into developing a mathematical model of the scattering of wave energy for a situation of ice-covered fluid. Our prime intention was to allow for a high degree of generality in the properties of the ice. In particular, our solution method was outlined for an arbitrarily shaped ice sheet for which the ice thickness and draught are permitted to vary. Furthermore, we allowed for situations of both full and partial ice-cover. We also wished to generate a solution method of low computational cost and this was achieved by pursuing an approximation method capable of delivering high accuracy at low dimensions and of attaining an approximation arbitrarily close to the full linear solution.

To describe the situation of ice-covered fluid, we used the model that is widely accepted at the present under linear theory. The fluid was assumed to possess some standard physical properties, namely homogeneity, incompressibility and irrotationality. This allowed the fluid motion to be defined through a velocity potential that must satisfy Laplace's equation throughout the fluid domain. An impermeable bed of finite depth was used to bound the fluid below and we permitted undulations in this surface.

The ice sheet was considered to behave like a 'thin' elastic plate. That is, as it flexes its properties are not deformed, which imposes the restriction that the amplitude of a passing wave cannot be too large and its length cannot be too short in relation to the thickness of the ice. In accepting such a model we have ignored features such as rotational inertia and compressibility; however, we included the property of flexure, which is believed to play the predominant rôle in the passage of flexural-gravity waves through ice-covered fluid (Robin, 1963). The physical properties of the ice were condensed into two functions, both of which vary with the ice thickness. One, a scaled version of the mass of the ice, varies linearly with the ice thickness, while the other, a scaled version of the flexural rigidity of the ice, is a cubic function of the ice thickness.

Using the thin-plate model of the ice sheet, it was possible to consider the stress experienced by the ice in terms of the displacement it undergoes at the interface between itself and the fluid. By linearising the position of this fluid-ice interface we obtained a fourth-order condition that describes the flexure of the ice in terms of the pressure exerted on it and a second-order condition that defines the position of the interface. These conditions couple the fluid and ice motions. In an ice-free domain they collapse to the regular free-surface condition.

We considered the time harmonic problem, in which an angular frequency is set that dictates a periodicity. This left two unknown functions, both dependent on the spatial coordinates only. One, the reduced velocity potential, exists throughout the fluid domain, the other, the reduced displacement of the fluid-ice interface, exists throughout the ice-covered region, so that it has no dependence on the vertical coordinate.

In order to fully pose the boundary value problem that defines these unknown functions it was necessary to impose lateral conditions that hold at the internal boundaries between ice-free and ice-covered domains or over corners in the geometry, as well as far-field conditions. The internal conditions take the form of jump conditions and conditions on the dynamics at an ice edge.

To construct a solution procedure, we introduced an alternative means of defining the unknown functions, in terms of a variational principle. To do so, Hamilton's principle was used to generate a functional for which the stationary condition coincides with the equations governing the boundary value problem. As such, the variational principle necessarily contained all of the correct physical information of the problem and was, indeed, the source of the internal lateral conditions that must be attached to the problem.

By reinterpreting the problem as a variational principle we were able to make use of the Rayleigh-Ritz method as our solution procedure. Here, we chose to restrict the vertical coordinate in the functional to a chosen, finite-dimensional trial space. In doing so, we created a stationary point of the functional over the restricted space, known as the MMA, and this approximates the unrestricted stationary point, which is the required full linear solution. It was shown that, to obtain the stationary point over the restricted space, we are required to solve a finite set of differential equations in the horizontal coordinates, with accompanying boundary conditions. The combination of the Rayleigh-Ritz method and the variational principle averages the vertical motion defined by the trial space through an integration process. This resulted in the absence of the vertical coordinate from the new set of governing equations, which constituted a substantial numerical saving.

It is possible to select the finite-dimensional trial space such that an approximation of a chosen degree of accuracy may be obtained. One means of improving accuracy was simply to increment the dimension of the space used; however, a higher-dimensional approximation leads to a need to solve a more complex system of equations to produce the MMA. This is not desirable as it increases the computational cost involved. In order to minimise the dimension required to gain accurate approximations, we selected our vertical modes, which form the basis of the trial space, so that they contained the perceived key features of the sought solution. Specifically, we applied a pointwise correspondence between the vertical modes of our varying geometry problem and the vertical modes of the full linear solution in the analogous uniform geometry problem.

At each horizontal point the vertical modes were produced by solving a dispersion relation, which results from the separation of variables in the analogous uniform problem, for the required number of roots. The resulting approximation was described as the natural approximation. The primary mode chosen, which corresponds to the real root of the dispersion relation, was that which supports propagating waves in domains of uniform geometry. As we assume the geometry to be uniform in the far-field, a substantial benefit of this choice is that the exact form of the radiation conditions is always satisfied by the MMA. We discussed the fact that the presence of ice has the tendency to elongate propagating waves, especially at higher frequencies.

In the full linear solution of the uniform problem, there are also infinitely many modes that support evanescent waves, which correspond to purely imaginary roots of the dispersion relation. When ice-cover is present there are an additional two 'complex' modes, produced by ‘complex’ roots, that typically support waves that attenuate as well as oscillate but may also merely attenuate.

Having chosen our trial space, it was subsequently discovered that the properties of the roots of the dispersion relation, in ice-covered domains, are non-trivial for the purposes of our approximation method. Our difficulties centred on the additional two roots, the complex roots, that appear in the case of ice-cover as opposed to a free-surface. As the geometry varies, it was shown that these complex roots are liable to coalesce on the imaginary axis and interact with the purely imaginary roots, which destroys the differentiability that is required of their corresponding vertical modes. The parameter régimes under which such bifurcations occur was expressed in terms of a single function and this was used to determine that only the primary purely imaginary root was capable of such bifurcations with physically realistic parameters.

The difficulty caused by these bifurcations was somewhat counteracted by the discovery that there is a two-fold degeneracy in the complete set of vertical modes, which are generated by the roots of the dispersion relation. This led us to make the choice to discard the modes relating to the complex roots. Consequently, for the uniform geometry problem, we reinterpreted the full linear solution in terms of a linearly independent set of vertical modes, with the horizontal waves that may attenuate as well as oscillate redistributed amongst the remaining modes.

Through a domain of varying ice-covered geometry, the issue of bifurcations may affect more than just the two complex roots. Specifically it may also affect the primary, purely imaginary root. In situations for which the problem of bifurcations persisted in the primary evanescent mode, which we wished to utilise in our trial space, we were forced to switch to an alternative expansion set but still retain the natural approximation in the far-field. Our choice was to exchange the purely imaginary roots of the dispersion relation for the values that are their upper bounds and that they tend to as they increase in magnitude, with the resulting approximation described as the hybrid approximation. The hybrid modes were, in fact, seen to be equivalent to using a Fourier cosine expansion for our trial space with the constant term replaced by the propagating mode. It was our conjecture that the use of the hybrid evanescent modes would slightly diminish the efficiency of the MMA, as these modes, unlike the natural modes, have no relation to the ice thickness.

The theoretical structure of our solution procedure was therefore complete. For the remainder of our work we looked to formulate the numerical calculation of the MMA in specific problems. Our initial study was made for two-dimensional configurations in which the geometry is considered to have a constant cross-section. Forcing in this problem was induced by a single incident wave that propagates from the far-field at a set angle to the cartesian coordinate frame. The governing equations of the MMA therefore reduced to a finite set of ordinary differential equations with accompanying boundary conditions.

In an interval of uniform geometry, it was possible to solve these ordinary differential equations to produce an analytic form for the MMA. The main feature of this solution was in the dimension-dependent terms that distinguished it from a truncated version of the full linear solution. These dimension-dependent terms appeared in place of the horizontal waves that were redistributed amongst the remaining modes when we removed the complex vertical modes from the full linear solution. Their dimension dependency was attributed to an awareness of all of the vertical modes missing from the MMA. In comparison, the approximation in an interval of ice-free fluid over an uniform bed is identical to the truncated version of the full linear solution.

The ramifications of the dimension-dependent terms in the MMA were investigated via a comparison to an eigenfunction matching method, whose solution has the form of a truncated version of the full linear solution in an interval of uniform geometry. Such a comparison required the use of piecewise uniform geometry and the classical problem of a semi-infinite ice sheet was chosen. In this problem, only the resolution of the scattering caused at a single ice edge was required and we investigated this in relation to differing ice thicknesses over a range of frequencies. Our results indicated that, at low dimensions, the MMA is better able to deal with the discontinuity and this was attributed to its construction through vertical averaging. This property was seen to become more evident when the discontinuity was exacerbated by thick ice and a high wave frequency. However, at other times, the high-dimensional refinements of the solution were seen to be slow in comparison to the method that used the exact values of the complex waves. This is most likely due to the complex waves being more significant than the high-order evanescent waves that are also missing from the trial space of the MMA.

Two two-dimensional problems, which utilised the ability of the MMA to admit situations in which the geometrical surfaces undulate, were formulated for numerical solution. In both, the varying geometry was permitted only over a finite ice-covered interval, with semi-infinite intervals of uniform geometry at either side. For one problem the semi-infinite intervals were ice-covered, so that the entire fluid domain was loaded. The incident wave is therefore scattered only by the geometrical undulations in the finite interval. In the other problem, the semi-infinite intervals were ice-free and the finite interval represented a solitary ice floe. In this problem, there were sources of scattering at the edges of the floe in addition to the undulating surfaces.

Over the finite interval of varying geometry, the governing differential equations of the MMA require numerical resolution. Combining the analytic form we derived for the solution in the semi-infinite intervals with the relevant jump conditions provided boundary values for the solution of the MMA, which was then found on the finite interval via a linear combination of numerically calculable functions. We were able to limit the number of these functions to two through suppression of the unknown amplitudes of the evanescent waves in the boundary conditions. In their original form the boundary conditions would have necessitated six linearly independent solutions for the single-mode approximation and this number would have then increased by two for each additional mode added.

For the more simple of the two problems, in which the ice-cover is complete, we began by studying the convergence rates of the natural and hybrid modes. It was seen that an approximation arbitrarily close to the full linear solution could be achieved with both expansion sets. As predicted, it was found that the convergence given by the natural modes was superior. Moreover, by also using a Fourier cosine expansion as a trial space, we witnessed the extra accuracy gained by inclusion of the mode that supports propagating waves in the natural and hybrid approximations.

In all of the problems of continuous ice-cover, chosen for solution by the MMA, high accuracy of the single-mode approximation was observed. For geometries that were clearly not slowly varying, although additional terms were required to achieve convergence in the qualitative detail, the accuracy of the single-mode approximation was still notable. A close relationship between the results produced by geometries that share a common ice thickness and fluid depth was also remarked upon. This prompted an analytic investigation, which was made in terms of the single-mode approximation. We found that, for most frequencies, the ice thickness is the predominant factor in determining the scattering of the incident wave. Variations to the fluid depth only become comparable for long incident waves. Furthermore, it was shown that a protrusion at the underside of the ice is a contributing factor in the scattering at mid to high frequencies, unlike the fluid depth, whose influence is negligible.

For the problem of a finite ice floe, the scattering caused by the ice edges was typically found to require a greater number of evanescent modes to achieve convergence in the MMA than was needed for undulating surfaces alone. Moreover, we observed that the presence of ice edges was detrimental to the accuracy of the low-dimensional approximations in a vicinity of the ice edges, at which point the evanescent waves are strongly activated. In extreme cases, this led to spurious phenomena in values sensitive to the accuracy of the approximations at the ice edges, such as the far-field response. However, through the addition of supplementary modes all discrepancies were quickly eradicated and high accuracy was again obtained at a relatively low cost.

Our results indicated that as the frequency increased, an ice edge has the tendency to reflect a greater proportion of the incident wave. This form of scattering becomes dominant in this limit, far outweighing that of an undulating surface, and is proportional to the thickness of the ice edge. However, we noted that there is a stage before the ice edge scattering dominates in which both sources of scattering are discernible. For waves existing beneath the ice that were short in relation to the length of the floe, we observed that there are frequencies for which locally disproportionate responses occur in the displacement experienced by the ice. This phenomenon was attributed to interaction between the scattering produced at either end of the floe and was also observed in a fine structure shown by the behaviour of the far-field.

An advantage of the MMA method of solution is that it allows for the inclusion of a physically correct Archimedean draught. It was shown that the addition of submergence could cause significant changes to the solution. In particular, we found that the inclusion of an Archimedean draught is important for thicker ice and for medium to high frequencies. It is for these régimes that the scattering caused by the submerged portion of the ice edge has a major rôle. We discovered that its main property is that of preventing the incident wave from penetrating beneath the ice to a certain extent. Consequently, our results showed that the ice floe experiences less displacement when a non-zero edge submergence is present.

A specific version of the complete ice-cover problem in two-dimensions was studied separately. In this problem, the geometrical variations that occur over the finite interval were of a periodic construction. For such a structure, in which the geometry may vary rapidly and we wish to study an arbitrary number of periods, a different numerical method is required to produce computational efficiency. This meant that we reformulated the problem by retaining the amplitudes of the evanescent waves, so that the scattering caused by the entire interval could be determined from the properties of a single period. To do so, a transfer matrix approach was utilised, which relates the complete set of amplitudes at either end of a period.

Our interest in the periodic problem stemmed predominantly from the existence of resonances caused by periodically undulating beds for free-surface flows. Following the work of previous authors in this field, we developed a wide-spacing approximation, which ignores the interaction of evanescent waves between adjacent periods but is illuminating in the analysis of resonance. Using the wide-spacing approximation, we were able to link the build-up of a resonance to an increasing number of periods when the eigenvalues of the transfer matrix lie in a certain configuration.

Resonances in periodic problems are well-known to occur around the so-called Bragg values. Although we found this to be the case when ice-cover is present, the elongation of propagating waves that occurs beneath an ice sheet meant that a Bragg value was less likely to be encountered by realistic parameters in such a situation. The resonances that we observed were strong in comparison to those found for free-surface flows. Specifically, we found that large responses were created by relatively few periods over large intervals and that this behaviour was maintained over a number of Bragg values. A feature discovered for ice-covered fluid, which is not known for free-surface flows, is the existence of a drift away from the Bragg value in the right as well as left direction, as the amplitude of the periodic geometry increases. A correspondence was made between leftward drift and thinning ice, and rightward drift and thickening ice.

The final configuration considered was one of a fully three-dimensional nature. This was the problem of an axisymmetric floe, forced by an incident plane wave. To efficiently formulate the solution of the MMA in these circumstances we transformed the horizontal coordinates from cartesian to polar, so that the geometrical functions varied only in terms of the radial coordinate. This allowed us to utilise the axisymmetry and expand the azimuthal dependence of the unknown functions in the form of Fourier cosine series, which we truncated to a dimension chosen to achieve a given degree of accuracy. Consequently, the governing equations of the MMA decoupled to leave a finite set of ordinary differential equations in the radial coordinate, with accompanying conditions at the ice edge. The reduction of our computations to a single coordinate constituted a significant numerical saving.

In a domain of uniform geometry it was again possible to obtain an analytic form for the MMA. This analytic form mirrored that produced in analagous two-dimensional situations, although the exponential functions that appeared there are replaced by Bessel functions in this case. For the axisymmetric floe problem, the analytic form was used in the ice-free region away from the floe, where the bed was assumed to be flat. In doing so we were able to easily ensure satisfaction of the Sommerfeld radiation condition as well as reproduce the incident wave. The analytic form was also of use when dealing with the singularity that arises at the centre of the ice floe due to the transformation to polar coordinates, without the need for complicated and costly numerical methods.

It was possible to make many inferences about the behaviour of circular floes by studying the problem in which the ice is restricted to uniform thickness. Thinner ice is more compliant with the incident wave and we observed near-plane waves, like the incident wave, travelling through the floe. On the other hand, when the ice becomes thicker, it is more resistant to the incident wave, and if a propagating wave does exist in the displacement of the floe then it is curved by its circular shape. We also observed the phenomenon of the damping of waves beneath the ice away from the edge.

A feature of axisymmetric floes is the prevalence of fine structure, which occurs in each of the azimuthal modes. As in the case of finite floes in two-dimensions, the fine structure was produced when the wave beneath the ice is short in comparison to the length of the floe, and leads to a locally disproportionate response in the displacement of the floe. The phase and magnitude of the peaks in the amplitudes that constitute this fine structure were found to be sensitive to the properties of the ice. For example, the addition of a thickness variation through the floe could displace such a peak and result in a vastly different response. However, away from these peaks mild variations to the ice thickness did not have a drastic effect. Similarly, the fine structure complicated the analysis of the introduction of an Archimedean draught. Although at relatively high frequencies, the property of a diminished displacement, when an edge submergence was included, was again present for an axisymmetric floe, the relationship was often broken by a peak in an amplitude that contributed to the solution. This meant that the Archimedean floe may experience a locally disproportionate response that outweighs that of the zero draught floe and results in a greater displacement when the submergence is included.

11.2 Future work

Possibilities for extending this work are numerous. To begin with there are many aspects of our work, both in the formulation of our solution procedure and the particular problems that we have studied, that may be elaborated upon or receive a more comprehensive examination. The former would be of interest if we believed that we could improve the accuracy given by the MMA in relation to numerical cost, either in a general sense or in relation to some particular quantity. In contrast, further study of the problems that we have formulated for numerical solution would probably be based on a desire to gain knowledge of some particular property of the model. Furthermore, the formulation of the MMA was made in the general three-dimensional setting. This was done specifically so that it would be available for any geometrical configuration that we may wish to study. Therefore, many more challenging problems and problems with greater physical relevance may be formulated and solved using the MMA. In this section we will elaborate on a few ideas for continuing our work.

Looking at the structure of MMA, the main area open for extended study is in the vertical modes that have been used. The prime aim here would be to seek a way of accelerating the convergence of the approximation. Although we have found that the natural approximation provides accurate solutions at a low numerical cost, it may be that there exists a more optimal choice of modes. For instance, it has been seen that the high-dimensional refinements of the MMA to the full linear solution may be slow in certain difficult situations. This is primarily in situations of partial ice-cover, where short incident waves strongly excite the evanescent waves around the ice edges. The inability of low-dimensional MMAs to exactly reproduce the full linear solution at these points was attributed to the lack of the complex modes in the trial space. It may be that it is possible to incorporate the complex modes in the trial space without causing numerical singularities and without the need to remove any of the important properties of the vertical structure in doing so, thereby resolving this issue.

A closely related issue is in further exploring the properties of the dimension-dependent wavenumbers of the approximation, which are denoted $\mu_{N,(i)}$ $(i = 1, 2)$. These quantities may be regarded as approximations of the complex roots of the dispersion relation, although their rôle is, in fact, as approximations of all of the roots of the dispersion relation that are not included in the MMA at dimension N. We have not studied the rate at which these approximate wavenumbers converge to the complex roots as the dimension, N, is increased, which is a property that may be relevant to the approximation. Consider, for example, the fact that the complex wavenumbers, like the propagating wavenumber, tend to a limit as the fluid depth is increased. However, the rate of convergence of the dimension-dependent wavenumbers is affected by the values of the purely imaginary roots, which continue to become smaller as the fluid depth increases. The result of this is that a greater dimension is required for the approximate wavenumbers to converge as the fluid depth increases, which will adversely affect the cost of producing the refined full linear solution with the MMA if the complex waves are strongly activated in a particular problem.

There is also scope for improving the alternative approximation that we use in situations for which the validity of the natural evanescent modes is compromised by bifurcations in the roots of the dispersion relation. Our method was to simply replace the purely imaginary roots with their limiting values, and we termed the resulting approximation the hybrid MMA. This choice has many advantages, not least that it is implemented at a low numerical cost. However, these replacement evanescent modes are completely unrelated to the thickness of the ice, a property that we have found to be of prime importance in the passage of flexural-gravity waves. We may therefore expect a more accurate approximation to be given if we are able to incorporate the ice thickness into the alternative evanescent modes. As it is only the root that exists in the first interval of the imaginary axis which has a strong dependence on the ice thickness, with all subsequent roots almost indistinguishable from their limiting values, it is likely that modifying the primary hybrid evanescent mode alone would be sufficient to improve the approximation. One option would be to interpolate between a number of chosen values of the root (or roots) present on the first interval of the imaginary axis.

There are many physical parameters available for variation in our model. Due to the constraints of this work we have only been able to deal with a few of those that we regard as important, namely the thickness of the ice and its draught. In particular, very little attention has been paid to the rôle of the bed in our results, and we have routinely assumed a flat bed of 10m-20m depth in our numerical models. If we were to closely study the influence of the bed, we may also wish to gain knowledge of the solution at this boundary. To do this in a situation in which the bed undulates, the addition of a 'bed mode', in the vein of Athanassoulis & Belibassakis (2005) or Chamberlain & Porter (2006), would be important. We would therefore wish to modify our trial space by including a mode which, unlike the natural modes, does not have a vanishing normal derivative at the bed. This would then allow the MMA to converge to the full linear solution at this point.

It would also be of interest to study the effect of variations in the material properties of the ice. For example, we could allow the value of Young's modulus, E, to fluctuate across the ice sheet. Such a study would be of relevance as the possibility of a varying Young's modulus has been noted by Fox *et al.* (2001). Implementing this example (or any other similar example) in our model would require a slight reformulation of the MMA. The flexural rigidity of the ice, β, would become not only a function of the ice thickness but also of Young's modulus. Similarly, the roots of the dispersion relation would also be functions of Young's modulus. Consequently, we would need to calculate all derivatives not only in terms of variations in the geometrical functions D, h and d but in E also. In practice, this would cause of little inconvenience, merely adding to the algebraic complexity.

There are a number of geometrical constructions that may be solved using the MMA, which would require only minor alterations to the formulations that appear in our work. Take the case of the periodic problem, which was studied in §8. In that chapter we considered a finite interval of periodic variations in an otherwise uniform ice sheet. The scattering was therefore caused solely by the periodic variations and we discovered the existence of resonance around Bragg values. In order to solve this problem we utilised a transfer matrix, P_0 say, that linked the amplitudes of the evanescent waves as well as the propagating waves at either side of an individual period. The transfer matrix, P_M say, for an interval of an arbitrary number, M, of these periods (and hence the scattering matrix for the entire interval) was then built-up from the transfer matrix for the single period, with $P_M = P_0^M$.

We could modify our transfer matrix approach to deal with an analogous problem in which there exists a single floe of finite length, with surfaces that undulate periodically. The transfer matrix, P_0, that operates between periods would be identical to the one that was calculated in the case of complete ice-cover. However, for the two periods that coincide with the ends of the floe, different transfer matrices, $\widetilde{P}_L$ and $\widetilde{P}_R$ say, would require calculation. In order to calculate these new transfer matrices we would need to solve problems that involve a single period of varying geometry, one end of which is attached to an interval of uniform ice and the other end forming an ice edge. The transfer matrix for the entire floe would then be composed as

$$P_M = \widetilde{P}_R P_0^{M-2} \widetilde{P}_L.$$

Although resonance would be produced around the Bragg values by the P_0 term in the same way that it was in the complete ice-cover problem, it would be of interest to see whether the inclusion of ice edges either strengthened or weakened these responses.

Alternatively, we could equally use the transfer matrix approach to study a situation in which we have an interval of any number of identical floes that are equally spaced, $\tilde{l}$m apart say, in an otherwise infinite ice-free interval. The relevant transfer matrix, P_0 say, for this problem would be one that relates amplitudes at the mid-points in the intervals of ice-free fluid between the floes. For consistency, we would place fictitious boundaries $\tilde{l}/2$m away from the floes at the extreme right and left. The transfer matrix for M floes, P_M say, would then be calculated as $P_M = P_0^M$. Such a problem would be of benefit in the study of multiple floe interactions. Furthermore, it is likely that resonances would appear, and, unlike the previous two periodic problems described, the parameter values that coincide with Bragg numbers would be physically plausible, as the incident wavenumber for each period is taken from the free-surface dispersion relation.

For the three-dimensional problem of an axisymmetric floe we would also wish to extend to situations that involve multiple floes. Our goal here would be to effectively model an arbitrary number of circular floes of differing radii and varying thicknesses, and in any alignment, interacting with one another. Such a model would begin to resemble a realistic configuration in the MIZ.

We are already able to calculate the scattering problem defined by each individual axisymmetric floe, so the issue is that of determining the interaction between these scattering processes, which in this case would take place in the ice-free regions between the floes. This is analogous to the way in which we solve two-dimensional problems for which more than one scatterer is present (e.g. periodic structures).

In order to formulate a solution procedure for this problem we would be likely to follow the method of Peter & Meylan (2004). Although their work was for floes of an arbitrary shape with a uniform thickness and a zero draught over an infinite bed, and therefore did not invoke any vertical averaging, their form for the scattered solution in the ice-free region between the floes would be very similar to that which we would use.

In brief, we would suppose that there are K floes and that, in addition to the global polar coordinate frame (r, θ), each floe is endowed with its own local polar coordinate system (r_j, θ_j) $(j = 1, \dots, K)$ with an origin set to coincide with the centre of the particular floe. For each floe, all unknown functions would then be expanded around the floe in a complete Fourier series, rather than a Fourier cosine series, as we may no longer assume symmetry in the local y-axis. In the local coordinate frame, the single-vertical-mode approximation, for example, would then be given by

$$\varphi(r_j, \theta_j) = \varphi_0(r_j) + \sum_{m=1}^{\infty} \mathrm{i}^m \{\varphi_m(r_j)\mathrm{e}^{\mathrm{i}m\theta_j} + (-1)^m \varphi_{-m}(r_j)\mathrm{e}^{-\mathrm{i}m\theta_j}\} \quad (j = 1, \dots, K),$$

where, assuming that the bed is flat, we have

$$\varphi_m(r_j) = A_{m,j}\mathrm{J}_m(k^{(0)}r_j) + B_{m,j}\mathrm{H}_m(k^{(0)}r_j) \quad (j = 1, \dots, K), \tag{11.1}$$

for the free-surface wavenumber $k^{(0)}$ and constant amplitudes $A_{m,j}$ and $B_{m,j}$, which are the unknowns of the problem. The Bessel functions of the first kind represent the forcing waves, which are comprised of the incident wave given in equation (9.17) that propagates from the far-field and we here rewrite as

$$\varphi_I(r,\theta) = \mathrm{I}_0 \left\{ \mathrm{J}_0(k^{(0)}r) + \sum_{m=1}^{\infty} \left(\mathrm{i}^m \mathrm{J}_m(k^{(0)}r)\mathrm{e}^{\mathrm{i}m\theta} + \mathrm{i}^{-m}\mathrm{J}_{-m}(k^{(0)}r)\mathrm{e}^{-\mathrm{i}m\theta} \right) \right\},$$

together with the propagating waves scattered by all of the other $(K-1)$ floes. In the multi-mode case the waves scattered by the other floes will consist of evanescent as well as propagating waves and we will have to make an allowance for this. The Hankel functions of the first kind are the scattered waves. Continuing with the specific example of the single-vertical-mode approximation, we have a means, given by the solution process outlined in §9, to relate each of the the scattered amplitudes, $B_{m,j}$, to its corresponding forcing amplitude, $A_{m,j}$, so that we may write $B_{m,j} = \mathfrak{F}_{m,j}(A_{m,j})$, for some known function $\mathfrak{F}_{m,j}$. This relation may be used to remove the scattered amplitudes $B_{m,j}$ whenever they appear, and therefore only the amplitudes $A_{m,j}$ $(j = 1, \ldots, K;\ m \in \mathbb{Z})$ must be found in order for us to determine the solution. Moreover, we can express the forcing amplitudes explicitly in terms of the amplitude of the incident wave, I_0, and the amplitudes of the waves scattered by the other floes, $B_{m,i}$ $(i = 1, \ldots, K;\ i \neq j)$. To do this, we would need to transform all of the relevant motion that will force a particular floe, i.e. the incident wave and the propagating waves scattered by the other floes, into its local coordinates via Graf's addition formula for Bessel functions. Therefore, the incident wave is written as

$$\begin{aligned}
\mathrm{I}_0\mathrm{J}_m(k^{(0)}r)\mathrm{e}^{\mathrm{i}m\theta} &= \mathrm{I}_0\mathrm{e}^{\mathrm{i}m\theta_{0,j}}\mathrm{J}_m(k^{(0)}r_{0,j})\mathrm{J}_0(k^{(0)}r_j) \\
&\quad + \mathrm{I}_0\mathrm{e}^{\mathrm{i}m\theta_{0,j}}\sum_{n=1}^{\infty}\{(-1)^n\mathrm{J}_{m+n}(k^{(0)}r_{0,j})\mathrm{e}^{\mathrm{i}n(\pi+\theta_{0,j})}\mathrm{J}_n(k^{(0)}r_j)\mathrm{e}^{\mathrm{i}n\theta_j} \\
&\qquad + \mathrm{J}_{m-n}(k^{(0)}r_{0,j})\mathrm{e}^{-\mathrm{i}n(\pi+\theta_{0,j})}\mathrm{J}_{-n}(k^{(0)}r_j)\mathrm{e}^{-\mathrm{i}n\theta_j}\},
\end{aligned} \tag{11.2a}$$

where $r_{0,j}$ represents the distance from the global origin to the jth local origin and $\theta_{0,j}$ is the corresponding angle. Similarly, to transform the waves scattered by the other floes we have

$$\begin{aligned}
B_{m,i}\mathrm{H}_m(k^{(0)}r_i)\mathrm{e}^{\mathrm{i}m\theta_i} &= B_{m,i}\mathrm{e}^{\mathrm{i}m\theta_{i,j}}\mathrm{H}_m(k^{(0)}r_{i,j})\mathrm{J}_0(k^{(0)}r_j) \\
&\quad + B_{m,i}\mathrm{e}^{\mathrm{i}m\theta_{i,j}}\sum_{n=1}^{\infty}\{(-1)^m\mathrm{H}_{m+n}(k^{(0)}r_{i,j})\mathrm{e}^{\mathrm{i}n(\pi+\theta_{i,j})}\mathrm{J}_n(k^{(0)}r_j)\mathrm{e}^{\mathrm{i}n\theta_j} \\
&\qquad + \mathrm{H}_{m-n}(k^{(0)}r_{i,j})\mathrm{e}^{-\mathrm{i}n(\pi+\theta_{i,j})}\mathrm{J}_{-n}(k^{(0)}r_j)\mathrm{e}^{-\mathrm{i}n\theta_j}\},
\end{aligned} \tag{11.2b}$$

where $r_{i,j}$ represents the distance from the ith local origin to the jth local origin and $\theta_{i,j}$ is the corresponding angle. If the azimuthal motion is approximated by truncating all infinite sums to M terms, then it is possible to obtain the amplitudes $A_{m,j}$ ($j = 1, \ldots K$; $m = -M, \ldots, M$) by solving a matrix system of dimension $(2M + 1)K$. This system of equations is derived by comparing the expansions (11.2a-b) to the form of the solution defined in equation (11.1). The extension to multiple vertical modes is straightforward.

As the interactions of floes rely on the scattering caused in a vicinity of each floe, a study of multiple floe interactions would need to be prefaced by a more thorough examination of the effect of a solitary floe on the free surface that surrounds it. We could then progress by adding a second floe and investigate the factors that affect the strength of the interactions between the two floes. There are many options here that could be considered such as the relative sizes of the two floes, their positions in relation to the incident wave, their distance apart from one another, their shape, their edge thicknesses and their submergences. We may, for example, expect a second floe that is placed directly 'downstream' of the first floe to be displaced to the greatest extent, as we have seen that the majority of the scattered wave lies in this direction. It may also be supposed that a realistic submergence would produce stronger interactions as a greater amount of scattering is caused when a portion of the ice edge is submerged. Another issue that could be of interest here is in whether the fine structure, which was observed in the solutions of individual floes, would be significant in multiple floe interactions. One possibility is that a disproportionately large response in the displacement of a particular floe could be accompanied by a relatively small displacement in the free-surface, thus leading to weaker interactions with other floes.

Once we have established a means of calculating the scattering properties of multiple three-dimensional floes, we may wish to make some general inferences about the amount of energy that passes through a pack of ice floes. That is, for a wave that is incident on a region that contains a number of floes, how much of the wave energy propagates through to the other side of the region? The findings of such an investigation could be applied to situations in which the edge of a large sheet of ice fractures into smaller floes, which then damps oceans waves so that it, in effect, provides a protective barrier for the inner ice. To analyse the overall damping properties of a region of ice floes we would need to keep some parameter values constant, say the density of the ice across the region in which they are contained and the average thickness of the ice. We would then be likely to pursue a statistical method by taking the average response of a large number of possible variants.

Another option in the three-dimensional axisymmetric setting would be to consider the problem in which the circular region is ice-free and the outer region is ice-covered. This situation models a 'pool' in a large expanse of ice. The formulation for this configuration would require a simple modification of the axisymmetric ice floe problem, and geometrical variations could, for example, be included in an annulus that surrounds the ice-free disc. In fact, the only amendment that we would need to make to the axisymmetric ice floe problem would be to apply the ice-ice jump conditions at the outer boundary of the annulus and the water-ice jump conditions at the inner boundary, rather than the opposite way around. We would then expand the scattered solution in the ice-free region in terms of Bessel functions of the first kind and in the ice-covered far-field in Hankel functions of the first kind, in order to satisfy the Sommerfeld radiation condition

$$r^{1/2}\left(\partial_r - \mathrm{i}k\right)\phi_S \to 0 \quad (r \to \infty),$$

where k represents the propagating wavenumber in the far-field and ϕ_S the scattered solution.

A related problem, described as the 'moon pool' problem, in which a rigid plate of uniform thickness surrounds a disc of open fluid has been studied previously by Molin (2001). In particular, resonances were discovered in the moon pool problem, and it would be of interest to study to what extent, if any, these resonances transfer into our elastic plate model.

The circular pool problem could then be extended to more general shapes. It is possible that certain configurations, such as ellipses, may be solved by performing transformations, although difficulties caused by the free-edge conditions may prove to be intractable. However, for most shapes we would undoubtedly have to resort to more numerical techniques and these would be highly dependent on the particular geometry of the pool.

If we were to consider a pool that was long in comparison to its width then it could be used to model the situation of a lead. Leads are familiar occurrences in ice sheets that are created when a crack is forced apart to leave an area of open water. These areas of open water are prone to refreezing, in which case they are described as refrozen leads. This situation could also be modelled by supposing that the pool contains ice of a different property (most probably due to its thickness) to that of the outer region.

Let us consider a straight lead that is long to the extent that there are points at which the scattering of cross-sections of the lead away from the ends are not influenced by their presence. We may therefore model this inner scattering problem in two-dimensions. So, let the finite interval $x \in (0, l)$ contain ice-free fluid and the two semi-infinite intervals at either end contain ice-covered fluid. A similar problem was studied by Chung & Linton (2005) using the residue calculus technique that they earlier applied for a semi-infinite ice sheet in Linton & Chung (2003). As in the case of a semi-infinite ice sheet, their model assumed that the ice was of a uniform thickness and had a zero draught. We could easily add not only a realistic draught but also variable geometry, say in the intervals $(-\hat{l}_0, 0)$ and $(l, l + \hat{l}_1)$, where the $\hat{l}_i$ $(i = 0, 1)$ are positive constants. This would mean for instance that the properties of the ice would be permitted to vary in a vicinity of the lead.

To solve this problem, supposing the bed to be flat throughout, we use equation (4.22) to derive the analytic expressions

$$\begin{aligned}\boldsymbol{\Psi}_N^{(-)}(x) &= \mathcal{C}^{(-)}\{\mathrm{e}^{\mathrm{i}\mathit{\Lambda}^{(-)}(x-\hat{l}_0)}\mathbf{A}^{(-)} + \mathrm{e}^{-\mathrm{i}\mathit{\Lambda}^{(-)}(x-\hat{l}_0)}\mathbf{B}^{(-)}\} \qquad (x < -\hat{l}_0),\\ \boldsymbol{\Psi}_N^{(+)}(x) &= \mathcal{C}^{(+)}\{\mathrm{e}^{\mathrm{i}\mathit{\Lambda}^{(+)}(l+\hat{l}_1-x)}\mathbf{A}^{(+)} + \mathrm{e}^{-\mathrm{i}\mathit{\Lambda}^{(+)}(l+\hat{l}_1-x)}\mathbf{B}^{(+)}\} \quad (x > l+\hat{l}_1),\end{aligned}$$

for the MMA in the intervals of uniform ice, where the vectors

$$\mathbf{A}^{(\pm)} = \left(A_0^{(\pm)}, 0, \ldots, 0\right)^T,$$

contain the incident amplitudes and

$$\mathbf{B}^{(\pm)} = \left(B_0^{(\pm)}, \ldots, B_N^{(\pm)}, B_{-1}^{(\pm)}, B_{-2}^{(\pm)},\right)^T,$$

the reflected amplitudes. In the ice-free interval the expression for the MMA, which is given by equation (4.30), is

$$\boldsymbol{\Phi}_N^{(0)}(x) = \mathrm{e}^{\mathrm{i}\Lambda x}\mathbf{A}^{(0)} + \mathrm{e}^{-\mathrm{i}\Lambda x}\mathbf{B}^{(0)}, \tag{11.3}$$

where $\mathbf{A}^{(0)}$ and $\mathbf{B}^{(0)}$ are full vectors of length $(N+1)$ and contain unknown constants. In the intervals of varying geometry, $(-\hat{l}_0, 0)$ and $(l, l+\hat{l}_1)$, the MMA must satisfy the differential system (4.4), and the solutions are linked at the connected ice boundaries, $x = -\hat{l}_0$ and $x = l + \hat{l}_1$ by the jump conditions (4.10a-b) and at the ice edges, $x = 0$ and $x = l$, by the conditions (4.11a-b). As in previous problems, we write the solution in intervals of varying geometry as linear combinations of numerically calculable functions, here

$$\boldsymbol{\Psi}(x) = \mathrm{i}\mathcal{L}_{0-}(x)(\mathbf{A}^{(-)} - \mathbf{B}^{(-)}) + \mathrm{i}\mathcal{L}_{1-}(x)(\mathbf{A}^{(0)} - \mathbf{B}^{(0)}) \quad (-\hat{l}_0 < x < 0),$$

and

$$\boldsymbol{\Psi}(x) = \mathrm{i}\mathcal{L}_{0+}(x)(\mathbf{A}^{(+)} - \mathbf{B}^{(+)}) + \mathrm{i}\mathcal{L}_{1+}(x)(\mathrm{e}^{\mathrm{i}\Lambda l}\mathbf{A}^{(0)} - \mathrm{e}^{-\mathrm{i}\Lambda l}\mathbf{B}^{(0)}) \quad (l < x < l + \hat{l}_1),$$

where the quantities $\mathcal{L}_{0\pm}$ are square matrices of dimension $(N+3)$ and $\mathcal{L}_{1\pm}$ are matrices of size $(N+3)\times(N+1)$. The columns of these matrices satisfy the differential system (4.4) with appropriate boundary values, which ensure that the MMA satisfies the conditions (4.10b) and (4.11b) at the relevant points. The scattered wave amplitudes are then obtained via application of the remaining conditions (4.10a) and (4.11a), which requires inversion of a matrix of dimension $(4N+8)$.

Again, this model may in a straightforward manner be modified to switch to the case of a refrozen lead. We would require the expression for the MMA in the lead, equation

(11.3), to be changed to the form for a uniform interval of ice-covered fluid, equation (4.22), and the conditions applied at the ends of this interval to be those for a connected ice sheet, equations (4.10a-b).

It is clear then that there is a wide range of avenues available for continuing our work, of which we have outlined just a few. In all of the ideas discussed above the problem is that of calculating the direct scattering caused by more challenging configurations. This assumes retention of the thin-elastic plate model of the ice, and linear and time-harmonic conditions.

However, there are many different approaches that can be explored. For example, rather than the direct problem, we may wish to look at an inverse problem in which we seek to reconstruct the shape of an ice floe given its scattering properties. Alternatively, we could incorporate a more sophisticated model of the ice, say by the inclusion of additional properties such as dissipation or by adding one or more of the rigid-body motions. These possibilities consitute sizeable undertakings and it is inappropriate to consider them further here.

Bibliography

ANDRIANOV, A. I. 2005 Hydroelastic analysis of very large floating structures. PhD thesis, Delft Uni. of Tech., The Netherlands.

ANDRIANOV, A. I. & HERMANS, A. J. 2003 The influence of water depth on the hydroelastic response of a very large floating platform. *Mar. Struct.* **16**(5), pp. 355–371.

ANDRIANOV, A. I. & HERMANS, A. J. 2004 Hydroelasticity of elastic circular plate. In *Proc. 19th Intl. Workshop on Water Waves & Floating Bodies* (ed. Landrini, M., Campana E.F., Iafrati, A.) Cortona, Italy.

BALMFORTH, N.J. & CRASTER, R.V. 1999 Ocean waves and ice sheets. *J. Fluid Mech.* **395**, pp. 89–124.

BELIBASSAKIS, K. A. & ATHANASSOULIS, G. A. 1999 A consistent coupled-mode theory for the propagation of small-amplitude water waves over variable bathymetry regions. *J. Fluid Mech.* **389**, 275–301.

BELIBASSAKIS, K.A. & ATHANASSOULIS, G.A. 2005 A Coupled-Mode Model for the Hydroelastic Analysis of Large Floating Bodies Over Variable Bathymetry Regions. *J. Fluid Mech.* **531**, pp. 221-249

BENNETTS, L. G., BIGGS, N. R. T. & PORTER, D. 2007 A multi-mode approximation to wave scattering by ice sheets of varying thickness. *J. Fluid Mech.* **579**, 413–443.

BERKOFF, J. C. W. 1973 Computation of combined refraction-defraction. In *Proc. 13th Intl. Conf. on Coastal Engng.,* Vancouver, Canada, pp. 471-490. ASCE.

BERKOFF, J. C. W. 1976 Mathematical models for simple harmonic linear water waves. *Delft Hydr. Rep.* W 154-IV.

CHAMBERLAIN, P. G. & BIGGS, N. R. T. 2006 Inverse water wave scattering by topography. *Conference presentation* British Applied Maths. Colloquium, Keele, UK.

Chamberlain, P. G. & Porter, D. 1995 The modified mild-slope equation. *J. Fluid Mech.* **291**, pp. 393–407.

Chamberlain, P.G. & Porter, D. 1995 Decomposition methods for wave scattering by topography with application to ripple beds. *Wave Motion* **22**, pp. 201–214.

Chamberlain, P. G. & Porter, D. 1999 Scattering and near-trapping of water waves by axisymmetric topography. *Wave Motion* **388**, pp. 335–354.

Chamberlain, P. G. & Porter, D. 2006 Multi-mode approximations to wave scattering by an uneven bed. *J. Fluid Mech.* **556**, pp. 421–441.

Chung, H. & Fox , C. 2002 Calculation of wave-ice interaction using the Wiener-Hopf technique. *NZ J. Math.* **31**, pp. 1–18.

Chung, H. & Linton, C.M. 2005 Reflection and transmission across a gap between two semi-infinite elastic plates on water. *Quart. J. Mech. Appl. Maths.* **58**(1), pp. 1–15.

Evans, D. V. & Davies, T. V. 1968 Wave-ice interaction. Davidson Lab - Stevens Institute of Technology, New Jersey **Report No. 1313**.

Evans, D. & Porter, R. 2003 Wave scattering by narrow cracks in ice sheets floating on water of finite depth. *J. Fluid Mech.* **484**, pp. 143–165.

Evans, D. & Porter, R. 2006 Scattering of flexural waves by multiple narrow cracks in ice sheets floating on water. *Wave Motion*, **43**(5), pp. 425–443.

Fox, C. 2001 A scaling law for the flexural motion of floating ice. *Proc. IUTAM Symp. on Scaling Lams in Ice Mechanics and Ice Dynamics* (ed. J. P. Dempsey & H. H. Shen), pp. 135–148. Dordrecht: Kluwer Academic.

Fox, C., Haskell, T. G. & Chung, H. 2001 Dynamic, in-situ measurment of sea-ice characteristic length. *Annal. Glaciol.* **33**, pp. 339–344.

Fox, C. & Squire, V. A. 1990 Reflection and transmission at the edge of shore fast sea ice. *J. Geophys. Res.* **95**(C7), pp. 11,629–11,639.

Fox, C. & Squire, V. A. 1991 Strain in shore fast ice due to incoming ocean waves and swell. *J. Geophys. Res.* **67**(C7), pp. 4,531–4,547.

Fox, C. & Squire, V. A. 1994 On the oblique reflexion and transmission of ocean waves at shore fast sea ice. *Phil. Trans. R. Soc. A*, **347**(5), pp. 185–218.

Greenhill, A. G. 1887 Wave motion in hydrodynamics. *Am. J. Math.*, **9**, pp. 62–112.

Hermans, A. J. 2003*a* Interaction of free-surface waves with a floating dock. *J. Engng. Maths.* **45**, pp. 39–53.

Hermans, A. J. 2003*b* The ray method for the deflection of a floating flexible platform in short waves. *J. Fluids Struct.* **17**, pp. 593–602.

Hermans, A. J. 2004 Interaction of free-surface waves with floating flexible strips. *J. Engng. Maths.* **49**, pp. 133–147.

Hobbs, P. V. 1974 Ice physics. London: Oxford University Press.

Hunkins, K. 1962 Waves on the Arctic Ocean. *J. Geophys. Res.* **67**(6), pp. 2,477–2,489.

Hutter, K. 1975 Floating sea ice plates and the significance of the dependence of the Poisson's ratio on brine content. *Proc. Roc. Soc.* **343**(1632), pp. 85–108.

Kashiwagi, M. 1998 A B-Spline Galerkin scheme for calculating hydroelastic response of a very large floating structure in waves. *J. Mar. Sci. Tech.* **3**, pp. 37–49.

Kerr, A. D. & Palmer, W. T. 1972 The deformations and stresses in floating ice plates. *Acta Mech.* **15**, pp. 57–72.

Khabakhpasheva, T. I. & Korobkin, A. A. 2002 Hydroelastic behaviour of compound floating plate in waves. *J. Engng. Maths.* **44**, pp. 21–40.

Lamb, H. 1932 Hydrodynamics. Cambridge.

Lighthill, J. 1978 Waves in fluids. Cambridge.

Linton, C. M. & Chung, H. 2003 Handbook of mathematical techniques for wave/structure interactions. Chapman & Hall.

Linton, C. M. & McIver, P. 2001 Reflection and transmission at the ocean/sea-ice boundary. *Wave Motion* **38**, pp. 43–52.

Liu, A. K. & Mollo-Christiensen, E. 1988 Wave propagation on a solid ice pack. *J. Phys. Oceanogr.* **18**, pp. 1,702–1,712.

Meylan, M. H. 2001 A variational equation for the wave forcing of floating thin plates. *Appl. Ocean Res.* **23**, pp. 195-206.

Meylan, M. H. 2002 Wave response of an ice floe of arbitrary geometry. *J. Geophys. Res.* **107**, pp. 1–11.

Meylan, M. H. & Squire V.A. 1994 The response of ice floes to ocean waves. *J. Geophys. Res.* **99**, pp. 891–900.

Meylan, M. H. & Squire V. A. 1996 Response of a circular ice floe to ocean waves. *J. Geophys. Res.* **101**, pp. 8869–8884.

Meylan, M. H., Squire V. A. & Fox, C. 1997 Towards realism in modelling ocean wave behaviour. *J. Geophys. Res.* **102**(C10), pp. 22,981–22,991.

Molin, B. 2001 On the piston and sloshing modes in moonpools. *J. Fluid Mech.* **430**, pp. 27–50.

Peter, M. A. & Meylan, M. H. 2004 Infinite depth interaction theory for arbitrary floating bodies applied to wave forcing of ice floes. *J. Fluid Mech.* **500**, pp. 145–167.

Peter, M. A., Meylan, M. H. & Chung, H. 2004 Wave scattering by a circular elastic plate in water of finite depth: a closed form solution. *IJOPE* **14**(2), pp. 81–85.

Peter, M. A., Meylan, M. H. & Linton, C. M. 2006 Water-wave scattering by a periodic array of arbitrary bodies. *J. Fluid Mech.* **348**, pp. 237–256.

Porter, D. 2003 The mild-slope equations. *J. Fluid Mech.* **494,** pp. 51–63.

Porter, R. 2004 Flexural-gravity wave diffraction by finite cracks of arbitrary shape in ice sheets. In *Proc. 19th Intl. Workshop on Water Waves & Floating Bodies* (ed. Landrini, M., Campana E.F., Iafrati, A.) Cortona, Italy.

Porter, R. 1997 Diffraction of waves by arbitrary configurations in ice sheets. To be submitted.

Porter, D. & Chamberlain, P.G. 1997 Linear wave scattering by two-dimensional topography. In *Gravity Waves in Water of Finite Depth* (ed. J. N. Hunt), pp. 335–354. Computational Mechanics, Southampton.

Porter, D. & Porter, R. 2000 Interaction of water waves with three-dimensional periodic topography. *J. Fluid Mech.* **434**, pp. 301–335.

Porter, D. & Porter, R. 2003 Scattered and free waves over period beds. *J. Fluid Mech.* **483,** pp. 129–163.

Porter, D. & Porter, R. 2004 Approximations to wave scattering by an ice sheet of variable thickness over undulating topography. *J. Fluid Mech.* **509**, pp. 145–179.

Porter, D. & Staziker, D. J. 1995 Extensions of the mild-slope equation. *J. Fluid Mech.* **300**, pp. 367–382.

PORTER, D. & STIRLING, D. S. G. 1990 Integral equations. A practical treatment, from spectral theory to applications. Cambridge.

ROBIN, G. DE Q. 1963 Wave propagation through fields of pack ice. *Phil. Trans. R. Soc.* **255**, pp. 313–319.

SHAPIRO, A. & SIMPSON, L. S. 1953 The effect of a broken ice field on water waves. *Trans. Am. Geophys. Union* **34**(1), pp. 36–42.

SQUIRE, V. A. 1978 Dynamics of ocean waves in a continuous sea ice cover. PhD thesis. Uni. Cambridge, UK.

SQUIRE, V. A. 1984*a* How waves break up inshore fast ice. *Polar Rec.* **22**, pp. 281–285.

SQUIRE, V. A. 1984*b* A theoretical, laboratory and field study of ice-coupled waves. *J. Geophys. Res.* **89,** pp. 8,069–8,079.

SQUIRE, V. A. 1995 Geophysical and oceanographic information in the marginal ice zone. *J. Geophys. Res.* **100(C1)**, pp. 997–998.

SQUIRE, V. A. 2007 Of ocean waves and sea-ice revisited. *Cold Reg. Sci Technol.* **49**(2), pp. 110–133.

SQUIRE, V. A. & DIXON T. W. 2000 An analytic model for wave propagation across a crack in an ice sheet. *Int. J. Offshore Polar* **10**(3), pp. 173–176.

SQUIRE, V. A. & DIXON T. W. 2001 How a region of cracked sea ice affects ice-coupled wave propagation. *Ann. Glaciol.* **33**, pp. 327–332.

SQUIRE, V. A., DUGAN, J. P., WADHAMS, P., ROTTIER P. J. & LIU, A. K. 1995 Of ocean waves and ice sheets. *Ann. Rev. Fluid Mech* **27**, pp. 115–168.

STAZIKER, D. J. 1995 Water wave scattering by undulating bed topography. PhD thesis, Uni. of reading, UK.

STUROVA, I. 2001 The diffraction of surface waves by an elastic platform floating on shallow water. *J. Appl. Maths. Mech.* **65**(1), pp. 109–117.

TAKAGI, K. 2002 Surface wave diffraction on a floating elastic plate. *Appl. Ocean. Res.* **24**, pp. 175–183.

TAKAGI, K., SHIMADA, K. & IKEBUCHI, T. 2000 An anti-motion device for a very large fl;oating structure. *Marine. Struct.* **13**, pp. 421–436.

TIMOSHENKO, S. & WOINOWSKY-KRIEGER, S. 1959 Theory of plates and shells, 2nd Edn. McGraw-Hill.

TKACHEVA, L. A. 2001 Surface wave diffraction on a floating elastic plate. *J. Fluid Mech.* **36**(5), pp. 776–789.

TKACHEVA, L. A. 2004 The diffraction of surface waves by a floating elastic plate at oblique incidence. *J. Appl. Math. Mech.* **68**(3), pp. 425–436.

TRANTER, C. J. 1968 Bessel functions with some physical applications. English Universities Press.

VAUGHAN, G. L. & SQUIRE, V. A. 2007 Scattering of ice-coupled waves by variable sea-ice terrain. *Annal. Glaciol.* **44**, pp. 88-94.

WADHAMS, P. 1973 The effect of sea ice cover on ocean surface waves. PhD thesis. Uni. Cambridge, UK.

WADHAMS, P. 1986 The seasonal ice zone. In *The Geophysics of Sea Ice,* (ed. Untersteiner, N.), pp. 825–891. New York: Plenum

WANG, C. & MEYLAN, M. H. 2002 The Linear wave response of a floating thin plate on water of variable depth. *Appl. Ocean Res.* **24**, pp. 163–174.

WANG, C., MEYLAN, M. H. & PORTER, R. 2007 The linear wave response of a periodic array of floating elastic plates. *J. Eng. Maths.* **57**(1), pp. 23–46.

WATANABE, E., UTSUNOMIYA, T. & WANG, C. M. 2004 Hydroelastic analysis of pontoon-type VLFS: a literature survey. *Eng. Struct.* **26**(2), pp. 245–256.

WEHAUSEN, J. N. & LAITONE, E. V. 1960 Surface waves. *Handbuch der Physik*, vol. XI. Springer.

WEITZ, M. & KELLER, J. B. 1950 Reflection of water waves from floating ice in water of finite depth. *Common. Pure. Appl. Math.* **3**(3), pp. 305–318.

WORLD METEOROLOGICAL ORGANISATION 1970 WMO sea-ice nomenclature, terminology, codes and illustrated glossary. WMO/OMM/BMO **259**, TP **145**. Geneva, World Meteorological Organisation.

WILLIAMS, T. D. 2006 The scattering of flexural-gravity waves by irregularities in arctic and antarctic sea ice. PhD thesis, Uni. of Otago, Dunedin, NZ.

WILLIAMS, T. D. & SQUIRE, V. A. 2002 Wave propagation across an oblique crack in an ice sheet. *Int. J. Offshore Polar* **12**(3), pp. 157–162.

WILLIAMS, T. D. & SQUIRE, V. A. 2004 Oblique scattering of plane waves by heterogeneities in sea-ice. *Proc. Roc. Soc.* **460**, pp. 3,469–3,497.

Williams, T. D. & Squire, V. A. 2006 Scattering of flexural-gravity waves at the boundaries between three floating sheets with applications. *J. Fluid Mech.* **569**, pp. 113–140.

Williams, T. D. & Squire, V. A. 2007a The effect of submergence on scattering across a transition between two floating flexible plates. *J. Fluid Mech.* Submitted.

Williams, T. D. & Squire, V. A. 2007b Wave scattering at the sea-ice/ice-shelf with other applications. *J. Appl. Math.* To appear.

Wu, C., Watanabe, E. & Utsunomiya, T. 1995 An eigenfunction matching method for analyzing the wave induced responses of an elastic floating plate. *Appl. Ocean Res.* **17**, pp. 301–310.

Appendix A

The coefficients of the MMA

Here we give the explicit formulae that are needed to calculate the coefficients $a_{j,i}$, $\mathbf{d}_{j,i}$, $b_{j,i}$, $v_{j,i}$ and $Q_{j,i}$ involved in the governing equations of the MMA, as well as their free-surface equivalents that take the superscript (0). These coefficients were defined in §3.2.1 in terms of a set of inner-products of the vertical modes and their derivatives, which are described in full below.

Let a general mode be defined as

$$w_i(x,y,z) = \varpi_i \cosh\{\kappa_i(z+h)\},$$

where the quantity κ_i, the weight ϖ_i and bed depth h are all functions of the horizontal cartesian coordinates. Following §3.2.1, we redefine this mode as

$$w_i(x,y,z) \equiv W_i(D,h,d,z),$$

so that it is a function of the geometrical variables D, h and d in addition to the vertical coordinate z. We therefore also regard κ_i and ϖ_i as functions of D, h and d.

If the mode w_i is a natural mode then $\kappa_i = k_i$ is a root of the (ice-covered) dispersion relation (3.13) and is indeed a function of D, h and d. Alternatively, w_i may be an evanescent mode in which case $\kappa_i = \tilde{k}_i \equiv \mathrm{i}\pi_i$, which is a function of h and d but not the ice thickness D. In an ice-free region $\kappa_i = k_i^{(0)}$, which is a root of the free-surface dispersion relation (3.16) and is a function of the bed depth h only.

From now on the notation

$$\mathrm{s}_i = \mathrm{s}_i(z) = \sinh \kappa_i(z+h), \quad \mathrm{c}_i = \mathrm{c}_i(z) = \cosh \kappa_i(z+h), \quad \mathrm{Z}(z) = z,$$

will be used for brevity. Recall that we have defined the inner-product notation

$$(f,g) = \int_{-h}^{-d} f g \,\mathrm{d}z.$$

Use of the free-surface equivalent, which is usually endowed with the superscript (0), will be implicit.

We wish to write the required inner-products of the vertical modes, in terms of inner-products of known hyperbolic functions only, so that, for example

$$(W_i, W_j) = \varpi_i \varpi_j (\mathrm{c}_i, \mathrm{c}_j).$$

In a case in which a derivative is present, we will make use of the equality

$$\partial_X W_i = \varpi_i (\partial_X \kappa_i) \mathrm{Z}\mathrm{s}_i + \varpi_i (\partial_X (\kappa_i h)) \mathrm{s}_i + (\partial_X \varpi_i) \mathrm{c}_i,$$

where X (and/or Y) $= D, h$ or d. This leads to the expression

$$(W_i, \partial_X W_j) \;=\; \varpi_i \varpi_j (\partial_X \kappa_j)(\mathrm{c}_i, \mathrm{Z}\,\mathrm{s}_j) + \varpi_i \varpi_j (\partial_X (\kappa_j h))(\mathrm{c}_i, \mathrm{s}_j) + \varpi_i (\partial_X \varpi_j)(\mathrm{c}_i, \mathrm{c}_j),$$

from which the further equality

$$\begin{aligned}
\partial_Y (W_i, \partial_X W_j) \;=\;& \{(\partial_Y \varpi_i)\varpi_j + \varpi_i (\partial_Y \varpi_j)\}\{(\partial_X \kappa_j)(\mathrm{c}_i, \mathrm{Z}\,\mathrm{s}_j) + (\partial_X (\kappa_j h))(\mathrm{c}_i, \mathrm{s}_j)\} \\
&+ \varpi_i \varpi_j \{(\partial_Y \partial_X \kappa_j)(\mathrm{c}_i, \mathrm{Z}\,\mathrm{s}_j) + (\partial_X \kappa_j)(\partial_Y (\mathrm{c}_i, \mathrm{Z}\,\mathrm{s}_j))\} \\
&+ \varpi_i \varpi_j \{(\partial_Y \partial_X (\kappa_j h))(\mathrm{c}_i, \mathrm{s}_j) + (\partial_X (\kappa_j h))(\partial_Y (\mathrm{c}_i, \mathrm{s}_j))\} \\
&+ \{\varpi_i (\partial_Y \partial_X \varpi_j) + (\partial_Y \varpi_i)(\partial_X \varpi_j)\}(\mathrm{c}_i, \mathrm{c}_j) \\
&+ \varpi_i (\partial_X \varpi_j)(\partial_Y (\mathrm{c}_i, \mathrm{c}_j)),
\end{aligned}$$

is straightforward to derive, as is

$$\begin{aligned}
(\partial_Y W_i, \partial_X W_j) \;=\;& \varpi_i \varpi_j (\partial_Y \kappa_i)(\partial_X \kappa_j)(\mathrm{Z}\,\mathrm{s}_i, \mathrm{Z}\,\mathrm{s}_j) + \varpi_i \varpi_j (\partial_Y (\kappa_i h))(\partial_X (\kappa_j h))(\mathrm{s}_i, \mathrm{s}_j) \\
&+ \varpi_i \varpi_j \{(\partial_Y (\kappa_i h))(\partial_X \kappa_j) + (\partial_Y \kappa_i)(\partial_X (\kappa_j h))\}(\mathrm{Z}\,\mathrm{s}_i, \mathrm{s}_j) \\
&+ (\partial_Y \varpi_i)\varpi_j (\partial_X (\kappa_j h))(\mathrm{c}_i, \mathrm{s}_j) + (\partial_X \varpi_j)\varpi_i (\partial_Y (\kappa_i h))(\mathrm{s}_i, \mathrm{c}_j) \\
&+ (\partial_X \varpi_j)\varpi_i (\partial_Y \kappa_i)(\mathrm{Z}\,\mathrm{s}_i, \mathrm{c}_j) + (\partial_Y \varpi_i)\varpi_j (\partial_X \kappa_j)(\mathrm{c}_i, \mathrm{Z}\,\mathrm{s}_j) \\
&+ (\partial_Y \varpi_i)(\partial_X \varpi_j)(\mathrm{c}_i, \mathrm{c}_j).
\end{aligned}$$

A.1 Inner-products of the hyperbolic functions

In order to evaluate the above expressions we will need to calculate a set of inner-products of hyperbolic functions. This can be done directly and we begin with those that do not contain any derivatives. Thus,

$$(\mathrm{c}_i, \mathrm{c}_j) = \begin{cases} \dfrac{\kappa_i \mathrm{s}_i(-d)\mathrm{c}_j(-d) - \kappa_j \mathrm{s}_j(-d)\mathrm{c}_i(-d)}{\kappa_i^2 - \kappa_j^2} & (i \neq j), \\ \dfrac{\mathrm{s}_i(-d)\mathrm{c}_i(-d) + \kappa_i H}{2\kappa_i} & (i = j), \end{cases}$$

$$(\mathrm{s}_i, \mathrm{s}_j) = \begin{cases} \dfrac{\kappa_i \mathrm{c}_i(-d)\mathrm{s}_j(-d) - \kappa_j \mathrm{c}_j(-d)\mathrm{s}_i(-d)}{\kappa_i^2 - \kappa_j^2} & (i \neq j), \\ \dfrac{\mathrm{s}_i(-d)\mathrm{c}_i(-d) - \kappa_i H}{2\kappa_i} & (i = j), \end{cases}$$

and

$$(\mathrm{c}_i, \mathrm{s}_j) = \begin{cases} \dfrac{\kappa_j + \kappa_i \mathrm{s}_i(-d)\mathrm{s}_j(-d) - \kappa_j \mathrm{c}_j(-d)\mathrm{c}_i(-d)}{\kappa_i^2 - \kappa_j^2} & (i \neq j), \\ -\dfrac{\mathrm{s}_i^2(-d)}{2\kappa_i} & (i = j). \end{cases}$$

These expressions may be used to aid calculation of the inner-product that contain an additional z dependency, with

$$(\mathrm{Z}\,\mathrm{c}_i, \mathrm{c}_j) = \begin{cases} -\dfrac{d\{\kappa_i \mathrm{s}_i(-d)\mathrm{c}_j(-d) - \kappa_j \mathrm{c}_i(-d)\mathrm{s}_j(-d)\} + \kappa_i(\mathrm{s}_i, \mathrm{c}_j) - \kappa_j(\mathrm{c}_i, \mathrm{s}_j)}{\kappa_i^2 - \kappa_j^2} & (i \neq j), \\ \dfrac{d^2 - h^2}{4} - \dfrac{d\mathrm{s}_i(-d)\mathrm{c}_i(-d) + (\mathrm{s}_i, \mathrm{c}_i)}{2\kappa_i} & (i = j), \end{cases}$$

$$(\mathrm{Z}\,\mathrm{s}_i, \mathrm{s}_j) = \begin{cases} -\dfrac{d\{\kappa_i \mathrm{c}_i(-d)\mathrm{s}_j(-d) - \kappa_j \mathrm{s}_i(-d)\mathrm{c}_j(-d)\} + \kappa_i(\mathrm{c}_i, \mathrm{s}_j) - \kappa_j(\mathrm{s}_i, \mathrm{c}_j)}{\kappa_i^2 - \kappa_j^2} & (i \neq j), \\ -\dfrac{d^2 - h^2}{4} - \dfrac{d\mathrm{s}_i(-d)\mathrm{c}_i(-d) + (\mathrm{s}_i, \mathrm{c}_i)}{2\kappa_i} & (i = j), \end{cases}$$

$$(\mathrm{Z}\,\mathrm{c}_i, \mathrm{s}_j) = -\frac{h\kappa_j + d\{\kappa_i \mathrm{s}_i(-d)\mathrm{s}_j(-d) - \kappa_j \mathrm{c}_i(-d)\mathrm{c}_j(-d)\} + \kappa_i(\mathrm{s}_i, \mathrm{s}_j) - \kappa_j(\mathrm{c}_i, \mathrm{c}_j)}{\kappa_i^2 - \kappa_j^2}$$

for $i \neq j$, and

$$(\mathrm{Z}\,\mathrm{c}_i, \mathrm{s}_i) = \frac{h - d\{\mathrm{c}_i^2(-d) + \mathrm{s}_i^2(-d)\} - (\mathrm{c}_i, \mathrm{c}_i) - (\mathrm{s}_i, \mathrm{s}_i)}{4\kappa_i}.$$

There are also two inner-products required that contain a z^2 term, these being

$$(\mathrm{Z}\,\mathrm{c}_i, \mathrm{Z}\,\mathrm{c}_j) = \frac{d^2\{\kappa_i \mathrm{s}_i(-d)\mathrm{c}_j(-d) - \kappa_j \mathrm{c}_i(-d)\mathrm{s}_j(-d)\} - 2\{\kappa_i(\mathrm{Z}\,\mathrm{s}_i, \mathrm{c}_j) - \kappa_j(\mathrm{Z}\,\mathrm{c}_i, \mathrm{s}_j)\}}{\kappa_i^2 - \kappa_j^2}$$

for $i \neq j$,

$$(\mathrm{Z}\,\mathrm{c}_i, \mathrm{Z}\,\mathrm{c}_i) = \frac{d^2 \mathrm{s}_i(-d)\mathrm{c}_i(-d) - 2(\mathrm{Z}\,\mathrm{c}_i, \mathrm{s}_i)}{2\kappa_i} - \frac{d^3 - h^3}{6},$$

$$(\mathrm{Z}\,\mathrm{s}_i, \mathrm{Z}\,\mathrm{s}_j) = \frac{d^2\{\kappa_i \mathrm{c}_i(-d)\mathrm{s}_j(-d) - \kappa_j \mathrm{s}_i(-d)\mathrm{c}_j(-d)\} - 2\{\kappa_i(\mathrm{Z}\,\mathrm{c}_i, \mathrm{s}_j) - \kappa_j(\mathrm{Z}\,\mathrm{s}_i, \mathrm{c}_j)\}}{\kappa_i^2 - \kappa_j^2}$$

for $i \neq j$, and

$$(\mathrm{Z}\,\mathrm{s}_i, \mathrm{Z}\,\mathrm{s}_i) = \frac{d^2\mathrm{s}_i(-d)\mathrm{c}_i(-d) - 2(\mathrm{Z}\,\mathrm{c}_i, \mathrm{s}_i)}{2\kappa_i} + \frac{d^3 - h^3}{6}.$$

Finally, we must find certain derivatives of the above inner-products, which are required to evaluate the term $\partial_Y(W_i, \partial_X W_j)$; these are calculated via Leibniz's rule to be

$$\begin{aligned}
\partial_Y(\mathrm{c}_i, \mathrm{c}_j) \;&=\; (\partial_Y\kappa_i)(\mathrm{Z}\,\mathrm{c}_i, \mathrm{s}_j) + (\partial_Y(\kappa_i h))(\mathrm{c}_i, \mathrm{s}_j) + (\partial_Y\kappa_j)(\mathrm{Z}\,\mathrm{s}_i, \mathrm{c}_j) \\
&\quad + (\partial_Y(\kappa_j h))(\mathrm{s}_i, \mathrm{c}_j) - (\partial_Y d)\mathrm{c}_i(-d)\mathrm{c}_j(-d) + (\partial_Y h),
\end{aligned}$$

$$\begin{aligned}
\partial_Y(\mathrm{c}_i, \mathrm{s}_j) \;&=\; (\partial_Y\kappa_i)(\mathrm{Z}\,\mathrm{s}_i, \mathrm{s}_j) + (\partial_Y(\kappa_i h))(\mathrm{s}_i, \mathrm{s}_j) + (\partial_Y\kappa_j)(\mathrm{Z}\,\mathrm{c}_i, \mathrm{c}_j) \\
&\quad + (\partial_Y(\kappa_j h))(\mathrm{c}_i, \mathrm{c}_j) - (\partial_Y d)\mathrm{c}_i(-d)\mathrm{s}_j(-d),
\end{aligned}$$

and

$$\begin{aligned}
\partial_Y(\mathrm{Z}\,\mathrm{c}_i, \mathrm{s}_j) \;&=\; (\partial_Y\kappa_i)(\mathrm{Z}\,\mathrm{s}_i, \mathrm{Z}\,\mathrm{s}_j) + (\partial_Y(\kappa_i h))(\mathrm{Z}\,\mathrm{s}_i, \mathrm{s}_j) \\
&\quad + (\partial_Y\kappa_j)(\mathrm{Z}^2\,\mathrm{c}_i, \mathrm{c}_j) + (\partial_Y(\kappa_j h))(\mathrm{Z}\,\mathrm{c}_i, \mathrm{c}_j) \\
&\quad + (\partial_Y d)d\mathrm{c}_i(-d)\mathrm{s}_j(-d).
\end{aligned}$$

The second derivative

$$\begin{aligned}
\partial_X\partial_Y(\mathrm{c}_i, \mathrm{c}_j) \;&=\; (\partial_X\partial_Y\kappa_i)(\mathrm{Zs}_i, \mathrm{c}_j) + (\partial_X\partial_Y\kappa_j)(\mathrm{Zc}_i, \mathrm{s}_j) \\
&\quad + (\partial_X\partial_Y(\kappa_i h))(\mathrm{s}_i, \mathrm{c}_j) + (\partial_X\partial_Y(\kappa_j h))(\mathrm{c}_i, \mathrm{s}_j) \\
&\quad + \{(\partial_X\kappa_i)(\partial_Y\kappa_j) + (\partial_Y\kappa_i)(\partial_X\kappa_j)\}(\mathrm{Zs}_i, \mathrm{Zs}_j) \\
&\quad + \{(\partial_X\kappa_i)(\partial_Y(\kappa_j h)) + (\partial_Y\kappa_i)(\partial_X(\kappa_j h)) \\
&\qquad + (\partial_X(\kappa_i h))(\partial_Y\kappa_j) + (\partial_Y(\kappa_i h))(\partial_X\kappa_j)\}(\mathrm{Zs}_i, \mathrm{s}_j) \\
&\quad + \{(\partial_X(\kappa_i h))(\partial_Y(\kappa_j h)) + (\partial_Y(\kappa_i h))(\partial_X(\kappa_j h))\}(\mathrm{s}_i, \mathrm{s}_j) \\
&\quad + \{(\partial_X\kappa_i)(\partial_Y\kappa_i) + (\partial_X\kappa_j)(\partial_Y\kappa_j)\}(\mathrm{Zc}_i, \mathrm{Zc}_j) \\
&\quad + \{(\partial_X\kappa_i)(\partial_Y(\kappa_i h)) + (\partial_Y\kappa_i)(\partial_X(\kappa_i h)) \\
&\qquad + (\partial_X\kappa_j)(\partial_Y(\kappa_j h)) + (\partial_Y\kappa_j)(\partial_X(\kappa_j h))\}(\mathrm{Zc}_i, \mathrm{c}_j) \\
&\quad + \{(\partial_X(\kappa_i h))(\partial_Y(\kappa_i h)) + (\partial_Y(\kappa_j h))(\partial_X(\kappa_j h))\}(\mathrm{c}_i, \mathrm{c}_j) \\
&\quad + (\partial_X d)\{((\partial_Y\kappa_i)d - (\partial_Y(\kappa_i h)))\mathrm{s}_i(-d)\mathrm{c}_j(-d) \\
&\qquad + ((\partial_Y\kappa_j)d - (\partial_Y(\kappa_j h)))\mathrm{c}_i(-d)\mathrm{s}_j(-d)\} \\
&\quad + (\partial_Y d)\{((\partial_X\kappa_i)d - (\partial_X(\kappa_i h)))\mathrm{s}_i(-d)\mathrm{c}_j(-d) \\
&\qquad + ((\partial_X\kappa_j)d - (\partial_X(\kappa_j h)))\mathrm{c}_i(-d)\mathrm{s}_j(-d)\} \\
&\quad + (\partial_X d)(\partial_Y d)\{\kappa_i\mathrm{s}_i(-d)\mathrm{c}_j(-d) + \kappa_j\mathrm{c}_i(-d)\mathrm{s}_j(-d)\},
\end{aligned}$$

is also of use when calculating the second derivative of the normalising weighting $\varpi_i = a_{i,i}^{-1/2}$.

A.2 Derivatives of the roots of the dispersion relation

Various derivatives of the quantity $\kappa_i = \kappa_i(D,h,d)$ appear in the inner-products above. These must also be given in an explicit form.

To begin with, let us assume that $\kappa_i = k_i$ is a root of the (ice-covered) dispersion relation, which we write as

$$f(k,D)\tanh(kH) = \kappa : \quad f(k,D) = (1 - \kappa\alpha(D) + \beta(D)k^4)k. \tag{A.1}$$

We will assume that the root k_i has been found by some means (see §3.2.2). In which case, its required first derivatives may then be calculated from

$$E_i(\partial_D k_i) = -(\partial_D f_i)\sinh(2k_iH), \quad E_i(\partial_d k_i) = 2f_ik_i, \quad E_i(\partial_h k_i) = -2f_ik_i,$$

where the notation $f_i = f(k_i,D)$ has been used. Similarly, $E_i = E(k_i)$, where the function E is defined as

$$E(k) = (\partial_k f(k))\sinh(2kH) + 2Hf(k).$$

The second derivatives then follow as

$$\begin{aligned} E_i(\partial_D^2 k_i) &= -(\partial_k E_i)(\partial_D k_i)^2 - (\partial_D^2 f_i)\sinh(2k_iH) \\ &\quad -2(\partial_D k_i)\{(\partial_k\partial_D f_i)\sinh(2k_iH) + 2H(\partial_D f_i)\cosh^2(k_iH)\}, \end{aligned} \tag{A.2a}$$

$$E_i(\partial_h^2 k_i) = -(\partial_k E_i)(\partial_h k_i)^2 - 4(\partial_h k_i)\{f_i + k_i(\partial_k f_i)\cosh^2(k_iH)\}, \tag{A.2b}$$

$$E_i(\partial_d^2 k_i) = -(\partial_k E_i)(\partial_d k_i)^2 + 4(\partial_d k_i)\{f_i + k_i(\partial_k f_i)\cosh^2(k_iH)\}, \tag{A.2c}$$

$$\begin{aligned} E_i(\partial_D\partial_h k_i) &= -(\partial_k E_i)(\partial_D k_i)(\partial_h k_i) - 2k_i(\partial_D f_i) - 2(\partial_D k_i)\{f_i + k_i(\partial_k f_i)\} \\ &\quad -(\partial_h k_i)\{(\partial_k\partial_D f_i)\sinh(2k_iH) + 2H(\partial_D f_i)\}, \end{aligned} \tag{A.2d}$$

$$\begin{aligned} E_i(\partial_D\partial_d k_i) &= -(\partial_k E_i)(\partial_D k_i)(\partial_d k_i) + 2k_i(\partial_D f_i) + 2(\partial_D k_i)\{f_i + k_i(\partial_k f_i)\} \\ &\quad -(\partial_d k_i)\{(\partial_k\partial_D f_i)\sinh(2k_iH) + 2H(\partial_D f_i)\}, \end{aligned} \tag{A.2e}$$

and

$$\begin{aligned} E_i(\partial_d\partial_h k_i) &= -(\partial_k E_i)(\partial_d k_i)(\partial_h k_i) + 2(\partial_h k_i)\{f_i + k_i(\partial_k f_i)\cosh(2k_iH)\} \\ &\quad -2(\partial_d k_i)\{f_i + k_i(\partial_k f_i)\}. \end{aligned} \tag{A.2f}$$

To evaluate the above expression we need derivatives of the functions f and E, and these are

$$\partial_k f = 1 - \kappa\alpha + 5\beta k^4, \quad \partial_D f = -D^{-1}k(\kappa\alpha - 3\beta k^4),$$

and

$$\partial_k^2 f = 20\beta k^3, \quad \partial_D^2 f = 6D^{-2}\beta k^5, \quad \partial_k\partial_D f = -D^{-1}(\kappa\alpha - 15\beta k^4),$$

and

$$\partial_k E = (\partial_k^2 f)\sinh(2kH) + 4H(\partial_k f)\cosh^2(kH).$$

The function E may be recognised as a scaled version of the derivative of the dispersion relation (A.1) with respect to k. As such, if it were to vanish at a particular root, k_i say, then k_i would necessarily be a multiple root of the dispersion relation. However, we would be unable to obtain its derivatives from equations (A.2a-g), as then $E_i = 0$. This corresponds to the comment made in §3.2.2 concerning the unboundedness of the constituent roots in the vicinity of a bifurcation.

Turning to the situation in which the ice is absent and the quantity $\kappa_i = k_i^{(0)}$ is a root of the free-surface dispersion relation

$$k^{(0)}\tanh(k^{(0)}h) = \kappa,$$

then, as previously mentioned, it is a function of the bed depth h only. The required first and second derivatives of $k_i^{(0)}$ are, respectively,

$$E_i^{(0)}(\partial_h k_i^{(0)}) = -2\left(k_i^{(0)}\right)^2,$$

and

$$E_i^{(0)}(\partial_h^2 k_i^{(0)}) = -4h\cosh^2(k^{(0)}h)(\partial_h k_i^{(0)})^2 - 4k_i^{(0)}(\partial_h k_i^{(0)})(1 + \cosh^2(k_i^{(0)}h)),$$

where

$$E_i^{(0)} = \sinh(2k_i^{(0)}h) + 2k_i h.$$

For the limiting values

$$\kappa_n = \mathrm{i}\pi_n = \mathrm{i}\frac{n\pi}{H},$$

which are used in the hybrid approximation, the expressions for the roots are trivial, but for completeness, we give them here. Thus,

$$\partial_h \pi_n = -\frac{n\pi}{H^2}, \quad \partial_d \pi_n = \frac{n\pi}{H^2},$$

and

$$\partial_h^2 \pi_n = \frac{2n\pi}{H^3}, \quad \partial_h\partial_d \pi_n = -\frac{2n\pi}{H^3}, \quad \partial_d^2 \pi_n = \frac{2n\pi}{H^3}.$$

Appendix B

Identities in two-dimensional problems

In this Appendix we derive an equation that can be used to show that for two-dimensional configurations the MMA maintains the energy balance that is satisfied by the full linear solution. We will then use this equation to deduce some of the identities that were used to analyse the scattering in a two-dimensional setting.

B.1 An energy balance equation

The energy equation that we will derive in this section is the extension of that which appeared in Porter & Porter (2004) in their equation (5.20) for the single-mode approximation.

Begin by letting the functions, $\boldsymbol{\Psi}_{(0)} = (\boldsymbol{\Phi}_{(0)}^T, \chi_{(0)}^{(1)}, \chi_{(0)}^{(2)})^T$, be defined as solutions of the governing differential equations of the MMA in two-dimensions, which were defined by equations (4.3a-b). Here we write the equations as

$$\mathfrak{H}(\boldsymbol{\Phi}_{(0)}, \chi_{(0)}^{(1)}) = \mathbf{0}, \quad \mathfrak{h}_1(\chi_{(0)}^{(1)}, \chi_{(0)}^{(2)}) = 0, \quad \mathfrak{h}_2(\boldsymbol{\Phi}_{(0)}, \chi_{(0)}^{(1)}, \chi_{(0)}^{(2)}) = 0,$$

where

$$\mathfrak{H}(\boldsymbol{\Phi}_{(0)}, \chi_{(0)}^{(1)}) \equiv \partial_x(A\partial_x\boldsymbol{\Phi}_{(0)}) + \widetilde{D}\partial_x\boldsymbol{\Phi}_{(0)} + (B - q^2A)\boldsymbol{\Phi}_{(0)} + \kappa\chi_{(0)}^{(1)}C\mathbf{f}, \tag{B.1a}$$

$$\mathfrak{h}_1(\chi_{(0)}^{(1)}, \chi_{(0)}^{(2)}) \equiv \beta(\partial_x^2 - q^2)\chi_{(0)}^{(1)} - \chi_{(0)}^{(2)}, \tag{B.1b}$$

and

$$\mathfrak{h}_2(\boldsymbol{\Phi}_{(0)}, \chi_{(0)}^{(1)}, \chi_{(0)}^{(2)}) \equiv (\partial_x^2 - q^2)\chi_{(0)}^{(2)} + \{(1-\nu)(\partial_x^2\beta) + 1 - \kappa\alpha\}\chi_{(0)}^{(1)} - \mathbf{f}^TC\boldsymbol{\Phi}_{(0)}. \tag{B.1c}$$

Now define the functions $\boldsymbol{\Psi}_{(1)} = (\boldsymbol{\Phi}^T_{(1)}, \chi^{(1)}_{(1)}, \chi^{(2)}_{(1)})^T$ as the solutions of the related system

$$\mathfrak{H}^*(\boldsymbol{\Phi}_{(1)}, \chi^{(1)}_{(1)}) = \mathbf{0}, \quad \mathfrak{h}_1(\chi^{(1)}_{(1)}, \chi^{(2)}_{(1)}) = 0, \quad \mathfrak{h}_2(\boldsymbol{\Phi}_{(1)}, \chi^{(1)}_{(1)}, \chi^{(2)}_{(1)}) = 0,$$

where

$$\mathfrak{H}^*(\boldsymbol{\Phi}_{(1)}, \chi^{(1)}_{(1)}) \equiv \partial_x(A\partial_x\boldsymbol{\Phi}_{(1)}) + \partial_x(\widetilde{D}\boldsymbol{\Phi}_{(1)}) + (B^T - q^2A)\boldsymbol{\Phi}_{(1)} + \kappa\chi^{(1)}_{(1)}C\mathbf{f}.$$

By applying the symmetries $A = A^T$ and $D = -D^T$ to the combination

$$\boldsymbol{\Phi}^T_{(1)}\mathfrak{H}(\boldsymbol{\Phi}_{(0)}, \chi^{(1)}_{(0)}) - (\mathfrak{H}^*(\boldsymbol{\Phi}_{(1)}, \chi^{(1)}_{(1)}))^T\boldsymbol{\Phi}_{(1)},$$

we arrive at the equality

$$\partial_x\{\boldsymbol{\Phi}^T_{(1)}A(\partial_x\boldsymbol{\Phi}_{(0)}) - (\partial_x\boldsymbol{\Phi}_{(1)})^TA\boldsymbol{\Phi}_{(0)} + \boldsymbol{\Phi}^T_{(1)}\widetilde{D}\boldsymbol{\Phi}_{(0)}\} + \kappa\mathbf{f}^TC\{\chi^{(1)}_{(0)}\boldsymbol{\Phi}_{(1)} - \chi^{(1)}_{(1)}\boldsymbol{\Phi}_{(0)}\} = 0. \tag{B.2a}$$

Similarly, by rearranging the terms $\chi^{(2)}_{(1)}\mathfrak{h}_1(\chi^{(1)}_{(0)}, \chi^{(2)}_{(0)}) - \chi^{(2)}_{(0)}\mathfrak{h}_1(\chi^{(1)}_{(1)}, \chi^{(2)}_{(1)})$ we find that

$$\begin{aligned}\partial_x\{\chi^{(2)}_{(1)}(\partial_x\chi^{(1)}_{(0)}) - \chi^{(2)}_{(0)}(\partial_x\chi^{(1)}_{(1)})\} - \{(\partial_x\chi^{(2)}_{(1)})(\partial_x\chi^{(1)}_{(0)}) - (\partial_x\chi^{(2)}_{(0)})(\partial_x\chi^{(1)}_{(1)})\} - \\ q^2\{\chi^{(2)}_{(1)}\chi^{(1)}_{(0)} - \chi^{(2)}_{(0)}\chi^{(1)}_{(1)}\} \quad &= 0,\end{aligned} \tag{B.2b}$$

and an analogous process for the combination

$$\chi^{(1)}_{(1)}\mathfrak{h}_2(\boldsymbol{\Phi}_{(0)}, \chi^{(1)}_{(0)}, \chi^{(2)}_{(0)}) - \chi^{(1)}_{(0)}\mathfrak{h}_2(\boldsymbol{\Phi}_{(1)}, \xi^{(1)}_{(1)}, \xi^{(2)}_{(1)})$$

produces

$$\begin{aligned}\partial_x\{\chi^{(1)}_{(1)}(\partial_x\chi^{(2)}_{(0)}) - \chi^{(1)}_{(0)}(\partial_x\chi^{(2)}_{(1)})\} - \{(\partial_x\chi^{(1)}_{(1)})(\partial_x\chi^{(2)}_{(0)}) - (\partial_x\chi^{(1)}_{(0)})(\partial_x\chi^{(2)}_{(1)})\} \\ -q^2\{\chi^{(1)}_{(1)}\chi^{(2)}_{(0)} - \chi^{(1)}_{(0)}\chi^{(2)}_{(1)}\} - \mathbf{f}^TC\{\chi^{(1)}_{(1)}\boldsymbol{\Phi}_{(0)} - \chi^{(1)}_{(0)}\boldsymbol{\Phi}_{(1)}\} \quad &= 0.\end{aligned} \tag{B.2c}$$

A linear combination of equations (B.2a-c) then gives

$$\begin{aligned}\partial_x\{\boldsymbol{\Phi}^T_{(1)}A(\partial_x\boldsymbol{\Phi}_{(0)}) - (\partial_x\boldsymbol{\Phi}_{(1)})^TA\boldsymbol{\Phi}_{(0)} + \boldsymbol{\Phi}^T_{(1)}\widetilde{D}\boldsymbol{\Phi}_{(0)}\} \\ -\kappa\partial_x\{\chi^{(1)}_{(1)}(\partial_x\chi^{(2)}_{(0)}) - \chi^{(1)}_{(0)}(\partial_x\chi^{(2)}_{(1)}) + \chi^{(2)}_{(1)}(\partial_x\chi^{(1)}_{(0)}) - \chi^{(2)}_{(0)}(\partial_x\chi^{(1)}_{(1)})\} \quad &= 0.\end{aligned} \tag{B.3}$$

Alternatively, we may express equation (B.3) in the more compact form

$$\partial_x\{\boldsymbol{\Psi}^T_{(1)}\mathcal{O}\mathcal{A}(\partial_x\boldsymbol{\Psi}_{(0)}) - (\partial_x\boldsymbol{\Psi}_{(1)})^T\mathcal{O}\mathcal{A}\boldsymbol{\Psi}_{(0)} + \boldsymbol{\Psi}^T_{(1)}\widetilde{\mathcal{D}}\boldsymbol{\Psi}_{(0)}\} = 0, \tag{B.4}$$

where the matrix

$$\mathcal{O} = \begin{pmatrix} I & \mathbf{0} & \mathbf{0} \\ \mathbf{0}^T & 0 & -\kappa \\ \mathbf{0}^T & -\kappa & 0 \end{pmatrix},$$

is of size $(N+3) \times (N+3)$.

Over an interval of suitably smooth geometry (x_0, x_1), that is geometry for which the operators (B.1a-c) are well defined, equation (B.4) may be integrated to give the energy balance

$$\left[\boldsymbol{\Psi}_{(1)}^T \mathcal{O}\mathcal{A}(\partial_x \boldsymbol{\Psi}_{(0)}) - (\partial_x \boldsymbol{\Psi}_{(1)})^T \mathcal{O}\mathcal{A}\boldsymbol{\Psi}_{(0)} + \boldsymbol{\Psi}_{(1)}^T \widetilde{\mathcal{D}}\boldsymbol{\Psi}_{(0)}\right]_{x=x_0}^{x_1} = 0. \tag{B.5}$$

This may be extended if both $\boldsymbol{\Psi}_{(\mathbf{i})}$ $(i = 0, 1)$ are subject to the jump conditions

$$(\mathcal{V}^T \mathcal{M}^{-1} \boldsymbol{\Psi}_{(i)})_+ = (\mathcal{V}^T \mathcal{M}^{-1} \boldsymbol{\Psi}_{(i)})_-,$$

and

$$\mathcal{V}_+^{-1}\{(\mathcal{A}\mathcal{M}\partial_x \boldsymbol{\Psi}_{(i)})_+ + (\mathcal{Q}\mathcal{N}\boldsymbol{\Psi}_{(i)})_+\} = \mathcal{V}_-^{-1}\{(\mathcal{A}\mathcal{M}\partial_x \boldsymbol{\Psi}_{(i)})_- + (\mathcal{Q}\mathcal{N}\boldsymbol{\Psi}_{(i)})_-\}.$$

In this case it can be shown by using the identity $Q - Q^T = \widetilde{D}$ that the above energy balance holds for any two points in an interval of ice-covered fluid, regardless of whether there are discontinuities in the geometry.

In an interval of ice-free fluid the energy balance (B.5) reduces to

$$\left[\boldsymbol{\Phi}_{(1)}^T A(\partial_x \boldsymbol{\Phi}_{(0)}) - (\partial_x \boldsymbol{\Phi}_{(1)})^T A\boldsymbol{\Phi}_{(0)} + \boldsymbol{\Phi}_{(1)}^T \widetilde{D}\boldsymbol{\Phi}_{(0)}\right]_{x=x_0}^{x_1} = 0.$$

Now suppose that the interval (x_0, x_1) extends from an ice-free interval into an ice-covered interval, and that the joining conditions

$$(V^T \boldsymbol{\Phi}_{(i)})_+ = (V^T \boldsymbol{\Phi}_{(i)})_-,$$

and

$$\mathcal{V}_+^{-1}\{(\mathcal{A}\mathcal{M}\partial_x \boldsymbol{\Psi}_{(i)})_+ + (\mathcal{J}\widetilde{\mathcal{N}}\boldsymbol{\Psi}_{(i)})_+\} = \mathcal{V}_-^{-1}\{(\mathcal{A}\mathcal{M}\partial_x \boldsymbol{\Psi}_{(i)})_- + (\mathcal{J}\widetilde{\mathcal{N}}\boldsymbol{\Psi}_{(i)})_-\},$$

apply at the ice edge, for $i = 0, 1$. The ice-covered and ice-free energy balance equations may then be combined, to give

$$\left[\boldsymbol{\Phi}_{(1)}^T A(\partial_x \boldsymbol{\Phi}_{(0)}) - (\partial_x \boldsymbol{\Phi}_{(1)})^T A\boldsymbol{\Phi}_{(0)} + \boldsymbol{\Phi}_{(1)}^T \widetilde{D}\boldsymbol{\Phi}_{(0)}\right]_{x=x_0} =$$
$$\left[\boldsymbol{\Psi}_{(1)}^T \mathcal{O}\mathcal{A}(\partial_x \boldsymbol{\Psi}_{(0)}) - (\partial_x \boldsymbol{\Psi}_{(1)})^T \mathcal{O}\mathcal{A}\boldsymbol{\Psi}_{(0)} + \boldsymbol{\Psi}_{(1)}^T \widetilde{\mathcal{D}}\boldsymbol{\Psi}_{(0)}\right]_{x=x_1}.$$

B.2 Identities involving the linearly independent functions

The energy balance (B.5) given above may be used to derive some of the identities that were used in our earlier work. Specifically, we wish to establish relationships between the linearly independent functions that are combined to form the MMA in two-dimensional problems. For instance, if the ice-cover is complete we define the MMA over an interval of varying geometry in equation (4.37) in terms of functions denoted $\mathcal{L}_{\pm}$. Similarly, in the case of a floe of a finite extent and a varying thickness, equation (4.37) defines the MMA in terms of different functions $\mathcal{L}_{\pm}$. There is also the problem of a periodic structure, for which the MMA is defined in each period by equation (8.3), where the linearly independent functions are denoted $\mathcal{L}_{\pm,(i)}$ $(i = 1, \ldots, M)$. In each case, the linearly independent functions satisfy the system of ordinary differential equations (4.4) that govern the MMA in two-dimensions. The energy balance (B.5) is therefore applicable to these functions.

B.2.1 Diagonality of the matrix $\mathcal{C}^T\mathcal{O}\mathcal{A}\mathcal{C}$

Before we seek relationships between the linearly independent functions, we must first prove an intermediate result that will facilitate our analysis. This is that the matrix $\mathcal{C}^T\mathcal{O}\mathcal{A}\mathcal{C}$ is diagonal. Recall that

$$\mathcal{C} = [\hat{\mathbf{c}}(\lambda_0), \ldots, \hat{\mathbf{c}}(\lambda_N), \hat{\mathbf{c}}(\lambda_{-1}), \hat{\mathbf{c}}(\lambda_{-2})],$$

where

$$\hat{\mathbf{c}}(\lambda_n) = \begin{pmatrix} \mathbf{I}_{n+1} \\ \gamma^{(1)}(\lambda_n) \\ \gamma^{(2)}(\lambda_n) \end{pmatrix}, \quad \gamma^{(1)}(\lambda_n) = \frac{k_n \sinh(k_n H)}{\kappa}, \quad \gamma^{(2)}(\lambda_n) = -\beta k_n^2 \gamma^{(1)}(\lambda_n),$$

for $n = 0, \ldots, N$,

$$\hat{\mathbf{c}}(\lambda_{-j}) = \begin{pmatrix} \upsilon_{N,(j)} \\ \gamma^{(1)}(\lambda_{-j}) \\ \gamma^{(2)}(\lambda_{-j}) \end{pmatrix}, \quad \gamma^{(1)}(\lambda_{-j}) = \frac{\mu_{N,(j)} \sinh(\mu_{N,(j)} H)}{\kappa},$$

and $\gamma^{(2)}(\lambda_{-j}) = -\beta \mu_{N,(j)}^2 \gamma^{(1)}(\lambda_{-j})$ for $j = 1, 2$. The vector $\upsilon_{N,(j)}$ is defined by

$$A\upsilon_{N,(j)} + \beta\gamma^{(1)}(\lambda_{-j})(K^2 + \mu_{N,(j)}^2 I)KS\mathbf{f} = \mathbf{0} \quad (j = 1, 2), \tag{B.8}$$

where the roots $\mu_{N,(j)}$ are calculated from

$$(\beta\mu_{N,(j)}^4 + 1 - \kappa\alpha) + \beta\mathbf{f}^T CA^{-1}(K^2 + \mu_{N,(j)}^2 I)KS\mathbf{f} = 0 \quad (j = 1, 2).$$

Evaluating the entries of the matrix $\mathcal{C}^T\mathcal{O}\mathcal{A}\mathcal{C}$ directly, we find that

$$\{\mathcal{C}^T\mathcal{O}\mathcal{A}\mathcal{C}\}_{j,i} = \left\{A + \frac{\beta}{\kappa}\left(KS\mathbf{f}\mathbf{f}^T K^3 S + K^3 S\mathbf{f}\mathbf{f}^T KS\right)\right\}_{j,i} \qquad (i, j = 1, \ldots, N+1), \quad \text{(B.9a)}$$

$$\{\mathcal{C}^T\mathcal{O}\mathcal{A}\mathcal{C}\}_{j,N+1+i} = \{\mathcal{C}^T\mathcal{O}\mathcal{A}\mathcal{C}\}_{N+1+i,j} = \{Av_{N,(i)} + \beta\gamma^{(1)}(\lambda_{-i})(K^2 + \mu_{N,(i)}^2 I)KS\mathbf{f}\}_j, \quad \text{(B.9b)}$$

for $j = 1, \ldots, N+1$ and $i = 1, 2$, and

$$\{\mathcal{C}^T\mathcal{O}\mathcal{A}\mathcal{C}\}_{N+1+j,N+1+i} = v_{N,(i)}^T A v_{N,(j)} + \kappa\beta\gamma^{(1)}(\lambda_{-i})\gamma^{(1)}(\lambda_{-j})(\mu_{N,(i)}^2 + \mu_{N,(j)}^2) \qquad \text{(B.9c)}$$

for $i, j = 1, 2$. We now wish to show that the off-diagonal entries are zero. Making use of the dispersion relation (3.13) and the definition of the coefficients $a_{j,i}$ given in (4.15), we find that, for the block defined in equation (B.9a), the off-diagonal entries ($i \neq j$) are

$$\begin{aligned}
& a_{j,i} + \frac{\beta}{\kappa} k_j \sinh(k_j H) k_i \sinh(k_i H)(k_j^2 + k_i^2) \\
= \; & \frac{1}{\kappa(k_j^2 - k_i^2)} \{\kappa\left(k_j \sinh(k_j H)\cosh(k_i H) - k_i \sinh(k_i H)\cosh(k_j H)\right) \\
& + \beta k_j \sinh(k_j H) k_i \sinh(k_i H)(k_j^4 - k_i^4)\} \\
= \; & \frac{1}{\kappa(k_j^2 - k_i^2)} \{\kappa\left(k_j \sinh(k_j H)\cosh(k_i H) - k_i \sinh(k_i H)\cosh(k_j H)\right) \\
& + k_j \sinh(k_j H)\left(\kappa\cosh(k_i H) + \kappa\alpha k_i \sinh(k_i H) - k_i \sinh(k_i H)\right) \\
& - k_i \sinh(k_i H)\left(\kappa\cosh(k_j H) + \kappa\alpha k_j \sinh(k_j H) - k_j \sinh(k_j H)\right)\} \\
= \; & \frac{1}{\kappa(k_j^2 - k_i^2)} \{\kappa\left(k_j \sinh(k_j H)\cosh(k_i H) - k_i \sinh(k_i H)\cosh(k_j H)\right) \\
& - \kappa\left(k_j \sinh(k_j H)\cosh(k_i H) - k_i \sinh(k_i H)\cosh(k_j H)\right)\} = 0.
\end{aligned}$$

The vanishing of the entries defined in (B.9b), which are all off-diagonal, is a trivial consequence of the definition of the vectors $v_{N,(i)}$ ($i = 1, 2$) given in (B.8). To show that the entries in equation (B.9c) are zero for $i \neq j$, we use the definition of the eigensystem (4.12a-b), which states that

$$(A(K^2 - \mu_{N,(i)}^2 I) - C\mathbf{f}\,\mathbf{f}^T KS)v_{N,(i)} + \kappa\gamma^{(1)}(\lambda_{-i})C\mathbf{f} = \mathbf{0}, \qquad \text{(B.10a)}$$

and

$$(\beta\mu_{N,(i)}^4 + 1 - \kappa\alpha)\gamma^{(1)}(\lambda_{-i}) - \mathbf{f}^T C v_{N,(i)} = 0, \qquad \text{(B.10b)}$$

for $i = 1, 2$. We deduce from the former that

$$\upsilon^T_{N,(j)}(AK^2 - C\mathbf{f}\,\mathbf{f}^T KS)\upsilon_{N,(i)} - \mu^2_{N,(i)}\upsilon^T_{N,(j)}A\upsilon_{N,(i)} + \kappa\gamma^{(1)}(\lambda_{-i})\upsilon^T_{N,(j)}C\mathbf{f} = 0 \tag{B.11}$$

for $i, j = 1, 2$. Then, taking the difference of the $(j, i) = (1, 2)$ and $(j, i) = (2, 1)$ cases of (B.11) results in the equality

$$(\mu^2_{N,(1)} - \mu^2_{N,(2)})\upsilon^T_{N,(2)}A\upsilon_{N,(1)} + \kappa(\gamma^{(1)}(\lambda_{-2})\upsilon^T_{N,(1)} - \gamma^{(1)}(\lambda_{-1})\upsilon^T_{N,(2)})C\mathbf{f} = 0. \tag{B.12}$$

Similarly, by using the cases $i = 1$ $i = 2$ of (B.10b), multiplied through by $\gamma^{(1)}(\lambda_{-2})$ and $\gamma^{(1)}(\lambda_{-1})$ respectively, and taking their difference, the identity

$$\beta(\mu^4_{N,(1)} - \mu^4_{N,(2)})\gamma^{(1)}(\lambda_{-1})\gamma^{(1)}(\lambda_{-2}) = (\gamma^{(1)}(\lambda_{-2})\upsilon^T_{N,(1)} - \gamma^{(1)}(\lambda_{-1})\upsilon^T_{N,(2)})C\mathbf{f} \tag{B.13}$$

follows. Combining equations (B.12)-(B.13) leads to

$$(\mu^2_{N,(1)} - \mu^2_{N,(2)})\upsilon^T_{N,(2)}A\upsilon_{N,(1)} + \kappa\beta(\mu^4_{N,(1)} - \mu^4_{N,(2)})\gamma^{(1)}(\lambda_{-1})\gamma^{(1)}(\lambda_{-2}) = 0,$$

and dividing through by $(\mu^2_{N,(1)} - \mu^2_{N,(2)})$ produces the required result. All off-diagonals have been accounted for and proof of the diagonality of the matrix $\mathcal{C}^T\mathcal{O}\mathcal{A}\mathcal{C}$ is complete.

B.2.2 Complete ice-cover

During our analysis of the scattering matrix, S, made in §4.4, it was stated that

$$\left[\mathcal{I}^T\Lambda\mathcal{C}^T\mathcal{O}\mathcal{A}\mathcal{C}\mathcal{I}\right]_{x=0_-}\mathfrak{b}_-\mathcal{L}_+(0) = \left[\mathcal{I}^T\Lambda\mathcal{C}^T\mathcal{O}\mathcal{A}\mathcal{C}\mathcal{I}\right]_{x=l_+}\mathfrak{b}_+\mathcal{L}_-(l), \tag{B.14}$$

where the linearly independent functions $\mathcal{L}_\pm$ are those used to calculate the MMA in the case of complete ice-cover. Recall that the operator

$$\mathfrak{b}_\pm\mathbf{v}(x) \equiv \mathcal{I}_1^T\mathcal{C}^{-1}(x_\pm)\mathcal{M}(x_\pm)\mathcal{V}^{-T}(x_\pm)\mathcal{V}^T(x_\mp)\mathcal{M}^{-1}(x_\mp)\mathbf{v}(x_\mp),$$

is a scalar quantity. We now wish to prove the statement (B.14).

Both $\mathcal{L}_\pm$ satisfy the differential equations (4.4) over the interval of varying geometry $(0, l)$. Additionally, these functions satisfy the boundary conditions

$$\left[\mathcal{V}^{-1}\{\mathcal{A}\mathcal{M}\partial_x\mathcal{L}_- + \widehat{\mathcal{Q}}_-\mathcal{L}_-\}\right]_{x=0_+} = (\mathcal{V}^{-1}\mathcal{A}\mathcal{M}\mathcal{C}\Lambda)^{(-)}\mathcal{I}_1, \tag{B.15a}$$

$$\left[\mathcal{V}^{-1}\{\mathcal{A}\mathcal{M}\partial_x\mathcal{L}_+ + \widehat{\mathcal{Q}}_-\mathcal{L}_+\}\right]_{x=0_+} = \mathbf{0}, \tag{B.15b}$$

$$\left[\mathcal{V}^{-1}\{\mathcal{A}\mathcal{M}\partial_x\mathcal{L}_- + \widehat{\mathcal{Q}}_+\mathcal{L}_-\}\right]_{x=l_-} = \mathbf{0}, \tag{B.15c}$$

and

$$\Big[\mathcal{V}^{-1}\{\mathcal{A}\mathcal{M}\partial_x\mathcal{L}_+ + \widehat{\mathcal{Q}}_+\mathcal{L}_+\}\Big]_{x=l_-} = -(\mathcal{V}^{-1}\mathcal{A}\mathcal{M}\mathcal{C}\Lambda)^{(+)}\mathcal{I}_1, \tag{B.15d}$$

which were originally defined in equations (4.38a-b). We will make use of the commutative properties

$$\mathcal{O}\mathcal{A} = \mathcal{A}\mathcal{O}, \quad \mathcal{O}\mathcal{Q} = \mathcal{Q}\mathcal{O}, \quad \mathcal{O}\mathcal{V} = \mathcal{V}\mathcal{O}, \tag{B.16a}$$

of the matrix $\mathcal{O}$, and also its 'near-commutative' properties

$$\mathcal{O}\mathcal{M} = \mathcal{M}^T\mathcal{O}, \quad \mathcal{O}\mathcal{N} = \mathcal{N}^T\mathcal{O}, \tag{B.16b}$$

all of which are easily established. We will also make use of the fact that the matrices $\mathcal{M}$ and $\mathcal{N}$ commute with $\mathcal{A}$, $\mathcal{Q}$ and $\mathcal{V}$.

As the functions $\mathcal{L}_\pm$ are solutions of the differential system (4.4) we may take $(\boldsymbol{\Psi}_{(1)}, \boldsymbol{\Psi}_{(2)}) = (\mathcal{L}_-, \mathcal{L}_+)$ and the interval $(x_0, x_1) = (0, l)$ in (B.5), so that

$$\Big[\mathcal{L}_+^T\mathcal{O}\mathcal{A}(\partial_x\mathcal{L}_-) - (\partial_x\mathcal{L}_+)^T\mathcal{O}\mathcal{A}\mathcal{L}_- + \mathcal{L}_+^T\widetilde{\mathcal{D}}\mathcal{L}_-\Big]_{x=0_+}^{l_-} = 0. \tag{B.17}$$

Consider the contribution to (B.17) from the boundary $x = 0_+$. Firstly, we may remove the derivatives via the boundary conditions (B.15a-b), with

$$\mathcal{L}_+^T(0)\mathcal{O}\mathcal{A}_\uparrow(\partial_x\mathcal{L}_-(0)) = \mathcal{L}_+^T(0)\mathcal{O}\left(-\mathcal{M}_\uparrow^{-1}\widehat{\mathcal{Q}}_-\mathcal{L}_-(0) + \mathcal{M}_\uparrow^{-1}\mathcal{A}_\uparrow^{-1}\mathcal{V}_\uparrow\mathcal{V}_\downarrow^{-1}\mathcal{A}_\downarrow\mathcal{M}_\downarrow\mathcal{C}_\downarrow\Lambda_\downarrow\mathcal{I}_1\right)$$

and

$$(\partial_x\mathcal{L}_+(0))^T\mathcal{O}\mathcal{A}\mathcal{L}_-(0) = -\mathcal{L}_+(0)^T\widehat{\mathcal{Q}}_-^T\mathcal{M}_\uparrow^{-T}\mathcal{O}\mathcal{L}_-(0),$$

where the subscript ↑ denotes evaluation of the quantity at 0_+ and likewise the subscript ↓ denotes evaluation of the quantity at 0_-. From equations (4.36a-b), we have the matrix $\widehat{\mathcal{Q}}_-$ defined as

$$\widehat{\mathcal{Q}}_- \;=\; \mathcal{Q}_\uparrow\mathcal{N}_\uparrow + \mathrm{i}\widetilde{\mathcal{Q}}_- \tag{B.19}$$

where

$$\widetilde{\mathcal{Q}}_- = \mathcal{V}_\uparrow\mathcal{V}_\downarrow^{-1}\mathcal{A}_\downarrow\mathcal{M}_\downarrow\mathcal{C}_\downarrow\Lambda_\downarrow\mathcal{F}\mathcal{C}_\downarrow^{-1}\mathcal{M}_\downarrow\mathcal{V}_\downarrow^{-T}\mathcal{V}_\uparrow^T\mathcal{M}_\uparrow^{-1},$$

We will now split the matrices $\mathcal{O}\mathcal{M}_\uparrow^{-1}\widehat{\mathcal{Q}}_-$ and $\widehat{\mathcal{Q}}_-^T\mathcal{M}_\uparrow^{-T}\mathcal{O}$ in terms of (B.19) and evaluate the their components. From the commutative relationships (B.16a-b), we find that

$$\mathcal{N}_\uparrow^T\mathcal{Q}_\uparrow^T\mathcal{M}_\uparrow^{-T}\mathcal{O} = \mathcal{O}\mathcal{M}_\uparrow^{-1}\mathcal{Q}_\uparrow^T\mathcal{N}_\uparrow,$$

so that

$$\mathcal{O}\mathcal{M}_\uparrow^{-1}\mathcal{Q}_\uparrow\mathcal{N}_\uparrow - \mathcal{N}_\uparrow^T\mathcal{Q}_\uparrow^T\mathcal{M}_\uparrow^{-T}\mathcal{O} = \widetilde{D}, \tag{B.20}$$

where we have again used the equality $Q - Q^T = \widetilde{D}$ and additionally $\mathcal{O}\widetilde{\mathcal{D}} = \widetilde{\mathcal{D}}$. For the second term, which includes the matrix $\widetilde{\mathcal{Q}}_-$ defined in (B.20), we find that

$$\begin{aligned}
& \mathcal{M}_\uparrow^{-T}\mathcal{V}_\uparrow\mathcal{V}_\downarrow^{-1}\mathcal{M}_\downarrow^{T}\mathcal{C}_\downarrow^{-T}\mathcal{F}\Lambda_\downarrow\mathcal{C}_\downarrow^{T}\mathcal{M}_\downarrow^{T}\mathcal{A}_\downarrow\mathcal{V}_\downarrow^{-T}\mathcal{V}_\uparrow^{T}\mathcal{M}_\uparrow^{-T}\mathcal{O} \\
= \; & \mathcal{M}_\uparrow^{-T}\mathcal{V}_\uparrow\mathcal{V}_\downarrow^{-1}\mathcal{M}_\downarrow^{T}\mathcal{C}_\downarrow^{-T}\mathcal{F}\Lambda_\downarrow\mathcal{C}_\downarrow^{T}\mathcal{O}\mathcal{A}_\downarrow\mathcal{C}_\downarrow\mathcal{C}_\downarrow^{-1}\mathcal{M}_\downarrow\mathcal{V}_\downarrow^{-1}\mathcal{V}_\uparrow\mathcal{M}_\uparrow^{-1} \\
= \; & \mathcal{M}_\uparrow^{-T}\mathcal{V}_\uparrow\mathcal{V}_\downarrow^{-1}\mathcal{M}_\downarrow^{T}\mathcal{C}_\downarrow^{-T}\mathcal{C}_\downarrow^{T}\mathcal{O}\mathcal{A}_\downarrow\mathcal{C}_\downarrow\mathcal{F}\Lambda_\downarrow\mathcal{C}_\downarrow^{-1}\mathcal{M}_\downarrow\mathcal{V}_\downarrow^{-1}\mathcal{V}_\uparrow\mathcal{M}_\uparrow^{-1} \\
= \; & \mathcal{O}\mathcal{M}_\uparrow^{-1}\mathcal{V}_\uparrow\mathcal{V}_\downarrow^{-1}\mathcal{A}_\downarrow\mathcal{M}_\downarrow\mathcal{C}_\downarrow\Lambda_\downarrow\mathcal{F}\mathcal{C}_\downarrow^{-1}\mathcal{M}_\downarrow\mathcal{V}_\downarrow^{-1}\mathcal{V}_\uparrow\mathcal{M}_\uparrow^{-1}.
\end{aligned}$$

Here we have again used (B.16a-b), as well as the diagonality of the matrix $\Lambda\mathcal{C}^T\mathcal{O}\mathcal{A}\mathcal{C}$. It follows that

$$\mathcal{O}\mathcal{M}_\uparrow^{-1}\widetilde{\mathcal{Q}}_- - \widetilde{\mathcal{Q}}_-^T\mathcal{M}_\uparrow^{-T}\mathcal{O} = 0. \tag{B.21}$$

Applying (B.20) and (B.21) to the contribution from the lower boundary in (B.17) gives

$$\begin{aligned}
& \Big[\mathcal{L}_+^T\mathcal{O}\mathcal{A}(\partial_x\mathcal{L}_-) - (\partial_x\mathcal{L}_+)^T\mathcal{O}\mathcal{A}\mathcal{L}_- + \mathcal{L}_+^T\widetilde{\mathcal{D}}\mathcal{L}_-\Big]_{x=0_+} \\
= \; & \mathcal{L}_+^T(0)\mathcal{O}\mathcal{M}_\uparrow^{-1}\mathcal{A}_\uparrow^{-1}\mathcal{V}_\uparrow\mathcal{V}_\downarrow^{-1}\mathcal{A}_\downarrow\mathcal{M}_\downarrow\mathcal{C}_\downarrow\Lambda_\downarrow\mathcal{I}_1 \\
= \; & \mathcal{I}_1^T\Lambda_\downarrow\mathcal{C}_\downarrow^T\mathcal{O}\mathcal{A}_\downarrow\mathcal{C}_\downarrow\mathcal{C}_\downarrow^{-1}\mathcal{M}_\downarrow\mathcal{V}_\downarrow^{-T}\mathcal{V}_\uparrow^T\mathcal{A}_\uparrow^{-1}\mathcal{M}_\uparrow^{-1}\mathcal{L}_+(0) \\
= \; & \big[\mathcal{I}_1^T\Lambda\mathcal{C}^T\mathcal{O}\mathcal{A}\mathcal{C}\mathcal{I}_1\big]_{x=0_-}\,\mathfrak{b}_-\mathcal{L}_+(0).
\end{aligned}$$

Here, we have again used the diagonality of the matrix $\mathcal{C}^T\mathcal{O}\mathcal{A}\mathcal{C}$.

Similarly, evaluating the contribution to (B.17) from $x = l_-$, we find that

$$\Big[\mathcal{L}_+^T\mathcal{O}\mathcal{A}(\partial_x\mathcal{L}_-) - (\partial_x\mathcal{L}_+)^T\mathcal{O}\mathcal{A}\mathcal{L}_- + \mathcal{L}_+^T\widetilde{\mathcal{D}}\mathcal{L}_-\Big]_{x=l_-} = \big[\mathcal{I}_1^T\Lambda\mathcal{C}^T\mathcal{O}\mathcal{A}\mathcal{C}\mathcal{I}_1\big]_{x=l_+}\,\mathfrak{b}_+\mathcal{L}_-(l).$$

The net result from these manipulations to (B.17) is the identity

$$\big[\mathcal{I}_1^T\Lambda\mathcal{C}^T\mathcal{O}\mathcal{A}\mathcal{C}\mathcal{I}_1\big]_{x=0_-}\,\mathfrak{b}_-\mathcal{L}_+(0) = \big[\mathcal{I}_1^T\Lambda\mathcal{C}^T\mathcal{O}\mathcal{A}\mathcal{C}\mathcal{I}_1\big]_{x=l_+}\,\mathfrak{b}_+\mathcal{L}_-(l),$$

which we were seeking.

B.2.3 Partial ice-cover

The analogous identity to (B.14) in the case of a finite ice floe is

$$\big[\mathbf{I}^T\Lambda A\mathbf{I}\big]_{x=0_-}\,\mathfrak{b}_-\mathcal{L}_+(0) = \big[\mathbf{I}^T\Lambda A\mathbf{I}\big]_{x=l_+}\,\mathfrak{b}_+\mathcal{L}_-(l).$$

The functionals are here defined as

$$\mathfrak{b}_\pm\mathbf{v}(x) \equiv \mathcal{I}_1^T\mathcal{V}^{-T}(x_\pm)\mathcal{V}^T(x_\mp)\widetilde{\mathcal{F}}\mathbf{v}(x_\mp).$$

The linearly independent solutions, $\mathcal{L}_\pm$, of the differential system (4.4) satisfy the boundary conditions (4.43a-b). For the purposes of this section, let

$$\mathcal{L}_\pm = \left(\mathbf{L}_\pm^T, \chi_\pm^{(1)}, \chi_\pm^{(2)}\right)^T,$$

where the vectors $\mathbf{L}_\pm$ satisfy the boundary conditions

$$\left[V^{-1}(A(\partial_x \mathbf{L}_-) + \widehat{Q}_- \mathbf{L}_-)\right]_{x=0_+} = (V^{-1}A\Lambda)^{(-)}\mathbf{I}_1,$$

$$\left[V^{-1}(A(\partial_x \mathbf{L}_+) + \widehat{Q}_- \mathbf{L}_+)\right]_{x=0_+} = \mathbf{0},$$

$$\left[V^{-1}(A(\partial_x \mathbf{L}_-) + \widehat{Q}_+ \mathbf{L}_-)\right]_{x=l_-} = \mathbf{0},$$

and

$$\left[V^{-1}(A(\partial_x \mathbf{L}_-) + \widehat{Q}_+ \mathbf{L}_-)\right]_{x=l_-} = -(V^{-1}A\Lambda)^{(+)}\mathcal{I}_1,$$

where the matrices

$$\widehat{Q}_\pm(x) = Q(x_\mp) \pm \mathrm{i}V(x_\mp)V^{-1}(x_\pm)A(x_\pm)\Lambda(x_\pm)FV^{-T}(x_\pm)V^T(x_\mp),$$

and $F = \mathrm{diag}\{0, 1, \dots, 1\}$ is a square matrix of dimension $(N+1)$.

The functions $\chi_\pm^{(j)}$ $(j = 1, 2)$ satisfy the no bending moment and shearing stress conditions, here written as

$$\chi_\pm^{(2)} + u(x)\chi_\pm^{(1)} = 0, \quad \partial_x\chi_\pm^{(2)} - u(x)\partial_x\chi_\pm^{(1)} + v(x)\chi_\pm^{(1)} = 0, \tag{B.23}$$

where $u(x) = \beta(x)(1-\nu)q^2$ and $v(x) = (\partial_x\beta(x))(1-\nu)q^2$.

It is more convenient in this case to use the energy balance in the form given in equation (B.3), so that

$$\begin{aligned}\big[\mathbf{L}_+^T A(\partial_x \mathbf{L}_-) - (\partial_x \mathbf{L}_+)^T A \mathbf{L}_- + \mathbf{L}_+^T \widetilde{D} \mathbf{L}_- \\ -\kappa\{\chi_+^{(1)}(\partial_x\chi_-^{(2)}) - \chi_-^{(1)}(\partial_x\chi_+^{(2)}) + \chi_+^{(2)}(\partial_x\chi_-^{(1)}) - \chi_-^{(2)}(\partial_x\chi_+^{(1)})\}\big]_{x=0_+}^{l_-} &= 0.\end{aligned} \tag{B.24}$$

Closely following the case of complete ice-cover, we have

$$\mathbf{L}_+^T(0)A_\uparrow(\partial_x \mathbf{L}_-(0)) = \mathbf{L}_+^T(0)\left(-\widehat{Q}\mathbf{L}_-(0) + V_\uparrow V_\downarrow^{-1}A_\downarrow\Lambda_\downarrow\mathbf{I}_1\right),$$

and

$$\begin{aligned}(\partial_x \mathbf{L}_+)^T A \mathbf{L}_- &= -(\widehat{Q}\mathbf{L}_-(0))^T \mathbf{L}_- \\ &= -\mathbf{L}_-(0)^T \widehat{Q}^T \mathbf{L}_-.\end{aligned}$$

We note that

$$\begin{aligned}\widehat{Q}_-^T &= (Q_\uparrow \pm \mathrm{i}V_\uparrow V_\downarrow^{-1} A_\downarrow \Lambda_\downarrow F V_\downarrow^{-T} V_\uparrow^T)^T \\ &= Q_\uparrow \pm \mathrm{i}V_\uparrow V_\downarrow^{-1} F \Lambda_\downarrow A_\downarrow^T V_\downarrow^{-T} V_\uparrow^T \\ &= Q_\uparrow^T \pm \mathrm{i}V_\uparrow V_\downarrow^{-1} A_\downarrow \Lambda_\downarrow F V_\downarrow^{-T} V_\uparrow^T.\end{aligned}$$

which uses the diagonality of $A_\downarrow$. This is a consequence of the orthogonality of the natural modes in ice-free intervals. We therefore have

$$\begin{aligned}\left[\mathbf{L}_+^T A(\partial_x \mathbf{L}_-) - (\partial_x \mathbf{L}_+)^T A \mathbf{L}_- + \mathbf{L}_+^T \widetilde{D} \mathbf{L}_-\right]_{x=0_+} &= \mathbf{L}_+^T(0) V_\uparrow V_\downarrow^{-1} A_\downarrow \Lambda_\downarrow \mathbf{I}_1 \\ &= \mathbf{I}_1^T \Lambda_\downarrow A_\downarrow \mathbf{I}_1 \mathbf{I}_1^T V_\downarrow^{-T} V_\uparrow^T \mathbf{L}_+(0) \qquad \text{(B.25a)} \\ &= \left[\mathbf{I}_1^T \Lambda A \mathbf{I}_1\right]_{x=0_-} \mathfrak{b}_- \mathbf{L}_+(0).\end{aligned}$$

Similarly,

$$\left[\mathbf{L}_+^T A(\partial_x \mathbf{L}_-) - (\partial_x \mathbf{L}_+)^T A \mathbf{L}_- + \mathbf{L}_+^T \widetilde{D} \mathbf{L}_-\right]_{x=l_-} = \left[\mathbf{I}_1^T \Lambda A \mathbf{I}_1\right]_{x=l_+} \mathfrak{b}_+ \mathbf{L}_-(l). \qquad \text{(B.25b)}$$

It remains to consider the terms including the functions $\chi_\pm^{(j)}$ $(j = 1, 2)$, namely

$$\left[\chi_+^{(1)}(\partial_x \chi_-^{(2)}) - \chi_-^{(1)}(\partial_x \chi_+^{(2)}) + \chi_+^{(2)}(\partial_x \chi_-^{(1)}) - \chi_-^{(2)}(\partial_x \chi_+^{(1)})\right]_{x=0_+}^{l_-}.$$

Consider the lower boundary $x = 0_+$, we substitute the functions $\chi_\pm^{(2)}$ for $\chi_\pm^{(1)}$ via the conditions (B.23) to give

$$\begin{aligned}&\left[\chi_+^{(1)}(\partial_x \chi_-^{(2)}) - \chi_-^{(1)}(\partial_x \chi_+^{(2)}) + \chi_+^{(2)}(\partial_x \chi_-^{(1)}) - \chi_-^{(2)}(\partial_x \chi_+^{(1)})\right]_{x=0_+} \\ =\;& \left[\chi_+^{(1)}(u\partial_x \chi_-^{(1)} - v\chi_-^{(1)}) - \chi_-^{(1)}(u\partial_x \chi_+^{(1)} - v\chi_+^{(1)}) - u\chi_+^{(1)}(\partial_x \chi_-^{(1)}) + u\chi_-^{(1)}(\partial_x \chi_+^{(1)})\right]_{x=0_+} \\ =\;& 0.\end{aligned} \qquad \text{(B.26a)}$$

Following an identical method at the upper limit $x = l_-$ gives

$$\left[\chi_+^{(1)}(\partial_x \chi_-^{(2)}) - \chi_-^{(1)}(\partial_x \chi_+^{(2)}) + \chi_+^{(2)}(\partial_x \chi_-^{(1)}) - \chi_-^{(2)}(\partial_x \chi_+^{(1)})\right]_{x=l_-} = 0. \qquad \text{(B.26b)}$$

Inserting equalities (B.25a-b) and (B.26a-b) into the energy balance (B.24) produces the required result (B.14).

B.2.4 The periodic problem

In the periodic problem we define the MMA in equation (8.3) for the mth period in terms of two matrices, $\mathcal{L}_{\pm,(m)}$, whose columns are linearly independent solutions of the differential system (4.4). We need only consider the first period ($m = 1$) and let

$$\mathcal{L}_{\pm,(0)} = \left[\xi_{\pm,(1)}, \ldots, \xi_{\pm,(N+3)}\right].$$

We may therefore express the boundary conditions for $\mathcal{L}_{\pm,(0)}$, which were defined in (8.5a-b), as

$$\left[\mathcal{V}^{-1}\{\mathcal{A}\mathcal{M}\partial_x\xi_{-,(i)} + (\mathcal{Q}\mathcal{N}\xi_{-,(i)}\}\right]_{x=0_+} = \left[\mathcal{V}^{-1}\mathcal{A}\mathcal{M}\mathcal{C}\Lambda\mathbf{I}_i\right]_{x=0_-},$$

$$\left[\mathcal{V}^{-1}\{\mathcal{A}\mathcal{M}\partial_x\xi_{+,(i)} + (\mathcal{Q}\mathcal{N}\xi_{+,(i)}\}\right]_{x=0_+} = \mathbf{0},$$

$$\left[\mathcal{V}^{-1}\{\mathcal{A}\mathcal{M}(\partial_x\xi_{-,(i)}) + (\mathcal{Q}\mathcal{N}\xi_{-,(i)}\}\right]_{x=l_{0-}} = \mathbf{0},$$

and

$$\left[\mathcal{V}^{-1}\{\mathcal{A}\mathcal{M}\partial_x\xi_{+,(i)} + (\mathcal{Q}\mathcal{N}\xi_{+,(i)}\}\right]_{x=l_{0-}} = \left[\mathcal{V}^{-1}\mathcal{A}\mathcal{M}\mathcal{C}\Lambda\mathbf{I}_i\right]_{x=l_{0+}}$$

for $i = 1, \ldots, N+3$.

We wish to prove the identities (8.15a-c). To do so, we use the energy balance (B.5) with $(\mathbf{\Psi}_{(0)}, \mathbf{\Psi}_{(1)})$ equal to the pairs $(\xi_{-,(i)}, \xi_{-,(j)})$, $(\xi_{+,(i)}, \xi_{+,(j)})$ and $(\xi_{+,(i)}, \xi_{-,(j)})$ for $(i, j = 1, \ldots, N+3)$. Noting the symmetry that

$$\left(\xi^T_{\pm,(i)}\mathcal{O}\mathcal{A}\xi_{\pm,(j)}\right)^T = \xi^T_{\pm,(j)}\mathcal{O}\mathcal{A}\xi_{\pm,(i)} \quad (i, j = 1, \ldots, N+3),$$

then we find that all of the calculations required for manipulation of the energy balance with the above three combinations of functions in order to produce the required results are given by

$$\left[\xi^T_{\pm,(i)}\mathcal{O}\mathcal{A}(\partial_x\xi_{+,(j)})\right]_{x=0_+} = -\left[\xi^T_{\pm,(i)}\mathcal{O}\mathcal{M}^{-1}\mathcal{Q}\mathcal{N}(\partial_x\xi_{+,(j)})\right]_{x=0_+}, \tag{B.28a}$$

$$\begin{aligned}\left[\xi^T_{\pm,(i)}\mathcal{O}\mathcal{A}(\partial_x\xi_{-,(j)})\right]_{x=0_+} &= -\left[\xi^T_{\pm,(i)}\mathcal{O}\mathcal{M}^{-1}\mathcal{Q}\mathcal{N}(\partial_x\xi_{-,(j)})\right]_{x=0_-} \\ &\quad + \left[\mathcal{I}_j\Lambda_\downarrow\mathcal{C}^T_\downarrow\mathcal{M}_\downarrow\mathcal{A}_\downarrow\mathcal{V}^{-T}_\downarrow\mathcal{V}^T_\uparrow\mathcal{M}^{-T}_\uparrow\mathcal{O}\xi_{\pm,(i)}\right]_{x=0},\end{aligned} \tag{B.28b}$$

$$\begin{aligned}\left[\xi^T_{\pm,(i)}\mathcal{O}\mathcal{A}(\partial_x\xi_{+,(j)})\right]_{x=l_-} &= -\left[\xi^T_{\pm,(i)}\mathcal{O}\mathcal{M}^{-1}\mathcal{Q}\mathcal{N}(\partial_x\xi_{-,(j)})\right]_{x=l_+} \\ &\quad - \left[\mathcal{I}_j\Lambda_\uparrow\mathcal{C}^T_\uparrow\mathcal{M}_\uparrow\mathcal{A}_\uparrow\mathcal{V}^{-T}_\uparrow\mathcal{V}^T_\downarrow\mathcal{M}^{-T}_\downarrow\mathcal{O}\xi_{\pm,(i)}\right]_{x=l},\end{aligned} \tag{B.28c}$$

and

$$\left[\xi^T_{\pm,(i)}\mathcal{O}\mathcal{A}(\partial_x\xi_{-,(j)})\right]_{x=l_-} = -\left[\xi^T_{\pm,(i)}\mathcal{O}\mathcal{M}^{-1}\mathcal{Q}\mathcal{N}(\partial_x\xi_{+,(j)})\right]_{x=l_+}, \tag{B.28d}$$

where the subscripts ↑ and ↓ are used to denote evaluation from the upper and lower limits respectively. Using equalities (B.28a-d) in the energy balance (B.5) for the three cases $(\mathbf{\Psi}_{(0)}, \mathbf{\Psi}_{(1)}) = (\xi_{-,(i)}, \xi_{-,(j)})$, $(\xi_{+,(i)}, \xi_{+,(j)})$ and $(\xi_{+,(i)}, \xi_{-,(j)})$, and again using $Q - Q^T = \widetilde{D}$

and $\mathcal{O}\widetilde{\mathcal{D}} = \widetilde{\mathcal{D}}$, leads to

$$\left[\mathcal{I}_j \Lambda_\downarrow \mathcal{C}_\downarrow^T \mathcal{M}_\downarrow \mathcal{A}_\downarrow \mathcal{V}_\downarrow^{-T} \mathcal{V}_\uparrow^T \mathcal{M}_\uparrow^{-T} \mathcal{O} \xi_{+,(i)}\right]_{x=0} = \left[\mathcal{I}_i \Lambda_\downarrow \mathcal{C}_\downarrow^T \mathcal{M}_\downarrow \mathcal{A}_\downarrow \mathcal{V}_\downarrow^{-T} \mathcal{V}_\uparrow^T \mathcal{M}_\uparrow^{-T} \mathcal{O} \xi_{+,(j)}\right]_{x=0}, \tag{B.29a}$$

$$\left[\mathcal{I}_j \Lambda_\downarrow \mathcal{C}_\downarrow^T \mathcal{M}_\downarrow \mathcal{A}_\downarrow \mathcal{V}_\downarrow^{-T} \mathcal{V}_\uparrow^T \mathcal{M}_\uparrow^{-T} \mathcal{O} \xi_{-,(i)}\right]_{x=l} = \left[\mathcal{I}_i \Lambda_\downarrow \mathcal{C}_\downarrow^T \mathcal{M}_\downarrow \mathcal{A}_\downarrow \mathcal{V}_\downarrow^{-T} \mathcal{V}_\uparrow^T \mathcal{M}_\uparrow^{-T} \mathcal{O} \xi_{-,(j)}\right]_{x=l}, \tag{B.29b}$$

and

$$\left[\mathcal{I}_j \Lambda_\downarrow \mathcal{C}_\downarrow^T \mathcal{M}_\downarrow \mathcal{A}_\downarrow \mathcal{V}_\downarrow^{-T} \mathcal{V}_\uparrow^T \mathcal{M}_\uparrow^{-T} \mathcal{O} \xi_{+,(i)}\right]_{x=0} = \left[\mathcal{I}_i \Lambda_\downarrow \mathcal{C}_\downarrow^T \mathcal{M}_\downarrow \mathcal{A}_\downarrow \mathcal{V}_\downarrow^{-T} \mathcal{V}_\uparrow^T \mathcal{M}_\uparrow^{-T} \mathcal{O} \xi_{-,(j)}\right]_{x=l}, \tag{B.29c}$$

for $i, j = 1, \ldots, N+3$. The final results (8.15a-c) then follow straightforwardly by collecting the combinations of i and j to form the matrix versions of (B.29a-c)

$$\mathfrak{Q}_0(0_+)\mathcal{L}_{+,(0)}(0) = \left(\mathfrak{Q}_0(0_+)\mathcal{L}_{+,(0)}(0)\right)^T,$$

$$\mathfrak{Q}_0(l_{0-})\mathcal{L}_{-,(0)}(l_0) = \left(\mathfrak{Q}_0(l_{0-})\mathcal{L}_{-,(0)}(l_0)\right)^T,$$

and

$$\mathfrak{Q}_0(0_+)\mathcal{L}_{+,(0)}(0) = \left(\mathfrak{Q}_0(l_{0-})\mathcal{L}_{-,(0)}(l_0)\right)^T,$$

where

$$\mathfrak{Q}_0(x_\pm) = \Lambda(x_\mp)\mathcal{C}^T(x_\mp)\mathcal{M}(x_\mp)\mathcal{A}(x_\mp)\mathcal{V}^{-T}(x_\mp)\mathcal{V}^T(x_\pm)\mathcal{M}^{-T}(x_\pm)\mathcal{O}.$$

Through use of the energy balance that was derived in the first section of this Appendix, in §B.2 we have been able to deduce a set of identities, which involve the linearly independent functions that must be calculated over intervals of varing geometry in two-dimensional problems in order to obtain the MMA. These identities enable us to obtain relations between the scattering coefficients, which appear in the main text.

Appendix C

A circular uniform floe

During our investigation of the circular floe of uniform thickness and zero draught forced by a plane wave, we produced expressions for the single-mode approximation that hold under certain circumstances. These approximations were given in §10; however, many of the details of the calculations were suppressed for presentational purposes. Here, we will provide those details.

C.1 The régime $kH \ll \sinh(kH)$

We assumed that the bed was sufficiently deep in relation to the length of the incident wave that the régime $kH \ll \sinh(kH)$ would apply. This was then used to write the complex wavenumbers $\mu_{(j)}$ $(j = 1, 2)$ and the corresponding weights, $\upsilon_{(j)}$ $(j = 1, 2)$, in terms of terms of the propagating wavenumber beneath the ice, namely k.

For the single-mode approximation the complex wavenumbers, $\mu_{(j)}$ $(j = 1, 2)$, are defined by the quartic equation

$$c_4\mu_{(j)}^4 + c_2\mu_{(j)}^2 + c_0 = 0,$$

where

$$c_0 = k^3 \sinh(kH)\cosh(kH) + a\frac{1-\kappa\alpha}{\beta},$$

$$c_2 = k\sinh(kH)\cosh(kH),$$

$$c_4 = a = \frac{\sinh(kH)\cosh(kH) + kH}{2k}.$$

This quartic may be solved straightforwardly for the squared quantities $\mu_{(j)}^2$, and we have that

$$\mu_{(j)}^2 = -\frac{c_2}{2c_4} - (-1)^j \mathrm{i}\left(\frac{4c_0c_4 - c_2^2}{4c_4^2}\right)^{1/2}.$$

Taking the two terms that appear in the above expression separately, we apply $kH \ll$

$\sinh(kH)$, so that we may treat $\cosh(kH)$ and $\sinh(kH)$ as being identical and eliminate the terms that do not involve these hyperbolic functions, to give

$$\begin{aligned}\frac{c_2}{2c_4} &= \frac{k^2\sinh(kH)\cosh(kH)}{\sinh(kH)\cosh(kH)+kH}\\ &\approx k^2,\end{aligned}$$

and

$$\begin{aligned}\frac{4c_0c_4-c_2^2}{4c_4^2} &= \frac{k^4\sinh(kH)\cosh(kH)(\sinh(kH)\cosh(kH)+2kH)}{(\sinh(kH)\cosh(kH)+kH)^2}+\frac{1-\kappa\alpha}{\beta}\\ &\approx k^4+\frac{1-\kappa\alpha}{\beta}.\end{aligned}$$

We wish to remove the value κ from the second expression as its value varies with the wavenumber k, and this is achieved by using the dispersion relation (3.13) as follows

$$\begin{aligned}k^4+\frac{1-\kappa\alpha}{\beta} &= \kappa\frac{\cosh(kH)}{\beta k\sinh(kH)}\\ &= \frac{(1+\beta k^4)\cosh(kH)}{\beta(\cosh(kH)+\alpha k\sinh(kH))}\\ &\approx \frac{1+\beta k^4}{\beta(1+\alpha k)}.\end{aligned}$$

Therefore, we have the approximation

$$\mu_{(j)}^2 \approx -k^2-(-1)^j\mathrm{i}\left(\frac{1+\beta k^4}{\beta(1+\alpha k)}\right)^{1/2}, \tag{C.2}$$

for $kH \ll \sinh(kH)$. If additionally the parameters are such that $1 \gg \alpha k$ and $1 \ll \beta k^4$, then we have the simplification

$$\frac{1+\beta k^4}{\beta(1+\alpha k)} \approx k^4,$$

whence

$$\mu_{(j)}^2 \approx -(1+(-1)^j\mathrm{i})k^2. \tag{C.3}$$

Therefore, the complex wavenumbers are approximated by

$$\mu_{(1)} \approx 2^{1/4}k\mathrm{e}^{\mathrm{i}3\pi/8}, \quad \mu_{(2)} \approx 2^{1/4}k\mathrm{e}^{\mathrm{i}5\pi/8}, \tag{C.4}$$

when the régimes $kH \ll \sinh(kH)$, $1 \gg \alpha k$ and $1 \ll \beta k^4$ hold. For the parameters given in §2.1 these régimes translate to

$$kD \ll 1.11, \quad k^4D^3 \gg 2.20\times 10^{-5},$$

which imposes some bounds on the value of the wavenumber, k, relative to the ice thickness D. With the geometries and wave periods that we commonly use these conditions are usually satisfied, for instance, if $D = 1$m and $H = 20$m, then for a wave period of $\tau = 2.5$secs

$$kD = 1.06 \times 10^{-1} \ll 1.11, \quad k^4 D^3 = 1.28 \times 10^{-4} \gg 2.20 \times 10^{-5},$$

and the conditions are met.

We note that the approximate values of the complex wavenumbers (C.2) are determined by the propagating wavenumber and the geometrical parameters α and β. Furthermore, the simplified approximation (C.4) is in terms of the propagating wavenumber only. In both cases the complex wavenumbers form a symmetric pair, $\mu_{(1)} = -\overline{\mu}_{(2)}$, and have a magnitude which is of the order of the propagating wavenumber.

We now turn to the weights, $\upsilon_{(j)}$ ($j = 1, 2$), of the complex waves. As we deal primarily with the displacement function, it is pertinent to consider the scaled quantities $\hat{\upsilon}_{(j)} = \upsilon_{(j)} k \sinh(kH)/\gamma(\mu_{(j)})\kappa$. Using the definition of $\upsilon_{(j)}$, which is given in equation (10.2) we have that

$$\begin{aligned} \hat{\upsilon}_{(j)} &= -\frac{2\beta k^2 \sinh(kH)(k^2 + \mu_{(j)}^2)}{\sinh(kH)\cosh(kH) + kH} \times \frac{k \sinh(kH)}{\kappa} \\ &= -\frac{2\beta k^2 \sinh(kH)(k^2 + \mu_{(j)}^2)}{\sinh(kH)\cosh(kH) + kH} \times \frac{\cosh(kH) + \alpha k \sinh(kH)}{1 + \beta k^4} \\ &\approx -\frac{2(1 + \alpha k)\beta k^2 (k^2 + \mu_{(j)}^2)}{1 + \beta k^4}, \end{aligned} \tag{C.5}$$

which holds if $kH \ll \sinh(kH)$. The quantity $\gamma(\mu_{(j)})$ is arbitrary and is usually set as in equation (4.21); however, its value will not have a bearing on the final approximations. If the additional conditions $1 \gg \alpha k$ and $1 \ll \beta k^4$ hold, then using the relevant approximation of the complex wavenumbers (C.3), we deduce that

$$k^2 + \mu_{(j)}^2 \approx k^2 - (1 + (-1)^j \mathrm{i})k^2 = -(-1)^j \mathrm{i} k^2,$$

and the approximation of the weights (C.5) simplifies to

$$\hat{\upsilon}_{(j)} \approx (-1)^j 2\mathrm{i}. \tag{C.6}$$

Let us assume that the most simple expressions for the wavenumbers, $\mu_{(i)}$ ($i = 1, 2$), and corresponding weights, $\upsilon_{(i)}$, which are given in equations (C.4) and (C.6), hold. Then the single-mode approximation, which is a combination of the functions $\varphi_m(r) \equiv \widetilde{\varphi}_m(r) A_m$

$(m = 0, \ldots, M)$, where

$$\widetilde{\varphi}_m(r) = \mathrm{J}_m(kr) - \sum_{i=1,2} \hat{v}_{(i)} \frac{\triangle_m(kR, \mu_{(i_-)}R)}{\triangle_m(\mu_{(i)}R, \mu_{(i_-)}R)} \mathrm{J}_m(\mu_{(i)}r), \tag{C.7}$$

and $\triangle_m$ is defined in equation (10.6a-b), is therefore dependent on the values of the propagating wavenumber k, the radius of the floe R and the amplitudes A_m.

Each amplitude A_m is dependent on the properties of the ice-covered region and also the region away from the ice, specifically the free-surface wavenumber $k^{(0)}$, and their values are obtained via the condition

$$\left\{ \mathrm{H}_m(k^{(0)}R) \frac{a}{a^{(0)}} \frac{v^{(0)}}{v} \left(\partial_r \widetilde{\varphi}_m(R)\right) - \left(\partial_r \mathrm{H}_m(k^{(0)}R)\right) \frac{v^{(0)}}{v} \widetilde{\varphi}_m(R) \right\} A_m = -\frac{2\mathrm{i}}{\pi R}, \tag{C.8}$$

where we assume the bracketed quantity on the left-hand side is non-vanishing. In the régime $kH \ll \sinh(kH)$ we may make use of the approximations

$$\frac{a}{a^{(0)}} \frac{v^{(0)}}{v} \approx \frac{2k_0^{(0)}}{k + k^{(0)}} \frac{\sinh(kH)}{\sinh(k^{(0)}H)}, \quad \frac{v}{v^{(0)}} \approx \frac{k + k^{(0)}}{2k} \frac{\sinh(kH)}{\sinh(k^{(0)}H)}. \tag{C.9}$$

These were given earlier in the main text in equations (7.8a-b). As discussed in the main text, it is actually the scaled amplitudes

$$\widetilde{A}_m = \frac{\mathrm{I}_0 k \sinh(kH)}{\kappa} A_m \quad (m = 0, \ldots, M),$$

where I_0 is the incident amplitude, that we consider in order to make inferences about the properties of the floe, as these quantities have the correct physical dimension of metres.

The expression (C.7) may be simplified by noting that the symmetry $\mu_{(2)} = -\overline{\mu_{(1)}}$ of the complex wavenumbers leads to the relationship in their corresponding Bessel functions

$$\mathrm{J}_m(\mu_{(2)}r) = (-1)^m \overline{\mathrm{J}_m(\mu_{(1)}r)}, \quad \partial_r \mathrm{J}_m(\mu_{(2)}r) = (-1)^m \overline{\partial_r \mathrm{J}_m(\mu_{(1)}r)}.$$

Furthermore, we then have that the functions $\mathscr{X}_m$ and $\mathscr{Y}_m$ are such that

$$\mathscr{X}_m(\mu_{(2)}r) = (-1)^m \overline{\mathscr{X}_m(\mu_{(1)}r)}, \quad \mathscr{Y}_m(\mu_{(2)}r) = (-1)^m \overline{\mathscr{Y}_m(\mu_{(1)}r)},$$

and this may be used in the definition of the quantities $\triangle_m(kR, \mu_{(i_-)}R)$ and $\triangle_m(\mu_{(i)}R, \mu_{(i_-)}R)$ to show that

$$\triangle_m(kR, \mu_{(2)}R) = (-1)^m \overline{\triangle_m(kR, \mu_{(1)}R)},$$

and

$$\begin{aligned}\triangle_m(\mu_{(1)}R, \mu_{(2)}R) &= (-1)^m \left\{ \mathscr{X}_m(\mu_{(1)}R)\overline{\mathscr{Y}_m(\mu_{(1)}R)} - \overline{\mathscr{X}_m(\mu_{(1)}R)}\mathscr{Y}_m(\mu_{(1)}R) \right\} \\ &= (-1)^m 2\mathrm{i}\Im\mathrm{m}\left(\mathscr{X}_m(\mu_{(1)}R)\overline{\mathscr{Y}_m(\mu_{(1)}R)} \right).\end{aligned}$$

Also noting that the approximate values of the weights, $\hat{v}_{(i)}$ $(i = 1, 2)$, given in equation (C.6), are such that $\hat{v}_{(1)} = \overline{\hat{v}_{(2)}}$, we deduce that

$$\begin{aligned}\sum_{i=1,2} \hat{v}_{(i)} \frac{\triangle_m(kR, \mu_{(i_-)}R)}{\triangle_m(\mu_{(i)}R, \mu_{(i_-)}R)} \mathrm{J}_m(\mu_{(i)}r) &= \frac{(-1)^m \hat{v}_{(1)} \overline{\triangle_m(kR, \mu_{(1)}R)} \mathrm{J}_m(\mu_{(1)}r)}{(-1)^m 2\mathrm{i}\Im\mathrm{m}\left(\mathscr{X}_m(\mu_{(1)}R)\overline{\mathscr{Y}_m(\mu_{(1)}R)} \right)} \\ &\quad - \frac{(-1)^m \overline{\hat{v}}_{(1)} \triangle_m(kR, \mu_{(1)}R) \overline{\mathrm{J}_m(\mu_{(1)}r)}}{(-1)^m 2\mathrm{i}\Im\mathrm{m}\left(\mathscr{X}_m(\mu_{(1)}R)\overline{\mathscr{Y}_m(\mu_{(1)}R)} \right)} \\ &= -\frac{\Im\mathrm{m}\left(\hat{v}_{(1)} \overline{\triangle_m(kR, \mu_{(1)}R)} \mathrm{J}_m(\mu_{(1)}r) \right)}{\Im\mathrm{m}\left(\mathscr{X}_m(\mu_{(1)}R)\overline{\mathscr{Y}_m(\mu_{(1)}R)} \right)}.\end{aligned}$$

The original form of the functions $\widetilde{\varphi}_m$ $(m = 0, \ldots, M)$, given in equation (C.7), may therefore be written as

$$\widetilde{\varphi}_m = \mathrm{J}(kr) - \frac{\Im\mathrm{m}\left(\hat{v}_{(1)} \overline{\triangle_m(kR, \mu_{(1)}R)} \mathrm{J}_m(\mu_{(1)}r) \right)}{\Im\mathrm{m}\left(\mathscr{X}_m(\mu_{(1)}R)\overline{\mathscr{Y}_m(\mu_{(1)}R)} \right)}. \tag{C.10}$$

C.2 The régime $kR \gg 1$

By making assumptions about the relationship between the wavenumbers k and $k^{(0)}$, and the radius R, we may deduce approximations of the amplitudes beneath the ice, $\widetilde{A}_m$, and hence infer certain behaviour about the response of the floe in these circumstances. To begin with we suppose that the radius is large in comparison to the incident wavelength as well as the wavelength beneath the ice, so that $k^{(0)}R \gg 1$ and $kR \gg 1$. As the wavelength beneath the ice is typically greater than in the open water, satisfaction of $kR \gg 1$ is sufficient.

For the régime $kR \gg 1$ we are able to utilise the limits of the Bessel function of the first kind (which are given in Tranter, 1968, for example)

$$\begin{aligned}\mathrm{J}_m(kR) \sim \left(\frac{2}{\pi kR} \right)^{1/2} &\left\{ \cos\left(kR - \frac{2m+1}{4\pi} \right) \sum_{j=0}^{\infty} \frac{(-1)^j \Gamma(m+j+1/2)}{j!\Gamma(m-j+1/2)(2kR)^{2j}} \right. \\ &\left. - \sin\left(kR - \frac{2m+1}{4\pi} \right) \sum_{j=0}^{\infty} \frac{(-1)^j \Gamma(m+j+3/2)}{(j+1)!\Gamma(m-j+3/2)(2kR)^{2j+1}} \right\},\end{aligned}$$

to find that

$$\mathrm{J}_m(kR) \;\sim\; \left(\frac{2}{\pi kR}\right)^{1/2} \cos\left(kR - \frac{2m+1}{4\pi}\right), \tag{C.11a}$$

for $m = 0, \ldots, M$, where Γ is the Gamma function. It follows that its derivative satisfies

$$\partial_r \mathrm{J}_m(kR) \sim -k\left(\frac{2}{\pi kR}\right)^{1/2} \sin\left(kR - \frac{2m+1}{4\pi}\right) \tag{C.11b}$$

for $m = 0, \ldots, M$. Similarly, for large $k^{(0)}R$ the Hankel function of the first kind has the asymptotic behaviour

$$\mathrm{H}_m(k^{(0)}R) \sim \left(\frac{2}{\pi k^{(0)}R}\right)^{1/2} \mathrm{e}^{\mathrm{i}k^{(0)}R - \mathrm{i}\frac{2m+1}{4\pi}}, \tag{C.11c}$$

and

$$\partial_r \mathrm{H}_m(k^{(0)}R) \sim \mathrm{i}k^{(0)}\left(\frac{2}{\pi k^{(0)}R}\right) \mathrm{e}^{\mathrm{i}k^{(0)}R - \mathrm{i}\frac{2m+1}{4\pi}}, \tag{C.11d}$$

for $m = 0, \ldots, M$, which are also give in Tranter (1968).

From our above approximations of the complex wavenumbers, we have $\mathrm{O}(|\mu_{(i)}|) = \mathrm{O}(k)$ $(i = 1, 2)$. Thus, the argument $\mu_{(i)}R$ is large and we use the asymptotic limit of the Bessel function of the first kind to find the expressions

$$\mathrm{J}_m(\mu_{(i)}R) \sim \left(\frac{1}{2\pi\mu_{(i)}R}\right)^{1/2} \mathrm{e}^{\Im\mathrm{m}(\mu_{(i)})R}\mathrm{e}^{-\mathrm{i}\Re\mathrm{e}(\mu_{(i)})R + \mathrm{i}\frac{2m+1}{4\pi}}, \tag{C.11e}$$

and

$$\partial_r \mathrm{J}_m(\mu_{(i)}r_0) \sim -\mathrm{i}\mu_{(i)}\left(\frac{1}{2\pi\mu_{(i)}R}\right)^{1/2} \mathrm{e}^{\Im\mathrm{m}(\mu_{(i)})R}\mathrm{e}^{-\mathrm{i}\Re\mathrm{e}(\mu_{(i)})R + \mathrm{i}\frac{2m+1}{4\pi}}. \tag{C.11f}$$

Note the presence of an exponentially growing factor in these limits.

Consider the functions

$$\mathscr{X}_m(w) = \left(w^2 - (1-\nu)m^2\right)\mathrm{J}_m(w) + w(1-\nu)(\partial_w \mathrm{J}_m(w)), \tag{C.12a}$$

and

$$\mathscr{Y}_m(w) = \left(w^2 + (1-\nu)m^2\right)w(\partial_w \mathrm{J}_m(w)) - (1-\nu)m^2\mathrm{J}_m(w). \tag{C.12b}$$

For large arguments w, using the above asymptotic limits of the Bessel functions and the fact that $\partial_{kr} = \partial_r/k$, we find that $\mathrm{J}_m(w)$ and $\partial_w \mathrm{J}_m(w)$ are of the same order of magnitude if we ignore the oscillatory terms. The leading order terms in the functions (C.12a-b) are therefore

$$\mathscr{X}_m(w) \approx w^2\mathrm{J}_m(w), \quad \mathscr{Y}_m(w) \approx w^3\partial_w \mathrm{J}_m(w), \tag{C.13}$$

for large w.

The above approximations of the functions $\mathscr{X}_m(w)$ and $\mathscr{Y}_m(w)$ are of use in calculating the values of $\triangle_m(kR, \mu_{(1)}R)$ and $\mathscr{X}(\mu_{(1)}R)\overline{\mathscr{Y}(\mu_{(1)}R)}$, which appear in the simplified definition of the functions $\widetilde{\varphi}_m$ given in equation (C.10). We also require an approximation for the derivative $\partial_r\widetilde{\varphi}_m$, for which an expression in terms of $\triangle_m(kR, \mu_{(1)}R)$ and $\mathscr{X}(\mu_{(1)}R)\overline{\mathscr{Y}(\mu_{(1)}R)}$ is easily obtained via equation (C.10).

Using approximations (C.13) and (C.11e-f) we have

$$\begin{aligned}
\mathscr{X}(\mu_{(1)}R)\overline{\mathscr{Y}(\mu_{(1)}R)} &\approx \mu_{(1)}^2 R^2 \mathrm{J}_m(\mu_{(1)}R) \times \overline{\mu_{(1)}^3 R^3 \partial_{\mu_{(1)}r}\mathrm{J}_m(\mu_{(1)}R)} \\
&\approx \mu_{(1)}^2 R^2 \left(\frac{1}{2\pi\mu_{(1)}R}\right)^{1/2} \mathrm{e}^{\Im\mathrm{m}(\mu_{(1)})R}\mathrm{e}^{-\mathrm{i}\Re\mathrm{e}(\mu_{(1)})R+\mathrm{i}\frac{2m+1}{4\pi}} \\
&\qquad \times \mathrm{i}\overline{\mu_{(1)}^3 R^3}\left(\overline{\frac{1}{2\pi\mu_{(1)}R}}\right)^{1/2} \mathrm{e}^{\Im\mathrm{m}(\mu_{(1)})R}\mathrm{e}^{\mathrm{i}\Re\mathrm{e}(\mu_{(1)})R-\mathrm{i}\frac{2m+1}{4\pi}} \\
&= \mathrm{i}|\mu_{(1)}|^4 R^4 \frac{\mu_{(1)}}{2\pi|\mu_{(1)}|}\mathrm{e}^{2\Im\mathrm{m}(\mu_{(1)})R},
\end{aligned}$$

from which it follows that

$$\begin{aligned}
\Im\mathrm{m}\left(\mathscr{X}(\mu_{(1)}R)\overline{\mathscr{Y}(\mu_{(1)}R)}\right) &\approx |\mu_{(1)}|^4 R^4 \frac{\Re\mathrm{e}(\mu_{(1)})}{2\pi|\mu_{(1)}|}\mathrm{e}^{2\Im\mathrm{m}(\mu_{(1)})R} \\
&\approx \frac{k^4R^4}{\pi}\cos\left(kR - \frac{2m+1}{4\pi}\right)\mathrm{e}^{2\Im\mathrm{m}(\mu_{(1)})R}.
\end{aligned} \tag{C.14}$$

where we have used the approximation of $\mu_{(1)}$ given in equation (C.4) to deduce the latter approximation. Again using (C.13) and (C.11e-f), along with (C.11a-b), in (10.6a-b) we find that

$$\begin{aligned}
\triangle_m(kR, \mu_{(1)}R) &\approx k^2R^2\mathrm{J}_m(kR) \times \mu_{(1)}^3 R^3 \partial_{\mu_{(1)}r}\mathrm{J}_m(\mu_{(1)}R) \\
&\qquad - \mu_{(1)}^2 R^2 \mathrm{J}_m(\mu_{(1)}R) \times k^3R^3\partial_{kr}\mathrm{J}_m(kR) \\
&= k^2\mu_{(1)}R^5\left\{\mu_{(1)}\mathrm{J}_m(kR)\partial_{\mu_{(1)}r}\mathrm{J}_m(\mu_{(1)}R) - k\mathrm{J}_m(\mu_{(1)}R)\partial_{kr}\mathrm{J}_m(kR)\right\} \\
&\approx \frac{k^2\mu_{(1)}^2R^4}{\pi}\left(\frac{1}{k\mu_{(1)}}\right)^{1/2}\mathrm{e}^{\Im\mathrm{m}(\mu_{(1)})R}\mathrm{e}^{\mathrm{i}\Re\mathrm{e}(\mu_{(1)})R-\mathrm{i}\frac{2m+1}{4\pi}} \\
&\qquad \times\left\{k\sin\left(kR - \frac{2m+1}{4\pi}\right) - \mathrm{i}\mu_{(1)}\cos\left(kR - \frac{2m+1}{4\pi}\right)\right\},
\end{aligned}$$

We now note that, from (C.6)

$$\Im\mathrm{m}\left(\hat{v}_{(1)}\overline{\triangle_m(kR, \mu_{(1)}R)}\mathrm{J}_m(\mu_{(1)}r)\right) \approx -2\Re\mathrm{e}\left(\overline{\triangle_m(kR, \mu_{(1)}R)}\mathrm{J}_m(\mu_{(1)}r)\right), \tag{C.15}$$

and we therefore evaluate

$$\begin{aligned}
\overline{\triangle_m(kR,\mu_{(1)}R)}\mathrm{J}_m(\mu_{(1)}r) &\approx \frac{k^2\overline{\mu_{(1)}}^2R^4}{\pi}\left(\frac{1}{k\overline{\mu_{(1)}}}\right)^{1/2}\mathrm{e}^{\Im\mathrm{m}(\mu_{(1)})R}\mathrm{e}^{-\mathrm{i}\Re\mathrm{e}(\mu_{(1)})R+\mathrm{i}\frac{2m+1}{4\pi}}\times \\
&\quad \left\{k\sin\left(kR-\frac{2m+1}{4\pi}\right)+\mathrm{i}\overline{\mu_{(1)}}\cos\left(kR-\frac{2m+1}{4\pi}\right)\right\} \\
&\quad \times\left(\frac{1}{2\pi\mu_{(1)}R}\right)\mathrm{e}^{\Im\mathrm{m}(\mu_{(1)})R}\mathrm{e}^{\mathrm{i}\Re\mathrm{e}(\mu_{(1)})R-\mathrm{i}\frac{2m+1}{4\pi}} \\
&= \frac{k^2R^4}{\pi}\left(\frac{1}{2\pi kR}\right)^{1/2}\mathrm{e}^{2\Im\mathrm{m}(\mu_{(1)})R}\frac{\overline{\mu_{(1)}}^2}{|\mu_{(1)}|}\times \\
&\quad \left\{k\sin\left(kR-\frac{2m+1}{4\pi}\right)+\mathrm{i}\overline{\mu_{(1)}}\cos\left(kR-\frac{2m+1}{4\pi}\right)\right\} \\
&\approx -\frac{k^4R^4}{2^{1/4}\pi}\left(\frac{1}{2\pi kR}\right)^{1/2}\mathrm{e}^{2\Im\mathrm{m}(\mu_{(1)})R}(1+\mathrm{i})\times \\
&\quad \left\{\sin\left(kR-\frac{2m+1}{4\pi}\right)+\mathrm{i}2^{1/4}\mathrm{e}^{5\pi/8}\cos\left(kR-\frac{2m+1}{4\pi}\right)\right\},
\end{aligned}$$

which leads to the approximation

$$\begin{aligned}
&\Re\mathrm{e}\left(\overline{\triangle_m(kR,\mu_{(1)}R)}\mathrm{J}_m(\mu_{(1)}r)\right) \\
\approx\ & -\frac{k^4R^4}{2^{1/4}\pi}\left(\frac{1}{2\pi kR}\right)^{1/2}\mathrm{e}^{2\Im\mathrm{m}(\mu_{(1)})R}\left\{\sin\left(kR-\frac{2m+1}{4\pi}\right)\right. \\
&\left.-2^{1/4}\sin\left(\frac{5\pi}{8}\right)\cos\left(kR-\frac{2m+1}{4\pi}\right)-2^{1/4}\cos\left(\frac{5\pi}{8}\right)\cos\left(kR-\frac{2m+1}{4\pi}\right)\right\},
\end{aligned} \tag{C.16}$$

where we have again used our approximation of $\mu_{(1)}$ given in (C.4). Combining the approximations (C.14), (C.15) and (C.16), we then deduce that

$$\begin{aligned}
&\frac{\Im\mathrm{m}\left(\hat{v}_{(1)}\overline{\triangle_m(kR,\mu_{(1)}R)}\mathrm{J}_m(\mu_{(1)}r)\right)}{\Im\mathrm{m}\left(\mathscr{X}(\mu_{(1)}R)\overline{\mathscr{Y}(\mu_{(1)}R)}\right)} \\
\approx\ & \left\{\frac{2^{3/4}k^4R^4}{\pi}\left(\frac{1}{2\pi kR}\right)^{1/2}\mathrm{e}^{2\Im\mathrm{m}(\mu_{(1)})R}\left(\sin\left(kR-\frac{2m+1}{4\pi}\right)\right.\right. \\
&\left.\left.-2^{1/4}\cos\left(\frac{5\pi}{8}\right)\cos\left(kR-\frac{2m+1}{4\pi}\right)-2^{1/4}\cos\left(\frac{5\pi}{8}\right)\cos\left(kR-\frac{2m+1}{4\pi}\right)\right)\right\} \\
&\div\left\{\frac{k^4R^4}{\pi}\cos\left(kR-\frac{2m+1}{4\pi}\right)\mathrm{e}^{2\Im\mathrm{m}(\mu_{(1)})R}\right\} \\
=\ & \frac{2^{1/4}}{\cos(3\pi/8)}\left(\frac{1}{\pi kR}\right)^{1/2}\left\{\sin\left(kR-\frac{2m+1}{4\pi}\right)\right. \\
&\left.+2^{1/4}\cos\left(\frac{3\pi}{8}\right)\cos\left(kR-\frac{2m+1}{4\pi}\right)-2^{1/4}\cos\left(\frac{3\pi}{8}\right)\sin\left(kR-\frac{2m+1}{4\pi}\right)\right\},
\end{aligned}$$

and then that

$$\begin{aligned}&\frac{\Im\mathrm{m}\left(\hat{v}_{(1)}\overline{\triangle_m(kR,\mu_{(1)}R)}\mathrm{J}_m(\mu_{(1)}r)\right)}{\Im\mathrm{m}\left(\mathscr{X}(\mu_{(1)}R)\overline{\mathscr{Y}(\mu_{(1)}R)}\right)}\\ \approx\ & \left(\frac{2}{\pi kR}\right)^{1/2}\left\{2^{1/2}\cos\left(kR-\frac{2m+1}{4\pi}\right)+2^{-1/4}\csc(\pi/8)\sin\left(kR-\frac{2m+1}{4\pi}\right)\right\},\end{aligned}\tag{C.17}$$

where the final expression follows from straightforward manipulations using trigonometric identities. Similarly, to gain an approximation for $\partial_r\widetilde{\varphi}_m$, we note that

$$\Im\mathrm{m}\left(\hat{v}_{(1)}\overline{\triangle_m(kR,\mu_{(1)}R)}\partial_r\mathrm{J}_m(\mu_{(1)}r)\right)\approx-2\Re\mathrm{e}\left(\overline{\triangle_m(kR,\mu_{(1)}R)}\partial_r\mathrm{J}_m(\mu_{(1)}r)\right),$$

and calculate the approximation

$$\begin{aligned}&\overline{\triangle_m(kR,\mu_{(1)}R)}\partial_r\mathrm{J}_m(\mu_{(1)}r)\\ \approx\ & \frac{k^2\overline{\mu_{(1)}}^2R^4}{\pi}\left(\frac{1}{k\overline{\mu_{(1)}}}\right)^{1/2}\mathrm{e}^{\Im\mathrm{m}(\mu_{(1)})R}\mathrm{e}^{-\mathrm{i}\Re\mathrm{e}(\mu_{(1)})R+\mathrm{i}\frac{2m+1}{4\pi}}\left\{k\sin\left(kR-\frac{2m+1}{4\pi}\right)\right.\\ &\left.+\mathrm{i}\overline{\mu_{(1)}}\cos\left(kR-\frac{2m+1}{4\pi}\right)\right\}(-\mathrm{i}\mu_{(1)})\left(\tfrac{1}{2\pi\mu_{(1)}R}\right)\mathrm{e}^{\Im\mathrm{m}(\mu_{(1)})R}\mathrm{e}^{\mathrm{i}\Re\mathrm{e}(\mu_{(1)})R-\mathrm{i}\frac{2m+1}{4\pi}}\\ =\ & \frac{k^2R^4}{\pi}\left(\frac{1}{2\pi kR}\right)^{1/2}|\mu_{(1)}|\mathrm{e}^{2\Im\mathrm{m}(\mu_{(1)})R}\left\{\mathrm{i}k\overline{\mu_{(1)}}\sin\left(kR-\frac{2m+1}{4\pi}\right)\right.\\ &\left.-\overline{\mu_{(1)}}^2\cos\left(kR-\frac{2m+1}{4\pi}\right)\right\}\\ \approx\ & \frac{k^4R^4}{\pi}2^{1/4}k\left(\frac{1}{2\pi kR}\right)^{1/2}\mathrm{e}^{2\Im\mathrm{m}(\mu_{(1)})R}\left\{\mathrm{i}2^{1/4}\mathrm{e}^{\mathrm{i}5\pi/8}\sin\left(kR-\frac{2m+1}{4\pi}\right)\right.\\ &\left.+(1+\mathrm{i})\cos\left(kR-\frac{2m+1}{4\pi}\right)\right\}\end{aligned}$$

whence

$$\begin{aligned}&\Re\mathrm{e}\left(\overline{\triangle_m(kR,\mu_{(1)}R)}\partial_r\mathrm{J}_m(\mu_{(1)}r)\right)\\ \approx\ & \frac{k^4R^4}{\pi}2^{1/4}k\left(\frac{1}{2\pi kR}\right)^{1/2}\mathrm{e}^{2\Im\mathrm{m}(\mu_{(1)})R}\left\{2^{1/4}\sin\left(\frac{5\pi}{8}\right)\sin\left(kR-\frac{2m+1}{4\pi}\right)\right.\\ &\left.-\cos\left(kR-\frac{2m+1}{4\pi}\right)\right\}.\end{aligned}$$

We therefore have the approximation

$$\begin{aligned}
&\frac{\Im\mathrm{m}\left(\hat{v}_{(1)}\overline{\triangle_m(kR,\mu_{(1)}R)}\partial_r \mathrm{J}_m(\mu_{(1)}r)\right)}{\Im\mathrm{m}\left(\mathscr{X}(\mu_{(1)}R)\overline{\mathscr{Y}(\mu_{(1)}R)}\right)} \\
&\approx -\left\{\frac{k^4R^4}{\pi}2^{1/4}k\left(\frac{1}{2\pi kR}\right)^{1/2}\mathrm{e}^{2\Im\mathrm{m}(\mu_{(1)})R}\left(2^{1/4}\sin\left(\frac{5\pi}{8}\right)\sin\left(kR-\frac{2m+1}{4\pi}\right)\right.\right. \\
&\qquad\left.\left.-\cos\left(kR-\frac{2m+1}{4\pi}\right)\right)\right\} \div \left\{\frac{k^4R^4}{\pi}\cos\left(kR-\frac{2m+1}{4\pi}\right)\mathrm{e}^{2\Im\mathrm{m}(\mu_{(1)})R}\right\} \\
&= -\frac{2^{3/4}}{\cos(3\pi/8)}k\left(\frac{1}{\pi kR}\right)^{1/2}\left\{2^{1/4}\sin\left(\frac{5\pi}{8}\right)\sin\left(kR-\frac{2m+1}{4\pi}\right)\right. \\
&\qquad\left.-\cos\left(kR-\frac{2m+1}{4\pi}\right)\right\} \\
&= k\left(\frac{2}{\pi kR}\right)^{1/2}\left\{2^{1/4}\csc\left(\frac{\pi}{8}\right)\cos\left(kR-\frac{2m+1}{4\pi}\right)\right. \\
&\qquad\left.+2^{1/2}\cot\left(\frac{\pi}{8}\right)\sin\left(kR-\frac{2m+1}{4\pi}\right)\right\}.
\end{aligned} \tag{C.18}$$

Inserting the approximations (C.17)-(C.18) into the expression (C.10) for $\widetilde{\varphi}_m$ and the equivalent expression for $\partial_r\widetilde{\varphi}_m$ gives

$$\widetilde{\varphi}_m(R) \sim \left(\frac{2}{\pi kR}\right)^{1/2} X_m, \quad \partial_r\widetilde{\varphi}_m(R) \sim -k\left(\frac{2}{\pi kR}\right)^{1/2} Y_m \quad (m = 0,\dots,M)$$

where

$$X_m = (1-2^{1/2})\cos\left(kR-\frac{2m+1}{4\pi}\right) - 2^{-1/4}\csc\left(\frac{\pi}{8}\right)\sin\left(kR-\frac{2m+1}{4\pi}\right),$$

and

$$Y_m = 2^{1/4}\csc\left(\frac{\pi}{8}\right)\cos\left(kR-\frac{2m+1}{4\pi}\right) + \left(1+2^{1/2}\cot\left(\frac{\pi}{8}\right)\right)\sin\left(kR-\frac{2m+1}{4\pi}\right),$$

as in §10.1. These approximations hold in the régimes $kH \ll \sinh(kH)$, $\alpha k \ll 1 \ll \beta k^4$ and $kR \gg 1$.

It is now a simple matter to substitute our above approximations of $\widetilde{\varphi}_m$ and $\partial_r\widetilde{\varphi}_m$, along with the asymptotic limits of the Hankel functions (C.11c-d) and approximations of the coefficients (C.9) into the equation from which the amplitudes are obtained, (C.8), to give

$$\begin{aligned} &-\frac{2}{\pi R}\left(\frac{k^{(0)}}{k}\right)^{1/2} \mathrm{e}^{k^{(0)}R-\frac{2m+1}{4\pi}} \frac{\sinh(kH)}{\sinh(k^{(0)}H)}\left\{\frac{2k}{k+k^{(0)}}kY_m+\mathrm{i}\frac{k+k^{(0)}}{2k}k^{(0)}X_m\right\}\widetilde{A}_m \\ \approx\ & -\frac{2\mathrm{i}k\sinh(kH)}{\pi R k^{(0)}\sinh(k^{(0)}H)}. \end{aligned}$$

By cancelling terms common to either side we are left with

$$\left\{\frac{2k^2}{k^{(0)}(k+k^{(0)})}Y_m+\mathrm{i}\frac{k+k^{(0)}}{2k}X_m\right\}\widetilde{A}_m \approx \mathrm{i}\left(\frac{k}{k^{(0)}}\right)^{3/2}\mathrm{e}^{-\mathrm{i}k^{(0)}R+\mathrm{i}\frac{2m+1}{4\pi}}, \tag{C.19a}$$

from which approximations to the amplitudes $\widetilde{A}_m$ may be calculated.

Now, we assume that the wavelength beneath the ice is far longer than that in the surrounding free-surface (i.e. $k \ll k^{(0)}$), which is often the case when the frequency is not especially small and the ice is not very thin (see figure 5.10(a)). Disregarding the influence of the oscillatory terms in X_m and Y_m, we have that the term in the bracketed quantity on the left hand side of approximation (C.19a) involving X_m will outweigh that which involves Y_m. Consequently, we deduce the simplified expression

$$\widetilde{A}_m \approx \frac{2}{X_m}\left(\frac{k}{k^{(0)}}\right)^{5/2}\mathrm{e}^{-\mathrm{i}k^{(0)}R+\mathrm{i}\frac{2m+1}{4\pi}} \quad (m=0,\ldots,M), \tag{C.19b}$$

when $k \ll k^{(0)}$.

Equations (C.19a-b) give the required approximations that are quoted in equations (10.19a-b). These approximations are validated numerically in figure 10.1.

C.3 The régime $kR \ll 1$

We now consider the opposing limit in which the radius of the floe is small in comparison to the two wavelengths involved in the problem. This situation is described by the régimes $kR \ll 1$ and $k^{(0)}R \ll 1$, and as before the relative sizes of the two wavenumbers means that we need only specify one of these régimes, here $kR \ll 1$.

We will once again make use of standard asymptotic limits of the Bessel functions in our chosen régime. In this case, the arguments of the Bessel functions at the interface between the ice-covered and ice-free domains are small, and beneath the ice we have that

$$\mathrm{J}_m(kR) \sim \frac{1}{m!}\left(\frac{kR}{2}\right)^m, \quad [\partial_r \mathrm{J}_m(kr)]_{r=R} \sim \begin{cases} -\dfrac{k^2R}{2} & (m=0), \\ \dfrac{k(kR)^{m-1}}{2^m(m-1)!} & (m\neq 0). \end{cases} \tag{C.20a}$$

Recall that we have assumed conditions such that the approximations (C.4) of the complex wavenumbers hold. Hence arguments involving the complex wavenumber, $\mu_{(i)}$ $(i = 1, 2)$, will also be small, so that the same limit applies, and thus

$$\mathrm{J}_m(\mu_{(i)}R) \sim \frac{1}{m!}\left(\frac{\mu_{(i)}R}{2}\right)^m, \quad [\partial_r \mathrm{J}_m(\mu_{(i)}r)]_{r=R} \sim \begin{cases} -\dfrac{\mu_{(i)}^2 R}{2} & (m = 0), \\ \dfrac{\mu_{(i)}(\mu_{(i)}R)^{m-1}}{2^m(m-1)!} & (m \neq 0). \end{cases} \tag{C.20b}$$

Note that, as opposed to the large floe régime, there is no oscillatory part in the limits of the Bessel functions here, which would lead to exponential growth when their arguments have a complex component.

Referring to (C.20a-b) we deduce that, as the complex wavenumbers are of the same order of magnitude as the propagating wavenumber beneath the ice, the corresponding Bessel functions of the first kind are also of the same order of magnitude, with

$$\mathrm{J}_m(kR) = \mathrm{O}\left((kR)^m\right), \quad \mathrm{J}_m(\mu_{(i)}R) = \mathrm{O}\left((kR)^m\right),$$

$$k^{-1}[\partial_r \mathrm{J}_m(kr)]_{r=R} = \begin{cases} \mathrm{O}\left(k^2 R\right) & (m = 0), \\ \mathrm{O}\left((kR)^{m-1}\right) & (m \neq 0), \end{cases}$$

and

$$[\partial_r \mathrm{J}_m(\mu_{(i)}r)]_{r=R} = \begin{cases} \mathrm{O}\left(kR\right) & (m = 0), \\ \mathrm{O}\left((kR)^{m-1}\right) & (m \neq 0), \end{cases}$$

for $i = 1, 2$. Furthermore, the functions $\triangle_m(kR, \mu_{(i)})$ and $\triangle_m(\mu_{(i)}, \mu_{(i_-)})$ are of the same order of magnitude. It then follows that the function φ_m is of the same order of magnitude as the Bessel functions $\mathrm{J}_m(kR)$ and $\mathrm{J}_m(\mu_{(i)}R)$, so that

$$\widetilde{\varphi}_m(R) \sim \hat{g}_m(kR)^m, \quad \partial_r\widetilde{\varphi}_m(R) \sim \begin{cases} \tilde{g}_0 k^2 R & (m = 0), \\ \tilde{g}_m k^m R^{m-1} & (m \neq 0), \end{cases} \tag{C.21}$$

where the constants $\hat{g}_m$ and $\tilde{g}_m$ are of order 1 whose values can be calculated but will not be needed.

This information will be used to deduce the relative magnitudes of the amplitudes $\widetilde{A}_m$ $(m = 0, \ldots, M)$, which are obtained from equation (C.8). We therefore require the relevant limits of the Hankel functions for the small argument kR, and these are

$$\mathrm{H}_m(k^{(0)}R) \sim \begin{cases} \dfrac{2\mathrm{i}}{\pi}\ln(k^{(0)}R) & (m = 0), \\ -\dfrac{\mathrm{i}(m-1)!}{\pi}\left(\dfrac{2}{k^{(0)}R}\right)^m & (m \neq 0), \end{cases} \tag{C.22a}$$

and

$$[\partial_r \mathrm{H}_m(k^{(0)}r)]_{r=R} \sim \begin{cases} \dfrac{2\mathrm{i}}{\pi R} & (m=0), \\ \dfrac{\mathrm{i}m!}{\pi R^{m+1}}\left(\dfrac{2}{k^{(0)}}\right)^m & (m \neq 0). \end{cases} \tag{C.22b}$$

Applying the limits (C.22a-b) and the approximations of the coefficients given in (C.9) to equation (C.8), for $m=0$ we have

$$\left\{\frac{2\mathrm{i}}{\pi}\ln(k^{(0)}R)\frac{2k_0^{(0)}}{k+k^{(0)}}\frac{\sinh(kH)}{\sinh(k^{(0)}H)}(\partial_r\widetilde{\varphi}_0(R)) - \frac{2\mathrm{i}}{\pi R}\frac{k+k^{(0)}}{2k}\frac{\sinh(kH)}{\sinh(k^{(0)}H)}\widetilde{\varphi}_0(R)\right\}\widetilde{A}_0$$
$$\approx -\frac{2\mathrm{i}}{\pi R}\frac{k\sinh(kH)}{k^{(0)}\sinh(k^{(0)}H)},$$

which simplifies to

$$\left\{\frac{k+k^{(0)}}{2k}\hat{g}_0 - (kR)^2\ln(k^{(0)}R)\frac{2k_0^{(0)}}{k+k^{(0)}}\tilde{g}_0\right\}\widetilde{A}_0 \approx \frac{k}{k^{(0)}}. \tag{C.23}$$

We now consider equation (C.23) in terms of orders of magnitude of the small quantities kR and $k^{(0)}R$. It is legitimate to ignore the first of the bracketed terms as $(kR)^2\ln(k^{(0)}R) \ll 1$, whence

$$\widetilde{A}_0 = \mathrm{O}\left(\left(\frac{k}{k^{(0)}}\right)^2\right). \tag{C.24}$$

Similarly, for $m \neq 0$, we begin by substituting the limits of the Bessel functions into equation (C.8) to give

$$\left\{R(m-1)!\left(\frac{2}{k^{(0)}R}\right)^m\frac{2k_0^{(0)}}{k+k^{(0)}}(\partial_r\widetilde{\varphi}_m(R)) + m!\left(\frac{2}{k^{(0)}R}\right)^m\frac{k+k^{(0)}}{2k}\widetilde{\varphi}_m(R)\right\}\widetilde{A}_m \approx 2\frac{k}{k^{(0)}},$$

and then simplify this expression using (C.21), which results in

$$2^{m-1}(m-1)!\left\{\frac{2k_0^{(0)}}{k+k^{(0)}}\tilde{g}_m + m\frac{k+k^{(0)}}{2k}\hat{g}_m\right\}\widetilde{A}_m \approx \left(\frac{k^{(0)}}{k}\right)^{m-1}. \tag{C.25}$$

If the bracketed terms on the left-hand side of (C.25) are of an identical order of magnitude and we cannot progress directly to a clear expression for $\widetilde{A}_m$. However, if we return to the situation $k^{(0)} \gg k$, then the second term outweighs the first and

$$\widetilde{A}_m = \mathrm{O}\left(\left(\frac{k^{(0)}}{k}\right)^{m-2}\right) \quad (m = 1, \ldots, M), \tag{C.26}$$

follows.

We may condense the results (C.23) and (C.25) into

$$G_m(k,k_0)\widetilde{A}_m = \mathrm{O}\left(\frac{k^{(0)}}{k}\right)^{m-1} \qquad (m = 0,\ldots,M),$$

where the function G_m is such that

$$G_0(k,k^{(0)}) = \frac{k+k^{(0)}}{2k}\hat{g}_0 - (kR)^2\ln(k^{(0)}R)\frac{2k_0^{(0)}}{k+k^{(0)}}\tilde{g}_0,$$

and

$$G_m(k,k^{(0)}) = (m-1)!2^{m-1}\left\{\frac{2k_0^{(0)}}{k+k^{(0)}}\tilde{g}_m + m\frac{k+k^{(0)}}{2k}\hat{g}_m\right\} \qquad (m = 1,\ldots,M).$$

This order of magnitude holds for $kR \ll 1$ and the conditions $kH \ll \sinh(kH)$ and $\alpha k \ll 1 \ll \beta k^4$. If additionally $k^{(0)} \gg k$ then we have the more usable results (C.24) and (C.27), which may be written as

$$\widetilde{A}_m = \mathrm{O}\left(\left(\frac{k^{(0)}}{k}\right)^{m-2}\right) \qquad (m = 0,\ldots,M). \tag{C.27}$$

In the main text the above results were given in equations (10.22)-(10.23) and were displayed graphically in figure 10.2.

Notation Index

Symbol	Description	Reference
x, y, z	Cartesian coordinates	figure 2.1
r, θ	polar coordinates	equation (9.6)
n, s	normal & tangential coordinates	page 22
∂_x	partial/full derivative with respect to x	page 18
∇	horizontal gradient operator	page 18
$(f, g)^*$	the inner product of f and g	equation (3.19)
$\langle\cdot\rangle$, $\langle\langle\cdot\rangle\rangle$	jump in the included quantity across a contour & a surface, respectively	page 25
D, H	ice thickness & fluid depth	figure 2.1
d	undisturbed position of fluid-ice interface	figure 2.1
h	bed depth	figure 2.1
ω	angular frequency	equation (2.8)
τ	wave period	page 20
κ	frequency parameter	equation (2.10)
α	scaled ice mass	equation (2.10)
β	scaled flexural rigidity	equation (2.5)
ρ_i, ρ_w	ice & fluid densities	section 2.1
E	Young's modulus	page 19
ν	Poisson's ratio	page 19
g	gravity	page 19
ϕ^*	reduced velocity potential	equation (2.8)
η	reduced displacement function	equation (2.8)
$L_\Omega{}^*$, I_Γ	functionals	section 2.2
Γ	internal boundary/ice edge	figures 2.2-2.3
u	auxiliary function	page 27
$\mathfrak{M}$, $\mathfrak{S}$	bending moment & shearing stress operators	equations (2.22a-b)
ϵ	normalised displacement	equation (5.13)
$w_n{}^*$	vertical modes	page 30
$\{w_0, \ldots, w_N\}$	trial space	page 30

---

[*] A superscript (0) is added to indicate when the quantity is evaluated in an ice-free domain.

Symbol	Description	Reference
${\psi_N}^*$	approximate reduced velocity potential	equation (3.1)
χ	approximate reduced displacement function	page 31
${\varpi_n}^*$	weight function	page 37
${\varphi_n}^*$	amplitude functions	equation (3.1)
${\Phi_N}^*$	vectors of amplitude functions	page 33
Ψ_N	vector of amplitude functions and approximate displacement functions	equation (4.5)
λ^*	incident wavelength	page 40
${k_0}^*$	real roots of the dispersion relation /propagating wavenumber	page 40
$k_n = \mathrm{i}{\sigma_n}^*$ $(n \geq 1)$	purely imaginary roots of the dispersion relation	page 41
$\tilde{k}_n = \mathrm{i}\pi_n$ $(n \geq 1)$	limiting values of the purely imaginary roots	equation (3.43)
μ_i $(i = 1, 2)$	complex roots of the dispersion relation	page 41
$\upsilon_{i,j}$	redistribution weights of the complex waves	equation (3.40)
$\mu_{N,(i)}$ $(i = 1, 2)$	approximate complex roots/ dimension-dependent wavenumbers of the MMA in a domain of uniform geometry	equation (4.20)
$\upsilon_{N,(i,j)}$	approximate redistribution weights/ dimension-dependent eigenvector entries	equation (4.26)
$\mathcal{C}$	matrix of the eigenvectors of the MMA in a domain of uniform geometry	equation (4.24)
C, S, K	diagonal matrices	equations (4.13a-b)
$P^{(X)*}$, $P^{(X,Y)*}$	inner-products of the vertical modes	section 3.2.1
${a_{j,i}}^*$, ${b_{j,i}}^*$, ${\widetilde{\mathbf{d}}_{j,i}}^*$	coefficients of the governing differential equations of the MMA	page 32
A^*, B^*, $\widetilde{D}^*$	respective matrices of above coefficients	page 33

Symbol	Description	Reference
$\mathcal{A}$, $\mathcal{B}$, $\widetilde{\mathcal{D}}$	respective extensions of above matrices to include the coefficients of the fourth-order displacement equation	page 55
$Q_{j,i}{}^*$, $v_{j,i}{}^*$	coefficients of the jump conditions of the MMA	equations (3.8)-(3.9)
Q^*, V^*	respective matrices of above coefficients	equations (3.8)-(3.9)
$\mathcal{Q}$, $\mathcal{V}$	respective extensions of above matrices to dimension $(N+3)$	page 56
$\mathcal{M}$, $\mathcal{N}$, $\widetilde{\mathcal{M}}$, $\widetilde{\mathcal{N}}$	matrices containing the coefficients of the displacement boundary conditions	page 57
S	scattering matrix	page 65
$R_{\pm}$, $T_{\pm}$	reflection & transmission coefficients	equation (4.44)
$\mathbf{I}_n$, $\mathcal{I}_n$	nth column of the identity matrix of size $(N{+}1)$ and $(N{+}3)$, respectively	
$\mathbf{f}$	vector of 1s	page 33
$\widetilde{\mathcal{F}}$	identity matrix appended with two colums of zeros	page 67
ϑ	incident angle in the two-dimensional problem	page 53
$A^{(\pm)*}$, $B^{(\pm)*}$	incident & reflected amplitudes in two-dimensional problems	equation (4.1a)
l	length of obstruction in two-dimensional problems	figures 4.1-4.2
e^{M}	diagonal matrix of the exponential values of the diagonal entries of the matrix M	equation (4.23)
$\mathcal{O}$	matrix associated with the two-dimensional energy balance equation	equation (4.48)
I_0	incident amplitude in the axisymmetric problem	equation 170
R	radius of axisymmetric floe	figure 9.2
J_m, H_m	Bessel & Hankel functions of the first kind of order m	